Nonlinear interactions in random seas and crest-height statistics for sea-states in finite water depth

Sotiria Eleni Zve

Imperial College London

Department of Civil and Environmental Engineering
Imperial College London

Thesis submitted for the degree of Doctor of Philosophy

Declaration of originality

All the work presented in this thesis is that of the author. Any work or contributions made by others is referenced appropriately.

Copyright declaration

The copyright of this thesis rests with the author and is made available under a Creative Commons Attribution Non-Commercial No Derivatives licence. Researchers are free to copy, distribute or transmit the thesis on the condition that they attribute it, that they do not use it for commercial purposes and that they do not later, transform or build upon it. For any reuse or redistribution, researchers must make clear to others the licence terms of this work.

Abstract

The present thesis concerns an investigation on the effect of nonlinear wave-wave interactions on the statistical properties of random wave fields, with particular focus on the effect of nonlinearity above second-order in wave steepness. This investigation is put into a practical perspective by devising a prediction methodology for the short-term crest-height distribution; a key input for the design and safety assessment of offshore structures and vessels.

The effect of nonlinearity is examined using a Higher-Order Spectral Model (HOSM), which is thoroughly validated. Particular focus has been devoted to establishing the effect of the progressive development of *near-resonant* interactions on the most likely magnitude of the largest waves arising in a 3-hour storm in a statistically reliable manner. In this respect, the present research aimed to fill a long unanswered research question regarding the quantification of the effect of energy focusing or defocussing arising from such interactions in finite water depth, in which the presence of wave-induced 'mean flow' has problematised many researchers so far.

The presented results indicate that in uni-directional seas, energy focusing is relevant in relative water depths of $k_p d > 1.36$ [1] and energy defocussing in $k_p d < 1.36$. This is in line with insights gained from previous works based on elementary wave interactions, and has a direct consequence on the crest-height distributions of the *free waves*, which are shown to deviate from the theoretical linear predictions. More importantly, it has been shown that, whilst energy focusing quickly attenuates with the introduction of directionality in $k_p d \gtrsim 1.36$, this is not the case for the effect of energy defocussing in $k_p d \lesssim 1.36$. The latter is shown to persist for sea-states of increased directionality. As such, with the *bound-wave* contributions leading to the nonlinear increase of the total crest heights and the *near-resonant* interactions leading to a decrease in $k_p d \lesssim 1.36$, wave nonlinearity is shown to include two *competing* processes.

The proposed crest-height model includes the parameterisation of the effect of energy focusing/defocusing based on the *dynamic kurtosis* and the bound-wave contributions upon the *skewness* and *bound kurtosis*; the latter coupled to the *dynamic kurtosis* to account for the *coupling* of the two nonlinear processes. With all avail-

[1] k_p being the wavenumber associated to the spectral peak frequency and d being the water depth

able analytical or theoretical solutions failing to provide an accurate prediction for all aforementioned statistical parameters, their prediction has been achieved by employing methodologies from the field of Machine Learning. The proposed crest-height model, which is valid in the effective depth range of $k_p d \in [0.5, 8]$, is extensively validated against an independent set of numerical, experimental and field-data results. While it is shown to consistently outperform the standard-industry Forristall (2000) model. Finally, an extension of the proposed crest-height model to account for the effect of wave breaking is presented based on a pragmatic approach.

Acknowledgements

I would firstly like to thank my supervisors for the guidance, inspiration and support I have received. I have been very fortunate to have Prof. Chris Swan as my main supervisor. His guidance and encouragement have been fundamental for the completion of this work. I must also thank my second supervisor, Prof. Graham Hughes, for his valuable inputs and guidance on practical matters. While I should not forget to appreciate the initial inputs of Dr. Johannes Spinneken and thank him for broadening my understanding in various research matters, for giving me the opportunity to pursue the present PhD and for securing the initial financial support of this project through the Energy Futures Lab (EFL) Director of Education PhD Scholarship.

Moreover, the contribution of Dr. Yiannis Karmpadakis for providing the extensive field database used in the thesis along with useful initial inputs is greatly appreciated.

I have been very lucky for sharing my time as a PhD student with wonderful colleagues. Yiorgos, Mark, Emma, Daniel, Ivo, Caroline, Cleo, Tom and Alex have contributed to creating a great social environment. Special thanks to Vishnu, Emily and Liliane for their friendship and unconditional support; the journey would not have been as pleasant without you.

Many thanks also to Becky and Fionnuala for helping with all administrative matters and to the Research Computing Service team for making the vast amount of simulations possible, and for providing guidance in resolving any occurring issues.

Finally, the contribution of people from the non-academic environment has been fundamental in putting things into a broader perspective. Many thanks to my father for his support, especially during the writing-up stage. Mother thank you for the wholehearted encouragement in every professional step in my life, your fighting spirit and unconditional love. I would also like to thank three very special people Litsa, Kleoparta and Fani; thank you for your friendship, high spirit, and always stimulating discussions. Last but not least, I would like to thank my twin sister Lilian for encouraging my interest in research and for all stimulating discussions about statistics!

Contents

Declaration of originality **3**

Copyright declaration **5**

Abstract **7**

Acknowledgements **9**

Table of contents **11**

List of figures **15**

List of tables **29**

Nomenclature **31**

1 Introduction **35**

1.1 Engineering context 35

1.2 Physical perspective 38

1.3 Designer's perspective 43

1.4 Research aims 45

1.5 Thesis layout 47

2 Background and Methodology **50**

2.1 Characterisation of real seas 51

2.1.1 Omni-directional wave spectrum 51

2.1.2 Directional wave spectrum 52

2.2 Water-wave solutions and nonlinear effects 54

2.2.1 Mathematical formulation 54

2.2.2 Linear and second-order wave solutions 56

2.2.3 Higher-Order effects . . . 59
2.2.4 Overview of higher-order numerical wave modelling . . . 66
2.2.5 Higher-Order Spectral Method (HOSM) . . . 67
2.2.6 Harmonic separation method within HOSM . . . 69
2.3 Stochastic wave modelling . . . 75
2.3.1 Statistics of a Gaussian stochastic process . . . 78
2.3.2 Generation of an initial linear random wavefield within HOSM 81
2.3.3 Nonlinear crest-height models . . . 85
2.4 Summary . . . 89

3 Statistical properties of uni-directional sea-states 90
3.1 Motivation . . . 91
3.2 Relevant previous works . . . 93
3.2.1 Numerical and experimental investigations . . . 93
3.2.2 Analytical uni-directional solutions for the statistical moments 95
3.3 Test cases and numerical setup . . . 98
3.4 Validation considerations . . . 102
3.4.1 Crest-height distributions . . . 102
3.4.2 Near-limiting deterministic wave groups . . . 110
3.5 Effect of nonlinear wave-wave interactions on the statistics of uni-directional random wavefields . . . 113
3.5.1 Preliminary considerations . . . 117
3.5.2 Influence of effective water depth . . . 122
3.5.3 Influence of sea-state steepness . . . 139
3.5.4 Influence of spectral bandwidth . . . 143
3.6 On the applicability of analytical uni-directional solutions for the statistical moments . . . 149
3.6.1 Dynamic kurtosis . . . 149
3.6.2 Skewness and bound kurtosis . . . 152
3.7 Chapter outcomes . . . 156

4 Statistical properties of directional sea-states 158
4.1 Previous works . . . 159
4.1.1 Numerical and experimental investigations . . . 159

4.1.2 Directional solutions for the statistical moments 161
4.2 Objectives 165
4.3 Test cases and numerical setup 166
4.4 Validation considerations 169
4.5 Effect of nonlinear wave-wave interactions on the statistics of directionally spread random wavefields 170
4.5.1 Preliminary results 170
4.5.2 Influence of effective water depth 174
4.5.3 Influence of sea-state steepness 182
4.5.4 Influence of directionality 187
4.5.5 Influence of spectral bandwidth 194
4.6 On the applicability of analytical solutions for the statistical moments in directional seas 198
4.6.1 Dynamic kurtosis 199
4.6.2 Skewness and bound kurtosis 203
4.7 Chapter outcomes 210

5 On the effective prediction of crest-height distributions 213
5.1 Previous research 214
5.2 Calibration of a fully nonlinear crest-height model 215
5.2.1 Empirical link between the crest-height distribution and the statistical moments 215
5.2.2 Prediction of the statistical moments using meta-modelling techniques 227
5.3 Assessing the performance of a new crest-height model 249
5.3.1 Numerical crest-height distributions used in the calibration process 250
5.3.2 Validation of HOE-EANN against numerical crest-height distributions of the test dataset 251
5.3.3 Validation of HOE-EANN against crest-height distributions from experimental data 254
5.3.4 Comparison between HOE-EANN and field data 257
5.4 Wave-breaking correction 270
5.5 Conclusions 282

6 Concluding remarks **285**
6.1 Research contributions 286
6.1.1 Improved physical insights 286
6.1.2 Improved engineering approaches 289
6.2 Recommendations for future work 290

References **294**

Appendices **318**

A Approximating the tail of the Cartwright & Longuet-Higgins (1956) distribution **319**
A.1 Level up-crossing rate 319
A.2 A lower bound for the distribution of local extrema 321

B Finite-depth theoretical solutions for the statistical moments and additional comparisons to numerical results **324**
B.1 The uni-directional solution of Janssen & Onorato (2007) for the dynamic kurtosis 324
B.2 The uni-directional solution of Janssen (2009) for the skewness and bound kurtosis 332
B.3 The directional solution of Janssen (2017) for the skewness, bound kurtosis and dynamic kurtosis 335

C Additional aspects of HOSM simulations **341**
C.1 Numerical setup of directional simulations 341
C.2 Spatial resolution 342
C.3 Spatial homogeneity in directional simulations 344
C.4 Separation of nonlinear contributions in directionally spread seas . . . 345

D Spectral evolution within directional HOSM simulations **363**
D.1 Evolution of the free-wave spectra 363
D.2 Spectral energy transfers 365
D.3 Time-evolution of mean directional spread and the effect of bound waves 369

E Statistical moments arising in second-order sea-states **372**

E.1 On the performance of Equation 4.4 in predicting the skewness 372
E.2 On the relation between the skewness and kurtosis 375

F Acceleration method for obtaining the second-order free surface 378

G On the applicability of the Gram-Charlier series 381
G.1 Probability density function of the free surface 382
G.2 Crest-height exceedance distribution 385

H Short description of additional meta-models 391
H.1 Gaussian Process Emulator 391
H.2 Support Vector Machines for regression 394

I Range of validity of the Ensemble Artificial Neural Network predictions 398

J On the performance of the Karmpadakis & Swan (2022) model 401
J.1 Test cases 401
J.2 Assessment of the fully nonlinear predictions: Comparison to numerical and field data 403
J.3 Assessment of the breaking-corrected predictions: Comparison to experimental and field data 408

List of figures

1.1 Photographs of the Stolt Surf tanker encountering a freak wave reaching a height of about $22m$ above mean water level in the North Pacific Ocean. 36
1.2 The time record of the 'New Year Wave' recorded at the Draupner platform in the North Sea on 1^{st} January 1995. 37
1.3 Photographs of damaged or destroyed platforms in the Golf of Mexico due to wave-in-deck loading. 39

2.1 The resonance loop of Phillips (1960). 62
2.2 The resonant interaction kernel of Janssen & Onorato (2007), normalised with respect to the deep-water value. 65
2.3 Segments of input free-surface traces used for applying the phase manipulation method. 72
2.4 Spatial traces of the nonlinear harmonic contributions around a large wave event. 73
2.5 Ensemble-averaged spectra of nonlinear contributions in two different effective water depths. Comparison of second-order spectra arising from HOSM simulation and SORWT. 74
2.6 Contour plot of the spectral energy ($\frac{1}{2}a^2$) of the extracted harmonic contributions in $k_p d = 5.03$. 76
2.7 Contour plot of the spectral energy ($\frac{1}{2}a^2$) of the extracted harmonic contributions in $k_p d = 0.87$. 77
2.8 An example of a time-trace of the free-surface elevation and definition of a zero-crossing wave. 79
2.9 JONSWAP spectral shapes and frequency bandwidth parameters. . . . 80
2.10 Crest-height probability of exceedance distribution normalised with respect to the Rayleigh prediction arising from linear simulations using random vs deterministic amplitudes. 83
2.11 Convergence of the statistical parameters of skewness and kurtosis for varying spectral discretisation. 84

3.1 Theoretically predicted skewness parameter for narrow-banded uni-directional sea-states against relative water depth. 96
3.2 Theoretically predicted bound kurtosis parameter for narrow-banded uni-directional sea-states against relative water depth. 97
3.3 Effect of finite water depth on the Benjamin-Feir Index. 98
3.4 Comparison between experimentally and numerically obtained normalised crest-height exceedance probability distributions, for uni-directional sea-states generated in the ICL wave basin (d=1.25m). 105
3.5 Comparison between experimentally and numerically obtained normalised crest-height exceedance probability distributions, for uni-directional sea-states generated in the ICL wave basin (d=0.50m). 106

3.6 Comparison between experimentally and numerically obtained normalised crest-height exceedance probability distributions, for uni-directional sea-states generated in the QUB wave basin. 107
3.7 Comparison between experimentally and numerically obtained normalised crest-height exceedance probability distributions, for uni-directional sea-states generated in the ICL double-ended wave flume. 108
3.8 Comparison of the fully nonlinear spatial wave profile between HOSM and MFBEM for uni-directional linearly focused wave groups of steepness $Ak_p = 0.08$ and evolution time $t_f = 20T_p$. 114
3.9 Comparison of the fully nonlinear spatial wave profile between HOSM and MFBEM for uni-directional linearly focused wave groups of steepness $Ak_p = 0.18$ and evolution time $t_f = 20T_p$. 115
3.10 Comparison of the fully nonlinear spatial wave profile between HOSM and MFBEM for uni-directional linearly focused wave groups of steepness $Ak_p = 0.18$ and evolution time $t_f = 40T_p$. 116
3.11 Temporal evolution of the ensemble-averaged dynamic kurtosis for uni-directional sea-states of $\gamma = 2.5$ and $\frac{1}{2}H_s k_p = 0.005$, 0.105 in different relative water depths using different ramp-function lengths. 118
3.12 The shape of the ramp function within HOSM and the definition of an effective evolution time within the ramp function. 119
3.13 Temporal evolution of the ensemble-averaged dynamic kurtosis in uni-directional sea-states with $\gamma = 2.5$ and $\frac{1}{2}H_s k_p = 0.105$ in different relative water depths using different ramp-function lengths, with incorporation of an effective evolution time associated with the ramp function. 120
3.14 Contour plot of the spectral energy ($\frac{1}{2}a^2$) of the second-harmonic for sea-states with $\gamma = 2.5$ and $\frac{1}{2}H_s k_p = 0.105$ using different ramp-function lengths in two different relative water depths. 121
3.15 Temporal evolution of the ensemble-averaged skewness and bound kurtosis for uni-directional sea-states with $\gamma = 2.5$ and $\frac{1}{2}H_s k_p = 0.105$ in different relative water depths using different ramp function lengths, with incorporation of an effective evolution time associated to the ramp function. 122

3.16 Normalised crest-height exceedance probability distributions arising in uni-directional sea-states with $\gamma = 2.5$ and $\frac{1}{2}H_s k_p = 0.105$ showing the effect of evolution time and relative water depth. 124
3.17 Temporal evolution of the crest height normalised with respect to the Rayleigh prediction corresponding to a probability of exceedance of $Q = 10^{-3}$. Uni-directional sea-states with $\gamma = 2.5$ and $\frac{1}{2}H_s k_p = 0.105$ in different relative water depths, showing the effect of sample variability and its progressive reduction. 126
3.18 Normalised crest-height exceedance probability distributions of the free waves arising in uni-directional sea-states with $\gamma = 2.5$ and $\frac{1}{2}H_s k_p = 0.105$ showing the effect of evolution time and relative water depth. . 129
3.19 Probability of exceedance of the crest heights of the free waves normalised with respect to the Rayleigh prediction at steady state for sea-states with $\gamma = 2.5$ and $\frac{1}{2}H_s k_p = 0.105$ in different effective water depths. 131
3.20 Temporal evolution of the free-wave contribution to the crest heights normalised with respect to the Rayleigh prediction corresponding to a probability of exceedance of $Q = 10^{-3}$ in uni-directional sea-states with $\gamma = 2.5$ and $\frac{1}{2}H_s k_p = 0.105$ in different relative water depths. . . 132
3.21 Scatter of the normalised total crest heights against the normalised crest heights of the free waves for individual wave events corresponding to $Q \lesssim 2.5 \cdot 10^{-1}$, along with comparison of the quantile-to-quantile crest heights for uni-directional sea-states with $\gamma = 2.5$ and $\frac{1}{2}H_s k_p = 0.105$ at steady state. 136
3.22 Normalised total bound-wave crest amplification along with the underlying contributions of increasing order for uni-directional sea-states of $\gamma = 2.5$ and $\frac{1}{2}H_s k_p = 0.105$ at steady state, with comparison to the uni-directional Forristall (2000) predictions. 137
3.23 Temporal evolution of the bound-wave contribution to the crest heights normalised with respect to the Rayleigh prediction corresponding to a probability of exceedance of $Q = 10^{-3}$ for uni-directional sea-states with $\gamma = 2.5$ and $\frac{1}{2}H_s k_p = 0.105$ in different relative water depths. . . 139

3.24 Effect of sea-state steepness on the time-and ensemble-averaged dynamic kurtosis and on the time-averaged crest height of the free waves normalised with respect to the Rayleigh prediction at $Q = 10^{-3}$ for uni-directional sea-states with $\gamma = 2.5$ in different relative water depths. 140
3.25 Effect of sea-state steepness on the time-averaged bound-wave contributions to the crest height normalised with respect to the Rayleigh prediction at $Q = 10^{-3}$ for uni-directional sea-states with $\gamma = 2.5$ in different relative water depths. 142
3.26 Effect of sea-state steepness on the time-averaged crest height of the total free surface normalised with respect to the Rayleigh prediction at $Q = 10^{-3}$ for uni-directional sea-states with $\gamma = 2.5$ in different relative water depths. 143
3.27 Effect of spectral bandwidth (γ) on the temporal evolution of the ensemble-averaged dynamic kurtosis and the crest height of the free waves normalised with respect to the Rayleigh prediction at $Q = 10^{-3}$ for sea-states with $\frac{1}{2}H_s k_p = 0.105$ in different relative water depths. . 145
3.28 Effect of spectral bandwidth (γ) and relative water depth on the ensemble-averaged dynamic kurtosis and the time-averaged normalised with respect to the Rayleigh prediction crest height of the free waves at $Q = 10^{-3}$ for uni-directional sea-states of $\frac{1}{2}H_s k_p = 0.105$. 147
3.29 Effect of spectral bandwidth (γ) and relative water depth on the time-averaged bound-wave contributions normalised with respect to the Rayleigh prediction at $Q = 10^{-3}$ for uni-directional sea-states of $\frac{1}{2}H_s k_p = 0.105$. 148
3.30 Effect of spectral bandwidth (γ) and relative water depth on the time-averaged crest height normalised with respect to the Rayleigh prediction at $Q = 10^{-3}$ for uni-directional sea-states of $\frac{1}{2}H_s k_p = 0.105$. . . . 149
3.31 Temporal evolution of the bandwidth parameter $q_p = 1/(\pi Q_p)$ normalised with respect to the initial value q_{p0} for different relative water depths and spectral bandwidths. 150

3.32 Comparison of the time-and ensemble-averaged dynamic kurtosis at steady state arising from HOSM simulations to the narrow-band predictions of Mori & Janssen (2006), Janssen & Onorato (2007) and Fedele (2014). 152
3.33 Comparison of the time-and ensemble-averaged skewness and bound kurtosis arising from HOSM simulations to the narrow-band predictions of Janssen (2009) for uni-directional sea-states of varying spectral bandwidth and effective water depth with $\frac{1}{2}H_s k_p = 0.105$. 153
3.34 Relative nonlinear change of crest heights at $Q = 10^{-3}$ against the statistical moments for all available uni-directional sea-state simulations. 155

4.1 Effect of finite water depth and directionality on the prediction of dynamic kurtosis. 164
4.2 Theoretically predicted skewness and bound kurtosis parameters for narrow-banded directional sea-states against relative water depth. . . 165
4.3 Comparison between experimental and numerical data describing normalised crest-height exceedance probability distributions for directional sea-states generated in the ICL and QUB wave basins. 171
4.4 Temporal evolution of the ensemble-averaged dynamic kurtosis for directional sea-states of $\frac{1}{2}H_s k_p = 0.005$ and 0.105, $\gamma = 2.5$ and $\sigma = 10°$ in different relative water depths using different ramp-function lengths. 173
4.5 Normalised crest-height exceedance probability distributions arising in directional sea-states of $\sigma_\theta = 10°$, $\gamma = 2.5$ and $\frac{1}{2}H_s k_p = 0.105$ showing the effect of evolution time and relative water depth. 175
4.6 Crest-height probability of exceedance distribution of the free waves normalised with respect to the Rayleigh prediction and normalised bound-wave amplifications at steady state, with comparison to the directional Forristall (2000) predictions for directional sea-states of $\sigma_\theta = 10°$, $\gamma = 2.5$ and $\frac{1}{2}H_s k_p = 0.105$. 178
4.7 Temporal evolution of the normalised with respect to the Rayleigh prediction crest height, and its underlying contributions, at $Q = 10^{-3}$ for directional sea-states of $\sigma_\theta = 10°$, $\gamma = 2.5$ and $\frac{1}{2}H_s k_p = 0.105$ in different relative water depths, with comparison to equivalent uni-directional results. 181

4.8 Effect of sea-state steepness on the time-and ensemble-averaged dynamic kurtosis and on the time-averaged crest height of the free waves normalised with respect to the Rayleigh prediction at $Q = 10^{-3}$ in directional sea-states with $\sigma_\theta = 10°$ and $\gamma = 2.5$ in different relative water depths. 184
4.9 Effect of sea-state steepness on the time-averaged bound-wave contributions and the total crest heights at $Q = 10^{-3}$, both normalised with respect to the Rayleigh prediction, in directional sea-states with $\sigma_\theta = 10°$ and $\gamma = 2.5$ in different relative water depths. 186
4.10 Effect of directionality on the time-and ensemble-averaged dynamic kurtosis, the time-averaged free-wave crest height at $Q = 10^{-3}$ normalised with respect to the Rayleigh prediction and the integrated frequency difference terms for sea-states with $\frac{1}{2}H_s k_p = 0.105$ and $\gamma = 2.5$ in different relative water depths. 188
4.11 Effect of directionality on the time-averaged bound-wave contributions and its underlying harmonics at $Q = 10^{-3}$ normalised with respect to the Rayleigh prediction for sea-states with $\frac{1}{2}H_s k_p = 0.105$ and $\gamma = 2.5$ in different relative water depths. 192
4.12 Effect of directionality on the time-averaged crest height of the total free surface at $Q = 10^{-3}$ normalised with respect to the Rayleigh prediction for sea-states with $\frac{1}{2}H_s k_p = 0.105$ and $\gamma = 2.5$ in different relative water depths. 193
4.13 Effect of spectral bandwidth on the time-and ensemble-averaged dynamic kurtosis and the time-averaged free-wave crest height normalised with respect to the Rayleigh prediction at $Q = 10^{-3}$ for directional sea-states with $\frac{1}{2}H_s k_p = 0.105$ and $\sigma_\theta = 10°$ in different relative water depths. 196
4.14 Effect of spectral bandwidth on the time-averaged bound-wave contributions and crest height of the total free surface at $Q = 10^{-3}$, both normalised with respect to the Rayleigh prediction, for directional sea-states with $\frac{1}{2}H_s k_p = 0.105$ and $\sigma_\theta = 10°$ in different relative water depths. 197

4.15 Comparison of the time-and ensemble-averaged dynamic kurtosis at steady state arising from HOSM simulations and the narrow-band predictions of Janssen (2017) for sea-states of varying directionality and constant steepness. 200
4.16 Effect of directionality on the wave-induced 'mean flow'. Comparison between numerical data based on spectral integration and the theoretical narrow-band predictions of Janssen (2017) for sea-states of $\frac{1}{2}H_s k_p = 0.105$ and $\gamma = 2.5$. 202
4.17 Comparison of the time-and ensemble-averaged skewness and bound kurtosis arising from HOSM simulations to the narrow-band predictions of Janssen (2017) for directional sea-states of varying spectral bandwidth and effective water depth with $\frac{1}{2}H_s k_p = 0.105$ and $\sigma_\theta = 10°$. 204
4.18 Comparison between the time-and ensemble-averaged skewness arising from HOSM simulations and the predictions of Equation 4.4 for sea-states of (A) varying effective water depth and spectral bandwidth, (B) varying steepness, (C) varying directionality and (D) all sea-states. 207
4.19 Total kurtosis and bound kurtosis against measured skewness arising from HOSM simulations. 210

5.1 Examples of approximating the nonlinear contributions to tail of the normalised crest-height distribution with linear fits. 217
5.2 Slope, a_t, and offset, b_t, expressed as a function of the total kurtosis and skewness, respectively, together with second-order polynomial fits. 218
5.3 Slope, a_1, and offset, b_1, parameters against the dynamic kurtosis, along with second-order polynomial fits. 220
5.4 Relative reduction of the initial value of the kurtosis for uni-directional and directional simulations against the relative water depth. 220
5.5 Slope, a_2, and offset, b_2, parameters against the skewness parameter, along with second-order polynomial fits. 221
5.6 Slope, a_2, and offset, b_2, parameters against $\lambda_3 \cdot f_{c,1}(\lambda_{40}^d)$ and $\lambda_3 \cdot f_{c,2}(\lambda_{40}^d)$, respectively; along with second-order polynomial fits. 222
5.7 Slope, a_2, and offset, b_2, parameters against $(\lambda_3 + \lambda_{40}^b) \cdot f_{c,1}(\lambda_{40}^d)$ and $(\lambda_3 + \lambda_{40}^b) \cdot f_{c,2}(\lambda_{40}^d)$, respectively; along with second-order polynomial fits. 223

5.8 Slope, a_3, and offset, b_3, parameters against λ_{40}^b; along with second-order polynomial fits. 225
5.9 Slope, a_3, and offset, b_3, parameters against $f_{c,3}\lambda_{40}^b$ and $f_{c,4}\lambda_{40}^b$, respectively; along with second-order polynomial fits. 226
5.10 Training dataset depicted in the input variable space, showing the original sea-states used for the HOSM simulations, along with additional 'boundary' points of zero sea-state steepness. 230
5.11 Schematic of a feed-forward ANN architecture. 232
5.12 Variation of the average mean-square-error with respect to the number of neurons per hidden layer for different number of hidden layers. . . 235
5.13 Comparison of the ANN predictions to the target values of the statistical parameters; individual ANN predictions vs ensemble averaged predictions. 236
5.14 Variation of the ANN predictions with relative water depth, $k_p d$, for different γ values. Results for an ANN architecture consisting of 5 and 9 neurons per hidden layer. 238
5.15 Same as in Figure 5.14 but this time single ANN with $\epsilon_{MSE} < \epsilon_{MSE_{10}}$ are considered. 239
5.16 Variation of the ensemble median ANN predictions with relative water depth, $k_p d$, for different γ values and directional spreads σ_θ. Results for an ANN architecture consisting of 2 hidden layers and 5 neurons per hidden layer. 242
5.17 Predictions of EANNB and EANNU for sea-states corresponding to the 'boundary' points. 243
5.18 Variation of the ensemble median ANN predictions of the skewness with increase in the sea-state steepness: the effect of 'boundary' points. 244
5.19 Examples of the predictive performance of SVM and GPE in capturing the statistical moments. 246
5.20 Comparison of the EANN predictions against the time-averaged ensemble-averaged values of the statistical moments arising from additional HOSM simulations (Table 5.4). 249

5.21 Comparison of the HOE-EANN crest-height model predictions to numerical results from HOSM simulations used in the calibration of HOE-EANN- uni-directional sea-states. 252
5.22 Comparison of the HOE-EANN crest-height model predictions to numerical results from HOSM simulations used in the calibration of HOE-EANN- directional sea-states with $\sigma_\theta = 10°$. 253
5.23 Histogram of the relative deviation between the HOE-EANN predicted crest-height at $Q = 10^{-3}$ and the corresponding crest-height from numerically (HOSM) obtained crest-height distributions. 254
5.24 Normalised crest-height distributions arising in directional sea-states of $\sigma_\theta = 30°$. Comparison of the HOE-EANN crest-height model predictions to numerical results from HOSM simulations belonging to the test dataset. 255
5.25 Normalised crest-height distributions arising in directional sea-states of $\sigma_\theta = 3°$. Comparison of the HOE-EANN crest-height model predictions to numerical results from HOSM simulations belonging to the test dataset. 256
5.26 Comparison of the HOE-EANN crest-height predictions to experimental crest-height distributions for sea-states of moderate steepness. 258
5.27 Example of a measured spectral energy density, along with a fitted JONSWAP spectrum. 261
5.28 Histograms of $H_s/H_{s,target}$, $T_p/T_{p,target}$ and γ/γ_{target}. 262
5.29 Convergence of mean γ with respect to the number of 20-min sea-states used for its evaluation. 262
5.30 Comparison of the HOE-EANN predictions to crest-height distributions from field data: deep-water sea-states $S1$ and $S2$. 266
5.31 Comparison of the HOE-EANN crest-height predictions to distributions from field data with $k_p d$ laying between 1.35 and 1.8. 267
5.32 Comparison of the HOE-EANN crest-height predictions to distributions from field data with $k_p d$ laying between 0.8 and 1.25. 269
5.33 Comparison of the HOE-EANN crest-height predictions to experimental crest-height distributions of $k_p d = 2.03$ and $\frac{1}{2} H_s k_p = 0.16$ 270

5.34 Variation of steepness s and s' with effective water depth $k_p d$ for different spectral shapes (γ) 272
5.35 Calibration of f_b as a function of s'. 273
5.36 Comparison of the HOE-EANN and HOE-EANN-B crest-height predictions to distributions from experimental data for sea-states of moderate steepness in $k_p d \in (1.22, 3.5)$. 275
5.37 Comparison of the HOE-EANN and HOE-EANN-B crest-height predictions to distributions from experimental data for sea-states of severe steepness in $k_p d \in (1.22, 2.0)$. 276
5.38 Comparison of the HOE-EANN and HOE-EANN-B crest-height predictions to distributions from field data for sea-states in $k_p d = 0.8$. . . . 277
5.39 Available sea-states for additional validation of the HOE-EANN (-B) model and the proposed limit of validity. 278
5.40 Comparison of the HOE-EANN and HOE-EANN-B crest-height predictions to distributions from experimental data for sea-states with $k_p d > 1.0$ and $\sigma_\theta = 10°$. 279
5.41 Comparison of the HOE-EANN and HOE-EANN-B crest-height predictions to distributions from experimental data for sea-states with $k_p d > 1.0$ and $\sigma_\theta = 20°$. 280
5.42 Comparison of the HOE-EANN and HOE-EANN-B crest-height predictions to distributions from field data for sea-states laying close to the limit of validity of the EANN predictions. 283

A.1 Probability of exceedance of normalised local maxima for different spectral bandwidths. Comparison between the exact form of Cartwright & Longuet-Higgins (1956) and Equation A.12. 323

B.1 Variation of the normalised resonant interaction kernel, the relative change in wave speed with respect to the deep-water relative change and the normalised wave-induced mean flow with relative water depth. 327
B.2 Comparison between the uni-directional narrow-band theoretical solution of Janssen & Onorato (2007) for the dynamic kurtosis and the numerical results obtained using HOSM for different definitions for the spectral bandwidth and sea-state steepness. 330

B.3 Comparison between the uni-directional narrow-band theoretical solution of Janssen & Onorato (2007) for the dynamic kurtosis, evaluated using the sea-state parameters recommended by ECMFW (Janssen, 2017), and the numerical results obtained using HOSM. 331
B.4 Comparison between the uni-directional narrow-band theoretical solutions of Janssen (2009), for the skewness and bound kurtosis, and the numerical results obtained using HOSM. Comparisons for different definitions of the relative water depth, with and without including the effect of wave-induced mean flow. 334
B.5 Temporal evolution of the directionality factor J with non-dimensional time for different values of the parameter R. 336
B.6 Variation of the normalised wave-induced mean flow with relative water depth for different values of the parameter R. 337
B.7 Comparison between the directional narrow-band theoretical solutions of Janssen (2017), for the skewness and bound kurtosis, and the numerical results obtained using HOSM. Comparisons for different definitions of the relative water depth and spectral bandwidth. 340

C.1 Effect of spatial increment on the crest-height distribution. 344
C.2 Spatial variation of the ensemble-averaged significant wave-height and kurtosis normalised by the linear (target) values. 345
C.3 Normalised crest-height distribution of exceedance obtained arising from HOSM simulations of directional sea-states for varying nonlinear order M. 347
C.4 Spatial profiles (along the x-axis) of wave events, normalised with respect to H_s, corresponding to a probability of exceedance of $Q = 10^{-4}$ for the sea-states presented in Figure C.3 and for varying nonlinearity order M. 349
C.5 Effect of the nonlinearity order M on the temporal evolution of the ensemble-averaged statistical moments for directional sea-states of $\frac{1}{2}H_s k_p = 0.105$, $\gamma = 2.5$ and $\sigma = 10^\circ$ in different relative water depths. 350

C.6 Effect of the nonlinearity order M on the temporal evolution of the normalised with respect to the Rayleigh prediction crest height, and its underlying contributions, at $Q = 10^{-3}$ for directional sea-states of $\sigma_\theta = 10°$, $\gamma = 2.5$ and $\frac{1}{2}H_s k_p = 0.105$ lying in different relative water depths. 352
C.7 Contour plot of the spectral energy ($\frac{1}{2}a^2$) of the total free-surface elevation in $k_p d = 5.03$ and 0.87 arising in directional JONSWAP ($\gamma = 2.5$) sea-states with $\frac{1}{2}H_s k_p = 0.105$ and $\sigma_\theta = 10°$. 353
C.8 Contour plot of the spectral energy ($\frac{1}{2}a^2$) of the extracted harmonic contributions for a directional sea-state with $\frac{1}{2}H_s k_p = 0.105$, $\sigma_\theta = 10°$ and $\gamma = 2.5$ in $k_p d = 5.03$ using $M = 5$ and $T_a = 4T_p$. 356
C.9 Contour plot of the spectral energy ($\frac{1}{2}a^2$) of the extracted harmonic contributions for a directional sea-state in $k_p d = 0.87$ with $\frac{1}{2}H_s k_p = 0.105$, $\sigma_\theta = 10°$ and $\gamma = 2.5$ using $M = 5$ and $T_a = 4T_p$. 357
C.10 Contour plot of the spectral energy ($\frac{1}{2}a^2$) of the second-harmonic for directional sea-states with $\frac{1}{2}H_s k_p = 0.105$, $\sigma_\theta = 10°$ and $\gamma = 2.5$ using different ramp-function lengths in two different relative water depths. 360
C.11 Contour plot of the spectral energy ($\frac{1}{2}a^2$) of the zeroth-harmonic for directional sea-states with $\frac{1}{2}H_s k_p = 0.105$, $\sigma_\theta = 10°$ and $\gamma = 2.5$ using different ramp-function lengths in two different relative water depths. 361
C.12 Contour plot of the spectral energy ($\frac{1}{2}a^2$) of the third-harmonic for directional sea-states with $\frac{1}{2}H_s k_p = 0.105$, $\sigma_\theta = 10°$ and $\gamma = 2.5$ using different ramp-function lengths in two different relative water depths. 362

D.1 Normalised ensemble-averaged two-dimensional wavenumber spectra of the free waves for different evolution times and relative water depths. 366
D.2 Energy movements in directional wave spectra of the free waves for different relative water depths. 368
D.3 Temporal evolution of the mean directional spread normalised with respect to its initial value for different frequency bands. The relative effect of near-resonant interactions and bound-wave contributions for sea-states in different relative water depths. 370

E.1 Comparison of the time-and ensemble-averaged skewness arising from SORWT simulations to the predictions of Equation 4.4. (A) for directional sea-states of $\frac{1}{2}H_s k_p = 0.105$ and $\sigma_\theta = 10°$ and (B) for an extensive data set of 120 sea-states. 374
E.2 Bound kurtosis against measured skewness arising from SORWT simulations. 376

G.1 Comparison of the probability density function of the free surface arising from uni-directional HOSM simulations to to the Gram-Charlier series predictions for the freely propagating part of the free surface and the total free surface for sea-states of different relative water depth. 384
G.2 Comparison between Λ and Λ_{app} for the full set of available HOSM simulations. 387
G.3 Comparison of crest-height distributions arising from HOSM simulations to Gram-Charlier series predictions. 388
G.4 Histogram of relative deviation between the crest heights corresponding to an exceedance probability level of $Q = 10^{-3}$ obtained from the Gram-Charlier series crest-height model and from HOSM simulations. 389

H.1 Illustration of the principal elements of the SVM formulation. 395

I.1 Variation of the EANN predictions for the statistical moments with sea-state steepness for different effective water depths, together with the proposed range of validity of the predictions. 400

J.1 Sea-state characteristics used for assessing the performance of the Karmpadakis & Swan (2022) model, represented in the (S_1, U_r) parameter space. 402
J.2 Histogram of relative deviations between the predicted crest heights by Karmpadakis & Swan (2022) at an exceedance probability level of $Q = 10^{-3}$ and the corresponding crest heights from numerical (HOSM) data. 405
J.3 Histogram of the relative deviations between the predicted crest-heights by HOE-EANN at an exceedance probability level of $Q = 10^{-3}$ and the corresponding crest heights from numerical (HOSM) data. 406

J.4 Comparison of the Karmpadakis & Swan (2022) predictions to crest-height distributions from field data for non-breaking sea-states. 407
J.5 Comparison of the Karmpadakis & Swan (2022) predictions to experimental crest-height distributions for sea-states with $\sigma_\theta = 10°$. 409
J.6 Comparison of the Karmpadakis & Swan (2022) predictions to experimental crest-height distributions for sea-states with $\sigma_\theta = 20°$. 410
J.7 Comparison of the Karmpadakis & Swan (2022) predictions to crest-height distributions from field data for breaking sea-states. 411

List of tables

3.1 Sea-state parameters relating to the study of the effect of sea-state steepness in uni-directional seas. 99
3.2 Sea-state parameters relating to the study of the effect of spectral bandwidth and relative water depth in uni-directional seas. 100
3.3 Numerical setup of HOSM for uni-directional simulations. 101
3.4 Sea-state parameters of experimental studies used for validating the uni-directional HOSM simulations. 103
3.5 Numerical setup of MFBEM simulations used for validating HOSM. . . 112

4.1 Sea-state parameters relating to the study of the effect of sea-state steepness in directional seas. 167
4.2 Sea-state parameters relating to the study of the effect of directionality. 168
4.3 Sea-state parameters relating to the study of the effect of spectral bandwidth and relative water depth in directionally spread seas. . . . 168

5.1 Absolute relative deviation of the ANN predictions; single vs ensemble preditions. 237
5.2 Absolute relative deviation, ϵ_r of the ANN predictions using different level of acceptable error ϵ_{MSE}; single vs ensemble median ANN predictions; ANNs consisting of 2 hidden layers of 5 neurons. 239
5.3 Comparison of error measures of the employed meta-models. 245

5.4 Sea-state characteristics of the test dataset. 248
5.5 Comparison of error measures of the meta-models' performance upon the test-data set. 248
5.6 List of field data sources. 259
5.7 Accuracy of different methods for estimating the peak frequency. . . . 263
5.8 List of sea-states extracted from field data. 265

C.1 Numerical setup of HOSM for directional simulations. 342

H.1 Characteristics of the GPE configuration. 393
H.2 Characteristics of the SVM configuration. 397

List of key symbols and abbreviations

η	Free surface elevation
η_c^b	Bound-wave contribution to the zero-crossing crest height
η_c^d	Zero-crossing crest height of the free-waves part of the free-surface elevation
η_c	Zero-crossing crest height of the total free-surface elevation
γ	Peak-enhancement factor of the JONSWAP spectrum
λ_{40}^b	Bound kurtosis
λ_{40}^d	Dynamic kurtosis
λ_3	Skewness
ω	Circular wave frequency
σ_η	Standard deviation of the free-surface elevation
σ_ω	Root-mean-square (or standard deviation) of a narrow-banded frequency spectrum
σ_θ	Root-mean-square (or standard deviation) of the directional spreading function
θ	Angle of wave propagation
d	Water depth
f	Wave frequency
H_s	Significant wave height
k	Wavenumber
k_p	Wavenumber corresponding to the spectral peak period

l_p	Wavelength corresponding to the spectral peak period
Q	Probability of exceedance
S_1	Deep-water steepness parameter based on the spectral mean period
T_1	Spectral mean period
T_p	Spectral peak period
Ur	Ursell parameter
ALS	Accidental Limit State
ANN	Artificial Neural Network
BMNLS	Bandwidth Modified Non-Linear Shröndiguer
DSF	Directional Spreading Function
ECMFW	European Centre for Medium-Range Weather Forecasts
GPE	Gaussian Process Emulator
HOE-EANN	Higher-Order Empirical - Ensemble Artificial Neural Network
HOSM	Higher-Order Spectral Method
ICL	Imperial College London
JONSWAP	JOnit North Sea WAve Programme
LRWT	Linear Random Wave Theory
MFBEM	Multiple-Flux Boundary Element Method
PDF	Probability Density Function
QUB	Queen's University Belfast
RMSE	Root-Mean-Square Error
SORWT	Second-Order Random Wave Theory

SVM	Support Vector Machines
ULS	Ultimate Limit State
ZE	Zakharov Equation

1
Introduction

1.1 Engineering context

Many of today's human activities take place in, or are dependant upon, ocean environments. Oceans provide routes for trade and access to some of the largest energy sources available on our planet. However, the complexity of the physical processes determining the state of the sea has led to the scientific community's rather slow but steady progress towards its understanding and effective prediction. This lack of knowledge has not prevented the expansion of marine or offshore industry but has imposed significant risks, both human and economic.

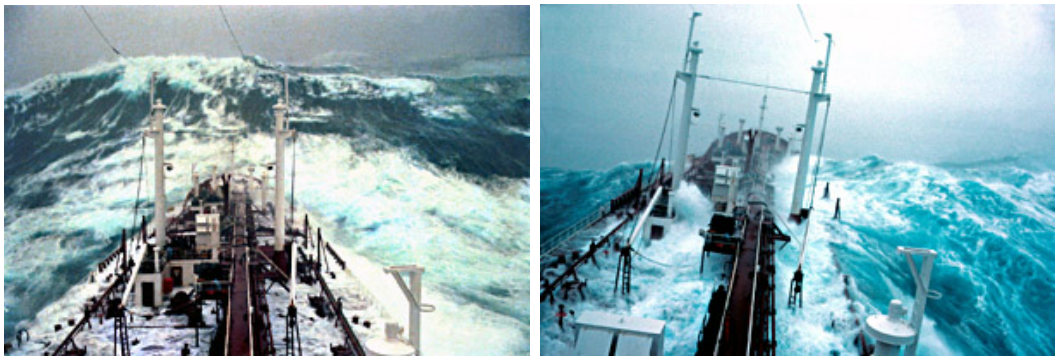
The turning point for the development of modern oceanography was World War II; accurate weather predictions giving significant military advantage for seaborne invasions. Notable examples include the American-British invasion of French North Africa during Operation Torch and the 'D-Day Landings' of the Allied forces in Normandy. At this time, weather predictions were mainly based on civilian or military weather observers in different locations passing on information to the meteorologists. The need for a more accurate approach was clearly apparent.

With the end of World War II and the beginning of the 'golden age' in economic development in North America and Western Europe, offshore oil extraction started its growth; the first offshore oil platform being constructed off the coast of Louisiana in 1947. The ground-breaking paper on wave forces on cylinders by Morison et al. (1950) noted that "*This paper is essentially a preliminary report submitted at this time*

because of the current importance of wave forces in the design of offshore structures.". This clearly highlighted the urgency with which research had to move forward at the time.

From then until now, ocean operations have expanded massively, with the seaborne trade consisting of the 80% of the total world trade and more than 1300 offshore oil platforms operating around the globe. These developments led to a sustained research effort to improve our understanding of ocean waves and their interaction with structures.

Modern oceanographic centres operating at a national or international level, such as the European Centre for Medium-Range Weather Forecasts (ECMFW), can provide marine operators and related industries with wave forecasts using specialised numerical models, including WAM (The Wamdi Group, 1988), WAVEWATCH-III (WW3DG, 2019) and SWAN (Booij et al., 1999), coupling the wind action to wave growth (The WISE Group et al., 2007). The output of such models, which consists mainly of the sea-state severity, dominant wave frequency, mean wave direction and angular spreading of wave energy, is a crucial input to the planning of marine operations and vessel route optimisation (see, for example, Vettor & Guedes Soares 2016).



(A) (B)

Figure 1.1: Photographs of the Stolt Surf tanker encountering a freak wave reaching a height of about $22m$ above mean water level in the North Pacific Ocean, captured in 1977 by Karsten Petersen (retrieved from NOAA)

However, the occurrence of the so-called *freak* or *rogue* waves that are substantially higher than their surrounding waves adds to the complexity of the required modelling. Such waves cannot be predicted by the above wave models and are often associated with moderately severe sea conditions that might otherwise be considered 'safe'.

Such waves have long been part of the anecdotal stories recorded over many 100's of years. More recently, photographic evidence has emerged, an example of which is provided in Figure 1.1. However, the first reliable measurement, and hence scientific proof of their actual existence, came when the so-called 'New Year Wave' was recorded at the Draupner platform in the North Sea on 1^{st} January 1995. This wave event, the record of which is shown in Figure 1.2, was characterised by a maximum crest elevation of $\eta_c = 18.5m$ above mean sea level. In contrast, the significant wave height, H_s, representing the average height of the highest 1/3 of waves was estimated to be $11m$. The ratio of $\eta_c/H_s \approx 1.7$ is abnormally high.

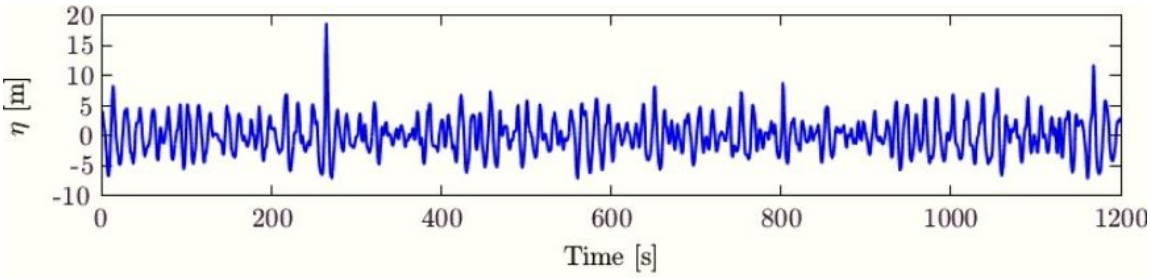


Figure 1.2: The time record of the 'New Year Wave' recorded at the Draupner platform in the North Sea on 1^{st} January 1995. Adapted from Latheef (2014).

Following the event at Draupner, the occurrence of freak waves became a focus of much research; large multi-party academic and industry projects and specialised workshops dedicated to explaining this undoubtedly threatening phenomenon. Notably, the analysis of an extensive field database including 122 million individual waves conducted by Christou & Ewans (2011) concluded that freak waves are more common than what was perhaps expected, with more than 3500 rogue waves detected in the analysis. However, many of these waves were small and not of practical engineering significance.

Nevertheless, freak waves are believed to be responsible for many of the weather-related accidents reported in the maritime and offshore industries, posing serious risks to the human safety and economic stability. Indicatively, between 2001 and 2010, 755 ship accidents associated with bad weather conditions have been reported by the International Maritime Organisation (IMO), with no clear human error associated with them (Zhang & Li, 2017). While an earlier analysis of a similar database conducted by Toffoli et al. (2005) has reported that the majority of accidents associated with bad weather did not occur in the most severe sea-states. Given that

the most severe sea-states will naturally be avoided when planning a ship's route, this observation links to the presence of abnormally high waves when compared to expectations.

Adding to the list of potential hazards that wave action can pose, Hurricanes Katrina (2005), Rita (2005), Gustav (2008) and Ike (2008) have caused serious issues for the U.S. energy supply. This arose, in part, because the extraction of oil had to be suspended in many cases (Ilbeigi & Dilkina, 2018), but also because of the serious damage or even collapse that these extreme environmental events caused to offshore infrastructure (Knabb et al. 2006a,b, Berg 2009, Cruz & Krausmann 2008). Indicatively, in the final reports published by the Mineral Management Service of the U.S. Department of the Interior (MMS, 2007, 2010) a total number of 44, 69 and 60 platforms were destroyed during Hurricanes Katrina, Rita and Gustav/Ike, respectively. Notably, the majority of the cases reporting structural failure were associated with wave-in-deck loading. The implications being that failure was associated with one very large wave crest capable of penetrating into the deck of the structure. Such events involve a very large increase in the applied load, which the structure was not designed to resist.

Figure 1.3 presents photographs of the damage such extreme loads can produce. These examples are cases reported within MMS (2007, 2010) reports; presenting either local damage (Figure (a)), global failure (Figure (b)) or complete wash-away of the deck (Figure (c)).

Based on the above, it is clear that an accurate prediction of the most probable maximum crest height within a storm is of utmost importance for both the safe design of new structures and the re-assessment of existing ones. To put this into perspective, a relatively small increase of the crest elevation by 1 to 2 meters compared to what is predicted based on the current design practice can lead to unexpected platform failures.

1.2 Physical perspective

Over the years, attempts to define the mechanisms that lead to the formation of exceptionally large waves such as the Draupner wave (Haver & Andersen, 2000) and/or other famous freak waves like the Andrea wave (Magnusson & Donelan,



(a) (b)

(c)

Figure 1.3: Photographs of damaged or destroyed platforms in the Golf of Mexico due to wave-in-deck loading. Adopted from MMS (2007, 2010).

2013) led to two main hypotheses.

The first hypothesis argues that exceptionally large waves can form when linear independent wave components come into phase at one point in space and time. Driven by linear frequency dispersion, this process can create a transient single wave event, which is higher than the surrounding waves. However, neither the magnitude nor the shape of the wave events produced by linear arguments agrees with observations. As the observed wave crests are steeper, have shallower troughs and are higher than what linear superposition predicts. To account for this, the hypothesis argues that when Stoke's type nonlinear interactions are included, the nonlinear features of the observed waves are adequately captured (Walker et al. 2004, Fedele & Tayfun 2009, Fedele et al. 2016, Benetazzo et al. 2017, Häfner et al. 2021).

The second hypothesis suggests that a rogue wave can form due to the so-called *modulational instability* phenomenon. In which an initially quasi-regular, or very narrow-band, wave train destabilises due to nonlinear interactions involving energy exchange between the freely propagating wave components. Such wave propagation is driven by changes in the dispersive properties due to third-order (in wave steepness) nonlinear interactions (Dysthe & Trulsen 1999, Osborne et al. 2000, Chabchoub et al. 2012, Wang et al. 2018).

To this end, advancements by Baldock et al. (1996), Johannessen & Swan (2001), Johannessen & Swan (2003) and Gibson & Swan (2007) have revealed both experimentally and numerically that the maximum wave event within a deterministic wave group, not initially defined by a very narrow-band frequency spectrum but broader and, hence, more representative of real sea conditions, cannot be captured by Stoke's type interactions. Much of the observed maximum wave-crest amplification was due to the nonlinear evolution of the free-wave regime induced by the same type of interactions responsible for the modulational instability phenomenon. This behaviour was more prominent in unidirectional waves, reducing as the directional distribution of energy broadened. However, the evolution of such wave groups was dominated by linear frequency dispersion and was weakly affected by nonlinear (steepness-driven) dispersion; essentially providing a bridge to the two hypotheses, discussed above.

Whilst additional hypotheses have been proposed over the years, such as the role of ambient currents, atmospheric forcing, crossing seas and variable bathymetry (Kharif & Pelinovsky 2003, Belibassakis et al. 2014, Ducrozet & Gouin 2017, Gram-

stad et al. 2018) the relevance of the above two main hypotheses (in the absence of additional effects) still remains to be resolved for sea-states involving a realistic spread of energy in both frequency and direction.

Based on the above, the effect of finite water depth is of particular interest as (1) the nonlinear interactions become increasingly more important, (2) the majority of the reported freak waves have been detected in intermediate water depths, including both Draupner and Andrea, and many of those reported by Christou & Ewans (2011) and (3) the majority ($\approx 70\%$) of the structural failures reported in the aftermath of Hurricanes Rita, Katrina, Gustav and Ike concerned water depths below $60m$.

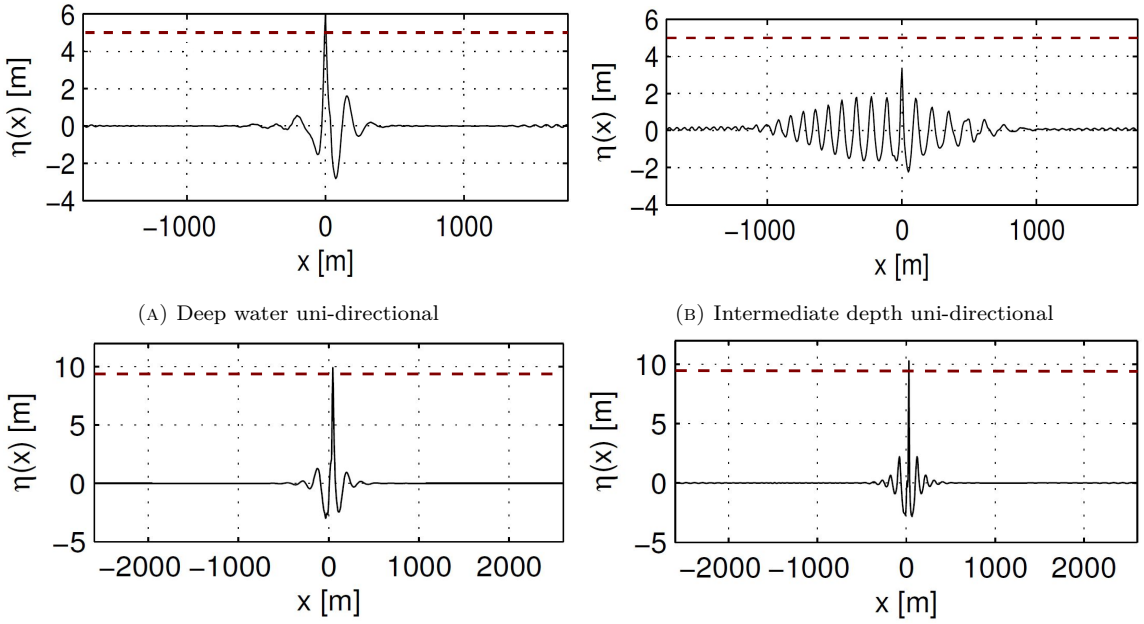
To this end, the comparison of the evolution of realistic bandwidth focused wave groups in deep and finite water depths presented by Katsardi (2007) and Katsardi & Swan (2011) has highlighted certain key physical phenomena associated with both the effect of water depth and the role of short-crestedness or directionality. The key messages arising from this earlier study will be briefly outlined as they provide critical background to the complexities underpinning the problem.

Figure 1.4 presents examples of the spatial wave profiles of 4 fully nonlinear wave groups at the time of their maximum elevation; the top two corresponding to uni-directional conditions and the bottom two, directional or short-crested conditions. In all plots, the red horizontal dashed line refers to the maximum elevation predicted in the absence of nonlinear effects. The results were numerically calculated using the fully nonlinear wave model proposed by Bateman et al. (2001, 2003).

Regarding the uni-directional cases, in deep water (Figure 1.4(A)) wave nonlinearity leads to the substantial increase of the wave-crest elevation ($\approx 25\%$). In contrast, the complete opposite was observed in finite water depth (Figure 1.4(B)). In this latter case, the crest elevation is $\approx 33\%$ below the linear prediction, and the wave group defined by a truncated quasi-regular wave train. In both cases, an in-depth analysis of the various nonlinear effects revealed that nonlinear wave-wave interactions above second-order in wave steepness, similar to those responsible for triggering the effect of modulational instability, were mostly responsible for this behaviour.

However, for the directional wave groups the 'picture' changes completely. First, the amplification of the wave crests in deep water is less significant ($\approx 5\%$) and the attenuation of the highest crest in intermediate depth, observed in uni-directional conditions, is reversed; the maximum elevation being higher than the linear predic-

tion by as much as $\approx 7\%$.



(A) Deep water uni-directional

(B) Intermediate depth uni-directional

(C) Deep water directional

(D) Intermediate depth directional

Figure 1.4: Spatial profiles of wave groups at the time of maximum elevation, simulated using the fully nonlinear wave model of Bateman et al. (2001) (extracted from Katsardi (2007)). (A) & (C) deep water, (B) & (D) intermediate depth of $15m$. In all cases the dominant wave period is $10s$, while the directional results represent conditions with root-mean-square angular spreading of $\approx 30°$. The linearly predicted maximum elevation in the uni-directional cases is $5m$ and in the directional cases $9.5m$. Finally, the input amplitude spectrum of the wave events is defined according to Tromans et al. (1991) using a JONSWAP spectrum of $\gamma = 2.5$ (see §2.1).

In this respect, when considering realistic directional sea-states, there is accumulated evidence from both experimental and field data to suggest that third-order nonlinear interactions lead to the amplification of the largest crest heights compared to industry-standard second-order predictions in both deep (Latheef & Swan 2013, Latheef 2014) and finite water depth (Karmpadakis et al. 2019a, Karmpadakis et al. 2019b), as long as severe wave breaking does not occur. While more recently, Karmpadakis & Swan (2020) have indicated that correcting linear free-surface records for second-order Stoke's type interactions is not sufficient to explain the wave shapes observed in both experimental and field measurements. However, the aforementioned studies did not attempt to directly isolate the various nonlinear effects in random free-surface records.

Based upon these results, some important questions arise with regard to the role of nonlinear interactions in realistic sea-states:

1. What is the effect of the different nonlinear wave-wave interactions on the wave crests?

2. Do wave interactions related to modulational instability play a key role in the formation of large wave events?

3. Is modulational instability relevant to sea-states of intermediate water depth?

4. How important are Stoke's type nonlinear interactions above second-order, and how do they depend upon the sea-state characteristics?

5. What is the role of directionality in different water depths, and how does it affect the various nonlinear interactions?

Building upon existing insights gained from the aforementioned studies, these questions will be answered in the present study.

1.3 Designer's perspective

For the safe and efficient design of offshore structures, the design process should address both the complex physical processes associated with the wave motion and the inherently stochastic nature of waves. The challenge from this standpoint lies in the fact that the full set of possible wave events that a structure may encounter during its lifetime is typically represented by a single *design* crest height, linked to a pre-specified *annual probability of exceedance*. According to international standards such as the BS-EN-ISO-19901-1 (2015), NORSOK-N-003 (2014) and DNV-RP-C205 (2014) this probability is typically defined as 10^{-2} for an Ultimate Limit State (ULS) design and as 10^{-4} for an Accidental Limit State (ALS) design; the latter being relevant to wave-in-deck loading.

To specify the design crest height, first, a *long-term* analysis of the sea conditions for a given geographic location must be performed. To this end, given the unsteady nature of the environmental conditions in any given site, these are usually segmented into shorter periods. These periods typically last 20 min to 3 hours, during which the environmental conditions are assumed to be *stationary*. During this stationary period, a *sea-state* is defined by the significant wave height, H_s, representing the average height of the largest one-third of waves and the peak period or dominant

wave period, T_p. While other parameters, such as the mean wave direction and angular distribution of energy, can be included for a more accurate description.

A full long term analysis then usually requires the specification of the joint probability density function of H_s and T_p, which can be determined either from free-surface measurements at the site of interest or most often from a *hindcast* analysis using wave models like WAM or WAVEWATCH-III. This approach is referred to as the *initial-distribution method*. Whilst it does not take into account the correlation between the sea-states, it has the advantage of utilising the highest possible number of sea-states. Other methods for conducting a long term analysis include the *peak-over-threshold* method. This relies on the identification of storm events that exceed a certain severity threshold or the *block maxima* method in which the most severe sea-states within a time window are selected. Both methods indirectly account for the correlation between the sea-states. However, with the scarcity of the storm events and the limited duration of either the free-surface measurements or the hindcast analysis, these two later methods can suffer from statistical uncertainty (Vanem, 2015).

Regardless of the methodology used for a long term analysis, a second source of uncertainty needs to be taken into account. This refers to the specification of the *short-term* crest-height probability distribution *within a sea-state*. The final estimation of the 'design conditions' requires the convolution of the long-term probability of occurrence of a sea-state or a storm with the short-term probability of the maximum crest heights within the sea-state. However, this process can be time-consuming if the free surface is simulated either experimentally or numerically via a Monte-Carlo approach. To avoid this, simplified methods, such as the environmental contour line approach (Haver & Kleiven, 2004), are often adopted.

The present thesis concerns the accurate estimation of the *short-term* crest-height probability distribution. A failure to accurately predict this can result in serious errors in calculating the design crest height and associated wave loads. To this end, in common design practices the short-term crest-height predictions incorporate nonlinear effects up to second-order in wave steepness (Forristall, 2000), thereby ignoring potentially important nonlinear effects that arise from higher-order nonlinear wave interactions.

An accurate prediction of the largest waves arising in a sea-state is also a funda-

mental input to the effective route design for shipping; the purpose being to avoid green water inundation or other destructive events. Whilst wave forecast models do not provide information about the individual waves within a sea-state, they are often coupled with analytical ways of predicting the largest wave events. Particularly, ECMFW has embedded a freak-wave warning system, which relies on the analytical estimation of a set of statistical parameters, namely the skewness, bound kurtosis and dynamic kurtosis. These parameters are integral measures which correlate with the possible influence of nonlinear wave-wave interactions. Indeed, they are used as input to analytical formulas for the prediction of the largest waves. However, these estimations rely on unrealistic narrow-band assumptions regarding the energy distribution in both frequency and direction. This could potentially lead to the over-estimation of the effect of modulational instability or the inaccurate estimation of the Stoke's type interactions.

1.4 Research aims

The present research aims to further our understanding of the effects of nonlinear wave interactions in realistic broad-banded sea-states, and to provide guidance as to how these can be effectively incorporated into the prediction of the largest waves arising therein. Based on this, the specific research goals are outlined as follows:

- Using a fully nonlinear phase-resolving wave model based on a Higher-Order Spectral Method (HOSM), to assess the effect of second and higher-order wave interactions on the statistical properties of uni-directional sea-states.
  - In doing this, to explore the effect of finite water depth, and identify if crest-amplification due to nonlinear interactions relating to deep-water modulational instability is relevant. This part of the research sits along side the theoretical grounds set by Janssen & Onorato (2007). Their analysis states that modulational instability ceases to exist for narrow-band sea-states when the dominant wave component is longer than about 4.6 times the water depth owing to the stabilising effect of the wave-induced mean flow. Specifically, in the narrow-band limit for the spectral bandwidth, the wave-induced mean flow is associated with a nonlinear wave

component having a wavenumber that tends to zero and, hence, inducing horizontal velocities in the form of a uniform current. Whilst these arguments are at odds with the evolution of wave groups in intermediate water depth presented by Katsardi & Swan (2011), its relevance to realistic bandwidth sea-states needs to be clarified.

  - Identify the importance of Stoke's type interactions on the magnitude of the largest waves arising in realistic bandwidth sea-states. In this respect, explore the overall validity of the second-order crest-height model of Forristall (2000) adopted within many international standards.
  - Explore the link of the statistical moments of skewness, bound kurtosis and dynamic kurtosis to the nonlinear crest elevation of the most likely maximum wave-crest arising in 3-hour sea-states of different effective water depth, steepness and spectral bandwidth.
  - Assess the validity of narrow-band theoretical solutions of the aforementioned statistical parameters.

- Extend the analysis of uni-directional sea-states to directionally spread seas.
  - Particularly, to explore how the outcomes of the analysis regarding directional seas change with an incremental increase in the directional spread, and to identify if modulational instability and the effects of the wave-induced mean flow apply in these realistic sea-states.
  - Assess the validity of the predictions for skewness, bound kurtosis and dynamic kurtosis according to the latest ECMFW freak-wave warning system (Janssen, 2017).
  - Assess the validity of other available methods for the prediction of the statistical moments, particularly those that are not governed by an underlying assumption of narrow-bandwidth.

- Using the results outlined above, parameterise a crest-height distribution based on fully nonlinear simulations that include all relevant nonlinear effects. To fully validate the proposed model based on additional numerical, experimental and field data. The utilised field free-surface data records originate from 6

platforms located in the North Sea and belong to the vast databases originally analysed by Makri (2018) and Karmpadakis (2018).

1.5 Thesis layout

The scope of the thesis outlined above is addressed as follows:

Chapter 2 presents the key theoretical background and methodologies relevant to the present study. In particular, the methodology for separating the various nonlinear contributions from fully nonlinear simulations is presented and validated. Additional aspects relating to the statistically appropriate initialisation of a wavefield are also discussed in detail.

Chapter 3 addresses the statistical properties of uni-directional nonlinear wavefields. The chapter starts with an account of the available theoretical solutions for the prediction of the statistical moments based on a narrow-band assumption; highlighting, in more detail, the questions that have been raised. An extensive validation of the numerical simulations is presented. This includes:

1. a comparison of numerically predicted fully nonlinear crest-height distributions using HOSM to experimental data originating from three different laboratory facilities, and

2. a comparison of the evolution of fully nonlinear wave groups predicted using HOSM and an alternative wave model proposed by Hague & Swan (2009).

Following on key considerations for the suppression of spurious wave components at the initialisation stage of the simulations are presented. Taken together these provide new insights regarding the time development of the nonlinear interactions in various water depths. The effect of the nonlinear evolution time, sea-state steepness, spectral bandwidth and effective water depth on the crest-height distribution and its underlying nonlinear contributions is thoroughly accounted for. Part of this investigation regards the assessment of the applicability of the Forristall (2000) model, highlighting the conditions in which it is expected to perform well and when its validity becomes questionable. Finally, the validity of the narrow-band solutions for the statistical moments is assessed.

Chapter 4 deals with the statistical properties of directional wavefields. Following a similar structure to the previous chapter, it commences with the presentation

of available theoretical solutions for the statistical moments relevant to directional sea-states, again based on a narrow-band assumption. This is followed by a brief validation study; with the aim being to extend the confidence gained from the earlier uni-directional simulations to directional seas. The chapter follows with the presentation of important insights regarding the effect of sea-state steepness, directionality and spectral bandwidth on the various nonlinear interactions. The sea-states are simulated over many tens of dominant wave periods, highlighting the time required for the nonlinear evolution to reach a steady-state. In addition, the appropriateness of the second-order directional model of Forristall (2000) is assessed, highlighting these cases in which the model performs well despite the presence of profound nonlinear effects beyond second-order. The chapter concludes with comparisons between numerically obtained values for the statistical moments and the theoretical predictions. In this respect, the effect of wave-induced mean flow is thoroughly assessed.

Building upon the insights gained from Chapters 3 and 4, **Chapter 5** is devoted to the effective prediction of the short-term crest-height distribution. The proposed approach makes use of the extensive set of numerical simulations presented in the previous chapters and treats each nonlinear contribution separately. The calibration of the proposed model relies on a combination of empirical fitting and machine learning. This enables the predictions to be based solely upon four sea-state parameters: the sea-state steepness, the degree of directional spread, the effective water depth and the spectral bandwidth. Subsequently, the predictions of the proposed crest-height model are compared to crest-height distributions arising from several possible sources. These include additional numerical simulations, laboratory experiments and field data. Finally, as wave breaking is not explicitly modelled within HOSM, the HOSM simulations have been restricted to non-breaking conditions. To this end, a simplified wave-breaking correction to the proposed crest-height model is calibrated based on available experimental data. This extends the range of applicability of the model to higher sea-state steepnesses. The advancements of the proposed model over existing state-of-the-art approaches (the inclusion of higher-order nonlinear interactions in crest-height modelling in finite water-depth) are discussed in detail. These state of the art approaches include either an analytical formulation using the so-called Gram-Charlier series (Tayfun & Fedele, 2007) or empirical fits to experimental and field data (Karmpadakis & Swan, 2022).

The thesis concludes in **Chapter 6**, where the key contributions of the present study are highlighted and suggestions for future work are provided.

2
Background and Methodology

The present chapter presents the background relevant to the present thesis and sets the ground for the analysis that follows in the subsequent chapters.

This chapter commences in §2.1 with a brief introduction of the various concepts that underpin the characterisation of real seas from an engineering perspective. Following on §2.2 presents nonlinear effects arising from wave-wave interactions at a second-order of the wave steepness and above. The crucial roles of steepness, bandwidth, finite water depth and directionality are highlighted. Building upon these insights, available analytical and numerical solutions to the water-wave mathematical problem are considered; with a special focus on the simulation of random sea-states. To this end, the Higher-Order Spectral Method (HOSM) is identified as the most suitable model for the investigations that follow. The HOSM model is combined with an existing methodology for separating the various nonlinear effects. The applicability of this approach in the present setting is discussed and validated. Finally, §2.3 briefly reviews the statistical concepts appropriate to random free-surface records and presents important considerations for the reliable initialisation of random wavefields within HOSM.

2.1 Characterisation of real seas

2.1.1 Omni-directional wave spectrum

The characterisation of the distribution of the energy across frequencies for wind seas has been the topic of extensive field studies conducted at the 60s and 70s. The most notable work on this subject is undoubtedly that of Hasselmann et al. (1973), which was conducted in the North Sea. The outcome of this study is the extensively used JONSWAP (JOint North Sea WAve Programme) wave spectrum, defined by Equation 2.1[1],

$$S_{\eta\eta}(\omega) = \frac{\alpha g^2}{\omega^5} \exp\left(-\beta \frac{\omega_p^4}{\omega^4} \right) \gamma^{\exp\left(-\frac{-(\omega-\omega_p)^2}{2\omega_p^2 \sigma^2} \right)} \tag{2.1}$$

where, ω is the circular wave frequency, ω_p the circular wave frequency corresponding to the peak of the spectrum, γ is the peak enhancement factor, α is the Phillip's parameter (Phillips, 1958), $\beta = 1.25$, $\sigma = 0.07$ for $\omega \leq \omega_p$ and $\sigma = 0.09$ otherwise.

Within this description, the Phillip's parameter, α, is typically linked to the velocity of the wind and the fetch length (see Longuet-Higgins 1969, Hasselmann et al. 1973, Donelan et al. 1985). Nonetheless, it is, in essence, a scaling factor for the energy level of the spectrum and does not alter the spectral shape.

The γ factor controls the 'peakedness' of the spectrum or, in effect, its spectral bandwidth. A high γ value corresponds to a 'young' sea-state or fetch-limited sea-state, in which the majority of the energy is centralised around the spectral peak. As a sea-state develops, it loses its peakedness, and γ reduces. For $\gamma = 1$, the JONSWAP wave spectrum coincides with the Pierson-Moscowitz spectrum for fully developed seas (Pierson & Moskowitz, 1964).

A JONSWAP spectrum is appropriate to a wave system generated by a local wind field. When a wave system has left the storm and has travelled over long distances, the energy is significantly down-shifted in frequency, and the high-frequency tail ceases to exist. The latter effect is explained by (1) the absence of significant wind forcing, which adds energy to the high-frequencies, (2) the higher rates of energy dissipation at higher frequencies due to wave breaking and (3) the fact that high

[1]It is noted that the spectrum given in Equation 2.1 is a variance density spectrum, which needs to be multiplied by ρg to represent energy, where ρ is the density of the water and g is the acceleration due to gravity.

frequency freely propagating components of the original storm travel at much slower speeds due to frequency dispersion; hence they separate from the lower frequencies over long distances. It is possible that such a system, often referred to as *swell*, enters a new storm location. In this scenario, two wave systems generally travelling in different mean directions, coexist and give rise to a so-called mixed sea. The frequency spectra of mixed seas are usually double-peaked; their parameterisation having been discussed by Ochi & Hubble (1977), Guedes Soares (1984) and Torsethaugen & Haver (2004) amongst others. The present research focuses on single-peaked JONSWAP spectra. As a result, mixed-seas spectra are not further discussed.

As mentioned in the introduction to this thesis a sea-state is usually defined by the significant wave height and spectral peak period (H_s, T_p). In defining a design wave spectrum based upon these values, the peak period is matched to the peak frequency of the JONSWAP wave spectrum (according to $T_p = 2\pi/\omega_p$) and the spectrum is scaled such that,

$$H_s = 4\sqrt{m_0} \tag{2.2}$$

where m_0 is the zeroth spectral moment defined by $m_0 = \int_0^\infty S_{\eta\eta}(\omega)d\omega$, and is equal to the variance, σ_η^2, of the zero-mean free-surface elevation, η. Hence, $\sigma_\eta^2 = E[\eta^2] = m_0$, where $E[\,\cdot\,]$ is the mean operator.

The spectral definition for H_s should not be confused with the original definition of Sverdrup & Munk (1947), which expresses the significant wave height as the average of the highest 1/3 of the waves in a sea-state. This earlier definition is both sensitive to the duration of a time record and to the spectral bandwidth (Goda, 2000). When adopted, it has been shown to lead to discrepancies between commonly used crest-height models and observations (see for example Latheef 2014). To avoid such difficulties, Equation 2.2 is used throughout the remainder of this thesis.

2.1.2 Directional wave spectrum

The JONSWAP wave spectrum does not include information on the directional properties of a sea-state and, hence, its short-crestedness. This is taken into account through a so-called Directional Spreading Function (DSF). This acts as a multiplier to the omni-directional JONSWAP spectrum to yield an energy distribution in both frequency and direction,

$$S_{\eta\eta}(\omega,\theta) = S^x_{\eta\eta}(\omega)D(\omega,\theta) \tag{2.3}$$

where, θ represents the angle of wave propagation and $D(\omega, \theta)$ is the DSF which must satisfy $\int_0^{2\pi} D(\omega, \theta) d\theta = 1$, so that the total energy of the omni-directional spectrum is maintained. Moreover, $S^x_{\eta\eta}$ here refers to the omni-directional spectrum, with x denoting the axis of the mean wave propagation.

Several DSFs have been proposed in the literature. These broadly lie in two categories: (1) these that incorporate frequency-dependent spreading and (2) these that are frequency-independent. Models that lie in the first category include example Mitsuyasu et al. (1975), Donelan et al. (1985) and Ewans (1998); all of which have been derived based on the analysis of field data. These consistently show higher spreading angles at frequencies above the spectral peak. Nonetheless, frequency-independent DSFs are often employed in both experimental (for example: Onorato et al. 2009a, Latheef & Swan 2013 and Karmpadakis et al. 2019a) and numerical investigations (for example: Toffoli et al. 2009 and Toffoli et al. 2010a). In fact, it has been shown experimentally by Latheef & Swan (2013) that the magnitude of the largest wave crests observed in deep-water random sea-states is dominated by the spread of energy around the spectral peak. Hence, it is not greatly influnced by frequency-dependence in the DSF.

In the present research, a frequency-independent Gaussian DSF is employed, its functional form given by,

$$D(\theta) = \frac{A}{\sigma_\theta \sqrt{2\pi}} \exp\left(- \frac{(\theta - \theta_m)^2}{2\sigma_\theta^2} \right) \tag{2.4}$$

where θ_m is the angle of mean wave propagation and A a scaling parameter, so that the DSF integrates to 1.

Alternative functional forms of frequency independent DSFs include the '$cosine-2s$' function introduced by Cartwright (1961), the DNV proposed '$cosine-n$' function DNV-RP-C205 (2014) and the '$sech-\beta$' function of Donelan et al. (1985). However, all of the above forms give similar angular spreading if their parameters are adjusted appropriately.

Having established the form of the wave spectrum appropriate to the characterisation of a random sea-state, the following section focuses on the mathematical and numerical modelling of random sea-states, with particular focus on the effect of nonlinear wave interactions.

2.2 Water-wave solutions and nonlinear effects

2.2.1 Mathematical formulation

When describing ocean waves that travel on the water surface, a number of assumptions are commonly employed. Specifically, it is assumed that the fluid (water) is incompressible and inviscid and that the flow is irrotational. The assumed incompressibility ensures a constant density across the water column. The absence of viscous effects prohibits the development of turbulence due to, for example, bottom friction or wave breaking, whereas the assumption of irrotationality ensures zero vorticity in the wavefield. Hence, a velocity potential, $\phi(x, y, z, t)$, can be defined everywhere in a three-dimensional fluid domain.

Within this definition, (x, y) defines a horizontal plane. While z points vertically upwards and has its origin on the still water level or the level of the quiescent water in the absence of waves. The gradient of the velocity potential yields the velocity field,

$$\mathbf{u} = \nabla\phi \tag{2.5}$$

where $\mathbf{u} = (u_x, u_y, u_z)$ and ∇ is the spatial gradient operator, $\nabla = (\frac{\partial}{\partial x}, \frac{\partial}{\partial y}, \frac{\partial}{\partial z})$.

Mass continuity applies throughout the fluid domain. Given the assumed incompressibility, this is expressed through the well-known Laplace equation,

$$\nabla \cdot \mathbf{u} = \nabla^2\phi = 0 \tag{2.6}$$

which becomes the governing fluid equation.

To fully define the mathematical problem, the boundaries of the fluid domain need to be determined, along with the physical constraints acting upon them. The most complicated boundary is the free surface of the water body, denoted as $\eta(x, y, t)$. This deforms free surface deforms due to the waves in both space and time. Hence, its shape is not known *a priori*. This boundary needs to satisfy two conditions.

First, the pressure on the water surface should be constant. This implies that no wind action is taken into account. Hence, it is assumed that the waves have already been generated and propagate within the fluid domain. This constant pressure constraint defines the so-called Dynamic Free Surface Boundary Condition (DFSBC).

Adopting the unsteady Bernoulli equation, it can be expressed as

$$\frac{\partial \phi}{\partial t} + \frac{1}{2}(\nabla^2 \phi) + g\eta = 0 \tag{2.7}$$

where g is the gravitational acceleration and the pressure has been set to zero without loss of generality.

The second constraint is the Kinematic Free Surface Boundary Condition (KFSBC). This expresses the fact that the free surface should be a streamline. In other words, that the velocity of the fluid normal to the free surface should equal the velocity of the free surface along this normal. The KFSBC is expressed as,

$$\frac{\partial \eta}{\partial t} + \frac{\partial \phi}{\partial x}\frac{\partial \eta}{\partial x} + \frac{\partial \phi}{\partial y}\frac{\partial \eta}{\partial y} - \frac{\partial \phi}{\partial z} = 0 \tag{2.8}$$

Both the DFSBC and KFSBC are nonlinear, and must be solved on the surface that cannot be known a priori. This complicates the solution of the governing Laplace equation, making its solution a non-trivial task. In addition, both conditions contain time-dependent quantities, which implies that a time marching procedure is needed to solve the problem.

In addition, an impermeable bed defines the bottom boundary of the fluid domain. This condition requires the fluid velocity normal to the boundary to be zero, and it is expressed as,

$$\frac{\partial \phi}{\partial \mathbf{n}} = 0 \tag{2.9}$$

where, $\mathbf{n}$ is the unit vector normal to the bed, the bed assumed to be horizontal at a constant depth of $z = -d$.

The lateral boundary conditions are often assumed periodic, defining open boundaries or 'open ocean' conditions. Alternatively, if the fluid domain is treated as a closed tank, it is supplied with appropriate wave-making and wave-absorbing boundary conditions. The present thesis primarily considers wave solutions with open lateral boundaries. When this is not the case, it is explicitly mentioned in the relevant section.

2.2.2 Linear and second-order wave solutions

Linear Random Wave Theory (LRWT)

Airy (1845) was the first to solve the water-wave problem; albeit subject to significant simplifications. Specifically, a Taylor series expansion was applied to the free-surface boundary conditions about the still water level ($z = 0$). By retaining only the first-order terms of this expansion, the DFSBC and KFSBC can be simplified to:

$$\begin{aligned} \frac{\partial \phi^{(1)}}{\partial t} + g\eta^{(1)} &= 0|_{z=0} \\ \frac{\partial \eta^{(1)}}{\partial t} - \frac{\partial \phi^{(1)}}{\partial z} &= 0|_{z=0}, \end{aligned} \tag{2.10}$$

where the superscript denotes the order of the term involved. By considering these boundary conditions, Airy (1845) derived the co-called linear wave theory. According to this theory, the free surface for a wave travelling under the effect of gravity is given by,

$$\eta^{(1)}(x, y, t) = a\cos(k_x x + k_y y - \omega t), \tag{2.11}$$

where ω is the circular wave frequency and $\mathbf{k} = (k_x, k_y)$ the wavenumber vector defined in the horizontal plane. The angle of the vector with respect to the x axis defines the direction of wave propagation, $\theta = tan^{-1}(k_y/k_x)$, and its magnitude, $k = |\mathbf{k}| = \sqrt{k_x^2 + k_y^2}$, is given by the linear dispersion relationship,

$$\omega^2 = gk\tanh(kd). \tag{2.12}$$

The derivation of this solution, on the basis of the boundary conditions of Equation 2.10, is based upon a linearisation of both the boundary conditions and, by consequence, the governing fluid equation representing mass continuity. In order for this to hold, it is necessary that the wave amplitude a is much smaller than both the wavelength, λ, and the water depth d; $a << \lambda$ and $a << d$.

The linear wave theory of Airy was derived for a monochromatic or regular wave train of angular frequency ω, propagating in the x-direction. Nonetheless, it provides the basis for representing a linear wavefield with multiple independent and freely propagating wave components having different frequencies and directions. This is achieved by simply superposing wave components of the form of Equation 2.11,

according to,

$$\eta^{(1)}(x,y,t) = \sum_{i=1}^{\infty} a_i \, cos(k_{x,i}x + k_{y,i}y - \omega_i t + \epsilon_i) \tag{2.13}$$

where the subscript i represents the i^{th} wave component and ϵ_i is an assigned phase angle; the latter randomly sampled from a uniform distribution in the interval $[0, 2\pi)$.

In defining the component amplitudes, two approaches are commonly adopted. The first, treats the amplitudes as deterministic quantities, given by,

$$a(\omega,\theta) = \sqrt{2S_{\eta\eta}(\omega,\theta)d\omega d\theta} \tag{2.14}$$

In contrast, the second approach treats the amplitudes as independent random variables, which are sampled from a Rayleigh distribution according to,

$$a(\omega,\theta) \sim R\Big(\sqrt{S_{\eta\eta}(\omega,\theta)d\omega d\theta}\Big) \tag{2.15}$$

where R(β) denotes the Rayleigh distribution with parameter β. This expression is derived on the basis that the following relationship should hold for the ensemble of wave amplitudes obtained from multiple realisations of Equation 2.13,

$$E[\frac{1}{2}a^2(\omega,\theta)] = S_{\eta\eta}(\omega,\theta)d\omega d\theta \tag{2.16}$$

where $E[\,\cdot\,]$ is the mean operator. Further discussion of the potential differences between these two approaches is provided in the context of stochastic wave modelling in Section 2.3. This linear representation of a wavefield is commonly referred to as Linear Random Wave Theory (LRWT). This provides the basis for the generation of waves in many experimental and numerical studies.

Second-Order Random Wave Theory (SORWT)

Nonlinear effects that can emerge when two freely propagating (first-order) wave components of different frequencies interact were considered by Longuet-Higgins & Stewart (1960). This solution followed the usual Taylor series expansion of the free-surface boundary conditions about the still water level, but retained terms up second-order. Using a perturbation series expansion method for the description of the various field variables, similarly to the Stokes (1847) wave solution for monochromatic wave trains, the free surface, pressure and velocity potential were expressed as a convergent

power series of the wave steepness, ak. Adopting this approach, the total free surface was expressed up to a second-order of wave steepness as,

$$\eta(x,y,t) = \eta^{(1)}(x,y,t) + \eta^{(2)}(x,y,t) + O((ak)^3) \tag{2.17}$$

where $\eta^{(1)}$ is the solution that satisfies the linear boundary conditions and $\eta^{(2)}$ the term added to $\eta^{(1)}$ so that the second-order boundary conditions are satisfied.

Within this solution, it was found that secondary (second-order) wave components, that ride upon the first-order ones, emerge. These second-order components, often referred to as second-order *bound* waves, are not freely propagating and they do not satisfy the linear dispersion equation. In particular, they consist of wave components at a *difference* frequency, $\omega_1 - \omega_2$, and at a *sum* frequency, $\omega_1 + \omega_2$; where ω_1 and ω_2 are the frequencies of the primary linear freely propagating wave components. The theory of Longuet-Higgins & Stewart (1960), applicable for collinear wave trains (or, in other words, waves travelling in the same direction) in arbitrary depth, was extended by Longuet-Higgins (1963) and Longuet-Higgins & Phillips (1962) to non-collinear waves (waves travelling in different directions).

Based on these theoretical developments, Sharma & Dean (1981) considered the interaction of multiple waves encountered in directional random seas, giving rise to the so-called Second-Order Random Wave Theory (SORWT). Within this theory the first-order part is given by LRWT, whereas the second-order contribution to the free surface, $\eta^{(2)}$, is given by the sum of interactions arising from all possible pairs of wave components:

$$\eta^{(2)}(x,y,t) = \frac{1}{4}\sum_{i=1}^{\infty}\sum_{j=1}^{\infty} a_i a_j \Big(A_{ij}^{-}\, cos(\psi_i - \psi_j) + A_{ij}^{+}\, cos(\psi_i + \psi_j) \Big) \tag{2.18}$$

with A^- and A^+ representing the second-order interaction kernels for the difference terms $(-)$ and sum terms $(+)$, respectively. Moreover, a_i and a_j are the amplitudes of the interacting pairs of the underlying linear wave components, and ψ_i and ψ_j the corresponding phases: $\psi_i = k_{x,i}x + k_{y,i}y - \omega_i t + \epsilon_i$.

From a physical point of view, the second-order difference terms are known to lead to a 'set-down' beneath wave groups containing large wave crests, as they are out of phase with the underlying linear process. In contrast, the second-order sum terms are in phase with the underlying linear process, leading to the increase and steepening

of large wave crests. However, they also induce a reduction (in magnitude) of the adjacent troughs. Moreover, the sum terms are responsible for the increase of the fluid velocities under large wave crests and the difference terms lead to the reduction of the fluid velocities lower in the water column. To this end, the difference terms are often interpreted as a return flow under large wave events that acts to balance the well-known Stoke's drift near the free surface.

The introduction of the second-order random wave theory has led to important advancements in understanding the nonlinearity of the waves encountered in both field and experimental observations of random sea-states; this is elaborated on in §2.3 in the context of stochastic wave modelling.

2.2.3 Higher-Order effects

Steady wave solution

Despite the improved description of waves provided by second-order theory, with an increase in wave steepness higher-order physics become increasingly more important.

For monochromatic waves in deep water, Stokes (1847) derived a third-order wave solution based again based on a small perturbation expansion, while Fenton (1985) extended it to fifth-order. The spatial profile within this solution, which is often referred to as *fifth-order Stoke's* solution, is given by,

$$\begin{aligned} k\eta(x) = {} & \epsilon\cos(kx) + \epsilon^2 B_{22}\cos(2kx) + \epsilon^3 B_{31}(\cos(kx) - \cos(3kx)) \\ & + \epsilon^4(B_{42}\cos(2kx) + B_{44}\cos(4kx)) \\ & + \epsilon^5(-(B_{53} + B_{55})\cos(kx) + B_{53}\cos(3kx) + B_{55}\cos(5kx)), \end{aligned} \tag{2.19}$$

where $\epsilon = kH/2$ is the wave steepness, with H the wave height, and the B coefficients are defined in Fenton (1985). Within this solution two important nonlinear effects emerge:

1. *Bound* wave contributions higher than second-order appear, the harmonic content of which matches the corresponding order of nonlinearity (or wave steepness). For example, the third-order bound contribution corresponds to a wave component of wavenumber $3k$, where k is the wavenumber of the primary freely propagating wave component.

2. The third and fifth-order contributions include *freely* propagating wave components of the primary (linear) wavenumber, k.

Moreover, at the third-order of the wave steepness and above, the dispersion of the freely propagating wave component is not only dictated by the effective water depth, kd, as in linear wave theory, but also by the wave steepness, ak. According to Stokes (1847), the third-order dispersion relation in deep water ($kd \to \infty$) is,

$$\omega^{(3)} = \omega^{(1)} \left(1 + \frac{1}{2} a^2 k^2\right) \tag{2.20}$$

where, $\omega^{(1)}$ is the linear frequency ($\omega^{(1)} = \sqrt{gk}$) and $\omega^{(3)}$ is the third-order result. This nonlinear change in frequency leads to an increase in the phase velocity or the speed of wave propagation; where $c = \omega/k$.

While the fifth-order Stokes solution offers an important contribution in understanding some important nonlinear effects that arise with increasing wave steepness, it fails to include the inherent unsteadiness encountered in random seas. Moreover, in trying to reproduce this solution in an experimental setting, one finds that this is not always possible. This is due to additional nonlinear effects that arise at a third-order of wave steepness and above and relate to the so-called *near-resonant* wave interactions. These are briefly reviewed as follows.

Resonant and near-resonant wave interactions

A *resonant* wave interaction occurs when $N-1$ wave components interact resonantly to transfer energy to a new, N^{th}, *freely* propagating wave component. In adopting this definition, the term *resonant* refers to the fact that, under such conditions, the wave motion has the mathematical form of a linear resonator. Unlike the non-resonant interactions (or the interactions that lead to bound wave components), the resonant interactions can lead to significant energy transfers among wave components and are responsible for the long-time evolution of the ocean wave spectra as described by Hasselmann (1962).

In order for these interactions to occur, the wavenumbers and frequencies of the

interacting wave components need to satisfy the following conditions,

$$\begin{aligned} \mathbf{k_i} &= \sum_{j=0}^{N-2} s_j \mathbf{k_j} \\ \omega_i &= \sum_{j=0}^{N-2} s_j \omega_j \end{aligned} \tag{2.21}$$

where $s_j = \pm 1$ and the wave component denoted with i refers to the free wave component to which energy is transferred. Moreover, in the above expressions the wavenumbers and frequencies are linked through the linear dispersion equation (Equation 2.12).

For the case of $N = 3$, the resonant *triad* interactions are defined by,

$$\mathbf{k_0} = \mathbf{k_1} \pm \mathbf{k_2} \quad \omega_0 = \omega_1 \pm \omega_2 \tag{2.22}$$

This type of resonance becomes relevant only in the shallow water limit in which $\tanh(kd) \to kd$ and $\omega^2 = k^2 gd$. To this end, it has been shown by Phillips (1960) that resonant triad interactions for deep-water gravity waves are not possible.

For $N = 4$ the interacting wave components are referred to as resonant *quartets* and need to satisfy,

$$\mathbf{k_0} + \mathbf{k_1} = \mathbf{k_2} + \mathbf{k_3} \quad \omega_0 + \omega_1 = \omega_2 + \omega_3 \tag{2.23}$$

The special case for which two of the wave components have the same wavenumber and frequency, i.e. $\mathbf{k_0} = \mathbf{k_1}$ and $\omega_0 = \omega_1$ has been studied by Phillips (1960). This particular case refers to the situation where one freely propagating wave component (of wavenumber $\mathbf{k_2}$) interacts resonantly with the second-order bound contribution of another component (of wavenumber $2\mathbf{k_0}$) to produce a fourth freely propagating wave (of wavenumber $\mathbf{k_3} = 2\mathbf{k_0} - \mathbf{k_2}$). The topology of the interacting wave components is depicted in the (k_x, k_y) domain by the so-called *'figure-8'* resonance loop. This is shown in Figure 2.1.

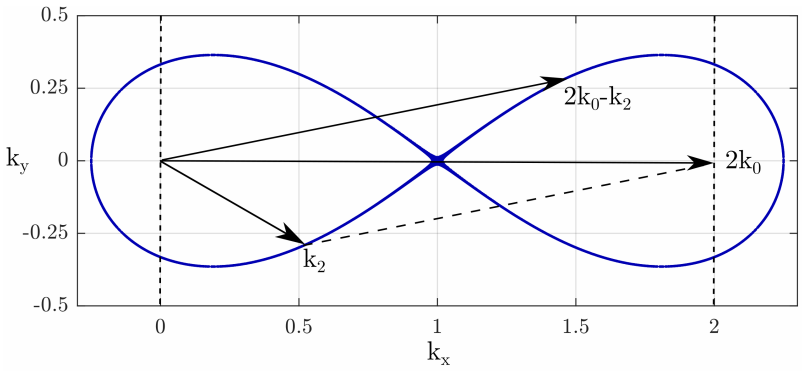


Figure 2.1: The resonance loop of Phillips (1960) in the (k_x, k_y) domain, where all wavevectors have been normalised by the magnitude of the primary wavenumber, $|\mathbf{k_0}|$. In this resonance loop, $\mathbf{k_1} = \mathbf{k_0}$ and energy is transferred to the wave component $\mathbf{k_3} = 2\mathbf{k_0} - \mathbf{k_2}$.

.

As such, this type of interactions can lead to directional energy transfers, which are often linked to the broadening of angular spreading above the spectral peak in ocean wave spectra (see, for example, Young et al. 1995, Ewans 1998).

Notably, the change in the wave speed of monochromatic waves arising at a third-order of wave steepness (as discussed previously in the context of the third-order Stoke's solution), is a manifestation of the effect of resonance for the special case of self-interaction; for $\mathbf{k_0} = \mathbf{k_1} = \mathbf{k_2} = \mathbf{k_3}$.

Benjamin & Feir (1967) was first to study the phenomenon that when a steep regular wave train (of frequency ω_0) is generated experimentally in deep water, it starts to disintegrate into an irregular waveform with a wider energy spectrum with distance from the wavemaker. Unlike an exact numerical simulation of a steep regular wave, the experimental generation of such a wave train is often accompanied by a small amplitude modulation due to imperfections in the wavemaking process. This small amplitude modulation effectively transfers a small proportion of the energy to wave components adjacent to the primary wave at frequencies $\omega_0(1 \pm \delta)$; these are often referred to as *sidebands*. It was found that this small energy 'leakage' was responsible for triggering the phenomenon of *near-resonance*. In this situation, the four-wave resonant conditions of Equation 2.23 are approximately, but not exactly satisfied.

The work of Benjamin & Feir (1967) showed that a necessary condition for triggering this instability, often referred to as modulational instability or Benjamin-Feir

instability, of a primary wave due to collinear disturbances (sidebands) is,

$$0 < \delta < \sqrt{2}ka, \tag{2.24}$$

where k and a are the wavenumber and amplitude of the primary wave, which together give a measure for the wave steepness. Moreover, this instability does not emerge immediately, but rather develops over a timescale of $O(1/(\omega_0 k^2 a^2))$ [1]. This required evolution time is much faster than the $O(1/(\omega_0 k^4 a^4))$ timescale of the Hasselmann-type (resonant) interactions (Hasselmann, 1962).

The Benjamin-Feir instability has attracted extensive research attention (see Yuen & Lake 1980 and Hammack & Henderson 1993). The reason for this was that the maximum elevation of a modulationally unstable wave train, under certain conditions, can reach as much as three times the initial wave amplitude or more (Henderson et al. 1999, Dysthe & Trulsen 1999, Chabchoub et al. 2012); owing to the dominance of nonlinear dispersion over (linear) frequency dispersion. Hence, the question as to whether this nonlinear process could be responsible for the formation of extreme waves in the ocean has been extensively considered.

The work of Benjamin & Feir (1967) was extended by Phillips (1967) to non-collinear disturbances. This work showed that the same type of instability occurs for wavevectors laying at the vicinity of the 'figure-8' resonance loop towards its interior. A corollary of this analysis is the well-known result that the instability ceases to exist for disturbances forming an angle greater than 35.26°. This is the maximum angle of vector $\mathbf{k}_2$ for which resonance can be achieved within the resonance loop and the angle at which the relative signs of the dispersive and the nonlinear terms change in the Non-Linear Shröndiguer equation (Yuen & Lake, 1982).

Considering a wave propagating in an arbitrary water depth, analytical considerations of Benjamin (1967) and Whitham (1974) have shown that the instability occurring in deep water due to *collinear* perturbations ceases to exist for effective water depths below $kd < 1.363$. Nonetheless, stability analysis for *non-collinear* perturbations has revealed that instabilities due to four-wave near-resonant interactions are possible for $kd < 1.363$ (see example Hayes 1973, McLean 1982a, Slunyaev et al. 2002). This result was confirmed experimentally by Toffoli et al. (2013).

[1] or equivalently a distance from the wavemaker $c_g/(\omega k^2 a^2)$, where c_g is the group velocity

These early stability analyses encouraged researchers to explore whether the above nonlinear effects are characteristic only in a deterministic wave setting, or if the same effects can can be triggered random sea-states. In the first attempts on this matter, the analytical works of Alber & Saffman (1978), Alber (1978), Crawford et al. (1980) and Janssen (1983) revealed that the effect of randomness has a stabilising effect on the modulational instability in deep water. However, it was shown that modulational instability still remained relevant for both collinear and transverse perturbations; with the intensity of the phenomenon being reduced due to the underlying randomness (Crawford et al., 1980).

In terms of numerically modelling these interactions, the so-called Zakharov equation (Zakharov, 1968) is often employed. This equation has been derived by Krasitskii (1994) to a fourth-order in wave steepness, and its numerical implementation is discussed in Annenkov & Shrira (2001). The Zakharov equation is particularly insightful as it separates the free-wave evolution due to resonance or near-resonance from the bound or static interactions. Following the compact notation of Krasitskii (1994), the equation for the free-wave evolution arising at third-order of the wave steepness is given by,

$$i\frac{\partial b_0}{\partial t} = \omega_0 b_0 + \int T_{0,1,2,3} b_1^* b_2 b_3 \delta_{0+1-2-3} d\mathbf{k}_{123} \tag{2.25}$$

where, $T_{0,1,2,3}$ is the resonant interaction kernel for four-wave interactions and δ is the Dirac delta function with $\delta_{0+1-2-3} = \delta(\mathbf{k_0} + \mathbf{k_1} - \mathbf{k_2} - \mathbf{k_3})$ and $d\mathbf{k}_{123} = d\mathbf{k}_1 d\mathbf{k}_2 d\mathbf{k}_3$. Moreover, the variable b_i relates to the complex amplitude, a_i, of the free wave with wavenumber k_i, according to, $b_i = (\omega_i/2g)^{-1/2} a_i$.

The magnitude of the resonant interaction kernel is of particular interest as it gives an insight into the intensity of the resonant wave interactions. In the original derivation of Krasitskii (1994), finite-depth effects were not included appropriately. This was discovered and resolved much latter by Janssen & Onorato (2007) (see also Stiassnie & Gramstad 2009 and Gramstad 2014), who provided a correct version for the self-interaction case ($\mathbf{k_0} = \mathbf{k_1} = \mathbf{k_2} = \mathbf{k_3}$).

Therefore, it is instructive, to explore the variation of the resonant interaction kernel of Janssen & Onorato (2007) with effective water depth; this variation being presented in Figure 2.2.

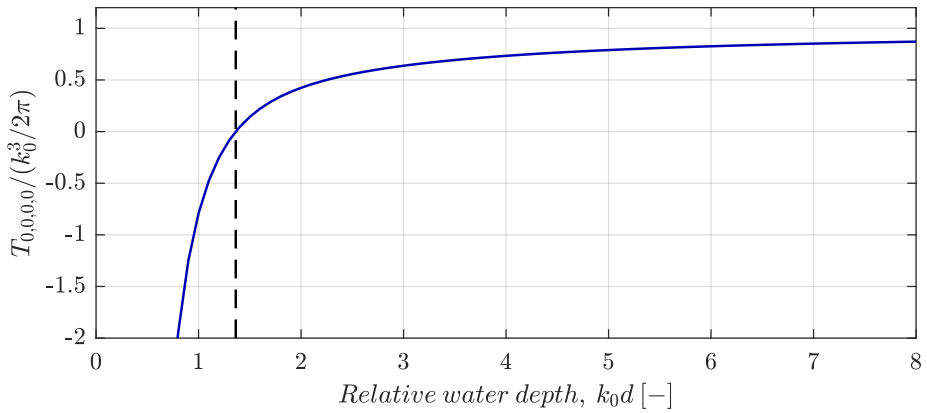


Figure 2.2: Variation of the resonant interaction kernel, $T_{0,0,0,0}$, of Janssen & Onorato (2007) with effective water depth. The kernel is normalised with respect to the deep-water value of $k_0^3/2\pi$, while the vertical black dashed line refers to $k_0 d = 1.363$.

.

From a physical perspective, when narrow-banded wave trains are concerned a positive value of the kernel leads to focusing of the wave energy, whereas a negative value leads to defocusing. Specifically, energy focusing is associated with increased free surface elevations when compared to linear theory. This increase is driven by energy transfers between freely propagating waves accompanied by an increase in the phase velocity of the free waves when they constructively interfere to form large wave events. This nonlinear process has already been described in the context of the Benjamin-Feir instability. In the defocusing case, nonlinear dispersion is such that it opposes the frequency dispersion. This reduces the ability of the free wave components to constructively interfere, and hence leads to reduced elevations. In observing Figure 2.2, the kernel changes sign at $kd = 1.363$. This is in accordance with previous analysis on the relation between dispersive and nonlinear terms using the two-dimensional Nonlinear Schrödinger equation and it is in agreement with the earlier stability analysis of Benjamin (1967) and Whitham (1974).

To put the above considerations into a practical perspective, it is worth noting that the resonant interaction kernel of Janssen & Onorato (2007) provides the basis for the freak wave warning system within the ECMFW (European Centre for Medium-range Weather Forecasts) weather forecasting modelling tool (see Janssen & Bidlot 2009, Janssen 2016).

The above theoretical considerations provide an important insight into the intensity of the near-resonant interactions in both a deterministic and an (idealised) random wave context involving a narrow spectral bandwidth. Indeed, this review has

highlighted that elementary wave interactions crucially depend upon the steepness, spectral bandwidth, directionality and effective water depth. As such, the extent to which these interactions affect the magnitude of the largest waves in realistic sea-states remains an open question. This is further reviewed in Chapters 3 and 4.

2.2.4 Overview of higher-order numerical wave modelling

Three main modelling approaches have traditionally been considered when modelling effects beyond second-order in random sea-states in both deep and transitional water depths. These are:

1. the Zakharov equation
2. the nonlinear Shröndiguer-type equations
3. the higher-order spectral methods

The Zakharov equation has been proven useful in studying elementary wave interactions (see example Stiassnie & Shemer 1987 and Annenkov & Shrira 2006) and the evolution of broad-banded deterministic wave groups (see Gibson & Swan 2007). However, its application to random sea-states is limited due to its high computational cost. In fact, Hadjigeorgiou et al. (2017) was the first to apply the numerical implementation of Annenkov & Shrira (2001) (including third-order resonant and second-order bound terms) to obtain crest-height statistics in uni-directional JONSWAP sea-states. However, with the computational cost of the solution scaling with order $O(N^4)$ (N being the number of wave components), its application to directionally spread sea-states was limited.

The simulation of directional random wavefields in deep water was first tackled numerically by Dysthe et al. (2003). In doing so, they used different versions of nonlinear Shröndiguer-type equations, including the bandwidth-modified version of Dysthe (1979) and Trulsen & Dysthe (1996) correct to fourth-order in wave steepness; referred to as BMNLS equation. While this first investigation covered Gaussian-shaped spectra in both frequency and direction, a subsequent investigation by Socquet-Juglard et al. (2005) studied the case of realistic JONSWAP spectra. Nonetheless, latter comparisons with experimental data indicated that the BMNLS equation can lead to significant underestimation of the largest crest heights arising in random sea-states (Xiao et al. 2013).

Regarding the numerical modelling in finite-depth conditions, the directional equivalent to the Non-Linear Shröndiguer equation is the so-called Davey-Stewartson (Davey & Stewartson, 1974) system of equations. This model essentially offers a special treatment for the mean flow and the mean free surface, relevant to finite depth conditions. Nonetheless, it still suffers from the typical bandwidth restrictions of the original Nonlinear Shröndiguer equation. Hence, it is not further considered.

Finally, the so-called Higher-Order Spectral Method (HOSM), which was derived independently by West et al. (1987) and Dommermuth & Yue (1987), is becoming increasingly popular in studying the evolution and nonlinearity that arises in random sea-states. This method, unlike the other types of models mentioned above, combines the following advantages,

1. no frequency or directional bandwidth limitations
2. modelling of both uni-directional and directionally spread sea-states
3. fully nonlinear free surface
4. computational efficiency (computational requirements scale according to $N \log_2 N$)
5. applicable to both deep and transitional water depths

Based on the above, HOSM is deemed the most appropriate modelling tool for the present analysis. To this end, the open-source numerical implementation of HOSM (West et al., 1987) provided by Ducrozet et al. (2016) is employed. However, for the purposes of the present investigation, the code has been modified to include user-defined inputs that are not restricted by the predefined options of the original code. In the subsequent sections, the HOSM model is briefly introduced, providing the key points of its formulation.

2.2.5 Higher-Order Spectral Method (HOSM)

The starting point for the derivation of HOSM are the KFSBC and DFSBC (in Section 2.2.1). Following Zakharov (1968), these are expressed in terms of the single valued free surface $\eta(x, y, t)$ and the potential at the free surface, $\phi^s(x, y, t) = \phi(x, y, \eta, t)$, according to:

$$\frac{\partial \phi^s}{\partial t} = -g\eta - \frac{1}{2}|\nabla_h \phi^s|^2 + \frac{1}{2}\Big(1 + |\nabla_h \eta|^2\Big)\Big(\frac{\partial \phi}{\partial z}\Big)^2 \tag{2.26}$$

$$\frac{\partial \eta}{\partial t} = \left(1 + |\nabla_h \eta|^2\right) \frac{\partial \phi}{\partial z} - \nabla_h \phi^s \cdot \nabla_h \eta \tag{2.27}$$

and applied on $z = \eta(x, y, t)$. In the above expressions ∇_h is the horizontal gradient operator $(\frac{\partial}{\partial x}, \frac{\partial}{\partial y})$ and $\frac{\partial \phi}{\partial z}|_{z=\eta}$ is the vertical velocity, which is the only non-free-surface quantity. The challenge in evaluating the evolution of the free surface lies in the fact that $\frac{\partial \phi}{\partial z}$ needs to be expressed in terms of the potential ϕ.

To tackle this, the potential is expressed as a series expansion about the mean water level, $z = 0$, as

$$\phi(x, y, t) = \sum_{m=1}^{M} \phi^{(m)}(x, y, t) \tag{2.28}$$

Based on this, the vertical velocity, $\frac{\partial \phi}{\partial z}$, is expanded in a similar way by simply differentiating Equation 2.28.

The implementation of Ducrozet et al. (2016) follows the approach of West et al. (1987), which keeps consistent ordering with respect to steepness for $\phi^{(m)}$; unlike the version of Dommermuth & Yue (1987). Using this approach, the elements, $\phi^{(m)}(x, y, t)$, of the above expansion are given by,

$$\begin{aligned}
\phi^{(1)}(x, y, 0, t) &= \phi^s(x, y, t) \\
\phi^{(2)}(x, y, 0, t) &= -\eta \frac{\partial \phi^{(1)}}{\partial z}(x, y, 0, t) \\
&\vdots \\
\phi^{(m)}(x, y, 0, t) &= -\sum_{k=1}^{m-1} \frac{\eta^k}{k!} \frac{\partial^k \phi^{(m-k)}}{\partial z^k}(x, y, 0, t)
\end{aligned} \tag{2.29}$$

where $\phi^{(m)}$ is of order m^{th} in steepness and M represents the order of nonlinearity. Interestingly, Onorato et al. (2007) has recovered the third-order Zakharov equation (Equation 2.25) analytically using $M = 3$, as both approaches are based on the Hamiltonian formalism for $\phi^s(x, y, t)$ and $\eta(x, y, t)$.

Based on the above expansions the original Dirichlet problem of Equations 2.26 and 2.27 for the complex boundary $z = \eta(x, y, t)$ is divided into M simpler Dirichlet subproblems for $z = 0$, which are numerically more tractable. Moreover, by introducing periodic lateral boundary conditions, the velocity potential and the free surface can be expressed as Fourier series of basis functions that satisfy the Laplace equation and the flat bed boundary conditions. Based on this later expansion, a Fast Fourier Transform is used to accelerate the numerical procedure.

Setting initial conditions for $\phi^s(x, y, t = 0)$ and $\eta(x, y, t = 0)$ the solution is time-marched using a fourth-order Runge-Kutta scheme with adaptive time-step. Thus, the HOSM scheme is a pseudo-spectral method, as the free-surface quantities are time-marched in the physical space, while the solution is obtained in the Fourier space. The solution for the free surface is then expressed as,

$$\eta(x, y, t) = \frac{1}{2}\Big[\sum_{l}^{N_x}\sum_{n}^{N_y} A_{ln}(t)e^{i(k_l x + k_n y)} + c.c.\Big] \tag{2.30}$$

where, $A_{ln}(t)$ are the time-dependent complex amplitudes, corresponding to a rectangular grid of wavenumbers $\mathbf{k} = (k_l, k_n) = (2\pi l/L_x, 2\pi n/L_y)$, ($L_x$,$L_y$) are the dimensions of the computational domain, and *c.c.* is the complex conjugate of the preceding term.

It is noted that the present investigation is restricted to sea-states of mild severity that are not dominated by the effects of wave breaking. As such, no energy dissipation mechanism within HOSM was employed to account for wave breaking.

While it should bee stressed out that throughout the course of the present study full dealiasing has been adopted in eliminating the numerical convergence issues when moving from the Fourier space to the physical space. More information on the HOSM scheme, including the dealiasing methodology, can be found in the following complementary sources: Tanaka (2001), Bonnefoy et al. (2010) and Ducrozet et al. (2016).

2.2.6 Harmonic separation method within HOSM

A drawback of HOSM is that the role of the nonlinear interactions of increasing order cannot directly be identified. Hence, the relative importance of the nonlinear interactions during the formation of extreme waves in random wavefields cannot be identified. To overcome this drawback, the phase manipulation method introduced by Fitzgerald et al. (2014) is employed.

Unlike previous applications of the method in the context of deterministic wave groups (Barratt et al., 2020), the method is to be applied in a random sea-state setting. To this end, it seeks to separate harmonics arising from wave components that are well separated in the frequency and wavenumber domain. As such, appropriate validation must be provided.

Methodology

The key idea behind this method is that by introducing several phase shifts to the input wave signal, the resulting measured nonlinear free-surface records (for different phase shifts) can be combined to produce separate signals of different nonlinear harmonic contributions. To this end, it can be viewed as an extension of the original two-phase manipulation method of Baldock et al. (1996), which was introduced to separate odd from even harmonics.

In applying this methodology to the nonlinear free surface, the different harmonic contributions can be viewed in a simple way by employing a Stokes solution up to 4th order, expressed as,

$$\begin{aligned}\eta(\psi) =&(a^2A_{20} + a^4A_{40}) + (a + a^3A_{31})cos(\psi) + (a^2A_{22} + a^4A_{42})cos(2\psi)\\ &+a^3A_{33}cos(3\psi) + a^4A_{44}cos(4\psi),\end{aligned} \tag{2.31}$$

where the first term in the expression represents a set-down term relevant to finite depth conditions, a is the linear input amplitude and the coefficients A are constants. Finally, $\psi = kx+\epsilon$ represents the phasing of the linear input wave and ϵ is the phase shift that is altered between simulations with values of $\epsilon = 0$, 90°, 180° and 270°.

By denoting the input free-surface records for different phase shifts, ϵ, with η_ϵ, the different harmonic contributions are given by the following algebraic relationships:

$$\eta^{1^{st}} = (a + a^3A_{31} + O(a^5))cos(\psi) = \frac{1}{4}(\eta_0 + \eta^H_{90} - \eta_{180} + \eta^H_{270}) \tag{2.32}$$

$$\eta^{2^{nd}} = (a^2A_{22} + a^4A_{42} + O(a^6))cos(2\psi) = \frac{1}{4}(\eta_0 - \eta_{90} + \eta_{180} - \eta_{270}) \tag{2.33}$$

$$\eta^{3^{nd}} = (a^3A_{33} + O(a^5))cos(3\psi) = \frac{1}{4}(\eta_0 + \eta^H_{90} - \eta_{180} - \eta^H_{270}) \tag{2.34}$$

$$\eta^{4^{th}} + \eta^{0^{th}} = a^2A_{20} + a^4A_{40} + a^4A_{44}cos(4\psi) + O(a^6)) = \frac{1}{4}(\eta_0 + \eta_{90} + \eta_{180} + \eta_{270}) \tag{2.35}$$

In the above equations, the superscript H refers to the Hilbert transform, which is applied to the spatially periodic free surface. It is noted that the 4^{th} and 0^{th} harmonics are given together using this harmonic separation method. When this method is applied to multi-chromatic waves, the separation of these two harmonic contributions is not straightforward, especially for broad-banded conditions. As in this case, their frequency range may overlap.

To overcome this difficulty, the separation of the 4^{th} and 0^{th} harmonics is based on a complimentary method to Fitzgerald et al. (2014), presented by Hann et al. (2014). This latter method considers 12 phase shifts of the input conditions with an increment of 30° starting from 0 and ending with 330°. The 0^{th} harmonic is then given by the following expression,

$$\eta^{0^{th}} = a^2 A_{20} + a^4 A_{40} = \frac{1}{12}(\eta_0 + \eta_{30} + \ldots + \eta_{300} + \eta_{330}) \tag{2.36}$$

Whereas to obtain the $4th$ harmonic, Equation 2.36 is subtracted from Equation 2.35. It should be noted that the term 'harmonic' contribution follows from the above monochromatic wave considerations and indicates contributions to the total free surface arising in different frequencies (and wavenumbers), which are affected by different types of nonlinear interactions.

Given that a mathematical proof of the applicability of this method in random sea-states is cumbersome, here it is verified using direct numerical simulations of a random sea-state. However, before proceeding to the validation of the method, it is important to distinguish which nonlinear contributions relevant to multi-chromatic wave interactions are expected to appear in the different harmonics of Equations 2.32-2.35:

1. The first harmonic ($\eta^{1^{st}}$) represents freely propagating waves that are naturally affected by third-order quartet resonant and near-resonant wave interactions; the former satisfying exactly the resonant conditions of Equation 2.21 and the latter nearly but not exactly.

2. The zeroth and second harmonics ($\eta^{0^{th}}$, $\eta^{2^{nd}}$) include the second-order in wave steepness bound-wave contributions representing the difference and sum terms, respectively, of Sharma & Dean (1981).

3. The third and fourth harmonics ($\eta^{3^{rd}}$, $\eta^{4^{th}}$) include bound-wave contributions of third and fourth-order in wave steepness, respectively.

Additionally, the even harmonics (second or fourth) could also contain freely propagating waves arising from fourth-order (quintet) resonant and near-resonant wave interactions. While the zeroth harmonic can theoretically include freely propagating waves arising from triad resonant and near-resonant interactions.

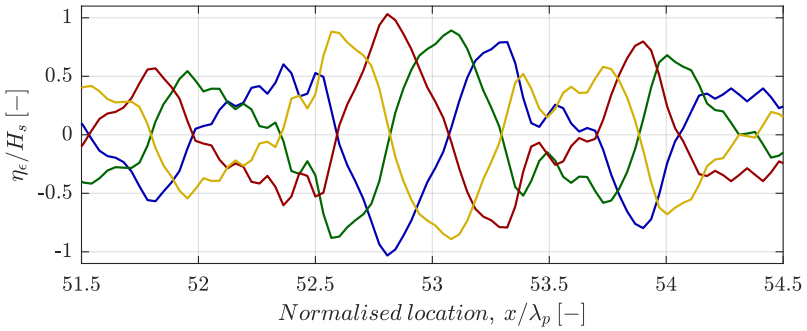


Figure 2.3: Segments of initial (input) free-surface traces (η_ϵ) having the same amplitude spectrum, but different phase shifts of ( ) 0°, ( ) 90°, ( ) 180° and ( ) 270°. The x-axis is normalised by the wavelength of the spectral peak frequency, λ_p, and the y-axis by the significant wave height H_s.

To illustrate the process of extracting the various nonlinear harmonics, a segment of initial (input) free-surface space traces defined by the same amplitude spectrum, but supplied with four different phase shifts is shown in Figure 2.3.

The various harmonic contributions around a large wave event are shown in Figure 2.4. As expected, the zeroth harmonic, representing frequency-difference terms, acts to reduce the total free surface and the intensity of the rest of the harmonics decreases with increasing nonlinear order.

Validation

To validate the phase manipulation method, two approaches are followed:

(1) The ensemble-averaged spectra of the zeroth and second harmonics arising from multiple realisations of a sea-state within HOSM are compared to the spectra of the corresponding second-order terms obtained using SORWT. To achieve such comparisons, the sea-state steepness is kept small ($\frac{1}{2}H_s k_p = 0.02$) such that (i) the free-wave evolution due to near-resonant effects is minimal, and (ii) fourth-order effects in the HOSM harmonics are entirely absent. To ensure like-to-like comparisons, the same set of linear inputs are used both within HOSM and SORWT.

(2) For a much steeper case of $\frac{1}{2}H_s k_p = 0.105$, the energy content of each harmonic in the frequency-wavenumber domain (obtained using a 2D-FFT of the entire space-time record) is compared against theoretical dispersion relationships. These relationships refer to: (i) the linear dispersion equation of Equation 2.12 for the first harmonic, and (ii) the dispersion relationships relevant to bound waves of a monochromatic wave train for the rest of the harmonics. As mentioned earlier,

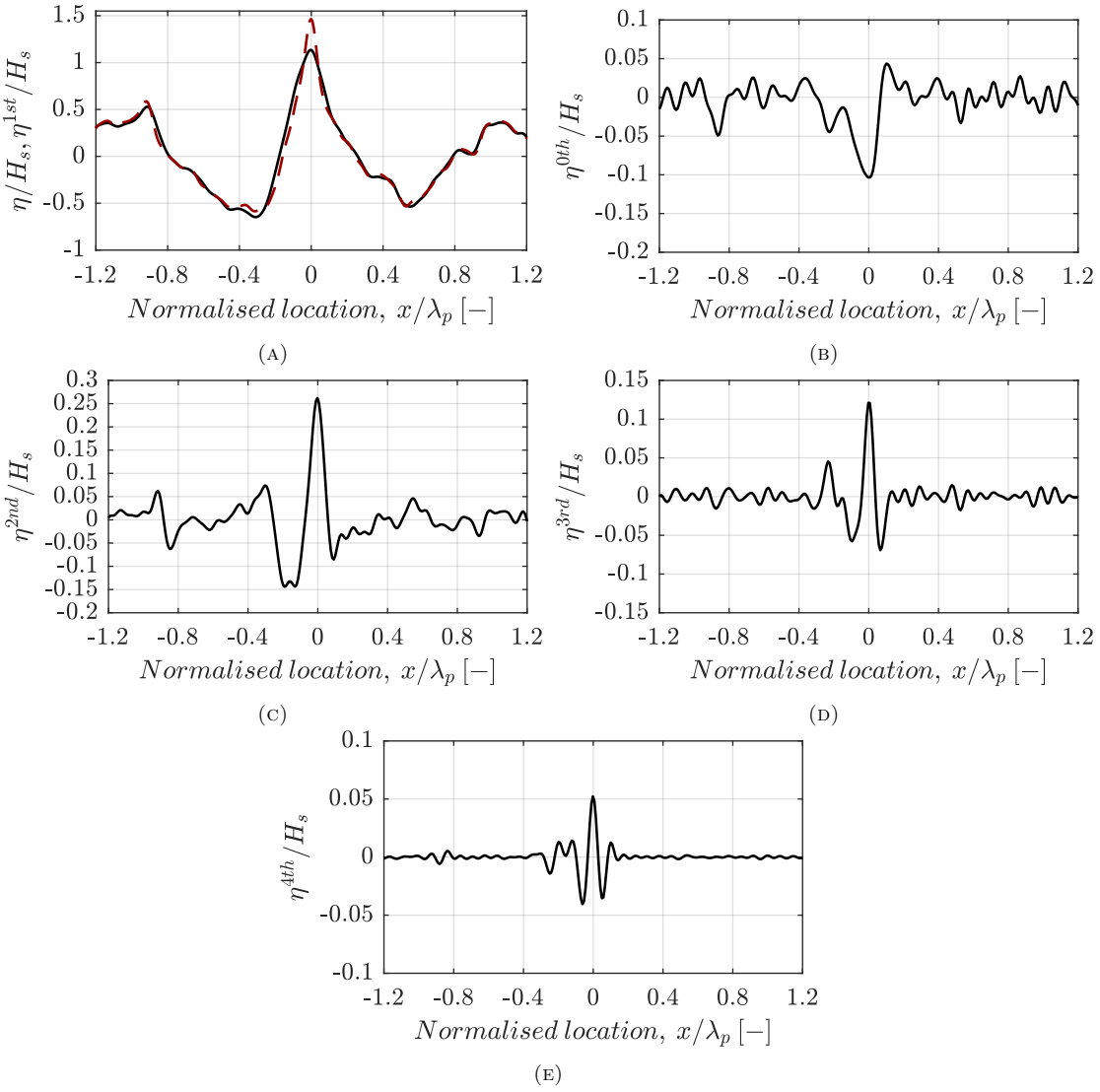
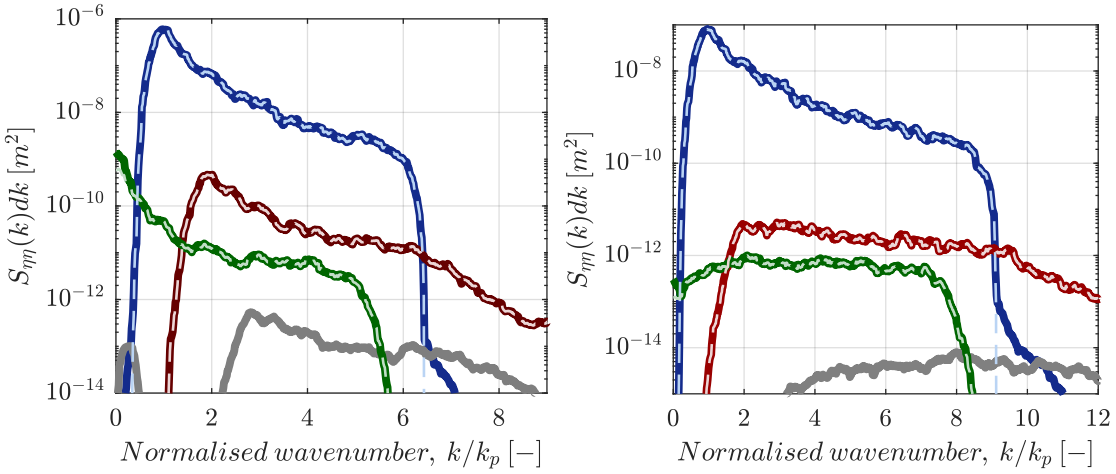


Figure 2.4: Spatial traces of the nonlinear harmonic contributions around a large wave event arising from the realisation of a JONSWAP ($\gamma = 2.5$) sea-state in a relative water depth of $k_p d = 5.03$ with $\frac{1}{2} H_s k_p = 0.105$. Sub-figure (A) presents the total free surface (η) denoted with (— —) along with the first harmonic (η^{1st}) denoted with (——). Sub-figures (B), (C), (D) and (E) present the zeroth ($\eta^{0^{th}}$), second ($\eta^{2^{nd}}$), third ($\eta^{3^{rd}}$) and fourth ($\eta^{4^{th}}$) harmonics respectively. In all sub-figures the x-axis is normalised by the wavelength of the spectral peak frequency, λ_p, and the y-axis by the significant wave height, H_s.



(A) (B)

Figure 2.5: Ensemble-averaged spectra of nonlinear contributions for JONSWAP ($\gamma = 2.5$) sea-states with steepness $\frac{1}{2}H_s k_p = 0.02$ and relative water depths of (A) $k_p d = 0.87$ and (B) $k_p d = 5.03$. Comparison between second-order spectra arising from HOSM and SORWT: ( ) for the linear inputs to both HOSM and SORWT, (/) for second-order difference/sum terms from SORWT, (/ / /) for the first ($\eta^{1^{st}}$), second ($\eta^{2^{nd}}$), zeroth ($\eta^{0^{th}}$) and third ($\eta^{3^{rd}}$) harmonics, respectively, arising from HOSM simulations at $t = 55T_p$. It is noted that the third harmonic is added for completeness, showing that it is indeed negligible.

bound waves ride upon the freely propagating waves and, hence, they travel faster than a free wave of the same wavenumber. Therefore, in a monochromatic setting, the phase speed of a bound wave is given by $c_n = n\omega/k$. Where n is the order of nonlinearity, and ω and k are the frequency and wavenumber of the underlying free wave, respectively. Moreover, based on the same reasoning, the zeroth harmonic contribution, containing frequency-difference terms, should travel slower than what linear theory predicts.

It is noted that the harmonic contributions within HOSM are not expected to satisfy exactly the aforementioned dispersion relationships, as the underlying free wave components are broad-banded. Nonetheless, the comparisons should reflect that the dispersion properties of each harmonic are different to the rest of the harmonics and, more importantly, that there is no unexpected free-wave energy in the bound harmonics.

In providing the required validations, JONSWAP wave spectra have been employed with $\gamma = 2.5$ in both deep ($k_p d = 5.03$) and transitional ($k_p d = 0.87$) water depth, covering the full range of effective water depths considered in the present thesis. The results for the validation point (1) above are shown in Figure 2.5. This demonstrates

that the second-order bound-wave spectra within HOSM are in excellent agreement with the ones obtained using SORWT.

Moreover, regarding validation-point (2), the results are presented in Figures 2.6 and 2.7, for $k_p d = 5.03$ and $k_p d = 0.87$ respectively. It is observed that the energy of each harmonic occupies a different area in the frequency-wavenumber space. This area is concentrated around the corresponding 'dispersion' line defined above for monochromatic waves. As such, the performance of the phase manipulation method appears correct.

It should be mentioned that in the deep-water case some small proportion of the energy of the zeroth harmonic is observed on the linear dispersion line (Figure 2.6 (C)). As mentioned above, if fourth-order quintet interactions are present, these would be included in the even harmonics. This explains the observation and is in line with earlier results presented by Gibson & Swan (2007) on the fully nonlinear evolution of deterministic wave groups in deep water. To this end, it should be stressed that a nonlinearity parameter $M = 5$ was adopted allowing for quintet interactions to be modelled. Moreover, further increase in the nonlinearity parameter yielded identical results.

Similarly, it is noted that a small proportion of energy of the third harmonic (Figure 2.6(D)) is located below the linear dispersion relationship. This can be explained by the fact that in a broad-band setting, third-order bound terms can include harmonics in difference frequencies ($\omega_1 - \omega_2 - \omega_3$) of the interacting primary wave components ($\omega_1, \omega_2, \omega_3$) as explained in Madsen & Fuhrman (2012). Specifically, three interacting components of frequencies in the range $\omega_1 \in [3, 3.5]\omega_p$, $\omega_2 \in [0.5, 1.0]\omega_p$ and $\omega_3 \in [0, 0.5]\omega_p$ cover the frequency-wavenumber region where slowly propagating energy is observed. It is noted that these components were not observed in Gibson & Swan (2007), presumably due to the reduced spectral bandwidth. To verify this further, the simulation of a narrower-banded spectrum ($\gamma = 5$) revealed a substantial reduction in these components.

2.3 Stochastic wave modelling

Having established the wave modelling tools appropriate for the calculation of random sea-state simulations, the remainder of this chapter focuses on the statistical

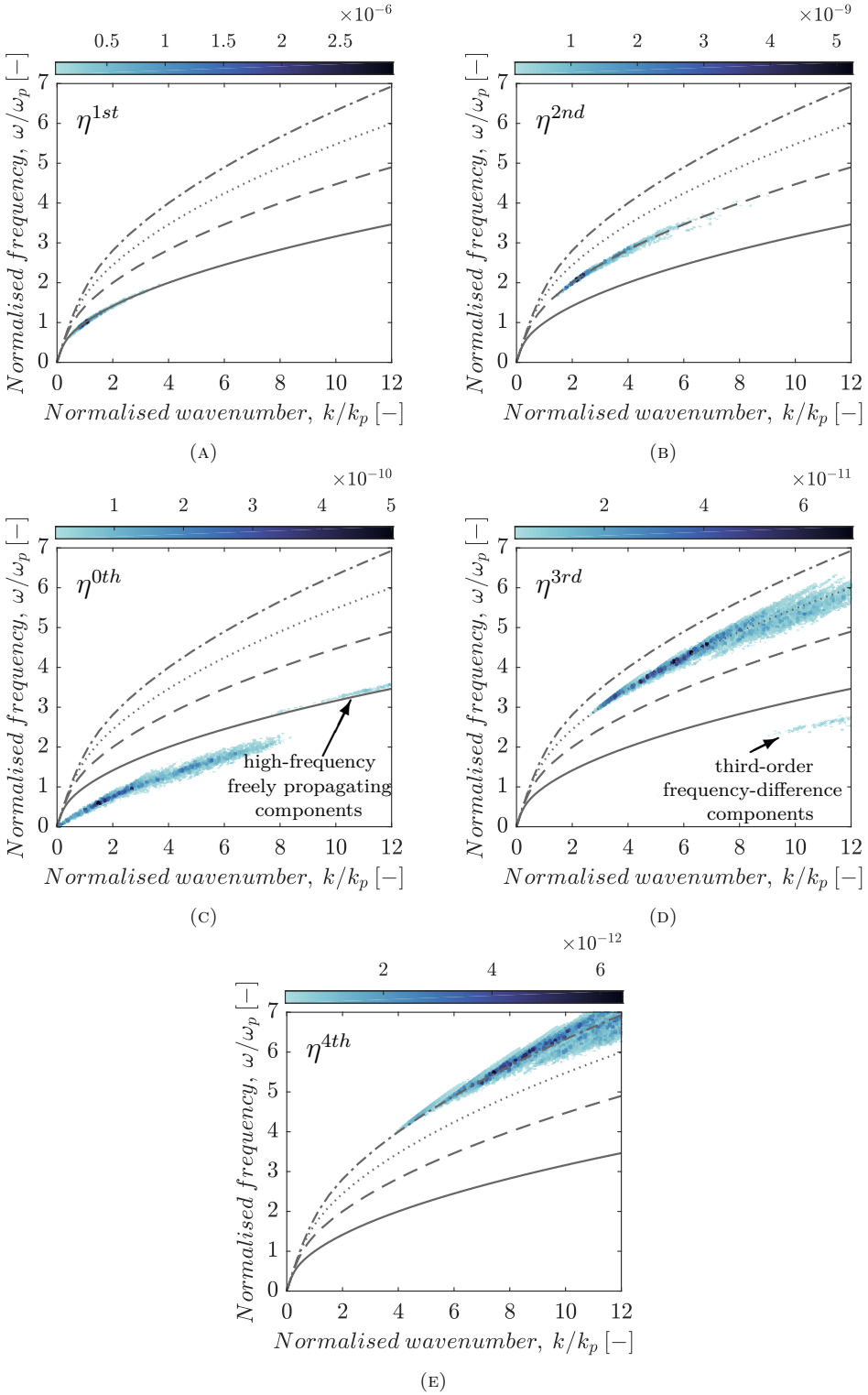


Figure 2.6: Contour plot of the spectral energy ($\frac{1}{2}a^2$) of the extracted harmonic contributions arising in a JONSWAP ($\gamma = 2.5$) sea-state of $\frac{1}{2}H_s k_p = 0.105$ and $k_p d = 5.03$: (A) first ($\eta^{1^{st}}$), (B) second ($\eta^{2^{nd}}$), (C) zeroth ($\eta^{0^{th}}$), (D) third ($\eta^{3^{rd}}$), and (E) fourth ($\eta^{4^{th}}$) harmonic contributions. The line (——) corresponds to the linear dispersion equation, while the lines (— — / · · · · / — · —) correspond to multiples of the dispersion relation, with $n = 2, 3$ and 4 respectively.

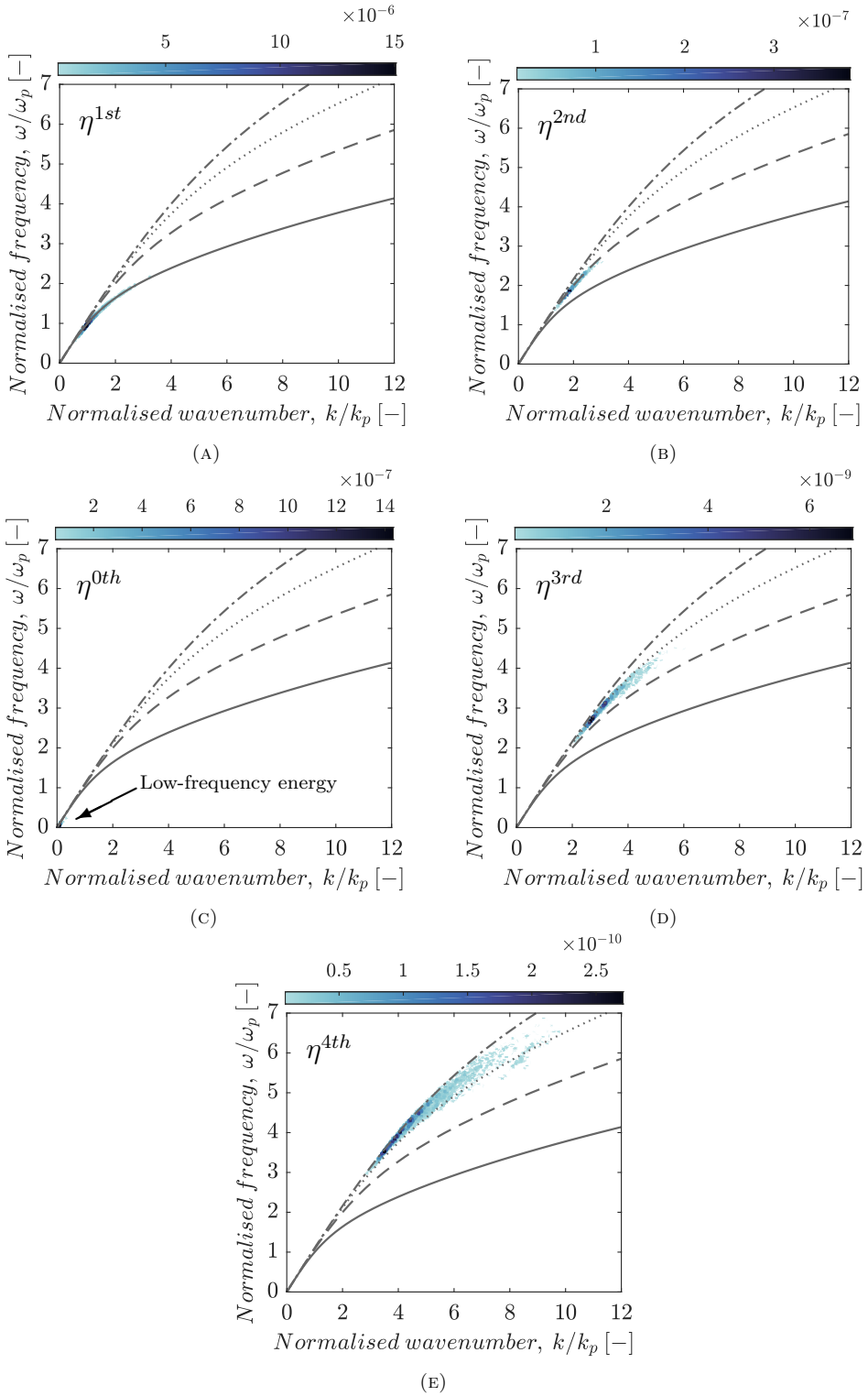


Figure 2.7: As Figure 2.6, but for $k_p d = 0.87$. It is noted that in the zeroth harmonic, the second-order difference terms are localised around lower wavenumbers-frequencies than in the deep-water case.

properties of random wavefields. Starting from the description of linear wave statistics in §2.3.1, the discussion continues in §2.3.2 with the initialisation of a linear random wavefield within HOSM. The section concludes with a review of nonlinear crest-height models in §2.3.3.

2.3.1 Statistics of a Gaussian stochastic process

In the absence of nonlinear effects a random sea-state at any location in the wavefield can be regarded as a Gaussian stochastic process, $\eta(t)$, with zero-mean and variance $\sigma_\eta^2 = m_0 = H_s^2/16$. Building upon the work of Rice (1945), Cartwright & Longuet-Higgins (1956) considered the probability of exceedance of local maxima, η_m, in such a process and showed that it is given by,

$$Q_m(\zeta) = \frac{1}{\sqrt{2\pi}}\Big[\int_{\zeta/\epsilon}^{\infty} e^{-\frac{1}{2}x^2}dx + (1-\epsilon^2)^{\frac{1}{2}} e^{-\frac{1}{2}\zeta^2}\int_{-\infty}^{\zeta(1-\epsilon^2)^{\frac{1}{2}}/\epsilon} e^{-\frac{1}{2}x^2}dx\Big] \tag{2.37}$$

where, $\zeta{=}\eta_m/\sqrt{m_0}$.

It can be observed that this equation depends on a single parameter ϵ,

$$\epsilon^2 = 1 - \frac{m_2^2}{m_0 m_4} \tag{2.38}$$

where, m_n refers to the n^{th} spectral moment defined by,

$$m_n = \int_0^{\infty} \omega^n S_{\eta\eta}(\omega)d\omega \tag{2.39}$$

The ϵ parameter is closely related to the bandwidth of the spectrum. For narrow-banded spectra, $\epsilon \to 0$ and the probability distribution of local maxima coincides with the probability distribution of the envelope of the process. This is given by the Rayleigh distribution (Rayleigh, 1880). In contrast, when the spectrum is broad-banded, $\epsilon \to 1$, the probability distribution of local maxima tends to the probability distribution of $\eta(t)$ itself, which is the Gaussian distribution. Based on these observations, the probability of exceedance of local maxima takes the following forms:

$$Q_m(\zeta) = e^{-\frac{1}{2}\zeta^2} \quad with \quad \zeta \in [0,\infty) \quad for \quad \epsilon \to 0 \tag{2.40}$$

$$Q_m(\zeta) = \frac{1}{\sqrt{2\pi}}\int_{\zeta}^{\infty} e^{-\frac{1}{2}x^2}dx \quad with \quad \zeta \in (-\infty,\infty) \quad for \quad \epsilon \to 1 \tag{2.41}$$

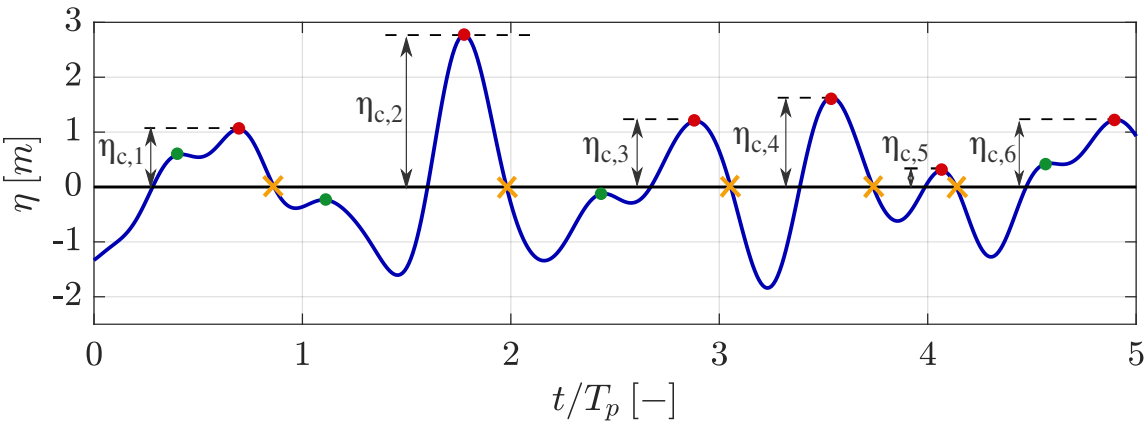


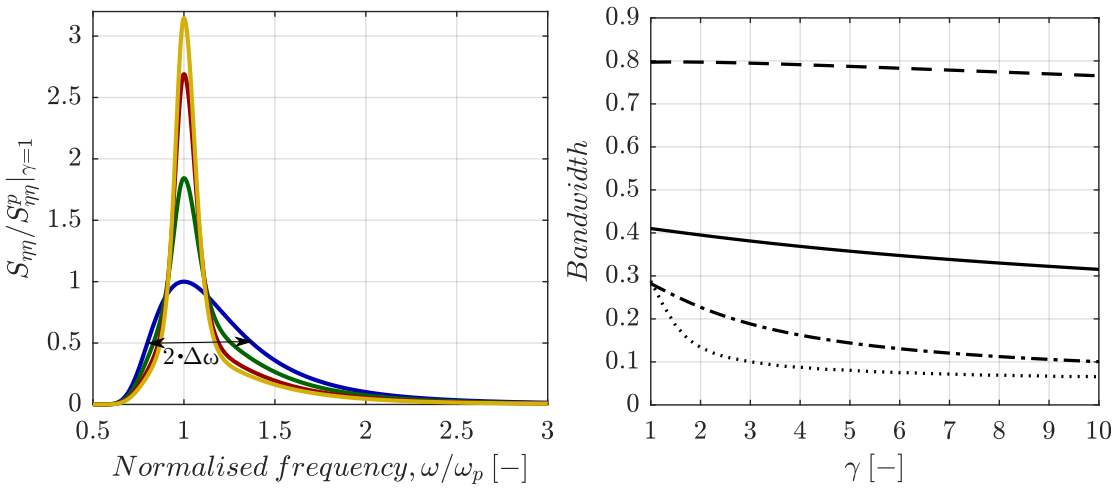
Figure 2.8: Example of a time-trace of the free-surface elevation, where zero-crossing waves are distinguished from local maxima. The crests of the zero-crossing waves are denoted with (•) and the additional local maxima are denoted with (•). Zero down-crossing points are denoted with (×) and the crest heights are denoted with $\eta_{c,i}$.

Building upon these results, it is shown in Appendix A that the tail of the full exceedance probability distribution of Cartwright & Longuet-Higgins (1956) can be approximated by,

$$Q_m(\zeta) = \sqrt{1-\epsilon^2}e^{-\frac{1}{2}\zeta^2} \tag{2.42}$$

provided $\epsilon \neq 1$. Hence, the higher the ϵ parameter, the lower the probability that a local maximum exceeds a certain level.

However, estimating wave statistics based on either Equation 2.37 or 2.42 can be overly sensitive to the energy allocated at high-frequencies; the latter being affected by the truncation of the spectral tail and/or noise from measuring procedures. To limit this, in engineering practice, the *zero-crossing* crest heights are typically considered (Forristall, 2000) instead of the local maxima. A zero-crossing crest height (η_c) is defined as the maximum elevation between consecutive zero up-(or down-) crossings of the zero-mean free surface; the former case involving zero-crossings with positive gradient ($\eta = 0 | \, d\eta/dt > 0$) and the latter with negative ($\eta = 0 | \, d\eta/dt < 0$). As such, within a zero-crossing analysis, any secondary local maxima between zero-crossings are discarded. To illustrate the above, Figure 2.8 presents a free-surface segment, where the zero down-crossing crest heights are marked with red markers and the discarded local maxima with green markers. The zero down-crossing crest heights are also denoted with $\eta_{c,i}$ (with i representing the i-th observation). Interestingly, when zero-crossing crest heights are considered, Boccotti (2015) has shown that the tail of their probability of exceedance can be approximated by the Rayleigh distribution



(A) (B)

Figure 2.9: (A) JONSWAP wave spectra with (/ / /) for $\gamma = 1$, 2.5, 5 and 7, respectively. The spectral shapes refer to the same energy content, while they have all been normalised with respect to the peak of the spectrum with $\gamma = 1$. While $\Delta\omega$ is defined for the spectrum of $\gamma = 1$. (B) Variation of the frequency bandwidth parameters as a function of γ: (——) for ν, (— —) for ϵ, (· · · ·) for $\Delta\omega/\omega_p$ and (— · —) for $\frac{1}{Q_p\sqrt{\pi}}$. Note that the inverse of Q_p is taken to represent the bandwidth and is divided by $\sqrt{\pi}$ for scaling purposes.

for any spectrum, assuming that at the vicinity of the largest wave events, laying at the tail of the distribution, secondary waves do not occur.

Based on the above, the ϵ parameter gives particular weight on the high-frequency tail of the distribution, owing to its dependence upon higher-order spectral moments. Therefore, ϵ does not reflect important spectral changes around the spectral peak. To this end, alternative measures of the spectral bandwidth have been sought; these proposed by Longuet-Higgins (1975) and Goda (2000) given in Equations 2.43 and 2.44 respectively,

$$\nu = \sqrt{m_0 m_2 / m_1^2 - 1} \tag{2.43}$$

$$Q_p = \frac{2}{m_0^2} \int_0^\infty f S_{\eta\eta}^2(f) df, \tag{2.44}$$

where f is the wave frequency. In addition, in many studies related to near-resonant effects, the half-width at half-maximum of the spectrum divided by the spectral peak circular frequency ($\Delta\omega/\omega_p$) is often used. To visualise the variation of the various bandwidth parameters in realistic-bandwidth sea-states, Figure 2.9 presents their dependence upon γ, along with the corresponding spectral shapes. Where $\Delta\omega$ is defined in Figure 2.9(A) for $\gamma = 1$.

Figure 2.9 confirms that ϵ is insensitive to important spectral changes, while the alternative parameters exhibit the expected decreasing trends with increasing γ. In particular, the parameter $\Delta\omega/\omega_p$ exhibits the largest variation. As $\Delta\omega/\omega_p$ is defined solely by the energy distribution around the spectral peak. These parameters will all be used in Chapters 3 and 4, to assess the performance of narrow-band theoretical solutions defining the intensity of nonlinear interactions in random sea-states.

In the section that follows the definitions given above are used in the context of HOSM random sea-state simulations. This focuses on the appropriate initialisation of the wavefields such that their statistics are in accordance with the properties of a Gaussian (linear) process also described above.

2.3.2 Generation of an initial linear random wavefield within HOSM

In Section 2.2.5, it was outlined that the initialisation of HOSM should be based upon an initial (linear) wavefield specified using LRWT. To achieve this, a set of phases and amplitudes of the input wave components must be defined. To define the spectral amplitudes, an appropriate representation of the spectrum in the wavenumber domain, $S_{\eta\eta}(k)$, is first required. Following Holthuijsen (2010), the transformation of a frequency-direction spectrum to a wavenumber spectrum in uni-directional conditions is given by,

$$S_{\eta\eta}(k) = S_{\eta\eta}(\omega)\frac{\partial\omega}{\partial k} = S_{\eta\eta}(\omega)c_g(\omega), \tag{2.45}$$

while for directionally spread conditions

$$S_{\eta\eta}(k_x, k_y) = S_{\eta\eta}(\omega, \theta)\frac{c(\omega)c_g(\omega)}{\omega}, \tag{2.46}$$

where c_g is the linear group velocity and c the linear phase velocity.

An appropriate definition of the input conditions requires the simulated free surface to be an *ergodic* process. In other words, the statistics arising from a single long realisation of Equation 2.13 should be the same as the statistics arising from multiple shorter realisations. In this context, the need for multiple shorter realisations of a sea-state stems from two competing factors:

1. The need to take into account the rarest of the wave events arising in each sea-

state. Assuming a sea-state of 3-hour duration, these events correspond to a probability level of as low as 10^{-3}. Unfortunately, these rare or maximum wave events are susceptible to large sample variability. Hence, a reliable estimation of their expected magnitude would typically require the simulation of two orders of magnitude more wave events, i.e. $\sim 100,000$.

2. The dimensions of the computational domain, along with the duration of the HOSM simulations are inevitably restrained by the inherent limitations associated with the computational resources. As such, a single HOSM simulation will typically produce a few hundred wave events at a single location in a wavefield.

According to Tucker et al. (1984) the ergodicity of random sea-state realisations depends upon the way the input amplitudes are treated. Specifically, whether they are treated as deterministic (Equation 2.14) or stochastic quantities (Equation 2.15). Tucker et al. (1984) argues that the first approach (deterministic) satisfies the ergodicity requirement provided that the number, N, of wave components used in the summation of Equation 2.13 is sufficiently high, $N \to \infty$. In contrast, the second approach (stochastic) is inherently valid, regardless of the number of wave components employed. However, how high N should be for the first approach to be valid remains unclear. To this end, difficulties in guarantying the ergodicity of directional random wavefields in an experimental context were addressed by Latheef et al. (2017). However, in an experimental context, the spectral resolutions are typically higher than what is viable within HOSM, and the problem of ergodicity arises from difficulties in guarantying the homogeneity. Here, the verification of the ergodicity refers to one-dimensional records. While the spatial homogeneity within directional HOSM simulations is verified subsequently in Appendix C in the context of Chapter 4.

To verify the ergodicity property of the initial wavefield within HOSM, linear space records for a JONSWAP sea-state of $\gamma = 2.5$ were generated using different spectral resolutions, combined with either deterministic or random amplitudes. Namely a number of spectral components were adopted. The number of spectral components were raised between $N_x = 128$, 256, 512, 1024, 2048 and 4096. Irrespective of the spectral resolution, the spatial resolution was held constant. In this way, any differences between the obtained results were unaffected by the sampling rate in x. To achieve this, the domain length varied such that the ratio N_x/L_x is held constant. This also guaranteed that the same maximum resolved wavenumber is

maintained between all cases; here corresponding to $\sim 4f_p$. In considering these tests, the number of realisations was varied for the different resolutions in order to maintain approximately the same number of wave events, and have the same resolved exceedance probability. Whereas to extract the wave crests, a zero-crossing analysis was applied to the spatial traces of the free surface along the x axis. Based on this approach, if the process is ergodic, the crest-height probability of exceedance of the amalgamated data sets should match the Rayleigh distribution.

Figure 2.10 presents the ratio of the simulated crests to the theoretical or target Rayleigh distribution, the vertical axis of the plots being much exaggerated but consistent. Sub-figure (A) corresponds to the random-amplitude approach, whereas sub-figure (B) corresponds to deterministic-amplitudes. In agreement with Tucker et al. (1984), the ergodicity property for the deterministic-amplitude approach is not guaranteed if the spectral resolution is not sufficiently high. For example, the crest heights can be underestimated by as much as 5% at a probability level of 10^{-3} for $N_x < 512$. In contrast, the random-amplitude approach remains valid irrespective of the spectral resolution. To this end, the present results are informative for practical applications and can be extended to other wave models/approaches if short duration random records are to be generated and amalgamated. In the subsequent investigations of Chapters 3 and 4 random amplitudes will be used throughout.

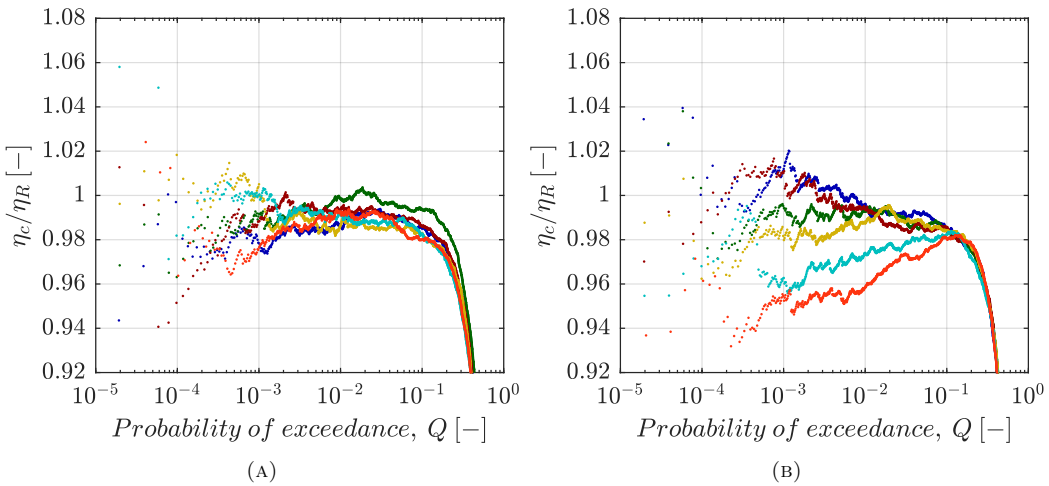
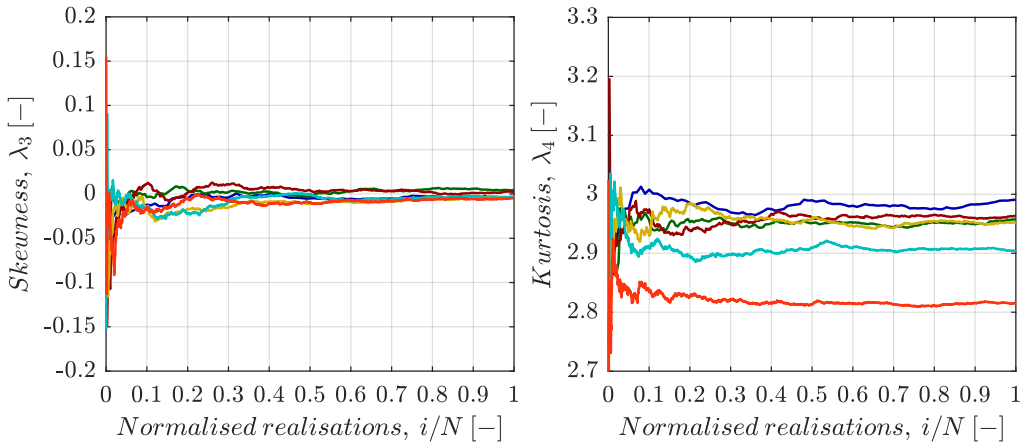


Figure 2.10: Crest-height probability of exceedance distribution normalised with respect to the Rayleigh prediction, η_c/η_R, for a JONSWAP sea-state with $\gamma = 2.5$, $T_p = 10s$ and $d = 125m$ arising from initial wavefields within HOSM obtained using LRWT. (A) random amplitudes and (B) deterministic amplitudes: ( ) N_x=4096, ( ) N_x=2048, ( ) N_x=1024, ( ) N_x=512, ( ) N_x=256, ( ) N_x=128.



(A) (B)

Figure 2.11: Convergence of the statistical moments for varying spectral discretisation. (A) Skewness and (B) Kurtosis: (——) $N_x = 4096$-$L_x/l_p = 280$, (——) $N_x = 2048$-$L_x/l_p = 140$, (——) $N_x = 1024$-$L_x/l_p = 70$, (——) $N_x = 512$-$L_x/l_p = 35$, (——) $N_x = 256$-$L_x/l_p = 18$, (——) $N_x = 128$-$L_x/l_p = 9$.

Furthermore, the appropriateness of the adopted discretisation within HOSM needs to be further verified with respect to the estimation of the initial statistical moments of skewness, λ_3, and kurtosis, λ_4, defined by:

$$\lambda_3 = \frac{E[\eta^3]}{\sigma_\eta^3} \quad \lambda_4 = \frac{E[\eta^4]}{\sigma_\eta^4}, \tag{2.47}$$

These parameters are widely used for the estimation of nonlinear effects in random seas and will be utilised throughout this thesis. Hence, the accuracy with which they are captured within the initial wavefields needs to be verified.

To this end, Figure 2.11 presents the average value of the two statistical parameters as a function of the normalised number of realisations, i/N_{max}, with random amplitudes in all cases. While the different lines refer to different spectral resolutions and consequently different domain lengths, the results demonstrate that the average values for both moments are converged in terms of the number of realisations in all cases. However, whilst the skewness meets the target value of zero irrespective of the domain length, the kurtosis is underestimated with decreasing domain length. However, it converges to within $\sim 1.5\%$ of the target value of 3 for $N_x \geq 512$.

Based on these results, it was decided to use a resolution of $N_x = 1024$ for unidirectional ($1D$) and $N_x = 512$ for directionally spread ($2D$) sea-state simulations. The latter resolution was chosen as a compromise between statistical reliability and

computational demand; directional simulations being computationally more demanding than uni-directional simulations.

In accordance with Gramstad et al. (2018), it was clear that the spectral bandwidth affected the convergence of the kurtosis. To address this, in all cases relevant to the present thesis, the selected resolutions yield an initial kurtosis that deviated from the target value by a maximum of 3.5%. Interestingly, the present results reveal that the majority of previous relevant studies adopted inadequately long domain lengths for the reliable estimation of kurtosis. This is particularly relevant to Toffoli et al. 2008b ($9l_p$), Toffoli et al. 2008a ($9l_p$), Toffoli et al. 2009 ($12l_p$), Toffoli et al. 2010a ($9l_p$).

2.3.3 Nonlinear crest-height models

Second-order crest-height modelling

Numerous studies have considered corrections to the Rayleigh distribution to account for second-order bound-wave nonlinearities. Perhaps the most notable early work on this subject was the model devised by Tayfun (1980) for narrow-banded deep-water sea-states. Following on Marthinsen & Winterstein (1992), Tayfun (2006), Fedele & Arena (2005), Fedele & Tayfun (2009) and Arena & Ascanelli (2010) (amongst others) seek to account for finite water depth, directional spreading and finite bandwidth. Nonetheless, the most commonly used second-order model and the one incorporated into international standards was proposed by Forristall (2000). This was derived on the basis of long-random simulations using SORWT, for both uni-directional and directionally spread JONSWAP spectra. This model defines the probability of a crest height, η_c, exceeding a threshold η as,

$$Q(\eta) = P(\eta_c > \eta) = \exp\left[-\left(\frac{\eta}{\alpha H_s}\right)^{\beta}\right] \tag{2.48}$$

with α and β given by,

$$\begin{aligned} \alpha &= 0.3536 + 0.2892S_1 + 0.1060Ur \\ \beta &= 2 - 2.1597S_1 + 0.0968Ur^2 \end{aligned} \tag{2.49}$$

for uni-directional sea-states and by,

$$\begin{aligned} \alpha &= 0.3536 + 0.2568S_1 + 0.08Ur \\ \beta &= 2 - 1.7912S_1 - 0.5302Ur + 0.284Ur^2 \end{aligned} \tag{2.50}$$

for directionally spread sea-states. In the above expressions, the sea-state severity is taken into account by the steepness parameter S_1 which is given by,

$$S_1 = \frac{2\pi}{g}\frac{H_s}{T_1^2}, \quad with \quad T_1 = 2\pi\frac{m_0}{m_1}, \tag{2.51}$$

and depth-dependence is expressed through the Ursell parameter, Ur,

$$Ur = \frac{H_s}{k_1^2 d^3}, \tag{2.52}$$

where k_1 is the wavenumber corresponding to T_1 and d is the water depth.

It is noted that in the latest work of Arena & Ascanelli (2010) very good agreement was demonstrated between their theoretical results and the fitted model of Forristall (2000) for uni-directional and directionally spread sea-states. In this thesis, the Forristall (2000) model is adopted as the appropriate second-order model due to its simplicity and engineering relevance.

Higher-order crest-height modelling

In the case that higher than second-order nonlinear effects are non-negligible, the crest-height distribution can no longer be based upon the SORWT. Evidence of this is provided in the laboratory data of Latheef & Swan (2013), Latheef et al. (2017) and Karmpadakis et al. (2019a). To address such cases, Tayfun & Lo (1990), building upon the work of Longuet-Higgins (1963), described the statistics of the wave envelope retaining terms up to third-order in Gram-Charlier series expansion. While following Tayfun & Fedele (2007) expressed the crest-height probability of exceedance as,

$$Q(\xi H_s) = P(\eta_c > \xi H_s) = \exp(-8\xi_0^2)[1 + \Lambda\xi_0^2(4\xi_0^2 - 1)] \tag{2.53}$$

where,

$$\xi = \xi_0 + 2\mu\xi_0^2. \tag{2.54}$$

Equation 2.54 defines the second-order crest-heights normalised by the H_s, following the second-order theory of Tayfun (1980). While the term in the square brackets in Equation 2.53 models the third-order correction to the estimated exceedance probability according to the Gram-Charlier series. As such, the crest-height probability of exceedance depends upon the parameters μ and Λ. The parameter μ is a steepness parameter defined by,

$$\mu = \lambda_{30}/3, \tag{2.55}$$

while Λ is given by,

$$\Lambda = \lambda_{40} + 2\lambda_{22} + \lambda_{04}. \tag{2.56}$$

In the above expressions, λ_{mn} refer to the normalised joint cumulants of η and $\hat{\eta}$, the latter representing the harmonic conjugate of η, and are evaluated according to,

$$\begin{aligned} \lambda_{mn} &= \frac{E[\eta^m \hat{\eta}^n]}{\sigma_\eta^{m+n}}, \quad for \quad m+n=3 \\ \lambda_{mn} &= \frac{E[\eta^m \hat{\eta}^n]}{\sigma_\eta^{m+n}} + (-1)^{m/2}(m-1)(n-1), \quad for \quad m+n=4 \end{aligned} \tag{2.57}$$

As such, the λ_{30} joint cumulant coincides with the skewness parameter (λ_3). While λ_{40} describes the excess kurtosis or $\lambda_4 - 3$. In the discussion that follows, the excess kurtosis will hereafter be simply referred to as the kurtosis, replacing the earlier definition in Equation 2.47 and used to reflect the effect of nonlinearity beyond second-order.

Based on the above, to apply the model of Equation 2.53 it is necessary to have an estimation of the normalised joint cumulants of the free surface. These are typically obtained from time histories of the free-surface elevation or theoretical predictions. For the latter case, the narrow-band limit of Λ is often used denoted with Λ_{app}, and it is given by $\Lambda_{app} = 8\lambda_{40}/3$. As it depends only upon λ_{40} for which theoretical predictions are available.

Finally, more recently, Karmpadakis & Swan (2022), as yet unpublished, have proposed a crest-height model that includes the effects of higher than second-order nonlinear interactions and the effect of wave breaking; the latter becoming crucial as the sea-state steepness increases and the effective water depth reduces.

Specifically, within this model, wave nonlinearity is taken into account based on the correction of the linearly predicted crest heights $\eta_c^{(1)}$ based on the Rayleigh

distribution. The second-order correction, $\eta_c^{(2)}$, is taken into account based on the theory of Tayfun (1980) and Tayfun (2006). While higher-order nonlinearity is taken into account as a correction to the second-order nonlinearity. The higher-order correction was calibrated empirically based on the departures of recorded crest-height distributions for non-breaking sea-states from the second-order predictions. Finally, a wave-breaking correction factor was calibrated based on the departures of breaking sea-states from the higher-order predictions.

The data used in the calibration of the model include experimentally generated sea-states of increasing steepness for $k_p d > 1$ and a subset of relatively severe (breaking) sea-states in $k_p d \approx 0.5$ recorded in the Southern North Sea. The model predictions depend upon the Ursell number, Ur, and the deep-water steepness parameter S_1, similarly to the Forristall (2000) model. As such, the predictions do not depend upon the directional spreading. While the spectral bandwidth is considered indirectly in the evaluation of Ur and S_1 through the wave period T_1.

Based on the above, the Karmpadakis & Swan (2022) model gives:

$$Q(\xi H_s) = P(\eta_c > \xi H_s) = \exp(-8\xi_0^2), \tag{2.58}$$

where

$$\begin{aligned} \xi &= \Big(\frac{\eta_c^{(1)}}{H_s} + \frac{\eta_c^{(2)}}{H_s} + \frac{\eta_c^{NL}}{H_s}\Big) \cdot f_{br} \\ &= \Big(\xi_0 + 2\mu\xi_0^2 + \kappa\mu\xi_0\Big) \cdot f_{br}. \end{aligned} \tag{2.59}$$

In the above expression, the terms in the parenthesis define the higher-order predictions, which are corrected for breaking through f_{br}, μ is given by Tayfun (2006) and κ is a sigmoid function depending on μ. The breaking factor is defined by $f_{br} = (A\xi_0 + B)$ with A and B depending on Ur and S_1. The functional form of κ, A and B can be found in Karmpadakis & Swan (2022). Importantly, f_{br} differs from unity (or in other words breaking is activated) when μ is greater than 0.065. Or equivalently when the estimated skewness λ_3 is greater than 0.195. Likewise, when $\mu = 0$ (small steepness) the Rayleigh distribution is recovered. Finally, further review material on additional existing methods for nonlinear crest-height predictions is provided in Chapter 5.

2.4 Summary

1. This chapter has provided a coherent review of nonlinear interactions arising at a second-order in wave steepness and above; specifically highlighting the importance of resonant and near-resonant interactions.

2. Building upon these considerations, an appropriate wave model for incorporating such interactions was sought; the Higher-Order Spectral Method (HOSM) identified as the most appropriate choice. In making this choice, the performance of HOSM in modelling such interactions in a random sea-state setting was verified.

3. Important considerations with regards to the appropriate selection of inputs within HOSM were also investigated. Specifically, it was demonstrated that high spectral resolutions need to be used with a deterministic amplitude approach to ensure that the free surface is ergodic. As a result, random amplitudes will be used in the Chapters that follow.

4. Finally, it was shown that the kurtosis of the free surface can be significantly underestimated if the computational domain length is not sufficiently long. Based on these considerations, the spectral resolution was set to consist of a minimum of 512 components.

3

Statistical properties of uni-directional sea-states

The present chapter presents a numerical investigation, using HOSM, of the role of near-resonant and bound-wave interactions in determining key statistical properties of uni-directional sea-states with a realistic bandwidth. Specifically, the purpose of the chapter is threefold:

1. To establish how the various nonlinear wave-wave interactions affect the short-term crest-height distribution, with a particular focus on the largest waves. In this regard, it will explore the effect of key sea-state characteristics, such as the sea-state steepness, effective water depth and spectral bandwidth.

2. To explore the applicability of existing theoretical narrow-band solutions for the statistical moments of skewness and kurtosis. As highlighted in §2.3.3, these moments are inherently connected to the nonlinear interactions arising in random wavefields and are used to obtain higher-order crest-height predictions. Therefore, assessing the applicability of these solutions in realistic bandwidth sea-states has important practical implications.

3. To investigate if the statistical moments (skewness and kurtosis) can explain the nonlinear contributions to the largest crest heights arising in realistic bandwidth sea-states.

The chapter commences in §3.1 with the motivation underpinning the present study. Subsequently, §3.2 presents relevant previous theoretical, numerical and experimental works, revealing the limitations of previous studies and highlighting in more detail the points where the chapter aims to contribute. §3.3 presents the set of sea-states simulated using HOSM, together with details of the adopted numerical setup. To ensure confidence in the present results, §3.4 presents a comparisons between numerically obtained crest-height distributions using HOSM and available experimental data. The experimental data originate from an extensive range of experimental facilities operating in various water depths; thereby enabling the validation of HOSM over the full range of conditions outlined in §3.3. Moreover, in §3.4 the HOSM model is validated against an alternative nonlinear wave model (Hague & Swan, 2009), comparing the wave profiles of near-limiting (non-breaking) deterministic wave groups. Whilst these preliminary validations may seem extensive, they are considered crucial in establishing the reliability of the adopted method. The main results of this investigation are then presented in §3.5 and §3.6; the former focusing on the effect of nonlinear interactions and the latter on assessing the validity of the theoretical solutions for the statistical moments. Finally, the chapter concludes in §3.7 with a summary of the main findings.

3.1 Motivation

Janssen (2003) was first to point out the importance of including third-order near-resonant interactions in the simulation of deep-water random wavefields. He demonstrated that near-resonant interactions induce a progressive deviation with time (or space) of the underlying freely propagating wavefield from Gaussianity or linearity. Notably, he demonstrated that this type of nonlinear evolution takes place over tens of dominant wave periods, as opposed to the long-term evolution of ocean wave spectra over thousands of dominant wave periods under the influence of exact resonant interactions; the latter evolution traditionally being included in operational wave forecasting models (Hasselmann, 1962), but the former not. Similar conclusions were drawn in earlier laboratory studies of quasi-deterministic focused waves, notable examples including Baldock et al. (1996) for unidirectional waves and Johannessen & Swan (2001) for directionally spread waves.

One of the most influential outcomes of the work of Janssen (2003) was that the intensity of near-resonant interactions arising in narrow-band uni-directional seas can be estimated based on a single factor referred to as Benjamin-Feir Index.This is defined as the ratio between the sea-state steepness and the spectral bandwidth, or, in other words, the ratio of nonlinearity over frequency dispersion.

Furthermore, with the reduction in effective water depth, the waves start to 'feel' the bottom, and the intensity of nonlinear interactions increases. At the same time, the waves become less dispersive, and hence the wave components interact for longer times. In considering finite-depth effects, the work of Janssen & Onorato (2007) has revealed that, as the effect of frequency dispersion attenuates with reducing effective water depth and under the presence of long-wave components resulting from second-order wave-wave interactions, near-resonance leads to the *defocusing* of the wave energy for $k_p d < 1.363$. In this respect, Janssen & Onorato (2007) found that this defocusing mechanism has a direct consequence on the value of the kurtosis of the underlying free waves, which was found to progressively reduce below the linearly predicted value. This observation is in direct contrast to the behaviour of the kurtosis in deep water, and is at odds with the laboratory observations reported by Baldock & Swan (1996).

A possible explanation for this lies in the fact that both the works of Janssen (2003) and Janssen & Onorato (2007) were restricted to narrow-banded Gaussian-shaped spectra. Consequently, the presence of a high-frequency tail relevant to realistic JONSWAP spectra could disrupt the above behaviour. This arises because the effect of frequency dispersion is enhanced, and because it imposes the different wave components to lay in different effective water depths.

The present study aims to fill exactly this gap: to explore the relevance of the findings of Janssen (2003) and Janssen & Onorato (2007) to realistic bandwidth sea-states; particularly focusing on identifying the role of near-resonant interactions on the formation of the largest waves. In addition, it aims to assess the equivalent effect of bound-wave interactions.

3.2 Relevant previous works

3.2.1 Numerical and experimental investigations

Deep water

The role of near-resonant interactions in realistic bandwidth sea-states was tackled experimentally by Stansberg (1994) and latter by Onorato et al. (2004). Both studies revealed a characteristic increase of the kurtosis with distance from the wavemaker. This is in qualitative agreement with the theoretical developments of Janssen (2003). Subsequently, Onorato et al. (2006) showed that the crest-height distributions from Onorato et al. (2004) deviated significantly from the second-order predictions. In accordance with the evolution of the kurtosis, the deviations increased with distance from the wavemaker. This confirmed that wave nonlinearity above second-order is likely to play an essential role in the formation of large wave events. This is directly confirmed by the laboratory observations of Baldock et al. (1996) and the fully nonlinear numerical calculations of Gibson & Swan (2007); both relating to deterministic wave groups.

Focusing on crest-height statistics, numerical simulations of uni-directional random sea-states of realistic JONSWAP spectra have been conducted by Toffoli et al. (2008b) using HOSM and by Hadjigeorgiou (2018) using both the Zakharov equation and HOSM. Whilst, both studies are important in that they demonstrated departures of the simulated crest heights from second-order theory, they were limited by a number of factors. First, neither of the above studies addressed the time evolution of the nonlinear interactions. Moreover, whilst the former study included the full nonlinearity of the problem, separation of the various harmonic contributions was not attempted. Finally, although the latter study did consider the different nonlinear terms separately, only bound terms up to second-order were specifically specified. To this end, the present study aims to fill these gaps by taking into account the entire nonlinear evolution process and by separating the effect of different nonlinear interactions.

Furthermore, Onorato et al. (2006) investigated three sea-state conditions, in which both steepness and spectral bandwidth were changed simultaneously. However, these two factors could be not equally important in broad-banded sea-states. To this end, experimental studies conducted by Shemer & Sergeeva (2009), Cherneva et al.

(2013) and Latheef (2014) have considered sea-states of increasing steepness whilst maintaining the same spectral shape. However, they either did not consider realistic spectral shapes (Shemer & Sergeeva, 2009), did not include a statistically significant number of wave cycles (Cherneva et al., 2013) or considered only a limited range of evolution distances from the wavemaker (Latheef, 2014). Unfortunately, the same limitations underpin equivalent studies that aimed to identify the effect of spectral bandwidth (Stansberg 1994, Shemer et al. 2010).

In the present investigation, the effect of steepness and spectral bandwidth will be explored separately. In addition, to provide conclusive results, the reduction of the statistical variability around the most likely maximum crest height arising in a 3-hour sea-state will be addressed.

Finite depth

Previous numerical studies in finite water depth are much less common than in deep water. Notable works on realistic bandwidth sea-states include those of Mori & Yasuda (2002), Fernández et al. (2016), Slunyaev et al. (2016) and Hadjigeorgiou (2018) all of which adopted HOSM. However, none of the above studies explored the validity of the Janssen & Onorato (2007) theory; the nonlinear interactions being taken into account as a whole.

Moreover, whilst the work of Mori & Yasuda (2002) provided some insights concerning the effect of relative water depth on the values of the skewness and kurtosis, the numerical simulations suffered from (1) the lack of statistical significance due to a very limited number of simulated wave events ($\sim$ 300) and (2) the adoption of deterministic input amplitudes; which has been shown in §2.3.2 to induce underestimation of the largest waves (and kurtosis).

In addition, from the above studies, only Fernández et al. (2016) considered the statistics of crest heights. They showed that crest-height amplification beyond the second-order predictions reduces with effective water depth. However, their analysis considered a rather limited set of three uni-directional sea-states in $k_p d \in [1.15, 1.78]$, characterised by a relatively narrow JONSWAP spectrum of $\gamma = 6$.

Finally, the experimental works of Karmpadakis et al. (2019a) and Gray (2020) in uni-directional seas have shown that crest-amplifications beyond second-order are relevant for $k_p d \in [0.88, 1.57]$. However, with the wave measurements undertaken

relatively close to the wavemaker (over distances of $\sim$ 1-2l_p and $\sim 5l_p$, respectively), it is yet unclear if the nonlinear interactions are fully developed.

Before proceeding, it is instructive to complement the above review with an account of relevant theoretical works. These works relate to the prediction of the statistical moments of skewness and kurtosis in various effective water depths. With these moments indicating the extent of the nonlinear interactions, this account will offer a better view of the present aims and is presented in §3.2.2.

3.2.2 Analytical uni-directional solutions for the statistical moments

In considering the relevance of the statistical moments to the present discussion, the skewness parameter, λ_3, expresses the degree of vertical asymmetry of the free surface induced by second-order *bound* contributions (see for example Longuet-Higgins 1963, Tayfun 1980) and it is often used within theoretical second-order crest-height models (Tayfun 2006, Fedele & Tayfun 2009, Arena & Ascanelli 2010). Interestingly, following Tayfun (2006), the skewness can be expressed as the summation of the contributions from the frequency-sum and frequency-difference terms: $\lambda_3 = \lambda_3^+ + \lambda_3^-$.

In contrast, the kurtosis parameter reflects how 'heavy' the tail of the respective distribution is. As such, it gives a measure for the likeliness of unexpectedly high or freak waves in the wavefield. Moreover, the kurtosis contains both a *dynamic* part due to near-resonant interactions (see e.g. Janssen 2003, Mori & Janssen 2006) and a *static* or *bound* part that is due to second and, primarily, third-order bound interactions (see Tayfun & Lo 1990 and Janssen 2009). As such, the total kurtosis can be expressed as the following summation,

$$\lambda_{40} = \lambda_{40}^d + \lambda_{40}^b \tag{3.1}$$

where, λ_{40}^d refers to the dynamic kurtosis and λ_{40}^b to the bound kurtosis.

Skewness (λ_3) and bound kurtosis (λ_{40}^b)

Marthinsen & Winterstein (1992) and Janssen (2009) have independently derived the expression for the skewness in the narrow-band limit for finite water depth conditions, the former based on the second-order theory of Longuet-Higgins & Stewart (1960)

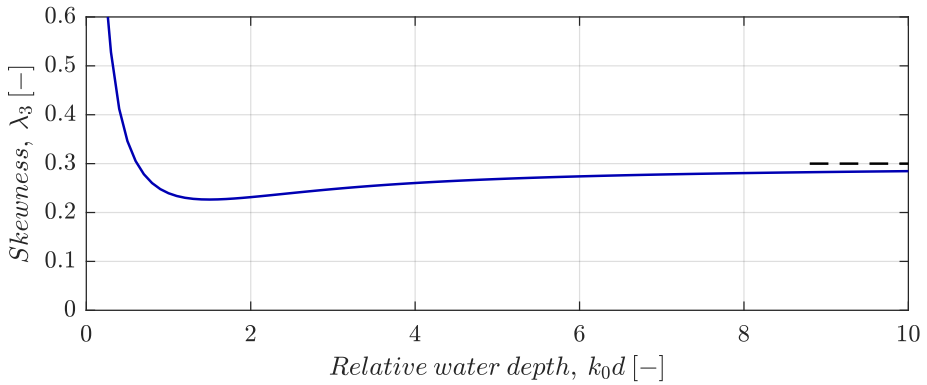


Figure 3.1: Theoretically predicted skewness parameter, λ_3, for narrow-banded uni-directional sea-states of steepness $\mu = \sigma_\eta k_0 = 0.1$ against relative water depth $k_0 d$. The horizontal black dashed line corresponds to the deep-water value given by $\lambda_3 = 3\mu$ (Mori & Janssen, 2006).

and the latter on the Zakharov equation in its canonical form (with separated free and bound-wave contributions). These solutions revealed that, similarly to deep-water conditions (Mori & Janssen, 2006), the skewness depends linearly upon the sea-state steepness, $\mu = \sigma_\eta k_0$ (with k_0 being the central wavenumber). The functional form of these solutions is provided in Appendix B.

Figure 3.1 presents the variation of skewness with relative water depth for an indicative steepness of $\mu = 0.1$, as predicted by both Marthinsen & Winterstein (1992) and Janssen (2009). This shows a characteristic increase in skewness with reduction in the effective water depth.

Similarly, Janssen (2009) also derived an analytical expression for the bound kurtosis, λ_{40}^b, in finite water depth, again based on a narrow-band assumption. In accordance to the analytical result of Mori & Janssen (2006) concerning deep-water conditions, it was shown that the bound kurtosis is proportional to the square of the characteristic steepness; the functional form of the solution being again provided in Appendix B. The variation of λ_{40}^b with relative water depth is shown in Figure 3.2. Once again, this exhibits a characteristic increase with reduced relative water depth. However, in this case, the increase is more rapid owing to the reduced effect of frequency difference terms.

Dynamic kurtosis (λ_{40}^d)

Janssen (2003) also employed the Zakharov equation to consider the numerical evaluation of the dynamic kurtosis and its evolution with time. More specifically, this

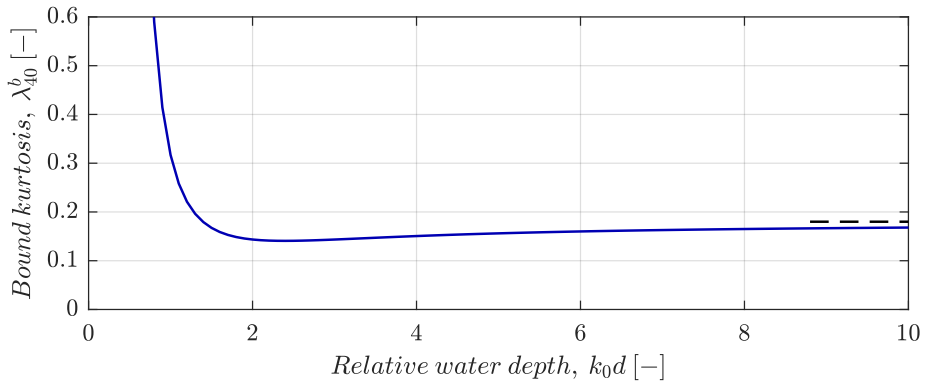


FIGURE 3.2: Theoretically predicted bound kurtosis parameter, λ_{40}^b, for narrow-banded uni-directional sea-states of steepness $\mu = \sigma_\eta k_0 = 0.1$ against relative water depth $k_0 d$. The horizontal black dashed line corresponds to the deep-water value given by $\lambda_{40}^b = 18\mu^2$ (Mori & Janssen, 2006).

evaluation included a multidimensional integration, in which each near-resonant interaction was weighted by the magnitude of the resonant interaction kernel, $T_{0,1,2,3}$, of Krasitskii (1994) (see Equation 2.25). Hence, assuming deep-water conditions with a narrow-band symmetric spectral energy around a central frequency, ω_0, the magnitude of the kurtosis will be governed by the magnitude of the self-interaction kernel $T_{0,0,0,0} = k_0^3/(2\pi)^2$ (with k_0 being the wavenumber corresponding to ω_0).

Based on this approach, Mori & Janssen (2006) showed that in the absence of spectral energy transfers the dynamic kurtosis in deep water evolves towards the steady-state value of,

$$\lambda_{40}^d = \frac{\pi}{\sqrt{3}} BFI^2 \tag{3.2}$$

where BFI refers to the Benjamin-Feir Index (originally derived by Janssen 2003):

$$BFI = \sqrt{2}\frac{k_0 \sigma_\eta}{\sigma_\omega/\omega_0} \tag{3.3}$$

with σ_ω being the standard deviation of the assumed symmetrical spectral shape.

For finite-depth conditions the expression of the nonlinear kernel $T_{0,0,0,0}$ is given by Janssen & Onorato (2007) (see Figure 2.2 and Appendix B) and the finite-depth version of BFI, denoted as B_s, becomes,

$$B_s^2 = BFI^2 \alpha_s, \quad a_s = -g\Big(\frac{c_g}{c_0}\Big)^2 \frac{(2\pi)^2 T_{0,0,0,0}}{k_0^4 \omega_0 \omega_0''} \tag{3.4}$$

where, c_g is the group velocity, c_0 the phase velocity and ω_0'' is second derivative of ω_0 with respect to k_0.

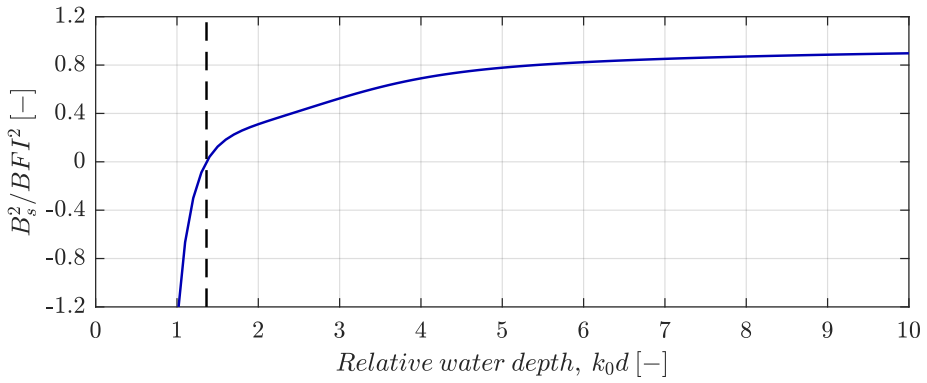


Figure 3.3: Effect of finite water depth on the Benjamin-Feir Index, expressed as the ratio Bs^2/BFI^2 for varying k_0d. The vertical black dashed line marks the theoretical relative water depth $k_0d = 1.363$.

To this end, it is instructive to visualise the ratio Bs^2/BFI^2 with effective water depth, as this expresses the equivalent variation of the dynamic-kurtosis predictions. This ratio is shown in Figure 3.3, where the characteristic change of the sign at $k_0d = 1.363$ is revealed, similarly to the magnitude of $T_{0,0,0,0}$ presented in Figure 2.2.

Taking the variation of the statistical moments as a whole, it is not clear whether nonlinear interactions would amplify the wave crests in $k_0d < 1.363$. As near-resonant effects and bound contributions seem to have a competing influence. However, all of this analysis is based on a narrow-band assumption.

In an attempt to account for the effect of spectral bandwidth Fedele (2014) has derived a bandwidth-corrected solution to Equation 3.2. This is given by,

$$\begin{aligned} \lambda^d_{40,F} &= \lambda^d_{40} \cdot \left[1 - 0.4(\sigma_k/k_0)^2\right] = \\ &= \lambda^d_{40} \cdot \left[1 - 1.6(\sigma_\omega/\omega_0)^2\right] \end{aligned} \tag{3.5}$$

where, σ_k is the standard deviation of the wavenumber spectrum and the transformation to the frequency spectrum (given in the second row of the equation) is based on $\sigma_\omega = \sigma_k/2$. This solution indicates that finite-bandwidth effects tend to decrease the value of the dynamic kurtosis. However, this is at best an approximation and the extent of the reduction remains to be clarified.

3.3 Test cases and numerical setup

With the aim of the present study being to identify the effects of sea-state steepness and spectral bandwidth on wave statistics in a wide range of effective water depths,

Table 3.1: Sea-state parameters relating to the study of the effect of sea-state steepness in uni-directional seas.

Set	k_pd [−]	γ [−]	σ_θ [°]	steepness/severity
U1	0.87	2.5	0	$\frac{1}{2}H_sk_p$ [−] = 0.005, 0.019, 0.039, 0.059, 0.085, 0.105 H_s/d [−] = 0.011, 0.044, 0.090, 0.136, 0.196, 0.243
U2	1.28	2.5	0	$\frac{1}{2}H_sk_p$ [−] = 0.005, 0.019, 0.039, 0.059, 0.085, 0.105 H_s/d [−] = 0.008, 0.030, 0.061, 0.092, 0.132, 0.164
U3	5.03	2.5	0	$\frac{1}{2}H_sk_p$ [−] = 0.005, 0.019, 0.039, 0.059, 0.085, 0.105 H_s/d [−] = 0.002, 0.008, 0.016, 0.023, 0.034, 0.042

the test cases are sub-divided into two parts, details of which are presented in Tables 3.1 and 3.2. Specifically, Table 3.1 presents the cases referring to the effect of sea-state steepness and Table 3.2 presents those referring to spectral bandwidth.

In considering Table 3.1 the effect of sea-state steepness is identified by incrementally increasing $\frac{1}{2}H_sk_p$, whilst maintaining all other parameters constant. Particularly, the sea-state steepness starts at $\frac{1}{2}H_sk_p = 0.005$ for which LRWT should hold and extends to $\frac{1}{2}H_sk_p = 0.105$; the latter allowing significant nonlinear interactions to occur, whilst ensuring that the largest waves arising in a 3-hour storm are non-breaking. In addition, the ratio of significant wave height over the water depth (H_s/d) is also added in Table 3.1 to represent the effect of finite water depth in the sea-state severity. In addition, a JONSWAP wave spectrum of $\gamma = 2.5$ is adopted throughout; this being a typical value used in engineering design.

Within the present investigation three effective water depths were employed: $k_pd = 0.87$, 1.28 and 5.03. These allowed the nonlinear interactions in the three different water-depth regimes ($k_pd < 1.36$, $k_pd \approx 1.36$ and $k_pd \gg 1.36$) to be studied. In considering these, it should be noted that in the shallowest case ($k_pd = 0.87$) all the input wave components lay within the transitional water-depth regime; $k_id > 0.50$, with i referring to the i^{th} wave component.

Regarding the second part of the study, to explore the effect of spectral bandwidth in any given effective water depth, the sea-state steepness was held constant at $\frac{1}{2}H_sk_p = 0.105$ and the γ parameter of the JONSWAP spectrum changed between 1, 2.5 and 5. To gain a complete understanding of the effective water depth, seven k_pd

Table 3.2: Sea-state parameters relating to the study of the effect of spectral bandwidth and relative water depth in uni-directional seas. The cases in parenthesis refer to sea-states already included in Table 3.1. While the cases with (*) refer to sea-states simulated using 5.000 random seeds.

Set	$\frac{1}{2}H_s k_p[-]$	$\gamma\,[-]$	$\sigma_\theta\,[^\circ]$	$k_p d\,[-]$
U4	0.105	1.0	0	5.03*, 3.50, 2.03, 1.57, 1.28*, 1.02, 0.87*
U5	0.105	2.5	0	(5.03*), 3.50, 2.03, 1.57, (1.28*), 1.02, (0.87*)
U6	0.105	5.0	0	5.03*, 3.50, 2.03, 1.57, 1.28*, 1.02, 0.87*

values were considered in the range $k_p d \in [0.87, 5.03]$, as shown in Table 3.2.

The numerical setup and relevant parameters used in the HOSM simulations are presented in Table 3.3. It is noted that each seed was simulated 12 times with different phase shifts such that the phase manipulation method, outlined in §2.2.6, could be applied. In addition, space-traces of the different harmonic contributions were obtained at time instances $t/T_p = 0$, 2, 4, 6, 8, 10, 12, 15, 25, 35, 45, 55, 65, 75, 85, 95, 105, 115 and 125, with a finer time-interval at the beginning of the simulations to capture any transient development of the nonlinear interactions. In analysing the generated data, the output amplitude spectra at each time-step were zero-padded to include 4096 components, or four times the output number of components, and the free surface reconstructed using an inverse Fourier Transform. In this way the spatial discretisation was reduced from ~ 25 points per wavelength to ~ 100, ensuring that the maximum wave crests were accurately captured. This corrects the small under-estimation of the crest heights with respect to the Rayleigh distribution observed in Figure 2.10 (a). Further discussion on this approach is given in Appendix C.

The base number of random seeds used throughout this study was 500, ensuring that at least $50,000$ wave events were captured from the ensemble of the free-surface records. In addition, to reduce the very large variability associated with the expected magnitude of the largest waves arising in a 3-hour sea state, a subset of cases were simulated using $5,000$ seeds. These cases are denoted with $(*)$ in Table 3.2.

Table 3.3: Numerical setup of HOSM for uni-directional simulations.

Parameter	Description	Value
HOSM parameters		
M [−]	Order of nonlinearity	5
n_x [−]	Number of nodes in x	2048
L_x/l_p [−]	Normalised domain length	70
$n_{x,pad}$ [−]	Number of nodes in x after zero-padding	8192
N_s [−]	Number of random seeds	500
T_{sim}/T_p[−]	Normalised duration of simulation	140
$\Delta\epsilon$ [deg]	Phase shifts used in the phase-manipulation method	0, 30, 60, 90, 120, 150, 180, 210, 240, 270, 300, 330
Computational resources		
$RAM[GB]$	Memory requirement	24
N_{proc} [−]	Number of processors	1
T_{proc} [h]	Processing time (including post-processing)	7

All 12 HOSM simulations for each seed (corresponding to 12 phase shifts) were combined in a single simulation routine using a MATLAB wrapper [1]. In this routine, the phase-manipulation method was also applied, along with the post-processing to extract the statistical properties of interest. As such, the computational resources noted in Table 3.3 refer not to a single HOSM simulation, but multiple HOSM simulations including post-processing.

Finally, in the course of the present simulations, the average of the maximum relative deviation of the total wave energy during the simulation period was $< 0.5\%$ for any given sea-state. While the maximum relative deviation of the total wave energy in any given seed was $\sim 1.0\%$. Therefore, energy was conserved to a very high accuracy ensuring the reliability of the simulations.

[1] MATLAB wrapper referring to a MATLAB routine which calls the HOSM excecutable

3.4 Validation considerations

3.4.1 Crest-height distributions

Before proceeding to the main results, it is important to validate the adopted HOSM model. Previous validation studies have focused on numerical convergence and stability (e.g. Ducrozet et al. 2007, Bonnefoy et al. 2010). However, this is itself important but not sufficient. To address this, crest-height exceedance distributions arising from HOSM will be compared to existing laboratory data.

Data sources

The experimental data employed in this task are presented in Table 3.4. Taken together, the data originate from a wide range of experimental facilities both at Imperial College London (ICL) and Queen's University Belfast (QUB), operating in different water depths. To distinguish between the different experimental facilities, a case name is assigned to each sea-state in Table 3.4. Specifically, the case names starting with 'ICB', 'ICDE' and 'QUB' refer to data obtained at the directional wave Basin at ICL, the Double-Ended flume at ICL and the wide wave tank at QUB, respectively.

The sea-states used for validation cover the full range of effective water depths used in the present study (Tables 3.1 and 3.2), ranging from $k_p d = 0.88$ to 3.5; the latter effectively representing deep-water conditions. Likewise, the selected sea-states from each experimental study have a steepness as close as possible to the maximum value of $\frac{1}{2}H_s k_p = 0.105$ in Tables 3.1 and 3.2.

Finally, the normalised distance of the measuring gauge to the wavemaker, x_G/l_p (l_p being the peak wavelength), is also added in Table 3.4; this is key information based on which an effective comparison between the HOSM simulations and experimental data can be performed. This is further described below.

Considerations

To achieve effective comparisons between laboratory data and HOSM simulations, it is vital to consider their difference in the generation/initiation of the wavefields and the process of nonlinear evolution. Specifically:

Table 3.4: Sea-state parameters of experimental studies used for validating the uni-directional HOSM simulations.

Case	Study	$H_s[m]$	$T_p\,[s]$	$d\,[m]$	$\gamma\,[-]$	$\frac{1}{2}H_sk_p$	k_pd	x_G/l_p
ICB1	McCarthy (2018)	0.066	1.2	1.25	2.5	0.092	3.50	2.1
ICB2	Latheef (2014)	0.105	1.6	1.25	2.5	0.086	2.03	1.1
ICB3		0.066	1.2	0.5	2.5	0.100	1.53	2.0
ICB4	Karmpadakis (2018)	0.090	1.4	0.5	2.5	0.110	1.22	1.6
ICB5		0.116	1.6	0.5	2.5	0.119	1.02	1.3
QUB1		0.120	1.6	0.6	2.5	0.115	1.15	1.2
QUB2	Karmpadakis (2018)	0.089	1.4	0.4	2.5	0.116	1.05	1.7
QUB3		0.111	1.8	0.5	2.5	0.097	0.88	1.1
ICDE1		0.101	1.4	0.7	2.5	0.113	1.57	4.8
ICDE2	Gray (2020)	0.099	1.4	0.7	4.0	0.110	1.57	4.8
ICDE3		0.097	1.4	0.7	6.0	0.109	1.57	4.8

1. In HOSM calculations, the computation starts with initial conditions in the wavenumber space corresponding to an initial wavefield in the physical space. While the spatial periodicity of the wavefield ensures spatial stationarity and homogeneity. Therefore, the nonlinear evolution takes place in *time*.

2. On the other hand, in a wave tank the simulation starts with a quiescent free surface, and there is a continuous flux of energy from the wavemaker to the water. In addition, to avoid the contamination of the wavefield from wave reflections from the downstream boundary of the tank, energy dissipation is achieved using wave dissipation mechanisms (for example, beach structures and or porous-type media). In this setting, the wavefield is homogeneous and stationary in time, and it evolves with distance from the wavemaker; i.e. the evolution takes place in *space*.

In this respect, following the nonlinear Shröndiguer equation (see Shemer & Dorfman 2008 and Chabchoub & Grimshaw 2016) to a leading order the link between the evolution distance (distance from the wavemaker), $x = x_G$, and the evolution time, t, is provided through the linear group velocity, c_g, associated to the spectral

peak: $x = c_g \cdot t$. Although this link is based on a narrow-band assumption, Toffoli et al. (2010a) demonstrated that it holds for realistic bandwidths as well. Hence, it was adopted in the present investigation.

Moreover, within HOSM an adjustment scheme is used to provide the transition between the initial (linear) wavefield to a fully nonlinear one, according to Dommermuth (2000) (see also Ducrozet et al. (2007)). This scheme is introduced to avoid the creation of spurious (error) waves due to the mismatch between linear inputs and the fully nonlinear free-surface boundary conditions. To achieve this, the nonlinear terms in the free-surface boundary conditions (Equations 2.26 and 2.27) are multiplied by a ramp function, given by,

$$g(t_R) = 1 - \exp\Big[-\Big(\frac{t_R}{T_a}\Big)^n\Big] \tag{3.6}$$

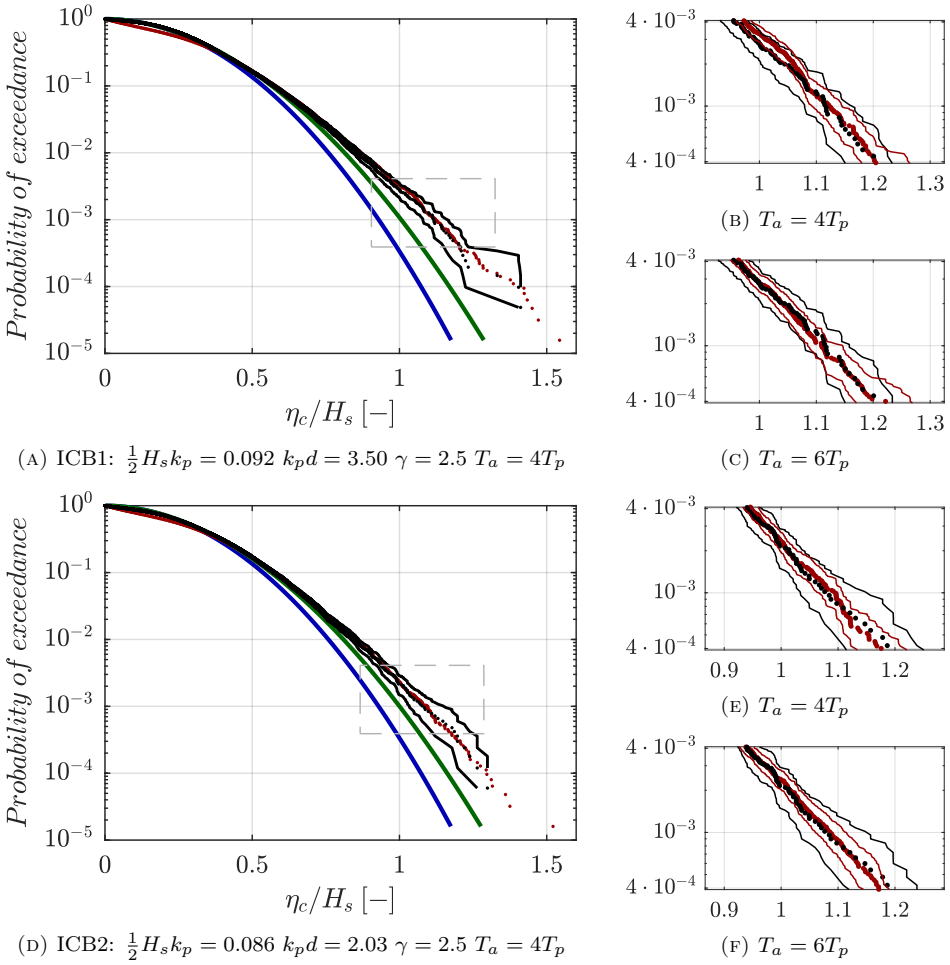
where, t_R refers to the simulation time including the ramping of the nonlinear terms, T_a defines the ramping duration and n is a shape parameter. At the beginning of the simulations, $g(0) = 0$, the free-surface boundary conditions are linear. While as t_R increases, $g(t_R)$ increases monotonically until it reaches a value of 1.

To provide effective comparisons between HOSM and experimental data, the evolution time, t, within HOSM was measured after the end of the ramp function; taken at the time it reaches a level of 99.5%. Moreover, to avoid any concerns with regards to the sensitivity of the HOSM results with respect to T_a, the simulations were performed using two different ramp-up times defined by $T_a = 4T_p$ and $6T_p$. In all cases the shape parameter was set to $n = 4$, following Dommermuth (2000).

Comparisons

Comparisons between the experimental crest-height exceedance probability distributions, normalised by the respective H_s, and the HOSM simulation results are shown in Figure 3.4 for the ICB cases with $d = 1.25m$, in Figure 3.5 for the ICB cases with $d = 0.5m$, in Figure 3.6 for the QUB cases and in Figure 3.7 for the ICDE cases.

In all figures, the left column presents the comparisons across the entire probability of exceedance, with the numerical data obtained using $T_a = 4T_p$. Within these figures, the Rayleigh and Forristall (2000) (2D) distributions have been added for reference. In addition, in comparing any two distributions based on sampled data, the inherent effect of sample variability must be accounted for. To achieve this, 95%



(A) ICB1: $\frac{1}{2}H_s k_p = 0.092$ $k_p d = 3.50$ $\gamma = 2.5$ $T_a = 4T_p$

(B) $T_a = 4T_p$

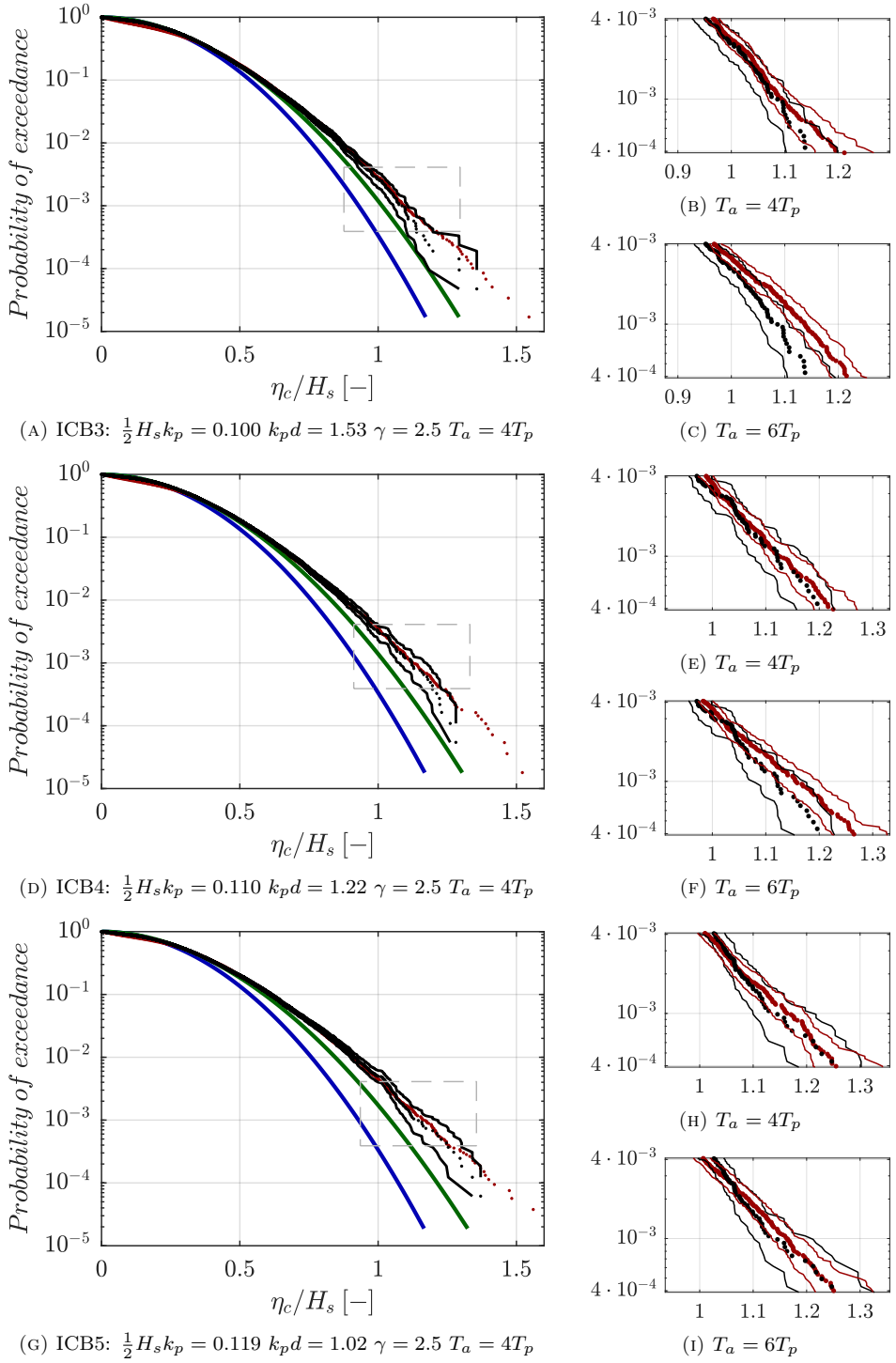
(C) $T_a = 6T_p$

(D) ICB2: $\frac{1}{2}H_s k_p = 0.086$ $k_p d = 2.03$ $\gamma = 2.5$ $T_a = 4T_p$

(E) $T_a = 4T_p$

(F) $T_a = 6T_p$

FIGURE 3.4: Comparison between experimentally (ICL basin, $d = 1.25m$) and numerically (HOSM) obtained normalised crest-height, η_c/H_s, exceedance probability distributions. (A) and (D) show the full probability distributions, where the HOSM results have been obtained using $T_a = 4T_p$. The different lines refer to: ( ) Rayleigh, ( ) Forristall (2000), ( ) HOSM, ( ) experiments, ( ) 95% confidence intervals. (B) and (E) show detailed views marked with a rectangle region in (A) and (D), respectively. Where confidence intervals have been added to the HOSM results denoted with ( ). (C) and (F) present the equivalent detailed views using $T_a = 6T_p$, showing that the results are independent of T_a.



(A) ICB3: $\frac{1}{2}H_s k_p = 0.100$ $k_p d = 1.53$ $\gamma = 2.5$ $T_a = 4T_p$

(B) $T_a = 4T_p$

(C) $T_a = 6T_p$

(D) ICB4: $\frac{1}{2}H_s k_p = 0.110$ $k_p d = 1.22$ $\gamma = 2.5$ $T_a = 4T_p$

(E) $T_a = 4T_p$

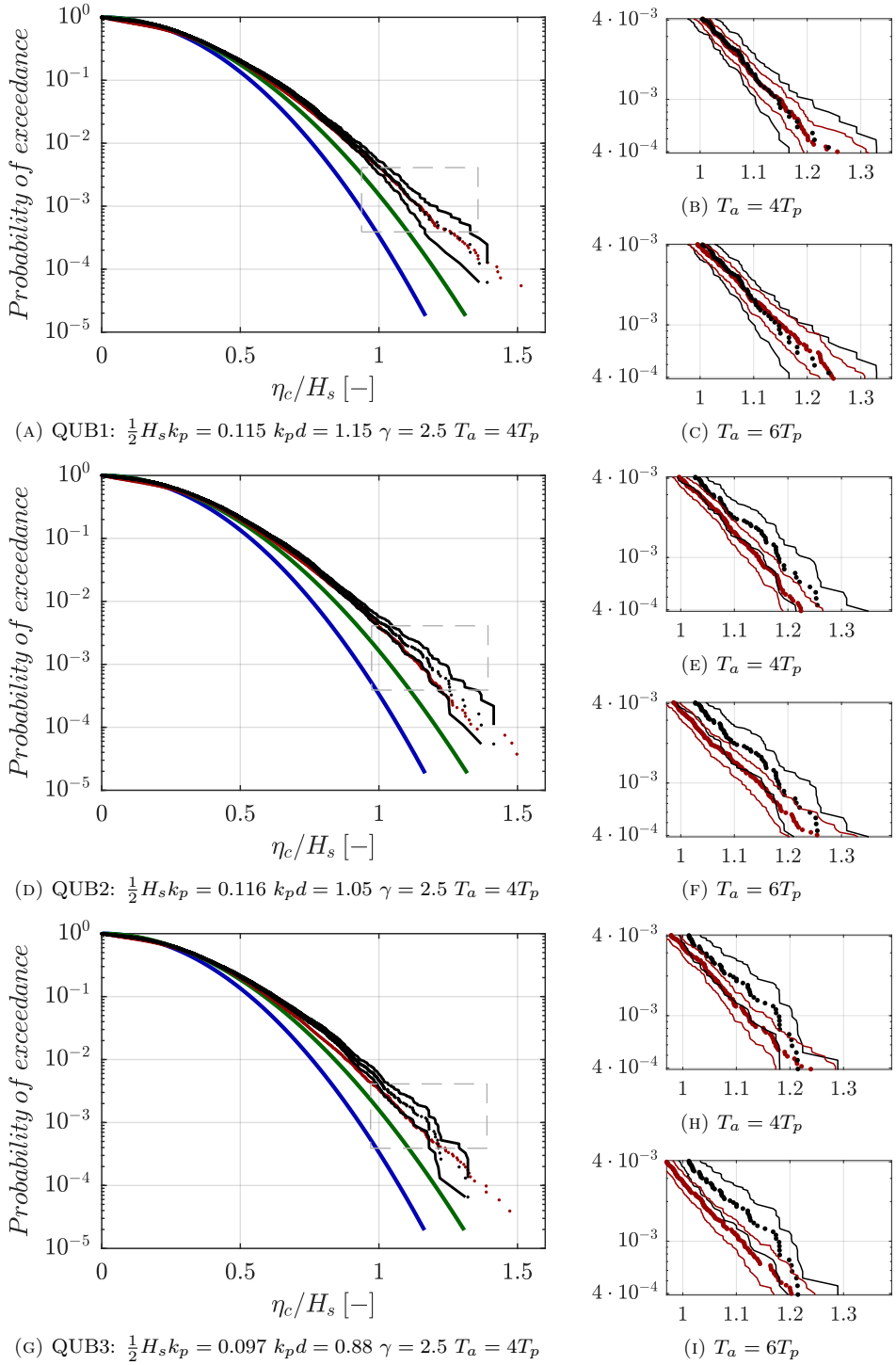
(F) $T_a = 6T_p$

(G) ICB5: $\frac{1}{2}H_s k_p = 0.119$ $k_p d = 1.02$ $\gamma = 2.5$ $T_a = 4T_p$

(H) $T_a = 4T_p$

(I) $T_a = 6T_p$

Figure 3.5: Comparison between experimentally (ICL basin, $d = 0.50m$) and numerically (HOSM) obtained normalised crest-height, η_c/H_s, exceedance probability distributions. (A), (D) and (G) show the full probability distributions, where the HOSM results have been obtained using $T_a = 4T_p$. The different lines refer to: (———) Rayleigh, (———) Forristall (2000), (•) HOSM, (•) experiments, (———) 95% confidence intervals. (B), (E) and (H) show detailed views marked with a rectangle region in (A), (D) and (G), respectively. Where confidence intervals have been added to the HOSM results denoted with (———). (C), (F) and (I) present the equivalent detailed views using $T_a = 6T_p$, showing that the results are independent of T_a.



(A) QUB1: $\frac{1}{2}H_s k_p = 0.115$ $k_p d = 1.15$ $\gamma = 2.5$ $T_a = 4T_p$

(B) $T_a = 4T_p$

(C) $T_a = 6T_p$

(D) QUB2: $\frac{1}{2}H_s k_p = 0.116$ $k_p d = 1.05$ $\gamma = 2.5$ $T_a = 4T_p$

(E) $T_a = 4T_p$

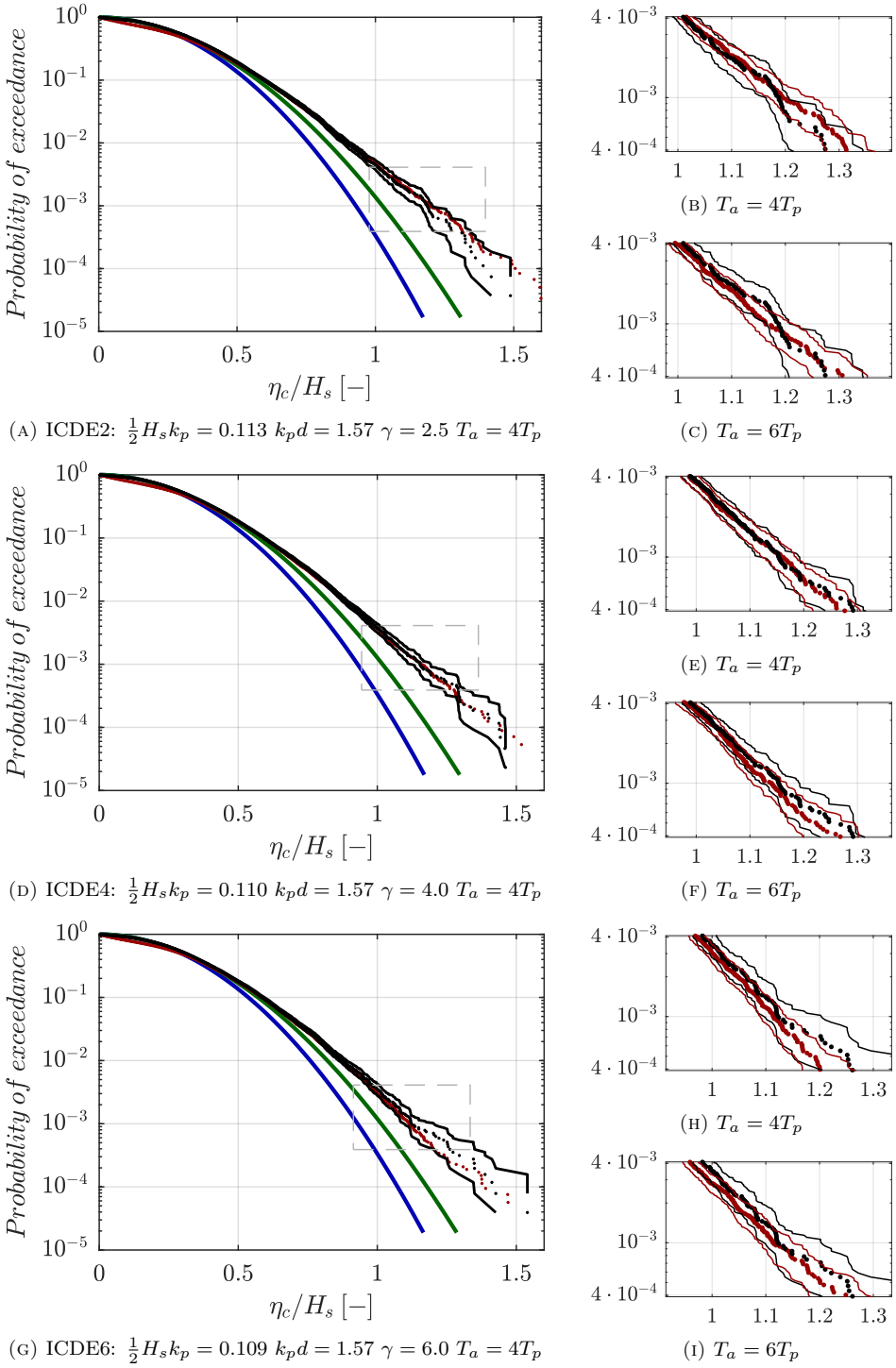
(F) $T_a = 6T_p$

(G) QUB3: $\frac{1}{2}H_s k_p = 0.097$ $k_p d = 0.88$ $\gamma = 2.5$ $T_a = 4T_p$

(H) $T_a = 4T_p$

(I) $T_a = 6T_p$

Figure 3.6: Comparison between experimentally (QUB basin) and numerically (HOSM) obtained normalised crest-height, η_c/H_s, exceedance probability distributions. (A), (D) and (G) show the full probability distributions, where the HOSM results have been obtained using $T_a = 4T_p$. The different lines refer to: (———) Rayleigh, (———) Forristall (2000), (•) HOSM, (•) experiments, (———) 95% confidence intervals. (B), (E) and (H) show detailed views marked with a rectangle region in (A), (D) and (G), respectively. Where confidence intervals have been added to the HOSM results denoted with (———). (C), (F) and (I) present the equivalent detailed views using $T_a = 6T_p$, showing that the results are independent of T_a.



(A) ICDE2: $\frac{1}{2}H_s k_p = 0.113$ $k_p d = 1.57$ $\gamma = 2.5$ $T_a = 4T_p$

(B) $T_a = 4T_p$

(C) $T_a = 6T_p$

(D) ICDE4: $\frac{1}{2}H_s k_p = 0.110$ $k_p d = 1.57$ $\gamma = 4.0$ $T_a = 4T_p$

(E) $T_a = 4T_p$

(F) $T_a = 6T_p$

(G) ICDE6: $\frac{1}{2}H_s k_p = 0.109$ $k_p d = 1.57$ $\gamma = 6.0$ $T_a = 4T_p$

(H) $T_a = 4T_p$

(I) $T_a = 6T_p$

Figure 3.7: Comparison between experimentally (ICL double-ended wave flume) and numerically (HOSM) obtained normalised crest-height, η_c/H_s, exceedance probability distributions. (A), (D) and (G) show the full probability distributions, where the HOSM results have been obtained using $T_a = 4T_p$. The different lines refer to: (——) Rayleigh, (——) Forristall (2000), (•) HOSM, (•) experiments, (——) 95% confidence intervals. (B), (E) and (H) show detailed views marked with a rectangle region in (A), (D) and (G), respectively. Where confidence intervals have been added to the HOSM results denoted with (——). (C), (F) and (I) present the equivalent detailed views using $T_a = 6T_p$, showing that the results are independent of T_a.

confidence intervals were obtained using the bootstrap method (Efron, 1979) based on 1000 re-samples of the original data. The confidence intervals of the experimental data have been added to all the comparisons. In contrast, the corresponding confidence intervals of HOSM simulations have been omitted from left-column figures to maintain clarity.

On the right hand columns of Figures 3.4, 3.5, 3.6 and 3.7 a detailed view of the comparisons is provided, focused around a probability of exceedance of $Q = 10^{-3}$; sub-figures (B), (E) & (H) corresponding to the marked rectangle appearing on the left hand side plots. The crest heights at this probability level are associated with the most likely maximum crest height in a 3-hour sea-state (full-scale) and they are not affected by the very large variability arising in lower probability levels. Hence, focusing on this area of the crest-height distribution provides both relevant and reliable comparisons. In these plots, confidence intervals of the numerical data have also been added for completeness. In addition, below each detailed view of sub-figures (B), (E) & (H), an identical detailed view is provided in sub-figures (C), (F) & (I). The numerical data in these latter plots correspond to a ramp function of $T_a = 6T_p$; comparisons between the two demonstrating that indeed the results are not overly sensitive to the ramp function's length.

Taking the comparisons in Figures 3.4, 3.5, 3.6 and 3.7 as a whole, the agreement between the experimental data and the HOSM simulations is very good; the differences between the two lying within the confidence intervals. More specifically, the average relative error [1] at the wave crest arising at $Q = 10^{-3}$ is 1.5% for $T_a = 4T_p$ and 2.3% for $T_a = 6T_p$. The maximum error is observed in QUB3 using $T_a = 6T_p$ and equals 5.8%, whereas the corresponding error for $T_a = 4T_p$ is 5%.

In interpreting the quality of the comparisons it should be stressed that whilst every effort was made to ensure the quality of experimental data (Latheef 2014, McCarthy 2018, Karmpadakis 2018 and Gray 2020), there are inevitably some limitations induced by (1) the wavemaking process, which is based on a first-order demand signal and (2) the level of wave absorption from the downstream wave dissipation boundary (beaches/porous media). The first limitation can potentially lead to the creation of unwanted freely propagating spurious waves. In addition, the second ef-

[1] the error has been calculated according to $2\frac{\eta_c^{HOSM}-\eta_c^{exp}}{\eta_c^{HOSM}+\eta_c^{exp}}$

fect can lead to the contamination of the wavefield with reflected waves. With the nonlinear interactions being more intense as the effective depth reduces, particularly the second-order difference terms, the first limitation is expected to affect the shallower cases more (Aknin, 2015). Regarding the second limitation, in the ICL facilities the wave reflections are typically below 5% (Masterton 2007, Gray 2020) and in the QUB facility below 7% (Karmpadakis, 2018). With the wave energy channelled in one direction in the present uni-directional sea-states, the level of wave reflections is expected to be higher in the present uni-directional sea-states, when compared to directional ones. Considering all the above factors, the discrepancies between experimental data and numerical data are within the expected range.

3.4.2 Near-limiting deterministic wave groups

Whilst the above validation is essential to demonstrate the reliability of the crest-height distributions obtained using HOSM; they do not provide information on the individual wave profiles. This is addressed in the present section which provides additional validation cases to ensure that HOSM captures the nonlinear physics correctly on a wave-by-wave basis. These cases refer to the comparison of fully nonlinear wave profiles of deterministic wave groups obtained using HOSM and an alternative fully nonlinear numerical wave model.

Multiple-Flux Boundary Element Method

The alternative wave model used to validate HOSM is based on the Boundary Element Method (BEM). The BEM makes use of the so-called Green's second identity and solves the water-wave boundary value problem in the physical space, an approach first proposed by Grilli et al. (1989). In particular, the model developed by Hague & Swan (2009) is employed here. This offers a special treatment for the so-called 'corner problem' [1] relevant to BEM applications. In tackling this problem, Hague & Swan (2009) make use of a Multiple-Flux approach. Hence, it will hereafter be referred to as MFBEM. For more details on the numerical implementation of MFBEM, the reader is referred to the original work of Hague & Swan (2009).

[1] The corner problem refers to the non-uniqueness of the outward potential flux at the corners of the computational domain.

The MFBEM model presents a numerical equivalent to a physical wave-flume, as the boundaries of the computational domain act similarly to the physical boundaries in an experimental setting. More specifically, they consist of (1) a wave-generation boundary, (2) an impermeable bottom boundary, and (3) a wave absorption boundary enhanced with an absorbing sponge layer in front to minimise wave reflections.

Within the present simulations, the numerical stability of MFBEM was ensured with the selection of an appropriate combination of spatial spacing, Δx, and time-step, Δt, such that the usual Courant number condition (see Grilli et al., 2001) is satisfied. In addition, the combination of a sponge layer of substantial length ($4l_p$) and a Sommerfield radiation condition at the downstream boundary ensured the effective absorption of the incident wave energy.

Details of simulations

In determining the inputs for the numerical wave-groups, the input amplitude spectrum was defined according to the theory of Lindgren (1970), Boccotti (1983) and Tromans et al. (1991). As such, it is proportional to the spectral energy of the assumed sea-state, here characterised by a JONSWAP spectrum with $\gamma = 2.5$. The input phases were adjusted such that all wave components came into focus at a predefined focal location and time under the effect of linear dispersion. Using this type of input in a linear simulation, the wave profile with the maximum elevation coincides with the most likely shape of a large wave event arising in a linear random sea-state. It, therefore, follows that the present simulations account for the nonlinear 'correction' to these incident wave events.

For the present comparisons three effective water depths are addressed ($k_p d = 0.87, 1.28$ and 5.03) and two (linear) steepnesses ($Ak_p = 0.08$ and 0.18, A defining the linear sum of the input amplitudes). The first steepness refers to wave groups of moderate nonlinearity, while the second refers to highly nonlinear near-limiting wave groups. For the first steepness, the evolution (or focus) time within HOSM was set to $t_f = 20T_p$ and for the second steepness two evolution times were considered, $t_f = 20T_p$ and $40T_p$. Comparisons between these cases aiming to address the effect of nonlinear evolution time. In all cases T_a was set to $4T_p$; the choice of T_a again found to not affect the results.

Following the discussion in the previous section, the evolution time within HOSM

is linked to the focus location within MFBEM according to the group velocity of the spectral peak. Therefore, the focus location is $x_f = 10,\ 14,\ 16.3l_p$ for $t_f = 20T_p$ and $x_f = 20,\ 28,\ 32.6l_p$ for $t_f = 40T_p$ in $k_pd = 5.03, 1.28$ and 0.87, respectively. With the different cases including different focus locations, x_f, the domain length within MFBEM was defined according to x_f. Hence, the computational resources used in the simulations varied between cases. Notably, with the computational requirements scaling according to $O(n^2)$ (with n being the number of computational nodes) the longest MFBEM simulations required more than two days of computation time. Finally, the parameters of the adopted numerical setup within the MFBEM are summarised in Table 3.5. Whereas the numerical setup within HOSM is presented in Table 3.3.

Table 3.5: Numerical setup of MFBEM simulations used for validating HOSM.

Parameter	Description	Value
$l_p/\Delta x\ [-]$	Number of free-surface nodes in x per wavelength corresponding to the spectral peak period T_p	80
$d/\Delta z\ [-]$	Number of vertical nodes (in z)	20-50
$T_p/dt\ [-]$	Number of time-steps per peak period	200
$L_{sponge}\ [-]$	Length of sponge layer	$4l_p$
$L_{domain}[-]$	Domain length	$x_f + 2l_p + L_{sponge}$

Comparisons between HOSM and MFBEM

The space-traces, $\eta(x)$, at the time of the maximum elevation and the envelope of the maximum elevation any time in the computational domain (both normalised with respect to the input amplitude sum, A) arising from the two wave models are compared in Figures 3.8 ($Ak_p = 0.08$, $t_f = 20T_p$), 3.9 ($Ak_p = 0.18$, $t_f = 20T_p$) and 3.10 ($Ak_p = 0.18$, $t_f = 40T_p$). Each figure contains three sub-plots referring to the three different effective water depths, $k_pd = 5.03$, 1.28 and 0.87 from top to bottom.

In considering these figures, the agreement between the two models is very good in all cases; both the maximum crest elevation and any wave asymmetries are in close agreement. Considering the results in more detail, for the lowest steepness cases (Figure 3.8), the wave traces and maximum elevation profiles are nearly symmetric. This arises because changes in the dispersive properties due to near-resonant

interactions are not significant. Likewise, any crest amplification due to the combination of near-resonant and bound-wave interactions remains less than $\sim 5\%$ in all cases.

For the higher steepness cases (Figures 3.9 and 3.10) the asymmetries are more pronounced due to the effect of nonlinear dispersion. Interestingly, in the two deepest cases the nonlinear interactions lead to crest-amplification by as much as $\sim 20\%$ in $k_p d = 5.03$. In contrast, the opposite is the case for the shallowest wave groups in $k_p d = 0.87$. This reduction is in line with insights gained from Katsardi & Swan (2011) on uni-directional deterministic wave-group evolution in this water depth. This explains the defocusing effect in terms of the near-resonant interactions.

3.5 Effect of nonlinear wave-wave interactions on the statistics of uni-directional random wavefields

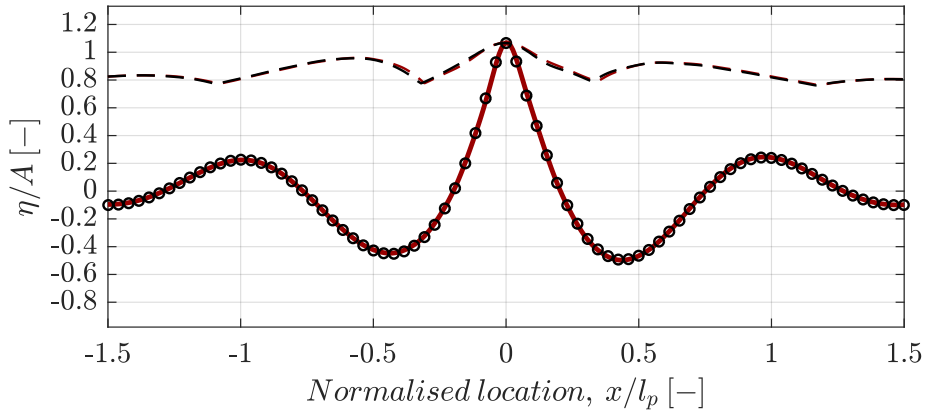
Having established the accuracy of the HOSM simulations, this section presents the results of the main investigation regarding the crest-height statistics in unidirectional nonlinear sea-states. Specifically:

1. §3.5.1 some additional verification of the random wave simulations and the effect of the ramp function on the nonlinear evolution. In the earlier validation sections of this chapter, it was shown that the crest-height statistics obtained for short evolution times are not particularly sensitive to the length of the ramp function. Nonetheless, with the aim of the main investigation being to study the effect of nonlinear interactions for longer evolution times, it was considered necessary to verify that the results which follow are indeed independent of the chosen ramp function.

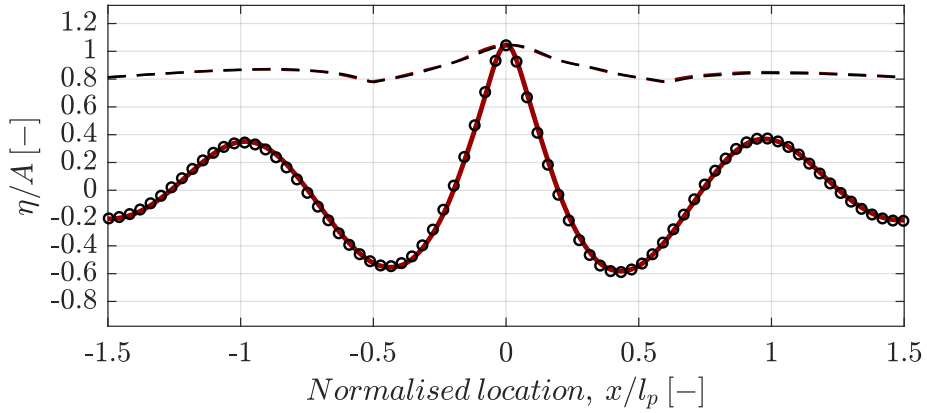
2. §3.5.2 presents the effect of nonlinear evolution on the statistical properties of random wavefields in different effective water-depth regimes; the focus being on the crest-height statistics.

3. Following, §3.5.3 concerns the role of sea-state steepness on the different nonlinear interactions.

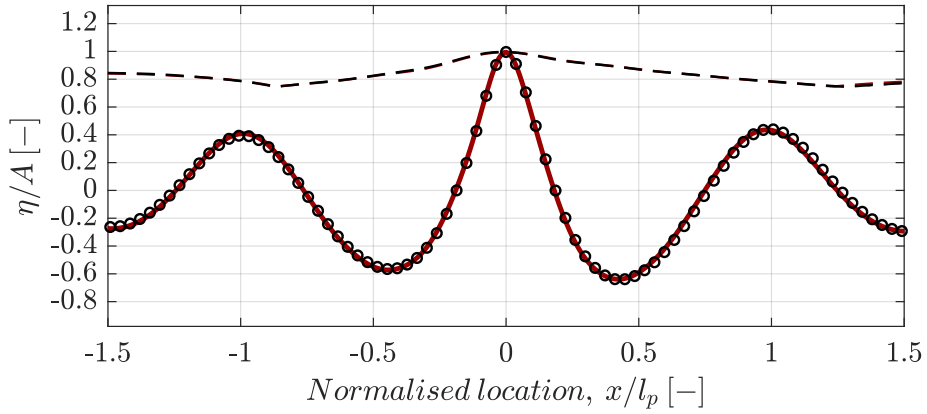
4. Finally, §3.5.4 provides an account of the effect of spectral bandwidth.



(a)

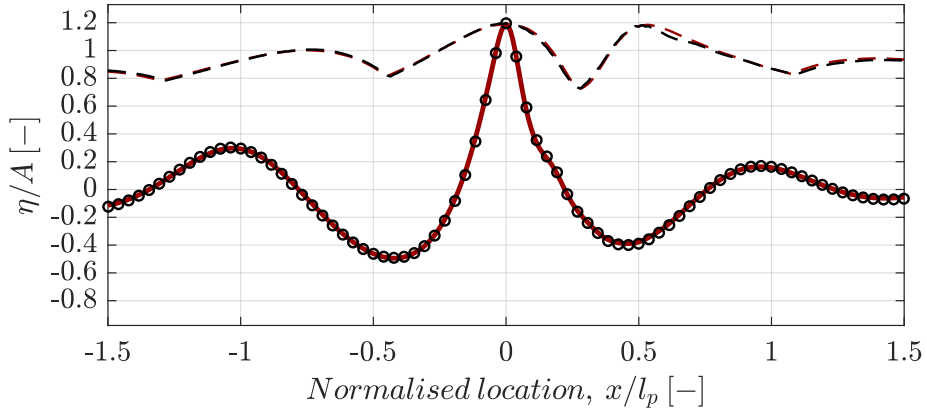


(b)

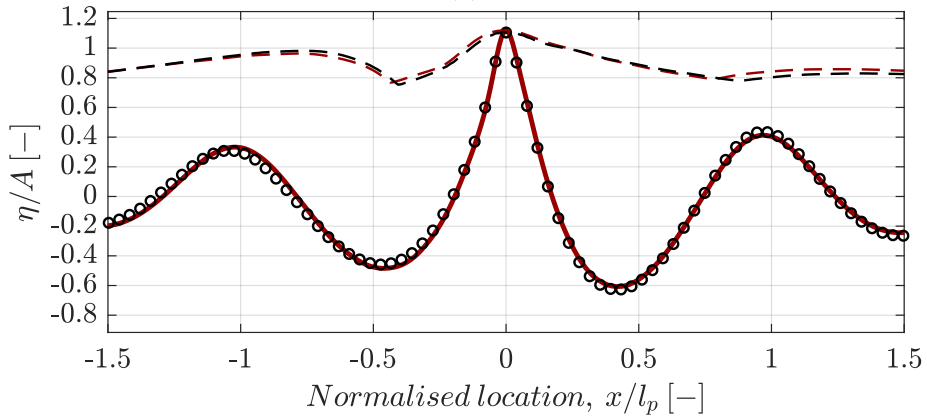


(c)

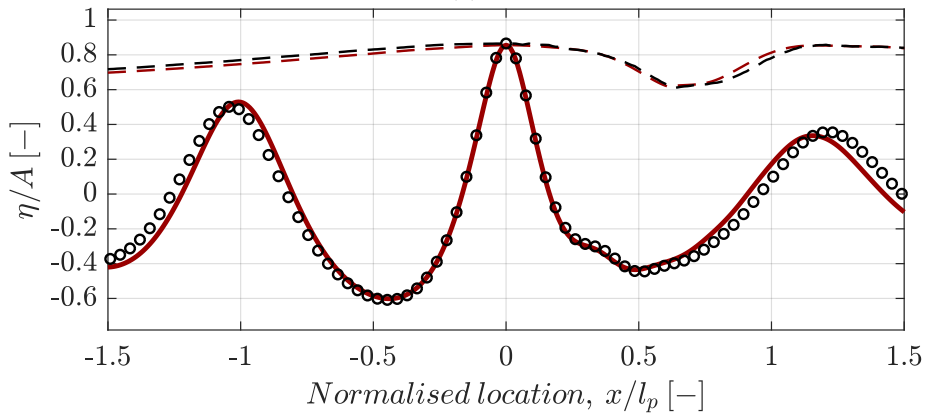
Figure 3.8: Comparison of the fully nonlinear normalised spatial profile of the free-surface elevation, η/A, at the time of maximum crest elevation between HOSM (———) and MFBEM (∘) for (linearly) focused wave groups of steepness $Ak_p = 0.08$. The variation in the maximum surface elevation in the computational domain at any time is also shown with (— —) for HOSM and (— —) for MFBEM. Sub-figure (A) for $k_pd = 5.03$, (B) for $k_pd = 1.28$ and (C) for $k_pd = 0.86$. The evolution time within HOSM is $t_f = 20T_p$. The horizontal axis is centred at the location of maximum elevation, and it is normalised by the peak wavelength l_p. Note that every fourth data point of the MFBEM simulations is plotted to maintain clarity.



(A)

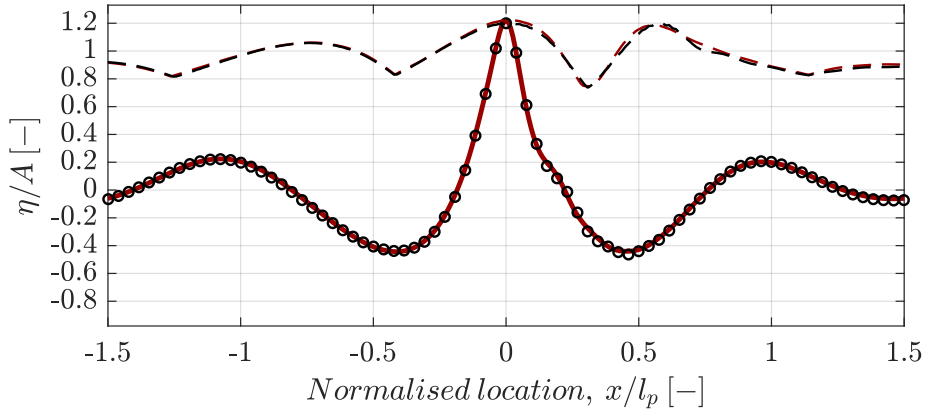


(B)

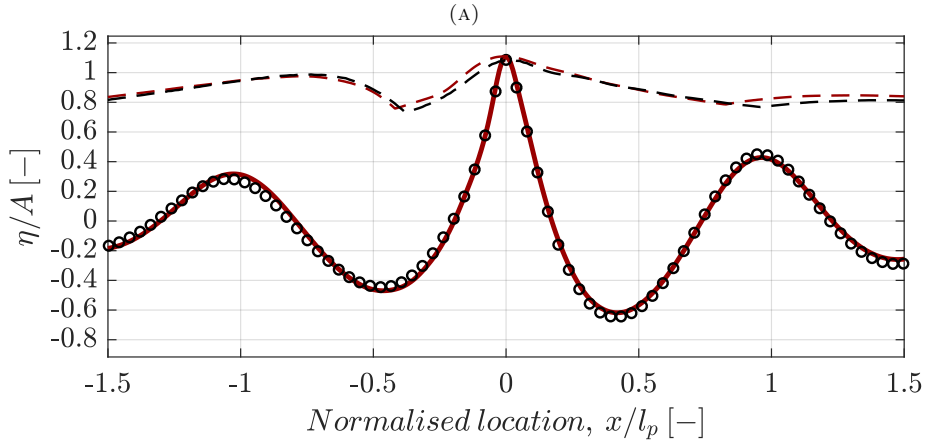


(C)

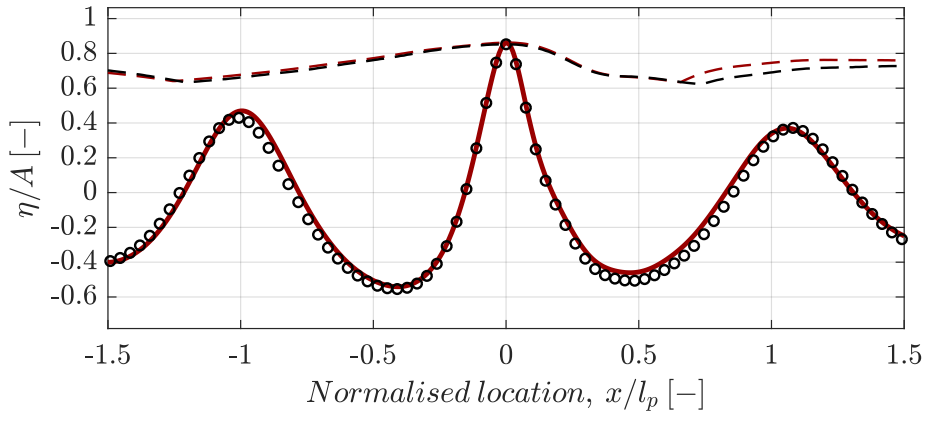
Figure 3.9: Comparison of the fully nonlinear normalised spatial profile of the free-surface elevation, η/A, at the time of maximum crest elevation between HOSM (———) and MFBEM (∘) for (linearly) focused wave groups of steepness $Ak_p = 0.18$. The variation in the maximum surface elevation in the computational domain at any time is also shown with (— —) for HOSM and (— —) for MFBEM. Sub-figure (A) for $k_pd = 5.03$, (B) for $k_pd = 1.28$ and (C) for $k_pd = 0.86$. The evolution time within HOSM is $t_f = 20T_p$. The horizontal axis is centred at the location of maximum elevation, and it is normalised by the peak wavelength l_p. Note that every fourth data point of the MFBEM simulations is plotted to maintain clarity.



(a)



(b)



(c)

Figure 3.10: Same as Figure 3.9, but for evolution time $t_f = 40T_p$ within HOSM.

3.5.1 Preliminary considerations

As mentioned above, this section presents preliminary results regarding the nonlinear evolution of the statistical properties of random wavefields. For this purpose, JONSWAP sea-states with $\gamma = 2.5$ were employed; the effective water depths defined by $k_p d = 0.87$, 1.28 and 5.03, corresponding to the three different water-depth regimes identified in §3.2. In performing these simulations, two sea-state steepnesses were selected, $\frac{1}{2}H_s k_p = 0.005$ and 0.105; the former representing a linear sea-state and the latter the steepest of the cases in Table 3.1. To explore whether the duration of the ramp function affects the nonlinear evolution process, 4 different ramp functions, defined by $T_a = 4$, 6, 8 and $10T_p$, were adopted.

Within these simulations, the freely propagating or dynamic part of the free surface was isolated using the phase-manipulation method (§2.2.6). To this end, the term 'free waves' will hereafter refer to the part of the free surface affected by third-order quartet near-resonant interactions; the free-wave energy associated with triad or quintet interactions being orders of magnitude smaller (§2.2.6). With the various nonlinear effects having been separated, the statistical moments of dynamic kurtosis, bound kurtosis and skewness were calculated at each time-step, once the initial ramping of the nonlinear terms ended [1]. In all cases, the time evolution of the ensemble-averaged (over 500 seeds) values was obtained.

To begin, the evolution the dynamic kurtosis for both sea-state steepnesses is shown in Figure 3.11, where $t = 0$ signifies the end of the ramp function. Considering, first, the smallest of steepnesses ($\frac{1}{2}H_s k_p = 0.005$), any nonlinear effects should be absent and the dynamic kurtosis should be zero during the entire duration of the simulation. This is exactly the case, as shown in Figure 3.11 (A). This confirms that any non-zero values for simulations of higher steepness will indeed be due to nonlinear evolution. The equivalent results for $\frac{1}{2}H_s k_p = 0.105$ are presented in Figure 3.11 (B). In this case, the dynamic kurtosis is shown to converge to the same steady-state value irrespective of the length of the ramp function. However, this is not the case for the initial stages of nonlinear evolution, a close-up shown in Figure 3.11 (C). For small times the results are shown to differ for different ramp-up durations; this is clearly a non-physical feature.

[1] In §3.4 it was noted that that the end of ramp was defined as it having reached a level of 99.5%

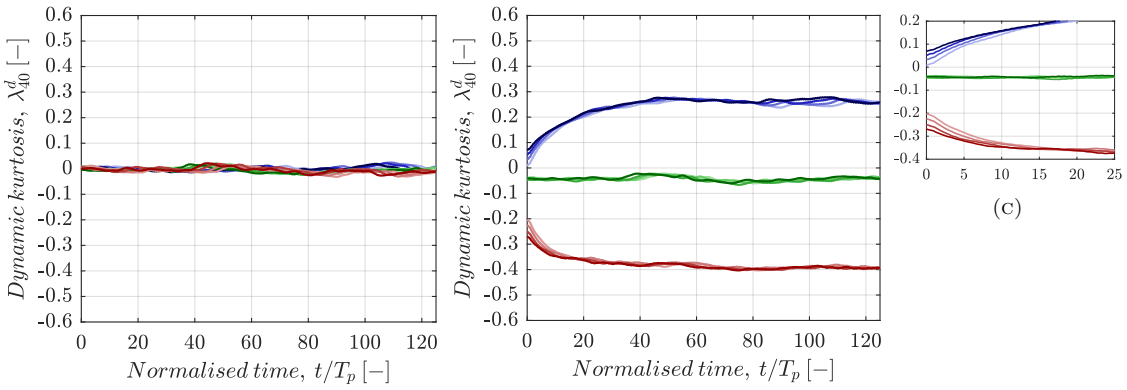
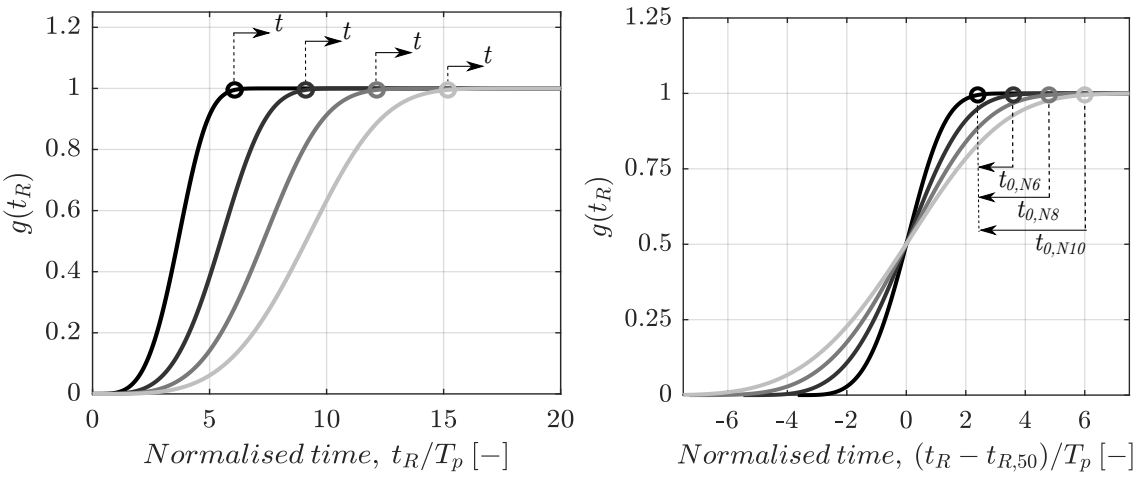


Figure 3.11: Temporal evolution of the ensemble-averaged dynamic kurtosis for different ramp function lengths in uni-directional sea-states with $\gamma = 2.5$. (A) for $\frac{1}{2}H_s k_p = 0.005$ and (B) for $\frac{1}{2}H_s k_p = 0.105$. (C) is a detailed view of (B) covering $t \in [0, 25]T_p$. The lines (/ / /) refer to $k_p d = 5.03$, (/ / /) to $k_p d = 1.28$ and (/ / /) to $k_p d = 0.87$; the different colour shades corresponding to $T_a = 4, 6, 8$ and $10T_p$, respectively. The horizontal time axis is normalised by the spectral peak period.

In interpreting this observation, it is instructive to visualise the shapes of the ramp functions. These are shown in Figure 3.12 (A). It is observed that as the length of the ramp function increases, the portion of time at which the ramp operates at high levels (closer to unity) increases. This means that there is inevitably more evolution taking place within the ramp function as the ramping lasts for longer. Hence, at the end of ramping time, the nonlinear evolution for different T_a is different.

In seeking to accommodate for this effect, an effective evolution time can be calculated based on the shapes of the ramp functions. To achieve this, the ramp functions were centred at the point at which they reach a level of 50%, as shown in Figure 3.12 (B). Subsequently, an effective evolution time for the longer ramp functions was calculated by treating the end of the shortest ramp ($T_a = 4T_p$) as a reference and measuring the time interval, t_0, between the end of the longer ramp functions and this reference point. This distance, denoted with $t_{0,N}$ ($N = T_a/T_p$) in Figure 3.12 (B), equals 1.2, 2.4 and $3.6T_p$ for $T_a = 6$, 8 and $10T_p$, respectively.

In accounting for this effective initial nonlinear evolution, Figure 3.13 presents comparable plots to Figures 3.11(B) and 3.11(C), but this time the numerical results incorporate an initial time-shift $t_{0,N}$. These results show that the evolution is almost identical for different T_a values, confirming that the results are indeed independent of the choice of T_a, provided the starting evolution time (at the end of the ramp function) is accounted for.



(A) (B)

Figure 3.12: (A) The shape of ramp functions for $T_a = 4, 6, 8$ and 10 denoted with (/ / /) respectively. (B) The ramp functions centred at the time they reach a level of 50%. An effective evolution time, t_0, is defined geometrically as the time-distance from the end of the longer ramp functions ($T_a/T_p = 6, 8$ and 10) to the end of the shortest function of $T_a = 4$. It is noted that the time axis in these plots refers to the ramping time t_R and the start of the evolution time t is defined at the end of ramp.

Additionally, it should be noted that, in theory, for $t = 0$, no nonlinear evolution should take place, hence the dynamic kurtosis should be zero. In observing Figure 3.13 (A), this is indeed the case for $k_pd = 5.03$, but not for the shallower cases of $k_pd = 0.87$ and 1.28. To correct this, the length of the ramp function could be reduced further. However, noting the work of Dommermuth (2000) on regular waves, a very short ramp function could result in the generation of unwanted spurious waves that can disrupt the entire simulations.

To identify whether the length of the ramp function could be further reduced or (even) be eliminated, ramp function lengths of $T_a = 0$ (no ramp), $2T_p$ and $4T_p$ were employed to generate random free surface records in $k_pd = 0.87$ and 5.03. A two-dimensional Discrete Fast Fourier Transform (2D-FFT) was then applied to the harmonic contributions of these records spanning in the time-interval $t \in [0, 50T_p]$; this interval marking the initial stage of evolution, where any spurious effects are expected to be more pronounced (Perignon et al., 2010). In undertaking these calculations, a Tukey window (Bloomfield, 2004) was applied in the time-axis before evaluating the 2D-FFT. This accounts for the non-periodicity of the signal.

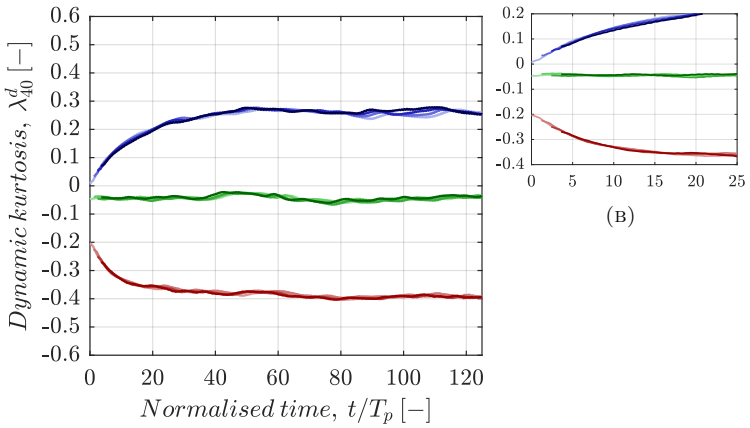


Figure 3.13: Temporal evolution of the ensemble-averaged dynamic kurtosis for different ramp function lengths in uni-directional sea-states with $\gamma = 2.5$ and $\frac{1}{2}H_s k_p = 0.105$. The results and colour reference is identical to Figures 3.11 (B) and (C), but this time the effective initial evolution time of $t_0 = 1.2, 2.4, 3.6T_p$ for $T_a = 4, 6, 8$ and 10, respectively, is incorporated in the plotting position.

To reduce the number of figures, only the results of the second-harmonic are discussed as follows. This harmonic was chosen because it was found to contain the highest portion of spurious waves. The resulting frequency-wavenumber energy spectra ($\frac{1}{2}a_i^2$) of the second-harmonic are shown in Figure 3.14. The results indicate that for $T_a = 0$ significant spurious free-wave energy, laying around the linear dispersion line, is detected in both effective water depths. For $T_a = 2T_p$ this energy is reduced (especially for $k_p d = 5.03$), but remains present. While it is eliminated for $T_a = 4T_p$ for both cases. The conclusions arising are therefore: (1) T_a cannot be reduced below $4T_p$ without including spurious wave generation and (2) the choice of $T_a = 4T_p$ is the shortest adequate ramp function [1].

To complete the verification of the simulations, the rest of the statistical moments should be considered as they contain information of additional interactions not included in the dynamic kurtosis To this end, Figure 3.15 presents the evolution of the skewness and bound kurtosis corresponding to the simulations outlined in Figure 3.13. In addition, the same initial time-shift as in Figure 3.13 has been applied. The results for the different ramp functions again overlap for the entire time record, highlighting once more the success of the time-shifting procedure and the independence

[1] It is noted that using an intermediate value of $T_a = 3T_p$ spurious waves were still present; the results being omitted for brevity.

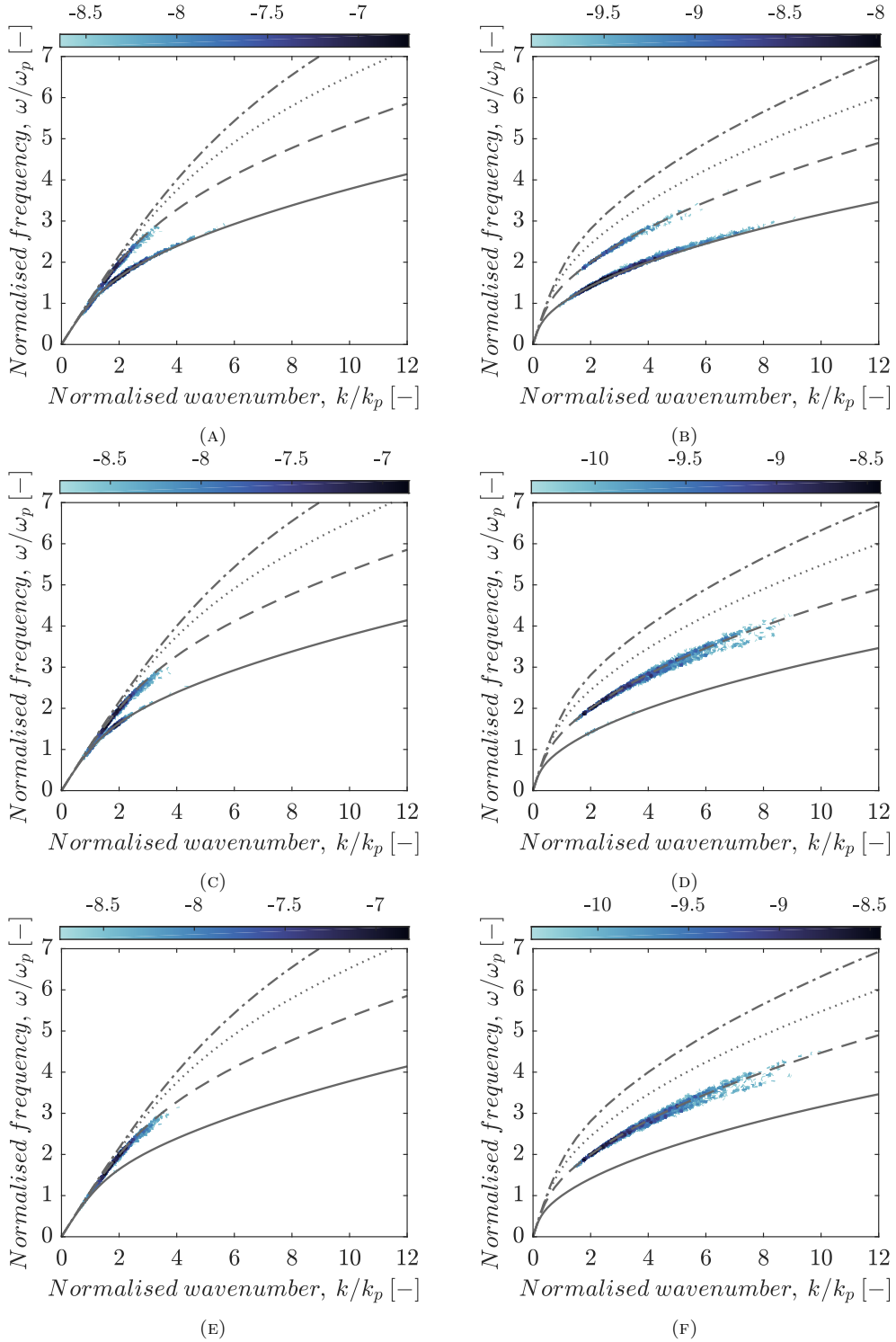
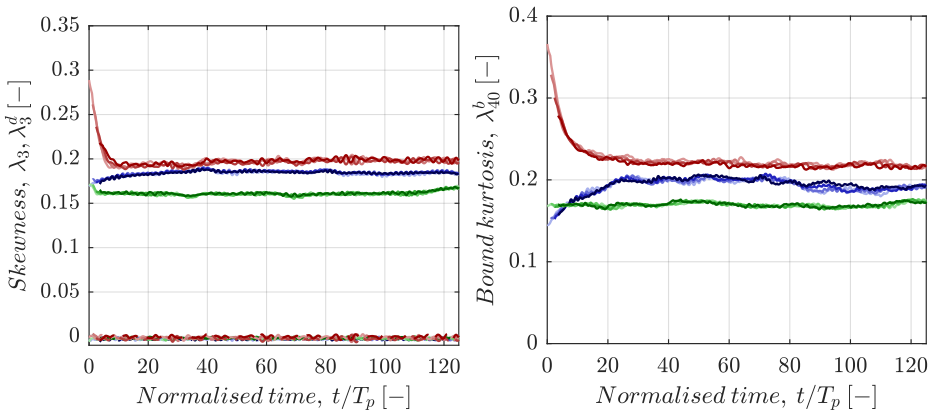


Figure 3.14: Contour plot of the spectral energy ($\frac{1}{2}a^2$) of the second-harmonic for different ramp-function lengths, for sea-states with $\gamma = 2.5$ and $\frac{1}{2}H_s k_p = 0.105$. Left column for $k_p d = 0.87$ and right column for $k_p d = 5.03$. (A)-(B) for $T_a = 0$, (C)-(D) for $T_a = 4T_p$ and (E)-(F) for $T_a = 6T_p$. The line (——) corresponds to the linear dispersion equation, while the lines (– – / ····· / –·–) correspond to integer multiples of the linear dispersion relation of 2, 3 and 4 respectively.



(A) (B)

Figure 3.15: Temporal evolution of the ensemble-averaged (A) skewness and (B) bound kurtosis for different ramp function lengths for uni-directional sea-states with $\gamma = 2.5$ and $\frac{1}{2}H_s k_p = 0.105$. The lines (/ / /) refer to $k_p d = 5.03$, (/ / /) to $k_p d = 1.28$ and (/ / /) to $k_p d = 0.87$; with the different colour shades corresponding to $T_a = 4, 6, 8$ and 10, respectively. Note that in (A) the skewness, λ_3^d, of the dynamic part of the free surface is also added for all water depths and corresponds to the horizontal lines at $\lambda_3 = 0$. In both cases the horizontal time-axis is normalised by the spectral peak period.

of the results with respect to the length of the ramp function.

An additional verification point is included in Figure 3.15(A), relating to the skewness parameter of the free waves (λ_3^d). Given that the separation of the harmonic contributions is valid, this skewness should be zero throughout the simulations. Figure 3.15(A) shows that this is indeed the case; confirming the accuracy of the simulations and the phase manipulation method.

3.5.2 Influence of effective water depth

This section explores how the crest-height statistics are affected by the nonlinear evolution in different effective water depths; particularly focusing on:

- the effect of evolution time on the crest-height distribution,
- the relative importance of near-resonant interactions vs bound-wave contributions at second-order and above on the crest heights, and
- the required number of simulated wave cycles for the reliable estimation of the expected crest height (and its underlying nonlinear contributions) at a probability of exceedance of $Q = 10^{-3}$; the latter corresponding (approximately) to the most likely maximum crest height in a 3-hour sea-state.

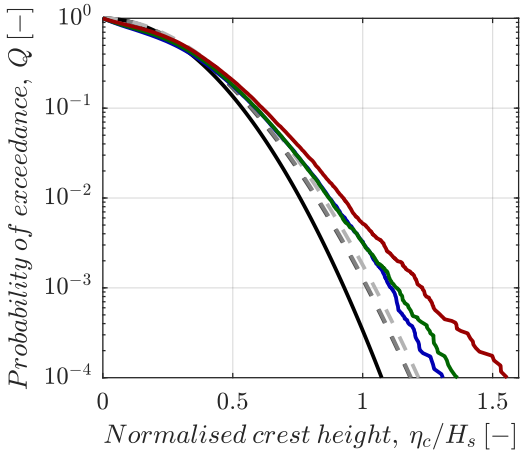
Time-evolution of the crest-height distribution

Figure 3.16 presents the normalised crest-height, η_c/H_s, exceedance probability distributions corresponding to the three nonlinear sea-states employed in the previous section, characterised by $\frac{1}{2}H_s k_p = 0.105$; each sub-figure corresponding to a different evolution time and containing results for all three effective water depths of $k_p d = 0.87$, 1.28 and 5.03. The selected evolution times refer to $t = 0$ (sub-figure (A)), $t = 4T_p$ (sub-figure (B)) and $t = 55T_p$ (sub-figure (C)) [1]. These cover the initial, transient and steady-state part of the nonlinear evolution of the statistical moments as presented in Figures 3.13 and 3.15.

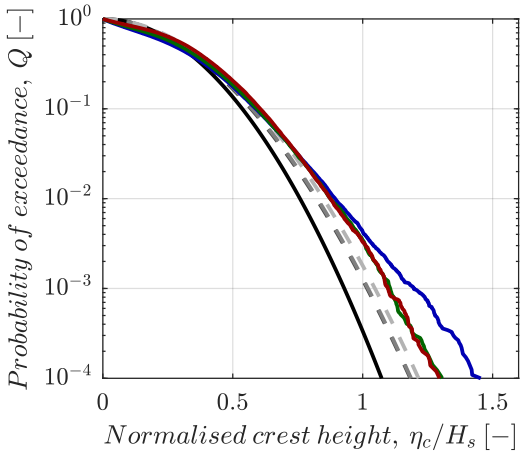
To assess the extent to which nonlinearity as a whole affects the crest heights, the (linear) Rayleigh distribution has been added in all sub-figures for reference. While the predictions of the widely used second-order crest-height model of Forristall (2000) have also been added to assess its performance. To this end, it should be stressed out that Forristall (2000) takes into account solely the effect of second-order bound terms in the absence of nonlinear evolution. Hence, whilst the Forristall (2000) predictions are influenced by the effective water depth, they remain unaffected by the nonlinear evolution time.

Considering, first, the results for $t = 0$ (sub-figure (A)), it is observed that the effective water depth affects profoundly the tail of the normalised crest-height distribution obtained from HOSM. Particularly, it is revealed that, whilst the relative crest height amplification for $k_p d = 5.03$ and 1.28 is of similar magnitude (at least for $Q > 10^{-3}$ where the sample variability is small), for $k_p d = 0.87$ the amplification is substantially higher (than the two deeper cases). In all effective water depths, the crest heights are shown to lay persistently above the Forristall (2000) predictions for $Q < 10^{-1}$, indicating the influence of nonlinear interactions beyond second-order. These observations are entirely in line with the outcomes of the experimental investigations conducted by Latheef & Swan (2013), Karmpadakis et al. (2019a) and Gray (2020) in that amplification of the wave crests above the second-order model of Forristall (2000) are relevant; evidence of which has already being presented in §3.4.1.

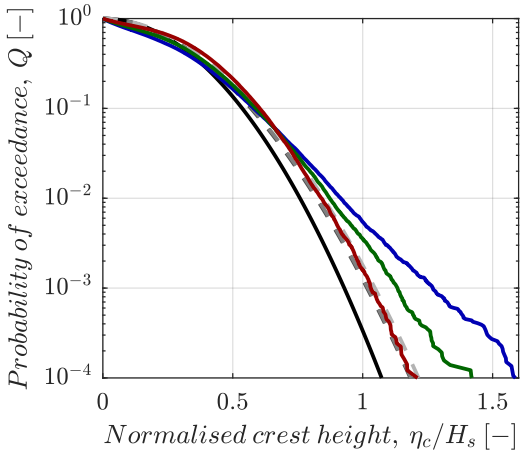
[1] Note that in connection with the discussion provided earlier with respect to the effect of the ramp function, the results in this section have been obtained on the basis of $T_a = 4T_p$. If this is not the case, it is mentioned explicitly in the discussion to follow.



(A)



(B)



(C)

Figure 3.16: Normalised crest-height, η_c/H_s, exceedance probability distributions in uni-directional sea-states with $\gamma = 2.5$ and $\frac{1}{2}H_s k_p = 0.105$ for different evolution times: (A) for $t = 0$, (B) for $t = 4T_p$ and (C) for $t = 55T_p$. The lines (/ /) correspond to $k_p d = 0.86$, 1.28 and 5.03, respectively. The Rayleigh distribution ( ) and Forristall (2000) distribution (/ /) for $k_p d = 0.86$, 1.28 and 5.03, respectively, are added for reference.

However, as the evolution time increases, significant changes to the above observations emerge. Specifically, for $t = 4T_p$ the effect of k_pd on tail of the crest height distribution is reversed compared to $t = 0$. At this time, the crest-height amplification for $k_pd = 0.87$ and 1.28 is of similar magnitude and the amplification for $k_pd = 5.03$ is higher than the two shallower cases.

For longer evolution ($t = 55T_p$) the results show that for $k_pd = 5.03$ the relative crest heights are further increased compared to $t = 4T_p$, whereas for $k_pd = 0.87$ they reduce. Notably, for the latter case the significant amplifications beyond the Forristall (2000) predictions for $t = 0$ are attenuated to an extent that the crest-height distribution matches the Forristall (2000) model.

However, in considering the above results, no accurate conclusions can be drawn concerning the extent of nonlinearity of the largest waves arising at probability levels of as low as $Q = 10^{-3}$; owing to the large sample variability. This lack of certainty regarding the expected crest height at this probability level is one of the main drawbacks of the majority (if not all) of the previous studies, and it will be addressed as follows.

To define the required number of simulated wave events to achieve an accurate estimation of the crest height at $Q = 10^{-3}$, the following procedure was followed:

1. The number of individual sea-state realisations or seeds, N_s, used to form the amalgamated data set of crest heights was progressively increased. With $N_s = 50$, 500 and 5000 seeds employed, datasets comprising of $\sim 5,000$, $50,000$ and $500,000$ crest heights were produced.

2. For each crest-height distribution, 95% confidence intervals were obtained using the bootstrap method (Efron, 1979).

3. The crest-height at an exceedance probability of $Q = 10^{-3}$ was extracted, along with the corresponding confidence interval.

The above procedure was applied to all 19 evolution times outlined in Section 3.3, allowing an investigation of the effect of evolution time on the crest-height at $Q = 10^{-3}$. The resulted time-evolution of this crest-height, normalised with respect to the Rayleigh prediction, along with the associated confidence intervals is shown in Figure 3.17; with sub-figures (a), (b) and (c) (& (d)) corresponding to $N_s = 50$, 500 and 5000, respectively.

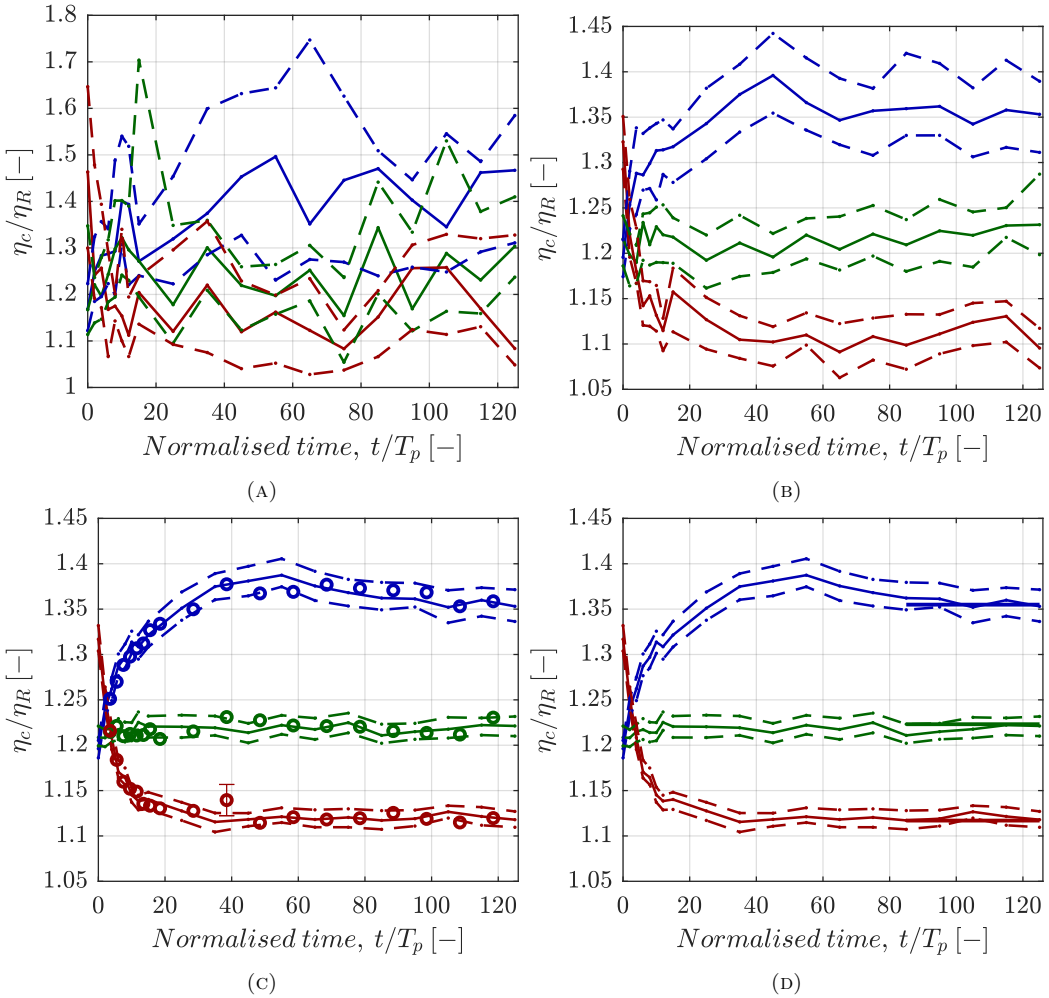


Figure 3.17: Temporal evolution of the crest height normalised with respect to the Rayleigh prediction, η_c/η_R, corresponding to a probability of exceedance of $Q = 10^{-3}$ for uni-directional sea-states with $\gamma = 2.5$ and $\frac{1}{2}H_s k_p = 0.105$. (A), (B) and (C) for $N_s = 50$, 500 and 5,000, respectively, using $T_a = 4T_p$. The lines (—●— / —●— / —●—) refer to $k_p d = 0.86$, 1.28 and 5.03, respectively. While the dash-dotted lines correspond to 95% confidence intervals. In (C) the markers (○ / ○ / ○) refer to additional simulations obtained using $T_a = 10T_p$ and $N_s = 5,000$ for $k_p d = 0.86$, 1.28 and 5.03, respectively, showing that the results are independent of T_a. (D) combines the results based on $N_s = 500$ and 5000. Specifically, the trends covering the entire time-axis are the same to those appearing in (C) for $T_a = 4T_p$. While the horizontal lines at $t \in [85, 125]$ correspond to the average crest height across the same interval extracted from the simulations based on $N_s = 500$.

In addition, to be entirely clear with respect to the effect of the ramp function, simulations using a longer ramp function of $T_a = 10T_p$ were also performed; the data appearing with open circular markers in sub-figure (c). In presenting these data the time-shifting outlined in §3.5.1 has again been applied. The data based on two different ramp functions are in a very good agreement, giving further confidence in the present results. However, it should be noted that for $T_a = 10T_p$ and $t \approx 40T_p$, an outlier is observed. This can be attributed to a very rare situation, where the crest height using $T_a = 10T_p$ lies beyond the confidence intervals of the results for $T_a = 4T_p$. This hypothesis was verified by supplying this point with its own confidence intervals. The two confidence intervals (for $T_a = 4T_p$ and $10T_p$) are shown to overlap, revealing that the two points can indeed originate from the same population.

In considering Figures 3.17(a), 3.17(b) and 3.17(c), the results demonstrate the crucial role of the number of random seeds adopted. Particularly, as the number of seeds increases, the variation of the crest-height with evolution time becomes clearer, and the range of the confidence intervals reduces significantly. Indicatively, for $N_s = 50$, this range is as much as $10-40\%$ of the linear crest height, for $N_s = 500$ is in the order of $5-10\%$, and for $N_s = 5,000$ is as low as $2-4\%$.

From a practical perspective, an important question to be asked is whether the ergodicity property holds for these simulations. In effect, whether the results using an increased number of seeds ($N_s = 5,000$) agree with the results obtained using a smaller number of seeds ($N_s = 500$). To verify this, the crest heights from the $N_s = 500$ simulations were time-averaged over the last $40T_p$ of the simulation time, during which the evolution has reached a steady state. This averaging acts as a second means of reducing the effect of sample variability. To this end, Figure 3.17 (d) presents the data of Figure 3.17 (c) based on $T_a = 4T_p$, together with the time-averaged crest height over $t \in [85, 125]$ extracted from the simulations using $N_s = 500$. The latter appears with horizontal lines at $t \geq 85T_p$. The results demonstrate an excellent agreement between the two approaches, thereby confirming that a number of 500 seeds is sufficient to capture the 'correct' crest-heights, as long as some averaging takes place.

Focusing on the physical effects emerging from Figure 3.17, and particularly from sub-figure (c) or (d), the effect of nonlinear evolution in the different effective water depths becomes evident:

1. in $k_pd = 5.03$ there is a significant increase in the nonlinear crest-height amplification with time. This is of the order of $\sim 13\%$,
2. in $k_pd = 1.28$ the nonlinear amplification remains steady for all times, and
3. in $k_pd = 0.87$ it reduces by $\sim 18\%$.

Importantly, for $t \lesssim 3T_p$ the nonlinear crest-height amplification is higher as the effective depth reduces, whereas for $t \gtrsim 3T_p$ the opposite holds. This outcome may have important implications on the expected extent of nonlinear phenomena arising in wave flumes. For example, if wave-structure interaction effects are of interest, the distance of the measuring gauge from the wavemaker may affect the extent of nonlinear wave loads and motions.

Having identified the importance of the nonlinear evolution on the crest-height amplification, the origins of the observed trends are sought. This focuses on the separate effects of near-resonant and bound-wave interactions.

Near-resonant interactions

The effect of the near-resonant interactions is revealed by considering the crest-height statistics of the underlying free waves; the bound-wave contributions having being removed. In this case, deviations from the Rayleigh distribution reflect the effect of energy focusing or defocusing. To this end, Figure 3.18 presents the normalised crest-height distributions of the free waves, η_c^d/H_S, corresponding to the results presented in Figure 3.16. Once again, the Rayleigh distribution is added for reference.

In considering the results of Figure 3.18, for $t = 0$ in $k_pd = 0.87$ the crest heights lie below the Rayleigh distribution. This reduction is consistent with the negative value of the dynamic kurtosis presented in Figure 3.13(a) and reflects the effect of energy defocusing in this effective water depth. Considering the two deeper cases, the crest heights agree with the Rayleigh distribution, demonstrating the absence of any focusing or defocusing mechanism. Once more, this is in line with the zero values of the dynamic kurtosis observed earlier.

For latter evolution times (sub-figures (b) and (c)), it is observed that (1) for $k_pd = 0.87$ the reduction of the crest heights becomes more pronounced compared to $t = 0$, (2) for $k_pd = 1.28$ the crest-height distribution does not seem overly affected by the evolution time, whereas (3) for $k_pd = 5.03$ the crest heights are increased

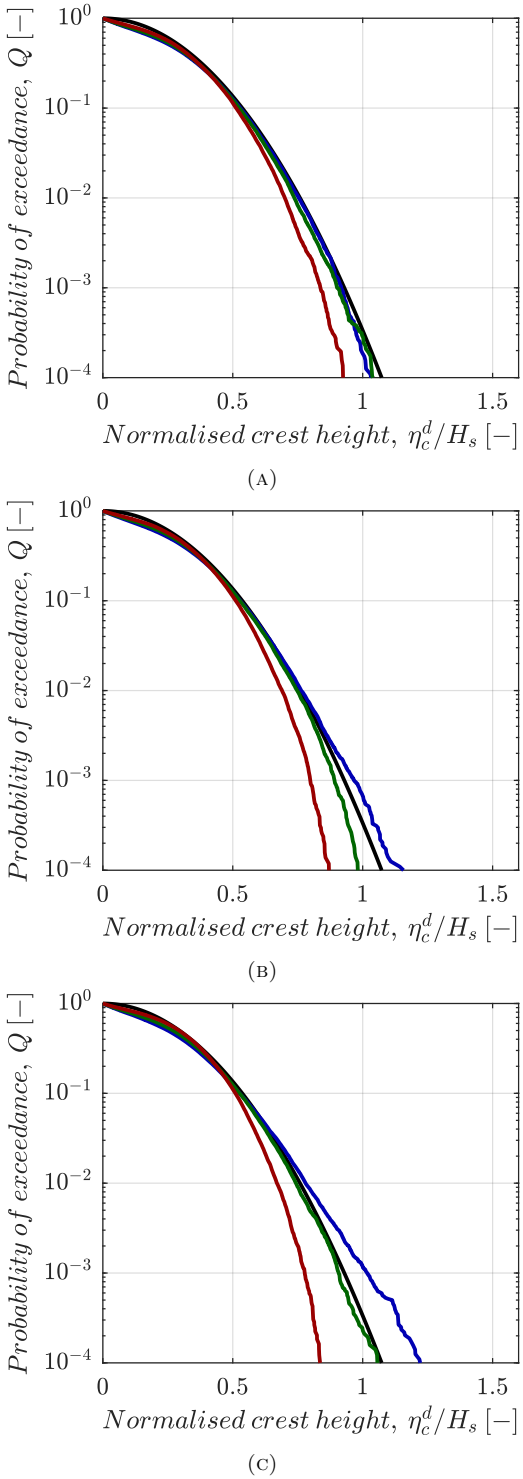


Figure 3.18: Normalised crest-height, η_c/H_s, exceedance probability distributions of the free waves in uni-directional sea-states with $\gamma = 2.5$ and $\frac{1}{2}H_s k_p = 0.105$ for different evolution times: (A) for $t = 0$, (B) for $t = 4T_p$ and (C) for $t = 55T_p$. The lines (/ /) correspond to $k_p d = 0.86$, 1.28 and 5.03, respectively. The Rayleigh distribution is shown with ( ).

compared to the linear prediction. This evolution of the crest-height distribution of the free waves is in line with the equivalent evolution of the crest-height distribution of the total free surface: in that for $k_p d = 0.87$ the crest heights decrease with time, while in $k_p d = 5.03$ they increase.

Interestingly, in Figure 3.18 the observed deviations from the Rayleigh (linear) prediction, from a statistical point of view, indicate that the various free wave components are not independent. To explain this, the necessary condition for a sea-state to be Gaussian (or linear) is the independent sampling of the phases and amplitudes of the various (free) wave components from their respective distributions (§2.2.2). Here the statistics of the free waves do not obey the linear predictions indicating that either the phases and/or amplitudes of the free waves are correlated and/or that they obey different distribution laws. To this end, Tang et al. (2021) has shown that in re-initiating evolved wavefields with independent uniformly distributed phases, the sea-state returns to a linear state. This suggests that it is the distribution of the phases that determines the free-wave statistics. To this end, Janssen (1983) and Janssen (2003) indicated that a necessary condition for modelling the development of near-resonant interactions is the abandonment of the homogeneity assumption adopted by Hasselmann (1962). This implies that the phases of the wave components must be correlated for inhomogeneities to occur, as noted by (Stiassnie et al., 2008). Taken together, whilst the nonlinear evolution can induce changes in the probability distribution of the amplitudes and phases, the correlation of the latter is sufficient for nonlinear statistics to occur. However, an account of these distributions is beyond the scope of this thesis. From a physical perspective, this argument is entirely in line with the so-called phase-locking of the side-bands to the primary wave during the development of the Benjamin-Feir instability.

Furthermore, the increased crest heights observed in deep water due to near-resonant interactions is entirely in line with the earlier works of Baldock et al. (1996) and Gibson & Swan (2007) on the evolution of uni-directional focused wave groups. Similarly, the reduction of the crest heights of the free waves in the shallowest case of $k_p d = 0.87$ agrees with the earlier investigation conducted by Katsardi & Swan (2011) on focused wave events in the same effective water depth. However, in the present study, the total crest heights are shown to be increased relative to the linear prediction. This differs from the results presented in Katsardi & Swan (2011), the

most likely explanation for this lies in the differences in the nonlinear dispersive properties of deterministic wave events as opposed to random wave records.

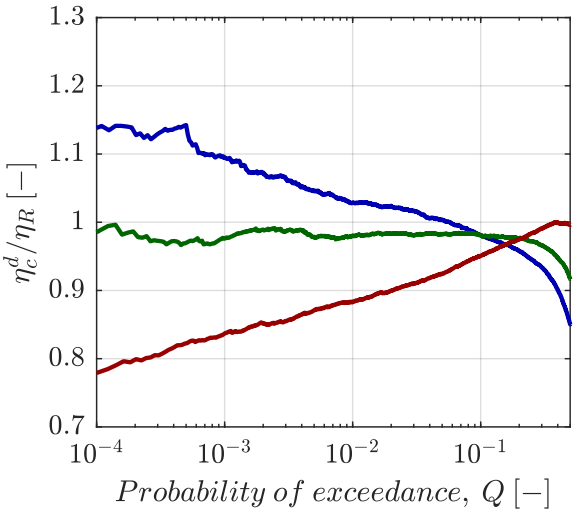


Figure 3.19: Probability of exceedance of the crest heights of the free waves normalised with respect to the Rayleigh prediction, η_c^d/η_R, in uni-directional sea-states with $\gamma = 2.5$ and $\frac{1}{2}H_s k_p = 0.105$ at $t = 55T_p$ with (— / — / —) referring to $k_p d = 0.87, 1.28$ and 5.03, respectively.

To further quantify the effect of near-resonant interactions, Figure 3.19 presents the ratio of the crest heights of the free waves over the Rayleigh prediction, corresponding to the steady-state part of the evolution ($t = 55T_p$). This shows that at a probability of exceedance level of $Q = 10^{-3}$, the crest heights are amplified by as much as 10% in $k_p d = 5.03$ and reduced by as much as 16% in $k_p d = 0.87$. Moreover, it is observed that near-resonant interactions affect the entire tail of the distribution ($Q < 10^{-1}$), indicating that wave modulation due to near-resonant interactions does not only affect the largest waves as it would have been expected, but also the smaller, more frequently occurring ones.

Based on the above, it is instructive to explore the full time-evolution of the effect of the near-resonant interactions. For this, the full set of simulations using $5,000$ seeds has been employed and the time-evolution of the crest height of the free waves, normalised with respect to the Rayleigh prediction, for $Q = 10^{-3}$ is presented in Figure 3.20. Similarly to Figure 3.17, the 95% confidence intervals are added; demonstrating the small effect of sample variability. To verify the ergodicity of the simulations, the time-averaged (for $t \in [85, 125]$) crest-heights from simulations using 500 seeds have also been added.

In considering Figure 3.20, it is interesting to note the direct equivalence to the

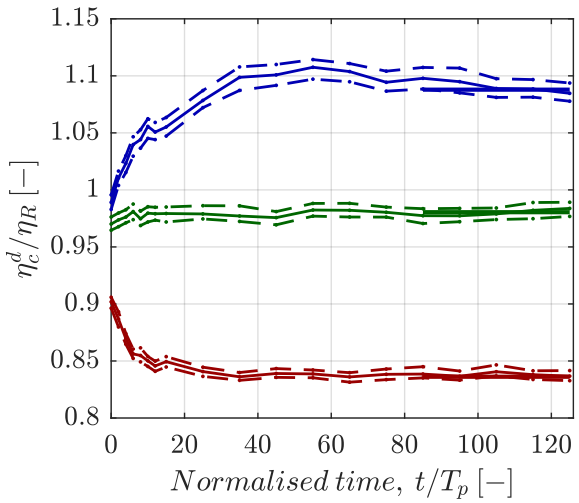


Figure 3.20: Temporal evolution of the free-wave contribution to the crest heights normalised with respect to the Rayleigh prediction, η_c^d/η_R, corresponding to a probability of exceedance of $Q = 10^{-3}$ for uni-directional sea-states with $\gamma = 2.5$ and $\frac{1}{2}H_s k_p = 0.105$. The lines (—●— / —●— / —●—) refer to $k_p d = 0.86$, 1.28 and 5.03, respectively. The dash-dotted lines correspond to 95% confidence intervals. While the horizontal lines at $t \in [85, 125]$ correspond to the average crest height across the same interval extracted from simulations based on $N_s = 500$.

evolution of the dynamic kurtosis, presented in Figure 3.13. This observation is important in that it puts all earlier works relating the prediction of the dynamic kurtosis in a practical context. Moreover, it links earlier theoretical or numerical works focusing on the dynamic kurtosis to the present investigation, particularly that of Janssen & Onorato (2007). In more detail,

1. for $k_p d = 5.03$, both the crest heights and the dynamic kurtosis are higher than the linear predictions. This is in line with Janssen (2003) and Janssen & Onorato (2007). The necessary time for the full development of near-resonant interactions is shown to be $t \approx 50T_p$. This appears to be in agreement with the so-called Benjamin-Feir time-scale ($O(1/(\epsilon^2\omega_0))$ [1]); corresponding to $O(58T_p)$ in the present case. The observed evolution of the dynamic kurtosis is in qualitative agreement to the theoretical evolution predicted by Mori & Janssen (2006) and Fedele (2014), as the kurtosis increases monotonically until it reaches a steady-state value. In this respect, considering equivalent numerical results presented by Janssen (2003), no overshoot is observed here owing to the rel-

[1] ϵ being the characteristic steepness $\sigma_\eta k_0$, k_0 the dominant wavenumber and ω_0 the dominant circular frequency

atively broad spectral bandwidth and moderate sea-state steepness (see also Janssen 1983).

2. for $k_p d = 1.28$, both the crest heights and the dynamic kurtosis lay slightly below the linear predictions. In considering this observation, it is instructive to mention that the majority (85%) of the wave energy lays in $f \in [0.5, 1.5]f_p$ corresponding to an effective-depth range $kd \in [1.09, 7.9]$. Thus, it is not certain as to whether near-resonant interactions would lead to focusing or defocusing of the wave energy in this case. The results indicate that the evolution is dictated by the spectral peak: a slightly reduced value of $k_p d$ compared to the theoretical value of 1.363 (where the theoretical sign of kurtosis changes sign according to Figure 3.3), corresponds to a slightly negative value of the dynamic kurtosis.

3. for $k_p = 0.87$, both the crest heights and the dynamic kurtosis lay below the linear predictions. Particularly, they decrease monotonically until they reach a steady state after about $t \approx 30T_p$. This is somewhat quicker evolution compared to $k_p d = 5.03$. Unfortunately, an estimation of the time-scale for the development of near-resonant interactions in finite water depth is not available. However, Onorato et al. (2009b) suggests that in shallow water the characteristic steepness that determines the time-scale of four-wave resonant interactions is σ_η/d. In employing this steepness instead of ϵ, the predicted time-scale of evolution is $O(10T_p)$. Hence, as perhaps expected, the time needed to reach a steady state in the present simulations lays between the deep-water and shallow-water estimated time-scales.

   Moreover, in considering the very initial stage of the evolution, it was pointed out earlier that the dynamic kurtosis does not start at zero. This non-zero value indicated that a fast evolution takes place within the ramp function. This observation is again in line with equivalent results presented by Janssen & Onorato (2007) for Gaussian spectra, in which the dynamic kurtosis is not initially zero [1]. In explaining this feature, it should be emphasised that the key mechanism that leads to the defocusing of the wave energy in this effective

[1] Note that in considering Figure 5 of Janssen & Onorato (2007), the time evolution of the dynamic kurtosis starts at a slightly higher time instance than 0.

water depth is the the transfer of energy to long-wave components through near-resonant triad interactions between pairs of wave components (see e.g. Janssen & Onorato 2007, Stiassnie & Gramstad 2009, Gramstad 2014). Whilst the time-scale for the development of these interactions is again not available for water of finite depth, existing literature suggests that resonant triads develop much faster than resonant quartets. For example, the time-scale for the development of triad interactions in gravity-capillary waves is of $O(1/(\epsilon\omega_0))$ (Hammack & Henderson, 1993), corresponding to $O(3T_p)$. Moreover, according to Onorato et al. (2009b) the time-scale for the development of resonant quartets in shallow water is of $O(1/(\sigma_\eta/d)^4)$, whereas the corresponding time-scale for resonant triads is $O((l^-/l_0)/(\sigma_\eta/d)^2)$ [1]; the latter being an order of magnitude smaller.

Therefore, given that the triad interactions are developed almost immediately, the evolution of quartet interactions also starts immediately; the development of which is at a much higher pace than in deep water. This explains the immediate reduction of the dynamic kurtosis and consequently of the free-wave crest heights.

Finally, the non-zero evolution at $t = 0$ for $k_p d = 0.87$ presents an additional source of uncertainty underpinning any comparisons between HOSM simulations and experimental data. This effect can perhaps explain the under-prediction of the crest heights obtained using HOSM in Figure 3.6(G). However, this factor was not found to be detrimental in achieving good overall comparisons.

Based on the above, the crest-height evolution presented in Figure 3.17 can, in large part, be explained by the crest-height evolution of the free waves (Figure 3.20). but not entirely. Nevertheless, the effect of bound-wave contributions also needs to be explored.

[1] Where l^- is the wavelength of the generated long waves and l_0 is the dominant wavelength. Here this ratio is estimated to be $O(5)$, when considering the central wavenumber of the low frequency components that nearly satisfy the linear dispersion relation

Bound-wave contributions

To identify the effect of bound waves on the crest-height distribution, the crest heights of the free waves can be subtracted from the crest heights of the total free surface. In doing so, two approaches are possible:

1. the extraction of the bound contributions for each individual wave (Adcock & Draper, 2015) and

2. the subtraction of the crest height of the free waves, η_c^d, from the crest height of the total free surface, η_c, corresponding to the same probability of exceedance in their respective distributions (Forristall, 2000), assuming an one-to-one correlation.

Whilst the first approach is physically more meaningful, the latter approach is of more practical interest as it identifies how bound contributions affect the crest-height distribution as a whole. As such, the latter approach is most commonly employed (see for example Tayfun & Fedele 2007, Fedele & Tayfun 2009, Latheef 2014).

To explore the difference between the two approaches and to assess the validity of the assumed one-to-one correlation of the second approach, Figure 3.21 compares:

- the scatter of the total crest heights against the crest heights of the free waves for each individual wave with $Q \lesssim 2.5 \cdot 10^{-1}$; thereby focusing on the most relevant events belonging to the tail of their respective distributions.

- the relation of the quantile-by-quantile crest heights of the free waves and the total free surface; often referred to as a 'Q-Q' representation.

In both cases, the deviation from the one-to-one line reflects the effect of bound contributions. The data in Figure 3.21 refer to the sea-states of the previous section ($\gamma = 2.5$, $\frac{1}{2}H_s k_p = 0.105$) for an evolution time $t = 55T_p$; each sub-figure corresponding to a different effective water depth.

In observing Figure 3.21, it can be seen that the crest heights of the free waves and the crest heights of the total free surface are highly correlated. However, the data exhibit some scatter owing to (i) the different bandwidths (or steepness) of the individual wave events and (ii) the presence of the frequency difference bound terms, the phasing of which affects the magnitude of the total crest heights. Therefore, with

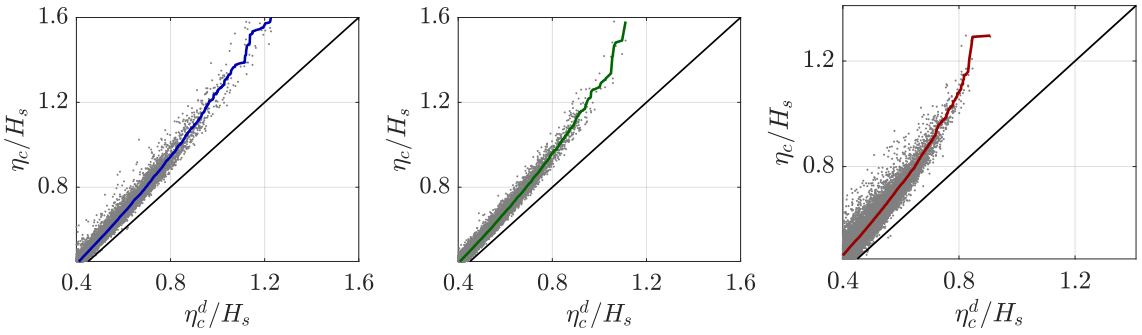


Figure 3.21: Scatter of the normalised total crest heights, η_c/H_s, against the normalised crest heights of the free waves, η_c^d/H_s, for individual wave events (•) corresponding to $Q \lesssim 2.5 \cdot 10^{-1}$, along with comparison of the quantile-to-quantile crest heights (——— / ——— / ———) for uni-directional sea-states of $\gamma = 2.5$ and $\frac{1}{2}H_s k_p = 0.105$ at $t = 55T_p$. (A) for $k_p d = 5.03$, (B) for $k_p d = 1.28$ and (C) for $k_p d = 0.87$. The diagonal lines (——) refer to the one-to-one relation.

point (ii) becoming more relevant as the water depth reduces, it is not surprising that the scatter of points is greater for the shallowest case of $k_p d = 0.87$ (Figure 3.21(C)). Taken together, the Q-Q line is shown to be a good representation of the expected link of the crest heights of the free waves and those of the total free surface. This suggests the relevance of the most commonly adopted approach (approach (2) defined above).

Following the second approach, to obtain the bound-wave contributions at *increasing* order, the following steps were followed:

1. the harmonic contributions were progressively added to the free-wave records,
2. a zero-crossing analysis was performed to the obtained record
3. the crest-height distribution was obtained by sorting the crest heights, and finally,
4. the crest heights at each exceedance probability were subtracted from the corresponding crest height of the record including up to the harmonic of the previous order.

In this procedure, the zeroth and second harmonics (representing the second-order bound terms as a whole) were taken together. Thus, to obtain, for example, the bound-wave contributions of the third harmonic, the ranked crest heights of the record $\eta^{1st} + \eta^{2nd} + \eta^{0th} + \eta^{3rd}$ were subtracted from the ranked crest heights of the record $\eta^{1st} + \eta^{2nd} + \eta^{0th}$, with due care over the sign.

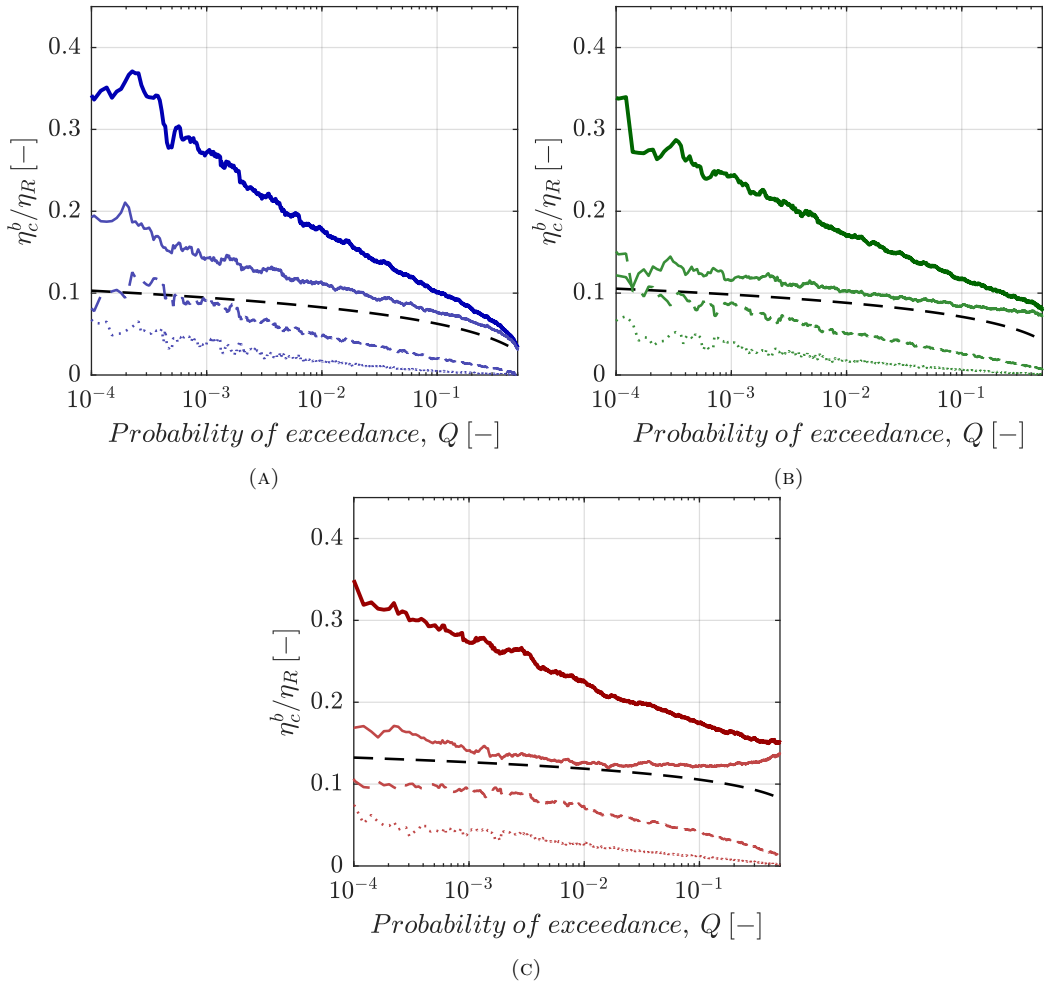


Figure 3.22: Normalised total bound-wave amplification, η^b/η_R, and its underlying contributions of increasing order at $t = 55T_p$, corresponding to (A) $k_pd = 5.03$, (B) $k_pd = 1.28$ and (C) $k_pd = 0.87$ for for uni-directional sea-states of $\gamma = 2.5$ and $\frac{1}{2}H_sk_p = 0.105$. The lines (/ /) refer to the total bound contributions, (/ /) to the second plus zeroth harmonic contributions, (/ /) to the third harmonic contribution and (/ /) to the fourth harmonic contribution. While, ( ) refers to the predicted amplification from the uni-directional Forristall (2000) model.

To illustrate the outcome of the above procedure, Figure 3.22 presents the total bound-wave amplifications along with the underlying contributions of increasing order based on the data presented in Figure 3.21.

In considering the results of Figure 3.22, it is shown that higher than second-order bound contributions are relevant in all water depths. Indicatively, the third-order bound-wave amplification at an exceedance probability level of $Q = 10^{-3}$ is as much as 10%. Whereas the equivalent fourth-order amplification is $3 - 4\%$, irrespective of the water depth.

Moreover, the nonlinear amplification of the Forristall (2000) model is also added in these plots, showing that the model captures the magnitude of the second-harmonic bound terms very well for $k_pd = 0.87$ and 1.28. However, this is not the case for $k_pd = 5.03$. To explain the discrepancies at $k_pd = 5.03$, it should be again emphasised that the Forristall (2000) model has been calibrated using SORWT. As such, it does not incorporate the evolution of the underlying free waves. With the underlying free waves for $k_pd = 5.03$ being amplified due to near-resonant interactions, it is not surprising that the Forristall (2000) model under-predicts the corresponding bound terms. Analogously, the observed agreement for $k_pd = 0.87$ is perhaps surprising if one considers that the underlying free waves are lower in magnitude compared to linear theory. To this end, it should also be stressed that the second-harmonic bound terms also include fourth-order contributions according to Equation 2.32. In fact, the slight underestimation of the second-harmonic bound terms for $k_pd = 1.28$, perhaps reflects this latter type of interactions. However, given the overall agreement with Forristall (2000) for $k_pd = 1.28$ and the fact that the magnitude of the fourth-harmonic bound terms is not overly sensitive to k_pd, it is believed that the effect of the fourth-order second-harmonic bound terms in $k_pd = 0.87$ is not significant. More importantly, taking into account that at $k_pd < 1.0$, the validity of the second-order theory is questioned, as indicated by Hadjigeorgiou (2018), the observed agreement in $k_pd = 0.87$ should/can not be treated as a means of extracting a physical interpretation. This will also be explored in Chapter 4.

Furthermore, to explore the origin of the observed trends of Figure 3.17(D), Figure 3.23 presents the time-evolution of the bound-wave contributions to the crest-height magnitude at $Q = 10^{-3}$ (using $N_s = 5000$); together with the time-averaged value using ($N_s = 500$). In considering Figure 3.23, the reduction of the bound-wave contributions with time for $k_pd = 0.87$ and their increase for $k_pd = 5.03$ is consistent with the magnitude of the underlying free waves; the latter were shown to decrease for $k_pd = 0.87$ and increase for $k_pd = 5.03$. The agreement of the results using either $N_s = 500$ or $N_s = 5000$ demonstrates, once more, the ergodicity of the simulations. Taken together Figures 3.17(D), 3.20 and 3.23, it has been shown to hold for the total amplification and the underlying nonlinear contributions; both free and bound.

Finally, it should be stressed out that without having separated the effects of near-resonant interactions from the bound-wave contributions, the results of Figure

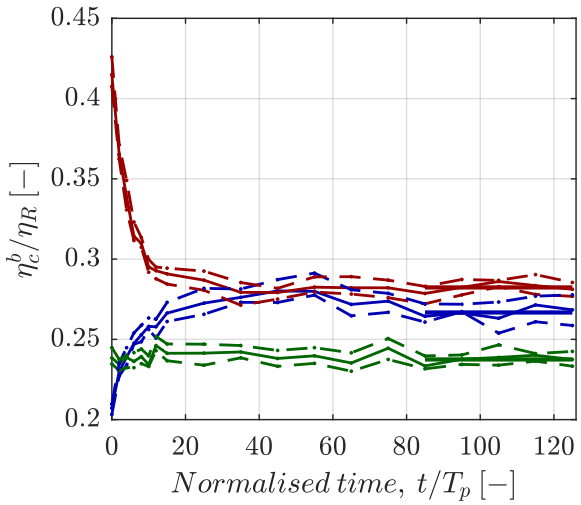


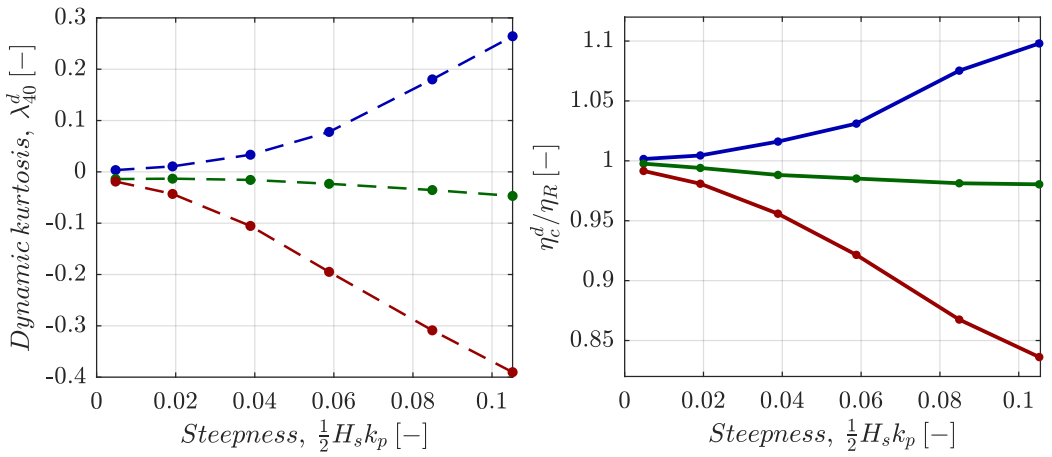
Figure 3.23: Temporal evolution of the bound-wave contribution to the crest heights normalised with respect to the Rayleigh prediction, η_c^b/η_R, at $Q = 10^{-3}$ for uni-directional sea-states with $\gamma = 2.5$ and $\frac{1}{2}H_s k_p = 0.105$. The lines (—●— / —●— / —●—) refer to $k_p d = 0.86$, 1.28 and 5.03, respectively. 95% confidence intervals using the bootstrap method are represented with dash-dotted lines. While the horizontal lines at $t \in [85, 125]$ correspond to the average crest height across the same interval extracted from simulations based on $N_s = 500$.

3.16(c) could have led to the misleading conclusion that nonlinearity above second-order becomes less relevant as the water depth is reduced. In reality, the present results suggest that the agreement of HOSM to the Forristall (2000) predictions stems from the competing influence of the nonlinear effects above second-order.

3.5.3 Influence of sea-state steepness

Having explored the effect of the nonlinear wave-wave interactions for a sea-state steepness $\frac{1}{2}H_s k_p = 0.1052$, it is interesting to explore how these results generalise for other sea-state steepnesses. Particularly, when focusing on the crest-height statistics, in particular, it is of interest to identify whether near-resonant interactions become relevant above a certain steepness or if their effect develops progressively with an increase in steepness.

To explore this, the sea-states of Table 3.1 were simulated using HOSM, and the phase manipulation method was again adopted to separate the various nonlinear contributions. In simulating these sea-states, 500 random seeds were generated; this choice having being justified by the accuracy with which the steady-state crest-height magnitude and its contributions are captured at $Q = 10^{-3}$, when averaged in the time interval $t \in [85, 125]$.



(A) (B)

Figure 3.24: Effect of sea-state steepness, $\frac{1}{2}H_s k_p$, for uni-directional sea-states with $\gamma = 2.5$ on (A) the time-and ensemble-averaged dynamic kurtosis with (–•– / –•– / –•–) referring to $k_p d = 0.87$, 1.28 and 5.03, respectively, and (B) time-averaged crest height of the free waves normalised with respect to the Rayleigh prediction, η_c^d/η_R, at $Q = 10^{-3}$ with (—•— / —•— / —•—) for $k_p d = 0.87$, 1.28 and 5.03, respectively.

Near-resonant interactions

In considering first the dynamic part of the free surface, Figure 3.24 presents the variation of the time-and ensemble-averaged dynamic kurtosis (sub-figure (A)) and the time-averaged normalised with respect to the Rayleigh (linear) predicted crest-height of the free waves at $Q = 10^{-3}$ (sub-figure (B)) with sea-state steepness.

From these figures, it is evident that there is a direct correspondence between the dynamic kurtosis and the nonlinear contributions to the crest heights of the free waves. Specifically, a negative kurtosis signifies a crest-height reduction compared to linear theory. In contrast, a positive kurtosis signifies crest-height amplification. Whilst this finding is (perhaps) expected, these results provide the first conclusive evidence on the relation of the two quantities for a wide range of sea-state steepnesses.

Examining the trends on Figure 3.24 in more detail, it is shown that for the smaller steepness and in accordance with one's expectation, both the dynamic kurtosis and the crest-height magnitude agree with the linear prediction. As the sea-state steepness increases, there is a progressive increase of the dynamic kurtosis in deep water. This appears approximately parabolic in shape and it is in qualitative agreement with the theoretical result outlined in Equation 3.2. Indicatively, the corresponding increase in the crest heights for sea-states with steepness $\frac{1}{2}H_s k_p = 0.059, 0.085$ and 0.105 is of the order of 3%, 7% and 10%, respectively. These results not only demon-

strate the need to include third-order near-resonant interactions when modelling uni-directional wavefields, but also cast doubt on the applicability of sorwt for relatively small sea-state steepnesses.

Moreover, for $k_p d = 1.28$ it is observed that the conclusions drawn in §3.5.2 can be extended to smaller steepnesses; supporting the previous finding that at this effective depth crest-height amplification due to near-resonance is not important.

Finally, for the shallowest case of $k_p d = 0.87$, it is shown that near-resonant interactions become important even for a steepness as low as $\frac{1}{2}H_s k_p = 0.039$, the observed reduction in the crest-height being of the order of 5%. In addition, in this case, the observed variation of the dynamic kurtosis with steepness is shown to be linear rather than parabolic for $\frac{1}{2}H_s k_p \geq 0.039$. This latter observation is at odds with the theoretical prediction based on Equation 3.2 and is believed to relate to the spectral bandwidth. Specifically, the adoption of a broad-banded spectrum is believed to limit a parabolic, unbounded, increase of the near-resonant interactions. This arises because a significant part of the wave energy will be deeper than the defocusing regime defined by $k_i d < 1.36$, with i representing the i-th wave component. As such, under the effect of nonlinear dispersion, both energy focusing and defocusing occurs in this effective water depth; the latter effect prevailing, but the extent of the change limited by the former. It is noted that the theoretical predictions based on Equation 3.2 have not been added in Figure 3.24(a) for clarity; a direct comparison to the simulation results being presented later in §3.6.

Bound-wave contributions

Having identified the influence of the sea-state steepness on the nonlinearity of the free waves, Figure 3.25 presents the equivalent variation of the steady-state (time-averaged) bound-wave amplification at $Q = 10^{-3}$ with increasing sea-state steepness. The corresponding amplification arising from the Forristall (2000) model has also been added for reference.

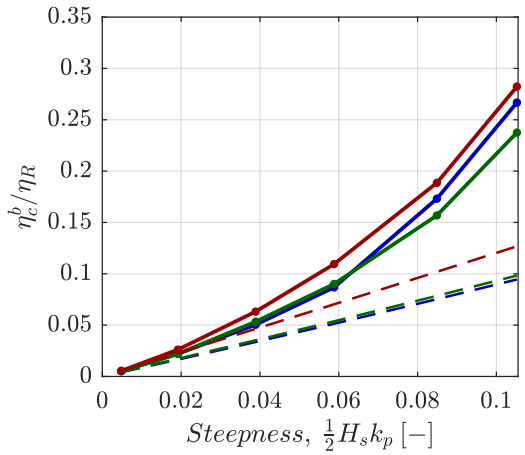


Figure 3.25: Effect of sea-state steepness, $\frac{1}{2}H_s k_p$, on the time-averaged bound-wave contribution to the crest height normalised with respect to the Rayleigh prediction, η_c^b/η_R, at $Q = 10^{-3}$ for uni-directional sea-states of $\gamma = 2.5$. Where (—●— / —●— / —●—) refer to HOSM results of $k_p d = 0.87$, 1.28 and 5.03, respectively. The Forristall (2000) predictions have also been added for reference, with (— — / — — / — —) corresponding to $k_p d = 5.03$, 1.28 and 0.87, respectively.

The results in Figure 3.25 show that the bound-wave contributions increase non-linearly with steepness. As expected, the rate of increase is more rapid than the second-order model of Forristall (2000). Overall they are consistently higher in the shallowest water depth, $k_p d = 0.87$, in qualitative agreement with Forristall (2000). However, the gradient of the increase in the deepest case of $k_p d = 5.03$ is higher than the shallower cases owing to the amplification of the crest heights of the underlying free waves observed in Figure 3.24(b). This effect could disrupt the ordering with respect to $k_p d$ if the steepness is increased further.

Total effect of nonlinear interactions

Taking the variation of the crest heights of the free waves and the bound-wave contributions together, Figure 3.26 presents the ratio of the total time-averaged crest height at $Q = 10^{-3}$ over the linear prediction and shows its variation with sea-state steepness. Once again: the Forristall (2000) predictions are added for reference.

These results show that for the deepest cases of $k_p d = 1.28$ and 5.03 the Forristall (2000) prediction consistently under-predicts the fully nonlinear crest heights. To quantify the observed differences, for a steepness as low as $\frac{1}{2}H_s k_p = 0.059$ the deviation from the Forristall (2000) prediction is $\sim 6\%$ for $k_p d = 5.03$ and it reduces to $\sim 2\%$ for $k_p d = 1.28$. Whereas, in the steepest sea-states ($\frac{1}{2}H_s k_p = 0.1052$) the corresponding deviations are as much as $\sim 24\%$ and $\sim 11\%$, respectively.

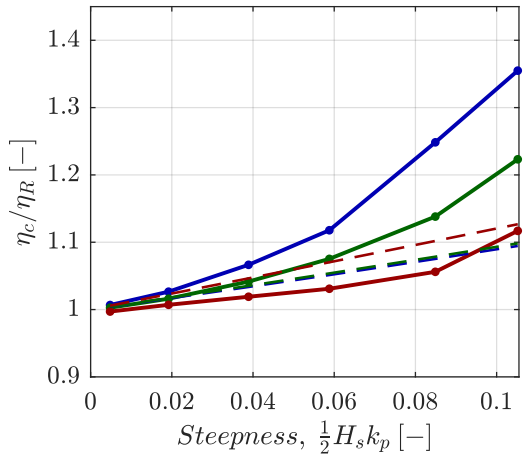


Figure 3.26: Effect of sea-state steepness, $\frac{1}{2}H_s k_p$, on the time-averaged crest height normalised with respect to the Rayleigh prediction, η_c/η_R, at $Q = 10^{-3}$ for uni-directional sea-states with $\gamma = 2.5$. Where (—●— / —●— / —●—) refer to HOSM results of $k_p d = 0.87$, 1.28 and 5.03, respectively. The Forristall (2000) predictions have also been added for reference, with (— — / — — / — —) corresponding to $k_p d = 5.03$, 1.28 and 0.87, respectively.

In contrast, for $k_p d = 0.87$, the Forristall (2000) prediction consistently over-predicts the total crest-height magnitude for $\frac{1}{2}H_s k_p < 0.1052$. However, for $\frac{1}{2}H_s k_p = 0.1052$, agreement is observed as indicated in §3.5.2. This is explained by the nonlinear increase of the bound-wave contributions combined with a quasi-linear decrease of the crest height due to third-order near-resonant interactions. Taken together, these results demonstrate that (1) near-resonant effects and bound-wave contributions have a competing influence on the total crest-height magnitude irrespective of the sea-state steepness, (2) for all steepnesses bound-wave contributions are higher than the attenuation due to near-resonant interactions, and (3) the agreement of the fully nonlinear crest-height distribution to the Forristall (2000) prediction observed in §3.5.2 is not expected to be valid for all cases in this effective water depth.

Having identified the crucial roles of the effective water depth and the sea-state steepness on the nonlinear interactions, the following section completes the present investigation by considering the role of spectral bandwidth.

3.5.4 Influence of spectral bandwidth

Time-evolution of near-resonant interactions

In considering the role of spectral bandwidth (essentially γ of the JONSWAP wave spectrum) on the intensity of near-resonant interactions, the presence of a long high-

frequency tail could enhance the effect of frequency dispersion over nonlinear wave modulation. Consequently, it remains uncertain if changes in γ will affect the nonlinear evolution process in the way that narrow-band theory predicts. The present section aims to investigate this by employing the sea-states presented in Table 3.2. with $k_p d = 5.03$, 1.28 and 0.87.

Figure 3.27 presents the time evolution of the ensemble-averaged kurtosis and the crest height of the free waves, normalised by the linear prediction, at $Q = 10^{-3}$. All three effective water depths are addressed. To obtain a reliable estimate of the latter quantity, the sea-states were simulated using 5000 random seeds; thereby keeping the effect of sample variability to a minimum (§3.5.2). Taken together, Figure 3.27 aims to identify if the dynamic kurtosis can explain the crest-height evolution across a broader set of sea-states. At a first glance, the data suggests that this is indeed the case; changes in the quantities being clearly correlated.

In detail the data reveals that as the spectral bandwidth decreases (γ increases), near-resonant interactions lead to increased deviations from the linearly predicted crest heights, provided the peak of the wave spectrum belongs to either the focusing or defocusing regime ($k_p d << 1.36$ or $k_p d >> 1.36$, respectively). Furthermore, decreases in the spectral bandwidth lead to increased interaction times between wave components, owing to attenuated frequency dispersion, and hence to increased wave modulations (i.e. local, nonlinear changes in dispersion leading to phase-locked wave components) once a steady state is reached. Moreover, the inverse relationship between the dynamic kurtosis and the spectral bandwidth at steady state is entirely in agreement with Equation 3.2.

Importantly, for the intermediate effective depth case of $k_p d = 1.28$, the spectral bandwidth is shown to have a negligible effect on the nonlinearity of the crest heights. This fact supports the notion that the effective water depth associated to the spectral peak, rather than the spread of energy at the tail of the wavenumber spectrum, determines the nature of the nonlinear evolution.

Moreover, in deep water for $\gamma = 5$ an overshoot is observed for both the dynamic kurtosis and the crest-height. This is not observed for lower γ values. This overshoot is a known effect and relates to the nonlinear evolution of narrow-banded spectra in deep water (see for example Onorato et al. (2004), Mori et al. (2007)). Following Janssen (1983), this is the random equivalent of the Fermi-Pasta-Ulam recurrence

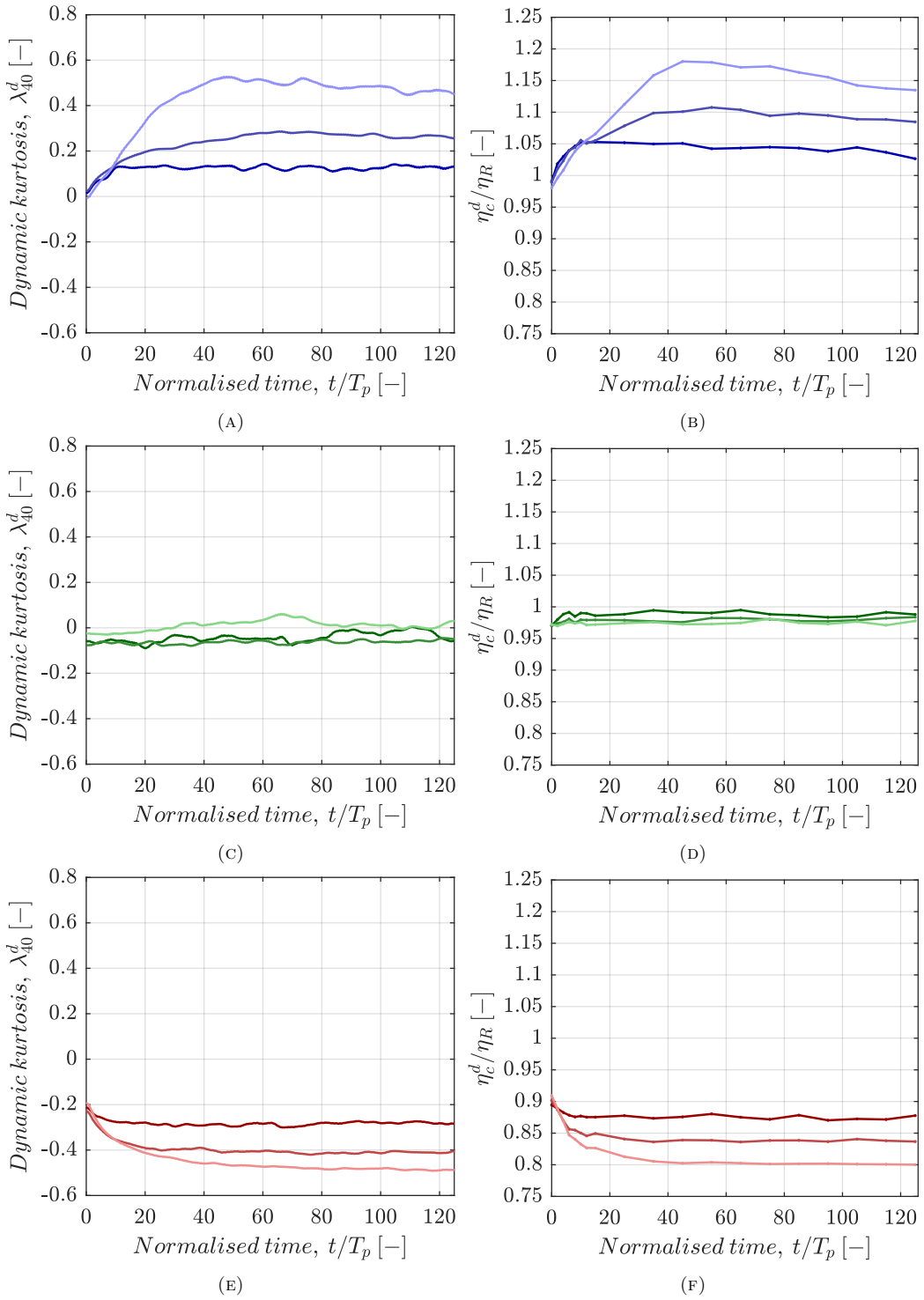


Figure 3.27: Effect of spectral bandwidth (γ) on the temporal evolution of (left column) the ensemble-averaged dynamic kurtosis, λ_{40}^d, and (right column) the crest height of the free waves normalised with respect to the Rayleigh prediction, η_c^d/η_R, at $Q = 10^{-3}$ for uni-directional sea-states with $\frac{1}{2}H_s k_p = 0.105$. (A),(B) refer to $k_p d = 5.03$ with (/ /) for $\gamma = 1.0, 2.5$ and 5.0, (C),(D) refer to $k_p d = 1.28$ with (/ /) for $\gamma = 1.0, 2.5$ and 5.0, and (E),(F) refer to $k_p d = 0.87$ with (/ /) for $\gamma = 1.0, 2.5$ and 5.0, respectively.

behaviour of wave modulation for a single quartet interaction (Lake et al., 1977). In the present case this is damped due to phase-mixing introduced by randomness (see also Stiassnie et al. 2008).

Focusing on the initial stage of the evolution ($t/T_p < 10$), the effect of spectral bandwidth appears somewhat reversed; owing to a faster evolution as the spectral bandwidth is increased. This effect becomes more evident in $k_pd = 5.03$ than in $k_pd = 0.87$; the initial stage of the evolution is not captured in its entirety in the shallowest water case. To verify this observation, it is instructive to consider the analytical works of Janssen (2003), Fedele et al. (2010) and Fedele (2014). Whilst these works are based on a narrow-band assumption, they can provide valuable qualitative insight into the origins of the different initial rates of nonlinear evolution. To this end, within these analytical developments, the time needed for the dynamic effects to be fully developed is invariant with changes in the spectral bandwidth, as long as an effective evolution time, $t' = (\sigma_k/k_0)^2\omega_0 t$, is introduced. Therefore, for a given effective evolution time, t', an increase in spectral bandwidth leads to a faster evolution when the original time t is considered. This is exactly as observed in the present results.

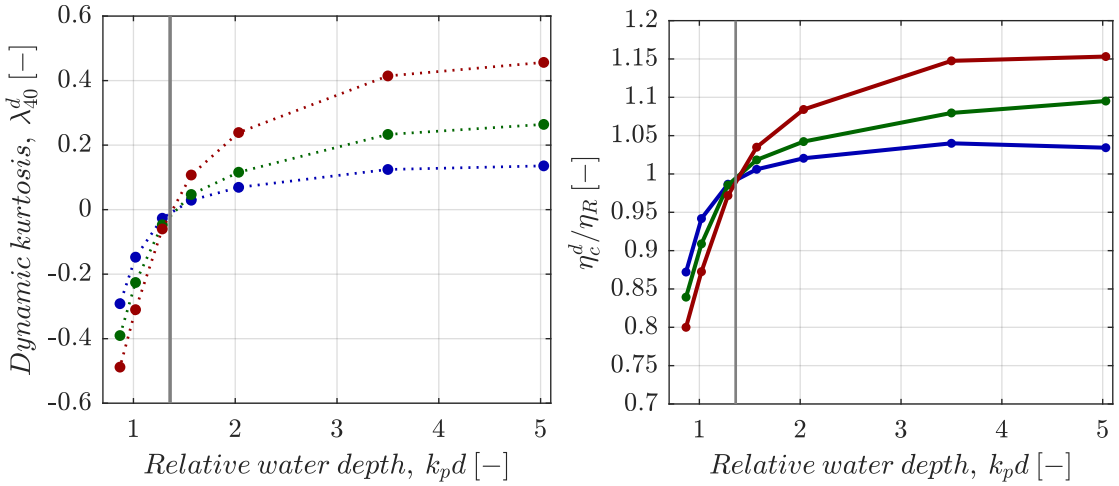
Nonlinear contributions in the steady state

Having identified the critical dependence of dynamic effects on the spectral bandwidth, the present section focuses on the relative importance of dynamic effects versus bound-wave contributions. For this, the entire set of sea-states presented in Table 3.2 is employed. With the employed sea-states including incremental changes in the effective water depth, the variation of the nonlinear interactions with effective water depth can be studied in detail. In addition, to maintain a compact presentation of the nonlinear effects, the investigation will focus on the steady-state part of the nonlinear evolution, for which wave nonlinearity becomes independent of the evolution time.

- ***Near-resonant interactions***

In considering first the dynamic part of the free surface, Figure 3.28(a) presents the variation of the time-and ensemble-averaged dynamic kurtosis, while the corresponding ratio of the nonlinear crest height of the free waves over the linear prediction

at $Q = 10^{-3}$ is presented in Figure 3.28(b). These results reveal that as the effective water depth approaches $k_p d = 1.36$, from either side of the effective water depth range, wave nonlinearity is affected less by the spectral bandwidth. This observation is entirely in line with the results presented in the previous section and, essentially, confirms a monotonic and gradual reduction of the effect of spectral bandwidth as $k_p d$ approaches 1.36. Once more, the value of the dynamic kurtosis is entirely consistent with the crest attenuation or amplification due to near-resonant interactions presented in Figure 3.28(b).



(a) (b)

Figure 3.28: Effect of spectral bandwidth (γ) and relative water depth on (a) the ensemble-averaged dynamic kurtosis (λ_{40}^d), with (/ /) corresponding to $\gamma = 1.0$, 2.5 and 5.0, respectively, and (b) the time-averaged normalised crest height of the free waves, η_c^d/η_R, at $Q = 10^{-3}$: with (/ /) referring to $\gamma = 1.0$, 2.5 and 5.0, respectively. The vertical line ( ) marks the theoretical relative water depth $k_p d = 1.363$. All results refer to uni-directional sea-states of $\frac{1}{2} H_s k_p = 0.105$.

- ***Bound-wave contributions***

Considering the bound-wave effects, Figure 3.29 presents their relative contribution to the linear crest-height for $Q = 10^{-3}$. It is shown that an increase in spectral bandwidth leads to an increase of the bound-wave contributions for all effective water depths. This is explained by the increased steepness of the individual waves with decreasing γ, as a higher proportion of the total wave energy is allocated to wavenumbers that are higher than the spectral peak. With the magnitude of the bound-wave contributions being inherently dependent upon the underlying wave steepness, it is not surprising that lower γ values lead to higher bound contributions.

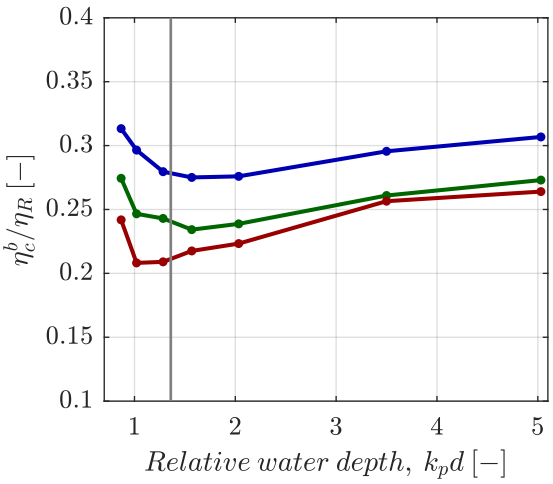


Figure 3.29: Effect of spectral bandwidth (γ) and relative water depth on the normalised bound-wave contributions, η_c^b/η_R, to the time-averaged crest height at $Q = 10^{-3}$, with (—●— / —●— / —●—) referring to $\gamma = 1.0$, 2.5 and 5.0, respectively. The vertical line (——) marks the relative water depth $k_pd = 1.363$ and it is added for reference. All results refer to uni-directional sea-states of $\frac{1}{2}H_sk_p = 0.105$.

- ***Dominant interactions***

Taking the results of Figures 3.28 and 3.29 together, it is interesting to observe that the third-order near-resonant and bound-wave interactions for $k_pd > 1.363$ are oppositely affected by the spectral bandwidth. Therefore, it is not obvious which type of interaction prevails. Indeed, it is unclear if the total crest heights are affected by the spectral bandwidth in this water-depth regime. To assess this, the total crest-height at $Q = 10^{-3}$ is shown in Figure 3.30. These results suggest that for $k_pd \in [1.36, 2.0]$ the effect of spectral bandwidth is dominated by bound-wave interactions. Alternatively, for deeper effective water depths, it is dominated by near-resonant interactions.

Moreover, with the crest amplification due to near-resonant interactions in $k_pd > 1.363$ being relatively small ($\sim 3\%$) for $\gamma = 1.0$, it is instructive to assess if, indeed, higher than second-order nonlinearity is important. To allow this, the Forristall (2000) model predictions for different spectral bandwidths have also been added in Figure 3.30. These comparisons indicate that even in the absence of important energy focusing, bound-wave contributions of higher-order lead to the amplification of the crests beyond the second-order predictions of Forristall (2000), by as much as $\sim 20\%$.

Finally, it is interesting to note that the agreement with Forristall (2000) observed

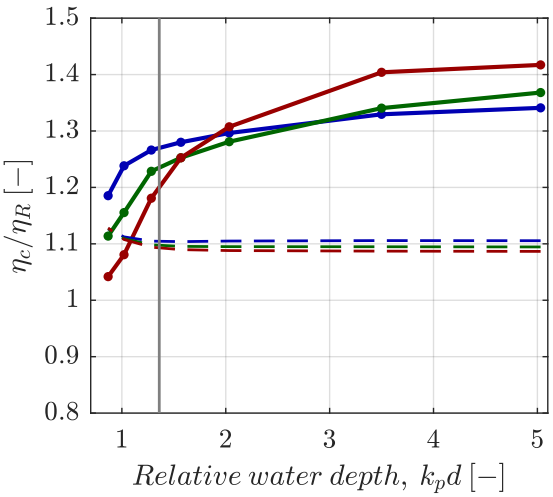


Figure 3.30: Effect of spectral bandwidth (γ) and relative water depth on the time-averaged normalised crest height, η_c/η_R at $Q = 10^{-3}$, with (—●— / —●— / —●—) referring to $\gamma = 1.0$, 2.5 and 5.0, respectively. The Forristall (2000) prediction has also been added for reference, with (— — / — — / — —) corresponding to $\gamma = 1.0$, 2.5 and 5.0, respectively. The vertical line (———) marks the theoretical relative water depth $k_pd = 1.363$. All results refer to uni-directional sea-states of $\frac{1}{2}H_sk_p = 0.105$.

earlier at $k_pd = 0.87$ holds only for $\gamma = 2.5$. Indeed, the balance of the dynamic effects over bound contributions is such that for $\gamma = 5$ the crest heights are attenuated with respect to Forristall (2000), while for $\gamma = 1.0$ they are amplified. To this end, the present results are entirely in line with Fernández et al. (2016) in that for $k_pd = 1.15$ and $\gamma = 6$ an agreement with Forristall (2000) was observed. However, the present analysis suggests that this agreement is to be expected for specific combinations of sea-state parameters, and it does not indicate the absence of nonlinear effects beyond second-order.

3.6 On the applicability of analytical uni-directional solutions for the statistical moments

3.6.1 Dynamic kurtosis

Having identified that the effect of near-resonant interactions on the crest-heights can be explained by the value of the dynamic kurtosis, the applicability of the narrow-band models for its prediction presented in §3.2.2 is of practical interest. Whilst this type of assessment has been performed for deep-water conditions (Mori et al. 2007,

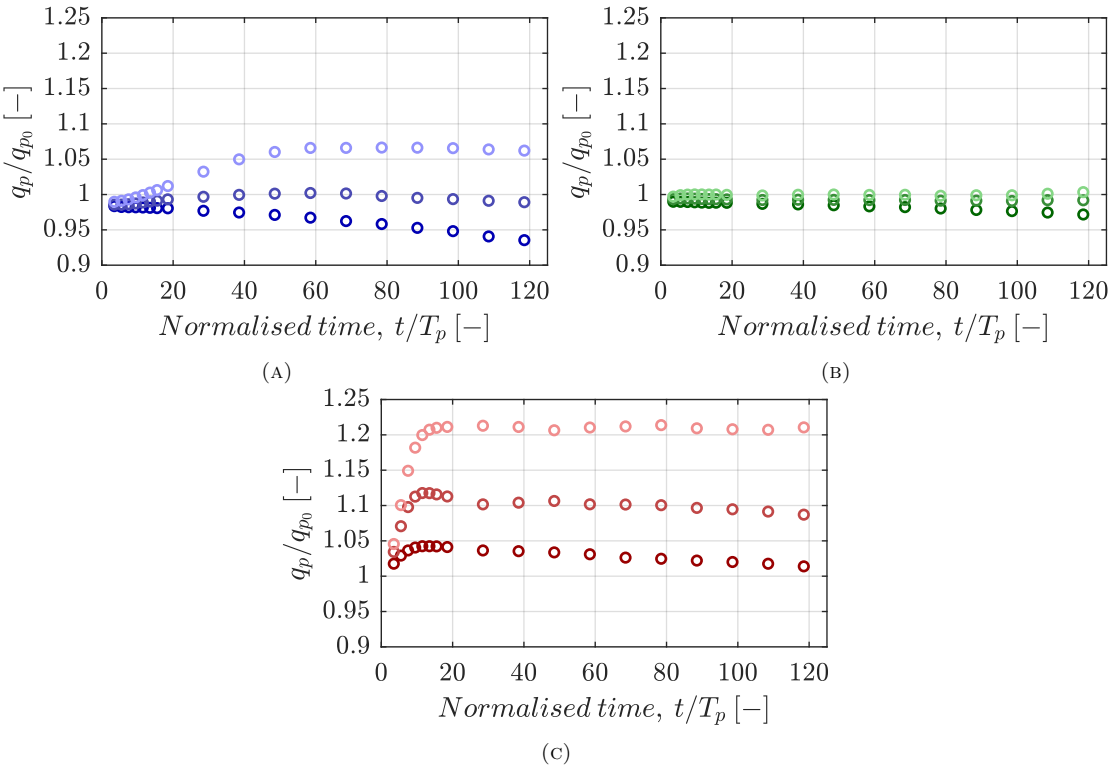


Figure 3.31: Temporal evolution of the bandwidth parameter $q_p = 1/(\pi Q_p)$ normalised with respect to the initial value q_{p0} for uni-directional sea-states of $\frac{1}{2}H_s k_p = 0.105$. (A) for $k_p d = 5.03$, (B) for $k_p d = 1.28$ and (C) for $k_p d = 0.87$. The different markers (○ , ○ , ○ / ○ , ○ , ○ / ○ , ○ , ○) refer to $\gamma = 1.0$, 2.5 and 5.0, respectively.

Fedele et al. 2010 and Tang et al. 2021) an equivalent assessment in finite water depth has not been previously performed.

To apply Equation 3.2, an estimate of the Benjamin-Feir Index (BFI) for realistic bandwidth sea-states is necessary. In the original definition of the BFI provided by Janssen (2003) a symmetric spectral shape was assumed, with the spectral bandwidth defined through the standard deviation of the frequency spectrum σ_ω. However, such a definition is not straightforward for the case of the JONSWAP spectra employed here. As such, different measures for the spectral bandwidth need to be considered. These consist of the parameters ν and $q_p = 1/(\sqrt{\pi Q_p})$, as presented in §2.3; the former allocating more weight to changes in the high frequencies and the latter to changes at the spectral peak.

Before employing these measures for predicting the dynamic kurtosis, it should be noted that they are not independent of time, as near-resonant interactions lead to energy transfers between wave components that can ultimately change the shape

of the free-wave spectrum. It was found that whilst the variation of ν with time was less than 3% for all cases, the variation of q_p was more significant. To this end, Figure 3.31, presents the time-variation of q_p based upon the free-wave spectrum. To reflect the relative change of q_p, the results are normalised with respect to the initial (input) value denoted with q_{p0}.

In exploring the trends observed in Figure 3.31, it is demonstrated that in deep water ($k_p d = 5.03$) (1) for $\gamma = 2.5$ the spectrum is initially in equilibrium, (2) for $\gamma = 5.0$ tends to broaden and (3) for $\gamma = 1.0$ it tends to narrow; these observations being qualitatively in line with the evolution of the amplitude spectrum of JONSWAP wave groups presented by Gibson (2004) and Gibson & Swan (2007). For the case of $k_p d = 1.28$, no spectral evolution is detected owing to the reduced energy transfers in this effect water depth. This is in accordance with numerical simulations presented by Janssen & Onorato (2007) for symmetric spectral shapes. Finally, for $k_p d = 0.87$, the spectrum tends to become broader for all initial spectra. This is in line with Janssen & Onorato (2007). More specifically, as perhaps expected, the narrower the initial spectrum, the larger the spectral changes; the energy transfers being stronger as the bandwidth decreases.

Having identified the extent of the spectral changes, it should be noted that it is not obvious whether the analytical solutions of Equation 3.2 should be based upon the initial or evolved spectral shapes. This is because these solutions do not address any spectral evolution. Within the present investigation, both initial and evolved values of the bandwidth parameters have been employed, and the best one is identified. Finally, in applying Equation 3.2, a characteristic steepness needs to be defined. This is taken as $k_p \sigma_\eta = k_p m_0^{1/2}$, which links to $\frac{1}{2} H_s k_p$ according to $k_0 \sigma_\eta = \frac{1}{4} H_s k_p$. Additional comparisons using alternative definitions for the sea-state steepness are presented in Appendix B (§B.1).

Figure 3.32 compares Equation 3.2 evaluated using both the initial and evolved bandwidth parameters for the sea-states presented in Figure 3.28(A). For completeness, the bandwidth corrected prediction of Equation 3.5, evaluated using the initial frequency spectrum is also added. However, the equivalent prediction based on the evolved spectra is omitted to ensure clarity in the plots. Moreover, whilst this correction has been derived upon deep-water arguments, its application has also been extrapolated into finite water depth. This correction, ranging between $12 - 16\%$ for

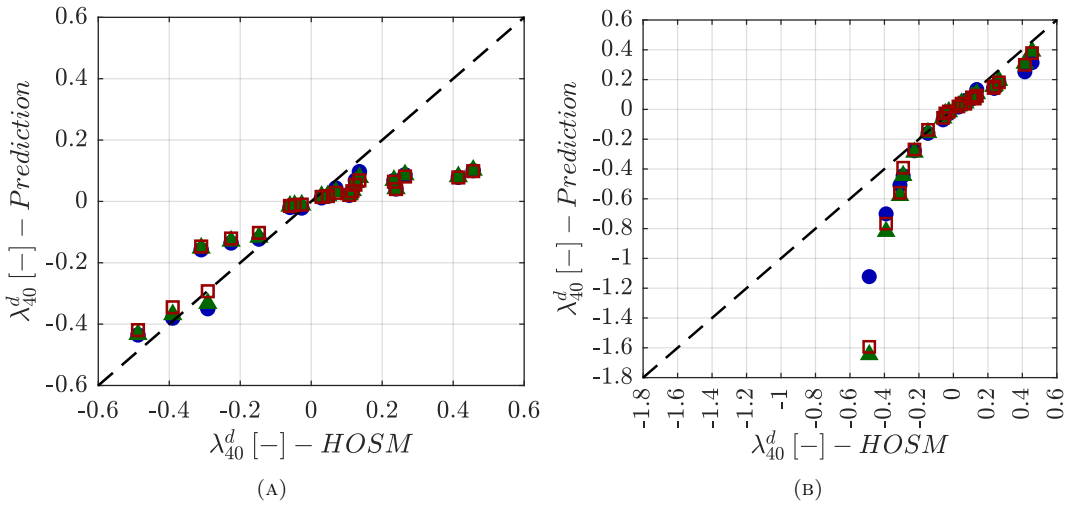


Figure 3.32: Comparison of the time-and ensemble-averaged dynamic kurtosis at steady state and the narrow-band predictions based on Equation 3.2 (•) for evolved spectra, (▲) for initial spectra, and on Equation 3.5 (□) applied upon the the initial spectra. The different sub-figures correspond to different definitions of spectral bandwidth: (A) for ν and (B) for $\frac{1}{Q_p\sqrt{\pi}}$. Note the different axis limits in the two plots.

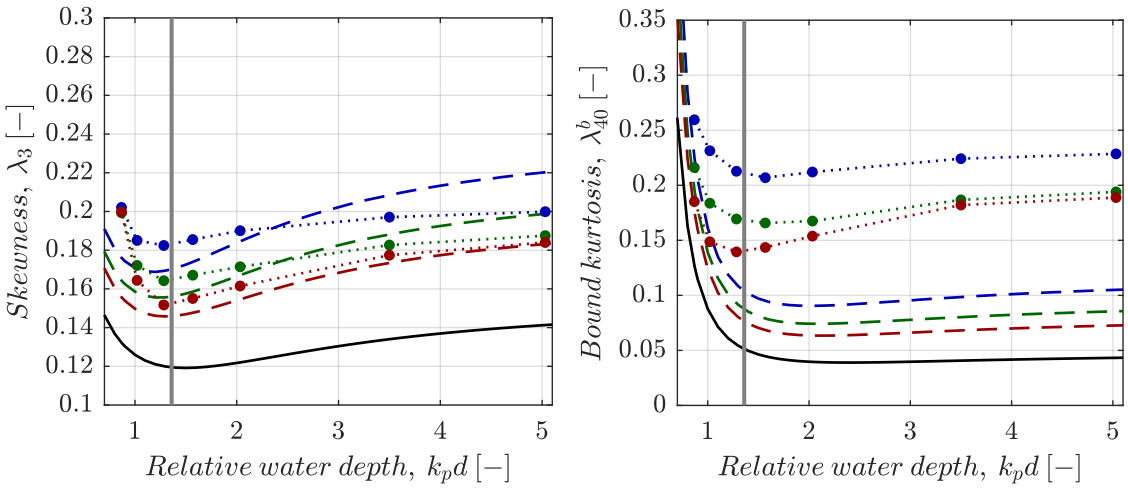
ν and $3-12\%$ for q_p, is not shown to be that significant.

Taken together, it is concluded that neither ν nor q_p can be used in a predictive manner across all the cases considered. Specifically, whilst ν leads to a reasonable agreement with observations for $\lambda_{40}^d < 0$, for $\lambda_{40}^d > 0$ the discrepancies are significant. In contrast, q_p gives good agreement for $\lambda_{40}^d > 0$, but fails to predict the lower values of the dynamic kurtosis. Furthermore, although the evolved q_p leads to improved predictions for $k_p d < 1.36$, the discrepancies remain very significant.

With ν being more sensitive to the spread of energy in the high-frequency tail, its outperformance over q_p for $\lambda_{40}^d < 0$, or equivalently for $k_p d < 1.36$, reveals the important role of the spectral tail on the intensity of near-resonant interactions. This is consistent with the data presented in Figure 3.24(A). In contrast, the outperformance of q_p over ν for $k_p d > 1.36$, suggests that the energy distribution around the spectral peak dominates the intensity of near-resonant interactions in this regime.

3.6.2 Skewness and bound kurtosis

To conclude this section, it is interesting to explore the applicability of the narrow-band theoretical solutions for the skewness and bound kurtosis of Janssen (2009) (§3.2.2). In applying these solutions, an effective central wavenumber has to be



(A) (B)

Figure 3.33: Comparison of the time-and ensemble-averaged (A) skewness (λ_3) and (B) bound kurtosis (λ^b_{40}) to the theoretical narrow-band solution of Janssen (2009) for uni-directional sea-states of $\frac{1}{2}H_sk_p = 0.105$. The numerical results are denoted with (· · ● · · / · · ● · · / · · ● · ·) for $\gamma = 1.0$, 2.5 and 5.0, respectively. The theoretical narrow-band predictions for the skewness and bound kurtosis are shown with (——) using $\sigma_\eta k_p$, and with (– – / – – / – –) using $\sigma_\eta k_m$ for $\gamma = 1.0$, 2.5 and 5.0, respectively. The vertical line (——) marks the relative water depth $k_pd = 1.363$ and it is added for reference.

selected. This aims to represent the wavenumber k_0 (§3.2.2) associated with a narrow symmetrically concentrated spectrum; this selection affecting both the estimation of the sea-state steepness, $\sigma_\eta k_0$, and effective water depth, k_0d. In making this selection, two wavenumber definitions have been employed: the peak wavenumber k_p and the mean wavenumber k_m, where k_m refers to the wavenumber corresponding to the mean frequency $\omega_m = m_1/m_0$ based upon the linear dispersion relationship such that $k_m = k(\omega_m)$ [1]. Whilst the former represents the location of the spectral peak, the latter is affected by the adopted spectral shape. In making these comparisons, the choice for representing the effective water depth was the wavenumber k_p. This was also the case for the dynamic effects (see Appendix B for further discussion). Comparisons using both definitions for the sea-state steepness (i.e. $\sigma_\eta k_p$ and $\sigma_\eta k_m$) are presented herein. Based on the above, the theoretical predictions for the skewness and bound kurtosis are compared to HOSM time-and ensemble-averaged steady-state values in Figures 3.33(A) and 3.33(B), respectively.

These comparisons indicate that the theoretical solution for the skewness pa-

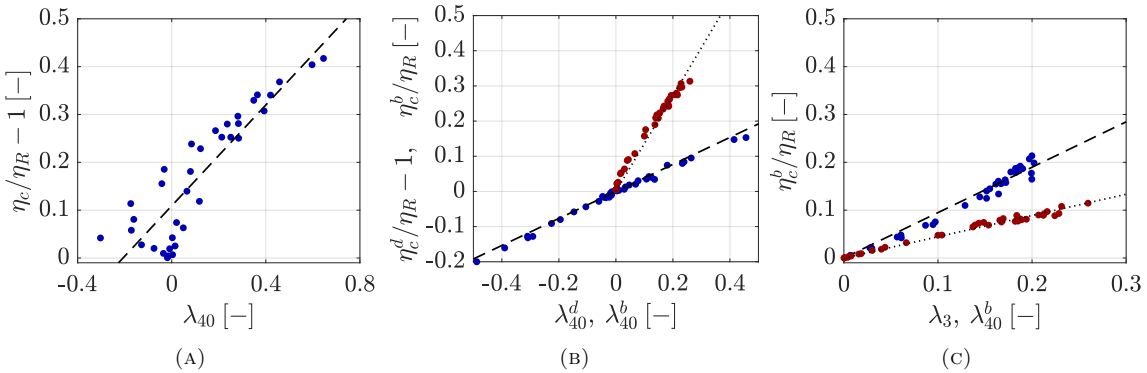
[1] This is identical to k_1 used within the Forristall (2000) model, presented in §2.3.3.

rameter severely under-predicts the numerical results when the steepness $\sigma_\eta k_p$ is employed. In contrast, the predictions based on $\sigma_\eta k_m$ appear more accurate. In fact, for the most narrow-banded sea-states of $\gamma = 5$ and for $k_p d > 1.2$ the predictions are very satisfactory. However, as the effective water depth reduces, the deviations become non-negligible. Indicatively, at $k_p d = 0.87$ the skewness is under-predicted by as much as $\sim 23\%$; most probably due to the over-prediction of the frequency-difference terms that tend to reduce the predicted values of the bound moments (see Appendix B). Moreover, the deviations also tend to increase with an increase in spectral bandwidth, owing to the progressive violation of the narrow-band assumption.

Similarly, the bound kurtosis is significantly under-predicted irrespective of the choice of the steepness parameter. However, once again the comparisons based on $\sigma_\eta k_m$ are better than these based on $\sigma_\eta k_p$. The observed discrepancies originate (1) from the inability of the narrow-band theory to capture the third-order bound-wave interactions arising in broad-banded sea-states and (2) from the coupling of the bound-wave contributions to the underlying dynamic effects. This coupling leads to both a progressive increase with time of the bound kurtosis in deep water and an attenuation as $k_p d$ reduces below 1.36 (Figure 3.15).

As a final remark, it is important to note the similarity between the variation of the skewness and bound kurtosis with effective water depth and spectral bandwidth, and the equivalent variation of the bound contributions presented in Figure 3.29. This observation adds value to the relevance of these statistical parameters. To quantify this and to demonstrate, in practice, how the statistical moments can relate to the largest waves encountered in random sea-states, Figure 3.34 presents how they relate to the crest-height and its contributions at $Q = 10^{-3}$ for the full set of the simulated sea-states employed in this chapter. Specifically,

- Figure 3.34(a) presents the variation of the the total crest heights relative to linear theory against the total kurtosis.
- Figure 3.34(b) presents the variation of crest-height induced by (1) the free waves against the dynamic kurtosis, and (2) the bound contributions against the bound kurtosis, and
- Figure 3.34(c) presents the variation of (1) the even-harmonic bound-wave contributions (essentially the sum of contributions from the zeroth, second and



(A) (B) (C)

FIGURE 3.34: Relative nonlinear change of crest heights at $Q = 10^{-3}$ against the statistical moments for all available uni-directional sea-state simulations. (A) total amplification, $\eta_c/\eta_R - 1$, vs total kurtosis, λ_{40}, (B) free-wave crest amplification, $\eta_c^d/\eta_R - 1$, vs dynamic kurtosis, λ_{40}^d, (•) and bound-waves amplification, η_c^b/η_R, vs bound kurtosis, λ_{40}^b, (•), and (C) even-harmonic bound-wave amplification vs skewness (•) and odd-harmonic bound-wave amplification vs bound kurtosis (•). In all plots the lines refer to best-fit linear fits.

fourth harmonics) against the skewness and (2) the odd-harmonic bound-wave contributions (essentially the contribution from the third-harmonic) against the bound kurtosis.

In all these sub-figures, the best-fit linear lines have been added.

In observing Figure 3.34(A), it is clear that the total kurtosis alone is unable to explain the magnitude of the largest waves. This was previously anticipated by Guedes Soares et al. (2003), Gramstad & Trulsen (2007), Xiao et al. (2013), Gramstad & Bitner-Gregersen (2019), Athanassoulis & Gramstad (2021) (amongst others). Evidence of this is provided by the significant scatter of the data points. However, when the effects of the near-resonant interactions and the bound contributions are isolated, Figure 3.34(B) shows that their respective effect on the largest crest heights can be largely explained by the dynamic and bound kurtosis, respectively. In addition, if one is interested in exploring further the individual harmonic contributions of the bound waves, Figure 3.34(C) shows that these can be expressed by the moments of skewness and bound kurtosis. In summary, Figure 3.34 demonstrates that the values of the statistical moments are relevant for engineering purposes, without having to assume any probability structure for the free surface (as is the case in the Gram-Charlier series expansion).

3.7 Chapter outcomes

The present chapter has provided an investigation of the near-resonant interactions versus bound-wave contributions on the statistical properties of uni-directional sea-states. The main outcomes of this investigation are summarised as follows:

1. It has been shown that near-resonant interactions lead to an increase of the crest heights for $k_p d > 1.36$, the crest heights are unaffected for $k_p d \approx 1.36$, and are reduced in $k_p d < 1.36$. With these regimes having already been predicted using narrow-band theory, the nonlinear evolution was shown to be dictated by the location of the spectral peak wavenumber k_p.

2. For sea-states in $k_p d < 1.363$, second and higher-order bound-wave contributions and third-order near-resonant interactions were found to have a competing influence on the total crest heights. For all cases considered, bound waves prevailed and, hence, the wave crests were found to be amplified when compared to the linear prediction. The total crest-height distribution for $k_p d = 0.87$ and $\gamma = 2.5$ agreed with the Forristall (2000) model. This result highlighted that considering the crest heights of the total free surface alone could lead to misleading conclusions regarding the presence of nonlinearity above second-order.

3. In considering the effect of sea-state steepness, it was found that the effect of near-resonant interactions increases progressively, without any step-change; casting doubt on the applicability of second-order theory, even for small sea-state steepnesses.

4. In introducing changes in the spectral bandwidth (by changing γ), it was found that near-resonant interactions were progressively affected less by these changes as $k_p d$ approaches the value of 1.363, from either side of the $k_p d$ range. For $k_p d > 1.363$, changes in spectral bandwidth oppositely affect the effect of near-resonant interactions and bound-wave contributions on the crest heights. Whereas this is not the case for $k_p d < 1.363$.

5. It has been shown that the evolution of the crest-height distribution of the free waves is directly linked to the corresponding evolution of the dynamic kurtosis.

6. Bound-wave contributions were found to be in accordance with the values of skewness and bound kurtosis for a wide range of sea-state conditions.

7. The performance of the analytical solutions for the dynamic kurtosis based on Mori & Janssen (2006) and Janssen & Onorato (2007) was assessed. It was found that the adopted measure for spectral bandwidth plays a crucial role in obtaining satisfactory predictions. The Goda (2000) parameter, Q_p, performed better for $k_p d > 1.363$, whereas the Longuet-Higgins (1975) ν parameter outperformed Q_p for $k_p d < 1.363$.

8. The narrow-band theoretical solutions for the statistical moments of skewness and bound kurtosis of Janssen (2009) were found to significantly under-predict the numerical results for the majority of the sea-states considered.

4

Statistical properties of directional sea-states

The previous chapter presented the crucial role of near-resonant and bound-wave interactions on the statistical properties of uni-directional sea-states, particularly highlighting the influence of effective water depth, sea-state steepness and spectral bandwidth on the crest-height statistics. The present chapter aims to extend this earlier investigation to directionally spread seas that more closely resemble realistic sea conditions.

Having established in Chapter 3 that the most likely magnitude of the largest waves arising in a 3-hour sea-state relates to the statistical moments of skewness, bound kurtosis and dynamic kurtosis, the present chapter aims to assess the predictions of directional solutions for these moments.

Following a similar structure to Chapter 3, the present chapter commences in §4.1 with an overview of previous analytical, numerical and experimental investigations. Following, §4.2 highlights in more detail the objectives of the investigation. Building upon these objectives, §4.3 presents the sea-state characteristics employed in the analysis. Subsequently, §4.4 presents a brief set of comparisons between numerically generated crest-height distributions using HOSM and experimental data originating from previous studies; the aim of these comparisons being to extend the validations presented in Chapter 3 to directional seas. The effect of nonlinear interactions on the statistical properties of directional random waves is presented in §4.5. Following on,

§4.6 assesses the performance of the current state-of-the-art prediction methodologies for the statistical moments. Finally, the chapter concludes in §4.7 with a summary of the main outcomes.

4.1 Previous works

4.1.1 Numerical and experimental investigations

Deep water

Over the last two decades much research has been conducted to better understand the nature of the largest waves arising in realistic directionally spread sea-states. In this regard, it is relatively well established through experimental studies (Stansberg 1994, Waseda 2006, Onorato et al. 2009a, Latheef & Swan 2013) and numerical (Onorato et al. 2002, Xiao et al. 2013, Hadjigeorgiou 2018) investigations that in deep water an increase in directionality leads to the reduction of nonlinearity.

Particularly, Latheef & Swan (2013) showed that, when non-breaking sea-states are considered, any deviations of the crest-height distribution from second-order theory reduce with an increase in directionality and a reduction of sea-state steepness. More recently, Hadjigeorgiou (2018) reproduced these results based on HOSM simulations. Both Latheef & Swan (2013) and Hadjigeorgiou (2018) attributed the reduction of the nonlinear crests with an increase in directionality to the reduction of the wave steepness of the underlying linear waves. Nonetheless, the extent to which near-resonant effects are responsible for this attenuation is, as yet, unknown.

To this end, the effect of nonlinear focusing in directionally spread seas has been traditionally studied using the BMNLS equation. Particularly, Gramstad & Trulsen (2007), and latter Mori et al. (2011), employed Gaussian spectra within the BMNLS equation and showed that there is a change in the magnitude of the dynamic kurtosis with increase in the directional spread. Nonetheless, whilst the above finding is interesting, it is of limited practical significance owing to the unrealistic spectral shapes employed. In this regard, Gramstad & Trulsen (2007) showed that this change is, at least in part, reproduced in JONSWAP spectra. However, with the BMNLS equation inherently suffering from bandwidth limitations, the JONSWAP spectra (both initial and resolved) were significantly truncated; the maximum resolved wavenumber k_x

being only two times the spectral peak. This limits the maximum resolved frequency component to only ~ 1.4 times the peak frequency. As such, the interpretation of these results should be treated with caution. Particularly because Xiao et al. (2013) have shown significant under-predictions of the crest heights obtained using BMNLS and the crest heights obtained using HOSM; the accuracy of the latter being demonstrated through comparisons to the experimental results of Onorato et al. (2009a).

Finite water depth

In finite water depth, the effect of directionality is less well established than in deep water. Toffoli et al. (2009) explored this effect using HOSM for realistic frequency and angular bandwidths; the focus of this work being on the statistical moments and the probability distribution function of the free surface. More recently, Hadjigeorgiou (2018) conducted a similar investigation using HOSM, but this time the crest-height distributions were considered. Both Toffoli et al. (2009) and Hadjigeorgiou (2018) demonstrated that with an increase in directionality, nonlinearity increases for effective water depths laying in $k_p d < 1.36$. This increase could stem either from the increase of bound-wave interactions (Forristall, 2000) or from energy focusing which is possible in this effective water depth regime for wave interacting in transverse directions (Hayes 1973, McLean 1982a, Toffoli et al. 2013). However, both Toffoli et al. (2009) and Hadjigeorgiou (2018) were incomplete in this regard as the nonlinearity was only addressed as a whole.

Moreover, there is contradictory evidence in the literature as to whether third-order nonlinearity is significant in directionally spread seas in finite water depth. Specifically, Fedele et al. (2016) showed that numerical crest-height distributions obtained using HOSM broadly agree with second-order crest-height predictions for sea-states of $\frac{1}{2}H_s k_p \approx 0.10$, $k_p d \in [1.36, 2.23]$, $\sigma_\theta \approx 20^\circ$ and $\gamma \approx 5$[1]. In line with findings presented by Fernández et al. (2016) for sea-states of $\frac{1}{2}H_s k_p = 0.13$, $k_p d \in [1.15, 1.78]$, $\sigma_\theta \approx 30^\circ$ and $\gamma = 6.0$. In contrast, Hadjigeorgiou (2018) demonstrated a small amplification beyond Forristall (2000) using HOSM. This was of the order of $2-3\%$ in the tail of the distribution for sea-states of $\frac{1}{2}H_s k_p \in [0.10, 0.11]$, $k_p d \in [0.9, 1.5]$, $\sigma_\theta \in [10, 20]^\circ$ and $\gamma = 2.5$.

[1]The γ value here is derived from the reported ν values, assuming a JONSWAP spectrum

In contrast, an extensive experimental study of finite water depth conditions conducted by Karmpadakis et al. (2019a) has shown significant departures of the measured crest heights from the Forristall (2000) predictions. These departures were in the order of 8% at an exceedance probability level of $Q = 10^{-3}$ and related to a wide range of non-breaking sea-state conditions of $\frac{1}{2}H_s k_p \in [0.1, 0.12]$, $k_p d \in [0.8, 1.56]$, $\sigma_\theta \in [10, 30]^\circ$.

Having reviewed previous research on the effect of directionality on the statistics of random seas, it is instructive to present how the current state-of-the-art operational forecasting systems for freak waves account for the wave nonlinearity. Janssen (2017) describes the adopted methodology within the ECMFW freak warning system. This relies on the analytical estimation of the dynamic kurtosis, bound kurtosis and skewness for a given directional wave spectrum. These solutions are reviewed in §4.1.2.

4.1.2 Directional solutions for the statistical moments

Dynamic kurtosis (λ_{40}^d)

Building upon the theoretical grounds set by Janssen (2003) and Mori & Janssen (2006), Fedele (2015) derived a directional narrow-banded (in both frequency and direction) analytical solution for the dynamic kurtosis in deep water [1]. Assuming that the spectral energy is symmetrically concentrated around central values of ω_0 and θ_0 and that the spread of energy is defined by the standard deviations σ_ω and σ_θ, in frequency and direction, Fedele (2015) argued that the dynamic kurtosis is evaluated according to,

$$\lambda_{40}^d = \frac{\pi}{\sqrt{3}} J(\tau; R) BFI^2, \tag{4.1}$$

where BFI is the Benjamin-Feir index defined in §3.3 and $J(\tau; R)$ is a time-dependent factor accounting for the effect of directionality:

$$J(\tau; R) = \frac{3\sqrt{3}}{\pi} \operatorname{Im} \int_0^\tau \frac{1}{\sqrt{1 - 2i\alpha + 3\alpha^2}\,\sqrt{1 + 2iR\alpha + 3R^2\alpha^2}} d\alpha, \tag{4.2}$$

[1] Related work by Janssen & Bidlot (2009) also attempted to produce a similar solution. However, an inconsistency in their adopted procedure was found and addressed by Fedele (2015).

where R is defined as $R = \sigma_\theta/(2\sigma_\omega/\omega_0)$ and expresses the relative importance of directional dispersion over frequency dispersion. τ is an effective evolution time defined as $\tau = (\sigma_\omega/\omega_0)^2\omega_0 t$.

Within Equation 4.1, for $R > 0$ the dynamic kurtosis tends to reduce to 0 in the limit $t \to \infty$. Prior that, it reaches a peak value at a time $\tau_c = 1/\sqrt{3R}$, which lays within the time-scales considered in this investigation (see Appendix B). In contrast, for uni-directional conditions ($R = 0$) the solution predicts a monotonic increase with time until a steady state is reached. This is in agreement with Mori & Janssen (2006). Furthermore, for $R > 1$, the dynamic kurtosis follows the same trend as described above for $R > 0$, but this time it is negative and much smaller in magnitude. A negative dynamic kurtosis signifies a defocusing of the wave energy that stems from interacting wave components that lay in both unstable and stable regions (according to the nonlinear Shröndiguer equation) as the directionality increases. This situation ultimately affects the nonlinear dispersion of different directional wave components in different ways. In the discussion that follows, only the maximum absolute value of the kurtosis through time will be considered, as this gives a unique prediction for each sea-state before the value drops to zero.

To account for finite water depth effects, Janssen (2017) extended the solution of Fedele (2015) using the Davey & Stewartson (1974) system of equations. The form of the solution of Janssen (2017) is identical to Equation 4.1, but this time finite depth affects are included in the evaluation of BFI and R. Based on these modifications, the evaluation of dynamic kurtosis according to Janssen (2017) is given by,

$$\lambda_{40}^d = \frac{\pi}{\sqrt{3}} J(\tau; R_s) B_{sd}^2, \tag{4.3}$$

where B_{sd} is the directional finite depth BFI, which includes a modification of the kernel $T_{0,0,0,0}$ accounting for the effect of directionality through R. Furthermore, $R_s = \beta_s R$, with β_s being a depth-dependent factor. The form of the modified kernel $T_{0,0,0,0}$ and β_s is shown in Appendix B. Before proceeding, it is instructive to explore how:

1. B_{sd} varies with the directionality factor, R, and effective depth, $k_0 d$.

2. the peak value of $J(\tau; R_s)$, $J_p(R_s)$, varies with R for different effective depths, $k_0 d$.

3. the final estimation of dynamic kurtosis varies with R for different effective depths, $k_0 d$; ultimately exploring if nonlinear focusing is predicted for $k_0 d < 1.363$ in directionally spread seas.

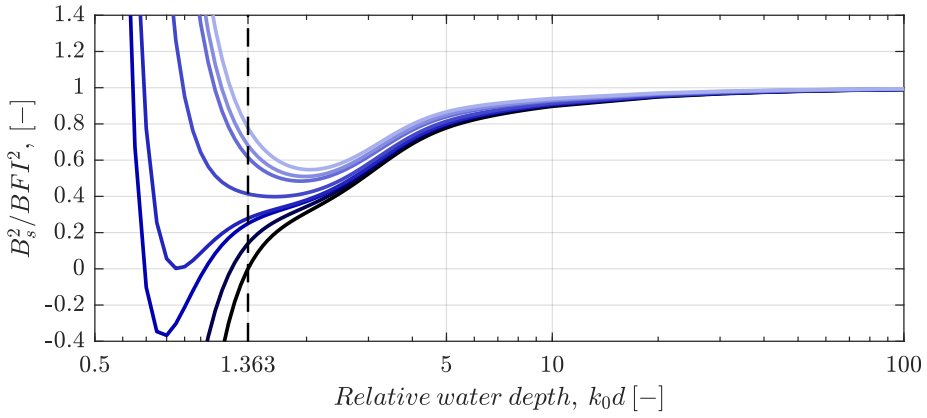
Figure 4.1 explores the above points. Specifically, Figure 4.1 (A) shows that as R increases the dynamic kurtosis increases; the increase being more pronounced as the effective depth reduces. Moreover, this increase and ultimate reversal in sign agrees with the notion that the interaction of non-collinear waves can lead to energy focusing in $k_p d < 1.36$ (Hayes, 1973). The explanation for this arises from the reduction of the wave-induced mean flow due to directionality.

In considering how $J_p(R_s)$ varies in different effective depths, Figure 4.1(B) shows that as $k_0 d$ reduces, $J_p(R_s)$ attenuates faster with increasing R. Thus, whilst in deep water $J_p(R_s)$ changes sign at $R = 1$, in finite water depth this value is reduced. More specifically, for $k_0 d = 0.87$ (the shallowest case considered herein) $J_p(R_s)$ is shown to change sign at $R \approx 0.38$. This relates to the reduced frequency dispersion as the effective water depth reduces, giving rise to a higher effective R factor and hence a quicker attenuation of $J_p(R_s)$ with R compared to deep water.

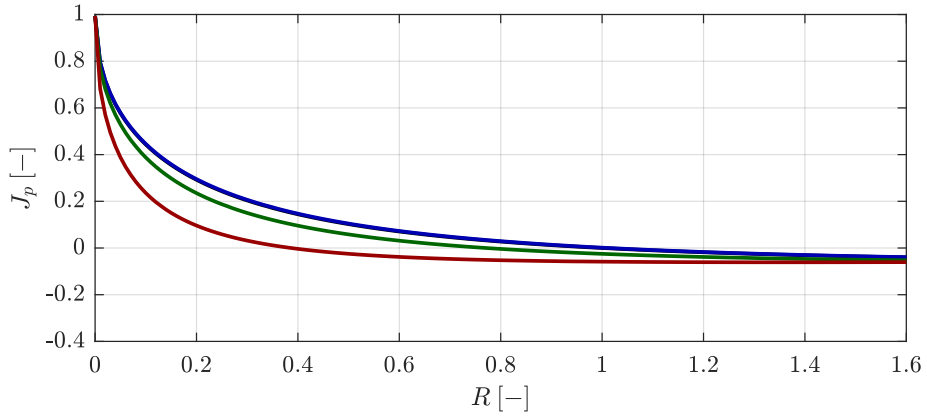
In combining B_{sd} and $J_p(R_s)$, the final prediction for the dynamic kurtosis, normalised with respect to the deep-water uni-directional case, is shown in Figure 4.1 (C) for $k_0 d = 100, 5, 1.28$ and 0.87. In deep water ($k_0 d = 100, 5$) the dynamic effects are shown to reduce with R in accordance with expectation, in $k_0 d = 1.28$ (laying close to the limit 1.363) the effect of directionality is minimal. However, in $k_0 d = 0.87$, despite the increase of B_{sd} with R observed in Figure 4.1 (A), the combined effect of B_{sd} and $J_p(R_s)$ leads to energy defocusing for the full range of the R parameter.

Skewness (λ_3) and bound kurtosis (λ_{40}^b)

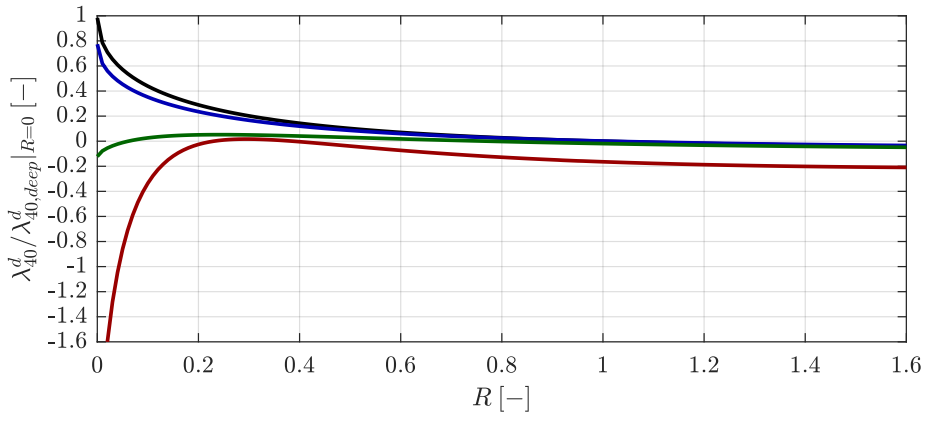
Janssen (2017) derived equivalent directional narrow-band solutions for the skewness and bound kurtosis in finite water depths. These also depend on R, similar to the dynamic kurtosis. The variation of the skewness and kurtosis based on Janssen (2017) with effective depth, $k_0 d$, for different directionality factors R and for a nominal steepness of $\sigma_\eta k_0 = 0.1$ is shown in Figure 4.2 ((A) for the skewness and (B) for the bound kurtosis); the functional form of the solutions given in Appendix B.



(A)



(B)



(C)

Figure 4.1: (A) Variation of B_{sd}^2/BFI^2 with relative water depth, k_0d, for different R: values of $R = 0, 0.1, 0.2, 0.23, 0.4, 0.8, 1.0$ and 1.4 denoted with (— / — / — / — / — / — / — / —), respectively. (B), (C) variation of $J_p(R_s)$ and $\lambda_{40}^d/\lambda_{40,deep}^d$ with R for different k_0d: values of $k_0d = 100, 5, 1.28$ and 0.87 denoted with (— / — / — / —), respectively. $\lambda_{40,deep}^d$ refers to the deep-water uni-directional prediction based on Equation 3.2. In (A) (— —) marks the k_0d value of 1.363 and it is added for reference.

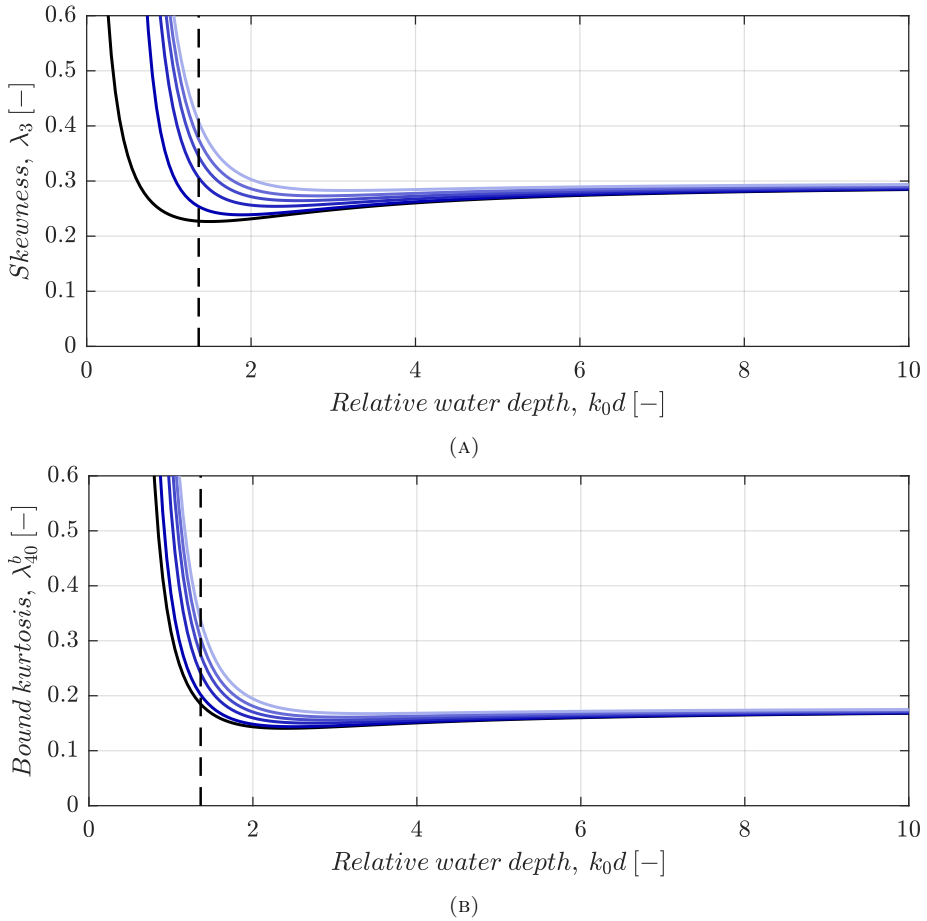


FIGURE 4.2: Theoretically predicted (A) skewness and (B) bound kurtosis for narrow-banded directional seas in varying relative water depth, $k_0 d$, for different R values and a steepness of $\sigma_\eta k_0 = 0.1$: values of $R = 0, 0.1, 0.4, 0.8, 1.4$ and 2.8 denoted with (—— / —— / —— / —— / —— / ——) and (– –) marks the theoretical $k_0 d$ value of 1.363.

Figure 4.2 shows that as R increases, the skewness and bound kurtosis again increase; the explanation again being reduction of the wave-induced mean flow. As the wave-induced mean flow in deep water vanishes so does the effect of R. As such, in deep water the estimated values for the statistical parameters coincide with the uni-directional prediction of Mori & Janssen (2006) (§3.2.2). Likewise for $R = 0$, the solution of Janssen (2017) is identical to the uni-directional case outlined in Janssen (2009).

4.2 Objectives

There is strong evidence in the literature for wave-crest amplifications beyond second-order in directionally spread sea-states in deep water; this amplification is reduced as

waves become more short-crested and less steep. However, the relative importance of the near-resonant interactions and bound-wave contributions remains unclear, particularly for broad-banded sea-states. Moreover, the role of finite water depth is more elusive, with contradictory outcomes presented in the literature. Based on the above, the following questions arise:

1. In deep water, is the nonlinear focusing due to near-resonant interactions identified for uni-directional seas relevant to deep water directional seas, and how is it affected by incremental changes in directionality?

2. For directional seas in finite water depth, is the nonlinear focusing identified in uni-directional seas reversed due to non-collinear interactions?

3. Does the additional effect of directional dispersion affect the dominant role of spectral bandwidth identified in uni-directional seas?

4. How are the bound-wave contributions affected by changes in directionality in different effective water depths?

5. Is the effect of evolution time as significant as in the uni-directional simulations?

The present chapter aims to answer these questions, with a particular focus on addressing the effect of sample variability on the estimation of the magnitude of the largest crest heights arising in a 3-hour sea-state. In addition, it aims to explore the validity of the Janssen (2017) solutions for the statistical moments; specifically identifying whether the trends observed in Figure 4.1 (c) for the dynamic kurtosis are indeed relevant to broad-banded sea-states simulated using HOSM.

4.3 Test cases and numerical setup

Given the above objectives, this section presents the sea-state characteristics and numerical setup within HOSM used in the present study.

To begin, the first goal of the investigation is to establish the role of finite water depth on the nonlinear interactions in directionally spread seas, and how these interactions are affected by the sea-state steepness. For this investigation, sea-states with $\sigma_\theta = 10°$, $\gamma = 2.5$ and increasing steepness were employed; the full details

Table 4.1: Sea-state parameters relating to the study of the effect of sea-state steepness in directional seas.

Set	$k_p d[-]$	$\gamma\,[-]$	$\sigma\,[^\circ]$	steepness/severity
D1	0.87	2.5	10	$\frac{1}{2}H_s k_p\,[-] = 0.005, 0.039, 0.059, 0.085, 0.105$ $H_s/d\,[-] = 0.011, 0.090, 0.136, 0.196, 0.243$
D2	1.28	2.5	10	$\frac{1}{2}H_s k_p\,[-] = 0.005, 0.039, 0.059, 0.085, 0.105$ $H_s/d\,[-] = 0.008, 0.061, 0.092, 0.132, 0.164$
D3	5.03	2.5	10	$\frac{1}{2}H_s k_p\,[-] = 0.005, 0.039, 0.059, 0.085, 0.105$ $H_s/d\,[-] = 0.002, 0.016, 0.023, 0.034, 0.042$

presented in Table 4.1. These allow a direct comparison to the uni-directional sea-states of Table 3.1. Second, to identify the effect of directionality in different effective water depths, sea-states of constant steepness ($\frac{1}{2}H_s k_p = 0.105$) and spectral bandwidth ($\gamma = 2.5$) were assigned different degrees of directional spreading, varying from $\sigma_\theta = 0$ (uni-directional) to 30° in increments of 5°; full details given on Table 4.2. Finally, to study the effect of frequency dispersion over directional dispersion, the γ parameter was varied, while holding the sea-state steepness and directionality constant; details given on Table 4.3. In all cases, the numerical setup adopted for the directional HOSM simulations, together with the required computational resources is presented in Table C.1.

Taken together, the employed sea-states comprise an extensive set of 48 sea-state conditions. This far exceeds any previous study using HOSM; the aim being to provide comprehensive insights on the dependence of the nonlinear interactions upon the different sea-state characteristics.

With a substantial increase in the computational effort required to model directional seas, the present investigation employs the four-phase manipulation method, presented in §2.2.6. This is in contrast to the more computationally demanding twelve-phase manipulation method employed for uni-directional seas. The four-phase manipulation does not separate the 4^{th} and 0^{th} harmonics. However, this limitation does not limit the effective separation of the free waves from the bound waves; this being the primary goal in applying the method.

In addition, in an analogy to uni-directional simulations, space-traces of the dif-

Table 4.2: Sea-state parameters relating to the study of the effect of directionality. The cases in parenthesis refer to sea-states already included in Table 4.1 and Table 3.1.

Set	k_pd [−]	γ [−]	$\frac{1}{2}H_sk_p$[−]	σ [°]
D4	0.87	2.5	0.105	(0), 5, (10), 15, 20, 25, 30
D5	1.28	2.5	0.105	(0), 5, (10), 15, 20, 25, 30
D6	5.03	2.5	0.105	(0), 5, (10), 15, 20, 25, 30

Table 4.3: Sea-state parameters relating to the study of the effect of spectral bandwidth and relative water-depth in directionally spread seas. The cases in parenthesis refer to sea-states already included in Table 4.1.

Set	$\frac{1}{2}H_sk_p$[−]	γ [−]	σ_θ [°]	k_pd [−]
D7	0.105	1.0	10	5.03, 3.50, 2.03, 1.57, 1.28, 1.02, 0.87
D8	0.105	2.5	10	(5.03), 3.50, 2.03, 1.57, (1.28), 1.02, (0.87)
D9	0.105	5.0	10	5.03, 3.50, 2.03, 1.57, 1.28, 1.02, 0.87

ferent harmonic contributions are obtained at time instances $t/T_p = 0$, 2, 4, 6, 8, 10, 12, 15, 25, 35, 45, 55 and 60; a finer interval being adopted at the beginning of the simulations to capture any transient development of the near-resonant interactions. The space traces in these calculations have been obtained along the x coordinate at lateral locations $y = (-5, 0, 5)l_p$ (where $y = 0$ signifies the centreline of the domain). The spatial distance of $5l_p$ ensured that the space traces in a single simulation were uncorrelated. In adopting this approach, the crest-height distribution for each sea-state at a given evolution time included at least $45,000$ waves using an amalgamated set of 330 individual random simulations. This ensured the reliable estimation of the crest-height elevations at an exceedance probability level of $Q = 10^{-3}$, as shown in Chapter 3. Moreover, the present directional simulations conserved energy to the same degree as the uni-directional simulations; the mean error being $< 0.5\%$ in any given sea-state and the maximum in any given seed $\sim 1.0\%$.

Furthermore, before proceeding, it should also be noted that the selected order of nonlinearity within HOSM was set to $M = 3$. In selecting this order, third-order near-resonant interactions are included in the simulations (Onorato et al., 2007). However, the fourth-order quintet interactions are omitted. Nonetheless, the latter could, in theory, be important for both deep and intermediate-depth conditions if the waves

are sufficiently steep and directionally spread (McLean 1982b, McLean 1982a and Francius & Kharif 2006). To be certain that the results have converged with respect to M, simulations with $M = 4$ and 5 were also performed for a sub-set of sea-states. These sea-states include the deepest and shallowest effective depths with $k_p d = 5.03$ and 0.87 with directional spreads $\sigma_\theta = 10°$ and 20°, and $\gamma = 2.5$. Appendix C presents the crest-height distributions along with samples of wave records. These confirm that the present results are indeed converged at $M = 3$.

With numerical convergence confirmed, the following section presents comparisons between experimentally measured crest-height distributions and numerical distributions obtained using HOSM; these comparisons providing the necessary validation.

4.4 Validation considerations

The experimental data employed in validating the directional sea-state simulations originate from the experimental studies outlined in §3.4 and refer to three sea-states generated in ICL in water depth of $d = 1.25m$ and $0.5m$ and in QUB in $d = 0.5m$. The experimental T_p was selected such that the full range of effective water depths employed in this study is covered, with $k_p d \in [0.88, 3.5]$. In addition, to perform effective comparisons, the evolution time in HOSM was linked to the evolution distance in the experiments based on the group velocity. Furthermore, the parameter T_a defining the ramp function was set to $4T_p$; as in Chapter 3 this value was found to be optimised.

With regard to the accuracy of both experimental and numerical crest-height distributions, spatial homogeneity must be ensured, such that the statistics are not dependent upon the spatial location within the wavefield. In the earlier experimental studies, this was the subject of much attention. In the present HOSM simulations, data confirming this are provided in §C.2.

Having previously discussed key aspects in comparing experimental vs numerical crest-height distributions, Figure 4.3 presents the relevant comparisons; the sea-state parameters defined in each sub-figure's caption. In accordance with the comparisons presented in §3.4, the sub-figures on the left present the full probability distribution of the normalised crest heights; the experimental data supplied with 95% confidence

intervals and the linear (Rayleigh) and second-order (Forristall, 2000) distributions added for reference. The right sub-figures present detailed views around an exceedance probability level $Q = 10^{-3}$, the confidence intervals on the numerical data having also been added. These comparisons show excellent agreement between the numerical and experimental data, both of which exhibit significant departures from the second-order Forristall (2000) model. These results confirm the ability of HOSM to simulate the full extent of the nonlinear interactions in directional seas accurately.

4.5 Effect of nonlinear wave-wave interactions on the statistics of directionally spread random wavefields

Having shown that HOSM simulations accurately reproduce the crest-height statistics, this section explores how the different nonlinear interactions are affected by the sea-state characteristics, particularly directionality, and the nonlinear evolution time.

4.5.1 Preliminary results

To gain an initial insight into the extent of the near-resonant interactions in directionally spread seas laying in different effective water depths, preliminary results will focus on the time-evolution of the dynamic kurtosis for sea-states of $\frac{1}{2}H_s k_p = 0.105$, $\gamma = 2.5$ and $\sigma = 10^\circ$ laying in the three effective depths, $k_p d = 5.03$, 1.28 and 0.87, investigated in Chapter 3.

Following the earlier approach adopted in §3.5.1, two different ramp function lengths were employed; the aim being to ensure that the results are independent of T_a. In addition, to further verify the simulations, sea-states with a very low steepness, $\frac{1}{2}H_s k_p = 0.005$, were simulated; in the absence of significant nonlinear interactions, the dynamic kurtosis should be zero.

Figure 4.4 concerns the time evolution of the dynamic kurtosis arising in these sea-states. These results shown that (1) the length of the ramp function does not affect the results for $\frac{1}{2}H_s k_p = 0.105$ and (2) the dynamic kurtosis for $\frac{1}{2}H_s k_p = 0.005$ is indeed zero; both observations enhancing the confidence on the nonlinear predictions. Moreover, in observing the results for $\frac{1}{2}H_s k_p = 0.105$, it is shown that at $t = 0$,

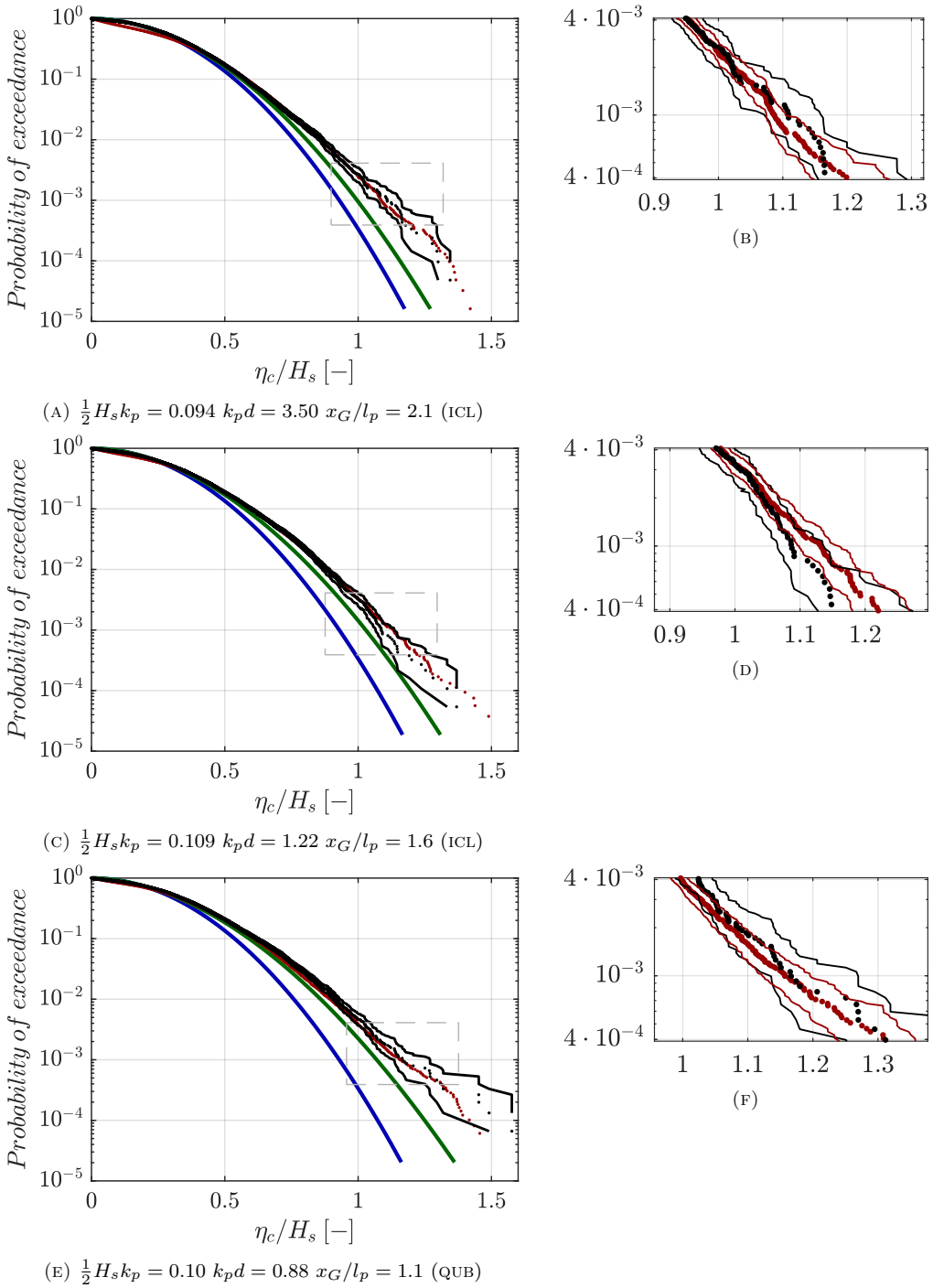


Figure 4.3: Comparison between experimental and numerical (HOSM) data describing normalised crest-height, η_c/H_s, exceedance probability distributions. (A), (C) and (E) show the full probability distributions. The different lines refer to: (——) Rayleigh, (——) Forristall (2000), (•) HOSM, (•) experiments and (——) 95% confidence intervals on the experimental results. (B), (D) and (F) show detailed views marked with a rectangle region in (A), (C) and (E), respectively. In these plots confidence intervals have been added to the HOSM results denoted with (——). All the sea-states are JONSWAP with $\gamma = 2.5$, characterised by a Gaussian DSF of $\sigma = 10°$. While the sea-state steepness $\frac{1}{2}H_sk_p$, effective water depth k_pd and normalised distance of the wave-gauge from the wavemaker x_G/l_p (l_p being the peak wave-length) are provided in the relevant caption.

signifying the end of the ramp function as defined in §3.4, the dynamic kurtosis is not 0 for all water depths. This indicates that nonlinear evolution occurs within the initial ramping of the nonlinear terms. Unfortunately, this is an inevitable feature of the HOSM simulations, as explained in §3.5.1, and relates to the need to adopt a ramp function of substantial length to avoid the creation of spurious waves.

In considering the physical effects that emerge from the results given in Figure 4.4:

1. In deep water ($k_p d = 5.03$), the energy focusing observed in uni-directional sea-states (Figure 3.13(A)) ceases to exist owing to the dominance of directional dispersion over nonlinear dispersive focusing. This result that is in agreement with Gramstad & Trulsen (2007) who based their analysis on the BMNLS equation. Specifically, there is slight energy defocusing in the initial stage of evolution; the value of the dynamic kurtosis laying slightly below zero. However, as time progresses, the dynamic kurtosis evolves towards zero. It is interesting to note that this type of evolution agrees with the theoretical prediction of Janssen (2017) for $R > 1$. To assess if Janssen (2017) predicts energy defocusing for this sea-state, different measures for the spectral bandwidth can be adopted when evaluating R. By employing ν, q_p and $\Delta\omega/\omega_p$, which progressively give more weight to the spectral peak (§2.3.1), the corresponding R values are 0.17, 0.37 and 1.15, respectively. Therefore, the theory of Janssen (2017) appears to predict energy defocusing provided $\Delta\omega/\omega_p$ is used to define the spectral bandwidth. This value is closer to the narrow-band assumption underpinning the theory. Whilst this appears promising, assessment of the solution of Janssen (2017) will be addressed in §4.6.

2. For $k_p d = 1.28$ it is shown that the evolution of kurtosis is very similar to the uni-directional results and in accordance to the theoretical prediction of Janssen (2017) (Figure 4.1(C)). In this case the effect of directionality on the dynamic kurtosis was minimal.

3. Finally, for $k_p d = 0.87$, energy defocusing similarly to the uni-directional results is observed for the full duration of the simulations. This arises due to the persistence of the effect of the wave-induced 'mean flow'. It is noted that in the narrow-band limit for the spectral bandwidth used within the solution of

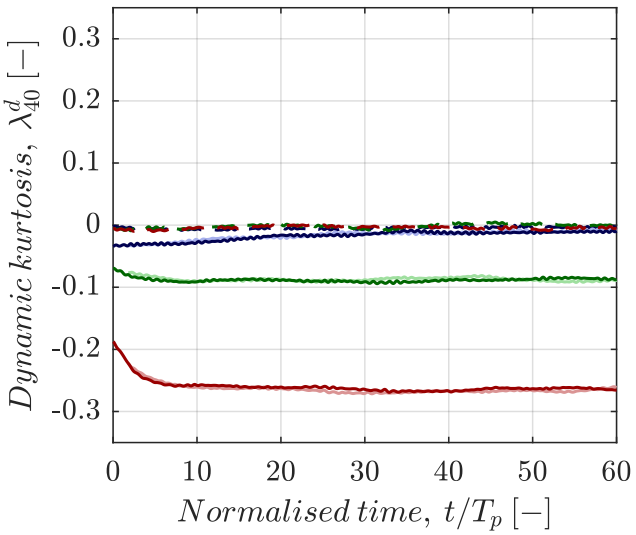


Figure 4.4: Temporal evolution of the ensemble-averaged dynamic kurtosis, λ_{40}^{d}, for directional sea-states of $\frac{1}{2}H_s k_p = 0.005$ and 0.105, $\gamma = 2.5$ and $\sigma = 10°$. The lines (/) refer to $k_p d = 5.03$, (/) to $k_p d = 1.28$ and (/) to $k_p d = 0.87$ for $\frac{1}{2}H_s k_p = 0.105$; the different colour shades corresponding to $T_a = 4$ and $10T_p$, respectively. The dashed lines refer to the results in adopting identical sea-state characteristics but this time $\frac{1}{2}H_s k_p = 0.005$. The horizontal time-axis is normalised by the spectral peak period, T_p.

Janssen (2017), the theory of which was described in §4.1.2, the wave-induced mean flow refers to a wave component with a wavenumber that tends to zero. This is distinguished from the wave-induced 'mean flow' associated with broad-banded sea-states, which involves very long freely propagating wave components of low wavenumbers spanning in a wider wavenumber range. In the former case, the wave-induced mean flow tends to induce a mean change in the free surface, whereas in the latter case, the wave-induced 'mean flow' involves oscillatory changes in the free surface. Hence, the quotes have been added in the latter case to distinguish it from the former. In either case, the mean flow or 'mean flow' is the result of triad resonant or near-resonant interactions arising at second-order in the wave steepness. In the presence of such long wave components, the quartet third-order near-resonant interactions lead to energy defocusing. This permanent effect of the quartet near-resonant interactions is in contrast to deep-water directional wave evolution that tends to return to zero as time progresses (see Mori et al. 2011, Xiao et al. 2013, Fedele 2015). This highlights, once more, the different nature of the near-resonant interactions as the water depth reduces.

Having verified the accuracy of the simulations and, in so doing, revealed some important features of the intensity of near-resonant interactions in directionally spread seas for different effective water depths, the effect of near-resonant interactions and bound-wave contributions on the crest-height statistics are explored in the sections to follow. Specifically, §4.5.2 deals with the effect of finite water depth, §4.5.3 the effect of steepness, §4.5.4 the effect of the directional spread and, finally, §4.5.5 the effect of spectral bandwidth.

4.5.2 Influence of effective water depth

Figure 4.5 presents crest-height distribution the normalised with respect to H_s for both the underlying free waves (sub-figures (A) and (C)) and total free-surface elevation ((B) and (D)) for sea-states with $\frac{1}{2}H_s k_p = 0.1052$, $\gamma = 2.5$ and $k_p d = 5.03, 1.28$ and 0.87. Two evolution times are considered: $t = 0$ on sub-figures (A) & (B) and $25T_p$ on sub-figures (C) & (D); the former corresponding to the initial stage on nonlinear evolution and the latter corresponding to that part of the dynamic kurtosis where a steady state has been reached. For reference, all sub-figures include the predictions of the (linear) Rayleigh model. In addition, the sub-figures concerning the total free surface also include the directional second-order Forristall (2000) predictions.

In considering the results on Figure 4.5, and contrasting these with the equivalent uni-directional results on Figure 3.16, the following observations arise:

1. *Crest heights of the free waves - Figures 4.5 (A), (C)*

    - Initially, for $t = 0$ there is a close similarity between the crest heights of the free waves in the uni-directional ($\sigma_\theta = 0$) and directionally spread ($\sigma_\theta = 10°$) simulations. Specifically, for $k_p d = 5.03$ and 1.28 the crest heights lay very close to the Rayleigh prediction. Whereas for $k_p d = 0.87$ the attenuation due to near-resonant interactions is comparable to the data presented in Figure 3.16 (A).
    - For the latter evolution time of $t = 25T_p$ it is observed that (1) in deep water, $k_p d = 5.03$, the crest heights are not amplified in directionally spread sea-states as they were in uni-directional seas (Figure 3.18), (2) for $k_p d = 1.28$ directionality does not seem to greatly affect the crest heights

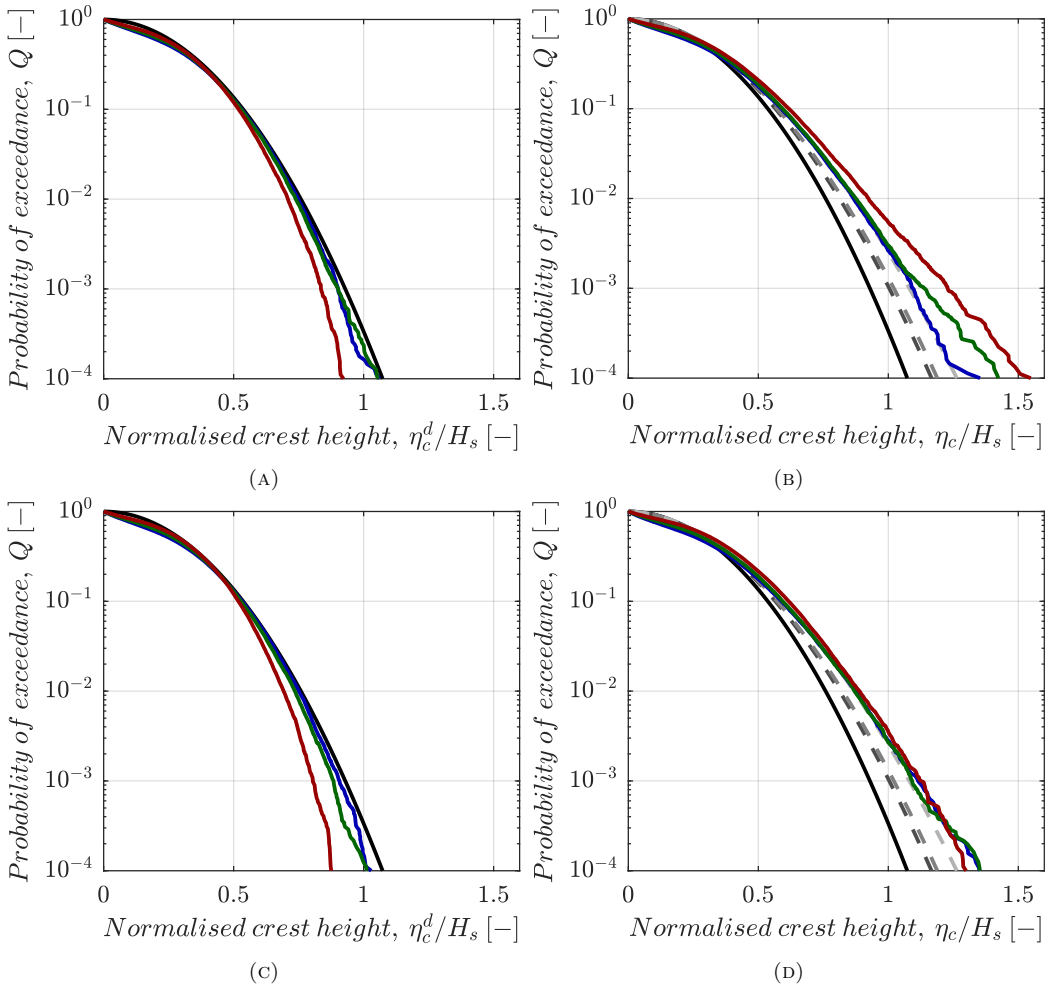


Figure 4.5: Normalised crest-height, η_c/H_s, exceedance probability distributions for directional sea-states of $\frac{1}{2}H_s k_p = 0.105$, $\gamma = 2.5$ and $\sigma_\theta = 10°$ for different evolution times: (A)-(B) for $t = 0$ and (C)-(D) for $t = 25T_p$. The left column refers to the crest heights of the free waves (η_c^d) and the right column to the total free surface (η_c). The lines (/ /) correspond to $k_p d = 0.86$, 1.28 and 5.03, respectively. The Rayleigh distribution ( ) and directional Forristall (2000) distribution (/ /) for $k_p d = 0.86$, 1.28 and 5.03 are added for reference.

of the free waves and (3) for $k_p d = 0.87$ the reduced crests observed in uni-directional sea-states is also present in directional sea-states.

Importantly, all of the above observations are consistent with the evolution of the dynamic kurtosis presented in Figure 4.4.

2. *Crest heights of the total free surface - Figures 4.5 (b), (d)*

   - Starting with the shallowest case of $k_p d = 0.87$, at both evolution times, the reduction of the free-wave crest heights is counteracted by the bound-wave contributions; the crest heights laying above the Rayleigh predictions. This observation is in line with the earlier analysis of uni-directional seas. Moreover, comparing the fully nonlinear crest heights to the Forristall (2000) prediction, the effect of evolution time becomes evident: for $t = 0$ the crest heights are substantially increased above Forristall (2000). In contrast, for $t = 25T_p$ they are in much closer agreement. Indicatively, the wave amplification above Forristall (2000) at an exceedance probability level of $Q = 10^{-3}$ is $\sim 14\%$ for $t = 0$ and $\sim 4\%$ for $t = 25T_p$. While the equivalent wave amplification beyond the linear (Rayleigh) predictions is $\sim 30\%$ and $\sim 20\%$, respectively, for the two evolution times considered. These results agree with experimental data reported by Karmpadakis et al. (2019a) concerning a short evolution time or distance from the wavemaker. In this latter study, a crest-amplification of $\sim 28\%$ was reported for the same probability level beyond the linear prediction for a sea-state similar to the present study. This was characterised by $k_p d = 0.81$, $\gamma = 2.5$, $\sigma = 10^\circ$ and $\frac{1}{2} H_s k_p = 0.11$. Interestingly, when the steady state crest heights are concerned, the present results also agree with the numerical data of Hadjigeorgiou (2018), who report a lower amplification of $\sim 17\%$ at this probability level for a similar sea-state of $k_p d = 0.9$, $\gamma = 2.5$, $\sigma = 10^\circ$ and $\frac{1}{2} H_s k_p = 0.11$.
   - Continuing with the two deeper cases of $k_p d = 1.28$ and 5.03, the crest height distributions show similar deviations from the theoretical distributions irrespective of t. It therefore appears that the evolution time is less important in the absence of significant nonlinear focusing or defocusing.

To quantify the effect of nonlinear interactions on the crest-height distributions in different effective water depths, Figure 4.6 presents the ratio of the various nonlinear contributions over the linear (Rayleigh) crest-height predictions for $t = 25T_p$. Specifically, sub-figure (a) concerns the normalised crest heights of the free waves and sub-figures (b)-(d) present the corresponding total bound-wave amplifications, along with the underlying harmonic contributions of the odd and even harmonics; each sub-figure corresponding to a different effective water depth.

In considering, first, Figure 4.6(a), near-resonant interactions lead to free-wave crest-height reduction in all effective water depths; the effect becoming more pronounced as the effective water depth reduces. Interestingly, this is shown to affect the entire tail of the probability distribution. Indicatively, the reduction at an exceedance probability level of $Q = 10^{-3}$ is in the order of 2%, 5% and 13.5% for $k_pd = 5.03, 1.28$ and 0.87, respectively. To highlight the effect of directionality, the corresponding reduction observed in the equivalent uni-directional sea-states in $k_pd = 1.28$ and 0.87 was $\sim 2.5\%$ and $\sim 16\%$, respectively, while the increase in $k_pd = 5.03$ was $\sim 10\%$.

Considering the total bound-wave contributions, the results demonstrate that they lay well above the directional second-order prediction of Forristall (2000) in all water depths; owing to higher than second-order nonlinear interactions. Specifically, the increase at $Q = 10^{-3}$ is in the order of $\sim 20\%$ for $k_pd = 5.03$ and 1.28 and of $\sim 35\%$ for $k_pd = 0.87$. In contrast, the corresponding increase predicted by Forristall (2000) is $\sim 10\%$ and $\sim 17\%$, respectively. Unfortunately, a direct comparison of the second-order bound terms with the Forristall (2000) prediction is not possible, as the even harmonics include additional fourth-order contributions. Taken together, whilst the second-order theory predicts an increase of the bound contributions with reduced effective water depths, it does not capture the full extent of bound contributions.

Having gained an insight into the effect of the various nonlinear interactions on the crest-height distribution for selected times, it is instructive to explore in more detail the time evolution of the nonlinearity. To achieve this, Figure 4.7 presents the time-evolution of the crest heights at an exceedance probability level of $Q = 10^{-3}$, together with the contributions of the free and bound waves. To gain a better view of the role of directionality, it directly contrasts the results to the equivalent uni-directional data presented in Figures 3.16 and 3.23. In more detail, the left column in Figure 4.7 presents the normalised crest heights of the total free surface, η_c/η_R,

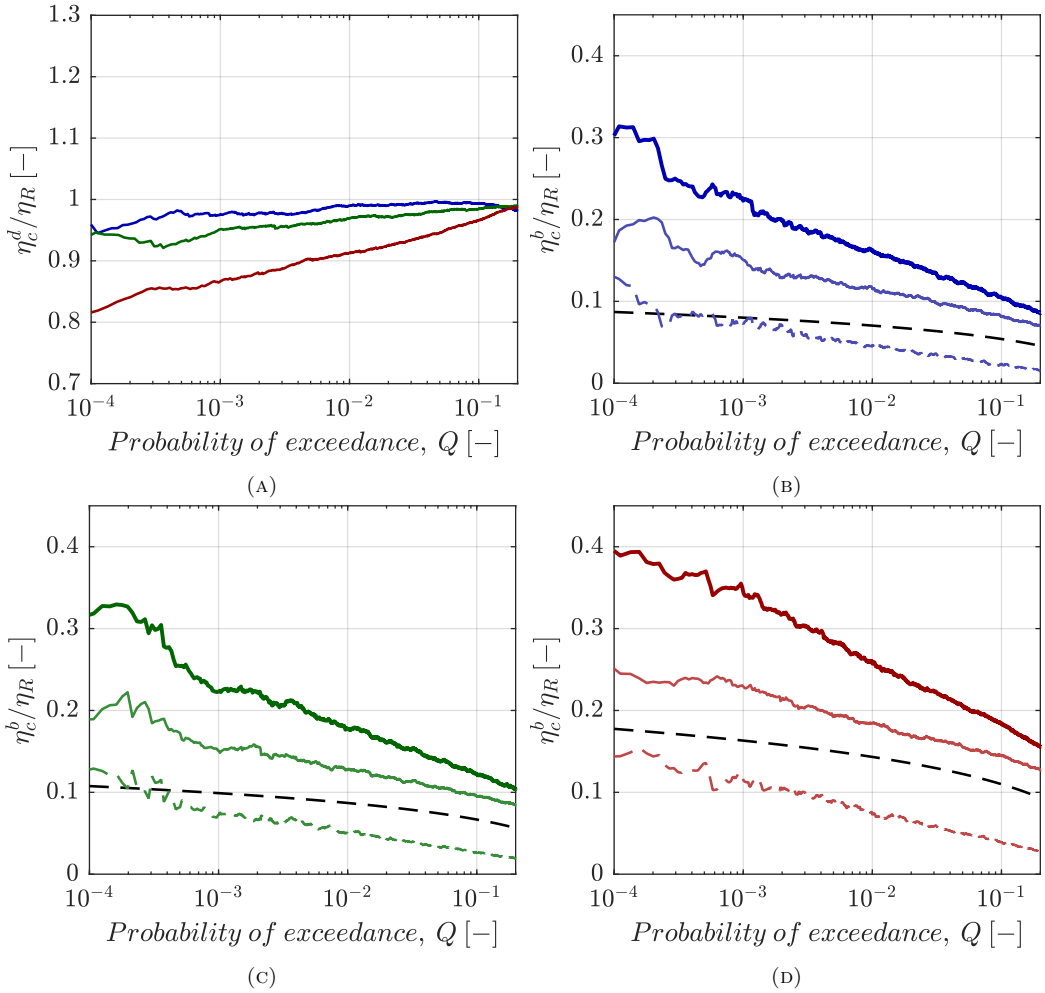


Figure 4.6: (a) Crest-height probability of exceedance distribution of the free waves normalised with respect to the Rayleigh prediction, η_c^d/η_R, ; (— / — / —) for $k_p d = 0.87, 1.28$ and 5.03, respectively. (b), (c) and (d) normalised total bound-wave amplification, η_c^b/η_R, and its underlying contributions of increasing order, corresponding to $k_p d = 5.03, 1.28$ and 0.87, respectively. All sub-figures correspond to $t = 25T_p$ for sea-states of $\frac{1}{2}H_s k_p = 0.105$, $\gamma = 2.5$ and $\sigma = 10°$. The lines (— / — / —) refer to the total bound-wave amplification, (— / — / —) to the even harmonics and (– – / – – / – –) to the third (odd) harmonic. The directional Forristall (2000) predictions (– –) are also added for reference.

and the underlying freely propagating part, η_c^d/η_R, and the left column presents the total bound-wave contributions, η_c^b/η_R. From top to bottom, the effective water depth decreases.

Before proceeding to the physical insights gained from such comparisons, two additional side issues should also be resolved. These refer to (1) the correct estimation of the steady state crest height at $Q = 10^{-3}$ and (2) that this estimation is unaffected by the length of the ramp function. Whilst these issues have been resolved in the context of the earlier uni-directional simulations, the nonlinear interactions exhibit a different intensity in directional seas and hence these key issues should be verified. To this end, Figure 4.7 presents results obtained using both $T_a = 4T_p$ and $10T_p$; the former shown with continuous lines and the latter with circular markers. Whilst this superimposition creates 'dense' data-plots, it leads to a compact presentation of the different effects.

In addition, to reflect the effect of sample variability at each evolution time the results for $T_a = 4T_p$ are supplied with 95% confidence intervals. These confidence intervals are relatively wide in that they show a variation of the total crest-height magnitude in the order of 7% of the linear predictions. Hence, to remove (to some extent) the effect of sample variability, an effective time averaging was performed to the results of both $T_a = 4T_p$ and $10T_p$, as highlighted in Chapter 3. These are depicted with horizontal continuous and dashed grey lines, respectively. For the present directional simulations, this average has been performed in the interval $t \in [10, 60]T_p$. This is wider than the corresponding interval in the uni-directional simulations, as the longest time to reach a steady state is shorter in the directional simulations. Therefore, by adopting this wider interval, the crest-heights are captured at least as accurately as in the uni-directional cases. Taking the results together, it is observed that (1) for individual time instances, the results for $10T_p$ lay within the confidence intervals of $4T_p$ and (2) the time-averaged values are nearly identical. As such, the results are independent of the choice of T_a.

Finally, additional considerations regarding the effect of the nonlinearity order M within HOSM on the different nonlinear contributions, the minimum required ramp function's length and the efficiency of the ramp function are presented in Appendix C. In summary, the results presented in Appendix C demonstrate that not only the total free-surface but also the underlying nonlinear contributions have converged to

within $\sim 1\%$ with respect to M at $M = 3$. Moreover, in agreement with Chapter 3, a minimum of $T_a = 4T_p$ was necessary to effectively suppress any spurious waves due to the linear initialisation of the wavefields. As such, the present results are independent of both M and the initial conditions.

Considering the physical effects that emerge from Figure 4.7 details are given as follows:

- **Free waves**: In directionally spread seas the crest height magnitude at an exceedance probability level of $Q = 10^{-3}$ is not affected by the evolution time for $k_p d = 1.28$ and 5.03. Whereas for $k_p d = 0.87$, for which dynamic effects still remain relevant, a steady state is reached after $t \approx 10T_p$. This is in accordance with the evolution of the dynamic kurtosis presented in Figure 4.4.

  In interpreting these results, it should be stressed that within HOSM, the spectrum is not stationary in time. To explore this, an investigation of the spectral evolution is provided in Appendix D. This reveals that the mean directional spreading evaluated over a frequency range of $f \in [0, 3f_p]$ increased considerably in time; owing to the progressive development of frequency-dependent spreading. However, for a frequency range of $f \in [0.9, 1.1]f_p$ the directional spreading remained largely unchanged. As such, the development of frequency-dependent spreading does not affect the crest-heights. This outcome is in line with the experimental study of Latheef & Swan (2013), which showed that the crest-height statistics both with frequency-dependent and frequency-independent spreading are dominated by the angular distribution around the spectral peak. However, the present results extend this finding to the situation where frequency dependence occurs naturally due to the development of near-resonant interactions rather than an initial imposed frequency-dependent spreading.

- **Bound waves**: At $t = 0$, for which nonlinear evolution is minimal, bound wave contributions are almost identical for both $\sigma_\theta = 0$ and $\sigma_\theta = 10^\circ$ in all water depths. These results reveal that bound-wave nonlinearity, in the absence of (significant) nonlinear evolution is not affected by the introduction of directionality, at least for $\sigma_\theta = 10^\circ$. For $k_p d = 5.03$, this outcome is in line with the deep water focused wave groups presented by Hadjigeorgiou (2018) simulated using second-order theory. Equivalently, regarding finite depth, Karmpadakis

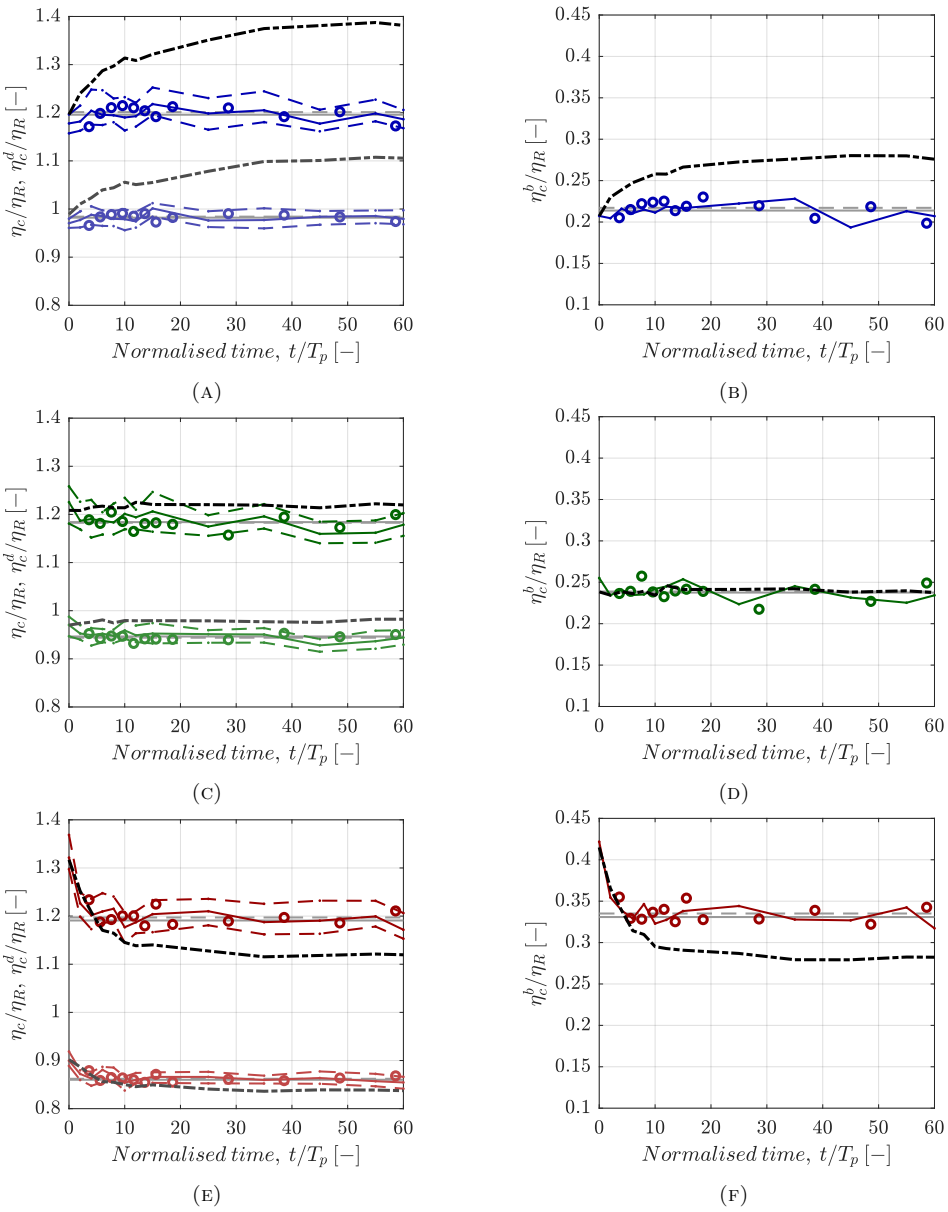


Figure 4.7: Temporal evolution of the normalised crest height, η_c/η_R, and its underlying nonlinear contributions corresponding to a probability of exceedance of $Q = 10^{-3}$ for directional sea-states of $\sigma_\theta = 10°$, $\gamma = 2.5$ and $\frac{1}{2}H_s k_p = 0.105$. The left column refers to the free-surface total and freely propagating part, and the right column to the total bound-wave contributions. The sub-figures (A), (B) refer to $k_p d = 5.03$, (C), (D) to $k_p d = 1.28$ and (E), (F) to $k_p d = 0.87$. In (A), (C) and (E) (—— / —— / ——) refer to the total free surface obtained using $T_a = 4T_p$. The same notation is also adopted in (B), (D) and (F) for the bound-waves part. While, the free-waves part is denoted with (—— / —— / ——). In all sub-figures the markers (○ / ○ / ○) and (○ / ○ / ○) refer to the results for the same sea-states obtained using $T_a = 10T_p$. The dash-dotted lines in (A), (C) and (E) correspond to 95% confidence intervals. In all sub-figures the time-averaged values for $t > 10T_p$ are denoted with (——) for $T_a = 4T_p$ and (— —) for $T_a = 10T_p$. Finally, the equivalent uni-directional results ($\sigma_\theta = 0$) presented in Figures 3.17, 3.20 and 3.23 have also been added for reference shown with (— · —) for the total free surface and bound contributions and (— · —) for the freely propagating part.

(2018) has shown that second-order bound-wave nonlinearity tends to increase with σ_θ, reaching a maximum at $\sigma_\theta = 15°$. With further increases in the directionality, second-order bound waves reduce. The fact that in the present results for $k_p d = 1.28$, bound waves are not affected by directionality can be explained by the slight reduction in the magnitude of the underlying free waves for $\sigma_\theta = 10°$, as shown in Figure 4.7(c). This reduction balances out the increase predicted by second-order theory. Unfortunately, for $k_p d = 0.87$, no insights can be gained using the second-order theory due to questions over its validity (§3.5.2). Moreover, as time progresses, for $k_p d = 5.03$ and 0.87, it is shown that the bound-wave contributions are greatly affected by directionality. Specifically, in $k_p d = 5.03$ and for $\sigma_\theta = 10°$ bound-wave contributions are lower when compared to $\sigma_\theta = 0$. This is due to the reduced magnitude of the underlying free waves. In contrast, for $k_p d = 0.87$ and for $\sigma_\theta = 10°$ they are higher when compared to $\sigma_\theta = 0$. This is due to the increased magnitude of the underlying free waves.

- **Total free surface**: Taken the effect of nonlinearity as a whole, Figure 4.7 shows that directionality does not affect the crest heights at early evolution times, in which the near-resonant interactions are not fully developed. However, once a steady state has established, directionality significantly decreases the crest heights in $k_p d = 5.03$, leaves the crest heights unaffected in $k_p d = 1.28$ and considerably increases the crest heights in $k_p d = 0.87$. These trends are primarily driven by the effect of nonlinear evolution, rather than static or bound interactions.

4.5.3 Influence of sea-state steepness

Having established the effects of directionality on both the near-resonant (dynamic) and bound wave interactions, this section concerns the transition of these two effects with an increase in wave steepness; adopting the sea-states of Table 4.1. In particular, the present section aims to explore (1) if with an increase of the sea-state steepness, the effect of near-resonant interactions is monotonic in all effective water depths, (2) how bound-wave amplification balances out the effect of energy defocusing, and (3) what is the implication of (1) & (2) on the performance of the Forristall (2000) model; the latter commonly used in design.

In exploring the above points, the steady-state part of the nonlinear evolution is considered for which a time-averaged (for $t \in [10, 60]T_p$) value of the crest height and its contributions at $Q = 10^{-3}$ allow a compact presentation of the results.

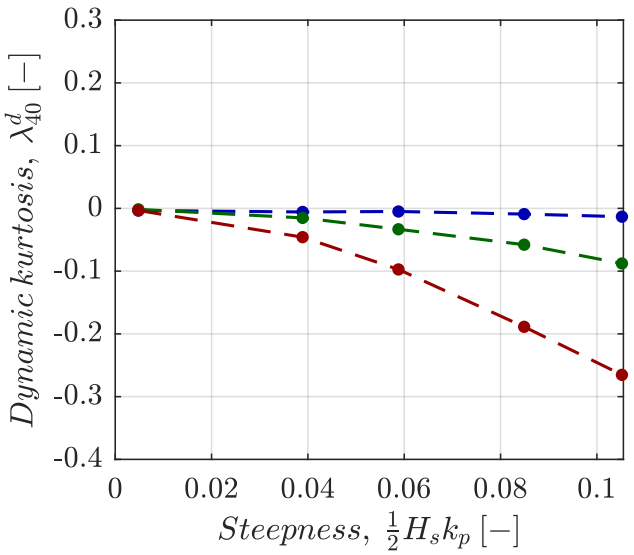
Near-resonant interactions

Considering first the dynamic effects, Figure 4.8 presents the variation of the dynamic kurtosis (sub-figure (A)) and the corresponding time-average of the crest height of the free waves, η_c^d, at $Q = 10^{-3}$, normalised by the Rayleigh prediction η_R (sub-figure (B)). Specifically, sub-figure (B) includes both the mean estimates and $\sim 95\%$ confidence intervals; the latter reflecting the variability around the mean predictions due to the finite sample of crest heights. These confidence intervals have been calculated on the basis of the central limit theorem, defined as $\pm 2\sigma_m$ were $\sigma_m = \sigma_c/\sqrt{N-1}$ is the standard deviation of the time-averaged values, σ_c the standard deviation of the set of crest heights of different evolution times and N to the number of time-instances used for calculating the time-averaged values. Figure 4.8, describes a monotonic transition from linearity ($\lambda_{40}^d = 0$, $\eta_c/\eta_R = 1$) to nonlinearity. This is similar to that observed in Figure 3.26.

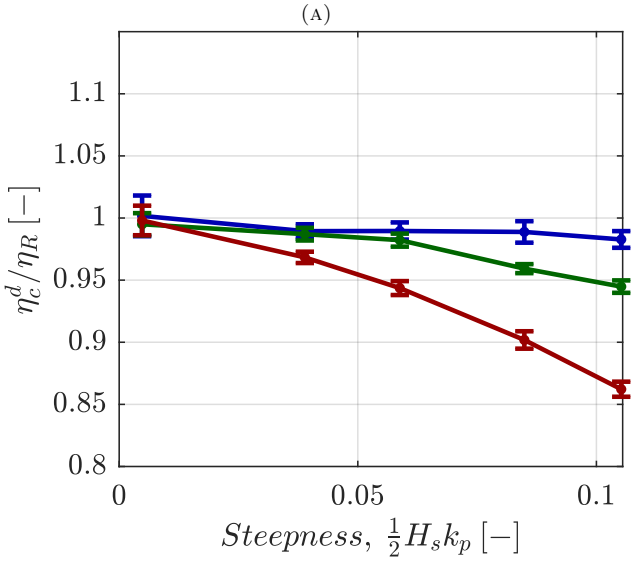
Interestingly, for $k_p d = 5.03$, the slight reduction of the crest heights observed in §4.5.2 persists even for lower steepnesses; indicating that directionality and frequency-bandwidth determine this behaviour. This observation is in accordance to the theoretical developments of Fedele (2015) and Janssen (2017), where energy focusing or defocusing is dictated by the parameter R. While it agrees with the numerical results of Annenkov & Shrira (2014) obtained based on the method of Janssen (2003) (the integration of the Zakharov equation), specifically, the transition of focusing to defocusing depends upon γ and not upon the sea-state steepness. Moreover, for $k_p d = 0.87$, the directional results remain consistently above the uni-directional data presented Figure 3.26; a direct overlaying of the latter results being omitted to avoid overloaded plots. As such, the role of directionality appears to be independent of the effect of sea-state steepness.

Bound-wave contributions

Considering the effect of bound waves, Figure 4.9(A) presents the the variation of the time-averaged bound-wave contributions at $Q = 10^{-3}$, with increasing sea-state



(A)



(B)

Figure 4.8: Effect of sea-state steepness, $\frac{1}{2}H_s k_p$, in directional sea-states with $\sigma_\theta = 10°$ and $\gamma = 2.5$ on (A) the time-and ensemble-averaged dynamic kurtosis with (—●— / —●— /—●—) referring to $k_p d = 0.87$, 1.28 and 5.03, respectively, and (B) on the time-averaged crest height of the free waves normalised with respect to the Rayleigh prediction, η_c^d/η_R, at $Q = 10^{-3}$ with (—●— / —●— / —●—) referring to $k_p d = 0.87$, 1.28 and 5.03, respectively. In (B) 95% confidence intervals have been added around the central estimates.

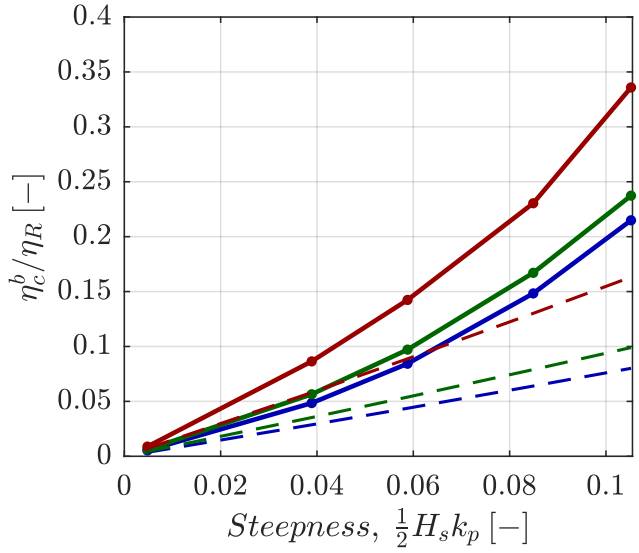
steepness; the Forristall (2000) predictions having been included to reflect the extent of second-order nonlinearity.

The HOSM results presented in Figure 4.9(A) show a nonlinear increase of the bound terms with steepness. This contradicts with the linear increase predicted by Forristall (2000). Once again, this is similar to the equivalent uni-directional results presented in Figure 3.25 and reflects the importance of bound terms beyond second-order. Within the present directional simulations, the gradient of the increase of the bound terms in $k_p d = 5.03$ appears lower compared to the equivalent uni-directional (Figure 3.25) results. This is due to the absence of nonlinear focusing. Taken together, the bound contributions are shown to increase with a reduction in the effective water depth; in qualitative agreement with both the theoretical variation of the statistical parameters of skewness and bound kurtosis (§4.1.2) and the Forristall (2000) model.

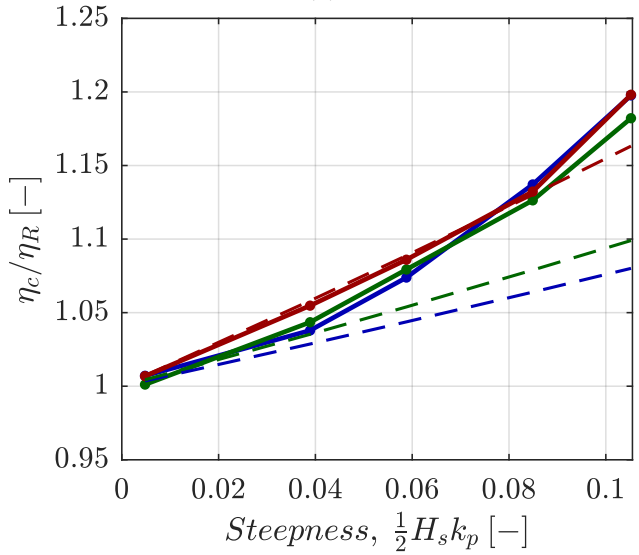
Total effect of nonlinear interactions

Taking the effect of nonlinearity as a whole, Figure 4.9(B) presents the time-averaged crest height of the total free surface at $Q = 10^{-3}$, normalised with respect to the Rayleigh prediction, together with the Forristall (2000) model predictions to assess its overall performance.

The observed trends reveal that the total nonlinear amplification does not vary greatly with changes in effective water depth. This is in contrast to the equivalent uni-directional results presented in Figure 3.26. This arises because of the reduced effect of the near-resonant interactions. Interestingly, for $k_p d = 0.87$, the results demonstrate that the attenuation of the crest heights due to near-resonant interactions is compensated by the bound-wave amplification in such a way that the numerical results agree with the Forristall (2000) predictions for $\frac{1}{2} H_s k_p \leq 0.085$. However, with further increases in steepness, the total crest heights lay above the Forristall (2000) predictions. This arises due to the more rapid increase of the bound terms when compared to the reduction of the free-wave crest height. To this end, as indicated earlier in Chapter 3, any agreement with the Forristall (2000) model in this effective water depth does not indicate the absence of nonlinearity above second-order, but rather the competing influence of the free and bound terms arising above second-order.



(A)



(B)

Figure 4.9: Effect of sea-state steepness, $\frac{1}{2}H_s k_p$, on the time-averaged (A) bound-wave contributions (η_c^b) and (B) total crest heights (η_c) at $Q = 10^{-3}$, both normalised with respect to the Rayleigh prediction (η_R) in directional sea-states with $\sigma_\theta = 10°$ and $\gamma = 2.5$. The lines (—●— / —●— / —●—) refer to $k_p d = 0.87$, 1.28 and 5.03, respectively. While the directional Forristall (2000) predictions are also added for reference, with (— — / — — / — —) referring to $k_p d = 0.87$, 1.28 and 5.03, respectively.

4.5.4 Influence of directionality

So far, the results have highlighted important changes that directionality induces in the intensity of nonlinear wave interactions. These changes were identified by contrasting results of $\sigma_\theta = 0$ to $\sigma_\theta = 10°$. The present section aims to extend the study the effect of directionality by increasing σ_θ from 0 to 30° in steps of 5°, whilst keeping all other sea-state parameters constant (as in Table 4.2).

Near-resonant interactions

To begin with the effect of near-resonant interactions, Figure 4.10 presents the variation, with σ_θ, of the time-and ensemble-averaged steady-state dynamic kurtosis in (A) and the corresponding time-averaged free-wave crest height at $Q = 10^{-3}$ normalised with respect to the linear prediction in (B). To indicate the variability around the mean estimates in (B), 95% confidence intervals have also been added.

From a physical perspective, the results reveal some important features. To begin, for $k_p d = 5.03$, the effect of directionality is immediate. With a directional spread of as low as $\sigma = 5°$, the crest amplification observed in uni-directional seas almost vanishes. Importantly, whilst sea-states with $\sigma_\theta = 0$ and $\sigma_\theta = 5°$ have the same spectral bandwidth, a parameter that was found in Chapter 3 to play a dominant role in the intensity of near-resonant interactions for $\sigma_\theta = 0$, this characteristic is no longer dominant in directionally spread seas. This observation highlights that the additional dispersion due to directionality (referred to as directional dispersion) prevails over the frequency dispersion: with the wave components interacting for shorter times under the influence of directional dispersion, wave modulations cease to exist.

Moreover, this sharp change between $\sigma_\theta = 0$ and $\sigma_\theta = 5°$ is indeed interesting, given that wave instabilities are still relevant for non-collinear interactions (see for example McLean 1982a, Kharif & Pelinovsky 2003, Crawford et al. 1980). In this regard, Toffoli et al. (2009) and Xiao et al. (2013) have shown an overshoot in the dynamic kurtosis for sea-states of similar bandwidth characteristics (i.e. $\gamma = 3$), sea-state steepness of $\frac{1}{2}H_s k_p = 0.13$ and 0.16, respectively, and a directional spread of $\sigma_\theta < 4°$; indicating the possible presence of energy focusing in sea-states with a very small directional spread. In addition, the present results are in qualitative agreement with the BMNLS-equation results of Gramstad & Trulsen (2007), in that the dynamic

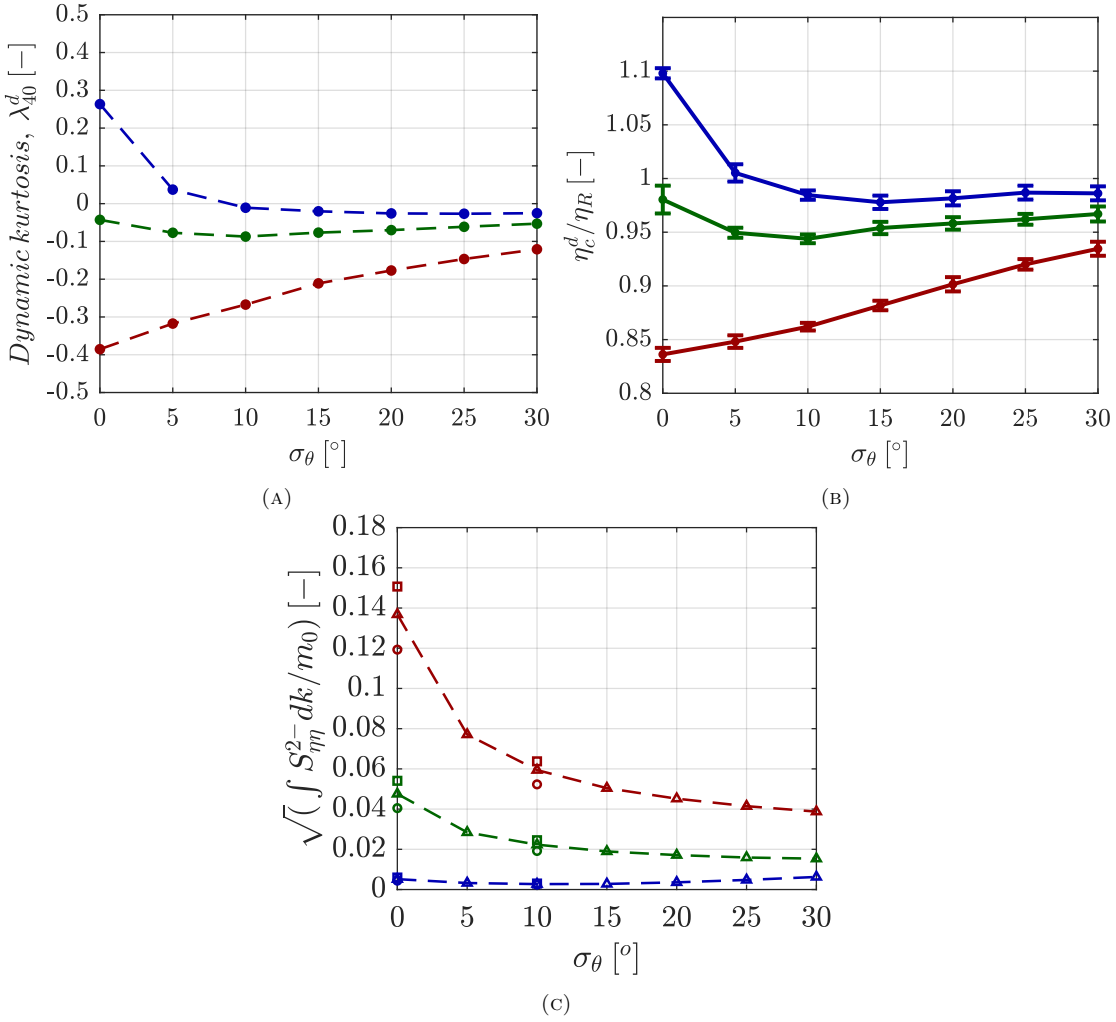


Figure 4.10: Effect of directionality (σ_θ) for sea-states with $\frac{1}{2}H_s k_p = 0.105$ and $\gamma = 2.5$ on (A) the time-and ensemble-averaged dynamic kurtosis, (B) the time-averaged free-wave crest height normalised with respect to the Rayleigh prediction, η_c^d/η_R, at $Q = 10^{-3}$ and (C) the integrated frequency difference terms in the interval $k \in [0, 0.3]k_p$. In the different plots the lines (–●–, –●–, –△– / –●–, –●–, –△– / –●–, –●–, –△–) correspond to $k_p d = 5.03, 1.28$ and 0.87, respectively. Note that in (B) 95% confidence intervals have been added around the central estimation of the crest-height magnitude. While in (C) at $\sigma_\theta = 0, 10°$ the markers (○/○/○) refer to $\gamma = 1.0$ and (□/□/□) refer to $\gamma = 5.0$, for $k_p d = 5.03, 1.28, 0.87$, respectively.

kurtosis quickly drops with the introduction of directionality and vanishes for $\sigma_\theta = 5°$. Taken together, the present results contribute to these earlier insights in that they confirm a similar behaviour for non-bandwidth-limited simulations for the first time. Importantly, they highlight the possibility of energy defocusing for directionally spread seas.

The data relating to the shallowest case, $k_p d = 0.87$, are novel in that no previous study has considered the effect of near-resonant interactions in this effective water depth. This is important because they reveal a very different directional dependence when compared to deep water. Specifically, the change in both the dynamic kurtosis and the expected crest-height of the free waves at $Q = 10^{-3}$ reduces more gradually than the equivalent deep-water results. Importantly, no energy focusing is observed due to non-collinear interactions.

Overall, the behaviour of the dynamic effects in $k_p d = 0.87$ is dictated by the wave-induced 'mean flow'; this is known to encourage a stabilisation of modulational instabilities and ultimate energy defocusing (Janssen & Onorato, 2007). In addition, whilst the effect of directional dispersion over frequency dispersion will still influence the results (Katsardi, 2007), it is shown not to be the dominating mechanism that controls the intensity of near-resonant interactions in this effective water depth. If this was the case, both the dynamic kurtosis and the crest-height magnitude would decrease rapidly, as in deep-water conditions.

To verify the above argument, a quantification of the wave-induced 'mean flow' is sought. For this, the ensemble-averaged spectral energy associated to the $0th$ harmonic (§2.2.6), $S^{2-}_{\eta\eta}$, has been integrated in the range $k/k_p \in [0, 0.3]$ for all water depths. This range was defined by re-considering Figure 2.5(A), where it is shown that there is a transfer of energy to low difference-frequency wavenumber components in the range $k \in [0, 0.3]k_p$ beyond the energy predicted by second-order theory. In adopting this range, any very long waves that nearly satisfy the dispersion relation can be isolated, thereby excluding the effect of bound terms. The variation of $\sqrt{\int S^{2-}_{\eta\eta} dk / m_0}$ with σ_θ is shown in Figure 4.10(C). This includes additional results based on other γ values to demonstrate the generality of the overall trends. Likewise, additional calculations have shown that the inclusion of other integration ranges ($k/k_p \in [0, 0.2], [0, 0.5]$) gave similar results.

Whilst the data in Figure 4.10(C) reveal that increasing directionality leads to

the reduction of the long-wave energy, it also shows that, as expected, this energy increases considerably with a reduction in effective water depth. However, for $k_p d = 5.03$, the long-wave energy does not reflect the energy of freely propagating components as frequency-difference bound terms lay away from the linear dispersion relationship (Figure 2.6(c)). Nonetheless, Figure 4.10(c) includes these results for reference, showing that the long-wave energy in deep water is minimal.

Finally, considering the intermediate effective water depth of $k_p d = 1.28$, Figure 4.10(b) shows that the effect of directionality is minimal. As the variation of the crest-height magnitude is less than $\sim 3.5\%$ across all σ_θ. However, a non-monotonic trend is observed as both the dynamic kurtosis and crest-height magnitude appear to be lowest for $\sigma_\theta = 10°$. The initial reduction for $\sigma_\theta \leq 10°$ is believed to relate to the effect of directional dispersion that affects the balance between energy focusing and defocusing for wave components at either side of $k_i d = 1.363$, making the effect of high-frequency tail weaker. However, as σ_θ increases further, the trend is found to be dominated by the reduction of the wave-induced 'mean flow' as observed in Figure 4.10(c).

Bound-wave contributions

Having established the effect of directionality on the free-wave statistics, Figure 4.11 (a) presents the equivalent effect on the bound-wave contributions at steady state. In interpreting the observed trends, it should be mentioned that the magnitude of the bound contributions can be affected by three factors: (1) the crest heights of the free waves, (2) changes in the local wavelength or wave slope $d\eta/dx$ (even in a linear sense) for different levels of directionality (see Latheef & Swan 2013, Hadjigeorgiou 2018 and Karmpadakis et al. 2019a) and (3) the balance between frequency-sum terms and frequency-difference terms. Keeping in mind these considerations, the following points can be drawn from Figure 4.11 (a):

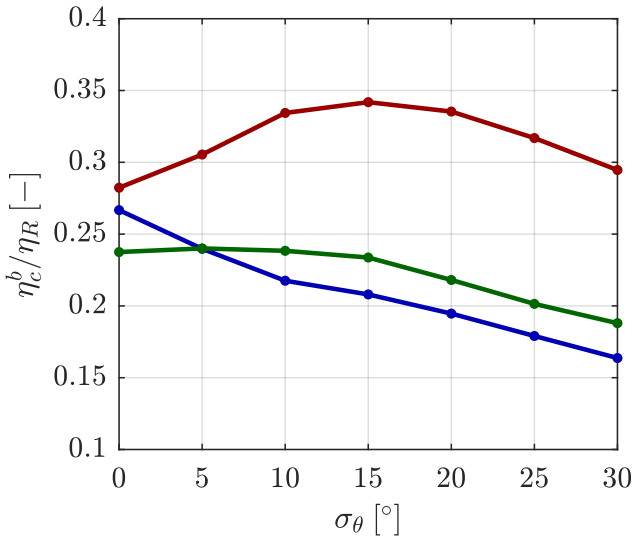
- For the deeper cases of $k_p d = 1.28$ and 5.03, the increase in directionality leads to a substantial reduction of the bound-wave contributions. For $k_p d = 1.28$, the change in magnitude of the underlying free waves was not significant (Figure 4.10(b)). Hence, the observed reduction in the bound-waves must be attributed to a decrease in the local wave steepness or $d\eta/dx$. In contrast, for $k_p d = 5.03$, the decrease for $\sigma_\theta \in [0, 10]°$ is more significant. The explanation for this lies

in the rapid decrease of the free-wave crests. For larger directional spreads, the observed reduction in the bound waves must again be explained by the decrease in the local steepness or $d\eta/dx$.

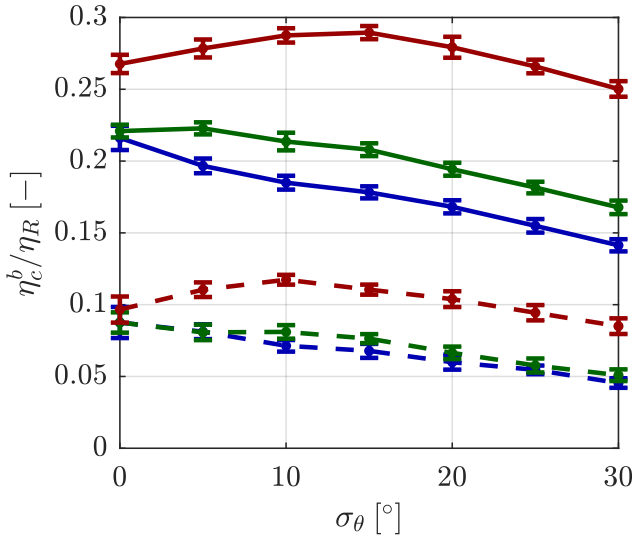
- For the shallowest case, $k_p d = 0.87$, the observed variation with σ_θ is distinctly different from the other two (deeper) cases. Indeed, the variation is non-monotonic; the bound terms increasing for $0 \leq \sigma_\theta \leq 15°$ and subsequently decreasing. The initial increase can be attributed to the increase of the free-wave crests, observed in Figure 4.10(b). In contrast, with further increase in directionality, the effect of $d\eta/dx$ dominates leading to a reduction in the bound waves.

However, the influence of the second-order difference terms should also be identified for a complete explanation of these results, not least because second-order difference terms become increasingly critical in $k_p d = 0.87$. To achieve this, the second and third harmonic contributions were isolated from the zeroth and fourth harmonic contributions; a separation of the latter two not being possible. The second and third harmonics can reflect the effect of the local (nonlinear) wave steepness and are presented in Figure 4.11(b) for all water depths; 95% confidence intervals being added as outlined in §4.5.3 to reflect the extent of sample variability. For $k_p d = 1.28$ and 5.03 the variation of these terms is monotonic as expected. However, for $k_p d = 0.87$, both the second-harmonic sum and third-harmonic terms exhibit a non-monotonic variation, similarly to the total bound contributions. The non-monotonic variation of the former arises due to changes in the underlying steepness, which is influenced by both the energy defocusing and linear changes induced by directionality. Whilst small, the non-monotonic variation of the terms presented in Figure 4.11(b) contradicts the predictions based on second-order theory; the sum terms reducing monotonically with an increase in σ_θ (Karmpadakis, 2018).

Having identified the effect of σ_θ on the near-resonant and bound-wave interactions, Figure 4.12 presents the amplification of the total crest heights. In the same figure, the second-order uni-directional and directional predictions of Forristall (2000) have been added for reference. For $k_p d = 5.03$ and 1.28, Figure 4.12 indicates that the overall effect of directionality is to decrease the total crest amplification. The relatively small crest attenuation of the near-resonant interactions, observed in Figure 4.10, is compensated by the larger bound-wave amplification. Overall, the



(A)



(B)

Figure 4.11: Effect of directionality (σ_θ) on the time-averaged bound-wave contributions normalised with respect to the Rayleigh prediction, η_c^b/η_R, at $Q = 10^{-3}$ for sea-states with $\frac{1}{2}H_s k_p = 0.105$ and $\gamma = 2.5$ in different relative water depths. (A) for the total bound-wave contributions, (B) for second-harmonic frequency-sum and third-harmonic terms. The lines (—●— , —●— / —●— , —●— / —●— , —●—) correspond to $k_p d = 5.03$, 1.28 and 0.87, respectively. In (B) the second-harmonic terms are given by the continuous lines and the third-harmonic terms by the dashed-lines.

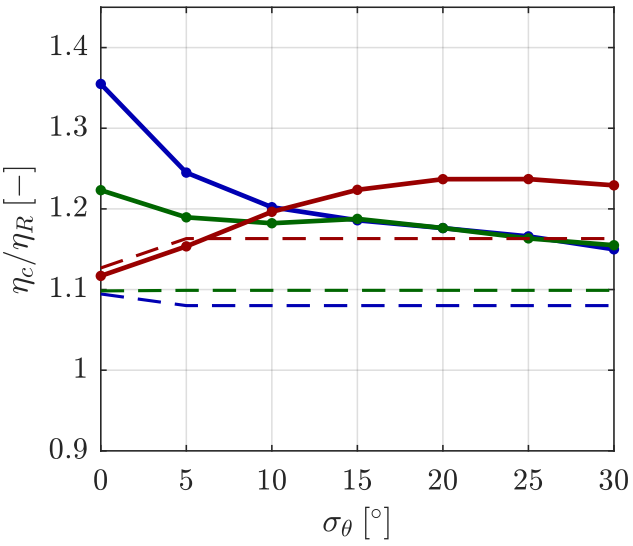


Figure 4.12: Effect of directionality (σ_θ) on the time-averaged crest height of the total free surface normalised with respect to the Rayleigh prediction, η_c/η_R, at $Q = 10^{-3}$ for sea-states with $\frac{1}{2}H_s k_p = 0.105$ and $\gamma = 2.5$ in different relative water depths. The lines (—●— / —●— / —●—) correspond to $k_p d = 5.03$, 1.28 and 0.87, respectively. While the Forristall (2000) predictions are added for reference, denoted with (– – / – – / – –) corresponding to $k_p d = 5.03$, 1.28 and 0.87, respectively.

crest heights are amplified when compared to the Rayleigh predictions. Moreover, the Forristall (2000) model is shown to under-predict the observed crest heights for all directional spreads. Indicatively, the amplification beyond the Forristall (2000) model is $\sim 5-6\%$ in $\sigma_\theta = 30°$.

In considering the shallowest effective water depth, $k_p d = 0.87$, the effect of directionality is in marked contrast to the two deeper cases. First, for $0 \leq \sigma_\theta \leq 15°$ the crest amplification increases with directionality and for $\sigma_\theta > 15°$ the amplification stays appropriately constant, close to the maximum observed. This trend is explained by (1) the steady increase of the free-wave crests, (2) the increase of the bound contributions until $\sigma_\theta = 15°$ and (3) the subsequent decrease for $\sigma_\theta > 15°$. In this later regime, the reduction in the bound waves is offset by an increase in the free waves. As such, the crest heights are virtually unaffected by directionality for $\sigma_\theta > 15°$.

It should be noted that the present results for $k_p d = 0.87$ contradict earlier experimental findings of Karmpadakis et al. (2019a) for sea-states in $k_p d = (0.81, 1.02)$, who showed that increases in directionality lead to a reduction in the crest heights. This qualitative difference when compared to the present results stems from the

different nonlinear evolution. Specifically, the present investigation concerned the steady-state part of the evolution. In contrast, the experimental data refer to a much shorter evolution time dictated by the distance between the wavemaker and the measuring point. As such, the near-resonant interactions are still in the developing stage.

4.5.5 Influence of spectral bandwidth

The present investigation concludes in this section with the effect of spectral bandwidth; induced by changes the latter based upon changes in γ according to Table 4.3. In effect, the sea-states outlined in Table 4.3 are closely related to the equivalent investigation in uni-directional seas (§3.5.4), the only difference being the inclusion of directionality ($\sigma_\theta = 10^\circ$).

Near-resonant interactions

In the context of uni-directional sea-states (§3.5.4), it was shown that the reduction in spectral bandwidth (increase in γ) leads to significant increases in the intensity of near-resonant interactions. At the same time, the results of the previous section show that when directional dispersion dominates, the extent of near-resonant interactions reduces; the balance between the two being dependant upon the effective water depth. Hence, the extent to which the spectral bandwidth in directionally spread seas affects the intensity of near-resonant interactions in different effective water depths needs to be resolved.

Figure 4.13(a) presents the variation of the time-and ensemble-averaged dynamic kurtosis and Figure 4.13(b) describes the equivalent variation of the time-averaged free-wave crest height normalised with respect to the Rayleigh prediction for $Q = 10^{-3}$. In considering these figures, irrespective of the effective water depth, the effect of spectral bandwidth is minimal. This is in direct contrast to the earlier uni-directional sea-state results (Figure 3.5.4). However, the weak dependence of near-resonant interactions observed in Figure 4.13 is in accordance with Figure 3.5.4.

The minimal dependence of the intensity of near-resonant interactions upon the spectral bandwidth for $k_p d = 5.03$, confirms that directional dispersion does not allow the development of the wave modulations observed in uni-directional seas. These results are in agreement with the earlier study of Gramstad & Trulsen (2007) based

on the BMNLS equation. However, despite the qualitative agreement of the present results to those of Gramstad & Trulsen (2007), given that comparisons between BMNLS and HOSM performed by Xiao et al. (2013) showed quantitative differences between the two models, the present results could not have been anticipated a-priori. Furthermore, the reduction of the effect of spectral bandwidth compared to uni-directional seas for $k_p d = 0.87$ is believed to originate from the equivalent reduction of the effect of spectral bandwidth on the wave-induced 'mean flow', as observed earlier in Figure 4.10(C).

Finally, it is interesting to note that whilst in uni-directional seas $k_p d = 1.363$ corresponds to a 'neutral' point for which neither energy focusing nor energy defocusing is observed, this is not the case in directional seas. Indeed, energy defocusing is observed. This is explained by the absence of the focusing mechanism due to the directional dispersion of the wave components laying in the uni-directional focusing regime and the persistent effect of the wave-induced 'mean flow' even in directional seas. Interestingly, this result is in qualitative agreement with the increase of the effective water depth at which the resonant interaction kernel of Stiassnie & Gramstad (2009) changes sign for non-collinear pairs of interacting waves as indicated by Hadjigeorgiou (2018).

Bound-wave contributions

To conclude our discussion of the nonlinear wave interactions, the extent of bound-wave contributions needs to be considered. Figure 4.14(A) presents the variation of the time-averaged bound-wave amplification normalised with respect to the Rayleigh prediction at $Q = 10^{-3}$. This is presented as a function of the effective water depth for different values of γ. The results are consistent with the earlier uni-directional simulations: the bound-wave contributions increasing with a reduction in effective water depth and being higher as the spectral bandwidth increases; the latter effect arising because of increased wave energy in the higher wavenumbers.

Comparing the variation of the normalised crest-height of the free waves (Figure 4.13) with the variation of the bound-waves (Figure 4.14(A)), the two types of interactions (free and bound) are shown to affect the the total crest height in opposite (competing) ways. Whilst the bound waves increase the crest heights, near-resonant interactions reduce them. It is therefore interesting to explore the total effect of non-

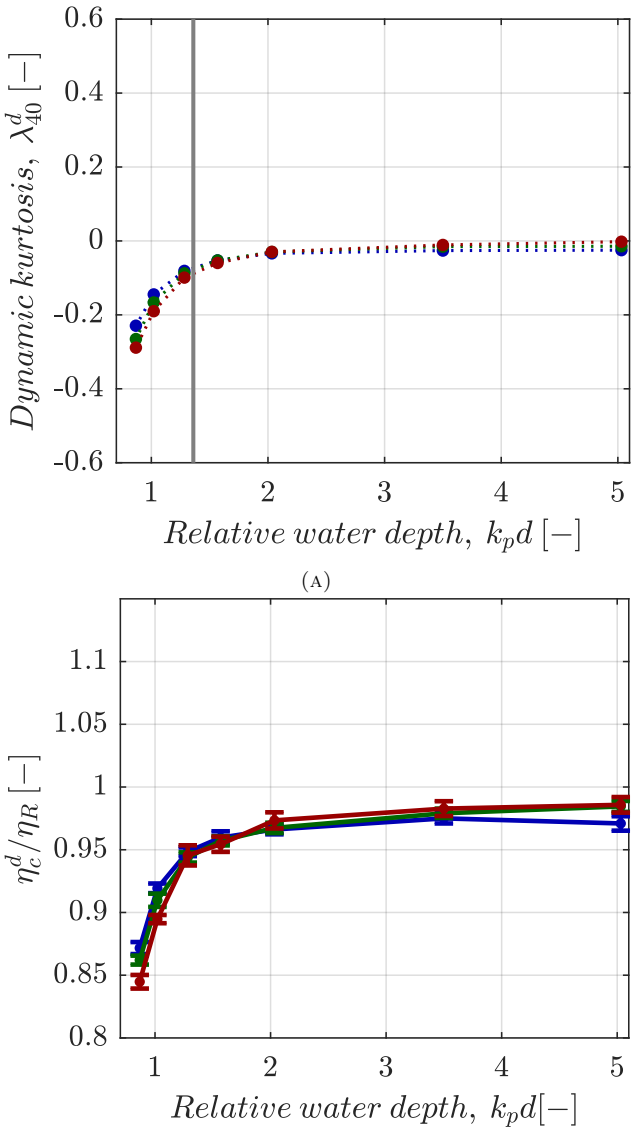
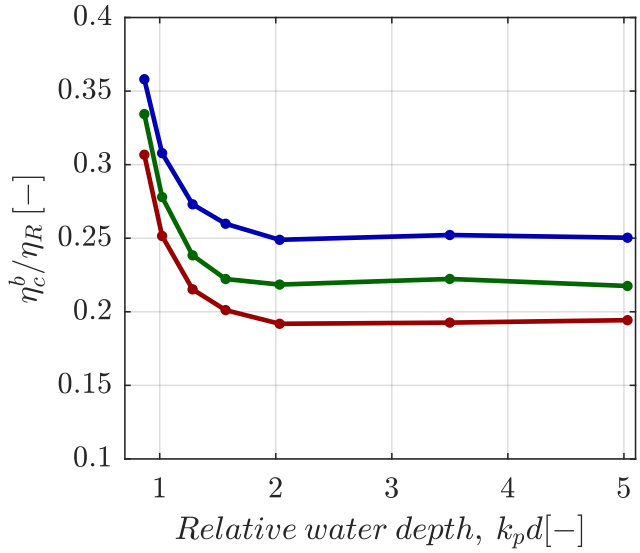
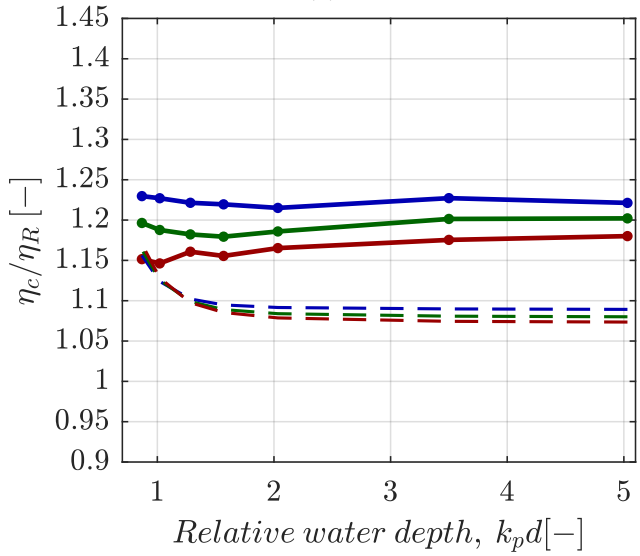


Figure 4.13: Effect of spectral bandwidth (γ) on (a) the time-and ensemble-averaged dynamic kurtosis and (b) the time-averaged free-wave crest height normalised with respect to the Rayleigh prediction at $Q = 10^{-3}$ for directional sea-states with $\frac{1}{2}H_s k_p = 0.105$ and $\sigma_\theta = 10°$. In the different lines ($\cdots\bullet\cdots$, —●— / $\cdots\bullet\cdots$, —●— / $\cdots\bullet\cdots$, —●—) correspond to $\gamma = 1.0, 2.5$ and 5.0, respectively. The vertical line (——) in (a) refers to the theoretical uni-directional effective water depth of $k_p d = 1.363$ and it is added for reference. While in (b) 95% confidence intervals have also been added around the central estimates.



(a)



(b)

Figure 4.14: Effect of spectral bandwidth (γ) on the time-averaged (a) bound-wave contributions (η_c^b) and (b) the crest height of the total free surface (η_c) at $Q = 10^{-3}$, both normalised with respect to the Rayleigh prediction (η_R), for sea-states with $\frac{1}{2}H_sk_p = 0.105$ and $\sigma_\theta = 10°$. The lines (—●— / —●— / —●—) corresponding to $\gamma = 1$, 2.5 and 5, respectively. While in (b) the Forristall (2000) predictions are also added for reference with (– – / – – / – –) corresponding to $\gamma = 1$, 2.5 and 5, respectively.

linearity on the crest heights. This is addressed in Figure 4.14(b). This reveals that the crest heights of the total free surface do not vary with the effective water depth, for all spectral bandwidths considered. This indicates that the reduced free-wave crest heights arising in lower effective water depths is balanced by the corresponding increase of the bound waves. Furthermore, unlike the equivalent uni-directional results (§3.5.4), the ordering effect of spectral bandwidth on the total crest heights is dictated by the bound-wave contributions over the entire effective water depth range.

Figure 4.14(b) also presents the predictions of the Forristall (2000) model. This is shown to significantly under-predict the numerical results. Specifically, the observed deviations increase as the effective depth increases for all γ values. Interestingly, for $k_p d = 0.87$ and $\gamma = 5.0$, the numerical results agree with Forristall (2000). This arises due to the greater attenuation of the crest heights due to near-resonant interactions compared to other γ values. However, the present analysis suggests that this agreement, in this effective water depth, does not signify the absence of nonlinear effects beyond second-order as previously argued (Fernández et al., 2016).

Finally, it is worth noting that both the effect of the near-resonant interactions and the bound contributions with increasing effective water depths, converges at $k_p d = 2$; this is in stark contrast to the uni-directional results (Figure 3.28 and 3.29). Hence, in directionally spread seas, $k_p d \geq 2$ reflects deep-water conditions, at least as far as the nonlinear terms are concerned.

4.6 On the applicability of analytical solutions for the statistical moments in directional seas

In §3.6 the nonlinear contributions to the crest heights of the largest waves arising in a 3-hour storm was linked to the values of the statistical moments of skewness, bound kurtosis and dynamic kurtosis. The present section assesses the theoretical predictions of these moments in directionally spread seas.

4.6.1 Dynamic kurtosis

In applying the theoretical solution of Janssen (2017) for the dynamic kurtosis, it should again be emphasised that this is based on a narrow-band assumption, in both direction and frequency. Therefore, assessing the applicability of this solution to sea-states with in realistic bandwidth is not straightforward. This arises, in part, because of the multiple definitions for the spectral bandwidth. Following §3.6, two definitions of the spectral bandwidth are employed: the parameters ν and q_p described in §2.3. In contrast, the angular bandwidth is uniquely defined by σ_θ.

In uni-directional sea-states, ν was shown to be the more suitable choice for predicting the dynamic kurtosis for $k_p d \leq 1.36$. Whereas, for $k_p d \geq 1.36$, q_p was found to outperform ν. However, in uni-directional seas the bandwidth parameter was only involved in the estimation of the BFI. In contrast, in directionally spread seas, it is also involved in the estimation of the directionality factor R which, in turn, affects the estimation of (1) the directional finite depth version of BFI, B_{sd}, and (2) the directionality factor J_p, as outlined in 4.1.2. Consequently, despite having already drawn conclusions regarding the suitability of each parameter in different effective depth ranges, both parameters are used in the present comparisons for all effective water depths. Finally, to be consistent with the equivalent uni-directional investigation, the sea-state steepness, used for calculating BFI, is defined by $k_p\sigma$.

Figure 4.15 presents the comparisons of the theoretical predictions of Janssen (2017) with the numerical results for sea-states of $\gamma = 2.5$, $\frac{1}{2}H_s k_p = 0.105$ and increasing directionality. Where available, data relating to different spectral bandwidths (γ) are also added. The sub-figures on the left involve theoretical predictions using ν and those on the right using q_p. In addition, from top to bottom each row corresponds to $k_p d = 5.03$, 1.28 and 0.87, respectively.

In making these comparisons, the following points are noted:

1. For $k_p d = 5.03$, the directional predictions based on either q_p and ν do not vary greatly. Moreover, they show limited variation with γ. This arises due to the reduced role of frequency dispersion. Interestingly, the q_p parameter leads to very good predictions for the entire σ_θ range, particularly, for $\gamma = 5$; the latter being closest to the narrow-band assumption.

2. Similarly, for $k_p d = 1.28$, the predictions based on both bandwidth parameters

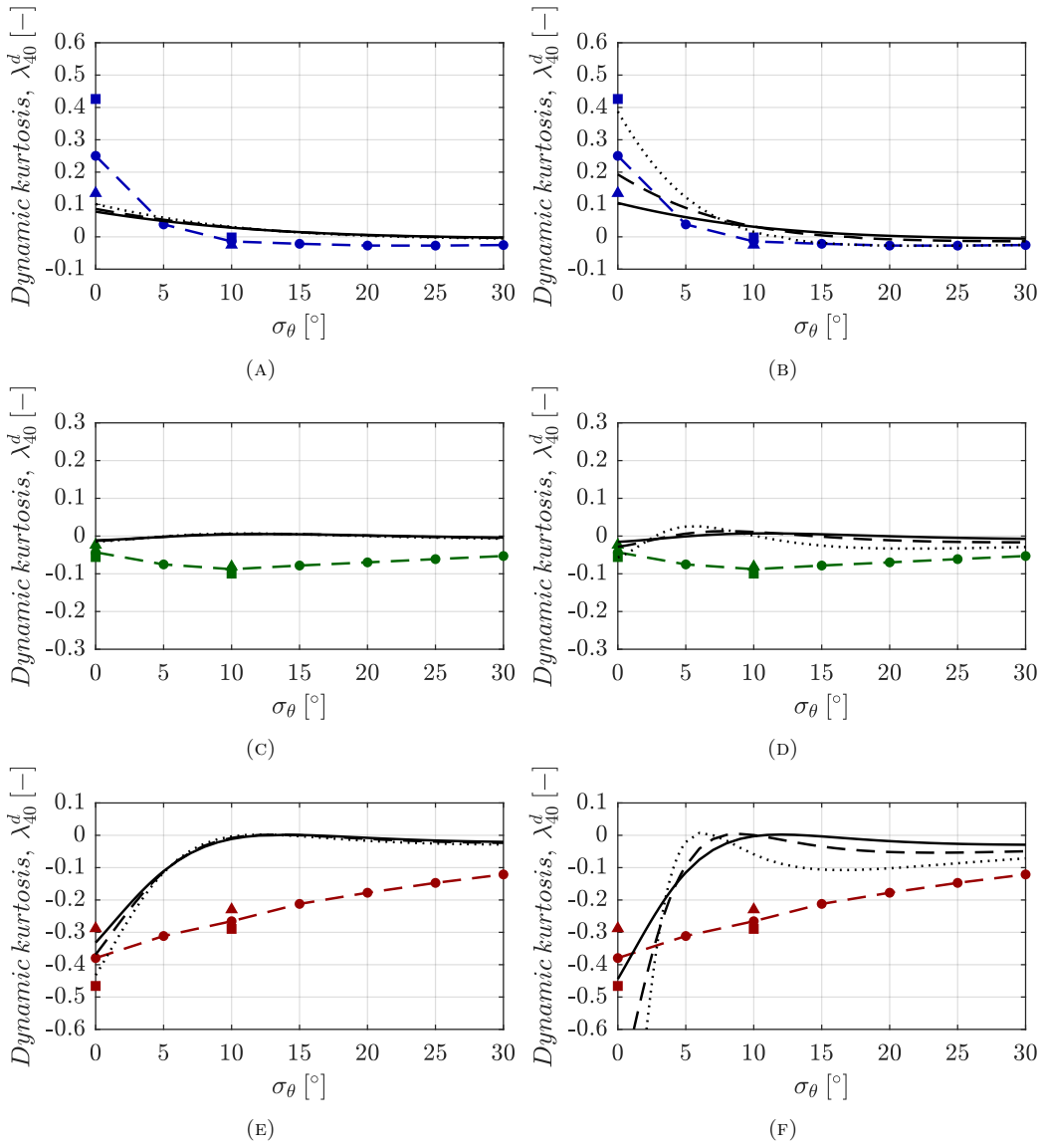


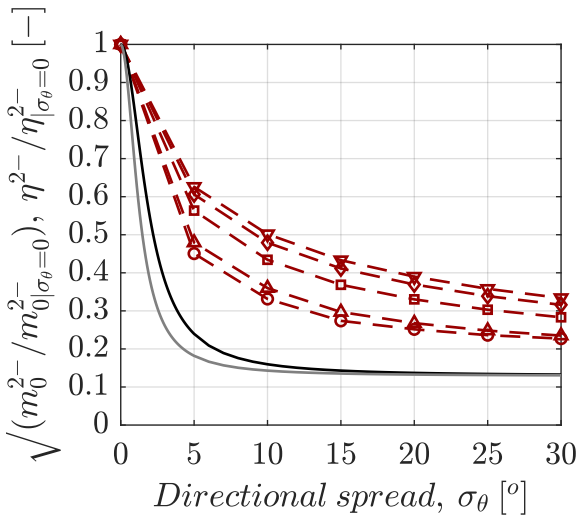
Figure 4.15: Comparison of the time-and ensemble-averaged dynamic kurtosis at steady state arising from HOSM simulations and the narrow-band predictions of Janssen (2017) for sea-states of varying directionality and $\frac{1}{2}H_s k_p = 0.105$. The left column presents comparisons using ν and the right column using q_p within the theoretical predictions (Equation 4.3). (A), (B) for $k_p d = 5.03$, (C), (D) for $k_p d = 1.28$ and (E), (F) for $k_p d = 0.87$. The lines (–●– / –●– / –●–) refer to the numerical results already presented in Figure 4.10(A) for sea-states with $\gamma = 2.5$ and varying σ_θ. The markers (■/■/■) refer to sea-states with $\gamma = 5$; and (▲/▲/▲) to sea-states with $\gamma = 1$. The theoretical predictions are shown with (—— / – – / · · · ·) for $\gamma = 1, 2.5$ and 5, respectively.

are clearly aligned; both predicting near zero values for the dynamic kurtosis, irrespective of the directional spread. Whilst ν is higher than q_p, leading to lower values of the R parameter and hence higher J_p, the Benjamin-Feir index, B_{sd}, based on ν is lower than that based on q_p. Therefore, the competing effect of these two factors leaves the predictions unchanged for different definitions of the spectral bandwidth. Moreover, it is shown that the theoretical predictions slightly over-predict the numerical results. This over-prediction probably originates from the under-estimation of the wave-induced mean flow. This argument is explored in the following point concerning the shallowest effective depth.

3. For $k_p d = 0.87$, it is shown that irrespective of the choice of the bandwidth parameter (ν or q_p), the theoretical solution significantly over-predicts the value of the dynamic kurtosis for $\sigma_\theta > 0$, for all spectral bandwidths (γ). To identify the origins of this discrepancy, the predicted wave-induced mean flow based on Janssen (2017) is compared to the numerical results. In this respect, as mentioned in the context of Figure 4.4, within the narrow-band theoretical solution of Janssen (2017) the wave-induced mean flow corresponds to an offset of the free surface or a wave of $k = 0$. Whereas for broad-banded simulations, the wave-induced 'mean flow' corresponds to low-frequency wave components of a wider wavenumber range [1]. Thus, an integration of the zeroth harmonic spectra needs to be performed, similar to that given in §4.5.4. For this, five wavenumber ranges were selected when quantifying the wave-induced 'mean flow'; all start at $k = 0$ and end at $k = 0.05, 0.1, 0.3, 0.5$ and $0.7k_p$.

Based on the above, Figure 4.16 presents the variation of the wave-induced mean flow as predicted theoretically by Janssen (2017) and numerically by HOSM for sea-states of $\gamma = 2.5$. In seeking to isolate the effect of directionality, the results have been normalised by the respective uni-directional values. The numerical results show an increased rate of reduction as the integration range narrows. This suggests that the uni-directional zeroth harmonic spectrum at very low wavenumbers is more concentrated close to $k = 0$ than the directional results. However, the trends exhibit a

[1] Again, the quotes being added when referring to the mean flow associated with broad-banded sea-states to reflect the weak oscillatory nature of the associated wave components when considered in the physical space.



(A)

Figure 4.16: Effect of directionality (σ_θ) on the wave-induced mean flow for sea-states of $\frac{1}{2}H_s k_p = 0.105$ and $\gamma = 2.5$. Comparison between numerical data based on spectral integration, $\int S_{\eta\eta}^{2-} dk$, and the theoretical narrow-band predictions, $\bar{\eta}$, of Janssen (2017). The different lines: (−○− /−△− /−□− /−◇− /−△−) refer to the numerical results, with the integration in k performed with an upper limit of $k = 0.05, 0.1, 0.3, 0.5$ and $0.7k_p$, respectively. While (—— , ——) refer to the theoretical predictions evaluated using ν and q_p, respectively. In all cases the results are normalised with respect to the values at $\sigma_\theta = 0$.

converged behaviour at either side of the maximum wavenumber range. This suggests that the estimation of the wave-induced 'mean flow' is accurate.

Moreover, the wave-induced mean flow within Janssen (2017) depends upon R which, in turn, depends upon the adopted definition of the spectral bandwidth. Therefore, the theoretical predictions were evaluated using both ν and q_p.

The comparisons between the theoretical estimates and the numerical results demonstrate that the theoretical estimates, irrespective of the adopted bandwidth parameter, significantly over-estimate the reduction of the wave-induced 'mean flow' with directionality. An observation that explains the significant over-prediction of the dynamic kurtosis for $k_p d = 0.87$ on Figure 4.15(E) and (F).

In summary, the comparisons in Figure 4.15 reveal that the solution of Janssen (2017) only performs very well for narrow-banded sea-states in deep water, where the solution essentially coincides with the original derivation of Fedele (2015). In contrast, the under-prediction of Janssen (2017) in finite water depth stems from the effect of spectral bandwidth on the rate of decrease of the wave-induced 'mean flow'.

4.6.2 Skewness and bound kurtosis

Solution of Janssen (2017)

The performance of Janssen (2017) in predicting the skewness and bound kurtosis is next assessed for the sea-states outlined in §4.5.5. This involves a fixed steepness, $\frac{1}{2}H_s k_p = 0.105$, and directionality, $\sigma_\theta = 10°$, varying effective water depth, $k_p d$, and spectral bandwidth, γ.

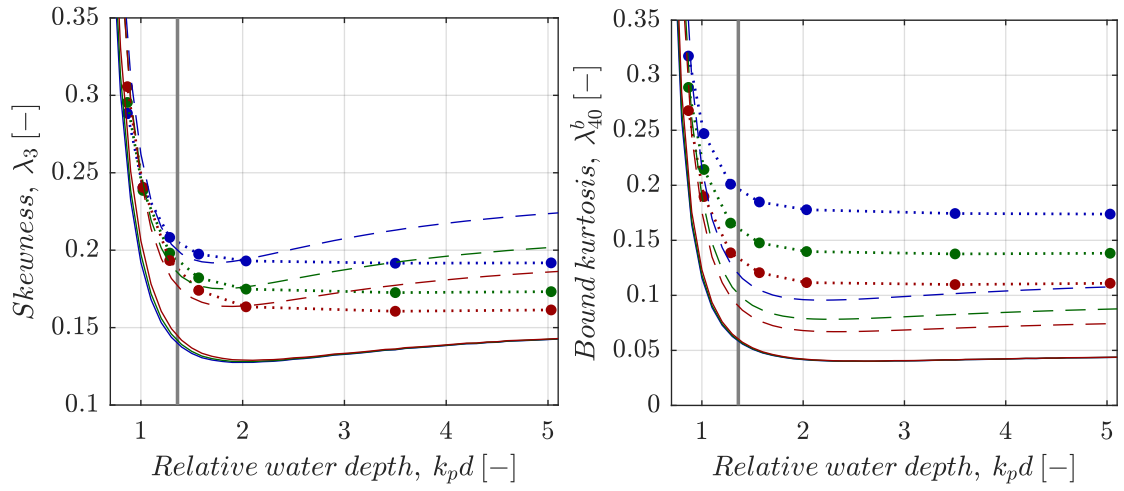
In applying this solution, the depth-dependence is based on the effective water depth $k_p d$ [1], while two definitions for the sea-state steepness have been adopted. These are (1) $\sigma_\eta k_p$ and (2) $\sigma_\eta k_m$, where k_m is the mean wavenumber as defined in §3.2.2. The first definition of steepness reflects the steepness of the dominant wave mode and the second definition reflects the mean steepness of the sea-state; the latter also being affected by the spectral bandwidth. Moreover, the spectral bandwidth parameter for estimating the wave-induced mean flow through R was ν. As this parameter led to better comparisons than q_p (details provided in Appendix B, §B.3).

Figure 4.17 presents the comparison between the theoretical predictions of Janssen (2017) and the numerical results using HOSM for both the skewness and bound kurtosis. These comparisons indicate that the theoretical solution evaluated using $\sigma_\eta k_p$ significantly underestimates both the skewness and bound kurtosis. This under-prediction stems from the fact that the steepness of the individual waves is not captured appropriately using a narrow-band assumption. Moreover, the spectral bandwidth does not significantly affect the predictions; signifying that changes in the wave-induced mean flow due to the spectral bandwidth are minimal.

Considering the theoretical results based on $\sigma_\eta k_m$ the predictions are much improved. However, the theoretical predictions are shown to over-predict the skewness as the effective water depth increases; this being in line with the fact that in deep water, the theoretical estimation is essentially an upper bound as explained in Longuet-Higgins (1963) and Tayfun (2006) (see Equation 40 in Tayfun (2006)). In contrast, the theoretical predictions under-estimate the bound kurtosis; highlighting the inappropriateness of the assumptions underpinning the narrow-band theory.

Having identified the inability of narrow-band solutions to predict the bound-wave

[1] Depth dependence upon $k_m d$ was also considered, but the results were less consistent.



(A) (B)

Figure 4.17: Comparison of the time-and ensemble-averaged (A) skewness (λ_3) and (B) bound kurtosis (λ_{40}^b) to the theoretical narrow-band solution of Janssen (2017) for directional sea-states of $\frac{1}{2}H_sk_p = 0.105$ and $\sigma_\theta = 10°$. The numerical results are denoted with (·· ● ·· / ·· ● ·· / ·· ● ··) for $\gamma = 1.0$, 2.5 and 5.0, respectively. The theoretical narrow-band predictions for the skewness and bound kurtosis are shown with (—— / —— / ——) using $\sigma_\eta k_p$, and with (– – / – – / – –) using $\sigma_\eta k_m$ for $\gamma = 1.0$, 2.5 and 5.0, respectively. In all cases the spectral bandwidth parameter ν has been used in evaluating R.

moments of skewness and bound kurtosis, the remainder of this section is devoted to assessing the applicability of non-bandwidth-limited solutions.

Prediction of skewness based on spectral integration

This section aims to explore if the skewness parameter predicted directly from second-order theory captures the results from fully nonlinear simulations. For this, the theories of Longuet-Higgins (1963), Vinje & Haver (1994) and Tayfun (1994) are employed here. These state that the skewness parameter can be evaluated analytically for a known sea-state spectrum of arbitrary bandwidth.

Recalling that the skewness is defined as $\lambda_3 = E[\eta^3]/\sigma_\eta^3$ (Equation 2.57), the numerator of the expression (coinciding with the third cumulant of the free surface), is given by,

$$E[\eta^3] = E[(\eta^{(1)})^2\eta^{(2)}] + O(m_2^3) = \\ = \frac{3}{2}\int_0^\infty\int_0^\infty\int_0^{2\pi}\int_0^{2\pi} S_{\eta\eta}(\omega_i,\theta_i)S_{\eta\eta}(\omega_j,\theta_j)[A_{ij}^+ + A_{ij}^-]d\theta_i d\theta_j d\omega_i d\omega_j + O(m_2^3) \tag{4.4}$$

assuming that a perturbation series assumption holds and neglecting the dynamic effects. In Equation 4.4, $\eta^{(1)}$ is the linear part of the free surface (Equation 2.13) and $\eta^{(2)}$ is the second-order part (Equation 2.18), m_2 is the second moment of the wave spectrum (Equation 2.39) and refers to the root-mean-square slope of the free surface, i.e $m_2 = E[(\partial\eta^{(1)}/\partial t)^2]$ [1]. Moreover, $S_{\eta\eta}(\omega, \theta)$ is the directional wave spectrum and $A_{ij}^{\pm}$ refer to the second-order interaction kernels between pairs of interacting wave components i and j (see Equation 2.18).

Figure 4.18 presents comparisons of the skewness calculated on the basis of Equation 4.4 to the HOSM simulation results. In considering Figure 4.18, sub-figure (A) presents comparisons for sea-states of $\sigma_\theta = 10^\circ$ of different γ and varying $k_p d$, these being the same sea-states employed previously in Figure E.1(A). Sub-figure (B) concerns sea-states of varying steepness with $\sigma_\theta = 10^\circ$ and $\gamma = 2.5$ and sub-figure (C) sea-states of varying directional spreading with $\frac{1}{2}H_s k_p = 0.105$ and $\gamma = 2.5$. As such, sub-figures (A), (B) and (C) cover the full set of simulated sea-states presented in §4.5.5, §4.5.3 and §4.5.4, respectively.

Considering, first, Figure (A), the comparisons show very good agreement between Equation 4.4 and the numerical results for $k_p d < 1$. However, for $k_p d > 1$ some deviations are observed as the spectral bandwidth is increased. Indicatively, for $k_p d = 5.03$ Equation 4.4 under-predicts the numerical results by $\sim 7\%$, $\sim 5\%$ and $\sim 3\%$ for $\gamma = 1, 2.5$ and 5, respectively. Based on these observations the following points can be made:

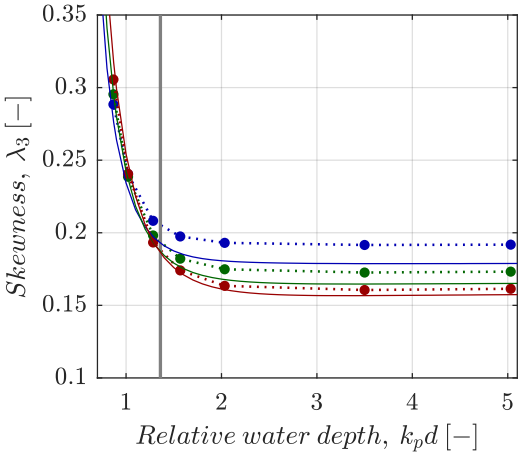
- Equation 4.4 performs better than the previously presented analytical solution of Janssen (2017) based on a narrow-band approximation.
- The improved agreement observed for low $k_p d$ values ($k_p d \leq 1$) arises from an over-prediction of Equation 4.4 due to the leading-order truncation of the solution as discussed in Appendix E in the context of SORWT.
- The under-prediction of Equation 4.4 for ($k_p d > 1$) most probably relates to the fourth-order contributions. These are expected to be higher for wider spectra owing to the occurrence of steeper waves.

[1] It is noted that whilst Vinje & Haver (1994) has expressed the error in truncation in terms of $E[(\partial\eta^{(1)}/\partial t)^2]$, Tayfun (1994) has adopted an alternative measure based on $E[(\nabla\eta^{(1)})^2]$, where ∇ is the horizontal gradient operator.

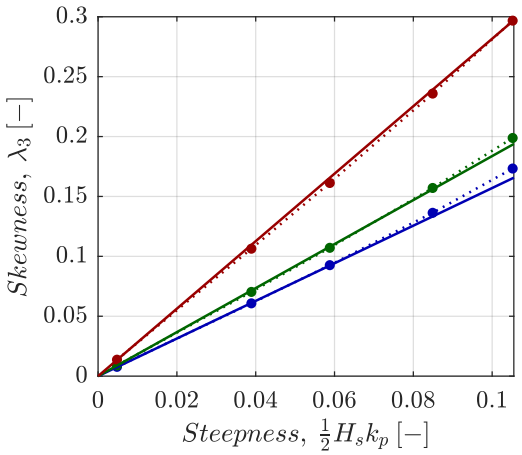
The above points are further verified when Figure 4.18(b) is considered. It is shown that whilst the the predictions of Equation 4.4 exhibit a linear variation with sea-state steepness, the HOSM results exhibit a degree of nonlinearity for $\frac{1}{2}H_s k_p \geq 0.059$ arising from fourth-order bound-wave interactions. This explains the under-predictions observed in Figure 4.18(a) in $k_p d > 1$, as suspected earlier. As the effective water depth reduces, for a moderate steepness of $\frac{1}{2}H_s k_p = 0.059$, Equation 4.4 is shown to slightly over-predict the HOSM results. This is consistent with the equivalent comparisons concerning SORWT (Figure E.1(a) in Appendix E). It would, therefore, appear that the agreement observed for $\frac{1}{2}H_s k_p = 0.105$ arises from the over-prediction of Equation 4.4 and the nonlinear increase of skewness in the HOSM simulations. However, the above deviations are all deemed small and the overall performance of Equation 4.4 is considered satisfactory for the sea-states in Figures 4.18(a) and (b).

In considering the effect of directionality, comparisons presented in Figure 4.18(c) suggest that Equation 4.4 performs reasonably well for directional sea-states. Importantly, the deviations are much smaller than those observed in uni-directional seas ($\sigma_\theta = 0$). In deep water ($k_p d = 5.03$), the deviations for $\sigma_\theta = 0$ are explained by the focusing of the underlying free-wave components which is not captured by Equation 4.4. Moreover, as the effective water depth is reduced, the under-prediction of Equation 4.4 persists and becomes very significant for $k_p d = 0.87$ and $\sigma_\theta = 0$; the skewness from HOSM being 36% above the prediction of Equation 4.4. This discrepancy arises from the inadequacy of second-order theory to capture the asymmetries of the free surface, as the effective water depth reduces. This was discussed by Tayfun & Alkhalidi (2020). In more detail, Tayfun & Alkhalidi (2020) pointed out that a significant under-prediction of the skewness is expected for long-crested narrow-band sea-states in finite water depth owing to the presence of anomalous troughs predicted by second-order theory. Such anomalous troughs are responsible for the non-validity of second-order theory with a reduction in effective water depth as quantified by Hadjigeorgiou (2018). In arguing this case, Hadjigeorgiou (2018) showed that the region in which second-order theory was invalid is critically dependant upon directionality. This explains the improved performance of Equation 4.4 in $k_p d = 0.87$ as the sea-states become more short crested.

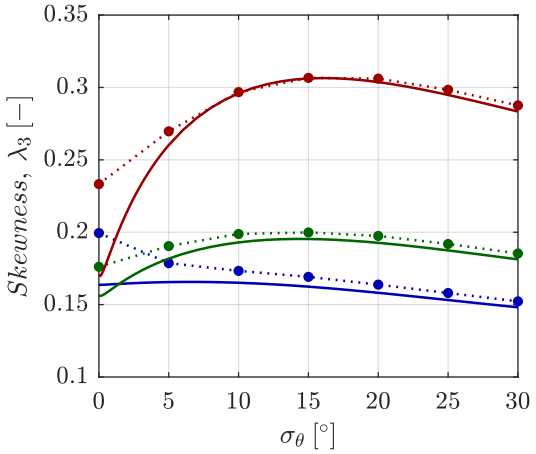
In summary, taking into account the full set of the available directional HOSM



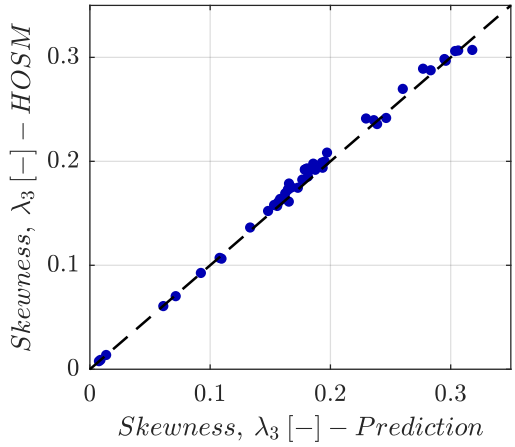
(A) Sea-states of $1/2H_sk_p = 0.105$, $\sigma = 10°$ and varying k_pd. All lines in blue, green, red refer to $\gamma = 1, 2.5, 5$, respectively. The vertical grey line refers to $k_pd = 1.36$ and it is added for reference.



(B) Sea-states of $\sigma = 10°$, $\gamma = 2.5$ and varying $1/2Hskp$. All lines in blue, green, red refer to $k_pd = 5.03, 1.28, 0.87$, respectively.



(C) Sea-states of $1/2H_sk_p = 0.105$, $\gamma = 2.5$ and varying σ_θ. All lines in blue, green, red refer to $k_pd = 5.03, 1.28, 0.87$, respectively.



(D) All sea-states of (A), (B) and (C) with $\sigma_\theta > 0$.

Figure 4.18: Comparison between the time-and ensemble-averaged skewness arising from HOSM simulations and the predictions of Equation 4.4; with the sub-figures' captions providing further explanation of each sub-figure's content. In sub-figures (A), (B) and (C) the lines (·•· / ·•· / ·•·) refer to HOSM results, the lines (— / — / —) refer to the predictions of Equation 4.4 divided by σ_η^3. Sub-figure (D) presents the predictions of skewness (based on Equation 4.4 divided by σ_η^3) against the numerical results using HOSM for all sea-states of (A), (B) and (C) with $\sigma_\theta > 0$. While the diagonal line (— —) defines perfect agreement.

simulations, Figure 4.18(d) presents a comparison between the predicted skewness (without change in the free-surface variance) using Equation 4.4 with the measured skewness from HOSM simulations. The comparisons show that whilst Equation 4.4 predicts consistently lower values, the deviations are small. Indicatively, the mean absolute relative error [1] is in the order of $\sim 3\%$ and the maximum relative error is $\sim 7\%$.

On the relation between skewness and kurtosis

With the skewness being relatively well predicted for arbitrary bandwidth, directionally spread seas, the present section focuses on the prediction of kurtosis and its contributions.

Regarding the relevance of this investigation, in trying to infer the extent of dynamic effects arising from measurements of the total free surface, many researchers have attempted to isolate the effect of the bound contributions using narrow-band estimates of the bound kurtosis (see, for example, Mori et al. 2007, Onorato et al. 2009a, Fedele et al. 2016, Fedele et al. 2019). However, these narrow-band estimates do not lead to accurate predictions, as revealed in both Chapter 3 and the present chapter. Hence, this approach can lead to misleading conclusions regarding the extent of any dynamic effects. Looking at the same problem from the opposite side, when estimating the dynamic effects is possible, knowing the bound kurtosis can correct for bound-wave effects. This way, comparisons to measured values of the total kurtosis arising either from field, experimental or numerical investigations are possible (see for example Mori et al. 2011 and Fedele 2015). The accurate prediction of the bound kurtosis can hence facilitate a clearer understanding of the free and bound-wave contributions.

Alternatively, following the results in Figure 3.34, a prediction of the bound kurtosis could be used directly to isolate the bound-wave contributions from the total most likely maximum crest height in a 3-hour storm.

Finally, given that the skewness and total kurtosis are used within the Gram-Charlier crest-height predictions, it would be instructive to explore the link between

[1] The mean absolute relative error is evaluated according to $\epsilon_r = \frac{1}{N}\sum_{i=1}^{N} |\frac{x_{p,i}-x_{t,i}}{x_{t,i}}|$, where i refers to the i-th observation, $x_{p,i}$ is the corresponding predicted value, $x_{t,i}$ is the observation or target value and N is the number of observations.

the two quantities, given that the skewness can be predicted accurately, as indicated above. To this end, for narrow-banded long-crested waves Marthinsen & Winterstein (1992) have shown that the second-order contribution to the bound kurtosis in deep water is given by $\lambda_{40}^b = 4/3\lambda_3^2$. While according to Janssen (2009) the equivalent third-order prediction for the bound kurtosis is given by $\lambda_{40}^b = 2\lambda_3^2$; the latter laying above the second-order prediction, as expected. Furthermore, previous studies have considered an empirical link between the skewness and kurtosis arising from measured experimental or field-data time series (see for example Jha 1997, Guedes Soares et al. 2003, Guedes Soares & Antão 2005 and Winterstein & Haver 2015). Nonetheless, the data appear significantly scattered in all of the above studies, possibly due to the large sample variability associated with the estimates of the statistical moments.

Based on these comments, the present section aims to:

1. Identify if the skewness and total kurtosis are linked in a meaningful (useful) way.

2. Explore the validity of the link between the skewness and bound kurtosis provided by Janssen (2009) given that the present data are not affected by (large) sample variability.

Figure 4.19(a) presents the measured values of the total kurtosis for all available directional sea-states against the measured values of skewness; the markers being coloured according to the effective water depth $k_p d$. The results show that, whilst in deep water, the scatter of the points is not significant, as the water depth reduces, the scatter becomes increasingly more important. This behaviour relates to the reduction of the dynamic kurtosis with a reduction in effective water depth. This suggests that bound-wave effects are not correlated to the wave dynamics. More importantly, the present results show that reduced values of the total kurtosis in the shallowest water depths do not (necessarily) originate from the dissipative effect of wave breaking as previously thought (Winterstein & Haver, 2015), as wave breaking is not modelled in the present simulations.

In this regard, it is instructive to remove the dynamic part of the kurtosis and explore the relationship between the skewness and the bound kurtosis. These results are depicted in Figure 4.19(b). To explain these results, the second-order solution of Marthinsen & Winterstein (1992) (i.e. $\lambda_{40}^b = 4/3\lambda_3^2$) and the third-order solution

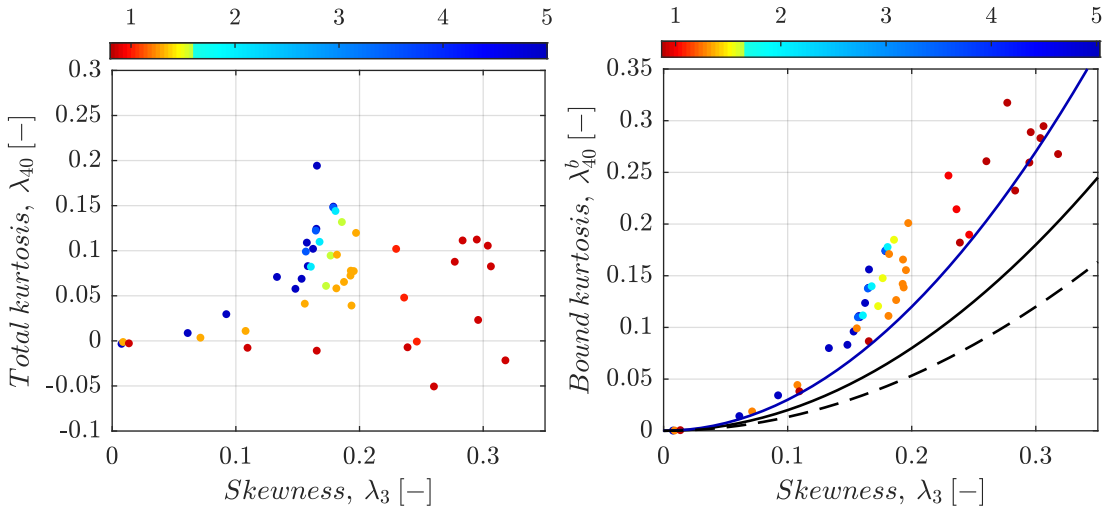


Figure 4.19: (A) total kurtosis and (B) bound kurtosis against measured skewness arising from HOSM simulations shown with (•); while the markers have been coloured according to the $k_p d$ value of each sea-state. In (B), the deep-water narrow-band second-order solution of Marthinsen & Winterstein (1992) (— —), the third-order narrow-band solution of Janssen (2009) (———) and the approximate third-order broad-band solution of Vinje & Haver (1994) (———) have been added for reference.

of Janssen (2009) (i.e. $\lambda^b_{40} = 2\lambda_3^2$) have been added for reference. To this end, the Marthinsen & Winterstein (1992) solution is shown to significantly under-predict the numerical results, demonstrating the important effects of nonlinearity beyond second-order. Note that the validity of this solution in the context of second-order theory is tested in Appendix E; with a relatively good agreement being observed. In addition, the under-prediction of Janssen (2009) demonstrates the inadequacy of a narrow-band solution to capture the effect of third-order bound waves in sea-states with realistic bandwidths. In an attempt to include the effects of spectral bandwidth, Vinje & Haver (1994) have proposed the simplified formula $\lambda^b_{40} = 3\lambda_3^2$, which is also added in Figure 4.19(B). It is shown that the Vinje & Haver (1994) formula leads to improved predictions compared to Janssen (2009). Nevertheless, the measured values are still significantly under-predicted.

4.7 Chapter outcomes

The present chapter was devoted to the statistical description of nonlinear, directionally spread, sea-states and the role of the underlying nonlinear contributions.

Regarding the effect of near-resonant interactions, the main findings of this study are outlined below:

1. Directionality immediately reduces the extent of energy focusing observed for $k_p d > 1.36$ in uni-directional seas (Chapter 3). This arises due to the effect of directional dispersion.

2. In contrast, for $k_p d < 1.36$, the effect of directionality is less profound. This arises because of the effect of the wave-induced 'mean flow'. In fact, for directionally spread seas, the 'neutral' effective water depth below which energy defocusing starts to become relevant is estimated to be $k_p d \approx 1.8$. The increase from 1.36 to 1.8 is induced by the effect of directional dispersion; this disrupts the balance between focusing and defocusing at $k_p d = 1.36$.

3. The energy-defocusing observed in $k_p d < 1.8$ for directionally spread seas contradicts the energy focusing predicted by the theoretical study of elementary wave interactions.

4. In line with earlier findings in Chapter 3, a direct link was observed between the values of the dynamic kurtosis and the deviation of the crest heights of the free waves from the theoretical (linear) Rayleigh distribution.

5. For sea-states with $\sigma_\theta = 10°$, the crest-reduction due to near-resonant interactions was found to be monotonic with an increase of the sea-state steepness.

6. The effect of spectral bandwidth was found to be less important when compared to uni-directional sea-states. In relatively deep water $k_p d > 1.8$, this signifies the dominant effect of directional dispersion. However in $k_p d < 1.8$, this effect arises from the reduced dependence of the wave-induced 'mean flow' on the spectral bandwidth when compared to uni-directional seas.

Furthermore, regarding the effect of bound-wave contributions on the crest-height statistics, the main outcomes are summarised below:

1. Bound-wave contributions become more significant with a reduction in effective water depth. In addition, irrespective of the effective water depth, they increase nonlinearly with an increase in the sea-state steepness, owing to nonlinear effects arising above second-order. This higher-order nonlinear increase is not included in the Forristall (2000) crest-height model.

2. Moreover, unlike the near-resonant interactions, the bound contributions are more sensitive to changes in spectral bandwidth; the bound contributions increasing as the spectral bandwidth increases.

3. Directionality also affects the bound-wave contributions as the effective water depth reduces. More specifically, in deep water ($k_p d = 5.03$), an increase in directionality leads to the reduction of the bound-wave contributions. However, for $k_p d = 0.87$, the bound-wave contributions increase with directionality up until $\sigma_\theta = 15°$, beyond this point they also start to decrease. This latter trend is influenced by the underlying steepness of the free waves. Importantly, the combined effect of near-resonant interactions and bound-wave contributions is the increase of the total crest heights with directionality up until $\sigma_\theta = 15°$, beyond which they are not affected by further increase in σ_θ.

This chapter also assessed available theoretical solutions for the statistical parameters of skewness, bound kurtosis and dynamic kurtosis. The relevant comparisons have shown:

1. That none of the solutions based on a narrow-band assumption performed adequately for the full range of conditions employed in the present study.

2. The abandonment of a narrow-band assumption led to satisfactory predictions of the skewness in directionally spread seas. However, no equivalent comparisons have been attempted for the kurtosis and its contributions, owing to the much-increased complexity and associated computational cost in evaluating these parameters.

5

On the effective prediction of crest-height distributions

Having established the importance of nonlinear interactions above second-order on the crest-heights arising in random seas (Chapters 3 and 4), the present chapter is devoted to the effective prediction of the fully nonlinear crest-height distribution. Such predictions are essential for design; combining the long-term distributions of metocean conditions with the short-term distributions of crests defines the crest-height corresponding to a specified annual probability of exceedance.

In the present chapter, a pragmatic approach is adopted to predict the fully nonlinear crest-height distribution. This approach is data-driven, taking advantage of the extensive set of HOSM simulations presented in Chapters 3 and 4. Moreover, to ensure the model is predictive, the proposed methodology relies on methods from the field of reliability analysis and machine learning. To validate the proposed approach, the model's performance is extensively assessed outside its calibration data set. To achieve the required validation, the model predictions are compared to crest-height distributions arising from additional HOSM simulations, previous experimental studies and field data recorded in the North Sea.

The present chapter commences in §5.1 with a review of previous studies dealing with higher-order crest-height predictions. Following on, §5.2 presents the calibration of the proposed crest-height model; the performance of the model is assessed in §5.3. Finally, §5.4 presents an approach to include the dissipative effect of wave breaking.

This occurs in very steep sea-states, and is applicable to both deep and finite water depths.

5.1 Previous research

To date, the most common approach to include nonlinearity above second-order in the statistical description of the crest heights is through the so-called Gram-Charlier series model of Tayfun & Fedele (2007) (see §2.3.3). The applicability/accuracy of this model has been tested on many occasions in the existing literature. However, in examining these studies, there is contradictory evidence concerning its effectiveness. Specifically, for uni-directional conditions, comparisons of Fedele et al. (2010) and Cherneva et al. (2009) to experimental data show significant under-prediction of the measured crest heights in deep water in the presence of energy focusing due to near-resonant interactions. Latheef (2014) show that the under-prediction persists even for directionally spread sea-states in $k_p d = 2$, albeit to a lesser extent. In contrast, comparisons conducted by Tayfun & Fedele (2007) and Zhang et al. (2016) to uni-directional experimental data of Onorato et al. (2006) and Onorato et al. (2009a), respectively, show no signs of under-prediction. In addition, comparisons to experimental and numerical data of directionally spread non-breaking sea-states in finite water depth conducted by Karmpadakis et al. (2019a) and Fedele et al. (2016), respectively, show very good agreement. Setting aside these differences, other difficulties remain. In §2.3 it was noted that whilst the model of Tayfun & Fedele (2007) provides the opportunity to express the crest-height distribution in a closed form, it suffers from the need to know *a-priori* the values of the statistical cumulants of the free surface. Hence, it is not a predictive model; the difficulties in predicting accurately such statistical quantities having already been highlighted in Chapters 3 and 4.

Apart from the Gram-Charlier series, additional approaches for including third-order nonlinearity in the free-surface statistics include the Hermite transformation of the free surface by Winterstein (1988) and the semi-empirical model proposed by Stansberg (2001); the latter including a Stokes-type second-order correction of the linear crests and an empirical correction for third-order nonlinear effects based on the kurtosis of the free-surface elevation. However, the approach of Winterstein (1988)

models the free-surface statistics and not the crest heights. The model of Stansberg (2001) has not found great popularity owing to the limited conditions upon which it has been calibrated and the somewhat heuristic approach in which nonlinearity is taken into account. Finally, Latheef (2014) proposed a perhaps more promising approach in which the nonlinear amplification arising in focused wave groups was used to correct the linear crest heights up to the third-order of the wave steepness. However, this model has been calibrated only for relatively deep-water conditions of $k_p d = 2$, and hence it does not cover the full extent of water depths considered in the present study.

Given the comments above, the applicability of the Gram-Charlier crest-height model of Tayfun & Fedele (2007) was tested as part of a preliminary investigation, since this is the only model that covers the full range of effective water depths considered in the present study. The results of this investigation are presented in Appendix G. This revealed that the model consistently under-predicts the crest-heights, especially when near-resonant interactions lead to significant focusing or defocusing of the wave energy. Thus, the formulation of the Gram-Charlier crest-height model of Tayfun & Fedele (2007) was abandoned as a starting point for calibrating the required crest-height model. As an alternative, the approach outlined in §5.2 was adopted.

5.2 Calibration of a fully nonlinear crest-height model

5.2.1 Empirical link between the crest-height distribution and the statistical moments

The proposed crest-height model originated from the insights given in Figure 3.34; the statistical moments of skewness, bound kurtosis and dynamic kurtosis being used to explain the crest heights and the underlying contributions at an exceedance probability of $Q = 10^{-3}$. As such, a link between the following quantities was sought:

1. The dynamic kurtosis and the crest-height distribution of the free waves.

2. The bound kurtosis and the odd-harmonic bound-wave contributions to the crest heights, the latter referring to the third-order in wave steepness bound waves.

3. The skewness and the even-harmonic bound-wave contributions to the crest heights, the latter referring to the second and fourth-order in wave steepness bound waves.

Parameterisation of the crest-height distribution

First, to isolate the effect of the nonlinear interactions on the crest-height distributions, the free waves (η_c^d) and the bound-wave contributions (η_c^b) of increasing order were normalised with respect to the Rayleigh prediction (η_R). Second, the corresponding exceedance probability distributions were approximated by linear fits. Given that the probabilities are given in a log-scale and that $Q \leq 10^{-1}$, the linear fits were expressed as,

$$\eta_c^d/\eta_R, \eta_c^b/\eta_R = a_j \cdot (\log_{10}(Q) + 1) + b_j \quad j = 1, 2, 3 \tag{5.1}$$

where the offset b_j corresponds to the magnitude of either η_c^d/η_R or η_c^b/η_R at $Q = 10^{-1}$ and a_j to the slope of the distribution for $10^{-4} < Q < 10^{-1}$; the lower Q limit being employed to exclude points at the very tail of the distribution exhibiting very large sample variability. In adopting these linear fits the following parameterisations were conducted:

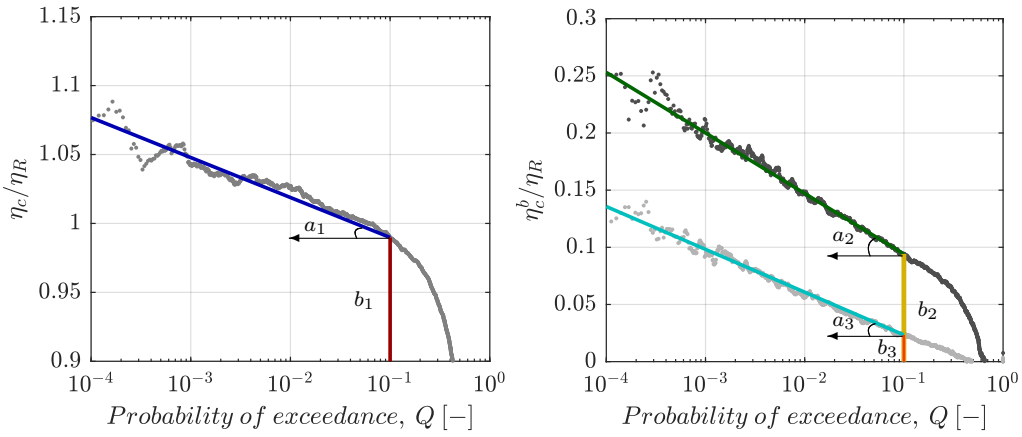
1. the crest-height distribution of the free waves was parameterised by the slope and offset parameters, a_1 and b_1,

2. the odd-harmonic bound-wave contributions were parameterised by the slope and offset parameters, a_2 and b_2, and

3. the even-harmonic bound-wave contributions were parameterised by the slope and offset parameters, a_3 and b_3,

These parameters are depicted in Figure 5.1.

The above linear fits were performed for the complete set of 84 available sea-state simulations presented in Chapters 3 and 4, full details given on Tables 3.1, 3.2, 4.1, 4.2 and 4.3, and for all available evolution times corresponding to the steady-state part of the nonlinear evolution. The resulting average root-mean-square error (RMSE) for all the performed fits was ~ 0.003 and the maximum RMSE was ~ 0.01. The latter value signifying that, at maximum, the standard deviation of the error



(A) (B)

FIGURE 5.1: Examples of approximating the nonlinear contributions to tail of the normalised crest-height distribution. (A) crests of free waves (η_c^d/η_R) and (B) bound contributions (η_c^b/η_R). The grey dots represent the numerical data using HOSM and coloured lines show the linear fits. (A) (———) slope a_1 and offset (———) b_1 for the free waves. (B) (———) slope a_2 and offset (———) b_2 for the even-harmonic bound-wave contributions, and (———) slope a_3 and offset (———) b_3 for the odd-harmonic bound-wave contributions. All offset parameters, b_j, are defined at a probability level of $Q = 10^{-1}$.

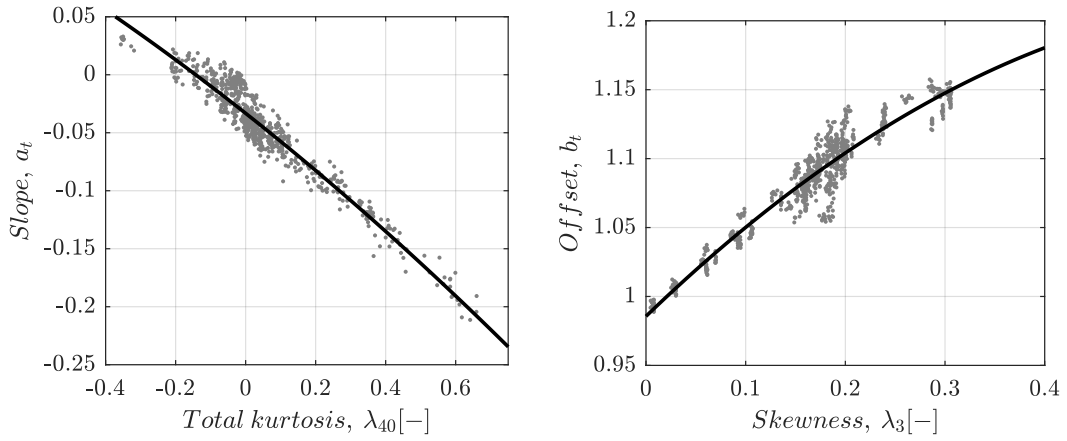
associated with the linear fits is in the order of 1% of the underlying Rayleigh crests. Consequently, approximating the tail of the exceedance probability distribution with linear lines is considered a successful approach. At this point it is important to note that the range of sea-states addressed was such that nonlinear amplification above second-order were expected, but the sea-state steepness was not so large that the crest-height distributions were dominated by the dissipative effect of wave breaking.

Expressing the linear fit parameters as a function of the statistical moments

Following Figure 3.34, the second step in calibrating the crest-height model was to associate the linear fit parameters (slopes and offsets) to the statistical moments of dynamic kurtosis, bound kurtosis and skewness.

- ***Total free surface***

However, before attempting this relatively complicated task, a simpler approach was first examined. This sought to explore whether the linear fit parameters corresponding to the total crest-height distribution (referred to as a_t for the slope and b_t for the offset) could be linked to the statistical moments of the total free surface, thereby avoiding the separation of the underlying contributions. In this respect, the



(A) (B)

Figure 5.2: (A) Slope, a_t, and (B) offset, b_t, expressed as a function of the total kurtosis and skewness, respectively; the lines (———) referring to best-fit second-order polynomials.

slope parameter correlated best to the total kurtosis, whereas the offset parameter to the skewness; the scatter of the data being presented in Figure 5.2, together with best-fit second-order polynomial curves.

The results in Figure 5.3 indicate that, whilst there is a correlation between the linear fit parameters and the statistical moments, the scatter is significant; the RMSE between the data points and the best-fit lines being 0.011 for both a_t and b_t, respectively. Indicatively, an error of 0.02 in both a_t and b_t can lead to an over-(or under-) prediction of the crest-height at $Q = 10^{-3}$ by as much as 5%. As such, this scatter prohibits the calibration of an accurate crest-height model. As a consequence, the link of the statistical parameters to the *underlying contributions* of the crest-height distribution was deemed necessary and is presented as follows.

- ***Dynamic part of the free surface***

As explained in Section 3.5.1 the elevation of the free waves gives rise to the dynamic kurtosis. Moreover, the associated contribution to the skewness parameter is zero. Thus, the parameters a_1 and b_1 were solely parameterised in terms of the dynamic kurtosis.

To this end, Figure 5.3 presents a_1 and b_1 as a function of the dynamic kurtosis; the latter extracted at the same time instance as a_1 and b_1. Again, second-order polynomial best-fit lines have been added in the respective plots. These are defined

by:

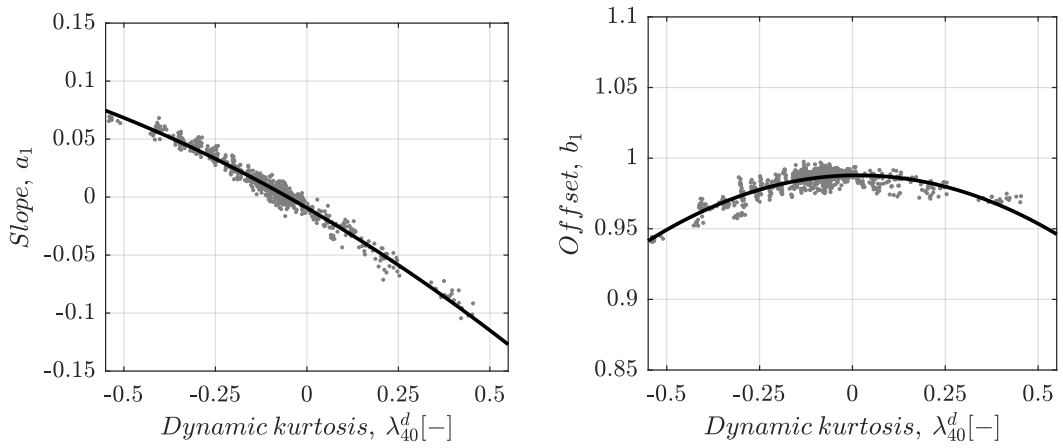
$$\begin{aligned} a_1 &= -0.009 - 0.183{\cdot}\lambda_{40}^d - 0.056{\cdot}(\lambda_{40}^d)^2 \\ b_1 &= 0.988 + 0.004{\cdot}\lambda_{40}^d - 0.146{\cdot}(\lambda_{40}^d)^2 \quad . \end{aligned} \tag{5.2}$$

In observing Figure 5.3, it becomes evident that the scatter of the data points is substantially reduced compared to Figure 5.2. Evidence of this is provided by the RMSE between the data points and the best-fit lines which is 0.005 for both a_1 and b_1. This is less than half of the error reported in the context of Figure 5.2.

From a physical perspective, the results show that a positive kurtosis leads to a negative slope parameter, a_1, signifying amplification with respect to the Rayleigh distribution (given that $(\log_{10}(Q)+1)$ is always negative). In contrast, the opposite holds for a negative kurtosis. These observations are entirely in line with earlier discussions provided in both Chapters 3 and 4 regarding the effect of near-resonant interactions on the crest-height distribution.

Furthermore, the offset parameter, b_1, reduces below unity as the magnitude of the dynamic kurtosis increases. This decrease of b_1, in the order of 5% in the most extreme cases, could potentially originate from the spectral broadening associated with sea-states of high (in magnitude) dynamic kurtosis as indicated in Figure 3.31. As with an increase in spectral bandwidth, the tail of the crest-height distribution converges to the Rayleigh distribution for lower Q. Whereas, for the cases of negative dynamic kurtosis, it could also originate from the defocusing of wave energy that tends to lower the crest heights. Additionally, it is noted that the offset parameter corresponding to zero dynamic kurtosis ($\lambda_{40}^d = 0$) lays slightly below the Rayleigh predictions with $b_1 = 0.988$. This arises due to the non-convergence of the, essentially linear, numerical distribution to a Rayleigh tail at $Q = 10^{-1}$ (as shown for example in Figure C.1(B)). To compensate for this effect, the corresponding slope parameter is slightly negative ($a_1 = -0.009$) at $\lambda_{40}^d = 0$. Nonetheless, this slight inconsistency with the linear narrow-band theory does not present any practical concerns.

Moreover, it should be noted that the horizontal axis Figure 5.3 refers to the measured ensemble-averaged dynamic kurtosis and not the de-biased value accounting for the effect of finite domain length (as noted in the context of Figure 2.11). More specifically, the finite domain length induces an initial reduction of the kurtosis (denoted as r_k), which is dependent upon the effective water depth and spectral bandwidth. To account for this effect, based on the available values of the initial



(A) (B)

Figure 5.3: (A) Slope, a_1, and (B) offset, b_1, parameters against the dynamic kurtosis; with the lines (——) referring to best-fit second-order polynomials.

kurtosis r_k was parameterised according to,

$$\begin{aligned} r_k &= r'_k / f_k \\ r'_k &= \begin{cases} 0.0038/k_p d^{0.41} + 0.0043 \; for \; \sigma_\theta = 0 \\ 0.0096/k_p d^{1.02} + 0.0145 \; for \; \sigma_\theta > 0 \end{cases} \\ f_k &= 1 - f_0 \cdot (\gamma/2.5 - 1) \end{aligned} \tag{5.3}$$

where $f_0 = 0.5$ for $\sigma_\theta = 0$ and $f_0 = 0.32$ for $\sigma_\theta > 0$.

To this end, Figure 5.4 presents the measured relative deviation of the initial kurtosis arising from the full set of both uni-directional and directional simulations, along with the expressions of Equation 5.3. The results show that indeed the reduction is small and does not pose any concerns for the convergence of the results.

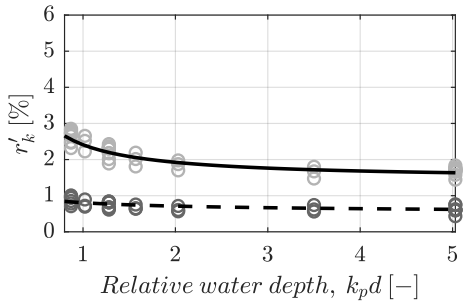


Figure 5.4: Relative reduction of the initial value of the kurtosis for uni-directional and directional simulations. against the relative water depth $k_p d$. The lines (– – / ——) refer to the best-fit lines for $\sigma_\theta = 0$ and $\sigma_\theta > 0$, respectively, given in Equation 5.3. While the markers (∘ / ∘) refer to measured values from HOSM simulations, for $\sigma_\theta = 0$ and $\sigma_\theta > 0$, respectively.

• ***Even-harmonic bound-wave contributions***

Considering next the even-harmonic bound-wave contributions, a natural first step is to parameterise the slope, a_2, and offset, b_2, as a function of the skewness. Indeed, the skewness has traditionally been used to represent the second-order nonlinearity in theoretical crest-height models (see, for example, Tayfun 1980, Fedele & Tayfun 2009 and Arena & Ascanelli 2010). To this end, the variation of a_2 and b_2 against the skewness parameter is presented in Figure 5.5 (sub-figures (A) and (B), respectively) along with best-fit polynomial functions. In considering these plots, it can be observed that whilst there is undoubtedly a link between a_2, b_2 and the skewness, there is also considerable scatter around the best-fit polynomial functions.

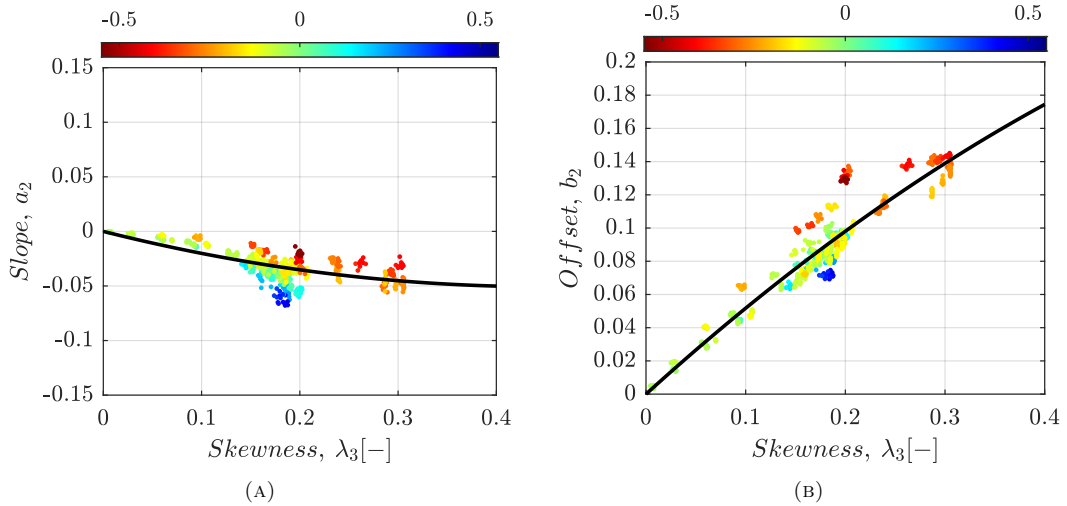


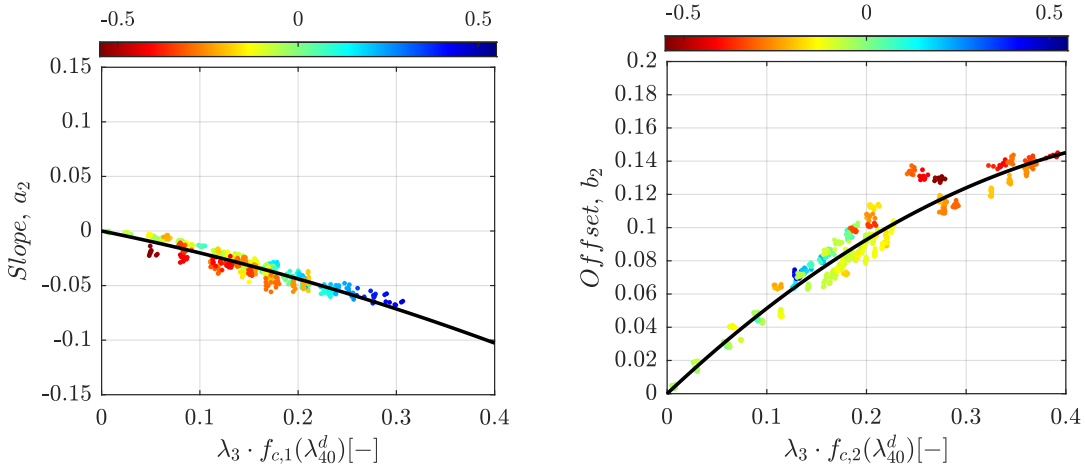
FIGURE 5.5: (A) Slope, a_2, and (B) offset, b_2, parameters against the skewness parameter, λ_3; with the lines (——) referring to best-fit second-order polynomials. The markers are coloured according to the value of the dynamic kurtosis.

To identify the origins of this scatter, the markers in both plots have been coloured according to the dynamic kurtosis. This colouring suggests that the dynamic effects do indeed relate to the observed variability. Specifically, for sea-states of large dynamic kurtosis, the slope parameter tends to exhibit a larger (in magnitude) slope a_2 than sea-states having the same skewness but lower dynamic kurtosis. In contrast, the corresponding offset parameter tends to be smaller. Likewise, for sea-states of low dynamic kurtosis, the slope a_2 tends to be smaller, while the offset tends to be higher than equivalent sea-states of the same skewness.

The above observations directly relate to earlier discussions provided in Chapters 3 and 4, in that the bound-wave contributions are linked to the magnitude of the

free-wave crests. Hence, with the crest heights of the free waves being amplified when the dynamic kurtosis is positive/negative, it is not surprising that a_2 is higher/lower.

Regarding the offset parameter, b_2, which reflects the magnitude of moderate crest heights at $Q = 10^{-1}$, a physical interpretation of the observed scatter is not so straightforward. A potential reason for the increase of b_2 in the shallowest cases characterised by a negative kurtosis is that second-order difference terms for relatively low waves may not be in anti-phase with the wave crests; owing to the weak constructive interference of the underlying free-wave components. Hence the scatter may not be related to the dynamic effects but rather to second-harmonic bound-wave effects. In deep water, the slight decrease in b_2 is most likely related to the corresponding decrease in b_1.



(A) (B)

Figure 5.6: (A) Slope, a_2, and (B) offset, b_2, parameters against $\lambda_3 \cdot f_{c,1}(\lambda_{40}^d)$ and $\lambda_3 \cdot f_{c,2}(\lambda_{40}^d)$, respectively; with the lines (———) referring to best-fit second-order polynomials. The markers are coloured according to the value of the dynamic kurtosis.

Taken together, given that the scatter observed in Figure 5.5 is associated with the value of the dynamic kurtosis, the inclusion of the latter on the horizontal axis could lead to more precise predictions for a_2 and b_2. To achieve this, and after trialling different functional forms, the following linear factors were applied,

$$\begin{aligned} f_{c,1}(\lambda_{40}^d) &= (1.4 \cdot \lambda_{40}^d + 1) \\ f_{c,2}(\lambda_{40}^d) &= (-0.8 \cdot \lambda_{40}^d + 1) \end{aligned} \tag{5.4}$$

for a_2 and b_2, respectively. These factors were defined to produce the largest possible reduction of the scatter in terms of the RMSE. In considering these factors, a zero

dynamic kurtosis leads to no change of the horizontal position of the points. A negative dynamic kurtosis shifts the data points to the left for a_2 and to the right for b_2. Whereas the opposite is the case for a positive dynamic kurtosis.

These factors serve as multipliers to the skewness parameter; the resulting variation of a_2 and b_2 against $\lambda_3 \cdot f_{c,1}(\lambda_{40}^d)$ and $\lambda_3 \cdot f_{c,2}(\lambda_{40}^d)$ is shown in Figure 5.6; the best-fit polynomial functions being superimposed. Indicatively, the RMSE associated to the polynomial fits in Figure 5.5 was ~ 0.01 for both a_2 and b_2. While in Figure 5.6 it has been reduced to ~ 0.005 and ~ 0.008 for a_2 and b_2, respectively.

Whilst the minimisation of the scatter in Figures 5.6(A) and 5.6(B) is evident, further improvement was sought, especially for b_2 where the fit is less satisfactory. It was found that when the bound kurtosis was added to the skewness parameter, the resulting variation of the data points was further reduced. Confirmation of this is shown in Figure 5.7. In this case the RMSE is ~ 0.003 and ~ 0.004 for a_2 and b_2, respectively. These values are lower than those associated with Figure 5.6 and less than half the original fits in Figure 5.5.

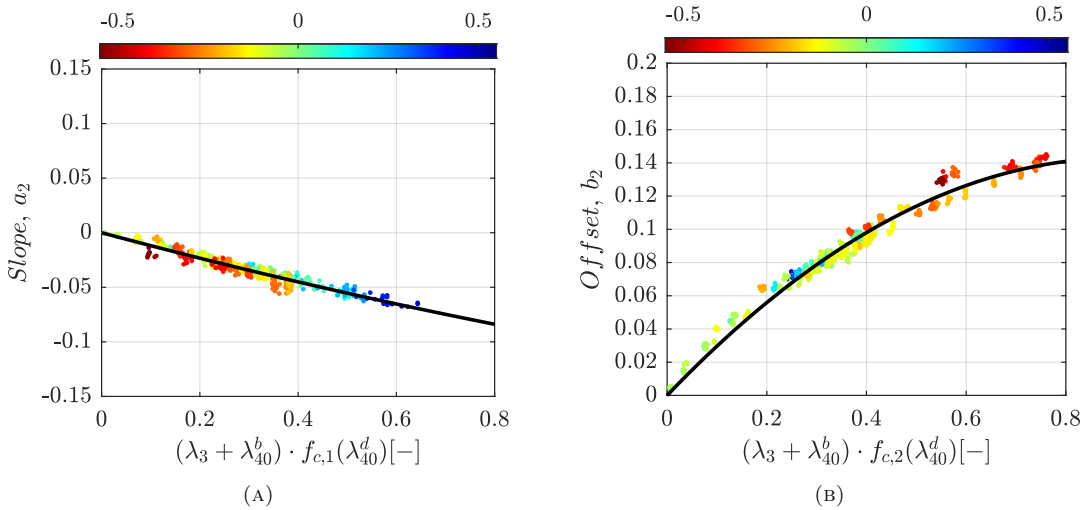


FIGURE 5.7: (A) Slope, a_2, and (B) offset, b_2, parameters against $(\lambda_3 + \lambda_{40}^b) \cdot f_{c,1}(\lambda_{40}^d)$ and $(\lambda_3 + \lambda_{40}^b) \cdot f_{c,2}(\lambda_{40}^d)$, respectively; with the lines (———) referring to best-fit second-order polynomials. The markers are coloured according to the value of the dynamic kurtosis.

This improved fit can be explained by the fact that the bound kurtosis reflects solely the magnitude of bound-wave contributions that add to the wave crests, unlike the skewness that also includes the effect of second-order difference terms that tend to reduce the wave crests. Therefore, given that the second-harmonic bound-wave contributions are inherently correlated to the third-harmonic bound-wave contributions

(§4.6), including the bound kurtosis when predicting the even-harmonic bound-wave contributions is used as a proxy for assigning more weight to bound terms that contribute positively to the crest-heights. This approach that is in line with the earlier discussion, in the context of Figure 5.5(b), with respect to the potential origins of the scatter in b_2.

Hence, the even-harmonic bound-wave contributions can be predicted based on the best-fit polynomial functions appearing in Figure 5.7. These are given by,

$$\begin{aligned} a_2 &= -0.121 \cdot c_2 + 0.0197 \cdot c_2^2 \\ b_2 &= 0.314 \cdot d_2 - 0.173 \cdot d_2^2 \end{aligned} \tag{5.5}$$

with,

$$\begin{aligned} c_2 &= (\lambda_3 + \lambda_{40}^b) \cdot f_{c,1}(\lambda_{40}^d) \\ d_2 &= (\lambda_3 + \lambda_{40}^b) \cdot f_{c,2}(\lambda_{40}^d); \end{aligned} \tag{5.6}$$

the optimum factors $f_{c,1}$ and $f_{c,2}$ are again given by Equation 5.4.

- ***Odd-harmonic bound-wave contributions***

To finalise the parameterisation of the crest-height distribution, the slope and offset parameters, a_3 and b_3, associated to the odd-harmonic bound-wave contributions remain to be specified. As the odd-harmonic bound-wave contributions are related to the bound kurtosis, λ_{40}^b, a natural first step is to explore the variation of a_3 and b_3 with λ_{40}^b. To this end, Figure 5.8 presents this variation along with best fit polynomial functions; sub-figure (a) concerning a_3 and sub-figure (b) b_3. Again, the data points have been coloured according to the value of the dynamic kurtosis.

In considering Figure 5.8, the scatter of points is again associated with the value of the dynamic kurtosis; the scatter being more significant for the parameter b_3. As the third-harmonic bound-wave contributions are relatively small compared to the rest of nonlinear contributions, the observed scatter in Figure 5.8 could perhaps be considered insignificant. However, in eliminating any systematic error induced by the parameterisation of the crest-height distribution, without much extra effort, correction factors accounting for the effect of dynamic kurtosis were again calibrated. Adopting a similar approach to the fitting of the even-harmonics, the correction factors again serve as multipliers to the variable on the horizontal axis, i.e. the

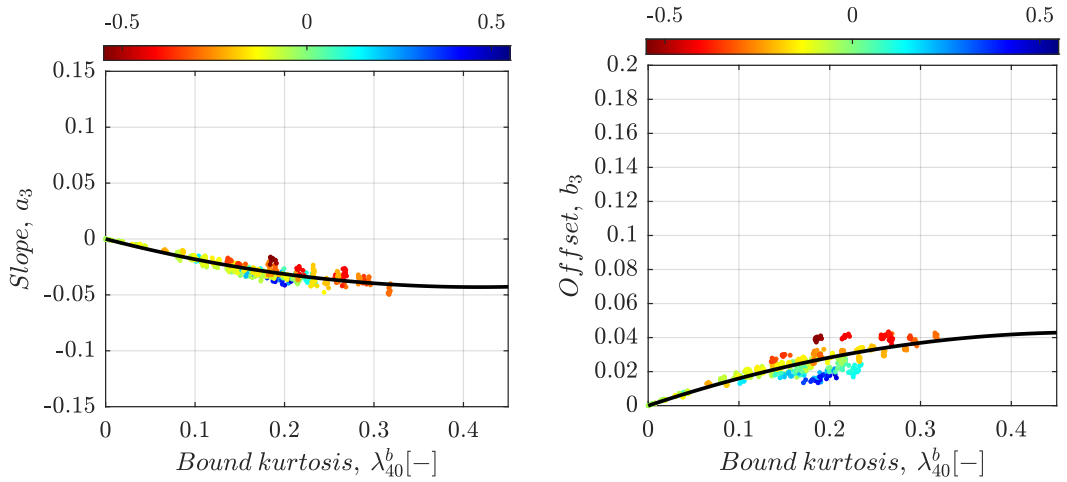


FIGURE 5.8: (A) Slope, a_3, and (B) offset, b_3, parameters against λ^b_{40}; with the lines ( ) referring to best-fit second-order polynomials. The markers are coloured according to the value of the dynamic kurtosis.

bound kurtosis in this case, and are given by:

$$\begin{aligned} f_{c,3}(\lambda^d_{40}) &= (0.7{\cdot}\lambda^d_{40} + 1) \\ f_{c,4}(\lambda^d_{40}) &= (-1.2{\cdot}\lambda^d_{40} + 1), \end{aligned} \tag{5.7}$$

with $f_{c,3}$ corresponding to a_3 and $f_{c,4}$ corresponding to b_3.

The variation of a_3 and b_3 with $f_{c,3}\lambda^b_{40}$ and $f_{c,4}\lambda^b_{40}$ are presented in Figure 5.9 along with best-fit polynomial functions. In contrasting Figure 5.9 to Figure 5.8 the reduction of the scatter, especially for b_3, becomes apparent. Quantifying this change, the RMSE associated to the polynomial fits in Figure 5.8 was ~ 0.004 for both a_3 and b_3. This reduces to ~ 0.003 and ~ 0.002 for a_3 and b_3, respectively, in Figure 5.9. To achieve this, the best-fit polynomial functions depicted in Figure 5.9 are defined by,

$$\begin{aligned} a_3 &= 0.183{\cdot}c_3^2 - 0.201{\cdot}c_3 \\ b_3 &= -0.213{\cdot}d_3^2 + 0.185{\cdot}d_3 \end{aligned} \tag{5.8}$$

with,

$$\begin{aligned} c_3 &= \lambda^b_{40}{\cdot}f_{c,3}(\lambda^d_{40}) \\ d_3 &= \lambda^b_{40}{\cdot}f_{c,4}(\lambda^d_{40}). \end{aligned} \tag{5.9}$$

These fits can be used for the prediction of the odd-harmonic bound-wave contributions given the values of the bound and dynamic kurtosis.

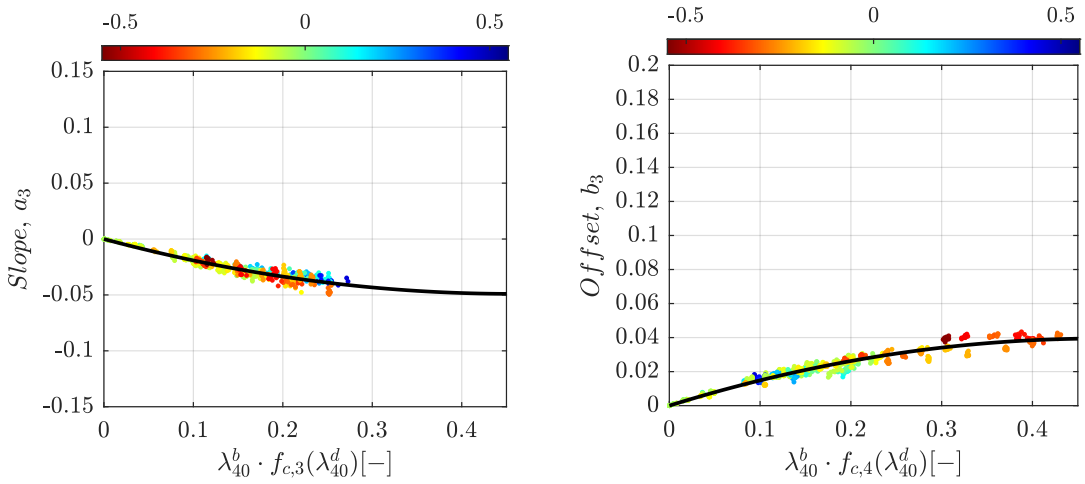


Figure 5.9: (A) Slope, a_3, and (B) offset, b_3, parameters against $f_{c,3}\lambda_{40}^b$ and $f_{c,4}\lambda_{40}^b$, respectively; with the lines ( ) referring to best-fit second-order polynomials. The markers are coloured according to the value of the dynamic kurtosis.

Summarising this section, the crest-height distribution arising in any sea-state irrespective of the relative water depth, spectral bandwidth, directional spread or steepness can be recovered based on the knowledge of the skewness, bound kurtosis and dynamic kurtosis. Based on the above, the remaining challenge is the effective prediction of the statistical moments, based on the sea-state parameters.

However, given that the current state-of-the-art solutions fail to provide reliable predictions for these moments (Chapters 3 and 4), their prediction remains a challenging task, mainly due to the wide range of conditions that the present study seeks to address. In a first attempt to address this, the derivation of empirical equations to predict the statistical moments was explored. Unfortunately, this proved not to be viable option; owing to the complexity of the observed relationships between the input sea-state parameters and the statistical moments; not least the high dimensionality of the problem. This is characterised by four input dimensions (for the steepness, directionality, spectral bandwidth and effective water depth). To resolve this, the research was directed to the field of the so-called *meta-modelling* analysis techniques lying in the fields of structural reliability analysis and machine learning.

In the context of ocean and coastal engineering, these techniques started emerging in the late 90s. Some of the key applications include the prediction of metocean parameters (Deo & Sridhar Naidu, 1998), the prediction of tides (Lee & Jeng, 2002), the prediction of the stability of armour layers in rubble-mound breakwaters (Mase

et al., 1995), and the assessment of wave over-topping over sea defences (van Gent et al., 2007).

To this end, the following section (§5.2.2) presents the application of these techniques in the present context; a brief introduction to the concept of meta-modelling is also provided.

5.2.2 Prediction of the statistical moments using meta-modelling techniques

Brief summary of meta-models and their use in the present context

The basic idea behind the meta-modelling techniques is that a response or output quantity arising from a computationally intensive simulation can be approximated by a so-called *meta-model*. This way, the meta-model acts as a simplified mathematical replacement of a computationally intensive simulation tool (here HOSM), enabling the user to predict the output quantity of interest for any set of inputs without the computational burden.

To calibrate any meta-model, a set of inputs and outputs arising from the computationally intensive simulation tool are required, referred to as the training dataset. Based on this training dataset, the so-called *hyper-parameters* inherent to any meta-model are optimised, aiming to minimise an error measure reflecting the deviation of the meta-model's predictions from the output data points.

Several types of meta-models have been developed over the years and the suitability of each one depends upon the problem at hand. Among these, the following categories can be identified:

1. Meta-models that in their mathematical formulation the *input variables* are *stochastic* quantities (for example polynomial chaos expansions) and those that are *deterministic* (examples of which will be provided below).

2. Meta-models that act as a *regression* tool and others that act as an *interpolation* tool. In the former case, they act as multidimensional best-fit approximators, and hence they do not necessarily replicate the outputs of the training dataset exactly. Whereas, in the latter case they do.

3. Meta-models that are themselves *deterministic* or *stochastic*. In the first case,

training the meta-model for a given training dataset multiple times will result in the same model (with the same values for the hyper-parameters). Whereas, in the second case, the meta-model will not be the same.

In the context of the present application, the input variables are deterministic quantities and consist of the sea-state parameters. Namely, the sea-state steepness, $\frac{1}{2}H_s k_p$, the effective water depth, $k_p d$, the directional spread, σ_θ and the spectral bandwidth, represented by γ. While the output variables of interest are the time- and ensemble-averaged values of the statistical moments. Consequently, despite the statistical moments being inherently stochastic quantities, their averaging over a large ensemble of random simulations makes them quasi-deterministic.

As such, regarding point (1) above, the second class of models will be considered. The most popular meta-modelling techniques lying in this class include:

1. the so-called Gaussian Process Emulators (GPE), often referred to as Kriging (see Santner et al. 2003, Rasmussen & Williams 2006)

2. the Support Vector Machines (SVM) (see Smola & Schölkopf 2004, Vapnik 2013)

3. the Artificial Neural Networks (ANN) (see Hagan et al. 1997, Hurtado & Alvarez 2001).

Regarding point (2) above, the SVM and ANN are regression tools, and the classic version of the GPE technique is an interpolation tool; both are regarded as relevant in the present context given that the outputs are quasi-deterministic. Finally, regarding point (3), the ANN is a stochastic meta-model, whilst the SVM and GPE are deterministic meta-models. To this end, the implication of employing a stochastic vs a deterministic meta-model will be discussed in the following sections in which these meta-models will be applied.

More generally, the reader is referred to Brunton et al. (2020) for further review on the application of machine learning tools in the field of fluid mechanics and to Simpson et al. (2001) for a review on the use of meta-models in engineering design. Finally, it is noted that it is beyond the scope of the present chapter to present in detail the mathematical formulation of the meta-models mentioned above and their training algorithms, the reader being referred to the provided references for further information. However, when necessary for the on-going discussion, a brief outline of the meta-model will be provided.

Training dataset

The training dataset used for calibrating the meta-models consists of the 84 sets of inputs-outputs arising from all available HOSM sea-state simulations. In considering this training dataset, most of the available sea-states have a sea-state steepness of $1/2H_sk_p = 0.105$. This leads to a somewhat under-representation of the input variable space. To resolve this, extra 'boundary' points for sea-states of zero sea-state steepness were added to the original training dataset, for which the output values for the statistical moments are zero according to theory. These extra data points cover the full range of possible combinations of the existing values of the remaining three sea-state parameters within the original training dataset, extending its size from 84 points to 231. Alternatively, HOSM simulations for sea-states of a very small steepness could have been performed to provide such points. However, this would induce excessive computational costs and it was abandoned as an option.

The original training dataset and the 'boundary' points are depicted in the multivariate matrix plot in Figure 5.10 with yellow markers/bars and blue markers/bars, respectively. In this figure, each subplot represents the scatter of points for each pair of sea-state parameters and the diagonals depict the corresponding histogram of data points for each sea-state parameter separately. In considering Figure 5.10 the logic behind employing the 'boundary' points becomes clearer. As considering for example the sea-states of $\gamma = 5$ and $\sigma_\theta = 10°$ simulated only for $1/2H_sk_p = 0.105$, which are represented by the top rightmost point in the scatter plot of $1/2H_sk_p$-vs-γ, they are supported by the added points at $1/2H_sk_p = 0$, depicted vertically below.

Having defined the training data set, the calibration of the different meta-models can be performed. For this, the Artificial Neural Network (ANN) approach is employed first; its application being discussed in the following.

Artificial Neural Network

- ***Description of the model***

With inspiration from the neural structure of the human brain, an artificial neural network consists of multiple interconnected computational units called neurons or perceptrons. Whilst there are numerous types of artificial neural networks eligible for supervised training (i.e. training using a dataset for the hyper-parameters

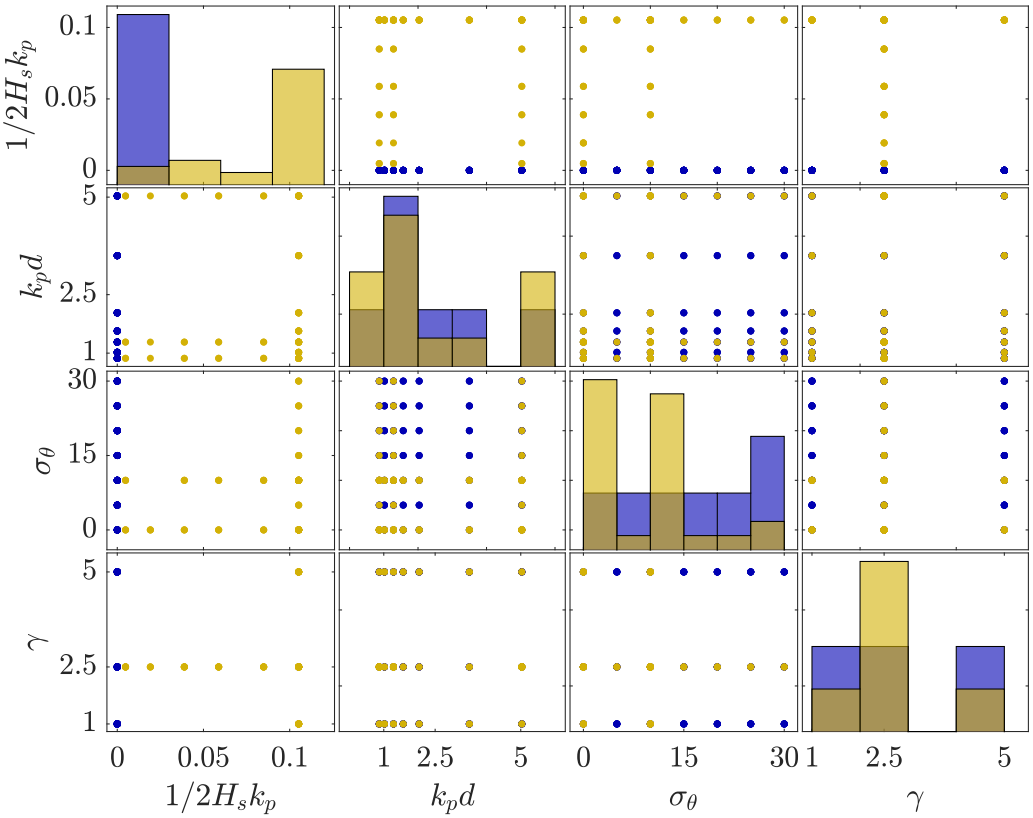


Figure 5.10: Training dataset depicted in the input variable space, showing the original sea-states used in the HOSM simulations with (•), along with additional 'boundary' points of zero sea-state steepness with (•). Each off-diagonal plot refers to the scatter of points for each pair of sea-state parameters. While the diagonal plots refer to the histogram of data points for each sea-state parameter; following the same colour notation as the scatter plots.

optimisation), the most widely used for problems of the present type is the so-called *multilayer perceptron*, a special case of a *feedforward network* with fully interconnected neurons. More specifically, a neural network of this type has the following architecture:

1. The *input* layer of neurons, each neuron corresponding to an input variable of the problem at hand.

2. Multiple *hidden* layers of neurons, applying a set of mathematical operations.

3. The *output* layer of neurons, each neuron corresponding to an output variable of the problem at hand.

Such a system is illustrated in Figure 5.11(A). The neurons in the input layer feed the values of the input parameters to the first hidden layer. While the neurons in the output layer have the same functionality as the neurons in the hidden layer; albeit their outputs are the final network's prediction. Furthermore, a multilayer perceptron can include multiple output variables. However, to keep the network architecture as simple as possible, a separate ANN was adopted for predicting each statistical moment. Hence, the output layer consists of a single neuron in the present case.

In more detail, within a multilayer perceptron, each connection between neurons contains a so-called *weight*, w. Each neuron, i, in the hidden layer, j:

1. receives the outputs, $A_{j-1} = (a_{1,j-1}, a_{2,j-1}, ..., a_{N_{j-1},j-1})$, of the neurons in the previous layer,

2. applies an activation function, f, to the sum of the weights multiplied by the output values of the previous layer $\sum W_j^T \cdot A_{j-1}$ $(W_j = (w_{1,j}, w_{2,j}, ..., w_{N_j,j}))$,

3. adds a *bias*, b_{ij}, and

4. evaluates its output value, a_{ij}, which is fed to the next layer of neurons.

as depicted in Figure 5.11(B).

To put the above in a mathematical perspective, the output value of a multilayer perceptron as depicted in Figure 5.11(A) is evaluated according to,

$$y_m = f_m\Big(\sum_{i=1}^{N_{m-1}} w_{i,m} \cdot a_{i,m-1}\Big) + b_m \tag{5.10}$$

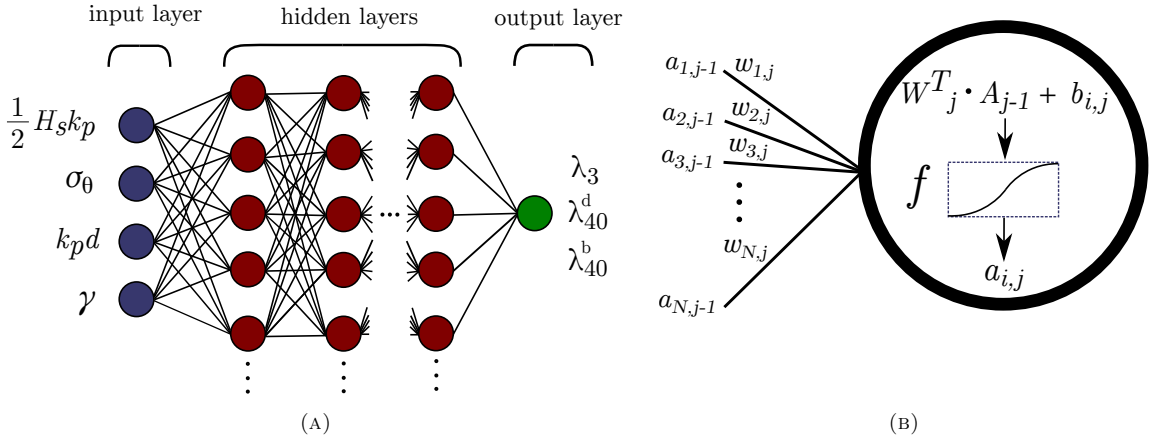


Figure 5.11: Schematic of a feed-forward ANN architecture. (A) a full neural network schematic with 4 neurons in the input layer, and an output layer of a single neuron. (B) a detailed view of the calculation procedure within a neuron i in layer (either hidden or output) j: $a_{i,j-1}$ representing the outputs of the neurons in the previous layer, $w_{i,j}$ the weights of the connections between the neurons in the previous layer and the current neuron, and $b_{i,j}$, f and $a_{i,j}$ the bias, activation function and output of the current neuron, respectively.

where, m is the total number of layers, N_{m-1} is the number of neurons in the last hidden layer, $w_{i,m}$ is the value of the weight connecting the neuron i in layer $m-1$ to the output neuron, $a_{i,m-1}$ are the outputs of the neurons in the last hidden layer, b_m is the bias of the output neuron and f_m is the activation function of the output neuron. While, the output of any neuron, i, in any given layer, j, is given by,

$$a_{i,j} = f\Big(\sum_{i=1}^{N_{j-1}} w_{i,j} \cdot a_{i,j-1}\Big) + b_{i,j} \tag{5.11}$$

where, symbols follow the same logic as in Equation 5.10. Finally, a linear activation function for f_m and a tangent sigmoid function for f is the most common choice for problems of the present type and have been employed in the present context.

Based on the above, training an artificial neural network aims to optimise the so-called *hyper-parameters*, comprising of the weights of the connections and the biases, such that the deviation of the network outputs from the outputs of the training dataset is minimised. This deviation is quantified by the mean-square error between the network outputs and the outputs of the training dataset, denoted as ϵ_{MSE}.

The training is implemented using a so-called *back-propagation* algorithm, supplied with early stopping criteria for enhancing the generalisation performance and for avoiding over-fitting (see Hagan et al. 1997). More specifically, applying the early

stopping criteria, the original training dataset is randomly divided into a reduced training dataset and a validation dataset. Then the back-propagation algorithm updates the hyper-parameters based on the gradient of ϵ_{MSE} with respect to the values of the hyper-parameters. However, the criterion for stopping the training is the minimisation of the mean-square error associated with the validation dataset, referred to as early stopping. This way, ϵ_{MSE} may not reach its lowest possible value, but the network's generalisation performance is superior. Whilst, several implementations of back-propagation exist, the Levenberg-Marquardt algorithm has been adopted here. This consists of a combination of gradient descent and Gauss-Newton algorithms, selected owing to its speed for solving medium size problems like the one herein. In the present study, the numerical implementation of the ANN provided by the deep-learning MATLAB toolbox has been adopted, as it is both robust and computationally efficient due to the automatic parallelisation of the numerical operations that MATLAB embeds.

Furthermore, in applying the back-propagation algorithm, the hyper-parameters are initialised with random values. As such, due to:

1. the complexity of the ANN architecture,
2. the random division of the reduced training and validation datasets, and
3. the random initialisation of the hyper-parameters,

the ANN is stochastic. Consequently, every time an ANN is trained, the values of the hyper-parameters and hence the predictions are not the same.

- ***Preliminary results***

To complete the architecture of the ANN, the number of hidden layers and the number of neurons per hidden layer should be defined. This is a crucial step as the performance of a multilayer perceptron can be highly dependent on the architecture of the hidden layers (Hagan et al., 1997). In the context of the present research and taking into account the stochastic nature of an ANN, the mean value of ϵ_{MSE} [1], $E[\epsilon_{MSE}]$, resulting from the training of 1,000 networks has been employed to define the optimum architecture.

[1] where ϵ_{MSE} is evaluated upon the entire training dataset (i.e. the reduced training and validation data sets combined)

To this end, Figure 5.12 presents the variation of $E[\epsilon_{MSE}]$ against the number of neurons in each hidden layer [1], for a different number of hidden layers. Where the number of neurons varies between 1 and 30, and the number of hidden layers varies from 1 to 4. Specifically, sub-figure (a) refers to networks trained to predict the skewness, sub-figure (b) the bound kurtosis and sub-figure (c) the dynamic kurtosis. Taking these results together, the error is shown to be minimised using two hidden layers and nine neurons per layer for all three output variables.

Furthermore, to demonstrate that the results of sub-figures (a), (b) and (c) are indeed converged with respect to the number of neural networks, sub-figure (d) presents the variation of the average error, $E[\epsilon_{MSE}]$, with respect to the number of networks for the optimum ann architecture. Where the values of $E[\epsilon_{MSE}]$ have been normalised by the average evaluated based on 1,000 networks. In considering the results in Figure 5.12(d), $E[\epsilon_{MSE}]$ is shown to be indeed converged using 1,000 networks.

- ***Ensemble predictions vs single predictions***

Whilst a single ann could potentially lead to reasonable predictions, given its stochastic nature, the adoption of an ensemble of anns could enhance the prediction performance. This approach, of employing multiple ann trained on the same data refers to the so-called ensemble methods (Perrone & Cooper, 1992) for output variance reduction and aims to remove the effect of randomness from the ann predictions.

To assess the merits of adopting this approach, Figure 5.13 presents

1. the outputs, y_m, of multiple single anns shown with grey markers,
2. the average, $E[y_m]$, of the outputs of 1,000 anns shown with blue markers, and
3. the median, $M[y_m]$, of the outputs of 1,000 anns shown with red markers

compared to the output values of the full training dataset. Specifically, the top row of sub-figures ((a) to (c)) corresponds to a different statistical moment. While the bottom row of sub-figures ((d) to (f)) presents detailed views of the former sub-figures, corresponding to the marked rectangle regions. These latter sub-figures are

[1] It is noted that the number of neurons in any hidden layer can in principle be different. However, for simplicity, here it is kept the same.

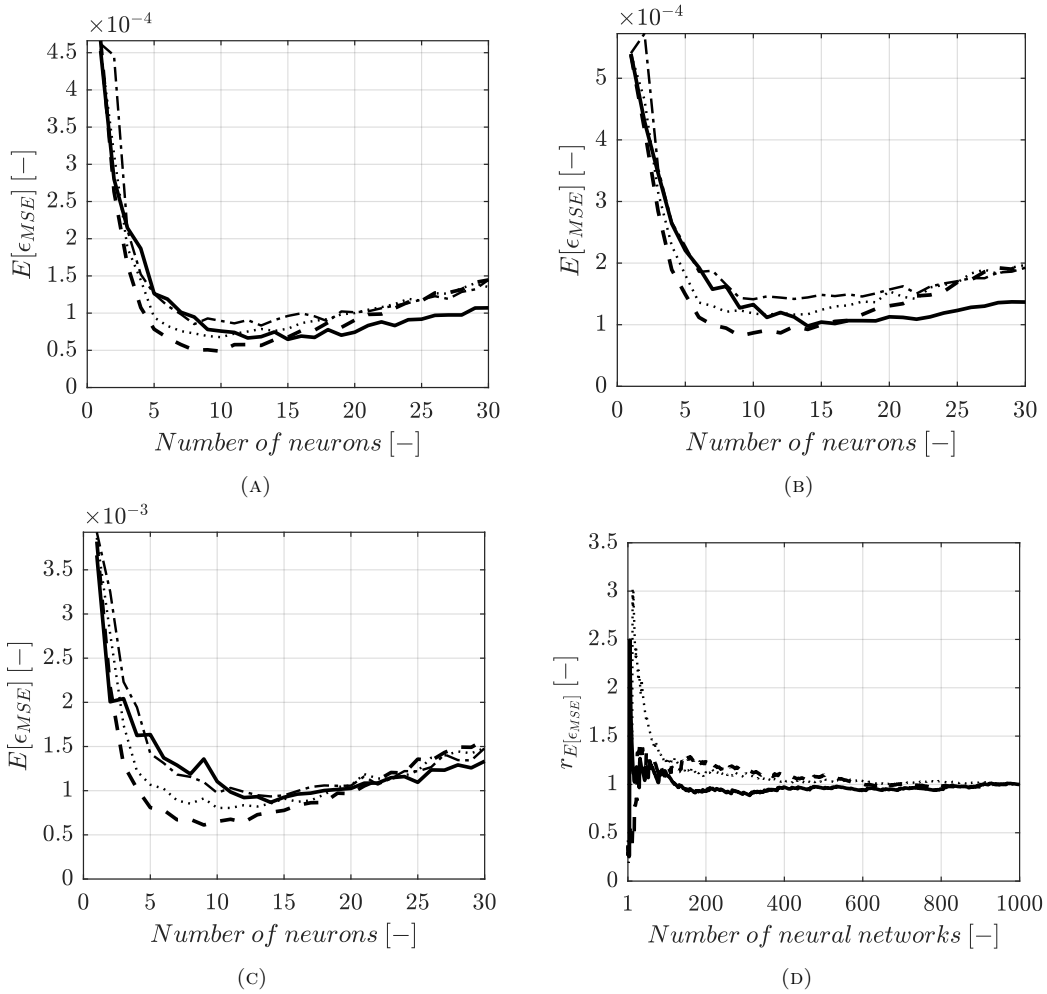


Figure 5.12: Variation of $E[\epsilon_{MSE}]$ with respect to the number of neurons per hidden layer for different number of hidden layers, $m' = m - 2$; with (———) for $m' = 1$, (– – –) for $m' = 2$, (·····) for $m' = 3$ and (– · –) for $m' = 4$. (A) for the skewness, (B) for the bound kurtosis and (C) for the dynamic kurtosis. While (D) presents the convergence of $E[\epsilon_{MSE}]$ with respect to the number of ANNs; with (———) for the skewness, (– – –) for the bound kurtosis, and (·····) for the dynamic kurtosis. Specifically, $r_{E[\epsilon_{MSE}]}$ represents the ratio of $E[\epsilon_{MSE}]$, evaluated for an increasing number of neural networks, over $E[\epsilon_{MSE}]$, evaluated using 1,000 neural networks.

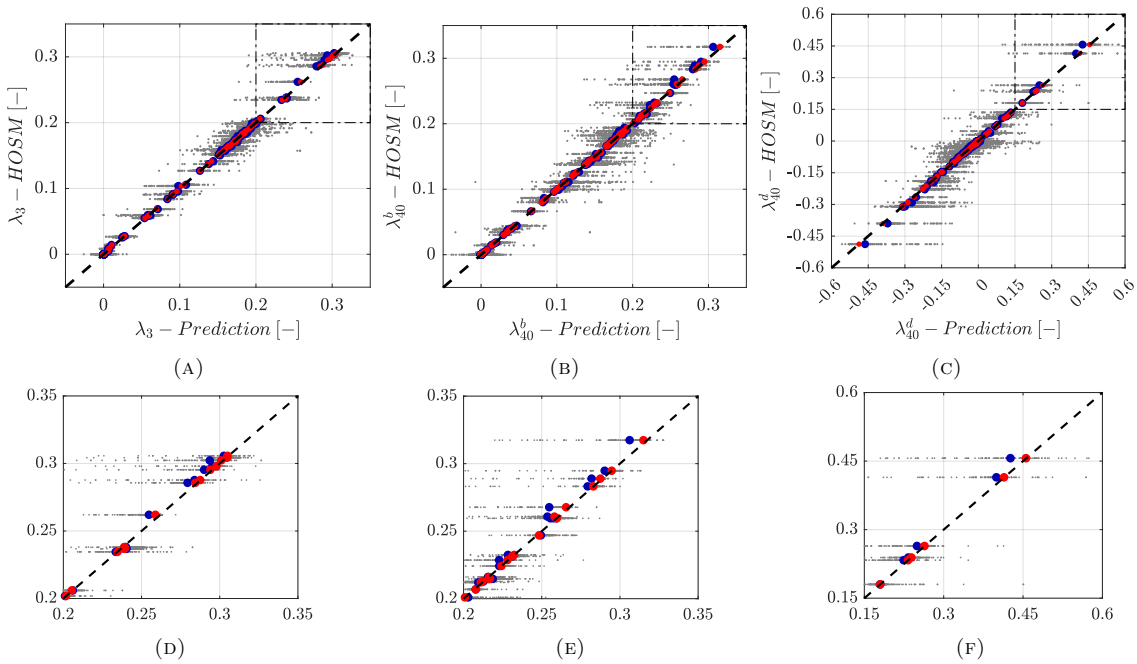


Figure 5.13: Comparison of the ANN predictions to the target values of the (A) skewness, (B) bound kurtosis and (C) dynamic kurtosis. Individual ANN predictions are shown with (•), ensemble averaged predictions are shown with (•) and ensemble median predictions are shown with (•); the diagonal line (— —) referring to perfect agreement. The sub-figures (D), (E) and (F) are detailed views of (A), (B) and (C), respectively, marked with a rectangle region (— · —) in the latter sub-figures. All results have been obtained using ANNs with 2 hidden layers and 9 neurons per hidden layer.

included to show in more detail the observations. The results in Figure 5.13 show that the predictions of single ANNs indeed exhibit substantial variability. However, by employing a central prediction using either $E[y_m]$ or $M[y_m]$ the predictions are very favourable; with the median, $M[y_m]$, outperforming slightly the mean, $E[y_m]$.

To quantify the difference between the single and ensemble predictions, Table 5.1 presents the values of the mean absolute relative deviation, ϵ_r, [1] of the ANN predictions. More specifically, for single ANN predictions, the values refer to the mean of ϵ_r across 1,000 ANNs and the values in parenthesis refer to the corresponding standard deviation. The results in Table 5.1 show that adopting a median prediction yields the lowest error.

[1]The mean absolute relative deviation is calculated according to $\epsilon_r = \frac{1}{N}\sum_{i=1}^{N}|\frac{x_{p,i}-x_{t,i}}{x_{t,i}}|$, where i refers to the the i-th observation, $x_{p,i}$ to the predicted value, $x_{t,i}$ to the observation or target value and N to the number of observations. While to avoid infinite numbers, the data with zero target values have been excluded.

Table 5.1: Absolute relative deviation of the ANN predictions; single vs ensemble preditions. For single ANNs the results refer to the average mean relative deviation of 1000 individual ANNs and the values in parenthesis refer to the corresponding standard deviation. For ensemble ANN predictions the results refer to the mean relative deviation. Note that only non-zero target values have been included in calculating the computed relative deviations, while the ANNs architecture consists of 2 hidden layers and 9 neurons per hidden layer.

ANN	λ_3	λ_{40}^b	λ_{40}^d
Single	0.044 (0.032)	0.275 (0.323)	0.184 (0.258)
Ensemble average	0.027	0.126	0.066
Ensemble median	0.017	0.078	0.021

At this point, it should perhaps be stressed out that Gramstad & Bitner-Gregersen (2019) have attempted to predict the kurtosis arising from HOSM simulations based on machine learning techniques. However, their results exhibited much more significant scatter than the present ones. Indicatively, in Gramstad & Bitner-Gregersen (2019), the mean-square error normalised by the variance of the target points was in the order of 0.10, whereas here it is only 0.0002; three orders of magnitude less.

- ***On the generalisation performance***

Having guaranteed that the error associated with the ANN predictions is kept to a minimum, the generalisation performance of the ANN predictions should also be assessed. This is essential because any meta-model could predict well the values of the training dataset, but fail to capture the true relationship between the input variables and the output variables (to generalise poorly). As mentioned earlier, this latter situation refers to over-fitting the training dataset. Although the back-propagation algorithm aims to avoid this, the generalisation performance needs to be assessed before the optimum ANN architecture can be defined.

To gain a first indication of the generalisation performance of the ensemble median ANN predictions, it is instructive to explore their variation with changes in the input variables. To this end, Figure 5.14 presents the ANN predictions for the dynamic kurtosis in varying effective water depths, $k_p d$, for sea-states of $\frac{1}{2} H_s k_p = 0.105$, $\sigma_\theta = 0$ and different JONSWAP spectra (γ values). To assess the effect of the ANN architecture on the generalisation performance, sub-figure 5.14(A) refers to ANNs with 9 neurons per hidden layer and sub-figure 5.14(B) to ANNs with 5 neurons per

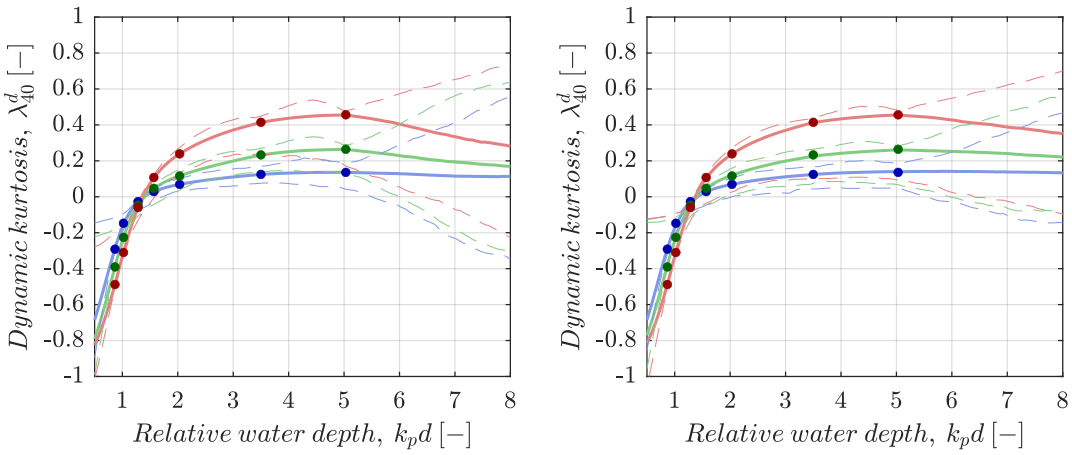


FIGURE 5.14: Variation of the ANN predictions with relative water depth, k_pd, for JONSWAP sea-states of $\frac{1}{2}H_sk_p = 0.105$, $\sigma_\theta = 0$ and different γ values. (A) for 9 neurons and (B) for 5 neurons per hidden layer. The lines (—— / —— / ——) correspond to the ensemble median ANN predictions, The lines (– – / – – / – –) refer to the 2.5% and 97.5% quantiles of the single ANN predictions. While the markers (• / • / •) correspond to HOSM results used in the training of the ANNs. In all cases the colour order refers to $\gamma = 1.0, 2.5$ and 5.0, respectively.

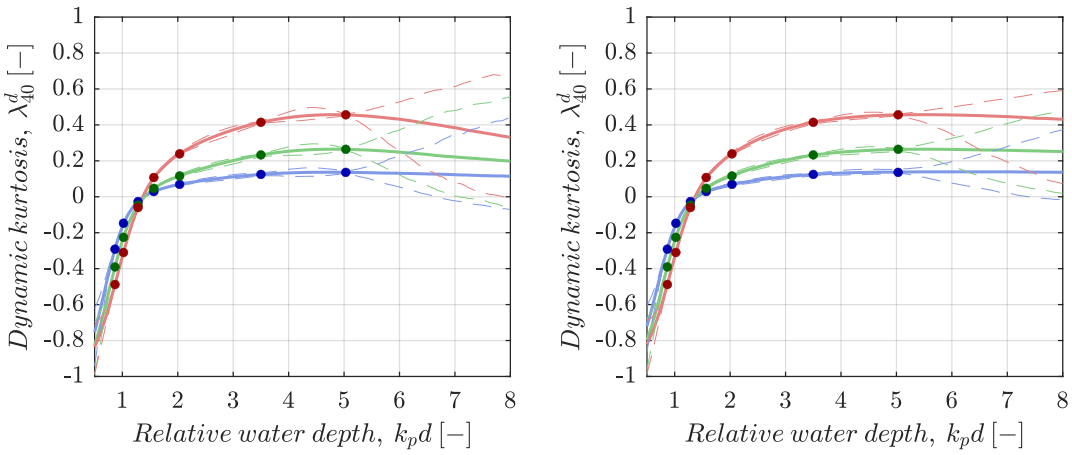
hidden layer. In each plot, the median predictions are shown with continuous lines, while the dashed lines refer to the 2.5% and 97.5% quantiles. In addition, when available, the values of the dynamic kurtosis belonging to the training dataset are also added.

The observed trends in Figure 5.14 demonstrate that, whilst the median predictions for both ANN architectures lead to satisfactory predictions of the data in the training dataset; they tend to generalise differently beyond the input variable range, especially for $k_pd > 5$. However, in considering these results, none of the two architectures leads to a satisfactory generalisation performance. From a physical perspective the predictions for $k_pd > 5$ should no longer be affected by k_pd; the conditions having converged to deep-water.

To resolve this, it was decided to discard ANNs of low performance. This lead to non-accurate estimates of even the data points of the training dataset. For this, the following steps were followed:

1. A selected quantile, p, of the scatter of ϵ_{MSE}, denoted as ϵ_{MSE_p}, was selected.

2. The training of the ANNs of the selected architecture was repeated, but this time any network of $\epsilon_{MSE} < \epsilon_{MSE_p}$ was discarded, whilst a target number of 1,000 networks was still maintained.



(A) (B)

FIGURE 5.15: Same as in Figure 5.14 but this time single ANN with $\epsilon_{MSE} < \epsilon_{MSE_{10}}$ are considered; whilst still maintaining a number of 1,000 single ANN.

To quantify the merit of adopting this approach, Table 5.2 presents the average and standard deviation of the mean absolute relative deviation, ϵ_r, of single ANNs using different quantiles, ϵ_{MSE_p} in the discarding process. Along with the ϵ_r of the ensemble median ANN predictions. The results in Table 5.2 refer to an ANN architecture consisting of 5 neurons per hidden layer; as this was shown in Figure 5.14 to generalise somewhat better than ANNs of 9 neurons per hidden layer.

TABLE 5.2: Absolute relative deviation of the ANN predictions using different level of acceptable error ϵ_{MSE}; single vs ensemble median ANN predictions. For single ANNs the results refer to the average mean relative deviation of 1000 individual ANNs and the values in parenthesis refer to the corresponding standard deviation. For ensemble median ANN predictions the results refer to the mean relative deviation. Note that only non-zero target values have been included in the calculation of the relative deviation.

Error threshold	Single			Ensemble median		
	λ_3	λ_{40}^{b}	λ_{40}^{d}	λ_3	λ_{40}^{b}	λ_{40}^{d}
N/A	0.064 (0.042)	0.407 (0.358)	0.243 (0.315)	0.032	0.173	0.042
$\epsilon_{MSE_{50}}$	0.037 (0.010)	0.236 (0.119)	0.098 (0.043)	0.025	0.134	0.042
$\epsilon_{MSE_{30}}$	0.032 (0.007)	0.205 (0.104)	0.082 (0.037)	0.023	0.121	0.037
$\epsilon_{MSE_{10}}$	0.026 (0.005)	0.158 (0.072)	0.067 (0.029)	0.020	0.108	0.036

In considering Table 5.2 it becomes evident that:

1. as the quantile p decreases the error of the predictions decreases,

2. the error of the single ANN predictions approaches the error of the ensemble predictions, and

3. the error of the ensemble median predictions for $p = 10$, is comparable to the error of the ensemble predictions for ANNs with 9 neurons per hidden layer as presented in Table 5.1.

To demonstrate the enhanced generalisation performance of ensemble median ANN predictions using a quantile of $p = 10$ in the discarding process, Figure 5.15 presents the equivalent to Figure 5.14 variation of the predictions for the dynamic kurtosis. While, again both ANN architectures of 5 and 9 neurons per hidden layer were adopted. In considering Figure 5.15 it is shown that:

1. For both ANN architectures, the variability of the single ANN predictions in the input variable range of the training dataset ($k_p d \in [0.87, 5.03]$) is minimal; as opposed to the very large variability observed in Figure 5.14. This observation essentially reflects the success of the discarding process. However, the variability of the single ANN predictions immediately increases for predictions outside the interval $k_p d \in [0.87, 5.03]$. This observation is crucial because it demonstrates that very successful single ANNs will not generalise well in principle; supporting further the adoption of the ensemble approach.

2. The ensemble median predictions of ANNs with 5 neurons per hidden layer exhibit better generalisation performance than the equivalent with 9 neurons per hidden layer. A result that is entirely in line with the notion that simpler ANN architectures lead to better generalisation performance (Hagan et al., 1997).

Taking the results presented in this section together, the final ANN predictions for the statistical moments will be based on error-truncated ($\epsilon_{MSE} < \epsilon_{MSE_{10}}$) ensemble median predictions derived from the training of multiple (1,000) ANNs of 2 hidden layers and 5 neurons per hidden layer.

To conclude this section, the generalisation performance of the ensemble median ANN predictions needs to be demonstrated in a wider set of cases. To this end, Figure

5.16 presents the predictions for all statistical moments with variation in relative water depth, $k_p d$, in the range $[0.8, 8.0]$ for sea-states of different JONSWAP spectra (γ) and directional spreads σ_θ having a steepness of $\frac{1}{2} H_s k_p = 0.105$. Again, where available, the data points belonging to the training dataset have been added. More specifically, the trends in Figure 5.16 have been obtained for $\gamma = 0.5, 1.0, 1.75, 2.5, 3.75, 5.0$ and 7.0; with the first and last values extending beyond the available values in the training dataset. Moreover, the sub-figures on the left column ((A), (C) and (E)) refer to sea-states of $\sigma_\theta = 0$, and the sub-figures on the right column ((B), (D) and (F)) refer to sea-states of $\sigma_\theta = 10°$. The top row of sub-figures refers to the predictions of skewness, the middle row the prediction of bound kurtosis and the bottom row the prediction of the dynamic kurtosis.

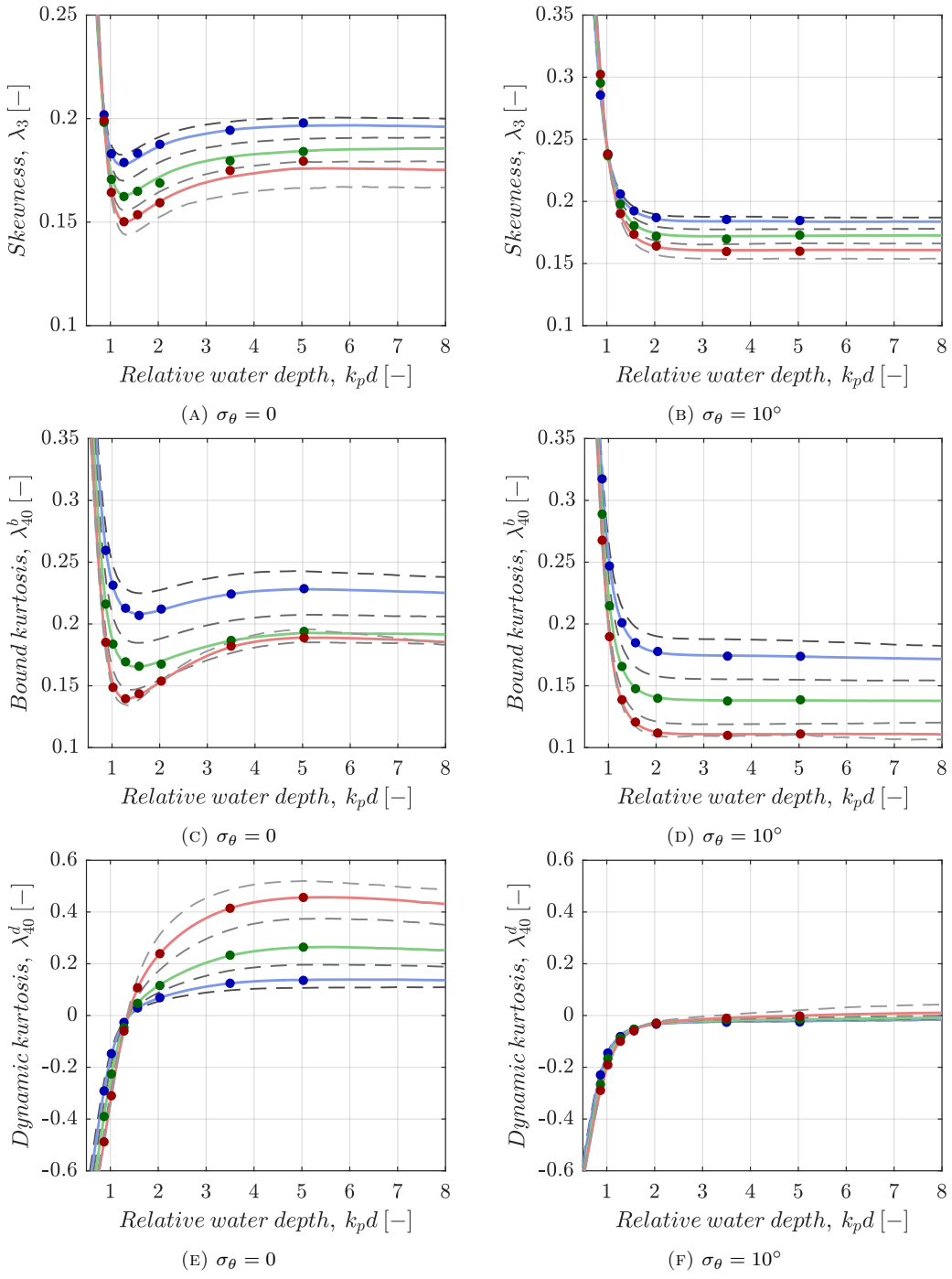
The results in Figure 5.16 demonstrate that the ensemble median ANN predictions based on error-truncation and 5 neurons per hidden layer:

1. Capture very well the values of the statistical parameters for sea-states belonging in the training dataset, as expected,
2. Interpolate well between the points for γ values included in the training dataset
3. At the same time, the predictions remain reasonable for γ values outside the training data.
4. They extrapolate very well for $k_p d$ values outside the input variable range of the training dataset.

Adopting this approach, the ensemble median ANN predictions will hereafter be referred to as EANN.

- ***The effect of 'boundary' points on the EANN predictions***

With the training dataset used by EANN including artificial points at zero steepness, the present section aims to clarify the effect of these 'boundary' points. To achieve this, the training of the individual ANNs was repeated using the same architecture (i.e. 5 neurons per hidden layer ANNs with error truncation) and a training dataset, which did not include the 'boundary' points. To differentiate between the two approaches:

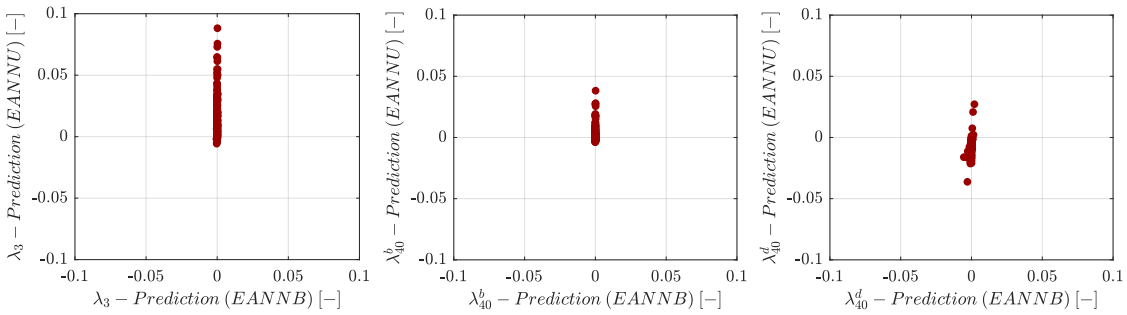


(a) $\sigma_\theta = 0$ (b) $\sigma_\theta = 10°$

(c) $\sigma_\theta = 0$ (d) $\sigma_\theta = 10°$

(e) $\sigma_\theta = 0$ (f) $\sigma_\theta = 10°$

Figure 5.16: Variation of the ensemble median ann predictions with relative water depth, k_pd, for jonswap sea-states of $\frac{1}{2}H_sk_p = 0.105$ and different γ. The sub-figures on the left column ((a), (c) and (e)) correspond to sea-states of $\sigma_\theta = 0$ and the sub-figures on the right column ((b), (d) and (f)) correspond to sea-states of $\sigma_\theta = 10°$. From top to bottom, (a) & (b) refer to the skewness, (c) & (d) to the bound kurtosis, and (e) & (f) to the dynamic kurtosis. In all sub-figures the lines (– – / —— / – – / —— / – – / —— / – –) correspond to the ensemble median ann predictions for $\gamma = 0.5, 1.0, 1.75, 2.5, 3.75, 5.0$ and 7.0, respectively. While the markers (• / • / •) correspond to the hosm results used in the training of the anns for $\gamma = 1.0, 2.5$ and 5.0, respectively. The ann predictions refer to an ann architecture consisting of 2 hidden layers and 5 neurons per hidden layer.



(A) (B) (C)

FIGURE 5.17: Predictions of EANNB and EANNU for sea-states corresponding to the 'boundary' points. (A) for the skewness, (B) for the bound kurtosis and (C) for the dynamic kurtosis.

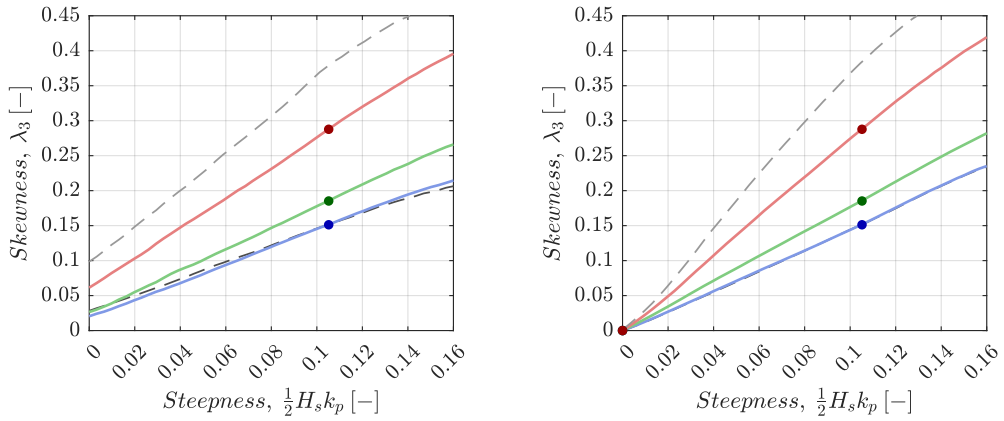
1. The EANN trained with the 'boundary' points *included* in the training dataset will be referred to as EANNB (with 'B' for bounded)

2. The EANN trained with the 'boundary' points *not included* in the training dataset will be referred to as EANNU (with 'U' for unbounded)

To assess the effect of including the boundary points in the training dataset, Figure 5.17 presents the predictions of both EANNB and EANNU for input parameters corresponding to the added 'boundary' points, where each sub-figure corresponds to a different statistical parameter. As expected, the EANNB predicts nearly zero values for all the statistical moments, whereas EANNU predicts non-zero values; the latter being physically incorrect.

To put the above into a more practical context, Figure 5.18 presents the variation of both EANNB and EANNU predictions of the skewness with increase in the sea-state steepness, for sea-states of $\sigma_\theta = 30°$ and $\gamma = 2.5$ in different effective water depths. Where available, the data points of the respective training datasets have been added.

The results in Figure 5.18 indicate the importance of including the 'boundary' points, as, without these, the EANNU predictions at zero steepness predict non-zero values of the statistical moments, especially for low $k_p d$ values. In addition, the 'boundary' points are shown to also affect the slope of the observed trends. Particularly, the latter observation can affect the predicted values beyond the range of $\frac{1}{2}H_s k_p$ used in the training (i.e. $\frac{1}{2}H_s k_p \in [0, 0.105]$). Given these results, the EANNB predictions are employed in the remainder of this chapter; for brevity these will simply be referred to as EANN.



(A) (B)

FIGURE 5.18: Variation of the ensemble median ANN predictions of the skewness with increase in the sea-state steepness, for sea-states of $\sigma_\theta = 30°$ and $\gamma = 2.5$ in relative water depths of $k_p d = 8.0, 5.03, 1.28, 0.87$ and 0.7 denoted with (— — / —— / —— / —— / — —) respectively. While the markers (• / • / •) correspond to the HOSM results used in the training of the respective ANNs with the colour order referring to $k_p d = 5.03, 1.28$ and 0.87, respectively. (A) for EANNU and (B) for EANNB predictions.

Assessing the generalisation performance based upon an independent test dataset and the use of other meta-models

• *Performance of other meta-models*

As mentioned earlier, in addition to ANN, other types of meta-models suitable for the present application include the GPE and the SVM. Unlike the ANN, these models have a fixed 'architecture' or mathematical formulation. While it is left to the user to define a set of options relating to (for example) the functional form of the so-called basis functions of the related expansions. These models will not be described here for brevity. However, a short description of is provided in Appendix H.

To define the optimum configuration of both GPE and SVM the performance measure used for their training is the so-called *leave-one-out* cross-validation error (see, for example, Meckesheimer et al. 2002). This error measure is calculated as follows:

1. The training dataset $T = \{[\mathbf{x_i}, y_i];\ i = 1..N\}$ of size N is copied N times, each time excluding a different data point.

2. A meta-model is then trained for each of the N copies and it is used to predict the excluded data point; this prediction being denoted with $M_{\ i}(\mathbf{x_i})$ (i

symbolising the excluded point from the training dataset).

3. Finally, the *leave-one-out* cross-validation error is evaluated according to,

$$\epsilon_{LOO} = \frac{1}{N}\sum_{i=1}^{N}(M_{\sim i}(\mathbf{x_i}) - y_i)^2 \tag{5.12}$$

where y_i is the output data point or observation within the original training dataset.

This procedure is an alternative to employing a randomly selected validation dataset used in the case of the ANN training, the advantage of which is the inclusion of the highest proportion of data each time the model is trained. However, having defined the optimum meta-model's configuration based on ϵ_{LOO}, the final model is trained based on the original training dataset of N elements.

To provide a quantitative comparison of the performance of the different meta-models, Table 5.3 presents the calculated *leave-one-out* cross-validation error, ϵ_{LOO}, the RMSE, $\sqrt{\epsilon_{MSE}}$ and the absolute mean relative deviation, ϵ_r. The *leave-one-out* cross-validation error essentially presents a measure of the generalisation performance of the models, the RMSE presents the standard deviation of the error of the predictions, and the absolute mean relative deviation reflects the expected deviation of the predictions from the target values. Considering these error measures, it is observed that whilst the GPE and SVM exhibit smaller $\sqrt{\epsilon_{MSE}}$ and ϵ_r errors than the EANN, the latter is associated with the smallest ϵ_{LOO}; signifying a better generalisation performance.

Table 5.3: Comparison of error measures of the employed meta-models.

Meta-model	$\sqrt{\epsilon_{LOO}}$			$\sqrt{\epsilon_{MSE}}$			ϵ_r		
	λ_3	λ_{40}^b	λ_{40}^d	λ_3	λ_{40}^b	λ_{40}^d	λ_3	λ_{40}^b	λ_{40}^d
EANN	0.0014	0.0015	0.0033	0.0007	0.0005	0.0016	0.020	0.108	0.036
SVM	0.0096	0.018	0.012	$1.2\,10^{-5}$	$1.3\,10^{-5}$	$5.5\,10^{-6}$	0.0002	0.0033	0.0002
GPE	0.0013	0.0018	0.0047	$O(10^{-7})$	$O(10^{-7})$	$O(10^{-7})$	$O(10^{-6})$	$O(10^{-6})$	$O(10^{-6})$

To illustrate the performance of GPE and SVM, Figure 5.19 presents examples of their predictions for different sea-state conditions. More specifically, sub-figures (A)

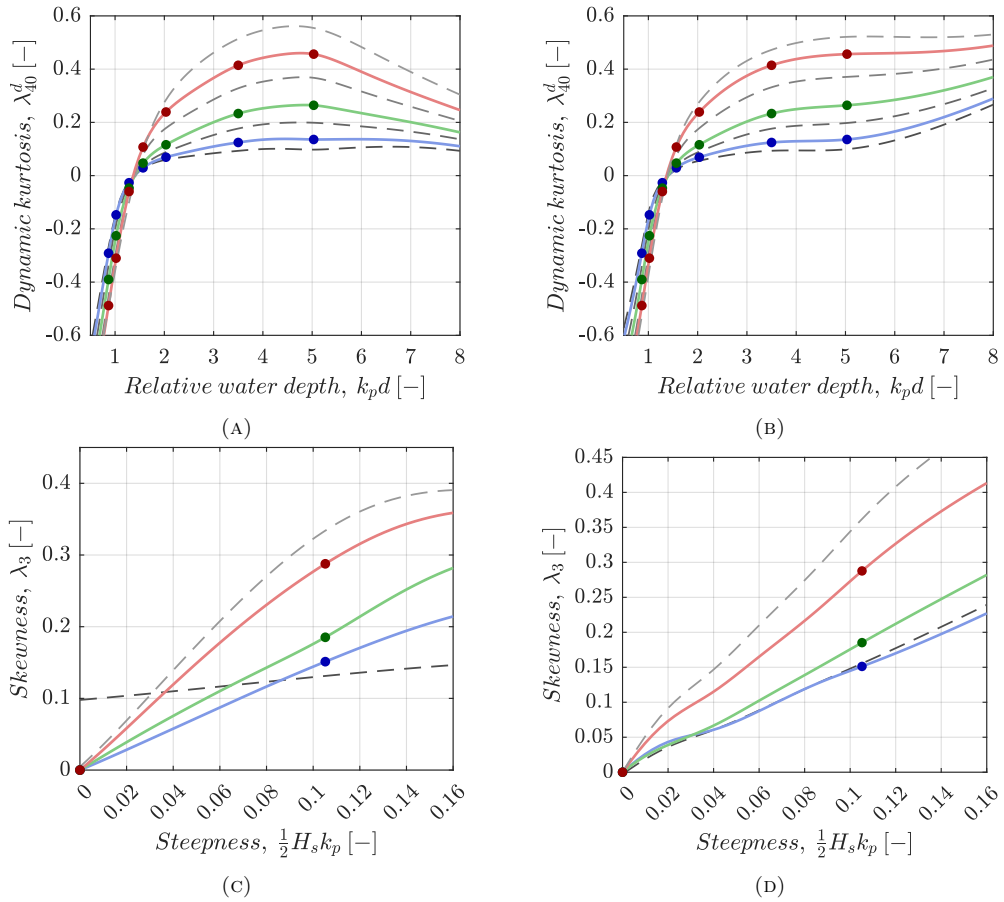


FIGURE 5.19: Examples of the predictive performance of (A)-(C) SVM and (B)-(D) GPE. Sub-figures (A)-(B) present the variation of the dynamic kurtosis with effective water depth, k_pd, for sea-states of $\frac{1}{2}H_sk_p = 0.105$, $\sigma_\theta = 0$ and different γ values; with lines (— — / —— / —— / —— / — —) referring to $\gamma = 0.5, 1.0, 1.75, 2.5, 3.75, 5.0$ and 7.0. and the markers (• / • / •) to the HOSM results with the colour order referring to $k_pd = 5.03, 1.28$ and 0.87, respectively. Sub-figures (C)-(D) present the variation of the skewness with sea-state steepness, $\frac{1}{2}H_sk_p$, for sea-states of $\sigma_\theta = 30°$, $\gamma = 2.5$ in different effective water depths. The lines (— — / —— / —— / —— / — —) refer to $k_pd = 8.0, 5.03, 1.28, 0.87$ and 0.7, respectively. While the markers (• / • / •) correspond to the HOSM results with the colour order referring to $k_pd = 5.03, 1.28$ and 0.87, respectively.

and (C) present the variation of their predictions for the dynamic kurtosis with effective water depth in uni-directional sea-states of different γ values and $\frac{1}{2}H_sk_p = 0.105$. While sub-figures (B) and (D) present the variation of their predictions with sea-state steepness for directional sea-states of $\sigma_\theta = 30°$ and $\gamma = 2.5$ in different effective water depths. Moreover, when available, the values of the respective moments obtained from the HOSM simulations, included in the training dataset, are also added for reference.

Taken the results presented in Figure 5.19 as a whole, GPE and SVM:

1. Predict the HOSM results very well.

2. Interpolate between the data points very well.

3. Extrapolate reasonably for γ values beyond the range of values contained in the training dataset (i.e. $\gamma \in [1, 5]$).

However, following the discussion around Figure 5.14, the extrapolation or generalisation performance of the predictions beyond the effective water depth range of $k_p d \in [0.87, 5.03]$ is questionable. The observed trends in sub-figures (A) and (B) do not exhibit a steady plateau for $k_p d > 5.03$. In addition, the skewness predictions of SVM for varying steepness, presented in (C), indicate an ineffective generalisation performance. More specifically, (1) for $k_p d = 8.0$ the predicted skewness at $\frac{1}{2} H_s k_p = 0$ is non-zero and (2) it is unexpectedly lower than the predictions in $k_p d = 5.03$ as $\frac{1}{2} H_s k_p$ increases. While for $k_p d < 1.0$ and $\frac{1}{2} H_s k_p > 0.105$ the predictions deviate significantly from the expected quasi-linear trend (see Figure 4.18(B)).

Based on the above discussion, and considering the equivalent Figures 5.16(E) and 5.18(B) associated with the EANN predictions, there is evidence that the EANN exhibits a better generalisation performance. This conclusion is also supported by the lower ϵ_{LOO} for this meta-model.

• Meta-models' predictions of an independent test dataset

To provide a quantitative and perhaps more conclusive assessment of the generalisation performance of the employed meta-models, a so-called *test* dataset is often employed. This dataset refers to additional data points not included in the original training dataset, with the generalisation performance of a meta-model being assessed upon how well these points are predicted. To obtain such dataset, a set of 9 additional sea-state simulations were performed using HOSM, the characteristics of which are presented in Table 5.4.

Within these additional simulations, the range of effective water depths extends beyond the range of the original training dataset. The employed directional spreads correspond to very long-crested and very short-crested sea-states with $\sigma_\theta = 3°$ and $30°$, respectively. For the more long-crested sea-states, the spectral bandwidth is defined by $\gamma = 1$, laying at the edge of the training dataset range. For the short-crested sea-states, γ is set to both 1 and 6; the latter value extending beyond the maximum

Table 5.4: Sea-state characteristics of the test dataset.

Set	$k_p d$ [−]	γ [−]	$\frac{1}{2}H_s k_p$ [−]	σ [°]
T1	0.80	1.0,6.0	0.10	30
T2	1.10	1.0,6.0	0.10	30
T3	8.00	1.0,6.0	0.10	30
T4	0.80	1.0	0.10	3
T5	1.10	1.0	0.10	3
T6	8.00	1.0	0.10	3

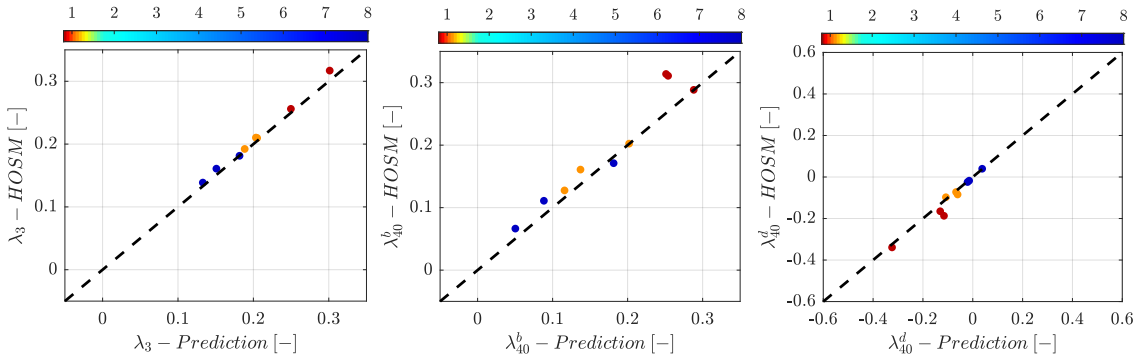
value of 5 adopted within the training dataset. Finally, the sea-state steepness is set to $\frac{1}{2}H_s k_p = 0.10$, which lays very close to the maximum sea-state steepness of the training dataset; a direct correspondence to this maximum value having been avoided to prevent unnecessarily favourable conditions. Taken together, the sea-states used to assess the generalisation performance are in no sense favourable; being either at the edges or (even) outside the training dataset range. Finally, it should be noted that very narrow-banded long-crested directional sea-states have not been considered. Such sea-states are unrealistic and do not, therefore, correspond to a regime of relevance for the present thesis (see also the discussion in §4.5.5).

To quantify the error of the meta-models' predictions based upon the test dataset, Table 5.5 presents the associated root-mean-square error, $\sqrt{\epsilon_{MSE}}$, and mean absolute relative deviation, ϵ_r. These results confirm that the error of the EANN predictions is lower than the other meta-models for all statistical moments.

Table 5.5: Comparison of error measures of the meta-models' performance upon the test-data set.

Meta-model	$\sqrt{\epsilon_{MSE}}$			ϵ_r		
	λ_3	λ_{40}^b	λ_{40}^d	λ_3	λ_{40}^b	λ_{40}^d
ANN	0.010	0.031	0.028	0.034	0.126	0.162
SVM	0.026	0.090	0.046	0.098	0.562	1.043
GPE	0.015	0.032	0.136	0.058	0.132	3.241

Furthermore, to visualise the EANN performance using the test dataset, Figure 5.20 presents the comparison between the EANN predictions against the values ob-



(A) (B) (C)

FIGURE 5.20: Comparison of the EANN predictions against the time-averaged ensemble-averaged values of the statistical moments arising from additional HOSM simulations (Table 5.4). (A) skewness, (B) bound kurtosis and (C) dynamic kurtosis.

tained from the HOSM simulations for all three statistical moments: (A) concerning the skewness, λ_3, (B) the bound kurtosis, λ_{40}^b and (C) dynamic kurtosis, λ_{40}^d. In all sub-figures, the markers have been coloured according to the $k_p d$ value of each sea-state. Taking these comparisons as a whole, the data points are shown to lay close to the one-to-one line, demonstrating the effective generalisation of EANN. However, as an exception, the bound kurtosis for the shallowest short-crested sea-states is under-predicted by $\sim 20\%$. This deviation is most likely associated with the strong gradients of the bound kurtosis in low effective water depths (see for example Figure 5.16(D)), leading to a mismatch between observations and predictions. However, with the rest of the statistical moments accurately predicted, it is to be explored whether this deviation affects the performance of the crest-height model predictions. This is assessed in detail in §5.3.2.

5.3 Assessing the performance of a new crest-height model

Having established a reliable prediction for the statistical moments, the proposed crest-height model is fully predictive; relying solely on the characteristics of the sea-state. In summary, obtaining the crest-height distribution involves the following steps:

1. Determining the sea-state parameters $\frac{1}{2}H_s k_p$, $k_p d$, σ_θ and γ.

2. Predicting the statistical moments based on the ensemble median ANN predictions (EANN).

3. Calculating the slope (a_1, a_2 and a_3) and offset (b_1, b_2 and b_3) parameters based on Equations 5.2, 5.5 and 5.8.

4. Evaluating the fully nonlinear corrections to the Rayleigh (linear) distribution according to:

$$\begin{aligned} r_1 &= a_1 \cdot (\log_{10}(Q) + 1) + b_1 \\ r_2 &= a_2 \cdot (\log_{10}(Q) + 1) + b_2 \\ r_3 &= a_3 \cdot (\log_{10}(Q) + 1) + b_3 \\ \eta_c &= (r_1 + r_2 + r_3) \cdot Hs \sqrt{-\log_e(Q)/8} \end{aligned} \tag{5.13}$$

   Equation 5.13 provides the prediction for the total crest heights, η_c, for pre-selected probabilities of exceedance, Q. In this respect, if one is interested in calculating the probability of exceedance of a pre-selected crest height, η_c, this can be based on $Q = \exp\left[-8\left(\frac{1}{r}\frac{\eta_c}{H_s}\right)^2\right]$, where $r = r_1 + r_2 + r_3$. However, with Q being involved in both the left-hand side and the right-hand side (within the factor r) of the expression, an iterative procedure would be required to evaluate Q. For the simplicity of the calculations the model will be evaluated for pre-selected Q rather than η_c, hence following Equation 5.13.

This crest-height model will hereafter be referred to as the Higher-Order Empirical - Ensemble Artificial Neural Network (HOE-EANN); its performance being assessed in the following sections.

5.3.1 Numerical crest-height distributions used in the calibration process

First, the assessment of HOE-EANN is performed against the sea-states used for its training; such assessment ensuring that the proposed model-formulation is indeed effective. To this end, Figures 5.21 and 5.22 present comparisons between the HOE-EANN predictions and numerical crest-height distributions corresponding to the steady-state part of the nonlinear evolution. Importantly, sea-states covering the full range of available effective water depths within the calibration dataset have been

included. More specifically, Figure 5.21 refers to uni-directional sea-states ($\sigma_\theta = 0$) and Figure 5.22 to directional sea-states of $\sigma_\theta = 10°$; each sub-figure referring to a different effective water depth. In all cases, the sea-states are characterised by the highest steepness used in the present study of $\frac{1}{2}H_s k_p = 0.105$, with $\gamma = 2.5$. Finally, all sub-figures include the Rayleigh (linear) distribution for reference.

Taking the full set of comparisons presented in Figures 5.21 and 5.22 together, the HOE-EANN model's performance is shown to be excellent. Indeed, the HOE-EANN predictions outperform the equivalent based on the Gram-Charlier series model (§2.3.3). These comparisons are presented in Appendix G.

Having explored the performance of HOE-EANN for a wide range of sea-state conditions presented in Figures 5.21 and 5.22, it is instructive to explore how the model performs for the full set of the sea-states used in its calibration. To this end, Figure 5.23 presets the relative deviation between the predicted crest-height magnitude at an exceedance probability level of $Q = 10^{-3}$, $\eta_{c,p}$, and the corresponding crest-height magnitude from the numerical crest-height distributions, $\eta_{c,s}$. Data from the full set of 84 sea-states and for all available evolution times at steady state have been included. Figure 5.23 (A) refers to the crest heights of the total free surface and 5.23 (B) to the crest heights of the free waves only.

Based on the results presented in Figure 5.23, it is observed that:

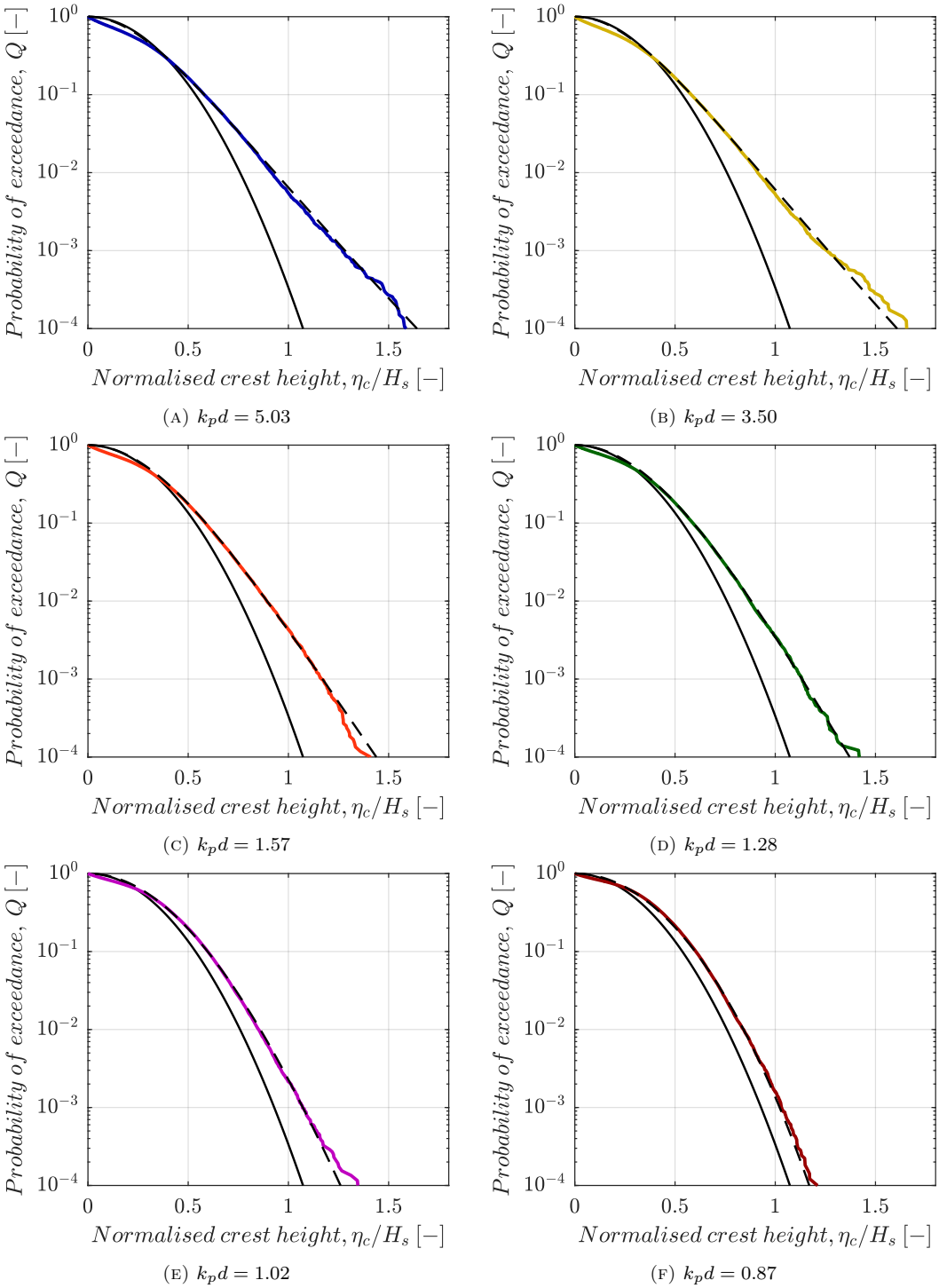
1. The HOE-EANN predictions are non-biased; the observed errors being centred around zero.

2. The relative deviation of the predictions for 90% of the cases is below 3%, whereas in the worst cases, it is below 4%. Deviations of this size are unavoidable given the inevitable sample variability.

3. HOE-EANN accurately predicts both the total nonlinearity of the crests and the underlying contributions.

5.3.2 Validation of HOE-EANN against numerical crest-height distributions of the test dataset

Unlike the previous results, this section aims to establish the validity of the predictions for sea-states that were not used in the model calibration. For this, the



(A) $k_pd = 5.03$ (B) $k_pd = 3.50$

(C) $k_pd = 1.57$ (D) $k_pd = 1.28$

(E) $k_pd = 1.02$ (F) $k_pd = 0.87$

Figure 5.21: Normalised crest-height distributions, η_c/H_s, arising in uni-directional sea-states. Comparison of the HOE-EANN crest-height model prediction to numerical results arising from HOSM simulations used in the calibration of HOE-EANN. Sea-states of $\frac{1}{2}H_sk_p = 0.105$ and $\gamma = 2.5$, each sub-figure corresponding to a different effective water depth: (A) $k_pd = 5.03$, (B) $k_pd = 3.5$, (C) $k_pd = 1.57$, (D) $k_pd = 1.28$, (E) $k_pd = 1.02$ and (E) $k_pd = 0.87$. In each sub-figure the coloured lines refer to numerical data, (— —) refers to the HOE-EANN predictions and (——) refers to the (linear) Rayleigh distribution. All the numerical results refer to steady-state conditions at an evolution time of $55T_p$.

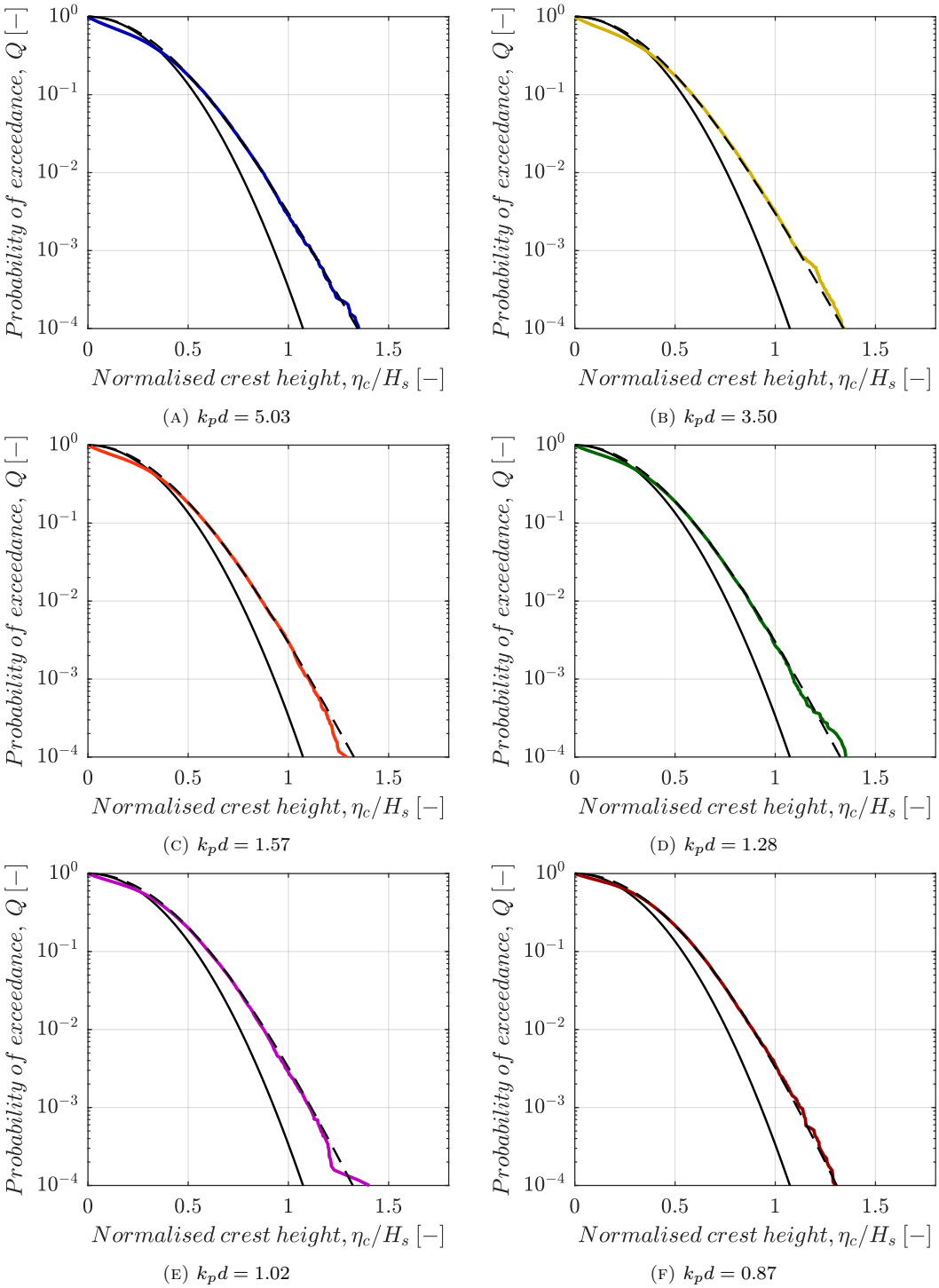
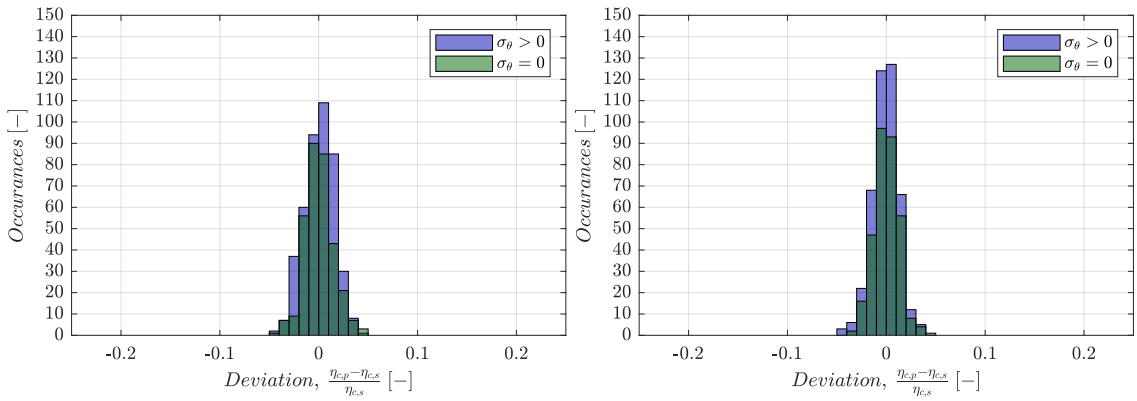


FIGURE 5.22: Normalised crest-height distributions, η_c/H_s, arising in directional ($\sigma_\theta = 10°$) sea-states. Comparison of the HOE-EANN crest-height model predictions to numerical results from HOSM simulations used in the calibration of HOE-EANN. Sea-states of $\frac{1}{2}H_sk_p = 0.105$ and $\gamma = 2.5$, each sub-figure corresponding to a different effective water depth: (A) $k_pd = 5.03$, (B) $k_pd = 3.5$, (C) $k_pd = 1.57$, (D) $k_pd = 1.28$, (E) $k_pd = 1.02$ and (E) $k_pd = 0.87$. In each sub-figure the coloured lines refer to numerical data, (— —) refers to the HOE-EANN predictions and (——) refers to the (linear) Rayleigh distribution. All the numerical results refer to steady-state conditions at an evolution time of $25T_p$.



(A) (B)

Figure 5.23: Histogram of relative deviation, $(\eta_{c,p} - \eta_{c,s})/\eta_{c,s}$, between the HOE-EANN predicted crest-height at an exceedance probability level of $Q = 10^{-3}$ and the corresponding crest-height from numerically (HOSM) obtained crest-height distributions. (A) for the total free surface and (B) for the dynamic part of the free surface.

sea-states of the test dataset (Table 5.4) have been employed. Once again, the comparisons of the HOE-EANN predictions to the numerical crest-height distributions correspond to the steady-state part of the nonlinear evolution ($t = 25T_p$). The comparisons presented in Figure 5.24 refer to sea-states with $\sigma = 30°$, while Figure 5.25 concerns sea-states with $\sigma = 3°$. The comparisons demonstrate that the HOE-EANN predictions are in excellent agreement with these additional data; confirming the effectiveness of the HOE-EANN model to provide predictions outside its training range.

5.3.3 Validation of HOE-EANN against crest-height distributions from experimental data

To verify that the HOE-EANN model is indeed applicable in a wider context, it will now be compared to experimental crest-height distributions. The experimental data was taken from Latheef & Swan (2013) in deep water and Karmpadakis et al. (2019a) in intermediate depths; all of the data generated in the directional wave basin at ICL. As HOE-EANN is a higher-order crest-height model that does not include the dissipative effect of wave breaking, the experimental data considered relate to sea-states of mild severity ($\frac{1}{2}H_s k_p \leq 0.11$). Moreover, the employed sea-states cover a wide range of effective water depths, with $k_p d$ ranging from 1.22 to 2.0; the latter referring effectively to deep-water conditions according to §4.5.4. Additionally, all

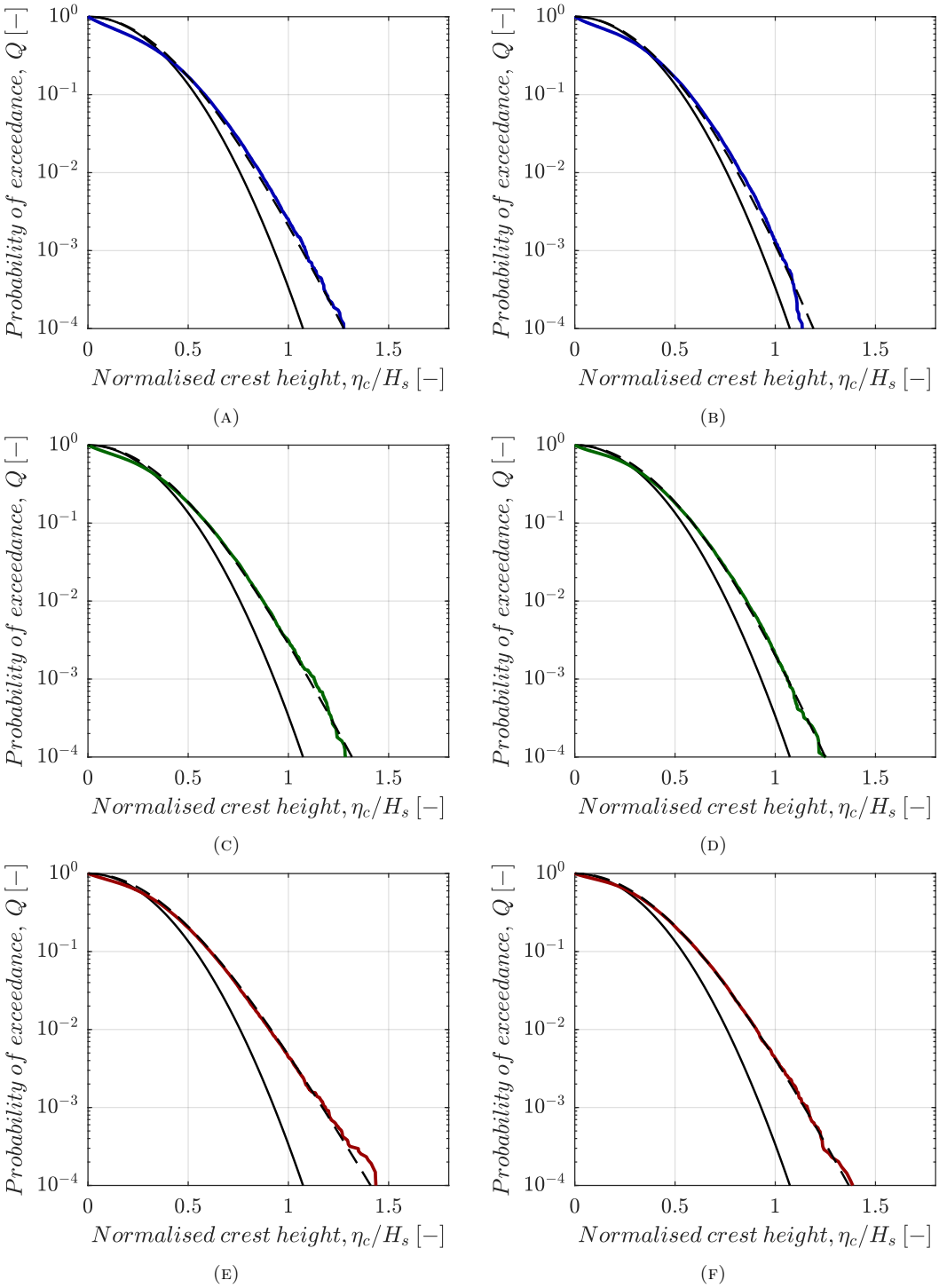


FIGURE 5.24: Normalised crest-height distributions, η_c/H_s, arising in directional sea-states of $\sigma_\theta = 30°$. Comparison of the HOE-EANN crest-height model predictions to numerical results from HOSM simulations belonging to the test dataset. In all cases, $\frac{1}{2}H_s k_p = 0.10$, with the left column referring to sea-states of $\gamma = 1$ and right column to sea-states of $\gamma = 6$. (A) & (B) for $k_p d = 8.0$, (C) & (D) for $k_p d = 1.1$, and (E) & (F) for $k_p d = 0.8$. In each sub-figure the coloured lines refer to numerical data, (— —) refers to the HOE-EANN predictions and (——) refers to the (linear) Rayleigh distribution. All the numerical results refer to steady-state conditions at an evolution time of $25T_p$.

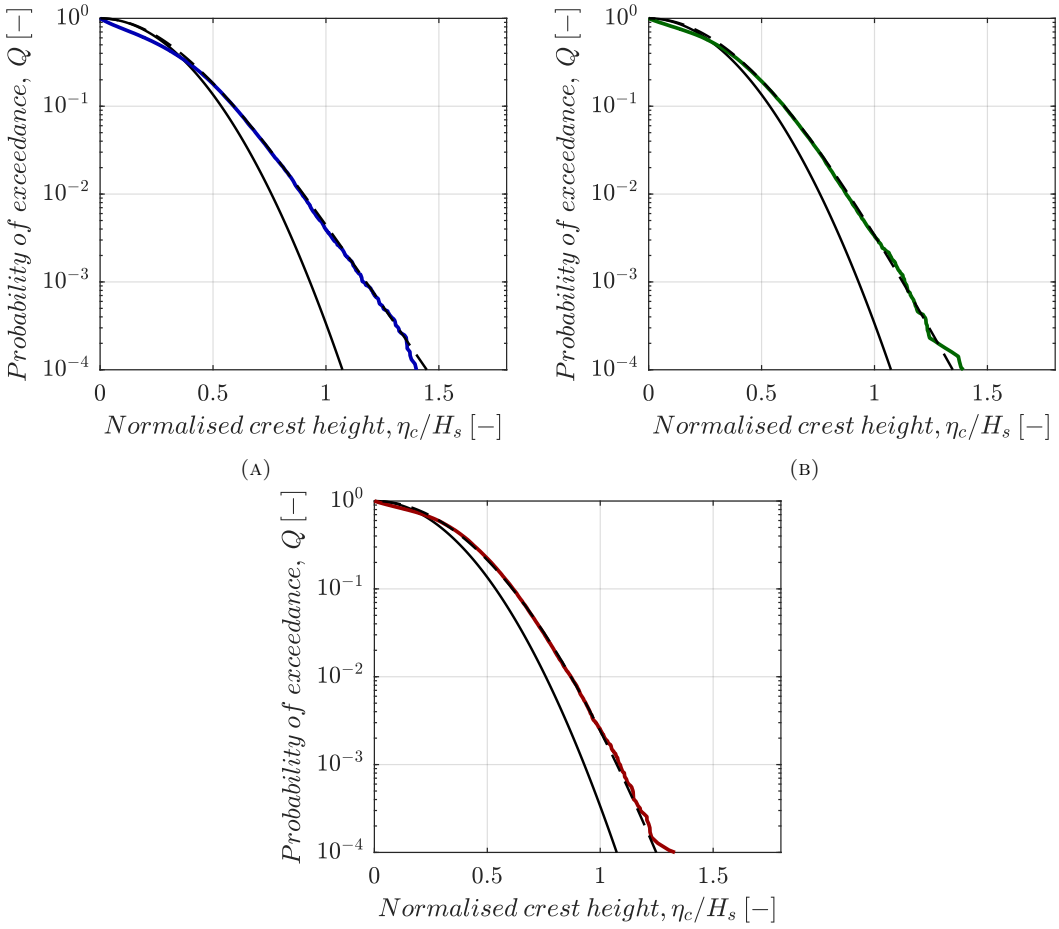


Figure 5.25: Normalised crest-height distributions, η_c/H_s, arising in directional sea-states of $\sigma_\theta = 3°$ and $\gamma = 1$. Comparison of the HOE-EANN crest-height model predictions to numerical results from HOSM simulations belonging to the test dataset. In all cases, $\frac{1}{2}H_s k_p = 0.10$; (A) for $k_p d = 8.0$, (B) for $k_p d = 1.1$, and (C) for $k_p d = 0.8$. In each sub-figure the coloured lines refer to numerical data, (— —) refers to the HOE-EANN predictions and (——) refers to the (linear) Rayleigh distribution. All the numerical results refer to steady-state conditions at an evolution time of $35T_p$.

the available directional spreads have been considered, ranging from 10° to 30°. The only omission is uni-directional sea-states and directional sea-states with $k_p d \lesssim 1.0$ as these would not correspond to steady-state conditions.

Figure 5.26 presents the comparison of the HOE-EANN predictions to the available experimental data; each sub-figure corresponding to a different sea-state, the characteristics of which are provided in the corresponding caption. To assist with an effective comparison, the 95% confidence intervals obtained using a bootstrap method (Efron, 1979) have been added to the experimental data. These indicate the effect of sample variability. Finally, the predictions of the linear (Rayleigh) and second-order (Forristall, 2000) models are also presented for reference. Taking the presented comparisons as a whole, HOE-EANN effectively predicts the amplification of the crest heights observed in laboratory data. Importantly, in all cases, any deviations lay within the confidence intervals when the largest waves arising in a 3-hour sea-state ($Q = 10^{-3}$) are considered.

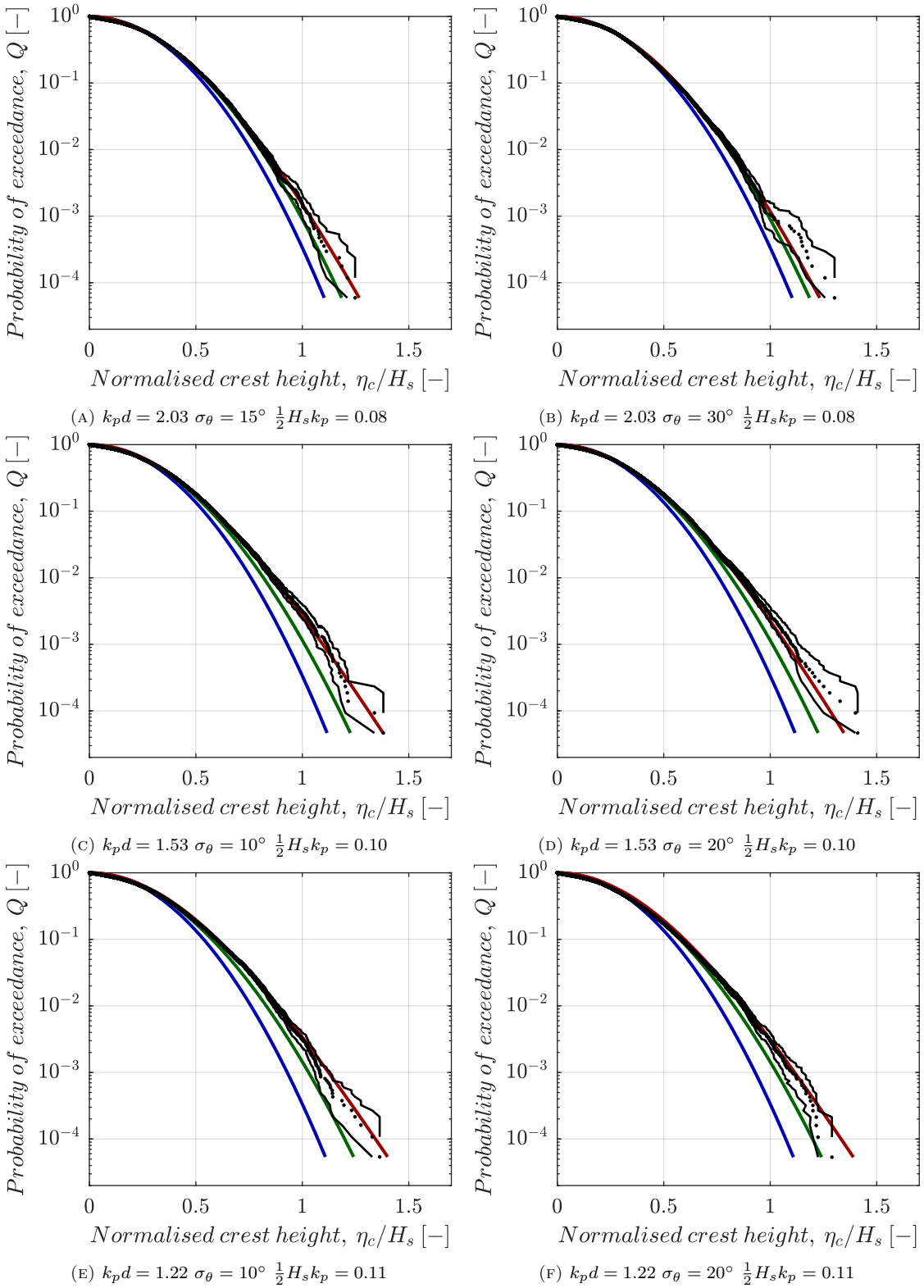
5.3.4 Comparison between HOE-EANN and field data

Having assessed the performance of the HOE-EANN model for an independent set of numerical and experimental data, it is of interest to explore whether the model performs equally well in predicting crest-height distributions arising from data measured in the field; the latter being the third and last potential source of obtaining crest-height distributions.

Analysis procedure

To obtain a wide range of effective comparisons, measured free-surface records acquired using WaveRadar REX installed in 6 platforms in the North Sea have been employed. The platforms' names, operator, duration of records and sampling rate are presented in Table 5.6. These data became available through the LoWiSh (Limits on Waves in Shallow water) III and LOADS Joint Industry Projects and have passed through a strict Quality Control (QC) procedure first developed by Christou & Ewans (2011) and further refined by Karmpadakis et al. (2020); the author of this thesis being provided with the quality controlled records. In summary, the QC procedure involves:

- Removal of tidal fluctuations.



(A) $k_pd = 2.03$ $\sigma_\theta = 15°$ $\frac{1}{2}H_sk_p = 0.08$

(B) $k_pd = 2.03$ $\sigma_\theta = 30°$ $\frac{1}{2}H_sk_p = 0.08$

(C) $k_pd = 1.53$ $\sigma_\theta = 10°$ $\frac{1}{2}H_sk_p = 0.10$

(D) $k_pd = 1.53$ $\sigma_\theta = 20°$ $\frac{1}{2}H_sk_p = 0.10$

(E) $k_pd = 1.22$ $\sigma_\theta = 10°$ $\frac{1}{2}H_sk_p = 0.11$

(F) $k_pd = 1.22$ $\sigma_\theta = 20°$ $\frac{1}{2}H_sk_p = 0.11$

Figure 5.26: Comparison of the HOE-EANN crest-height predictions to experimental crest-height distributions for sea-states of moderate steepness. The different lines refer to: (———) Rayleigh, (———) directional Forristall (2000), (———) HOE-EANN, (•) experiments, (———) 95% confidence intervals. The data in (A) and (B) originate from Latheef & Swan (2013), while the data in (C)-(F) originate from Karmpadakis et al. (2019a).

- Removal of unrealistically long wave events (with zero-crossing period greater than 25s).
- Removal of records with unrealistic spikes (greater than $5\sigma_\eta$).
- Removal of records for which the percentage of energy at low ($< 0.04Hz$) or high ($> 0.6Hz$) frequencies is more than 5%.

More details concerning the adopted QC can be found in the original references.

Table 5.6: List of field data sources.

Platform	Operator	Duration of records	Sampling frequecy $[Hz]$
Magnus	BP	1/2012 - 9/2014	2.0
Miller	BP	7/2011 - 9/2014	2.0
Gorm	Maersk	12/2001 - 12/2012 (non-continuous)	5.12
Tyra East	Maersk	9/2004 - 1/2013 (non-continuous)	5.12
Sean	Shell	10/2012 - 2/2017	4.0
AWG	Shell	10/2012 - 2/2017	4.0

With the duration of the field-data records spanning over many years, the records inevitably need to be segmented into shorter periods, over which the sea-state conditions can be assumed *stationary*. To this end, the following procedure was adopted to obtain the measured crest heights and the associated sea-state characteristics:

1. The sampled free-surface records were divided into 20-min segments.
2. For each segment, the energy spectral density was estimated using a Welch's overlapped segment averaging estimator with 5 sub-segments, each sub-segment being multiplied by a Blackman-Harris window function to avoid energy leakage.
3. The significant wave height, H_s, was computed using the zeroth spectral moment of the energy spectral density.
4. A JONSWAP spectrum was fitted to the measured energy spectral density using a standard least-squares minimisation algorithm.

5. The peak frequency, f_p, of the sea-state was defined as the peak of the fitted JONSWAP spectrum. Likewise the associated γ value of the JONSWAP spectrum was also obtained from the fitting described in 4.

6. A standard down-crossing analysis was performed in each 20-min record to identify individual wave cycles and hence the crest heights.

Aspects of the analysis procedure

Before proceeding to the comparison between the HOE-EANN model predictions and the crest-height distributions arising from the field data, it is instructive to first establish the reliability of the proposed analysis procedure. More specifically, it is of interest to assess the accuracy with which H_s, T_p and γ are captured. To achieve such assessment, linear simulations of JONSWAP sea-states were conducted using LRWT. Each sea-state was simulated 1,000 times using a different set of (input) random amplitudes and phases for a duration of three hours. The free surface was sampled at $4Hz$. Each 3-hour record was segmented into shorter, 20-min, records over which the above analysis procedure was applied. For each 20-min segment, the H_s, T_p and γ were blindly evaluated despite knowing *a-priori* their 'true' values.

At this point, it should be stressed that the peak period (or equivalent peak frequency) arising from fitting a JONSWAP spectrum differs from the peak period obtained directly from the measured spectral density. In the latter case, traditionally, the peak frequency is defined either by the maximum ordinate of the spectral density or, alternatively, by a 3-point parabolic fit around the maximum (Frigaard et al. 1997); the latter aiming to account for the effect of spectral discretisation. Whilst the choice of 3 points is somewhat arbitrary, it is one of the methods proposed by the International Association for Hydraulic Research (Frigaard et al. 1997) and it is adopted here without modification. To illustrate the difference between the two approaches, Figure 5.27 presents an example of a measured energy spectrum accompanied by a fitted JONSWAP spectrum. An inset detailing the area around the spectral peak is also provided. This defines the 3-point parabolic fit. In this plot, the red marker denotes the estimate of f_p as the maximum point of the fitted parabola, referred to as f_p^m, and the blue marker the f_p-estimate based on a JONSWAP fit, referred to as f_p^J.

In observing Figure 5.27, it can be seen that f_p^J is a more accurate estimator for

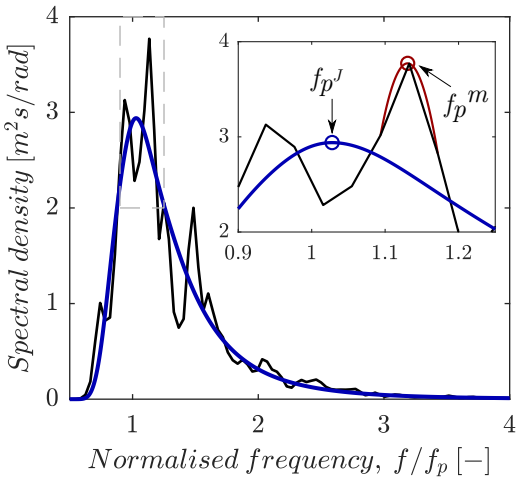


FIGURE 5.27: Example of a measured spectral energy density ( ), along with a fitted JONSWAP spectrum ( ) against the normalised frequency f/f_p; with f_p representing the input peak frequency of the LRWT simulations. The inset depicts the area marked with ( ) in more detail. In this inset the 3-point parabolic fit at the maximum measured spectral energy ( ) is also added. While the marker ( ) represents the point of the final estimation of f_p.

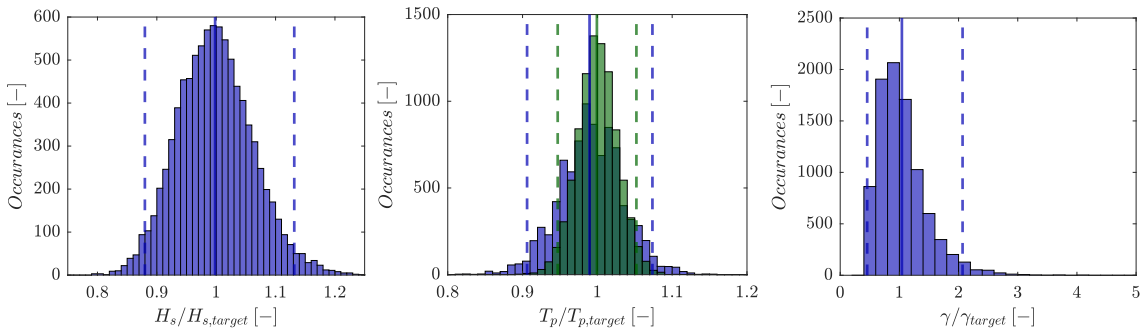
f_p than f_p^m. Indicatively, in this example, f_p^J is only marginally (2%) higher than the true value, while f_p^m is 13% higher. It is important to note that the consequence of this latter discrepancy propagates into both the estimation of k_pd and $\frac{1}{2}H_sk_p$. For example, for a sea-state of $T_p = 10s$ in a water depth of $100m$ ($k_pd = 4.0$), both k_pd and $\frac{1}{2}H_sk_p$ are over-estimated using f_p^m by $\approx 30\%$, while for an equivalent sea-state in $15m$ ($k_pd = 0.87$) by $\approx 15\%$.

To illustrate the effect of segmentation of the free-surface records on the measured values of H_s, T_p and γ, Figure 5.28 presents the histograms of:

1. the ratio of the estimated H_s over the true significant wave height denoted by $H_{s,target}$,
2. the ratio of the estimated T_p (using both methods detailed above) over the true spectral peak period denoted by $T_{p,target}$, and
3. the ratio of the estimated γ over the true peak enhancement factor γ_{target}.

for input JONSWAP spectra of $\gamma = 2.5$. In addition, the mean values and 95% confidence intervals of the above ratios are marked with vertical lines.

The results in Figure 5.28 demonstrate that H_s is expected to vary between $[0.88, 1.12]H_s$ with 95% confidence. Moreover, the spread of $T_p/T_{p,target}$ is much higher when the estimation of T_p is based on the peak of the measured spectral energy,



(A) (B) (C)

Figure 5.28: Histograms of (A) $H_s/H_{s,target}$, (B) $T_p/T_{p,target}$ and (C) γ/γ_{target}. In all plots, the continuous vertical lines represent the mean values. Whereas the dashed lines represent the 95% confidence intervals. In (B) (■) refers to $1/f_p^J$ and (■) refers to $1/f_p^m$, with the vertical lines following the same colour notation.

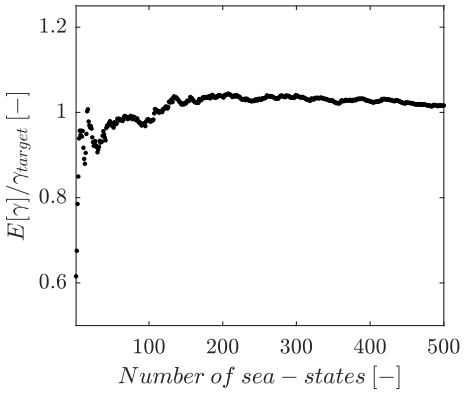


Figure 5.29: Convergence of mean γ, $E[\gamma]$, with respect to the number of 20-min sea-states used for its evaluation.

compared to the peak of the fitted JONSWAP spectrum; with the 95% confidence interval being $[0.90, 1.08]$ using the first approach and $[0.95, 1.05]$ using the second.

Finally, when considering γ, it is shown to exhibit much higher scatter than the other variables. However, it can be seen that the mean value is accurately captured. To this end, with (1) the mean value of γ in Figure 5.28(C) being evaluated upon an abundance of data and (2) keeping in mind that, in a realistic setting, the availability of sea-states is limited by the duration of the full records, it is instructive to explore how 'quickly' the mean value of γ converges to the target value. For this, Figure 5.29 presents the convergence of the mean γ, $E[\gamma]$, against the number of sea-states used for its evaluation. It can be seen that $E[\gamma]$ converges relatively quickly close to the target value; the number of sea-states necessary to reach satisfactory convergence ($\sim 95\%$) being ~ 40.

Given that failure to capture accurately f_p can have important consequences for the characterisation of a 20-min sea-state, other available methods for estimating f_p have been considered. These methods involve a spectral-density weighted integration of the recorded frequencies proposed independently by Sobey & Young (1986) and Read (1986), and Frigaard et al. (1997). According to Sobey & Young (1986) and Read (1986), the peak frequency can be estimated by the following expression,

$$f_p^n = \Big(\int_0^\infty f S(f)^n df \Big) / \Big(\int_0^\infty S(f)^n df \Big) \tag{5.14}$$

where the integration takes place over the entire f-range. The difference between Sobey & Young (1986) and Read (1986) lays on the adopted value for n; the former proposing $n = 8$ and the latter $n = 5$. However, Young (1995) demonstrated that the optimal value for n is 4, leading to the smallest observed scatter in f_p.

Furthermore, according to Frigaard et al. (1997) f_p can be estimated according to,

$$f_p^D = \Big(\int_{f_1}^{f_2} f S(f) df \Big) / \Big(\int_{f_1}^{f_2} S(f) df \Big) \tag{5.15}$$

where, f_1 and f_2 refer to the frequencies at intercepts of the spectral density at either side of the peak corresponding to 80% of the maximum.

Employing all four estimates for f_p ($f_p^m, f_p^J, f_p^n, f_p^D$) Table 5.7 presents the ratio of their mean estimates over the input or target $f_{p,target}$, along with lower and upper 95% confidence limits for linearly simulated JONSWAP sea-states of $\gamma = 1.5$, 2.5 and 3.5. Based on Table 5.7 the f_p estimated from fitting the JONSWAP spectra, f_p^J, is the optimal method. Unlike the other estimates, f_p^J is an unbiased estimator (mean value of 1.0) and leads to the narrowest confidence intervals.

Table 5.7: Accuracy of different methods for estimating the peak frequency, with r_p symbolising the ratio $f_p/f_{p,target}$.

f_p-estimator	$\gamma = 1.5$			$\gamma = 2.5$			$\gamma = 3.5$		
	$E[r_p]$	$P_{2.5\%}$	$P_{97.5\%}$	$E[r_p]$	$P_{2.5\%}$	$P_{97.5\%}$	$E[r_p]$	$P_{2.5\%}$	$P_{97.5\%}$
f_p^m	1.02	0.90	1.17	1.01	0.93	1.10	1.01	0.98	1.04
f_p^D	1.04	0.99	1.05	1.01	0.94	1.10	1.01	0.99	1.03
$f_p^{n=4}$	1.04	0.96	1.13	1.02	0.96	1.08	1.01	0.99	1.03
f_p^J	1.00	0.94	1.07	1.00	0.95	1.05	1.00	0.99	1.01

Finally, with regards to the other sea-state characteristics, the variability in H_s and the convergence of γ was found not to be affected by the (input) γ value.

Set of sea-states from field data

To extract statistically reliable crest-height distributions from field data, a grouping of 20-min sea-states has to be performed. To this end, in the course of the present analysis, the data-binning approach proposed by Karmpadakis (2018) was adopted. Within this approach, the crest heights of sea-states with H_s and T_p laying between specified intervals are amalgamated to form a representative crest-height distribution for a mean H_s and T_p. Interestingly, in considering the analysis of the previous section, this approach is entirely in line with the fact that both H_s and T_p are expected to vary when the record of the free surface is segmented into shorter 20-min records.

For each platform, the crest-height distribution for bins characterised by $\frac{1}{2}H_s k_p \approx 0.10$ has been mainly considered. While smaller steepnesses have been taken into account when necessary for the purposes of the discussion. Notably, the selected sea-state steepness $\frac{1}{2}H_s k_p \approx 0.10$ relates to the maximum steepness used in the calibration of the HOE-EANN model and typically represents the maximum steepness for which statistically reliable results can be obtained from field data in severe conditions.

The range of H_s and T_p values within the identified bins, along with the relevant non-dimensional sea-state parameters for each platform are presented in Table 5.8. These cover the full range of effective water depths considered in the present thesis ($k_p d \in [0.8, 4.0]$). Additionally, to provide a means of establishing the reliability of the extracted crest-height distributions, sea-states of the same $k_p d$ and $\frac{1}{2}H_s k_p$ arising from different platforms have been considered when available.

Importantly, Table 5.8 presents the water depth at platforms, the mean γ ($E[\gamma]$), and the number of available sea-states. In considering Table 5.8, the number of sea-states used for evaluating $E[\gamma]$ in each bin is sufficient to guarantee converged results according to the analysis of linearly simulated sea-states presented earlier.

Finally, for completeness, the estimation of γ according to the DNV-RP-C205 (2014) guidelines (based on the mean H_s and T_p for each bin) is also presented, denoted with γ_{DNV}. In contrasting the mean measured γ values and γ_{DNV}, the

former are found to be consistently higher than γ_{DNV}, highlighting perhaps the need to revisit the DNV-guidelines. However, this is left as a topic for future research, and it is not further explored here.

Table 5.8: List of sea-states extracted from field data.

Set	Platform	Depth $[m]$	H_s $[m]$	T_p $[s]$	$\frac{1}{2}H_s k_p$ $[-]$	$k_p d$ $[-]$	$E[\gamma]$ $[-]$	γ_{DNV} $[-]$	N_s $[-]$
S1	Magnus	189	8.8-9.4	10.7-14.3	0.10	4.2	2.6	1.9	66
S2	Miller	100	6.9-7.4	11.2-12.2	0.10	3.0	3.4	2.0	117
S3	Gorm	45	4.9-5.5	9.8-11.0	0.10	1.8	2.6	1.6	365
S4	Gorm	45	5.2-5.8	11.2-12.4	0.10	1.5	2.4	1.3	249
S5	Gorm	45	6.5-8.4	11.5-13.7	0.10	1.25	2.4	1.3	64
S6	Gorm	45	6.9-10.4	13.7-16.2	0.10	1.1	2.4	1.0	42
S7	Tyra East	40	4.6-5.2	10.0-11.2	0.10	1.6	2.8	1.3	371
S8	Tyra East	40	5.2-5.8	11.2-12.4	0.10	1.35	2.4	1.0	249
S9	Sean	32.3	4.1-4.6	9.0-10.0	0.10	1.6	2.2	1.7	79
S10	AWG	7.7	1.4-2.2	5.2-6.4	0.10	1.1	1.8	1.2	236
S11	AWG	7.7	1.3-1.9	5.5-6.7	0.10	1.0	1.7	1.0	892
S12	AWG	7.7	1.3-1.9	6.9-8.1	0.08	0.8	1.5	1.0	3444
S13	AWG	7.7	1.5-2.1	6.9-8.1	0.09	0.8	1.6	1.0	1957
S14	AWG	7.7	1.7-2.3	6.9-8.1	0.10	0.8	1.7	1.0	996

Comparisons

In applying the HOE-EANN model, all necessary (input) parameters are provided in Table 5.8, apart from the directional spread which is not available in the dataset. As such, the degree of directionality, σ_θ, has to be assumed. Considering that the standard deviation of the angular distribution associated with storm events typically ranges between 15 and 30° for frequencies around the spectral peak (Ewans, 1998), a value of $\sigma_\theta = 22°$ was adopted for all the sea-states of Table 5.8.

The first set of comparisons between crest-height distributions from field data and the HOE-EANN model are presented in Figure 5.30, where the linear (Rayleigh) and second-order (Forristall, 2000) distributions have also been added for reference. These comparisons concern the binned sea-states $S1$ and $S2$, both of which refer to deep-water conditions, and hence they should match one another. Apart from the

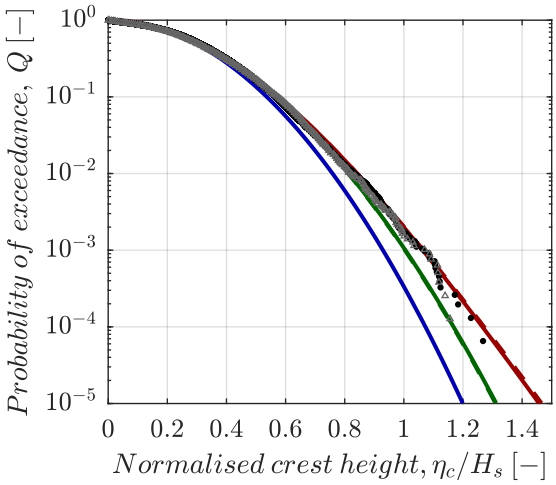
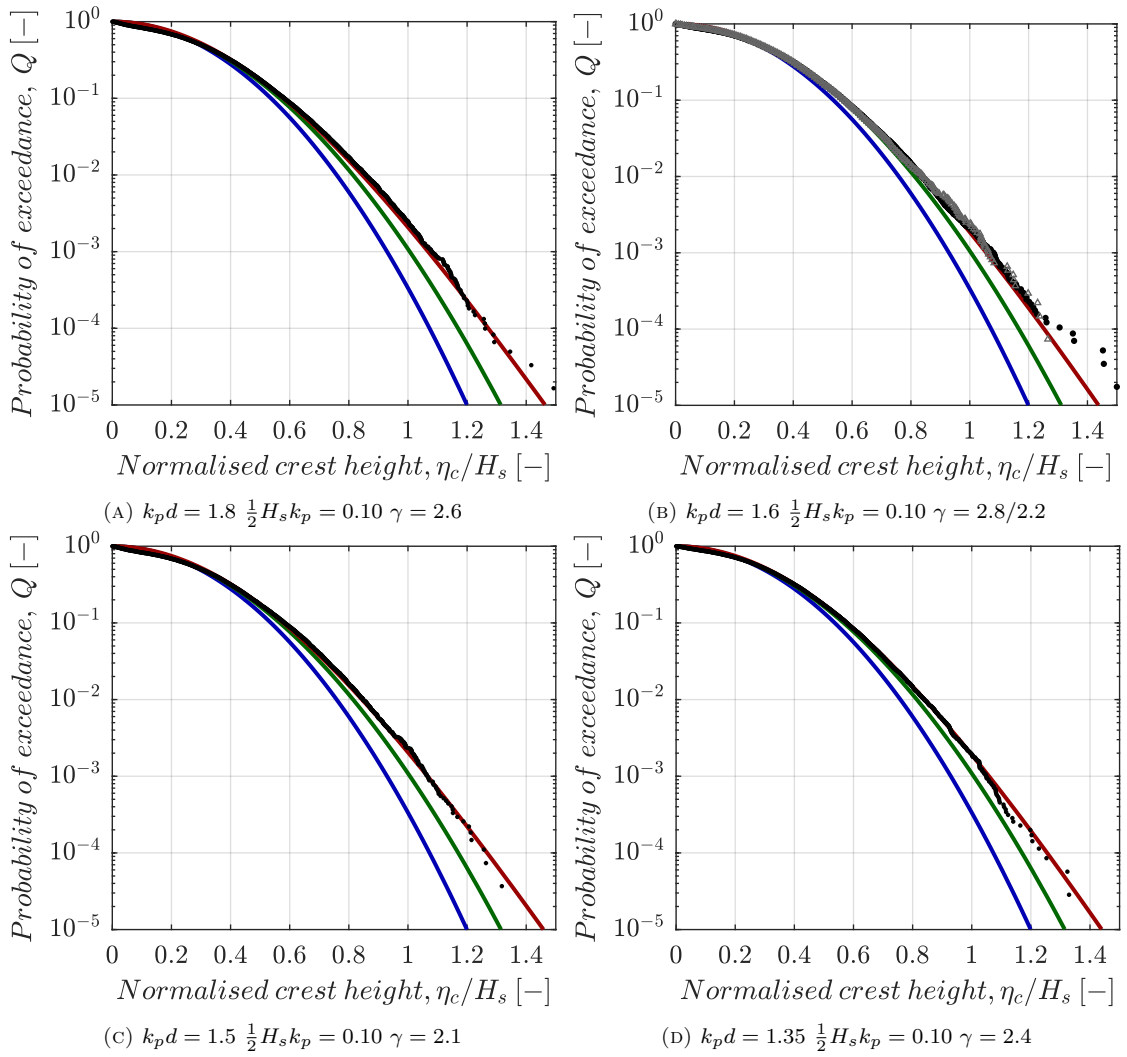


Figure 5.30: Comparison of the HOE-EANN crest-height predictions to distributions from field data: deep-water sea-states $S1$ and $S2$. The different lines refer to: (———) Rayleigh, (——— / – – –) directional Forristall (2000) for $\gamma = 2.6/3.4$, (——— / – – –) HOE-EANN $\gamma = 2.6/3.4$, (•) sea-state $S1$, (△) sea-state $S2$. Note that (———) and (– – –) nearly overlap.

very tail of the distributions, which are subject to large sample variability, this is indeed shown to be the case. A fact that demonstrates the success of the proposed approach in analysing the field data and the accuracy of the measurements. Moreover, the HOE-EANN model predictions agree very well with the measured data of both $S1$ and $S2$; with both predictions and data lying well above the standard Forristall (2000) model. Whereas, it is noted that despite γ being somewhat different for $S1$ and $S2$, neither the data nor the predictions are affected by this difference.

The logic of the comparisons presented in Figure 5.30 is continued in Figure 5.31 for sea-states of progressively lower $k_p d$. This data relate to sea-states S3, S4, S7 (in combination to S9) and S8 of Table 5.8 covering effective water depths in the range $k_p d \in [1.35, 1.8]$. The results, once more, demonstrate a very good agreement between the HOE-EANN model and the crest-height distributions from the field data; all of which depart from the Forristall (2000) model.

Continuing on, Figure 5.32 covers even lower effective water depths in the range $k_p d \in [0.8, 1.25]$. This data arise from sea-states S5, S6 (in combination to S10), S11, S12, S13 and S14. In the shallowest effective water depth it is important to note that sea-states of steepness $\frac{1}{2} H_s k_p = 0.08, 0.09$ and 0.10 have been considered in S12, S13 and S14 respectively. Considering first the sea-states S5, S6 and S11 (shown in sub-figures (A), (C) and (E), respectively), it is observed that HOE-EANN continues to be effective for $k_p d$ as low as 1.0. Considering next the sea-states at



(A) $k_pd = 1.8$ $\frac{1}{2}H_sk_p = 0.10$ $\gamma = 2.6$

(B) $k_pd = 1.6$ $\frac{1}{2}H_sk_p = 0.10$ $\gamma = 2.8/2.2$

(C) $k_pd = 1.5$ $\frac{1}{2}H_sk_p = 0.10$ $\gamma = 2.1$

(D) $k_pd = 1.35$ $\frac{1}{2}H_sk_p = 0.10$ $\gamma = 2.4$

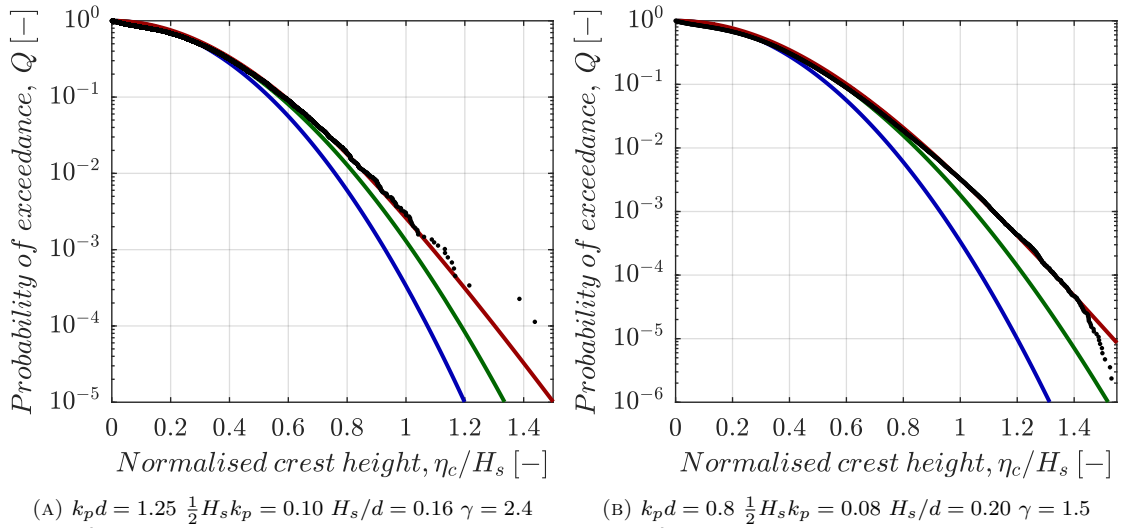
Figure 5.31: Comparison of the HOE-EANN crest-height predictions to distributions from field data for $k_pd \in [1.35, 1.8]$. The different lines refer to: ( ) Rayleigh, ( ) directional Forristall (2000), ( ) HOE-EANN, (•) field data. (A) sea-state $S3$, (B) sea-states $S7$&$S9$, (C) sea-state $S4$, and (D) sea-state $S8$.

$k_p d = 0.8$ (sub-figures (b), (d) and (f)), the tail of the crest-height distribution arising from field data is shown to progressively deviate from the HOE-EANN model as the sea-state steepness increases. More specifically, for $\frac{1}{2}H_s k_p = 0.08$ (sub-figure (b)) the HOE-EANN model performs very well for exceedance probabilities of as low as $4 \cdot 10^{-5}$. However, as the sea-state steepness increases, the deviation between the model predictions and the data start becoming noticeable at higher probabilities of exceedance.

This discrepancy is most likely associated with the dissipative effect of wave breaking, which tends to lower the crest-heights at the tail of the distribution (Latheef & Swan 2013, Karmpadakis et al. 2019a). This is captured neither by HOSM nor by the HOE-EANN model. In particular, in this effective water depth, wave breaking is expected to not only be affected by the wave steepness, $\eta_c k$ [1], but also by depth-limiting effects. This explains why it is only observed in $k_p d = 0.8$ for $\frac{1}{2}H_s k_p = 0.10$ and not in deeper effective water depths. Moreover, the relatively low γ values of these sea-states are also expected to intensify the effect of wave breaking, following laboratory results presented by Haley (2016) on realistic bandwidth focused wave groups of different γ values.

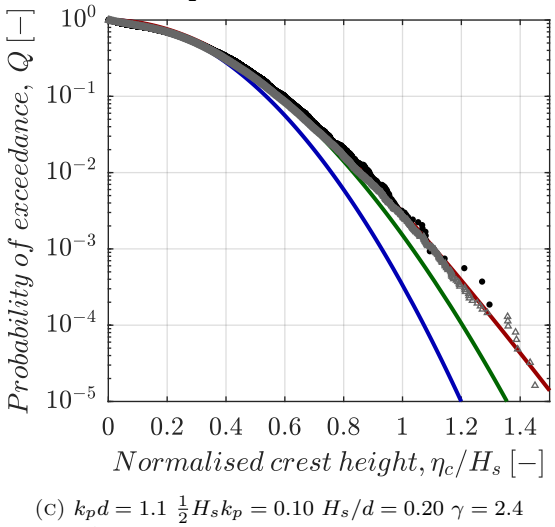
To summarise the results of the present section, it can be concluded that the HOE-EANN model captures very well an extensive range of crest-height distributions arising from the analysis of field data lying in the range $k_p d \in [0.8, 4.0]$, with nonlinear amplification beyond second-order being clearly identified. As such, the model outperforms the standard industry second-order model of Forristall (2000). To the author's knowledge, no previous crest-height model has been validated in this water depth range against field data, especially for such wide set of sea-states. Finally, it should be noted that the crest-height model presented by Karmpadakis (2018), which is based on an entirely different approach (linking crest heights to wave heights) has addressed much lower effective water depths. Moreover the crest-height model developed by Latheef (2014) based on focused wave groups addressed deep-water conditions, with no comparisons to field data being provided. Finally, Karmpadakis & Swan (2022) have presented comparisons of their model (§2.3.3) to crest-height distributions from field data for three binned sea-states with $k_p d = 4.0, 2.45$ and

[1] k referring to the wavenumber of the wave events in the broad sense, with multiple definitions being possible

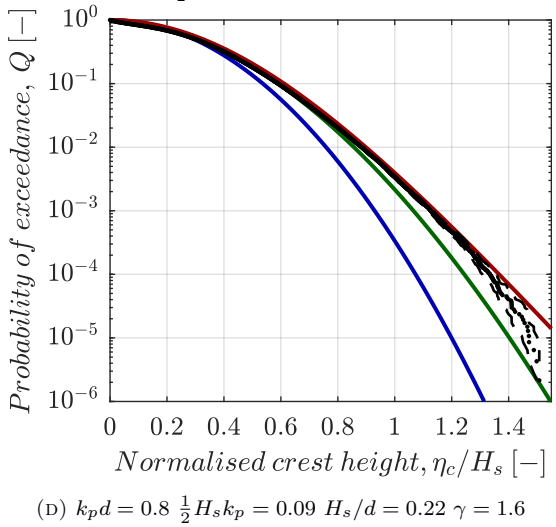


(A) $k_pd = 1.25$ $\frac{1}{2}H_sk_p = 0.10$ $H_s/d = 0.16$ $\gamma = 2.4$

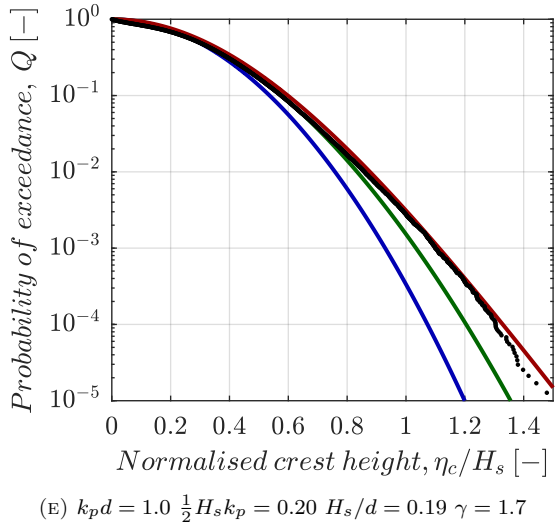
(B) $k_pd = 0.8$ $\frac{1}{2}H_sk_p = 0.08$ $H_s/d = 0.20$ $\gamma = 1.5$



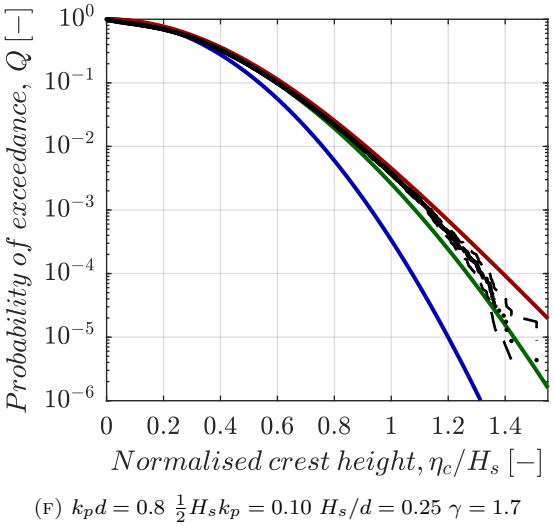
(C) $k_pd = 1.1$ $\frac{1}{2}H_sk_p = 0.10$ $H_s/d = 0.20$ $\gamma = 2.4$



(D) $k_pd = 0.8$ $\frac{1}{2}H_sk_p = 0.09$ $H_s/d = 0.22$ $\gamma = 1.6$



(E) $k_pd = 1.0$ $\frac{1}{2}H_sk_p = 0.20$ $H_s/d = 0.19$ $\gamma = 1.7$



(F) $k_pd = 0.8$ $\frac{1}{2}H_sk_p = 0.10$ $H_s/d = 0.25$ $\gamma = 1.7$

Figure 5.32: Comparison of the HOE-EANN crest-height predictions to distributions from field data for $k_pd \in [0.8, 1.25]$. The different lines refer to: (———) Rayleigh, (———) directional Forristall (2000), (———) HOE-EANN, (•) field data, (— —) 95% confidence intervals. (A) sea-state $S5$, (B) sea-state $S12$, (C) sea-state $S6/S10$, (D) sea-state $S13$, (E) sea-state $S11$, (F) sea-state $S14$.

1.16 and $\frac{1}{2}H_s k_p \in [0.08, 0.10]$. In considering these comparisons, the obtained crest-height distributions contained a fewer number of wave events and hence the sample variability was much larger than the one associated with the present data. While no cross-platform comparisons were obtained. Importantly, no comparisons were presented in $0.8 < k_p d < 1.1$, where the effect of near-resonant interactions is important.

5.4 Wave-breaking correction

The present section aims to extend the applicability of the HOE-EANN model to sea-states for which wave breaking becomes relevant; this extension being necessary if a full long-term analysis is to be performed. To demonstrate the consequences of not including the effect of wave breaking within HOE-EANN, Figure 5.33 presents the comparison of the HOE-EANN model predictions to the experimental crest-height distribution arising in a sea-state of $\frac{1}{2}H_s k_p = 0.16$ in $k_p d = 2.03$ with $\gamma = 2.5$ and $\sigma_\theta = 15°$ (obtained from Latheef & Swan (2013)). It can be seen that the HOE-EANN model over-predicts the measured crest heights. This is clearly due to the dissipative effect of wave breaking.

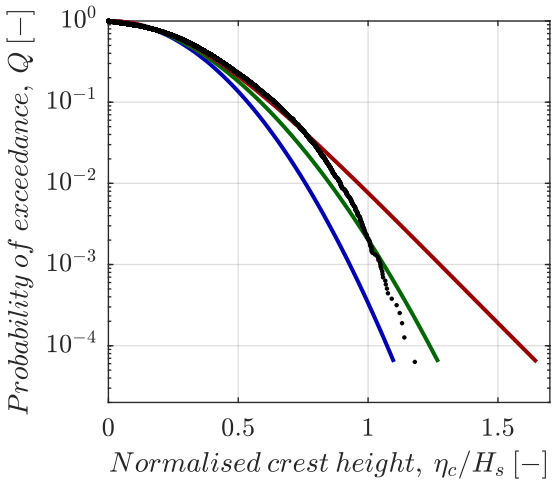


Figure 5.33: Comparison of the HOE-EANN crest-height predictions to experimental crest-height distributions with $k_p d = 2.03$, $\frac{1}{2}H_s k_p = 0.16$, $\gamma = 2.5$ and $\sigma_\theta = 15°$. The different lines refer to: (———) Rayleigh, (———) directional Forristall (2000), (———) HOE-EANN, (•) experimental data.

Inspired by the wave-breaking model proposed by Latheef (2014) which was calibrated based on linear quasi-deterministic focused wave groups (Lindgren 1970, Boccotti 1983 and Tromans et al. 1991), a wave-breaking correction can link the

steepness of the waves to the necessary attenuation of the crests predicted by HOEEANN. In the deep-water study of Latheef (2014) the relevant steepness was defined as $s = Ak_c$. Where A is the amplitude sum of focused wave events linked to a certain probability of exceedance, Q, according to the Rayleigh distribution,

$$A = H_s\sqrt{-log(Q)/8} \tag{5.16}$$

and k_c is the central wavenumber defined as,

$$k_c = \frac{1}{Ag}\sum_{n=1}^{\infty} a_n\omega_n^2 \tag{5.17}$$

where a_n is the amplitude of the wave components associated with the quasi-deterministic focused wave spectrum for a given sea-state (see §3.4.2) and ω_n is the circular frequency of the wave components. Unlike k_p, k_c incorporates the effect of spectral bandwidth. This becomes essential when wave breaking is considered.

In the present analysis, an alternative definition for the steepness was sought to account for depth-limiting wave breaking. For this, the form of the well-known Miche (1944) breaking criterion was employed, which defines the limiting wave height, H_b, of regular waves and is given by,

$$H_b k = 0.89\ \tanh(kd) \tag{5.18}$$

where, k is the wavenumber and d the water depth. In deep water ($\tanh(kd) \to \infty$) the limiting value of $H_b k$ comes independent of depth and equal to 0.89. Assuming that the wave height can be expressed as two times the wave amplitude, A, the criterion in deep water yields the well-known limiting steepness for regular waves $Ak \approx 0.44$ (Michell, 1893).

Retaining the analogy to Equation 5.18, depth-limiting effects can be taken into account in practical terms by considering an effective steepness, s',

$$s' = \frac{Ak_c'}{\tanh(k_c'd)} \quad k_c' = \frac{1}{Ag}\sum_{n=1}^{\infty}\frac{a_n\omega_n^2}{\tanh(k_nd)} \tag{5.19}$$

where k_c' is the finite-depth version of k_c.

To illustrate the effect of water depth on the estimation of the steepness, Figure

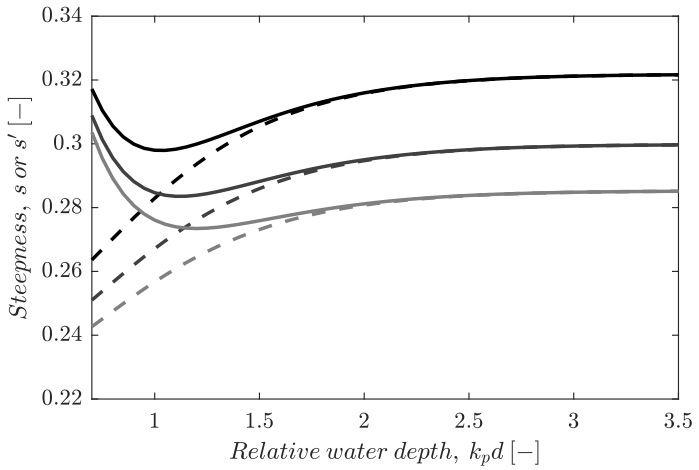


Figure 5.34: Variation of steepness s and s' with effective water depth k_pd for different spectral shapes (γ). s' is represented by (/ /) for $\gamma = 1.5, 2.5$ and 3.5, respectively. While s is represented by (/ / for $\gamma = 1.5, 2.5$ and 3.5, respectively.

5.34 presents the variation of s and s' with k_pd for $\gamma = 1.5, 2.5$ and 3.5, with an amplitude A corresponding to $Q = 10^{-3}$ for sea-states of $\frac{1}{2}H_sk_p = 0.12$.

Figure 5.34 shows that the steepness $s = Ak_c'$ reduces with effective water depth as waves are effectively narrower in bandwidth. However, this reduction is reversed for $k_pd \lesssim 1.0$ with the inclusion of $\tanh(k_c'd)$ in the denominator of s'.

Considering now the wave-breaking correction to the HOE-EANN model, it can be simply calibrated by defining the ratio,

$$f_b = \frac{\eta^Q_{c,exp} - A^Q}{\eta^Q_{c,p} - A^Q} \tag{5.20}$$

where, $\eta^Q_{c,exp}$ is the experimental crest height, $\eta^Q_{c,p}$ is the crest height predicted by HOE-EANN[1], A^Q is the linear crest height given by the Rayleigh distribution. While in all cases the superscript Q denotes that all values refer to a certain probability of exceedance, Q. This ratio essentially represents the attenuation of the nonlinear amplification effects due to wave breaking and can be multiplied to the sum of coefficients r_1, r_2 and r_3 in Equation 5.13 at every Q.

To calibrate f_b, a set of 22 crest-height distributions from the experimental studies of Latheef & Swan (2013), Karmpadakis et al. (2019a) and McCarthy (2018) were

[1]Note that the HOE-EANN model, in this case extrapolates beyond its calibration range. However, it has been thoroughly checked that the EANN predictions extrapolate reasonably beyond $\frac{1}{2}H_sk_p > 0.10$.

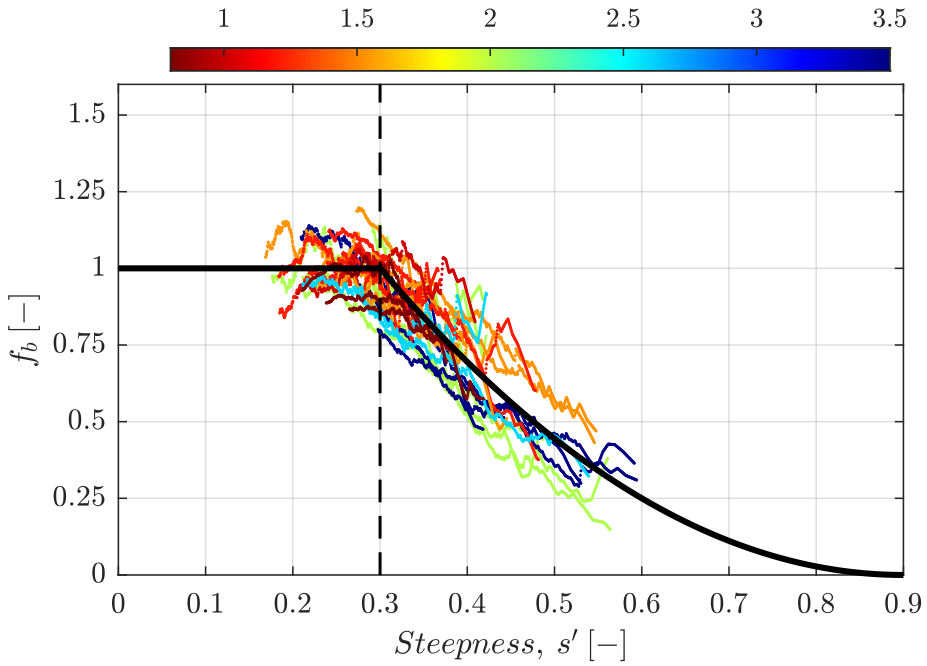


Figure 5.35: Calibration of f_b as a function of s'. The data from 25 sea-states are shown with coloured markers; the colour being according to the corresponding k_pd value. The best-fit trend is shown with (——), while the onset of wave breaking at $s' = 0.3$ is shown with (— —)

employed. These sea-states cover a range of $k_pd \in [1.02, 3.5]$, $\frac{1}{2}H_sk_p \in [0.10, 0.16]$ and $\sigma_\theta \in [10, 30]°$. Additionally, the crest-height distributions originating from field data at $k_pd = 0.8$ were also considered to cover the full range of validity of HOE-EANN in terms of k_pd. Finally, from each crest-height distribution, the crest heights at $Q < 10^{-1}$ were taken into account, similarly to the original calibration of the HOE-EANN.

The resulted variation of f_b with s', is shown in Figure 5.35 for the full set of sea-states. In each case the data are coloured according to the k_pd of the sea-state in which they occur. In considering Figure 5.35, it becomes evident that, whilst some scatter in f_b is observed owing to either the effect of sample variability or other factors that can affect the experimental results (particularly in relation to wave breaking), all experimental and field-data distributions follow a similar trend.

Importantly, wave breaking is shown to become relevant for $s' \gtrsim 0.30$: above this value, f_b starts dropping below unity. The limiting value $s' = 0.30$ is entirely in line with the earlier experimental study of Latheef (2014) based on focused waves. This demonstrates both the universality of the earlier result and the suitability of s' for calibrating f_b in finite water depth. To predict f_b based on s', a best-fit parabolic

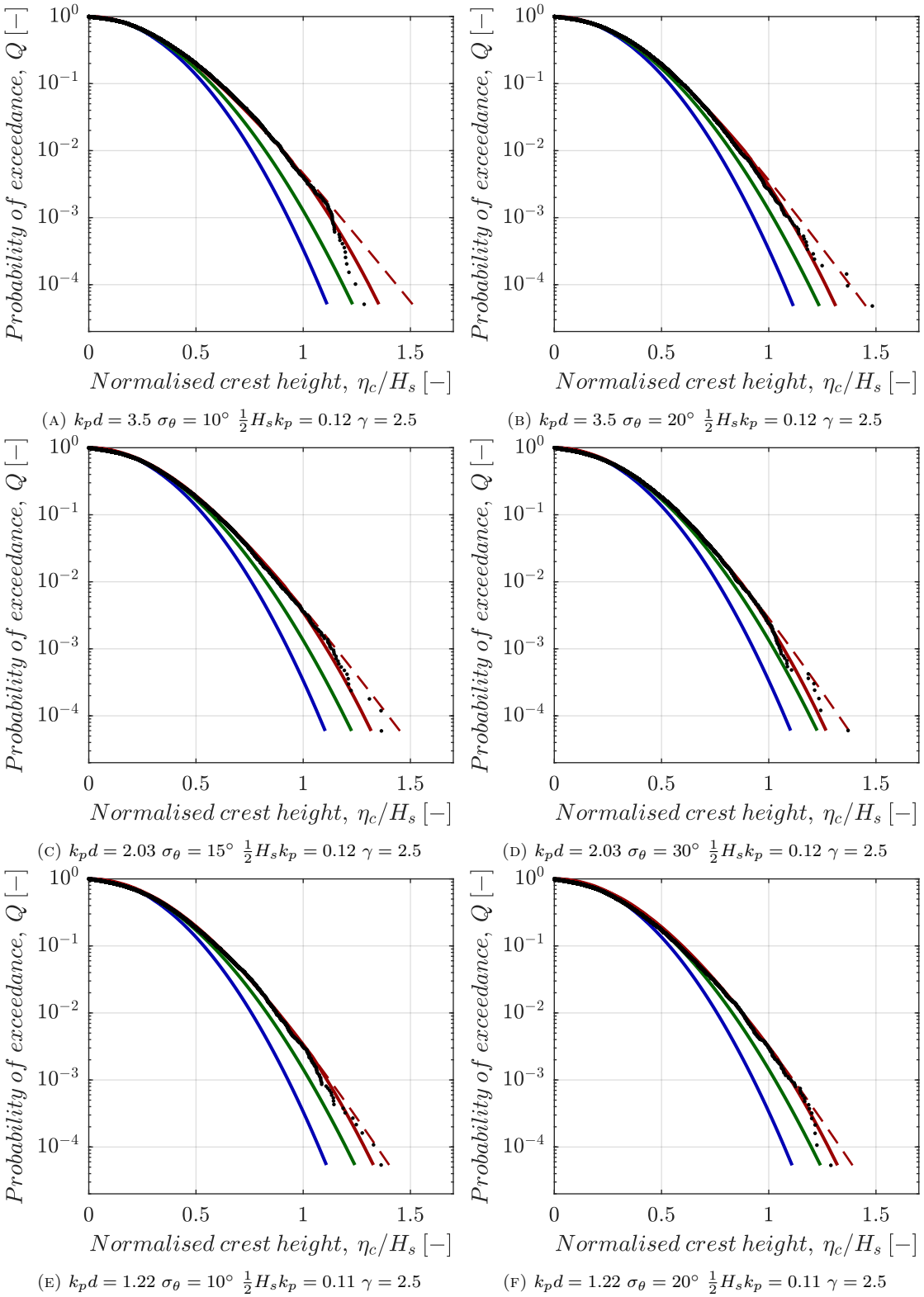
line was fitted to the experimental data for $s' \gtrsim 0.30$. This is given on Figure 5.35 and is defined as follows:

$$f_b = \begin{cases} 1.0 & s' < 0.3 \\ (1.667 \cdot (s' - 0.9))^2 & s' \geq 0.3 \end{cases} \tag{5.21}$$

Having defined f_b, its effectiveness in correcting the HOE-EANN predictions for the effect of wave breaking can be assessed. To differentiate between the original HOE-EANN predictions and the predictions that include f_b, the latter will be referred to as HOE-EANN-B. Figure 5.36 presents comparisons of both the HOE-EANN and the HOE-EANN-B predictions to the available experimental crest-height distributions associated with a sea-state steepness in the range $\frac{1}{2}H_s k_p = [0.11, 0.12]$; the exact sea-state conditions defined in the individual captions In all cases, the HOE-EANN-B is shown to outperform HOE-EANN, especially for the steepest of the cases ($\frac{1}{2}H_s k_p = 0.12$), where the effect of wave breaking is more noticeable.

Figure 5.37 concerns the most severe sea-states, presenting comparisons between both HOE-EANN and HOE-EANN-B and experimental crest-height distributions recorded in sea-states with steepness in the range $\frac{1}{2}H_s k_p = [0.14, 0.16]$. In this case, HOE-EANN leads to unrealistically high predictions, as previously noted. However, HOE-EANN-B successfully incorporates the effect of wave breaking; any small deviations being expected due to (1) the approximations underpinning the calibration of f_b and (2) the inherent statistical variability of the data at the lowest exceedance probability levels.

Finally, Figure 5.38 concerns the two breaking sea-states extracted from the field-data analysis presented earlier, namely $S13$ and $S14$ on Table 5.8. In considering the comparisons presented in Figure 5.38, f_b is once again shown to effectively capture the effect of wave breaking, even for sea-states with $k_p d$ as low as 0.8. Taking the results of the present section as a whole, the factor f_b, expressed as a function of s', successfully models the effect of wave breaking on the crest-height distribution.



(A) $k_pd = 3.5$ $\sigma_\theta = 10°$ $\frac{1}{2}H_sk_p = 0.12$ $\gamma = 2.5$

(B) $k_pd = 3.5$ $\sigma_\theta = 20°$ $\frac{1}{2}H_sk_p = 0.12$ $\gamma = 2.5$

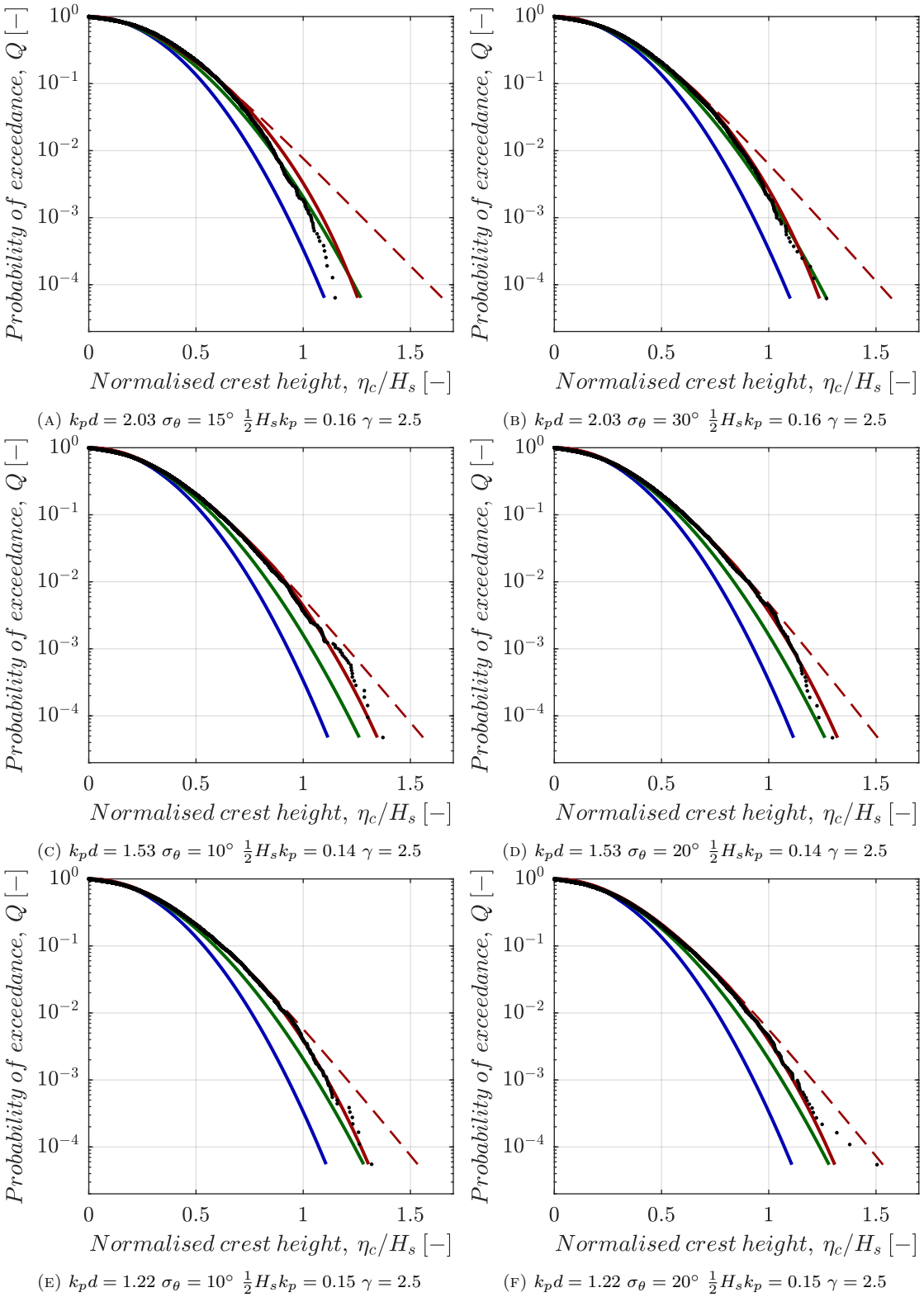
(C) $k_pd = 2.03$ $\sigma_\theta = 15°$ $\frac{1}{2}H_sk_p = 0.12$ $\gamma = 2.5$

(D) $k_pd = 2.03$ $\sigma_\theta = 30°$ $\frac{1}{2}H_sk_p = 0.12$ $\gamma = 2.5$

(E) $k_pd = 1.22$ $\sigma_\theta = 10°$ $\frac{1}{2}H_sk_p = 0.11$ $\gamma = 2.5$

(F) $k_pd = 1.22$ $\sigma_\theta = 20°$ $\frac{1}{2}H_sk_p = 0.11$ $\gamma = 2.5$

Figure 5.36: Comparison of the HOE-EANN and HOE-EANN-B crest-height predictions to distributions from experimental data for sea-states of $\frac{1}{2}H_sk_p \in [0.11, 0.12]$ and $k_pd \in [1.22, 3.5]$. The different lines refer to: (———) Rayleigh, (———) directional Forristall (2000), (———) HOE-EANN-B, (– – –) HOE-EANN, (•) experiments. The data in (A) and (B) originate from McCarthy (2018), in (C) and (D) from Latheef & Swan (2013), while in (E) and (F) from Karmpadakis et al. (2019a).



(A) $k_pd = 2.03$ $\sigma_\theta = 15°$ $\frac{1}{2}H_sk_p = 0.16$ $\gamma = 2.5$

(B) $k_pd = 2.03$ $\sigma_\theta = 30°$ $\frac{1}{2}H_sk_p = 0.16$ $\gamma = 2.5$

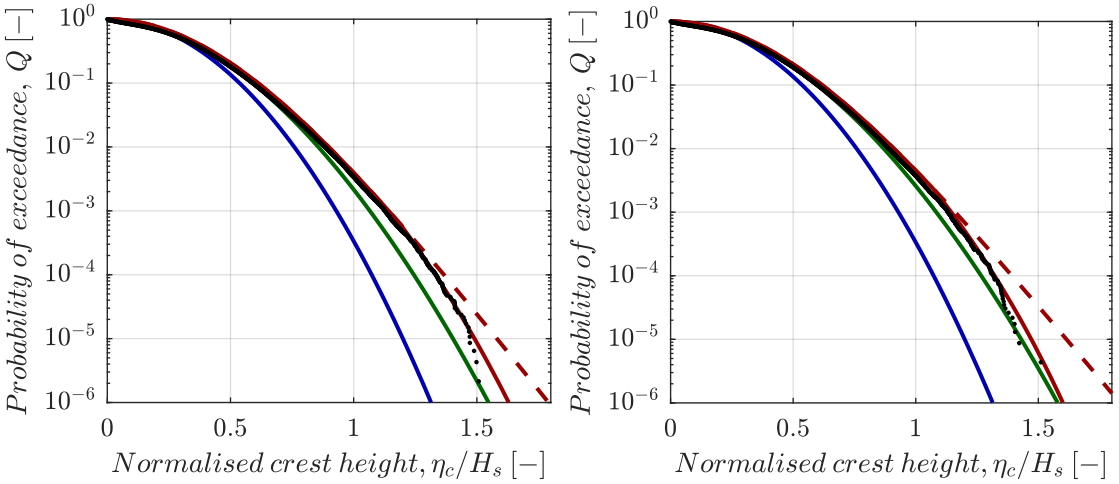
(C) $k_pd = 1.53$ $\sigma_\theta = 10°$ $\frac{1}{2}H_sk_p = 0.14$ $\gamma = 2.5$

(D) $k_pd = 1.53$ $\sigma_\theta = 20°$ $\frac{1}{2}H_sk_p = 0.14$ $\gamma = 2.5$

(E) $k_pd = 1.22$ $\sigma_\theta = 10°$ $\frac{1}{2}H_sk_p = 0.15$ $\gamma = 2.5$

(F) $k_pd = 1.22$ $\sigma_\theta = 20°$ $\frac{1}{2}H_sk_p = 0.15$ $\gamma = 2.5$

Figure 5.37: Comparison of the HOE-EANN and HOE-EANN-B crest-height predictions to distributions from experimental data for sea-states of $\frac{1}{2}H_sk_p \in [0.14, 0.16]$ and $k_pd \in [1.22, 2.0]$. The different lines refer to: (———) Rayleigh, (———) directional Forristall (2000), (———) HOE-EANN-B, (– – –) HOE-EANN, (•) experiments. The data in (A) and (B) originate from Latheef & Swan (2013) and in (C)-(F) originate from Karmpadakis et al. (2019a).



(A) $k_pd = 0.8$ $\sigma_\theta = 22°$ $\frac{1}{2}H_sk_p = 0.09$ $\gamma = 1.6$ (B) $k_pd = 0.8$ $\sigma_\theta = 22°$ $\frac{1}{2}H_sk_p = 0.10$ $\gamma = 1.7$

Figure 5.38: Comparison of the HOE-EANN and HOE-EANN-B crest-height predictions to distributions from field data for sea-states in $k_pd = 0.8$. The different lines refer to: (———) Rayleigh, (———) directional Forristall (2000), (———) HOE-EANN-B, (– – –) HOE-EANN, (•) field data. The data in (A) refer to sea-state $S13$ and the data in (B) refer to sea-state $S14$.

However, the effectiveness of the breaking model has thus far been assessed for the sea-states used in its calibration. Hence, it would be interesting to assess the validity of the predictions for a broader and independent set of sea-state conditions, specifically steeper and/or shallower sea-states. To perform such comparisons, the range of the applicability of the EANN predictions should be defined such that any extrapolation is reasonable. This definition is provided in Appendix I, where it is shown that the predictions for the statistical moments follow the expected trends for sea-states lying within the range $\frac{1}{2}H_sk_p < 0.19\tanh(k_pd)$.

Having defined the range of validity of the EANN predictions, additional comparisons to available experimental data for $k_pd > 1.0$ and field data for $k_pd < 1.0$ have been considered laying within the proposed range of validity; the field data being recorded in the AWG platform of Table 5.6. These additional sea-states are presented in Figure 5.39 in the $(k_pd, \frac{1}{2}H_sk_p)$ parameter space, together with the proposed range of validity of the EANN predictions and the data that have already been used either in the calibration or validation of the HOE-EANN-B model. It is shown that these additional sea-states are indeed either steeper or shallower than any data used thus far, and include sea-states close to the proposed limit of validity of the EANN predictions.

The comparisons to the additional experimental data in $k_pd > 1.0$ are presented in Figures 5.40 and 5.41; the former referring to sea-states with $\sigma_\theta = 10°$ and the latter

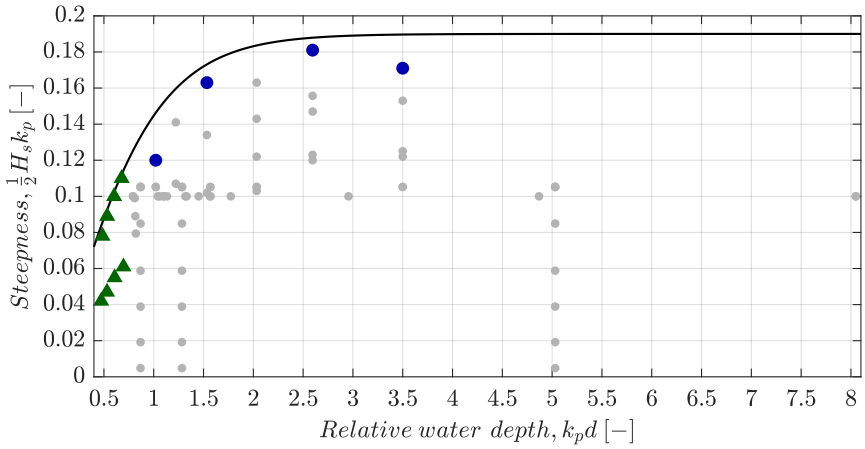


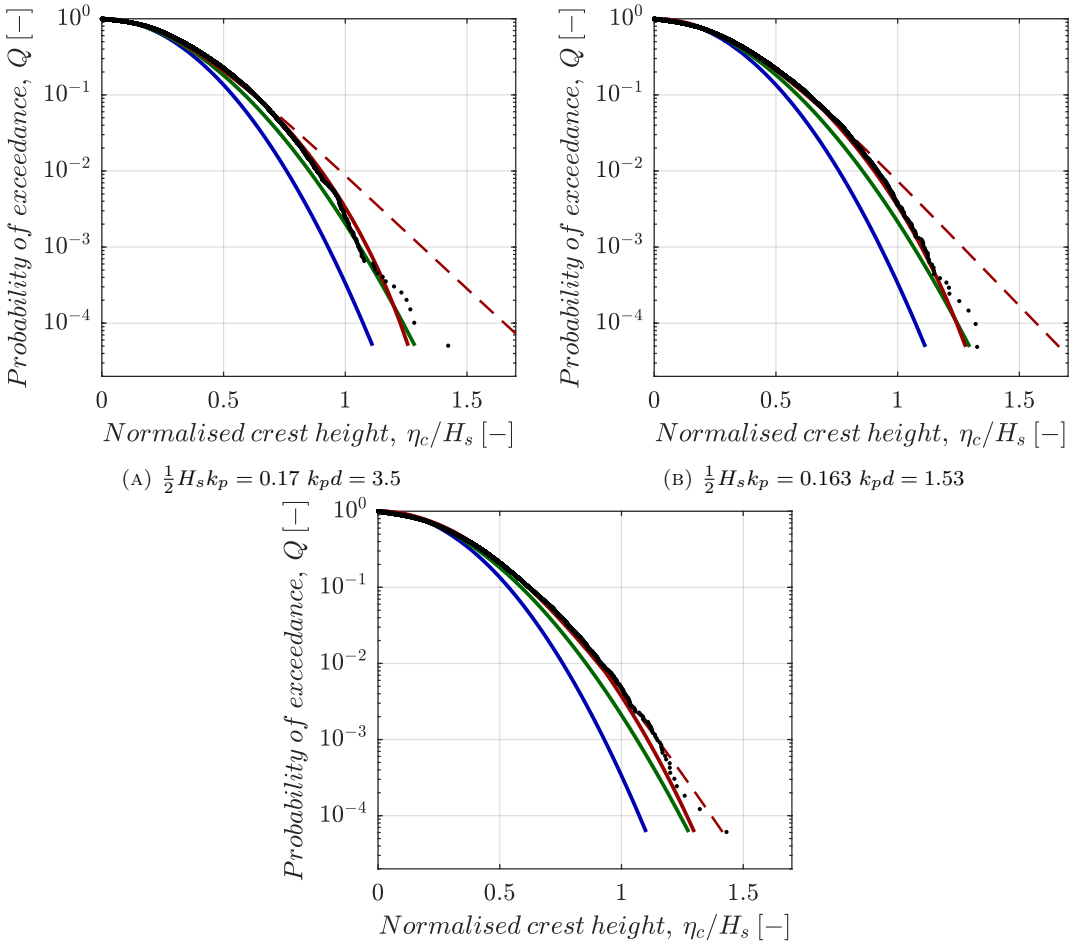
Figure 5.39: Available sea-states for additional validation of the HOE-EANN (-B) model and the proposed limit of validity. The data are presented in the $(k_p d, \frac{1}{2}H_s k_p)$ parameter space together with the data used in its calibration and validation thus far. The line (——) refers to the limit of validity of the EANN predictions for the statistical moments. Regarding the different markers, (•) refers to the additional experimental data and (▲) to the additional field data; while (•) refers to sea-states used in the calibration or validation thus far.

with $\sigma_\theta = 20°$ [1]. The sea-state characteristics are defined in caption of each sub-figure. In each case, the linear (Rayleigh) and second-order directional (Forristall, 2000) predictions are also added for reference. Considering these comparisons, the HOE-EANN-B model is shown to perform effectively even for sea-states not used in its calibration, with $k_p d$ as low as 1.02.

Comparisons between the HOE-EANN-B model and field data for $k_p d < 1$ are presented in Figure 5.42; the sea-state characteristics again being provided in each caption. To facilitate these comparisons, the linear (Rayleigh) and second-order (Forristall, 2000) predictions are also added for reference. Similarly to §5.3.4, the data-binning approach was followed to extract these distributions; the bin size being identical to sea-states S10-S14 in Table 5.8 recorded in the same platform. The number of sea-states in each bin was sufficient for an accurate estimation of γ. In accordance with the comparisons presented in Figures 5.30, 5.31 and 5.32, the degree of directional spreading was assumed to be $\sigma_\theta = 22°$.

Considering Figure 5.42, the sub-figures on the left refer to low steepness sea-states characterised by $H_s/d = 0.18$, for which the effect of wave breaking is not expected to be significant. Indeed, in these cases, the HOE-EANN and HOE-EANN-B

[1]Note that a sea-state with $\frac{1}{2}H_s k_p = 0.18$, $k_p d = 2.6$ and $\sigma_\theta = 10°$ is not available.

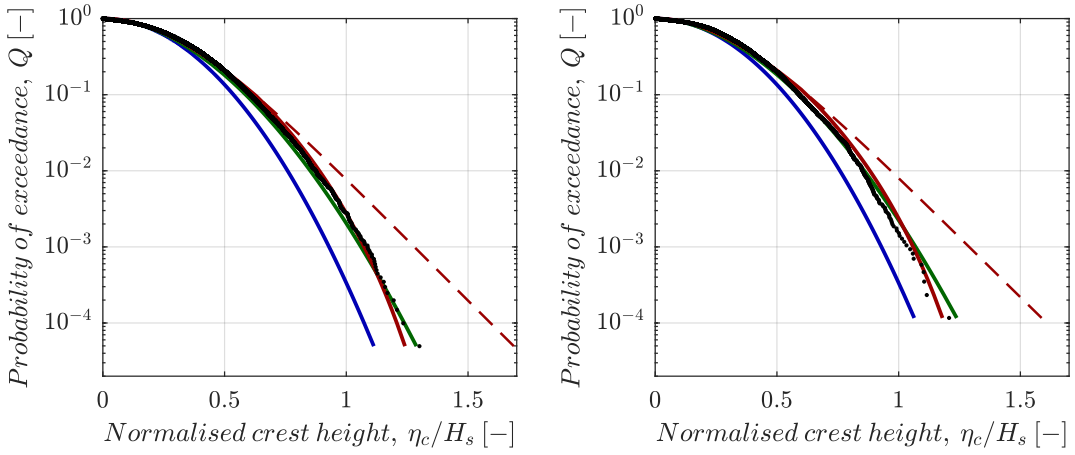


(A) $\frac{1}{2}H_s k_p = 0.17$ $k_p d = 3.5$

(B) $\frac{1}{2}H_s k_p = 0.163$ $k_p d = 1.53$

(C) $\frac{1}{2}H_s k_p = 0.12$ $k_p d = 1.02$

Figure 5.40: Comparison of the HOE-EANN and HOE-EANN-B crest-height predictions to distributions from experimental data in $k_p d > 1.0$ with $\sigma_\theta = 10°$. The employed sea-states lay close to the limits of validity of the EANN predictions. The different lines refer to: (———) Rayleigh, (———) directional Forristall (2000), (———) HOE-EANN-B, (– – –) HOE-EANN, (•) experimental data. The data in (A) originate from Latheef & Swan (2013) and in (B) & (C) originate from Karmpadakis et al. (2019a). For all sea-states $\gamma = 2.5$.



(A) $\frac{1}{2}H_s k_p = 0.17$ $k_p d = 3.5$

(B) $\frac{1}{2}H_s k_p = 0.18$ $k_p d = 2.6$

(C) $\frac{1}{2}H_s k_p = 0.163$ $k_p d = 1.53$

(D) $\frac{1}{2}H_s k_p = 0.12$ $k_p d = 1.02$

Figure 5.41: Same as Figure 5.40 but this time the sea-states are characterised by $\sigma_\theta = 20°$. The data in (A) & (B) originate from McCarthy (2018) and the data in (C) & (D) from Karmpadakis et al. (2019a). For all sea-states $\gamma = 2.5$.

predictions are identical as the breaking correction is not activated. Notably, the HOE-EANN model is very effective in capturing the nonlinearity arising in sea-states with k_pd as low as ~ 0.50. Interestingly, it is observed that whilst both observations and the HOE-EANN predictions exhibit amplification with respect to the Forristall (2000) distribution for $k_pd = 0.7$, this amplification is reduced as k_pd reduces further. Notably, for $k_pd = 0.53$ an agreement with Forristall (2000) is observed, whilst for an even lower effective water depth of $k_pd = 0.48$ the crest heights lay below Forristall (2000). This observation is due to the effect of energy defocusing in this water-depth regime that is not captured by any existing crest-height model. Indeed, the sea-states used by Karmpadakis & Swan (2022) to calibrate their model in $k_pd = 0.5$ were much steeper, with $\frac{1}{2}H_sk_p \approx 0.13$. As such, wave nonlinearity and significant breaking coexisted. Hence, the nonlinear crest-height corrections, which were calibrated upon data with $k_pd > 1$, are extrapolated significantly when the Karmpadakis & Swan (2022) model is applied in $k_pd \approx 0.5$. Indeed, independent comparisons presented in Appendix J show that Karmpadakis & Swan (2022) model significantly over-predicts the crest heights for sea-states of moderate steepness ($\frac{1}{2}H_sk_p \lesssim 0.105$) in $k_pd < 1.0$. The data used for assessing Karmpadakis & Swan (2022) in $k_pd < 1.0$ refer to both the field data presented in Figure 5.42 and the extensive set of HOSM simulations used to calibrate HOE-EANN. This over-prediction stems from the neglect of the effect of near-resonant interactions that tend to reduce the crest-heights.

Comparisons relating to steeper sea-states are presented in the right-hand-side sub-figures in Figure 5.42. Considering these latter comparisons, the HOE-EANN-B predictions are again found to be in very good agreement with the observations. Importantly, the wave breaking factor is shown to be very effective, even outside the original k_pd range ($k_pd \in [0.8, 3.5]$) upon which it was calibrated. Finally, the HOE-EANN predictions that do not include the effect of wave breaking are shown to lay below the Forristall (2000) predictions in all cases. This demonstrates that the competing effect of third-order near-resonant interactions and bound contributions leads to reduced crest-heights with respect to the industry-standard second-order Forristall (2000) model. In making these comparisons, questions should be raised as to the validity (convergence) of the second-order solution. This has been addressed by Hadjigeorgiou (2018). Assuming it is valid, it appears that both the effect of third-order near-resonant interactions and the wave breaking are responsible for the

over-estimation of the crest-heights by Forristall (2000).

Regarding the performance of Karmpadakis & Swan (2022) for the more severe sea-states at the right-hand-side of Figure 5.42, the model is again shown in Appendix J to over-estimate the observations. However, in this case, the extent of the over-prediction is reduced. This is because, with an increase in steepness, the model is applied closer to the data upon it was calibrated. In considering the advancements that HOE-EANN-B offers in relation to Karmpadakis & Swan (2022); three points should be noted:

1. Both models are applicable for sea-states in $k_p d > 1.0$. However, HOE-EANN-B better captures the nonlinear crests simulated using HOSM. The explanation for this is: (a) unlike Karmpadakis & Swan (2022), HOE-EANN-B includes the effect of directional spreading and spectral bandwidth and (b) the formulation of HOE-EANN-B is more effective.

2. HOE-EANN-B performs better than Karmpadakis & Swan (2022) for sea-states in $k_p d < 1.0$, as long as both models are applied within their range of applicability. To this end, it should be mentioned that the proposed range of validity of Karmpadakis & Swan (2022) extends to steeper sea-states than HOE-EANN-B.

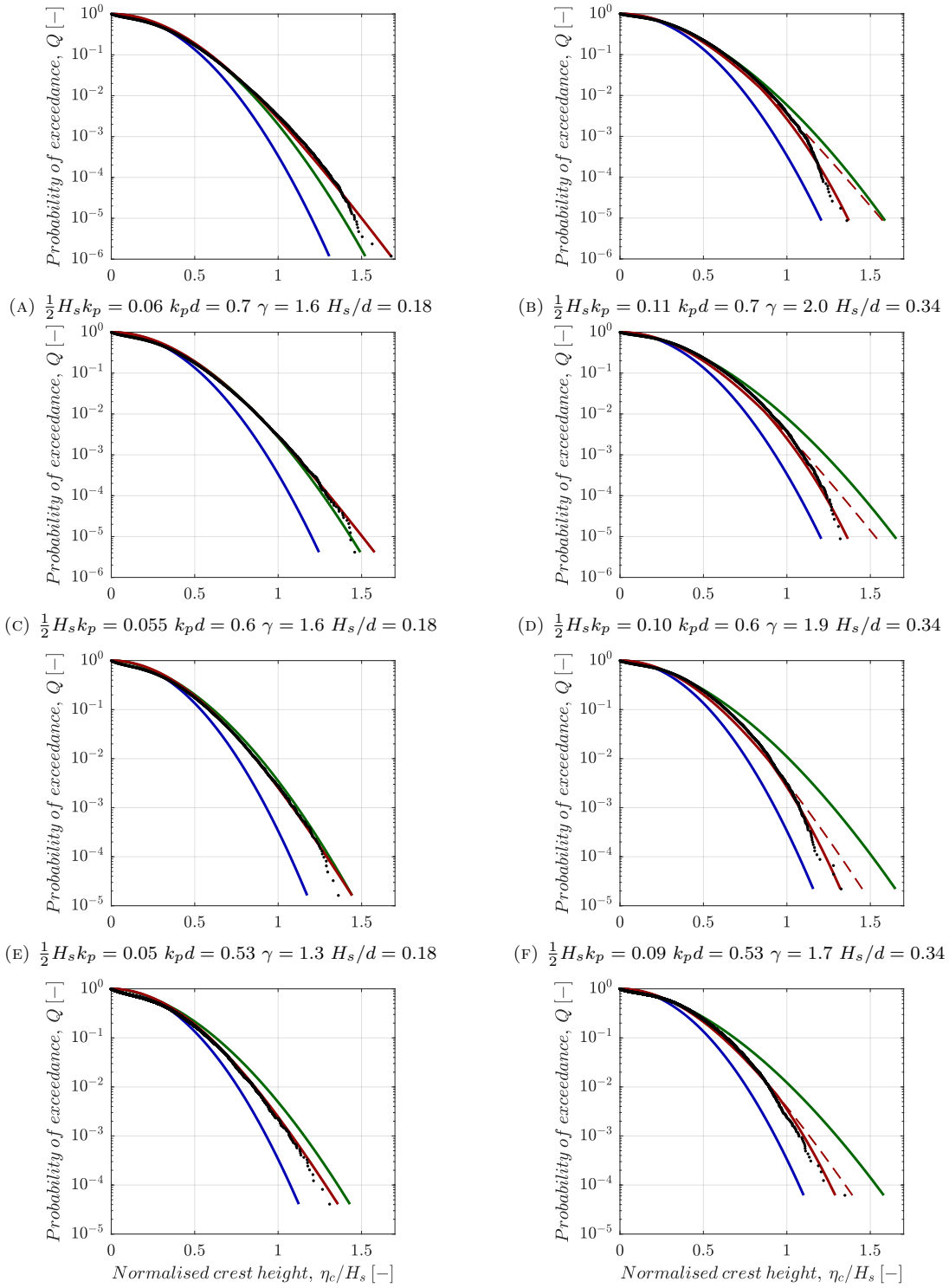
3. The discrepancies between Karmpadakis & Swan (2022) and field or numerical data in $k_p d < 1.0$ are due to the effect of near-resonant interactions, which are not accounted for by Karmpadakis & Swan (2022).

The above points are supported by additional comparisons presented in Appendix J.

5.5 Conclusions

The present chapter concerned the effective prediction of the fully nonlinear crest-height distribution arising in JONSWAP sea-states with an effective water-depth range of $k_p d \in [0.5, 8.0]$ and steepness $\frac{1}{2} H_s k_p < 0.19 \tanh(k_p d)$. In summary,

1. A novel approach was proposed for predicting the crest-height distribution that is fully predictive and takes into account the contributions from the different nonlinear interactions separately.



(A) $\frac{1}{2}H_s k_p = 0.06$ $k_p d = 0.7$ $\gamma = 1.6$ $H_s/d = 0.18$

(B) $\frac{1}{2}H_s k_p = 0.11$ $k_p d = 0.7$ $\gamma = 2.0$ $H_s/d = 0.34$

(C) $\frac{1}{2}H_s k_p = 0.055$ $k_p d = 0.6$ $\gamma = 1.6$ $H_s/d = 0.18$

(D) $\frac{1}{2}H_s k_p = 0.10$ $k_p d = 0.6$ $\gamma = 1.9$ $H_s/d = 0.34$

(E) $\frac{1}{2}H_s k_p = 0.05$ $k_p d = 0.53$ $\gamma = 1.3$ $H_s/d = 0.18$

(F) $\frac{1}{2}H_s k_p = 0.09$ $k_p d = 0.53$ $\gamma = 1.7$ $H_s/d = 0.34$

(G) $\frac{1}{2}H_s k_p = 0.04$ $k_p d = 0.48$ $\gamma = 1.4$ $H_s/d = 0.18$

(H) $\frac{1}{2}H_s k_p = 0.08$ $k_p d = 0.48$ $\gamma = 1.4$ $H_s/d = 0.34$

Figure 5.42: Comparison of the HOE-EANN and HOE-EANN-B crest-height predictions to distributions from field data in $k_p d < 1.0$ The left column refers to sea-states with $H_s/d = 0.18$ and the right column to $H_s/d = 0.34$. The sea-state characteristics are defined in the caption of each sub-figure. The different lines refer to: (———) Rayleigh, (———) directional Forristall (2000), (———) HOE-EANN-B, (– – –) HOE-EANN and (•) field data. The mean T_p corresponding to each data-bin is 8.7, 9.8, 11.0 and 12.2s, for each row of sub-figures respectively, and $d = 7.7$.

2. This approach relied on the empirical calibration of geometric coefficients that described the crest-height distribution based on the statistical moments of skewness, bound kurtosis and dynamic kurtosis.

3. The prediction of the statistical moments was achieved through a novel approach that relied on the Ensemble Artificial Neural Network approach. Where special care was devoted to guaranteeing a good generalisation performance. This approach outperformed other methods available from the field of so-called meta-modelling techniques.

4. The proposed crest-height model, referred to as HOE-EANN, was extensively validated against additional numerical, experimental and field data; with excellent comparisons being observed in all cases.

5. An extension to the HOE-EANN model to include the effect of wave breaking was also proposed. This extension was achieved by introducing a crest-attenuation factor calibrated based on a single steepness parameter using existing experimental data and present field data. The comparison of the breaking-corrected HOE-EANN model, referred to as HOE-EANN-B, against experimental and field-data crest-height distributions demonstrated the effectiveness of the proposed approach, even when applied outside the range upon which it was calibrated.

6
Concluding remarks

The safe and economical design of offshore structures or the effective planning of marine operations requires an accurate account of the largest waves that will be encountered during their lifetime. In this regard, the present thesis has focused on two main aspects: (1) the understanding of the mechanisms that lead to the formation of large waves in a variety of sea-states and (2) the calibration of a new model to effectively predict the short-term crest-height distribution. In achieving these two main goals, the present research has:

1. Thoroughly validated the Higher-Order Spectral Model (HOSM) applied to a very wide range of uni-directional and directional seas; covering deep to intermediate effective water depths in the range $k_p d \in [0.87, 5.03]$.

2. Separated the near-resonant and bound-wave interactions; identifying the conditions at which these two different types of interactions have either an *allied* or *competing* influence on the magnitude of the largest crest-heights.

3. Explored the suitability of the industry-standard second-order crest-height model of Forristall (2000).

4. Assessed the validity of the narrow-band theoretical solutions for the statistical moments of skewness, bound kurtosis and dynamic kurtosis, which are currently incorporated in operational freak-wave forecasting models.

5. Calibrated and thoroughly validated a new crest-height model. This model relies on (a) the accurate prediction of the statistical moments of skewness, bound kurtosis and dynamic kurtosis based on a set of 4 key sea-state parameters utilising tools from the field of machine learning and (b) the parameterisation of the crest-height distribution based on these three statistical parameters. This model was calibrated based on HOSM simulations that do not include the dissipative effect of wave breaking. To account for this effect, a wave-breaking correction factor was introduced, extending the applicability of the model to severe sea-states.

Section §6.1 presents a more detailed account of the main contributions. This is followed by §6.2 which makes recommendations for future research, building on successes outlined in this thesis.

6.1 Research contributions

6.1.1 Improved physical insights

Uni-directional sea-states

The analysis concerning uni-directional conditions has revealed some new physical insights:

(i) In sea-states with realistic frequency spectra, near-resonant interactions lead to the focusing of wave energy in $k_p d > 1.36$ and to defocusing in $k_p d \in [0.87, 1.36)$. This is in accord with earlier theoretical results based on a narrow-band assumption (Janssen & Onorato, 2007). However, the intensity of the energy defocusing is lower than narrow-band theory.

(ii) The time needed for the full development of near-resonant interactions is directly linked to their intensity; over 40 peak periods required to reach steady-state conditions in the most extreme cases.

(iii) The transient behaviour of the near-resonant interactions profoundly affects the crest-height distribution arising at different evolution times. Specifically,

for short evolution times, for which near-resonant interactions are not developed, the magnitude of the crest-heights is governed by Stoke's type or bound-wave interactions. As such, in the shallowest effective water depths, the crest heights appear higher than in deep water. However, this 'picture' changes as time evolves; the crest-heights in deep water being higher than in shallower conditions when a steady state is reached.

(iv) For uni-directional seas, the effect of sea-state steepness, spectral bandwidth and effective water depth on the most probable maximum crest height arising in a 3-hour storm was studied in detail. The key points of this investigation are summarised as follows:

a) The effect of near-resonant interactions monotonically increases with sea-state steepness; casting doubt on the validity of the second-order theory of Longuet-Higgins & Stewart (1960) and Sharma & Dean (1981) even for relatively small sea-state steepnesses.

b) Changes in spectral bandwidth affect the near-resonant interactions and bound-wave interactions differently; the former decreasing and the latter increasing with an increase in spectral bandwidth.

c) With a reduction in the effective water depth below $k_p d = 1.36$, bound-wave contributions and near-resonant interactions have a competing influence on the largest crest heights. However, the bound-wave contributions exceed the crest attenuation due to near-resonant interactions in all cases; giving rise to amplified crests compared to linear predictions.

Directional sea-states

The introduction of directionality was found to influence the above points regarding uni-directional seas in a variety of ways:

(i) In deep water ($k_p d \gtrsim 2.0$), the introduction of even a small degree of directional spreading ($\sigma_\theta = 5^\circ$) substantially reduces the energy focusing observed in uni-directional seas. Moreover, a further increase in σ_θ can lead to the inversion of the phenomenon; the waves being in a weak defocusing state for $\sigma_\theta \gtrsim 10^\circ$. In this regard, directional dispersion was found to dominate nonlinear dispersion; the latter being responsible for the energy focusing in uni-directional seas.

(ii) In intermediate water depth conditions of $k_p d \lesssim 1.0$, nonlinear dispersion effects are governed by the effect of the wave-induced 'mean flow'. An effect that persisted even in directional sea-states. Specifically, whilst directionality leads to an attenuation of the 'mean flow', its decrease with directionality is relatively weak. As such, near-resonant interactions attenuate the largest waves arising in directionally spread seas in this effective water-depth regime. This observation contrasts with the reduced importance of near-resonant interactions in deep-water conditions.

(iii) The effect of the evolution time is not relevant in deep-water directional seas; the near-resonant interactions being weak. This is not the case for water depths of $k_p d \lesssim 1.0$. In this case about 10 peak periods are required to reach a steady state for sea-states of $\sigma_\theta = 10°$. This observation may have significant implications for effective experimental modelling in directional wave basins operating in intermediate water depths.

(iv) Concentrating in this directional spreading ($\sigma_\theta = 10°$), for short evolution times, the crest heights were found to be larger as the effective water depth decreased. However, as steady-state conditions are reached, the magnitude of the largest waves is not affected by the effective water depth. This is explained by the balancing between nonlinear effects: the competing influence of near-resonant interactions and bound-wave contributions; the former attenuating the crest heights and the latter increasing them progressively with decreasing in $k_p d$.

(v) However, for larger directional spreads, the crest amplification was dependent upon $k_p d$; with the crest heights being more amplified as the effective water depth reduces.

(vi) The effect of spectral bandwidth in directionally spread seas was also addressed. Despite the profound effect of spectral bandwidth on the development of near-resonant interactions in uni-directional seas, its equivalent effect in directional seas was substantially reduced. However, it remained equally relevant when the bound contributions were considered.

6.1.2 Improved engineering approaches

1. The applicability of the Forristall (2000) model was assessed. It was found that, under the influence of third-order nonlinearity and above, the model significantly under-predicted the crest heights in deep water. However, as the effective water depth reduces, the deviations from the Forristall (2000) model were found to decrease. Interestingly, for an effective water depth of $k_p d = 0.87$ the fully nonlinear crest heights were found to be in a good agreement with Forristall (2000) for $\sigma_\theta \lesssim 10^\circ$ and $\gamma = 2.5$. However, with the nonlinear interactions isolated, this agreement was shown to be the result of the competing effects of the free and bound terms arising above second-order. Hence, it does not imply that no higher-order terms arise.

2. The complete set of available prediction methods for the skewness, bound kurtosis and dynamic kurtosis was assessed through comparisons to numerical results from HOSM simulations. In performing these comparisons, special care was devoted to obtaining statistically converged values from the numerical simulations. The analysis showed that none of the methods provides reliable predictions for the full set of simulations; casting doubts on the appropriateness of the current methods used for detecting freak waves within operational wave-forecasting models.

3. However, as an exception, the prediction of the skewness based on the theoretical formulation of Longuet-Higgins (1963) was found to be effective for directional sea-states. This motivated the research to explore the link between skewness and kurtosis. However, due to the dynamic effects and the broad range of effective water depths, such a direct link was not possible.

4. A new higher-order crest-height model was proposed. In doing so, its calibration had to deal with three challenging aspects:

   (i) The first aspect concerned parameterising the crest-height distribution in terms of a limited set of parameters. This was resolved by approximating the nonlinear contributions to the tail of the crest-height distribution with linear best-fit lines.

   (ii) The second aspect related to how the parameters defining these linear

fits could be predicted. This prediction was achieved by expressing the linear-fit parameters in terms of the measured values of skewness, bound kurtosis and dynamic kurtosis; demonstrating perhaps for the first time the practical relevance of these three parameters in a conclusive sense.

(iii) The third and final aspect related to predicting the skewness, bound kurtosis and dynamic kurtosis, given that all previous theoretical approaches fail to provide reasonable predictions. This was achieved by employing models from the field of machine learning, often referred to as meta-models, which enabled the prediction of the statistical moments based on a set of 4 sea-state parameters. More specifically, giving special attention to the generalisation performance of each meta-model, the Ensemble Artificial Neural Network approach was found to be exceptionally effective. This approach could potentially replace the existing analytical approaches adopted in operational wave-forecasting models.

5. The proposed model was thoroughly validated against an independent set of numerical, experimental and field data. This has not previously been achieved, setting an adhesive element into the relevance of the crest-height distributions originating from these three independent sources.

6. Finally, the range of applicability of the proposed model was extended to sea-states where wave breaking plays an important role. This extension was achieved by introducing a wave-breaking correction factor. This factor was calibrated based on a single steepness parameter defined on the basis of the well-known Miche (1944) criterion; thereby demonstrating its relevance to realistic sea-states. As a result, the developed model becomes relevant to even the very steepest sea-states.

6.2 Recommendations for future work

1. The present research focused on uni-modal wave systems. It could be extended to include bi-modal crossing sea-states. To this end, whilst Gramstad et al. (2018) have provided some insights on this matter for deep-water conditions, it would be interesting to first explore whether the methodology for separating

the various harmonic contributions is equally applicable in crossing seas and, subsequently, identify the role of the various nonlinear interactions in different effective water depths. In this regard, the presence of a second transverse wave system in wavenumber regions where the stability analysis of monochromatic waves predicts energy focusing would be very interesting to explore. This situation could potentially trigger the phenomenon of modulational instability and lead to even higher crest elevations in finite water depth. To this end, the applicability of the methodology developed in the present thesis for crest-height predictions could directly be explored, especially for the interesting case of co-existing wind waves and swell in directional seas.

2. The effect of ambient currents of different heading angles with respect to the mean wave direction and the effect of variable bathymetry would also be very important to explore, especially for realistic directional sea-states. For this purpose, both numerical simulations and wave-tank experiments could be used. For this, the new Wide Flow Basin in the hydrodynamics laboratory at Imperial College could be used to provide experimental measurements, as it enables the generation of both waves and currents. The author has been part of the hydrodynamic design of the current inlet configuration of this facility. Particularly, she provided CFD (Computational Fluid Dynamics) simulations for assessing the smooth establishment of the current profile along the tank.

3. In the present research, the focus clearly laid on crest-height statistics arising in a single location. However, the statistical properties of crest heights arising in an area would be interesting to explore. The values of skewness, bound kurtosis and dynamic kurtosis could again be used to calibrate a finite-area crest-height model, or this could be simply parameterised in terms of the single-point statistics.

4. The analysis of the field database (Chapter 5) revealed some deviations of the DNV-RP-C205 (2014) proposed formula for the prediction of the peak-enhancement factor of JONSWAP spectra. As a result, it would be worth carrying out a specialised study for assessing the proposed formula, not least because the spectral bandwidth of a sea-sate may play a vital role in the dynamic excitation of floating structures.

5. To this end, the presence of a structure in the wavefield, having dimensions that can produce significant reflection and/or diffraction of the incident wavefield, could produce fundamentally different crest height elevations. Importantly, the wavefield in front of the structure can exhibit much increased elevations. Moreover, in this area with the wave system including waves travelling in opposing directions, the process of wave breaking becomes more complicated and it would be interesting to explore if its effect on the crest heights could still be expressed as a function of the same steepness parameter employed in the present study. Finally, any link between the crest height elevations, or wave records in general, at a distance from the structure and wave-slamming events or wave-overtopping would also be interesting to explore.

6. In the present study, a numerical wave model was utilised based on the potential flow theory. Thus, sea-state conditions where wave breaking is not important were investigated. Alternatively, models that resolve for the full Navier-Stokes equations could be utilised to explore the effect of wave breaking in random directional sea-states. This approach would have an advantage over physical experiments, as it provides a complete description of the associated velocity fields.

   Nonetheless, the drawback of this approach is the high computational cost. Whilst there is a plethora of ways that this could be addressed, much of the added computational requirements stems from the excessive portion of the computational domain devoted to the effective wave generation and absorption, often referred to as *relaxation zones*. The use of relaxation zones could be avoided by adopting boundary conditions with wave absorption capabilities. To this end, building upon Spinneken et al. (2014) the author has presented an approach for optimising the configuration of such boundary conditions based on wavemaking theory and force feed-back control (Zve & Spinneken, 2016). Whilst this approach was implemented within the C++ version of the MFBEM (Hague & Swan, 2009) wave model, its implementation within a CFD model should be straightforward.

7. The applicability of the so-called designer wave approach would be interesting to explore. Particularly identifying if the nonlinear content and dispersion aris-

ing in isolated wave groups matches those arising in random sea-sates. Progress towards this direction has been made in the course of the present research. Specifically, building upon earlier works of Tromans & Vanderschuren (2004) and Gibson et al. (2007) the optimisation of the input conditions has been carried out for uni-directional seas. The proposed method is based on (1) the dimensional reduction of the input parameter space based on the Karhunen-Loeve expansion and (2) the optimisation of the input conditions based on the Inverse First-Order Reliability Method (IFORM). However, these results have not been included in the present thesis, which is already long. To this end, an extension of this work to directional sea-states is to follow.

8. Finally, a full long-term analysis of the crest heights using the new crest-height model presented in the present thesis could determine the most probable annual maximum crest height and its variability. These quantities are key input to the reliability assessment of both new and exiting (often ageing) structures. As part of earlier research, the author has conducted a quantification of the time-evolution of the probability of failure of a structurally degrading offshore platform due to corrosion (Zve et al., 2015). As such, the present research outcomes could aid in refining this earlier approach.

References

Adcock, T. A. A., & Draper, S. (2015). The second order contribution to wave crest amplitude - Random simulations and New Wave. International Ocean and Polar Engineering Conference. ISOPE-I-15-292. 135

Airy, G. B. (1845). *Tides and Waves: Extracted from the Encyclopaedia Metropolitana*. 56

Aknin, D. (2015). *Creating a shallow-water experimental wave environment*. Ph.D. thesis, Imperial College London. 110

Alber, I. E. (1978). The effects of randomness on the stability of two-dimensional surface wavetrains. *Proceedings of the Royal Society of London A: Mathematical, Physical and Engineering Sciences*, *363*(1715), 525–546. 64

Alber, I. E., & Saffman, P. G. (1978). *Stability of random nonlinear deep water waves with finite bandwidth spectra*. TRW, Defense and Space Systems Group. 64

Annenkov, S. Y., & Shrira, V. I. (2001). Numerical modelling of water-wave evolution based on the Zakharov equation. *Journal of Fluid Mechanics*, *449*, 341–371. 64, 66

Annenkov, S. Y., & Shrira, V. I. (2006). Role of non-resonant interactions in the evolution of nonlinear random water wave fields. *Journal of Fluid Mechanics*, *561*, 181–207. 66

Annenkov, S. Y., & Shrira, V. I. (2014). Evaluation of skewness and kurtosis of wind waves parameterized by JONSWAP spectra. *Journal of Physical Oceanography*, *44*(6), 1582–1594. 183

Arena, F., & Ascanelli, A. (2010). Nonlinear crest height distribution in three-dimensional ocean waves. *Journal of Offshore Mechanics and Arctic Engineering*, *132*(2), 021604. 85, 86, 95, 221

Athanassoulis, A. G., & Gramstad, O. (2021). Modelling of ocean waves with the Alber equation: Application to non-parametric spectra and generalisation to crossing seas. *Fluids*, *6*(8). 155

Baldock, T., & Swan, C. (1996). Extreme waves in shallow and intermediate water depths. *Coastal Engineering*, *27*(1), 21 – 46. 92

Baldock, T. E., Swan, C., & Taylor, P. H. (1996). A laboratory study of nonlinear surface waves on water. *Philosophical Transactions of the Royal Society of London A*, *354*, 649–676. 40, 70, 91, 93, 130

Barratt, D., Bingham, H. B., Taylor, P. H., van den Bremer, T. S., & Adcock, T. A. (2020). Linearization of the wave spectrum: A comparison of methods. In *ASME 2020 39th International Conference on Ocean, Offshore and Arctic Engineering*. American Society of Mechanical Engineers Digital Collection. 69

Bateman, W., Swan, C., & Taylor, P. (2003). On the calculation of the water particle kinematics arising in a directionally spread wavefield. *Journal of Computational Physics*, *186*(1), 70 – 92. 41

Bateman, W. J. D., Swan, C., & Taylor, P. H. (2001). On the efficient numerical simulation of directionally spread surface water waves. *Journal of Computational Physics*, *174*(1), 277 – 305. 41, 42

Belibassakis, K., Athanassoulis, G., & Gerostathis, T. (2014). Directional wave spectrum transformation in the presence of strong depth and current inhomogeneities by means of coupled-mode model. *Ocean Engineering*, *87*, 84–96. 40

Benetazzo, A., Ardhuin, F., Bergamasco, F., Cavaleri, L., Guimarães, P. V., Schwendeman, M., Sclavo, M., Thomson, J., & Torsello, A. (2017). On the shape and likelihood of oceanic rogue waves. *Scientific reports*, *7*(1), 8276. 40

Benjamin, T. B. (1967). Instability of periodic wavetrains in nonlinear dispersive systems. *Proceedings of the Royal Society of London. Series A. Mathematical and Physical Sciences*, *299*(1456), 59–6. 63, 65

Benjamin, T. B., & Feir, J. E. (1967). The disintegration of wave trains on deep water part 1. theory. *Journal of Fluid Mechanics*, *27*(3), 417–430. 62, 63

Berg, R. (2009). Tropical cyclone report: Hurricane ike, 1-14 september 2008. Tech. rep. 38

Bloomfield, P. (2004). *Fourier analysis of time series: An introduction*. John Wiley & Sons. 119

Boccotti, P. (1983). Some new results on statistical properties of wind waves. *Applied Ocean Research*, *5*(3), 134 – 140. 111, 270

Boccotti, P. (2015). *Wave mechanics and wave loads on marine structures*. Butterworth-Heinemann. 79

Bonnefoy, F., Ducrozet, G., Le Touzé, D., & Ferrant, P. (2010). Time domain simulation of nonlinear water waves using spectral methods. In *Advances In Numerical Simulation Of Nonlinear Water Waves*, (pp. 129–164). World Scientific. 69, 102

Booij, N., Ris, R. C., & Holthuijsen, L. H. (1999). A third-generation wave model for coastal regions: 1. model description and validation. *Journal of Geophysical Research: Oceans*, *104*(C4), 7649–7666. 36

Brunton, S. L., Noack, B. R., & Koumoutsakos, P. (2020). Machine learning for fluid mechanics. *Annual Review of Fluid Mechanics*, *52*(1), 477–508. 228

BS-EN-ISO-19901-1 (2015). Petroleum and natural gas industries — specific requirements for offshore structures part 1: Metocean design and operating considerations. 43

Cartwright, D. E. (1961). The use of directional spectra in studying the output of a wave recorder on a moving ship. In *National Institute of Oceanography, Wormley, Surray, UK, Presented at the Conference on Wave Spectra, Easton, Maryland*. 53

Cartwright, D. E., & Longuet-Higgins, M. S. (1956). The statistical distribution of the maxima of a random function. *Proceedings of the Royal Society of London A: Mathematical, Physical and Engineering Sciences*, *237*(1209), 212–232. 25, 78, 79, 319, 322, 323

Chabchoub, A., Akhmediev, N., & Hoffmann, N. (2012). Experimental study of spatiotemporally localized surface gravity water waves. *Physical Review E*, *86*(1), 016311. 40, 63

Chabchoub, A., & Grimshaw, R. H. J. (2016). The hydrodynamic nonlinear Schrödinger equation: Space and time. *Fluids*, *1*(3). 103

Cherneva, Z., Tayfun, M. A., & Guedes Soares, C. (2009). Statistics of nonlinear waves generated in an offshore wave basin. *Journal of Geophysical Research: Oceans*, *114*(C8). 214, 386

Cherneva, Z., Tayfun, M. A., & Guedes Soares, C. (2013). Statistics of waves with different steepness simulated in a wave basin. *Ocean Engineering*, *60*, 186–192. 93, 94, 386

Christou, M., & Ewans, K. (2011). Examining a comprehensive dataset containing thousands of freak wave events: Part 2 - analysis and findings. In *ASME 2011 30th International Conference on Ocean, Offshore and Arctic Engineering*, (pp. 827–837). American Society of Mechanical Engineers. 37, 41, 257

Crawford, D. R., Saffman, P. G., & Yuen, H. C. (1980). Evolution of a random inhomogeneous field of nonlinear deep-water gravity waves. *Wave Motion*, *2*(1), 1–16. 64, 187

Cristianini, N., Shawe-Taylor, J., et al. (2000). *An introduction to support vector machines and other kernel-based learning methods*. Cambridge university press. 394

Cruz, A., & Krausmann, E. (2008). Damage to offshore oil and gas facilities following hurricanes Katrina and Rita: An overview. *Journal of Loss Prevention in the Process Industries*, *21*(6), 620–626. 38

Davey, A., & Stewartson, K. (1974). On three-dimensional packets of surface waves. *Proceedings of the Royal Society of London. A. Mathematical and Physical Sciences*, *338*(1613), 101–110. 67, 162, 335

Deo, M., & Sridhar Naidu, C. (1998). Real time wave forecasting using neural networks. *Ocean Engineering*, *26*(3), 191–203. 226

DNV-RP-C205 (2014). Environmental conditions and environmental loads, recommended practice. 43, 53, 264, 291

Dommermuth, D. (2000). The initialization of nonlinear waves using an adjustment scheme. *Wave motion*, *32*(4), 307–317. 104, 119

Dommermuth, D. G., & Yue, D. K. P. (1987). A high-order spectral method for the study of nonlinear gravity waves. *Journal of Fluid Mechanics*, *184*, 267–288. 67, 68

Donelan, M. A., Hamilton, J., Hui, W. H., & Stewart, R. W. (1985). Directional spectra of wind-generated ocean waves. *Philosophical Transactions of the Royal Society of London A: Mathematical, Physical and Engineering Sciences*, *315*(1534), 509–562. 51, 53

Ducrozet, G., Bonnefoy, F., Le Touzé, D., & Ferrant, P. (2007). 3-D HOS simulations of extreme waves in open seas. *Natural Hazards and Earth System Science*, *7*(1), 109–122. 102, 104, 348

Ducrozet, G., Bonnefoy, F., Le Touzé, D., & Ferrant, P. (2016). HOS-ocean: Open-source solver for nonlinear waves in open ocean based on High-Order Spectral method. *Computer Physics Communications*, *203*, 245 – 254. 67, 68, 69

Ducrozet, G., & Gouin, M. (2017). Influence of varying bathymetry in rogue wave occurrence within unidirectional and directional sea-states. *Journal of Ocean Engineering and Marine Energy*, *3*(4), 309–324. 40

Dysthe, K. B. (1979). Note on a modification to the nonlinear Schrödinger equation for application to deep water waves. *Proceedings of the Royal Society of London. A. Mathematical and Physical Sciences*, *369*(1736), 105–114. 66

Dysthe, K. B., & Trulsen, K. (1999). Note on breather type solutions of the NLS as models for freak-waves. *Physica Scripta*, *1999*(T82), 48. 40, 63

Dysthe, K. B., Trulsen, K., Krogstad, H. E., & Socquet-juglard, H. (2003). Evolution of a narrow-band spectrum of random surface gravity waves. *Journal of Fluid Mechanics*, *478*, 1–10. 66, 363

Efron, B. (1979). Bootstrap Methods: Another Look at the Jackknife. *The Annals of Statistics*, *7*(1), 1 – 26. 109, 125, 257, 350

Ewans, K. C. (1998). Observations of the directional spectrum of fetch-limited waves. *Journal of Physical Oceanography*, *28*(3), 495 – 512. 53, 62, 265

Fedele, F. (2014). On certain properties of the compact Zakharov equation. *Journal of Fluid Mechanics*, *748*, 692–711. 20, 98, 132, 146

Fedele, F. (2015). On the kurtosis of deep-water gravity waves. *Journal of Fluid Mechanics*, *782*, 25–36. 161, 162, 173, 183, 202, 208, 335, 336

Fedele, F., & Arena, F. (2005). Weakly nonlinear statistics of high random waves. *Physics of Fluids*, *17*(2), 026601. 85

Fedele, F., Brennan, J., De León, S. P., Dudley, J., & Dias, F. (2016). Real world ocean rogue waves explained without the modulational instability. *Scientific reports*, *6*, 27715. 40, 160, 208, 214, 386

Fedele, F., Cherneva, Z., Tayfun, M., & Guedes Soares, C. (2010). Nonlinear Schrödinger invariants and wave statistics. *Physics of Fluids*, *22*(3), 036601. 146, 150, 214

Fedele, F., Herterich, J., Tayfun, A., & Dias, F. (2019). Large nearshore storm waves off the Irish coast. *Scientific reports*, *9*(1), 1–19. 208

Fedele, F., & Tayfun, M. A. (2009). On nonlinear wave groups and crest statistics. *Journal of Fluid Mechanics*, *620*, 221–239. 40, 85, 95, 135, 221

Fenton, J. D. (1985). Fifth order Stokes theory for steady waves. *Journal of Waterway, Port, Coastal and Ocean Engineering*, *111*(2), 216–234. 59

Fernández, L., Onorato, M., Monbaliu, J., & Toffoli, A. (2016). Occurrence of extreme waves in finite water depth. In *Extreme ocean waves*, (pp. 45–62). Springer. 94, 149, 160, 198

Fitzgerald, C. J., Taylor, P. H., Eatock Taylor, R., Grice, J., & Zang, J. (2014). Phase manipulation and the harmonic components of ringing forces on a surface-piercing column. In *Proc. R. Soc. A*, vol. 470. The Royal Society. 69, 71

Forristall, G. Z. (2000). Wave crest distributions: Observations and second-order theory. *Journal of Physical Oceanography*, *30*, 1931–1943. 8, 18, 20, 44, 46, 47, 48, 79, 85, 86, 88, 104, 105, 106, 107, 108, 123, 124, 125, 135, 137, 138, 139, 141, 142, 143, 148, 149, 153, 156, 160, 161, 170, 171, 174, 175, 176, 177, 178, 182, 185, 186, 191, 193, 197, 198, 211, 257, 258, 265, 266, 267, 268, 269, 270, 275, 276, 277, 278, 279, 281, 282, 283, 285, 289, 346, 347, 406, 407, 408, 409, 410, 411

Francius, M., & Kharif, C. (2006). Three-dimensional instabilities of periodic gravity waves in shallow water. *Journal of Fluid Mechanics*, *561*, 417–437. 169

Frigaard, P., Helm-Petersen, J., Klopman, G., Standsberg, C., Benoit, M., Briggs, M., Miles, M., Santas, J., Schäffer, H., & Hawkes, P. (1997). IAHR list of sea parameters: an update for multidirectional waves. In Mansard, Etienne (ed.) (Ed.) *Proceedings of the 27th IAHR Congress, San Francisco, 10-15 August 1997*. Canada: Canadian Government Publishing. 260, 263

Fructus, D., Kharif, C., Francious, M., Kristiansen, Ø., Clamond, D., & Grue, J. (2005). Dynamics of crescent water wave patterns. *Journal of Fluid Mechanics*, *537*, 155–186. 354

Gibson, R. (2004). *Wave interactions and wave statistics in directional seas*. Ph.D. thesis, Imperial College London. 151

Gibson, R., & Swan, C. (2007). The evolution of large ocean waves: The role of local and rapid spectral changes. *Proceedings of the Royal Society of London A: Mathematical, Physical and Engineering Sciences*, *463*(2077), 21–48. 40, 66, 75, 93, 130, 151, 354, 355

Gibson, R., Swan, C., & Tromans, P. (2007). Fully nonlinear statistics of wave crest elevation calculated using a spectral response surface method: Applications to unidirectional sea states. *Journal of physical oceanography*, *37*(1), 3–15. 293

Goda, Y. (2000). *Random seas and design of maritime structures*, vol. 33. World Scientific Publishing Company. 52, 80, 157

Gramstad, O. (2014). The Zakharov equation with separate mean flow and mean surface. *Journal of Fluid Mechanics*, *740*, 254–277. 64, 134

Gramstad, O., & Bitner-Gregersen, E. (2019). Predicting extreme waves from wave spectral properties using machine learning. *Volume 3: Structures, Safety, and Reliability*. 155, 237

Gramstad, O., Bitner-Gregersen, E., Trulsen, K., & Nieto Borge, J. C. (2018). Modulational instability and rogue waves in crossing sea states. *Journal of Physical Oceanography*, *48*(6), 1317–1331. 40, 85, 290

Gramstad, O., & Trulsen, K. (2007). Influence of crest and group length on the occurrence of freak waves. *Journal of Fluid Mechanics*, *582*, 463–472. 155, 159, 172, 187, 194, 195

Gray, A. (2020). *Extreme waves under significantwind stress*. Ph.D. thesis, Imperial College London. 94, 103, 109, 110, 123

Grilli, S. T., Guyenne, P., & Dias, F. (2001). A fully non-linear model for three-dimensional overturning waves over an arbitrary bottom. *International Journal for Numerical Methods in Fluids*, *35*(7), 829–867. 111

Grilli, S. T., Skourup, J., & Svendsen, I. (1989). An efficient boundary element method for nonlinear water waves. *Engineering Analysis with Boundary Elements*, *6*(2), 97–107. 110

Guedes Soares, C. (1984). Representation of double-peaked sea wave spectra. *Ocean Engineering*, *11*(2), 185–207. 52

Guedes Soares, C., & Antão, E. (2005). Comparison of the characteristics of abnormal waves on the North Sea and Gulf of Mexico. In *Rogue Waves 2004*. IFREMER Brest, France. 209

Guedes Soares, C., Cherneva, Z., & Antäo, E. (2003). Characteristics of abnormal waves in North Sea storm sea states. *Applied Ocean Research*, *25*(6), 337–344. 155, 209

Hadjigeorgiou, D. (2018). *Nonlinear wave interactions in realistic sea states*. Ph.D. thesis, Imperial College London. 93, 94, 138, 159, 160, 176, 180, 190, 195, 206, 281, 359

Hadjigeorgiou, D., Swan, C., & Christou, M. (2017). Numerical investigation of crest-height statistics in deep water. In *The 27th International Ocean and Polar Engineering Conference*. International Society of Offshore and Polar Engineers. 66

Häfner, D., Gemmrich, J., & Jochum, M. (2021). Real-world rogue wave probabilities. *Scientific Reports*, *11*(1), 1–11. 40

Hagan, M. T., Demuth, H. B., & Beale, M. (1997). *Neural network design*. PWS Publishing Co. 228, 232, 233, 240

Hague, C., & Swan, C. (2009). A multiple flux boundary element method applied to the description of surface water waves. *Journal of Computational Physics*, *228*(14), 5111–5128. 47, 91, 110, 292

Haley, J. F. (2016). *Fluid forcing in the crests of large ocean waves*. Ph.D. thesis, Imperial College London. 268

Hammack, J. L., & Henderson, D. (1993). Resonant interactions among surface water waves. *Annual review of fluid mechanics*, *25*(1), 55–97. 63, 134

Hann, M., Greaves, D., & Raby, A. (2014). A new set of focused wave linear combinations to extract non-linear wave harmonics. In *Twenty-ninth Int. Workshop on Water Waves and Floating Bodies, Osaka, Japan*, vol. 30, (pp. 61–64). 71

Hansen, N., & Ostermeier, A. (2001). Completely derandomized self-adaptation in evolution strategies. *Evolutionary computation*, *9*(2), 159–195. 393, 397

Hasselmann, K. (1962). On the non-linear energy transfer in a gravity-wave spectrum Part 1. general theory. *Journal of Fluid Mechanics*, *12*(04), 481–500. 60, 63, 91, 130

Hasselmann, K., Barnett, T., Bouws, E., Carlson, H., Cartwright, D., Enke, K., Ewing, J., Gienapp, H., Hasselmann, D., Kruseman, P., Meerburg, A., Müller, P., Olbers, D., Richter, K., Sell, W., & Walden, H. (1973). Measurements of wind-wave growth and swell decay during the Joint North Sea Wave Project (JONSWAP). Tech. rep., Deutches Hydrographisches Institut. 51

Haver, S., & Andersen, O. J. (2000). Freak waves: rare realizations of a typical population or typical realizations of a rare population? In *The Tenth International*

Offshore and Polar Engineering Conference. International Society of Offshore and Polar Engineers. 38

Haver, S., & Kleiven, G. (2004). Environmental contour lines for design purposes: why and when? In *ASME 2004 23rd International Conference on Offshore Mechanics and Arctic Engineering*, (pp. 337–345). American Society of Mechanical Engineers. 44

Hayes, W. D. (1973). Group velocity and nonlinear dispersive wave propagation. *Proceedings of the Royal Society of London. A. Mathematical and Physical Sciences*, *332*(1589), 199–221. 63, 160, 163

Henderson, K., Peregrine, D., & Dold, J. (1999). Unsteady water wave modulations: Fully nonlinear solutions and comparison with the nonlinear Schrödinger equation. *Wave Motion*, *29*(4), 341–361. 63

Holthuijsen, L. H. (2010). *Waves in oceanic and coastal waters*. Cambridge university press. 81

Huang, N. E., & Long, S. R. (1980). An experimental study of the surface elevation probability distribution and statistics of wind-generated waves. *Journal of Fluid Mechanics*, *101*(1), 179–200. 383

Hurtado, J. E., & Alvarez, D. A. (2001). Neural-network-based reliability analysis: A comparative study. *Computer Methods in Applied Mechanics and Engineering*, *191*(1), 113–132. Micromechanics of Brittle Materials and Stochastic Analysis of Mechanical Systems. 228

Hwang, P. A., Wang, D. W., Walsh, E. J., Krabill, W. B., & Swift, R. N. (2000). Airborne measurements of the wavenumber spectra of ocean surface waves. Part ii: Directional distribution. *Journal of Physical Oceanography*, *30*(11), 2768–2787. 369

Ilbeigi, M., & Dilkina, B. (2018). Statistical approach to quantifying the destructive impact of natural disasters on petroleum infrastructures. *Journal of Management in Engineering*, *34*(1), 04017042. 38

Janssen, P. A. E. M. (1983). Long-time behaviour of a random inhomogeneous field of weakly nonlinear surface gravity waves. *Journal of Fluid Mechanics*, *133*, 113–132. 64, 130, 133, 144

Janssen, P. A. E. M. (2003). Nonlinear four-wave interactions and freak waves. *Journal of Physical Oceanography*, *33*(4), 863–884. 91, 92, 93, 95, 96, 97, 130, 132, 146, 150, 161, 183

Janssen, P. A. E. M. (2009). On some consequences of the canonical transformation in the Hamiltonian theory of water waves. *Journal of Fluid Mechanics*, *637*, 1–44. 14, 20, 26, 95, 96, 152, 153, 157, 165, 209, 210, 324, 332, 334, 373

Janssen, P. A. E. M. (2016). Hamiltonian description of ocean waves and freak waves. In *Rogue and Shock Waves in Nonlinear Dispersive Media*, (pp. 117–157). Springer. 65

Janssen, P. A. E. M. (2017). *Shallow-water version of the freak wave warning system*. European Centre for Medium Range Weather Forecasts. 14, 22, 26, 46, 161, 162, 163, 165, 166, 172, 173, 183, 199, 200, 201, 202, 203, 204, 205, 324, 329, 331, 335, 336, 338, 339, 340

Janssen, P. A. E. M., & Bidlot, J.-R. (2009). *On the extension of the freak wave warning system and its verification*. European Centre for Medium-Range Weather Forecasts. 65, 161

Janssen, P. A. E. M., & Onorato, M. (2007). The intermediate water depth limit of the Zakharov equation and consequences for wave prediction. *Journal of Physical Oceanography*, *37*(10), 2389–2400. 14, 16, 20, 25, 26, 45, 64, 65, 92, 94, 97, 132, 133, 134, 151, 157, 189, 286, 324, 325, 326, 327, 328, 330, 331, 335

Jefferys, E. (1987). Directional seas should be ergodic. *Applied Ocean Research*, *9*(4), 186 – 191. 344

Jha, A. K. (1997). Nonlinear random ocean waves: Prediction and comparison with data. Tech. rep., Civil Engineering Department,Stanford University. 209

Johannessen, T. B., & Swan, C. (2001). A laboratory study of the focusing of transient and directionally spread surface water waves. *Proc. Roy. Soc. Lond. A*, *457*, 971–1006. 40, 91

Johannessen, T. B., & Swan, C. (2003). On the nonlinear dynamics of focused wave groups produced by the focusing of surface-water waves. *Proc. Roy. Soc. Lond. A*, *459*, 1021–1052. 40

Kac, M. (1943). On the average number of real roots of a random algebraic equation. *Bulletin of the American Mathematical Society*, *49*(4), 314–320. 320

Karmpadakis, I. (2018). *Wave statistics in intermediate and shallow water depths*. Ph.D. thesis, Imperial College London. 47, 103, 109, 110, 180, 191, 264, 268, 383, 402, 406

Karmpadakis, I., & Swan, C. (2020). On the average shape of the largest waves in finite water depths. *Journal of Physical Oceanography*, *50*(4), 1023–1043. 42

Karmpadakis, I., & Swan, C. (2022). A new crest height distribution for nonlinear and breaking waves in varying water depths. ***TBC - Draft Manuscript***. 15, 28, 29, 48, 87, 88, 268, 281, 282, 401, 402, 403, 404, 405, 406, 407, 408, 409, 410, 411, 412

Karmpadakis, I., Swan, C., & Christou, M. (2019a). Laboratory investigation of crest height statistics in intermediate water depths. *Proceedings of the Royal Society A*, *475*(2229), 20190183. 42, 53, 86, 94, 123, 161, 176, 190, 193, 214, 254, 258, 268, 272, 275, 276, 279, 280, 409, 410

Karmpadakis, I., Swan, C., & Christou, M. (2019b). Wave height and crest height distributions in shallow water: Analysis of field data. *Coastal Structures 2019*, (pp. 642–651). 42

Karmpadakis, I., Swan, C., & Christou, M. (2020). Assessment of wave height distributions using an extensive field database. *Coastal Engineering*, *157*, 103630. 257

Katsardi, V. (2007). Surface water waves in intermediate and shallow water depths. *Imperial College London*. 41, 42, 189

Katsardi, V., & Swan, C. (2011). The evolution of large non-breaking waves in intermediate and shallow water. I. Numerical calculations of uni-directional seas. In

Proceedings of the Royal Society of London A: Mathematical, Physical and Engineering Sciences, vol. 467, (pp. 778–805). The Royal Society. 41, 46, 113, 130, 327, 355

Kharif, C., & Pelinovsky, E. (2003). Physical mechanisms of the rogue wave phenomenon. *European Journal of Mechanics - B/Fluids*, *22*(6), 603 – 634. 40, 187

Kharif, C., & Ramamonjiarisoa, A. (1988). Deep-water gravity wave instabilities at large steepness. *The Physics of Fluids*, *31*(5), 1286–1288. 355

Kim, M.-H., & Yue, D. (1990). The complete second-order diffraction solution for an axisymmetric body. Part 2: Bichromatic incident waves and body motions. *Journal of Fluid Mechanics*, *211*, 557–593. 380

Knabb, R. D., Brown, D., & Rhome, J. R. (2006a). Tropical cyclone report: Hurricane rita, September 18-26, 2005. Tech. rep., National Hurricane Center. 38

Knabb, R. D., Rhome, J. R., & Brown, D. (2006b). Tropical cyclone report: Hurricane katrina, August 23-30, 2005. Tech. rep., National Hurricane Center. 38

Krasitskii, V. P. (1994). On reduced equations in the Hamiltonian theory of weakly nonlinear surface waves. *Journal of Fluid Mechanics*, *272*, 1–20. 64, 97

Lake, B. M., Yuen, H. C., Rungaldier, H., & Ferguson, W. E. (1977). Nonlinear deep-water waves: theory and experiment. Part 2: Evolution of a continuous wave train. *Journal of Fluid Mechanics*, *83*(1), 49–74. 146

Latheef, M. (2014). *Surface wave statistics in directionally spread seas*. Ph.D. thesis, Imperial College London. 37, 42, 52, 94, 103, 109, 135, 214, 215, 268, 270, 271, 273

Latheef, M., & Swan, C. (2013). A laboratory study of wave crest statistics and the role of directional spreading. *Proceedings of the Royal Society of London A: Mathematical, Physical and Engineering Sciences*, *469*(2152). 42, 53, 86, 123, 159, 180, 190, 254, 258, 268, 270, 272, 275, 276, 279

Latheef, M., Swan, C., & Spinneken, J. (2017). A laboratory study of nonlinear changes in the directionality of extreme seas. In *Proc. R. Soc. A*, vol. 473, (p. 20160290). The Royal Society. 82, 86, 344

Lee, T., & Jeng, D. (2002). Application of artificial neural networks in tide-forecasting. *Ocean Engineering*, *29*(9), 1003–1022. 226

Lindgren, G. (1970). Some properties of a normal process near a local maximum. *The Annals of Mathematical Statistics*, (pp. 1870–1883). 111, 270

Longuet-Higgins, M. S. (1963). The effect of non-linearities on statistical distributions in the theory of sea waves. *Journal of fluid mechanics*, *17*(03), 459–480. 58, 86, 95, 203, 204, 289, 382

Longuet-Higgins, M. S. (1969). On wave breaking and the equilibrium spectrum of wind-generated waves. *Proceedings of the Royal Society of London. A. Mathematical and Physical Sciences*, *310*(1501), 151–159. 51

Longuet-Higgins, M. S. (1975). On the joint distribution of the periods and amplitudes of sea waves. *Journal of Geophysical Research (1896-1977)*, *80*(18), 2688–2694. 80, 157

Longuet-Higgins, M. S. (1976). On the nonlinear transfer of energy in the peak of a gravity-wave spectrum: A simplified model. *Proceedings of the Royal Society of London. A. Mathematical and Physical Sciences*, *347*(1650), 311–328. 363, 364, 365, 367, 368

Longuet-Higgins, M. S., & Phillips, O. M. (1962). Phase velocity effects in tertiary wave interactions. *Journal of Fluid Mechanics*, *12*(3), 333–336. 58

Longuet-Higgins, M. S., & Stewart, R. W. (1960). Changes in the form of short gravity waves on long waves and tidal currents. *Journal of Fluid Mechanics*, *8*, 565–583. 57, 58, 95, 287

Madsen, P. A., & Fuhrman, D. R. (2012). Third-order theory for multi-directional irregular waves. *Journal of Fluid Mechanics*, *698*, 304–334. 75

Magnusson, A. K., & Donelan, M. A. (2013). The Andrea wave characteristics of a measured North Sea rogue wave. *Journal of Offshore Mechanics and Arctic Engineering*, *135*(3). 031108. 38

Makri, I. M. (2018). *Wave height and crest elevation statistics applicable to offshore wind turbines*. Ph.D. thesis, Imperial College London. 47

Marelli, S., & Sudret, B. (2014). *UQLab: A Framework for Uncertainty Quantification in Matlab*, (pp. 2554–2563). 393, 397

Marthinsen, T., & Winterstein, S. R. (1992). On the skewness of random surface waves. *All Days*. ISOPE-I-92-279. 85, 95, 96, 209, 210, 325, 326, 327, 375, 376, 377

Mase, H., Sakamoto, M., & Sakai, T. (1995). Neural network for stability analysis of rubble-mound breakwaters. *Journal of waterway, port, coastal, and ocean engineering*, *121*(6), 294–299. 226

Masterton, S. (2007). *Nonlinear wave-structure interaction: Scattering, forcing and dynamic response*. Ph.D. thesis, Imperial College London. 110

McCarthy, J. (2018). *Wave breaking in random seas*. Master's thesis, Department of Civil and Environmental Engineering, Imperial College London. 103, 109, 272, 275, 280, 409, 410

McLean, J. W. (1982a). Instabilities of finite-amplitude gravity waves on water of finite depth. *Journal of Fluid Mechanics*, *114*, 331–341. 63, 160, 169, 187, 354, 355

McLean, J. W. (1982b). Instabilities of finite-amplitude water waves. *Journal of Fluid Mechanics*, *114*, 315–330. 169

Meckesheimer, M., Booker, A. J., Barton, R. R., & Simpson, T. W. (2002). Computationally inexpensive metamodel assessment strategies. *AIAA journal*, *40*(10), 2053–2060. 244

Miche, M. (1944). Mouvements ondulatoires de la mer en profondeur constante ou décroissante. *Annales de Ponts et Chaussées, 1944, pp (1) 26-78,(2) 270-292,(3) 369-406*. 271, 290

Michell, J. H. (1893). XLIV. the highest waves in water. *The London, Edinburgh, and Dublin Philosophical Magazine and Journal of Science*, *36*(222), 430–437. 271

Miles, M. D., & Funke, E. R. (1989). A comparison of methods for synthesis of directional seas. *Journal of Offshore Mechanics and Arctic Engineering*, *111*(1), 43–48. 344

Mitsuyasu, H., Tasai, F., Suhara, T., Mizuno, S., Ohkusu, M., Honda, T., & Rikiishi, K. (1975). Observations of the directional spectrum of ocean waves using a cloverleaf buoy. *Journal of Physical Oceanography*, *5*(4), 750 – 760. 53, 365

MMS (2007). Assessment of fixed offshore platform performance in hurricanes Katrina and Rita, Final report. Tech. rep., U.S. Department of the Interior Mineral Management Service Engineering and Research Branch. 38, 39

MMS (2010). Assessment of damage and failure mechanisms for offshore structures and pipelines in hurricanes Gustav and Ike, Final report. Tech. rep., U.S. Department of the Interior Mineral Management Service Engineering and Research Branch. 38, 39

Mori, N., & Janssen, P. A. E. M. (2006). On kurtosis and occurrence probability of freak waves. *Journal of Physical Oceanography*, *36*(7), 1471–1483. 20, 95, 96, 97, 132, 157, 161, 162, 165, 386, 398

Mori, N., Onorato, M., & Janssen, P. A. E. M. (2011). On the estimation of the kurtosis in directional sea states for freak wave forecasting. *Journal of Physical Oceanography*, *41*(8), 1484–1497. 159, 173, 208

Mori, N., Onorato, M., Janssen, P. A. E. M., Osborne, A. R., & Serio, M. (2007). On the extreme statistics of long-crested deep water waves: Theory and experiments. *Journal of Geophysical Research: Oceans*, *112*(C9). 144, 149, 208

Mori, N., & Yasuda, T. (2002). Effects of high-order nonlinear interactions on unidirectional wave trains. *Ocean Engineering*, *29*(10), 1233 – 1245. 94

Morison, J. R., Johnson, J. W., & Schaaf, S. A. (1950). The force exerted by surface waves on piles. *Jounal of Petroleum Technology*, *189*(5), 149–154. 35

NORSOK-N-003 (2014). Actions and action effects. (NORSOK Standard, N-003). 43

Ochi, M., & Hubble, E. (1977). Six-parameter wave spectra. In *Coastal Engineering 1976*, (pp. 301–328). 52

Onorato, M., Cavaleri, L., Fouques, S., Gramstad, O., Janssen, P. A. E. M., Monbaliu, J., Osborne, A. R., Pakozdi, C., Serio, M., Stansberg, C. T., Toffoli, A., &

Trulsen, K. (2009a). Statistical properties of mechanically generated surface gravity waves: a laboratory experiment in a three-dimensional wave basin. *Journal of Fluid Mechanics*, *627*, 235–257. 53, 159, 160, 208, 214

Onorato, M., Osborne, A., & Serio, M. (2007). On the relation between two numerical methods for the computation of random surface gravity waves. *European Journal of Mechanics - B/Fluids*, *26*(1), 43 – 48. 68, 168

Onorato, M., Osborne, A. R., Janssen, P. A. E. M., & Resio, D. (2009b). Four-wave resonant interactions in the classical quadratic Boussinesq equations. *Journal of Fluid Mechanics*, *618*, 263–277. 133, 134

Onorato, M., Osborne, A. R., & Serio, M. (2002). Extreme wave events in directional, random oceanic sea states. *Physics of Fluids*, *14*(4), L25–L28. 159

Onorato, M., Osborne, A. R., Serio, M., Cavaleri, L., Brandini, C., & Stansberg, C. T. (2004). Observation of strongly non-gaussian statistics for random sea surface gravity waves in wave flume experiments. *Physical Review E*, *70*(6), 067302. 93, 144

Onorato, M., Osborne, A. R., Serio, M., Cavaleri, L., Brandini, C., & Stansberg, C. T. (2006). Extreme waves, modulational instability and second order theory: Wave flume experiments on irregular waves. *European Journal of Mechanics - B/Fluids*, *25*(5), 586 – 601. Rogue waves. 93, 214

Osborne, A. R., Onorato, M., & Serio, M. (2000). The nonlinear dynamics of rogue waves and holes in deep-water gravity wave trains. *Physics Letters A*, *275*(5), 386 – 393. 40

Perignon, Y. L., Bonnefoy, F., Ferrant, P., & Ducrozet, G. (2010). Non-linear initialization in three-dimensional high order spectra deterministic sea state modeling. *29th International Conference on Ocean, Offshore and Arctic Engineering: Volume 4*, 525–532. 119

Perrone, M. P., & Cooper, L. N. (1992). When networks disagree: Ensemble methods for hybrid neural networks. Tech. rep., Brown University, Providence Rhode Island, Institute for brain and neural systems. 234

Phillips, O. M. (1958). The equilibrium range in the spectrum of wind-generated waves. *Journal of Fluid Mechanics*, *4*(4), 426–434. 51

Phillips, O. M. (1960). On the dynamics of unsteady gravity waves of finite amplitude. Part 1. The elementary interactions. *Journal of Fluid Mechanics*, *9*(2), 193–217. 16, 61, 62, 364, 365, 367, 368

Phillips, O. M. (1967). Theoretical and experimental studies of gravity wave interactions. *Proceedings of the Royal Society of London. Series A. Mathematical and Physical Sciences*, *299*(1456), 104–119. 63

Pierson, W., & Moskowitz, L. (1964). A proposed spectral form for fully developed wind seas based on the similarity theory of sa kitaigorodskii. *Journal of geophysical research*, *69*(24), 5181–5190. 51

Rasmussen, C., & Williams, C. (2006). *Gaussian Processes for Machine Learning. Adaptive Computation and Machine Learning*. The MIT Press, Cambridge. 228, 393

Rayleigh, F. (1880). XII. on the resultant of a large number of vibrations of the same pitch and of arbitrary phase. *The London, Edinburgh, and Dublin Philosophical Magazine and Journal of Science*, *10*(60), 73–78. 78

Read, W. W. (1986). *Time series analysis of wave records and the search for wave groups*. Ph.D. thesis, James Cook University of North Queensland. 263

Rice, S. O. (1945). Mathematical analysis of random noise. *The Bell System Technical Journal*, *24*(1), 46–156. 78, 320, 321

Santner, T. J., Williams, B. J., Notz, W. I., & Williams, B. J. (2003). *The design and analysis of computer experiments*, vol. 1. Springer. 228

Sharma, J. N., & Dean, R. G. (1981). Second-order directional seas and associated wave forces. *Society of Petroleum Engineering*, *4*, 129–140. 58, 71, 287

Shemer, L., & Dorfman, B. (2008). Experimental and numerical study of spatial and temporal evolution of nonlinear wave groups. *Nonlinear Processes in Geophysics*, *15*(6), 931–942. 103

Shemer, L., & Sergeeva, A. (2009). An experimental study of spatial evolution of statistical parameters in a unidirectional narrow-banded random wavefield. *Journal of Geophysical Research: Oceans*, *114*(C1). 93, 94

Shemer, L., Sergeeva, A., & Liberzon, D. (2010). Effect of the initial spectrum on the spatial evolution of statistics of unidirectional nonlinear random waves. *Journal of Geophysical Research: Oceans*, *115*(C12). 94

Simanesew, A., Krogstad, H. E., Trulsen, K., & Nieto Borge, J. C. (2016). Development of frequency-dependent ocean wave directional distributions. *Applied Ocean Research*, *59*, 304–312. 363, 365, 367

Simpson, T. W., Poplinski, J., Koch, P. N., & Allen, J. K. (2001). Metamodels for computer-based engineering design: survey and recommendations. *Engineering with computers*, *17*(2), 129–150. 228

Slunyaev, A., Kharif, C., Pelinovsky, E., & Talipova, T. (2002). Nonlinear wave focusing on water of finite depth. *Physica D: Nonlinear Phenomena*, *173*(1), 77 – 96. 63

Slunyaev, A., Sergeeva, A., & Didenkulova, I. (2016). Rogue events in spatiotemporal numerical simulations of unidirectional waves in basins of different depth. *Natural Hazards*, *84*(2), 549–565. 94

Smola, A. J., & Schölkopf, B. (2004). A tutorial on support vector regression. *Statistics and computing*, *14*(3), 199–222. 228, 396, 397

Sobey, R. J., & Young, I. R. (1986). Hurricane wind waves—a discrete spectral model. *Journal of waterway, port, coastal, and ocean engineering*, *112*(3), 370–389. 263

Socquet-Juglard, H., Dysthe, K. B., Trulsen, K., Krogstad, H. E., & Liu, J. (2005). Probability distributions of surface gravity waves during spectral changes. *Journal of Fluid Mechanics*, *542*, 195–216. 66, 363, 383

Spinneken, J., Christou, M., & Swan, C. (2014). Force-controlled absorption in a fully-nonlinear numerical wave tank. *Journal of Computational Physics*, *272*(0), 127–148. 292

Stansberg, C. T. (1994). Effects from directionality and spectral bandwidth on non-linear spatial modulations of deep-water surface gravity wave trains. In *Coastal Engineering 1994*, (pp. 579–593). 93, 94, 159

Stansberg, C. T. (2001). Random waves in the laboratory–what is expected for the extremes? In *Rogue Waves 2000 (Brest, France, 2000)*, (pp. 289–301). Ifremer. 214, 215

Stiassnie, M., & Gramstad, O. (2009). On Zakharov's kernel and the interaction of non-collinear wavetrains in finite water depth. *Journal of Fluid Mechanics*, *639*, 433–442. 64, 134, 195

Stiassnie, M., Regev, A., & Agnon, Y. (2008). Recurrent solutions of Alber's equation for random water-wave fields. *Journal of Fluid Mechanics*, *598*, 245–266. 130, 146

Stiassnie, M., & Shemer, L. (1987). Energy computations for evolution of class i and ii instabilities of stokes waves. *Journal of Fluid Mechanics*, *174*, 299–312. 66

Stokes, G. (1847). On the theory of oscillatory waves. *Transactions of the Cambridge Philosophical Society*, *8*, 441. Reprinted in *Mathematical and Pysical Papers vol 1*, Cambridge University Press, pp. 197–229. 57, 59, 60

Sverdrup, H. U., & Munk, W. H. (1947). *Wind, sea and swell: Theory of relations for forecasting*. 601. U.S. Navy Hydrographic Office Washington. 52

Tanaka, M. (2001). A method of studying nonlinear random field of surface gravity waves by direct numerical simulation. *Fluid Dynamics Research*, *28*(1), 41. 69

Tang, T., Xu, W., Barratt, D., Bingham, H. B., Li, Y., Taylor, P. H., van den Bremer, T. S., & Adcock, T. A. A. (2021). Spatial evolution of the kurtosis of steep unidirectional random waves. *Journal of Fluid Mechanics*, *908*, A3. 130, 150

Tayfun, M. A. (1980). Narrow-band nonlinear sea waves. *Journal of Geophysical Research: Oceans*, *85*(C3), 1548–1552. 85, 87, 88, 95, 221

Tayfun, M. A. (1994). Distributions of envelope and phase in weakly nonlinear random waves. *Journal of Engineering Mechanics*, *120*(5), 1009–1025. 204, 205, 372

Tayfun, M. A. (2006). Statistics of nonlinear wave crests and groups. *Ocean Engineering*, *33*(11), 1589 – 1622. 85, 88, 95, 203, 398

Tayfun, M. A., & Alkhalidi, M. A. (2020). Distribution of sea-surface elevations in intermediate and shallow water depths. *Coastal Engineering*, *157*, 103651. 206, 325

Tayfun, M. A., & Fedele, F. (2007). Wave-height distributions and nonlinear effects. *Ocean Engineering*, *34*(11), 1631 – 1649. 48, 86, 135, 214, 215, 386, 401

Tayfun, M. A., & Lo, J.-M. (1990). Nonlinear effects on wave envelope and phase. *Journal of waterway, port, coastal, and ocean engineering*, *116*(1), 79–100. 86, 95, 386

The Wamdi Group (1988). The WAM model-A third generation ocean wave prediction model. *Journal of Physical Oceanography*, *18*(12), 1775–1810. 36

The WISE Group, L. C., Alves, J.-H., Ardhuin, F., Babanin, A., Banner, M., Belibassakis, K., Benoit, M., Donelan, M., Groeneweg, J., Herbers, T., Hwang, P., Janssen, P., Janssen, T., Lavrenov, I., Magne, R., Monbaliu, J., Onorato, M., Polnikov, V., Resio, D., Rogers, W., Sheremet, A., McKee Smith, J., Tolman, H., van Vledder, G., Wolf, J., & Young, I. (2007). Wave modelling-The state of the art. *Progress in Oceanography*, *75*(4), 603–674. 36

Toffoli, A., Benoit, M., Onorato, M., & Bitner-Gregersen, E. M. (2009). The effect of third-order nonlinearity on statistical properties of random directional waves in finite depth. *Nonlinear Processes in Geophysics*, *16*(1), 131–139. 53, 85, 160, 187, 364, 365, 369

Toffoli, A., Bitner-Gregersen, E., Onorato, M., & Babanin, A. V. (2008a). Wave crest and trough distributions in a broad-banded directional wave field. *Ocean Engineering*, *35*(17), 1784 – 1792. 85

Toffoli, A., Fernández, L., Monbaliu, J., Benoit, M., Gagnaire-Renou, E., Lefevre, J. M., Cavaleri, L., Proment, D., Pakozdi, C., Stansberg, C. T., Waseda, T., & Onorato, M. (2013). Experimental evidence of the modulation of a plane wave to oblique perturbations and generation of rogue waves in finite water depth. *Physics of Fluids*, *25*(9), 091701. 63, 160

Toffoli, A., Gramstad, O., Trulsen, K., Monbaliu, J., Bitner-Gregersen, E., & Onorato, M. (2010a). Evolution of weakly nonlinear random directional waves: Laboratory experiments and numerical simulations. *Journal of Fluid Mechanics*, *664*, 313–336. 53, 85, 104, 369

Toffoli, A., Lefèvre, J. M., Bitner-Gregersen, E., & Monbaliu, J. (2005). Towards the identification of warning criteria: Analysis of a ship accident database. *Applied Ocean Research*, *27*(6), 281 – 291. 37

Toffoli, A., Onorato, M., Bitner-Gregersen, E., Osborne, A. R., & Babanin, A. V. (2008b). Surface gravity waves from direct numerical simulations of the Euler equations: A comparison with second-order theory. *Ocean Engineering*, *35*(3), 367 – 379. 85, 93

Toffoli, A., Onorato, M., Bitner-Gregersen, E. M., & Monbaliu, J. (2010b). Development of a bimodal structure in ocean wave spectra. *Journal of Geophysical Research: Oceans*, *115*(C3). 363, 365, 367, 368, 370

Torsethaugen, K., & Haver, S. (2004). Simplified double peak spectral model for ocean waves. In *The Fourteenth International Offshore and Polar Engineering Conference*. International Society of Offshore and Polar Engineers. 52

Tromans, P., Anaturk, A., & Hagemeijer, P. (1991). A new model for the kinematics of large ocean waves-application as a design wave. In *The First International Offshore and Polar Engineering Conference*. International Society of Offshore and Polar Engineers. 42, 111, 270

Tromans, P. S., & Vanderschuren, L. (2004). A spectral response surface method for calculating crest elevation statistics. *Journal of Offshore Mechanics and Arctic Engineering*, *126*(1), 51–53. 293

Trulsen, K., & Dysthe, K. B. (1996). A modified nonlinear Schrödinger equation for broader bandwidth gravity waves on deep water. *Wave Motion*, *24*(3), 281–289. 66

Tucker, M. J., Challenor, P. G., & Carter, D. J. T. (1984). Numerical simulation of a random sea: A common error and its effect upon wave group statistics. *Applied Ocean Research*, *6*(2), 118 – 122. 82, 83

van Gent, M. R., van den Boogaard, H. F., Pozueta, B., & Medina, J. R. (2007). Neural network modelling of wave overtopping at coastal structures. *Coastal engineering*, *54*(8), 586–593. 227

Vanem, E. (2015). Uncertainties in extreme value modelling of wave data in a climate change perspective. *Journal of Ocean Engineering and Marine Energy*, *1*(4), 339–359. 44

Vapnik, V. (2013). *The nature of statistical learning theory*. Springer science & business media. 228

Vettor, R., & Guedes Soares, C. (2016). Development of a ship weather routing system. *Ocean Engineering*, *123*, 1–14. 36

Vinje, T., & Haver, S. (1994). On the non-gaussian structure of ocean waves. 204, 205, 210

Walker, D., Taylor, P., & Taylor, R. E. (2004). The shape of large surface waves on the open sea and the Draupner New Year wave. *Applied Ocean Research*, *26*(3), 73 – 83. 40

Wang, J., Ma, Q., Yan, S., & Chabchoub, A. (2018). Breather rogue waves in random seas. *Physical Review Applied*, *9*(1), 014016. 40

Waseda, T. (2006). Impact of directionality on the extreme wave occurrence in a discrete random wave system. In *Proceedings of 9th International Workshop on Wave Hindcasting and Forecasting, Victoria, Canada*. 159

West, B. J., Brueckner, K. A., Janda, R. S., Milder, D. M., & Milton, R. L. (1987). A new numerical method for surface hydrodynamics. *Journal of Geophysical Research: Oceans*, *92*(C11), 11803–11824. 67, 68

Whitham, G. B. (1974). *Linear and Nonlinear Waves*. John. 63, 65, 325

Winterstein, S. R. (1988). Nonlinear vibration models for extremes and fatigue. *Journal of Engineering Mechanics*, *114*(10), 1772–1790. 214

Winterstein, S. R., & Haver, S. (2015). Modelling shallow-water waves: Truncated hermite models and the ShallowWave routine. *Volume 3: Structures, Safety and Reliability*. V003T02A049. 209

WW3DG (2019). The wavewatch iii development group: User manual and system documentation of wavewatch iii version 6.07. Tech. Rep. 333. 36

Xiao, W., Liu, Y., Wu, G., & Yue, D. K. P. (2013). Rogue wave occurrence and dynamics by direct simulations of nonlinear wave-field evolution. *Journal of Fluid Mechanics*, *720*, 357–392. 66, 155, 159, 160, 173, 187, 195, 363, 370

Young, I. R. (1995). The determination of confidence limits associated with estimates of the spectral peak frequency. *Ocean Engineering*, *22*(7), 669–686. 263

Young, I. R., Verhagen, L. A., & Banner, M. L. (1995). A note on the bimodal directional spreading of fetch-limited wind waves. *Journal of Geophysical Research: Oceans*, *100*(C1), 773–778. 62

Yuen, H. C., & Lake, B. M. (1980). Instabilities of waves on deep water. *Annual Review of Fluid Mechanics*, *12*(1), 303–334. 63

Yuen, H. C., & Lake, B. M. (1982). Nonlinear dynamics of deep-water gravity waves. *Advances in applied mechanics*, *22*, 67–229. 63

Zakharov, V. E. (1968). Stability of periodic waves of finite amplitude on the surface of a deep fluid. *Journal of Applied Mechanics and Technical Physics*, *9*(2), 190–194. 64, 67, 325, 359

Zhang, H., Guedes Soares, C., Chalikov, D., & Toffoli, A. (2016). Modeling the spatial evolutions of nonlinear unidirectional surface gravity waves with fully nonlinear numerical method. *Ocean Engineering*, *125*, 60–69. 214

Zhang, Z., & Li, X.-M. (2017). Global ship accidents and ocean swell-related sea states. *Natural Hazards and Earth System Sciences*, *17*(11), 2041–2051. 37

Zve, & Spinneken (2016). Towards long random sea simulations in numerical wave tanks. In *Proceedings of the 26th International Offshore and Polar Engineering Conference (ISOPE)*. 292

Zve, E. S., Loukogeorgaki, E., & Angelides, D. C. (2015). Effect of zoning corrosion on the life-time structural reliability of a jacket offshore structure. In *The Twenty-fifth International Ocean and Polar Engineering Conference*. OnePetro. 293

Appendices

A

Approximating the tail of the Cartwright & Longuet-Higgins (1956) distribution

In §2.3.1 it was stated that the tail of the exceedance probability distribution of local maxima, η_m, arising in a linear (or Gaussian process), originally derived by Cartwright & Longuet-Higgins (1956), can be approximated by,

$$Q_m(\zeta) = \sqrt{1-\epsilon^2}e^{-\frac{1}{2}\zeta^2}, \tag{A.1}$$

provided $\epsilon \neq 1$. Where $\zeta = \frac{\eta_m}{\sqrt{m_0}}$, m_0 is the zeroth spectral moment and ϵ is given by Equation 2.38. In the following sections, the derivation of this expression is provided.

A.1 Level up-crossing rate

The starting point for deriving Equation A.1 is the so-called level *up-crossing rate*. This refers to the frequency at which a certain value of the free-surface elevation, $\eta(t)$ [2], or any stochastic process, is exceeded; the term 'up-crossing' referring to the fact that the slope of the free surface is positive at the crossing point.

[2]Note that the free surface here is denoted to be a function of time, but the derivation procedure is equivalently valid for a process being a function of space

This rate for a Gaussian stochastic process is given by Rice (1945). In deriving such rate, Rice (1945) defined the necessary condition for a stochastic process, $\eta(t)$, to exhibit an up-crossing of a level u some time between t and $t+\Delta t$, as $-\dot{\eta}(t)\Delta t < u-\eta(t) < 0$; $\dot{\eta}(t)$ being the time derivative of the process. This condition was derived on the basis that Δt is very small ($\Delta t \to 0$), and hence $\dot{\eta}$ can be regarded linear in the interval (t,$t+\Delta t$). Having defined this condition, following Rice (1945) the up-crossing rate, $\nu_+(u)$, is given by:

$$\nu_+(u) = \frac{\mathbf{d}}{\mathbf{d}\Delta t}\int_0^\infty \int_{u-\dot{\eta}(t)\Delta t}^{u} p(\eta(t),\dot{\eta}(t))d\eta d\dot{\eta} = \int_0^\infty \dot{\eta}(t)p(u,\dot{\eta}(t))d\dot{\eta}, \tag{A.2}$$

where p is the joint probability distribution function of the stochastic process and its time-derivative and $\mathbf{d}$ denotes differentiation.

In the case of a Gaussian process, p is given by the following bivariate normal distribution:

$$p(\eta(t),\dot{\eta}(t)) = \frac{1}{(2\pi)|\mathbf{\Sigma}|^{1/2}} e^{\left[-\frac{1}{2}\mathbf{X}^T\mathbf{\Sigma}^{-1}\mathbf{X}\right]}, \tag{A.3}$$

where

$$\mathbf{X} = \begin{bmatrix} \eta(t)^2 & \eta(t)\dot{\eta}(t) \\ \dot{\eta}(t)\eta(t) & \dot{\eta}(t)^2 \end{bmatrix} \tag{A.4}$$

and $\mathbf{\Sigma}$ is the covariance matrix of $\eta(t)$ and $\dot{\eta}(t)$, defined as,

$$\mathbf{\Sigma} = \begin{bmatrix} m_0 & 0 \\ 0 & m_2 \end{bmatrix}. \tag{A.5}$$

Where m_i denotes the i^{th} spectral moment given by Equation 2.39. Moreover, as the off-diagonal terms of $\mathbf{\Sigma}$ are zero, the Gaussian process is uncorrelated to its derivative process.

Combining Equations A.2 and A.3, Rice (1945) have shown that the level up-crossing rate for a Gaussian process is given by,

$$\nu_{\eta+}(u) = \frac{1}{2\pi}\sqrt{\frac{m_2}{m_0}} e^{-\frac{u^2}{2m_0}} \tag{A.6}$$

It has to be noted that equation A.6 was also independently derived by Kac (1943) in the context of roots of random polynomials. However it was formally proven by

Rice (1945) in the context of stochastic processes.

Furthermore, it is interesting to note that Equation A.6 also holds for the level down-crossing rate of the same process. While, when Equation A.6 is applied to $u = 0$, the zero-crossing rate is obtained. In the field of ocean engineering, this corresponds to the inverse of the spectral estimate of the mean zero-up-crossing wave period: $T_2 = 2\pi\sqrt{m_0/m_2}$.

Based on the above, considering now the crossings of the time-derivative process, $\dot{\eta}(t)$, which is also a Gaussian process, one can calculate the rate to which local maxima occur. This is based on the fact that the sufficient condition for a maximum to occur, is that $\dot{\eta}(t)$ is zero and its derivative, $\ddot{\eta}(t)$, is negative; the latter signifying a down-crossing. As such, the rate of local maxima of $\eta(t)$ coincides with the zero-down-crossing rate of $\dot{\eta}(t)$. Therefore, by using the moments of $\dot{\eta}(t)$ instead of $\eta(t)$ in Equation A.6 and setting the level u to zero, the rate of local maxima of $\eta(t)$ is given by, [1],

$$\nu_{\dot{\eta}-}(0) = \frac{1}{2\pi}\sqrt{\frac{m_4}{m_2}}. \tag{A.7}$$

Finally, the ratio of the number of local maxima to zero-crossings of $\eta(t)$ in a time period ΔT can be calculated as,

$$r = \frac{\nu_{\dot{\eta}-}(0)\Delta T}{\nu_{\eta+}(u)\Delta T} = \sqrt{\frac{m_0 m_4}{m_2^2}}. \tag{A.8}$$

Interestingly, r is related to the bandwidth parameter ϵ (Equation 2.38) according to: $\epsilon = \sqrt{1 - 1/r^2}$. The ratio r plays a fundamental role in describing the distribution of local maxima (or equivalently minima) of a Gaussian process. This is discussed in the following section.

A.2 A lower bound for the distribution of local extrema

For any level up-crossing of a random process, there is at least one local maximum of higher magnitude than that level. Specifically, in a given time interval, ΔT, the

[1] Note that the zeroth and second moments of $\dot{\eta}(t)$ are the second and fourth moments of $\eta(t)$, respectively

number of local maxima higher than a specified level u is equal to the number of level u up-crossings plus the number of positive local minima above the same level. Based on this, the following relationship holds for the number of local maxima,

$$N(\eta_m > u) = \nu_{\eta+}(u)\Delta T + N(\eta_n > u) \tag{A.9}$$

where N refers to the number of the argument, η_m to the local maxima and η_n to the local minima. To obtain the probability that a local maximum exceeds a level u, Equation A.9 should be divided by the total number of local maxima. The latter is given by Equation A.7 multiplied by T. Hence, following from Equation A.9 the probability that a local maximum, η_m, exceeds a level u is given by,

$$P(\eta_m > u) = \sqrt{\frac{m_0 m_4}{m 2^2}} e^{-\frac{u^2}{2m_0}} + P(\eta_m < -u) \tag{A.10}$$

where P refers to the probability of the argument. Moreover, the symmetry of the Gaussian process with respect to the zero mean level was used to replace $P(\eta_n > u)$ by $P(\eta_m < -u)$.

As u increases the $P(\eta_m < -u)$ reduces and thus for $u \to \infty$ the probability of exceedance of a local maximum becomes,

$$Q_m = P(\eta_m > u) = \sqrt{\frac{m_2^2}{m_0 m_4}} e^{-\frac{u^2}{2m_0}}. \tag{A.11}$$

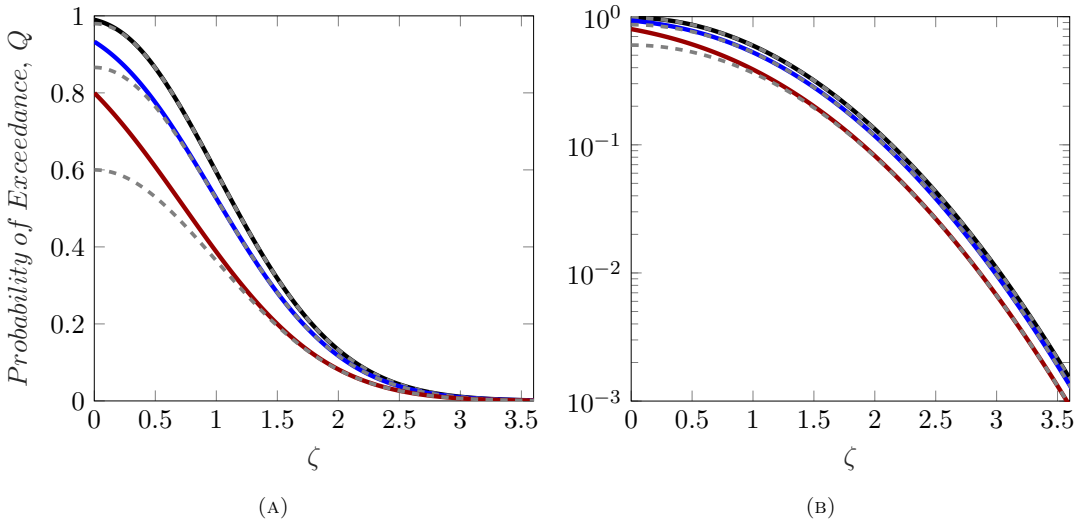
This can be expressed based on the parameter ϵ (Equation 2.38) according to,

$$Q_m = P(\eta_m > u) = \sqrt{1-\epsilon^2} e^{-\frac{u^2}{2m_0}} \tag{A.12}$$

Following Equation A.10, Equation A.11 consists of a lower bound of the true distribution of local maxima, which has been derived by Cartwright & Longuet-Higgins (1956) and was discussed in §2.3.1. Contrasting Equation A.12 to the Equation proposed by Cartwright & Longuet-Higgins (1956) (Equation 2.37), it can be observed that A.12 becomes exact for $\epsilon \to 0$ (narrow-band case) and as $\epsilon \to 1$ it breaks down; due to an infinite number of local maxima occurring above a level up-crossing.

Figure A.1 shows the comparison between Equation 2.37 and Equation A.12 for different values of the ϵ parameter. Specifically, the two sub-figures refer to the same results, with sub-figure (A) having a linear vertical axis and sub-figure (B)

logarithmic. As such, the former sub-figure emphasises the lower in magnitude local maxima, whereas the latter emphasises the higher and hence rarer ones. Finally, in both sub-figures the horizontal axis refers to the normalised local maxima: $\zeta = \frac{u}{\sqrt{m_0}}$. In considering Figure A.1, it is observed that Equation A.12 converges to Equation 2.37 at the tail of the distribution for all values of the ϵ parameter considered ($\epsilon = 0.2, 0.5$ and 0.8). However, as ϵ increases, Equation A.12 converges to Equation 2.37 for lower ζ.



(A) (B)

Figure A.1: Probability of exceedance of normalised local maxima, $\zeta = \frac{u}{\sqrt{m_0}}$, for different spectral bandwidths ϵ; comparison between the exact form of Cartwright & Longuet-Higgins (1956) (solid lines) and Equation A.12 (dashed lines): (A) for linear vertical axis and (B) for logarithmic vertical axis. The lines (/ /) refer to $\epsilon = 0.2, 0.5$ and 0.8, respectively. Note that only positive local maxima are shown.

B

Finite-depth theoretical solutions for the statistical moments and additional comparisons to numerical results

The present appendix presents the functional forms of the narrow-banded solutions of Janssen & Onorato (2007), Janssen (2009) and Janssen (2017) for the statistical moments. No account is provided to their derivation process, more information on which the reader is directed to the original references. In addition, present appendix provides additional comparisons to broad-banded numerical results based on HOSM. In doing so, considerations in applying a narrow-band solution to broad-banded seas are discussed in detail.

B.1 The uni-directional solution of Janssen & Onorato (2007) for the dynamic kurtosis

B.1.1 Theoretical solution

As mentioned in §3.2.2, the estimation of the dynamic kurtosis is based on the value of the so-called Benjamin-Feir index, given by Janssen & Onorato (2007) for

finite-depth conditions. In obtaining this index, Janssen & Onorato (2007) have pointed out that the wave-induced mean flow needs to be included in the derivation of the finite-depth self-interaction resonant kernel $T_{0,0,0,0}$ within the Zakharov (1968) equation. According to Janssen & Onorato (2007), the wave-induced mean flow translates to a shift in the mean free-surface for narrow-banded waves with central wavenumber, k_0. This shift is given by,

$$\bar{\eta} = a^2 k_0 \Delta, \quad \Delta = -\frac{1}{4}\frac{c_s^2}{c_s^2 - c_g^2}\Big[\frac{2(1-Q_0^2)}{Q_0} + \frac{1}{k_0 d}\Big], \tag{B.1}$$

where $c_s = \sqrt{gd}$ is the shallow-water wave speed, c_g is the group velocity given by $c_g = \omega_0' = 1/2c_0(1 + 2k_0 d/(\sinh(2k_0 d)))$ [1], c_0 is the wave speed (ω_0/k_0), a is the amplitude of the primary wave, d is the water depth and $Q_0 = \tanh(k_0 d)$. This result is entirely in agreement with an earlier derivation presented by Whitham (1974) using the so-called variational approach.

In addition, it should be noted that the the wave-induced mean flow has also been derived by Marthinsen & Winterstein (1992) on the basis of a Stoke's type narrow-band process. According to Marthinsen & Winterstein (1992) this is given by,

$$\bar{\eta} = -\frac{a^2 k_0}{2}\Big(\frac{g c_g/\omega}{gd - c_g^2} + \frac{gd}{(gd - c_g^2)\sinh(2kd))}\Big). \tag{B.2}$$

Both Equations B.1 and B.2 reveal that the wave-induced mean flow arises at second-order in wave-steepness. However, it differs from the classic monochromatic Stoke's wave set-down, as noted by Marthinsen & Winterstein (1992) (see also Tayfun & Alkhalidi (2020)); owing to the abandonment of a strict monochromatic assumption.

In accounting for the presence of the wave-induced mean flow, the finite-depth self interaction kernel within the Zakharov equation is given by (Janssen & Onorato, 2007):

$$T_{0,0,0,0} = \frac{k_0^3}{2\pi} X_0, \quad X_0 = \frac{9Q_0^4 - 10Q_0^2 + 9}{8Q_0^3} - \frac{1}{k_0 d}\Big(\frac{(2c_g - c_0/2)^2}{c_s^2 - c_g^2} + 1\Big). \tag{B.3}$$

This interaction kernel is used within the finite-depth Benjamin-Feir index in Equa-

[1] ω_0' refers to the first derivative of ω_0 with respect to k_0

tion 3.4, yielding the estimation of the dynamic kurtosis at steady state according to Equation 3.2.

Finally, the second derivative of ω_0 with respect to k_0, ω_0'', appearing in Equation 3.4, is given by,

$$\omega_0'' = -\frac{g}{4\omega_0 k_0 Q_0}\Omega'', \quad \Omega'' = [Q_0 - k_0 d(1-Q_0^2)]^2 + 4(k_p d)^2 Q_0^2(1-Q_0^2). \tag{B.4}$$

It is interesting to note that the value of the interaction kernel $T_{0,0,0,0}$ is also involved in the finite-depth nonlinear dispersion relationship. Specifically, in finite depth the third-order wave frequency, $\omega_0^{(3)}$, is given by,

$$\omega_0^{(3)} = \omega_0^{(1)} \cdot \left(1 + \frac{1}{2} T_{0,0,0,0} \frac{2\pi}{k_0 \tanh(k_0 d)} a^2\right), \tag{B.5}$$

where $\omega_0^{(1)} = \omega_0$ is the linear angular frequency given by $\omega_0^{(1)} = \sqrt{g k_0 \tanh(k_0 d)}$. Interestingly, in deep water, for which $T_{0,0,0,0} = k_0^3/2\pi$, Equation B.5 yields the well-known Stoke's change in the angular frequency already given in Equation 2.20.

At this point, it is perhaps instructive to visualise the variation with effective water depth, $k_0 d$, of:

- the resonant interaction kernel $T_{0,0,0,0}$, normalised with respect to the deep-water value of $k_0^3/2\pi$,
- the normalised wave-induced mean flow, $\bar{\eta}/(a^2 k_0)$ (given by both Janssen & Onorato 2007 and Marthinsen & Winterstein 1992), and
- the relative change in wave speed, $\Delta c/c_0 = (\omega_0^{(3)} - \omega_0^{(1)})/\omega_0^{(1)}$ due to third-order nonlinearity (Equation B.5) in relation to the deep-water relative change $\Delta c/c_0 = \frac{1}{2} a^2 k_0^2$ (Equation 2.20).

All of the above quantities are plotted in Figure B.1 against the relative water depth, $k_0 d$. These have been superimposed on the same plot such that their variation with $k_0 d$ can be directly compared.

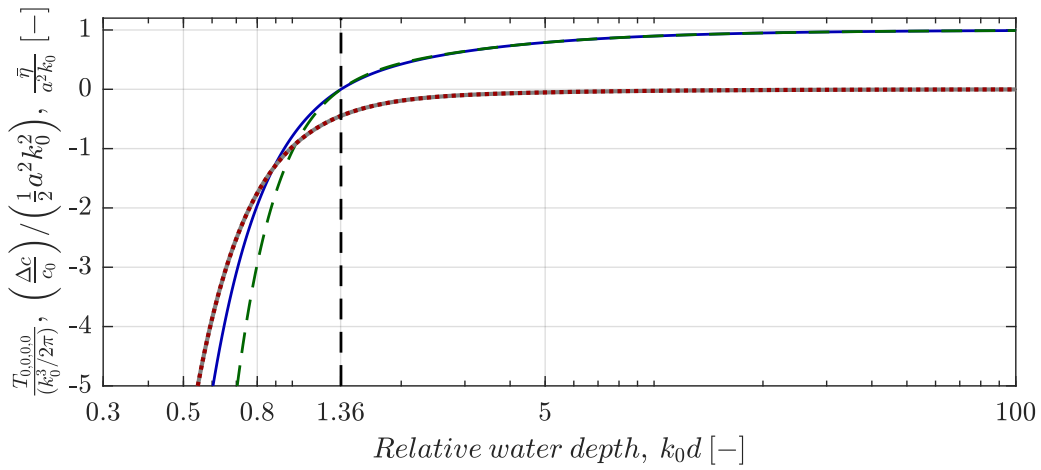


FIGURE B.1: Variation of the normalised resonant interaction kernel $T_{0,0,0,0}/(k_0^3/(2\pi))$ (——), the relative change in wave speed with respect to the deep-water relative change $(\Delta c/c_0)/(\frac{1}{2}a^2k_0^2)$ (– –) and the normalised wave-induced mean flow $\bar{\eta}/(a^2k_0)$; (——) denoting the solution of Janssen & Onorato (2007) and (·····) denoting the solution of Marthinsen & Winterstein (1992). All quantities are plotted against the relative water depth, k_0d. Finally, the effective water depth $k_0d = 1.363$, where both the resonant interaction kernel and the relative change in wave-speed change sign is shown with (— —).

Several points can be made in observing Figure B.1. These are listed as follows:

1. Under the effect of third-order resonant interactions, the phase-speed of a narrow-band wave train reduces in relation to the linear phase-speed for $k_0d < 1.36$ and it increases for $k_0d > 1.36$. This change in phase speed for wave components at different k_0d is most likely responsible for the elongation of uni-directional JONSWAP quasi-deterministic linearly focused wave groups in $k_pd = 0.86$ presented by Katsardi & Swan (2011). As low-frequency components travel slower than linearly predicted and high-frequency components travel faster. This change in wave speed leads to the non-focusing of wave energy. This explains the fact that the fully nonlinear crest-elevations presented by Katsardi & Swan (2011) lied below the linearly predicted elevations. A similar effect was also noted in Figures 3.9 and 3.10.

2. The expressions of Janssen & Onorato (2007) and Marthinsen & Winterstein (1992) for the wave-induced shift in the mean free-surface are in perfect agreement despite being derived using different approaches. This demonstrates the reliability of these solutions.

3. The wave-induced wave-induced shift in the mean free-surface does not vanish

at $k_0 d = 1.363$. Hence, energy focusing is possible even in the presence of wave-induced mean flow.

4. The rate at which the wave-induced shift in the mean free-surface and the resonant interaction kernel change with $k_0 d$ is not directly proportional. Nonetheless, the two quantities are shown to be related in the sense that they show a rapid decrease for $k_0 d < 1.363$. Combining this point with point (3), the value of the dynamic kurtosis cannot be directly inferred from the magnitude of the wave-induced shift in the mean free-surface.

B.1.2 Additional comparisons to numerical results

Having presented key aspects of the theoretical solution of Janssen & Onorato (2007), this section discusses the application of this solution, and particularly of Equation 3.2, to non-bandwidth limited sea-state conditions. Hence, the present section compliments the discussion already provided in §3.6, regarding the performance of Equation 3.2 in predicting the dynamic kurtosis arising in broad–banded uni-directional seas. In more detail, in applying Equation 3.2 to broad-banded seas, multiple definitions for the related sea-state parameters are possible. This makes the comparisons presented in §3.6 non-unique. For this reason, here additional comparisons between the theoretical predictions based on Equation 3.2 and the numerical (HOSM) results are presented for completeness. This is achieved by using different definitions for the sea-state parameters involved. These parameters refer to the definition of the spectral bandwidth and the sea-state steepness within the estimation of the BFI (Equation 3.3), as well as the definition of the central wavenumber k_0 within Equation 3.4.

To this end, Figure B.2 presents the comparisons between the theoretical predictions and the HOSM data for different effective water depths, $k_p d$, and JONSWAP spectra (different γ). At the left-hand-side sub-figures the bandwidth parameter $\frac{1}{\sqrt{\pi Q_p}}$, defined in Equation 2.44, was used to calculate BFI, whereas in the right hand-side sub-figure the bandwidth parameter ν, defined in Equation 2.43 was employed. In all comparisons, two steepnesses have been employed to represent the narrow-band steepness $k_0 \sigma_\eta$ in Equation 3.3 (σ_η^2 being the variance of the free surface). Specifically, the continuous lines refer to the steepness $k_p \sigma_\eta$, while the dashed lines refer to $k_m \sigma_\eta$ (where k_m is the wavenumber corresponding to the spectral mean

frequency $\omega_m = m_1/m_0$ according to the linear dispersion relationship [1]). Irrespective of the adopted steepness, the depth-dependence is taken according to k_p in all cases.

In observing Figure B.2, as already noted in §3.6, the use of $\frac{1}{\sqrt{\pi Q_p}}$ in $k_p d > 1.36$ is shown to lead to better predictions than ν. Whereas the opposite holds for sea-states with $k_p d < 1.36$, irrespective of the choice of steepness. However, the values of the dynamic kurtosis for $k_p d > 1.36$ (using $\frac{1}{\sqrt{\pi Q_p}}$), were found to be slightly under-predicted. This is also depicted in the left-hand side sub-figures of Figure B.2. To this end, Figure B.2 shows that when using the steepness $k_m \sigma_\eta$ the dynamic kurtosis is over-predicted. Hence, the adoption of an alternative wavenumber between k_p and k_m could potentially provide more satisfactory predictions.

To explore this, the wavenumber used for estimating the dynamic kurtosis within the ECMFW freak warning system (Janssen, 2017) has been employed, given by $k'_m = k(0.9\omega_m)$ (where $k(\omega)$ refers to the linear dispersion relationship). This wavenumber was adopted for both the steepness and relative water depth. Following again the ECMFW recommendations (Janssen, 2017), the bandwidth parameter $\frac{1}{\sqrt{\pi Q_p}}$ was adopted for these additional comparisons. These additional comparisons are shown in Figure B.3. It is shown that by employing the wavenumber, k'_m, which lays between k_0 and k_m, within Equation 3.2 leads to better predictions for $k_p d > 1.36$, than using either k_0 or k_m (Figure B.2).

Moreover, for $k_p d < 1.36$ the use $\frac{1}{\sqrt{\pi Q_p}}$ in conjunction with $\sigma_\eta k_0 = \sigma_\eta k'_m$ and $k_0 d = k'_m d$, leads to more satisfactory predictions than what was obtained on the basis of $\sigma_\eta k_0 = \sigma_\eta k_p$ and $k_0 d = k_p d$ in Figure B.2 when the same bandwidth parameter was adopted. This is not surprising given that k'_m reflects the importance of the high-frequency tail, which is not captured by $\frac{1}{\sqrt{\pi Q_p}}$. However, in this effective water depth regime ($k_p d < 1.36$), the use of ν in conjunction with $\sigma_\eta k_0 = \sigma_\eta k_p$ and $k_0 d = k_p d$ is still the most appropriate choice of parameters. Particularly, because in Figure B.3 the values of the dynamic kurtosis at $k_p d < 1.0$ are significantly over-predicted, especially for reducing bandwidth.

[1] Note that k_m defined in this Appendix is identical to k_1 defined in §2.3.3

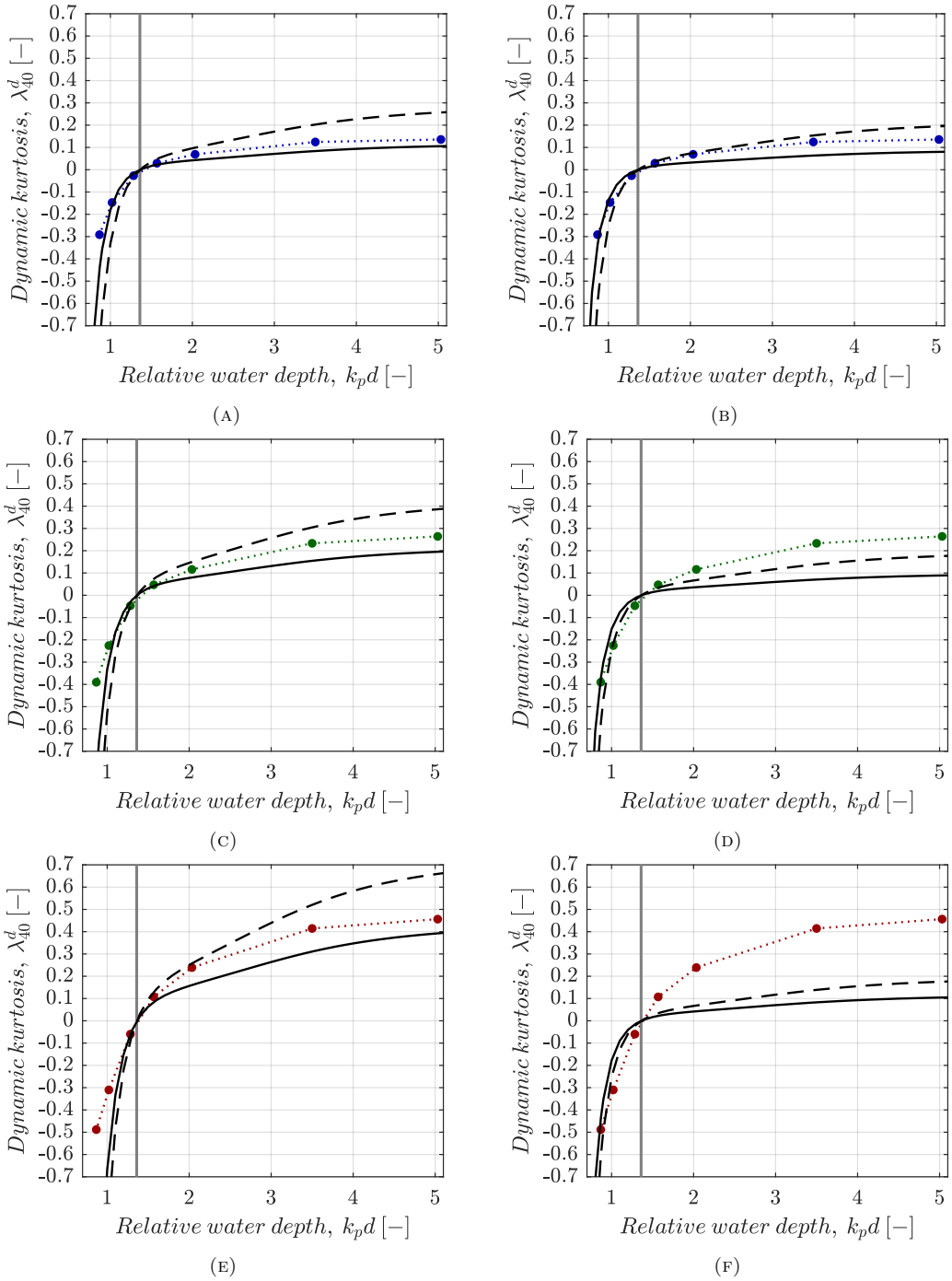


Figure B.2: Comparison between the uni-directional narrow-band theoretical solution of Janssen & Onorato (2007) for the dynamic kurtosis and the numerical results obtained using HOSM; left column for $\frac{1}{\sqrt{\pi Q_p}}$ and right column for ν. All sea-states are characterised by $\frac{1}{2}H_sk_p = 0.105$ and $\sigma_\theta = 0$. (A) and (B) for $\gamma = 1$, (C) and (D) for $\gamma = 2.5$, and (E) and (F) for $\gamma = 5$. The lines (·· ● ·· / ·· ● ·· / ·· ● ··) refer to HOSM results and the lines (—— / – –) to theoretical predictions using $\sigma_\eta k_p$ and $\sigma_\eta k_m$, respectively. The vertical line (——) in all sub-plots marks the theoretical value of $k_0d = 1.363$.

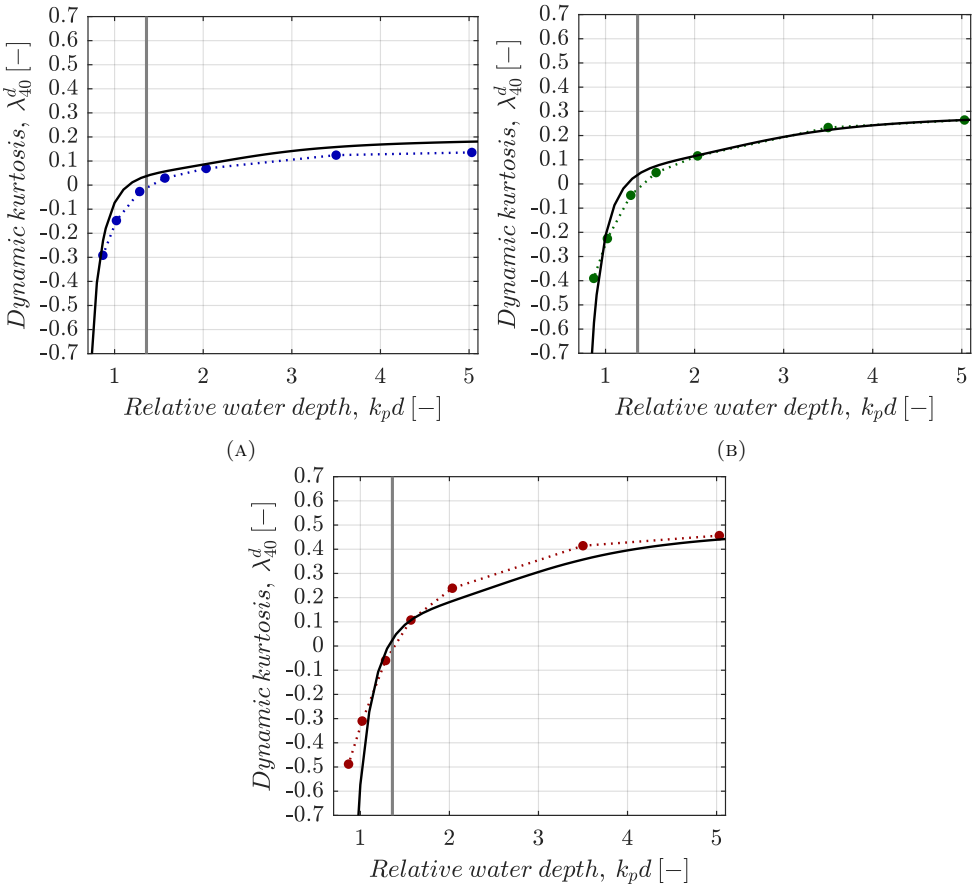


Figure B.3: Comparison between the uni-directional narrow-band theoretical solution of Janssen & Onorato (2007) for the dynamic kurtosis, evaluated using the sea-state parameters recommended by ECMFW (Janssen, 2017), and the numerical results obtained using HOSM. All sea-states are characterised by $\frac{1}{2}H_sk_p = 0.105$ and $\sigma_\theta = 0$. (A) for $\gamma = 1$, (B) for $\gamma = 2.5$ and (C) for $\gamma = 5$. The lines (· · ● · · / · · ● · · / · · ● · ·) refer to HOSM results and the lines (——) to the theoretical predictions. Again, the vertical line (——) in all sub-plots marks the theoretical value of $k_0d = 1.363$.

B.2 The uni-directional solution of Janssen (2009) for the skewness and bound kurtosis

B.2.1 Theoretical solution

Following from §3.2.2, Janssen (2009) derived closed-form solutions for the skewness and bound kurtosis appropriate for narrow-banded uni-directional random seas in arbitrary effective water depth conditions. These solutions have been compared to HOSM broad-banded results in Figure 3.33 and are provided here for completeness.

According to Janssen (2009), to the lowest significant order, the skewness parameter for a narrow-band wave train of central wavenumber, k_0, is given by,

$$\lambda_3 = 6\sigma_\eta k_0(\alpha + \Delta), \quad \alpha = \frac{3 - Q_0^2}{4Q_0^3}. \tag{B.6}$$

Likewise, the bound kurtosis is given by,

$$\lambda_{40}^b = 24(\sigma_\eta k_0)^2\Big[\beta + \kappa + 2(\alpha + \Delta)^2\Big], \quad \beta = \frac{24 + 3(1 - Q_0^2)^3}{64Q_0^6}, \quad \kappa = -\frac{\alpha^2}{2} \tag{B.7}$$

where Δ and Q_0 have already been been defined in the context of Equation B.1.

B.2.2 Additional comparisons to numerical results

As already indicated by Janssen (2009), with a reduction in effective water depth, the values of both skewness and bound kurtosis are greatly affected by the effect of the wave-induced mean flow (expressed through the parameter Δ). Specifically, the incorporation of the wave-induced mean flow was shown to substantially reduce both the skewness and the bound kurtosis. To this end, in the comparisons presented in Figure 3.33, the wave-induced mean flow was included in the theoretical predictions. As the wave-induced mean flow is the narrow-band equivalent of low-frequency frequency-difference terms that are inherently included in the simulation results. However, the wave-induced mean flow predicted based on a narrow-band assumption could be over-estimated. This effect could be responsible for the under-estimation of both the skewness and bound kurtosis observed in Figure 3.33.

In addition, the depth-dependence within Equations B.6 and B.7 is considered through the parameter Q_0, which in turn depends upon $k_0 d$. As mentioned earlier, in

a narrow-band sense, there is no ambiguity regarding the definition of k_0. However, this is not the case for realistic bandwidth sea-states; with k_p and k_m being the two main possible definitions

Based on the above, the application of Equations B.6 and B.7 to broad-banded sea-states is not straightforward. As there is ambiguity regarding the definition of (1) the effective water depth, $k_0 d$, (2) the sea-state steepness $\sigma_\eta k_0$ and (3) the inclusion or not of the effect of the wave-induced mean flow.

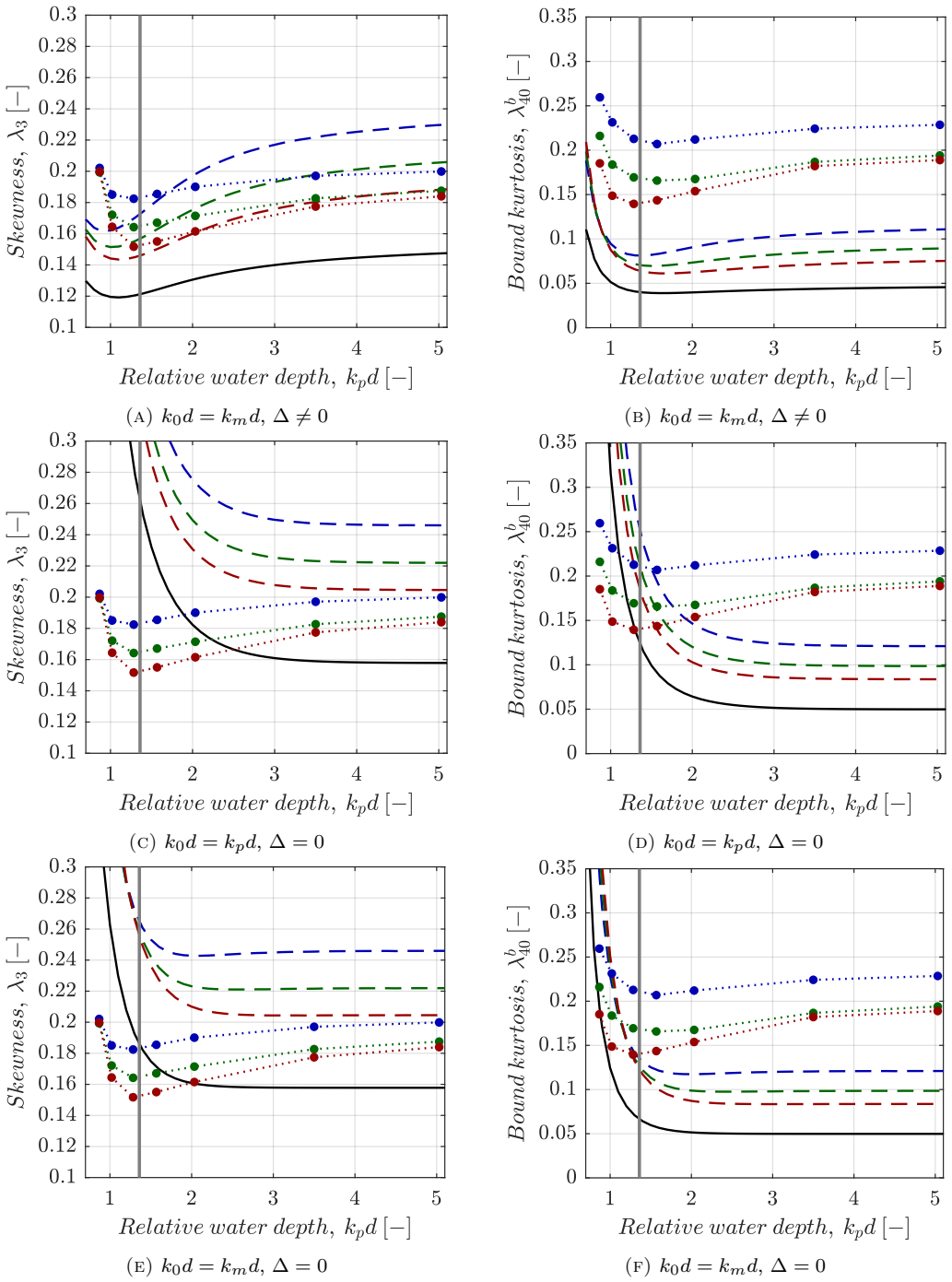
To determine the most suitable choice for these parameters, Figure B.4 presents additional to Figure 3.33 comparisons to the numerical results obtained using HOSM. Specifically, Figure 3.33 included comparisons in which depth dependence was considered based on $k_p d$, the sea-states steepness was defined using both $\sigma_\eta k_p$ and $\sigma_\eta k_m$ and the effect of wave-induced mean flow was included in the theoretical predictions. In contrast, the different sub-figures within Figure B.4 present the following comparisons:

- Sub-figures (A) and (B) present comparisons for the skewness and bound kurtosis respectively, where depth-dependence in the analytical solutions is taken into account according to $k_m d$. While the effect of the wave-induced mean flow is included.

- Sub-figures (C) and (D) present comparisons for the skewness and bound kurtosis respectively, where depth-dependence in the analytical solutions is taken into account according to $k_p d$. While the effect of the wave-induced mean flow is *not* included.

- Sub-figures (E) and (F) present comparisons for the skewness and bound kurtosis respectively, where depth-dependence in the analytical solutions is taken into account according to $k_m d$. While effect of the wave-induced mean flow is *not* included.

The comparisons in Figure B.4 demonstrate that none of the employed approaches gives satisfactory agreement to the HOSM data. This once again confirms the inappropriateness of the narrow-band solutions. Specifically, in contrasting Figures 3.33(A) and 3.33(B) to Figures B.4(A) and B.4(B), respectively, it is revealed that depth-dependence is better captured when the k_p is adopted. While the omission of



(A) $k_0d = k_md$, $\Delta \neq 0$ (B) $k_0d = k_md$, $\Delta \neq 0$

(C) $k_0d = k_pd$, $\Delta = 0$ (D) $k_0d = k_pd$, $\Delta = 0$

(E) $k_0d = k_md$, $\Delta = 0$ (F) $k_0d = k_md$, $\Delta = 0$

Figure B.4: Comparison between the uni-directional narrow-band theoretical solutions of Janssen (2009), for the skewness and bound kurtosis, and the numerical results obtained using HOSM All sea-states are characterised by $\frac{1}{2}H_sk_p = 0.105$ and $\sigma_\theta = 0$. The left column refers to the skewness and the right column to the bound kurtosis. In (A) and (B) $k_0d = k_md$ and the effect of the wave-induced mean flow is included. In (C) and (D) $k_0d = k_pd$ and the effect of the wave-induced mean flow is *not* included. In (E) and (F) $k_0d = k_md$ and the effect of the wave-induced mean flow is *not* included. The lines (·· ● ·· / ·· ● ·· / ·· ● ··) correspond to the numerical results for $\gamma = 1.0$, 2.5 and 5.0, respectively. The theoretical narrow-band solution is denoted with (——) using a steepness of $\sigma_\eta k_p$, and with (– – / – – / – –) using $\sigma_\eta k_m$ for $\gamma = 1.0$, 2.5 and 5.0, respectively.

the effect of the wave-induced mean-flow leads to significant over-prediction of the skewness in all cases, as well as of the bound kurtosis for low effective water depths.

B.3 The directional solution of Janssen (2017) for the skewness, bound kurtosis and dynamic kurtosis

As noted in §4.1.2, Janssen (2017) has provided directional solutions for the statistical parameters of skewness, bound kurtosis and dynamic kurtosis, that account for the effect of directionality. For completeness of the discussion, here, the functional form of these solutions will be provided along with complimentary comparisons to HOSM data.

B.3.1 Theoretical solution

The directional finite-depth solution of Janssen (2017) bridges the uni-directional finite-depth solution of Janssen & Onorato (2007) and the deep-water directional solution of Fedele (2015). This was achieved by employing the Davey & Stewartson (1974) system of equations, which provides special treatment for the effect of the wave-induced mean flow in finite water depth. Therefore, first, the solution of Fedele (2015) will be described before presenting the finite-depth solution of Janssen (2017).

Repeating from §4.1.2, according to Fedele (2015), the dynamic kurtosis for deep-water narrow-banded, in both frequency and direction, sea-states is expressed as:

$$\lambda_{40}^{d} = \frac{\pi}{\sqrt{3}} J(\tau; R) BFI^2, \tag{B.8}$$

where BFI is the Benjamin-Feir index defined in Equation 3.3. Moreover, $J(\tau; R)$ is a time dependent factor evaluated according to:

$$J(\tau; R) = \frac{3\sqrt{3}}{\pi} \operatorname{Im} \int_0^{\tau} \frac{1}{\sqrt{1 - 2i\alpha + 3\alpha^2}\,\sqrt{1 + 2iR\alpha + 3R^2\alpha^2}} d\alpha, \tag{B.9}$$

where R is defined by $R = \delta_\theta/(2\delta_\omega) = \sigma_\theta/(2\sigma_\omega/\omega_0)$ and expresses the relative importance between the directional dispersion and the frequency dispersion; with $R = 0$

signifying uni-directional conditions. While, τ is given by $\tau = (\sigma_\omega/\omega_0)^2\omega_0 t$.

Figure B.5 shows the time-evolution of $J(\tau; R)$ for different values of R as a function of the non-dimensional time τ (sub-figure B.5(A)) and the non-dimensional time t/T_p (sub-figure B.5(B)). In the former, the spectral bandwidth σ_ω/ω_0 has been taken as $1/(\sqrt{\pi}Q_p)$, assuming a JONSWAP spectrum of $\gamma = 2.5$.

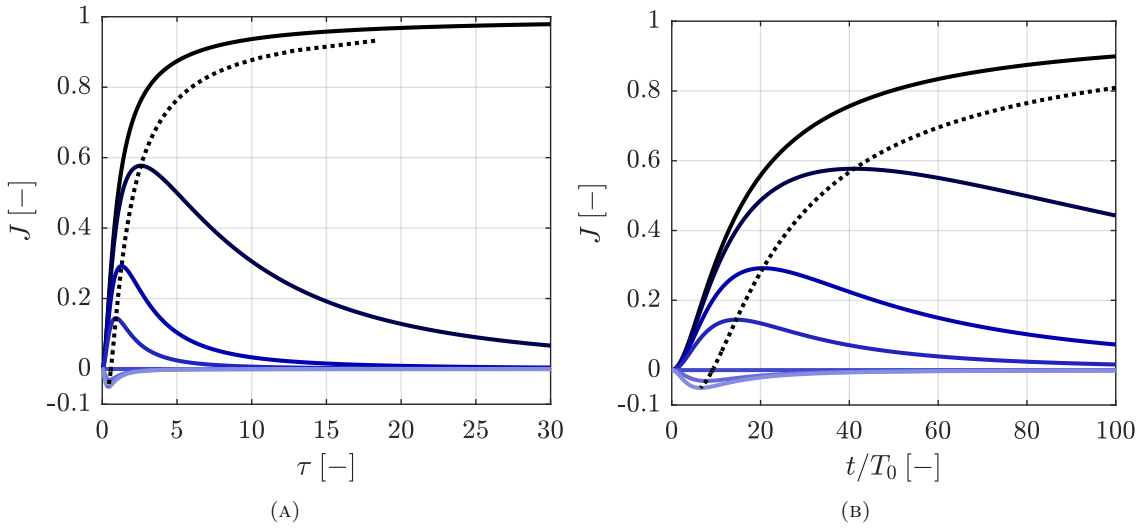


Figure B.5: Temporal evolution of the directionality factor J with non-dimensional time for different values of the parameter R. The two sub-figures refer to the same trends but with different non-dimensional time on the horizontal axis; sub-figure (A) for τ and sub-figure (B) for t/T_p. The different lines (/ / / / / /) correspond to $R = 0, 0.05, 0.2, 0.4, 1, 1.4$ and 2, respectively. While the line ( ) marks the points at which the dynamic kurtosis maximises for different R values. This is given by $\tau_c = 1/\sqrt{3R}$.

The take-out message from Figure B.5 is that the theoretical predictions for the dynamic kurtosis in directionally spread seas peak within the duration of the HOSM simulations; the latter being of $\sim 60T_p$ duration. This is important in that it demonstrates that the simulations are sufficiently long such that the numerical HOSM results could directly be compared to the theoretical predictions. Interestingly, for $t \to \infty$ the theoretical solution predicts that the dynamic kurtosis tends to 0 in directional sea-states ($R > 0$).

Considering now the finite-depth solution of Janssen (2017), the key difference to Fedele (2015) is the inclusion of the effect of the wave-induced mean flow, relevant to finite-depth conditions. According to Janssen (2017), the wave-induced mean flow

for a narrow-band directional wave train is expressed as,

$$\bar{\eta} = a^2 k_0 \Delta_d, \quad \Delta_d = \Delta + \frac{1}{4}\frac{c_g}{Q_0}\frac{2c_0 + c_g(1-Q_0^2)}{c_s^2 - c_g^2}\frac{R}{R+\alpha_\omega/2} \tag{B.10}$$

where Δ has been defined in the context of Equation B.1 and α_ω is given by,

$$\alpha_\omega = \frac{c_0^2}{c_g^2}\left(1 - \frac{c_g^2}{c_s^2}\right) \tag{B.11}$$

As such, the wave-induced mean flow is affected by the factor R. Notably, when the latter is set to zero (uni-directional conditions), the uni-directional solution of Equation B.1 is recovered.

To gain a better understanding on how R affects the magnitude of the wave-induced mean flow, $\bar{\eta}$, Figure B.6 presents the variation of $\bar{\eta}/(a^2k_0)$ with effective water depth $k_0 d$ for different values of R. It is shown that as R increases, the set-down reduces. This reduction in the set-down leads to the increase of the directional finite-depth BFI, B_{sd}, presented in Figure 4.1(A).

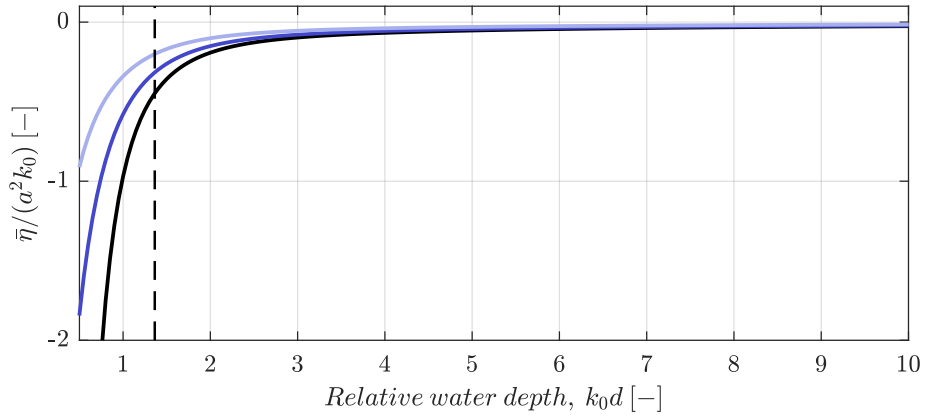


FIGURE B.6: Variation of the normalised wave-induced mean flow, $\bar{\eta}/(a^2k_0)$, with relative water depth, $k_0 d$, for different values of the parameter R: $R = 0, 0.4$ and 1.4, denoted with (— / — / —), respectively. The effective water depth $k_0 d = 1.363$, denoted with (– –), is added for reference.

In this respect, B_{sd} is defined by Equation 3.4. However, this time the uni-directional finite-depth kernel, $T_{0,0,0,0}$, is replaced by its directional version, $T^d_{0,0,0,0}$. This is defined by,

$$T^d_{0,0,0,0} = \frac{k_0^3}{2\pi}\Big(X_0 + X_d\Big), \tag{B.12}$$

where X_0 has been defined in the context of Equation B.3 for uni-directional sea-

states and X_d accounts for the effect of directionality. This is given by,

$$X_d = \frac{[c_0 + c_g(1 - Q_0^2)/2]^2}{Q_0(c_s^2 - c_g^2)} \frac{R}{R + \alpha_\omega/2}. \tag{B.13}$$

To complete the definition of the directional solution of Janssen (2017), following the discussion in §4.1.2, the finite-depth version of the parameter R, referred to as R_s, needs to be defined. This is involved in the calculation of the factor $J(\tau; R_s)$ within Equation B.9 and is given by,

$$R_s = \beta_s R, \quad \beta_s = -2\Big(\frac{c_g}{c_0}\Big)^3 \frac{Q_0 g}{k_0 \omega_0 \omega_0''}. \tag{B.14}$$

In the above expression, the factor β_s is linked to the depth factor α_s in Equation 3.4 according to:

$$\alpha_s = \frac{1}{2}\frac{X_0}{Q_0}\Big(\frac{c_0}{c_g}\Big)\beta_s. \tag{B.15}$$

It is noted that the resulted variation of $J(\tau; R_s)$ with R for different effective water depths was presented in Figure 4.1(b), hence no further discussion will be provided here.

Finally, as pointed out in §4.1.2, the change in the wave-induced mean flow due to directionality also affects the estimates for the skewness and bound kurtosis. Specifically, the directional estimates of these parameters follow from Equations B.6 and B.7, in which the parameter Δ is replaced by the parameter Δ_d of Equation B.10. It is noted that the effect of including Δ_d in estimating the skewness and bound kurtosis has already been discussed in the context of Figure 4.2.

B.3.2 Additional comparisons to numerical results

In §B.1 and B.2 it was pointed out that the way a narrow-band solution can be applied to broad-banded seas is non-unique. Hence, here additional comparisons between the theoretical predictions of Janssen (2017) for the statistical parameters of skewness and bound kurtosis to numerical (HOSM) results arsing in directional simulations are provided. These comparisons complement the ones already presented in Figure 4.17. Specifically, the theoretical predictions presented in Figure 4.17 have been obtained by employing the peak wavenumber, k_p, for reflecting depth dependence (i.e. $k_0 d = k_p d$) and ν as a measure of spectral bandwidth within the

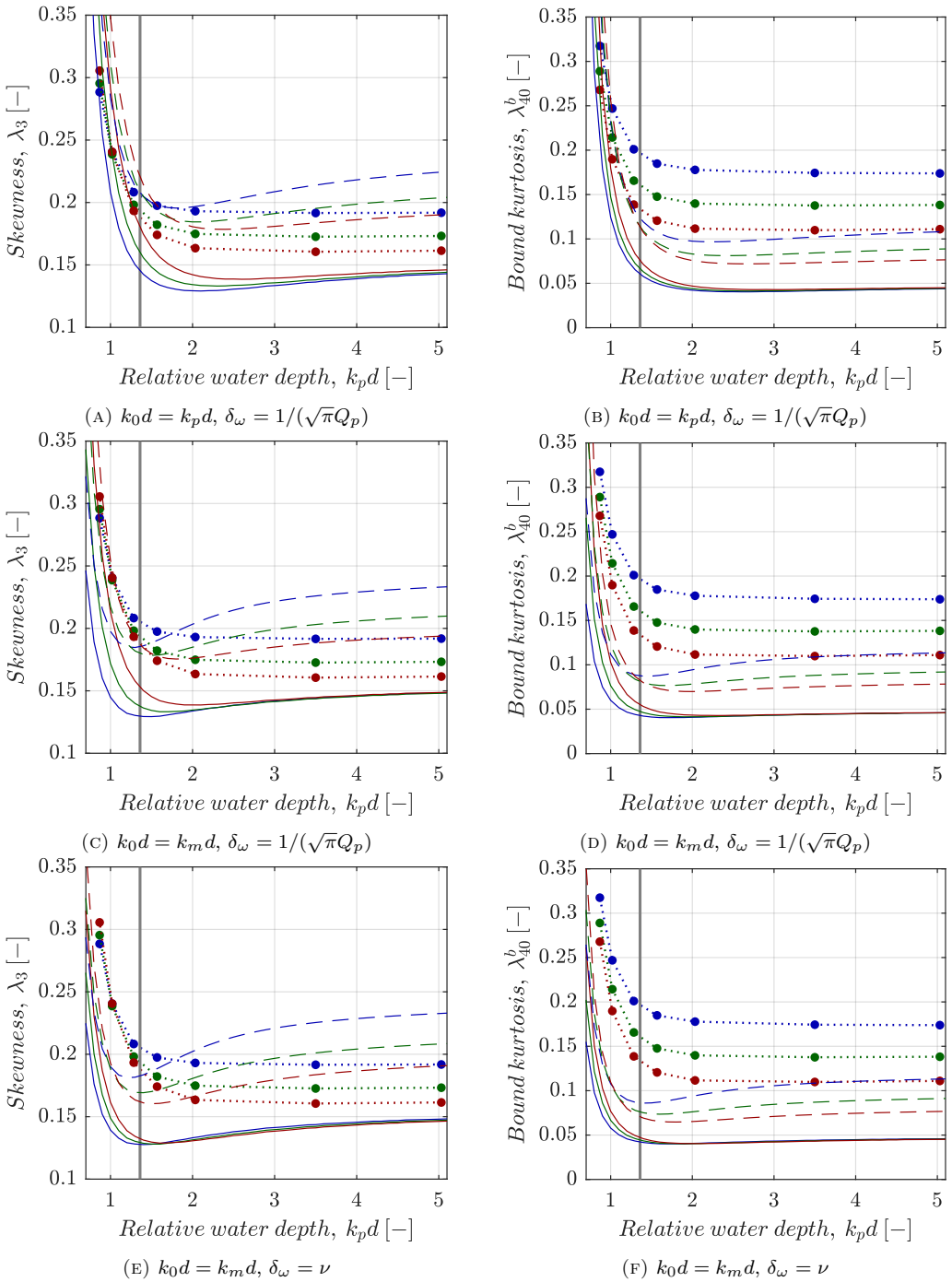
parameter R.

To this end, Figure B.7 presents the same set of comparisons as Figure 4.17, but depth dependence and spectral bandwidth are considered in alternative ways. Specifically, in Figure B.7 the left-hand side sub-figures refer to the skewness parameter and the right-hand side sub-figures to the bound kurtosis. In particular, the evaluation of the theoretical predictions:

- in sub-figures (A) and (B) has been based on $k_0 d = k_p d$, but this time the spectral bandwidth is taken as $\delta_\omega = 1/(\sqrt{\pi} Q_p)$;
- in sub-figures (C) and (D) has been based on $k_0 d = k_m d$ and a spectral bandwidth parameter $\delta_\omega = 1/(\sqrt{\pi} Q_p)$; and
- in sub-figures (E) and (F) has been based on $k_0 d = k_m d$ and a spectral bandwidth parameter ν.

While in all cases, the theoretical predictions are obtained using $\sigma_\eta k_p$ and $\sigma_\eta k_m$ as the steepness parameter.

The comparisons presented in Figure B.7 support the conclusion drawn upon the comparisons presented earlier in Figure 4.17 in that the Janssen (2017) solutions are not able too capture the values of the statistical moments arising in broad-banded directional HOSM simulations. As none of the combination of parameters leads to satisfactory predictions. Notably, the combination of $k_0 d = k_p d$ and ν adopted in Figure 4.17 appears to lead to the most favourable predictions. Finally, it was found that in adopting the ECMFW proposed wavenumber k'_m did not improve any of the presented comparisons.



(A) $k_0d = k_pd$, $\delta_\omega = 1/(\sqrt{\pi}Q_p)$ (B) $k_0d = k_pd$, $\delta_\omega = 1/(\sqrt{\pi}Q_p)$

(C) $k_0d = k_md$, $\delta_\omega = 1/(\sqrt{\pi}Q_p)$ (D) $k_0d = k_md$, $\delta_\omega = 1/(\sqrt{\pi}Q_p)$

(E) $k_0d = k_md$, $\delta_\omega = \nu$ (F) $k_0d = k_md$, $\delta_\omega = \nu$

Figure B.7: Comparison of the directional narrow-band theoretical solutions of Janssen (2017), for the skewness and bound kurtosis, and the numerical results obtained using HOSM. All sea-states are characterised by $\frac{1}{2}H_sk_p = 0.105$ and $\sigma_\theta = 10°$. The left column refers to the skewness and the right column to the bound kurtosis. In (A) and (B) $k_0d = k_pd$ and $\delta_\omega = 1/(\sqrt{\pi}Q_p)$. In (C) and (D) $k_0d = k_md$ and $\delta_\omega = 1/(\sqrt{\pi}Q_p)$. In (E) and (F) $k_0d = k_md$ and $\delta_\omega = \nu$. The lines (·●·/·●·/·●·) correspond to HOSM data for $\gamma = 1$, 2.5 and 5, respectively. The theoretical predictions evaluated upon the steepness $k_p\sigma_\eta$ are shown with (——/——/——), while evaluated upon the steepness $k_m\sigma_\eta$ are shown with (– –/– –/– –). These latter lines correspond to $\gamma = 1$, 2.5 and 5, respectively.

C

Additional aspects of HOSM simulations

The present appendix presents additional aspects relating to the random sea-state simulations using HOSM, presented through the thesis. These aspects refer to:

1. The effect of the spatial resolution within HOSM on the crest-height statistics, presented in §C.2.

2. Verification of the spatial homogeneity within directional sea-state simulations, presented in §C.3.

3. Verification for the reliable extraction of the harmonic contributions within directional HOSM simulations, presented in §C.4.

The present appendix commences in §C.1 with the numerical setup used within the directional simulations presented in Chapter 4. While the above aspects follow.

C.1 Numerical setup of directional simulations

The adopted numerical setup for the directional sea-state simulations within HOSM and the required computational resources are presented in Table C.1.

Table C.1: Numerical setup of HOSM for directional simulations. The values in parenthesis refer to simulations with $\sigma_\theta \geq 20°$. While the duration of the simulations includes the ramp-up time of the nonlinear terms and refers to the duration when a ramp of $T_a = 10T_p$ is adopted. For lower T_a the duration was reduced accordingly. The number of processors refers to those used for running the MATLAB wrapper, while HOSM is run in serial mode.

Parameter	Description	Value
HOSM parameters		
M [−]	Order of nonlinearity	3
n_x [−]	Number of nodes in x	1024
n_y [−]	Number of nodes in y	256(512)
L_x/l_p [−]	Normalised domain length in x	35
L_y/l_p [−]	Normalised domain length in y	20
$n_{x,pad}$ [−]	Number of nodes in x after zero-padding	4096
$n_{y,pad}$ [−]	Number of nodes in y after zero-padding	512
N_s [−]	Number of random seeds	330
T_{sim}/T_p[−]	Normalised duration of simulation	75
$\Delta\epsilon$ [deg]	Phase-shifts used in the phase-manipulation method	0, 90, 180, 270
Computational resources		
$RAM[GB]$	Memory requirement	48 (96)
N_{proc} [−]	Number of processors	4
T_{proc} [h]	Processing time (including post-processing)	26 (52)

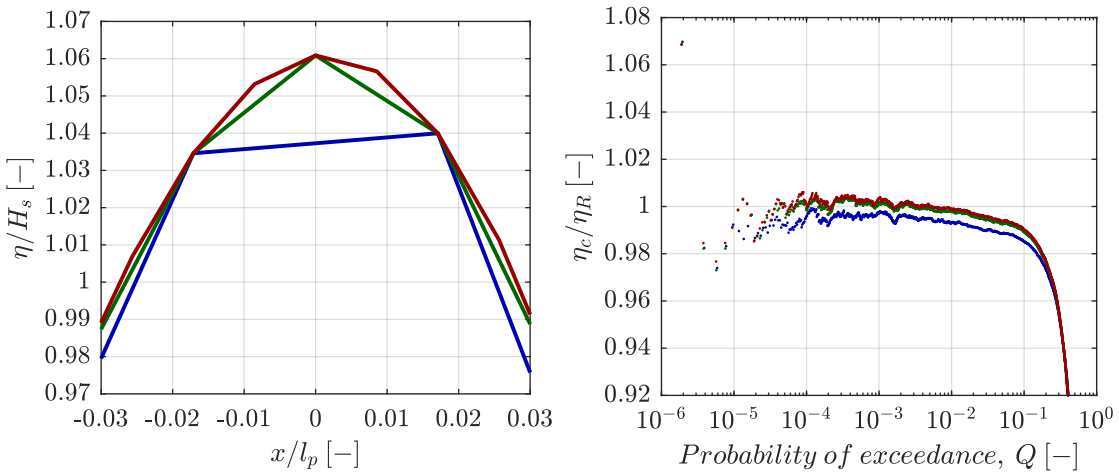
C.2 Spatial resolution

This section discusses the effect of the spatial resolution within HOSM on the crest-height statistics. As described in §2.3.2, the spatial resolution within HOSM is imposed by the combination of (1) the domain length and (2) the number of spectral components. In turn, the combination of these two factors dictates the maximum resolved wavenumber, which needs to be high enough to avoid an excessive truncation of the wave spectrum and low enough to achieve a good spectral resolution

(especially around the spectral peak).

Prioritising therefore an effective modelling of the adopted spectral form, within the analysis presented in Chapters 3 and 4, the choice of the domain length and number of spectral components was such that the spatial increment, Δx, was $\Delta x \approx l_p/30$. In adopting this spatial increment, Figure 2.10 (A) has shown that the ratio of the measured crest-heights arising from linear simulations over the Rayleigh-predicted target values approaches unity, but it does not appear to reach the desired value of 1; with measured crest-heights laying $\sim 1-2\%$ below the target values. To this end, a finer Δx was adopted to investigate whether the spatial increment was responsible for this small discrepancy. This was achieved by zero-padding the original spectrum, whilst maintaining the same spectral resolution as the HOSM simulations.

Figure C.1 (A) shows the spatial profile of a selected wave-crest in a close-up reproduced using finer spatial increments of $\Delta x \approx l_p/60$ and $\Delta x \approx l_p/120$. Figure C.1 (A) demonstrates that with the original resolution, the magnitude and shape of the event are not captured as accurately as when a finer resolutions is adopted. This affects the crest-height distribution as a whole, as shown in Figure C.1 (B). In more detail, with a reduction in the spatial increment to $\Delta x \approx l_p/120$, the tail of the crest-height distribution is shown to converge to the target Rayleigh distribution with great accuracy; the discrepancies being less then $\sim 0.3\%$ around $Q = 10^{-3}$. It is noted that in eliminating the possible effect of sample variability on these trends, the linear sea-states were simulated using $4,000$ seeds. Therefore, to avoid an unwanted underestimation of the recorded crest heights, within the uni-directional and directional simulations presented in Chapters 3 and 4, respectively, the output amplitude spectra were zero-padded and the free-surface reconstructed at every time-step, so that $\Delta x \approx l_p/120$.



(A) (B)

Figure C.1: Effect of spatial increment, Δx, on the crest-height distribution: (A) free surface elevation around a large wave crest and (B) crest-height probability of exceedance distribution normalised with respect to the Rayleigh prediction. The different lines refer to: ( ) for $\Delta x \approx l_p/30$, ( ) for $\Delta x \approx l_p/60$ and ( ) for $\Delta x \approx l_p/120$. The data are obtained from initial wavefields within HOSM obtained using LRWT for a uni-directional sea-state with $k_p d = 5.03$ and $\gamma = 2.5$.

C.3 Spatial homogeneity in directional simulations

Spatial homogeneity is an important property that should be guaranteed within the wavefield, so that the wave characteristics are independent of the location within the wavefield.

In an experimental setting, a relatively coarse angular resolution, imposed by inherent restrictions on the minimum amplitude of waves that a paddle can generate successfully, can lead to a non-homogeneous generated wavefield, as outlined by Jefferys (1987) and Miles & Funke (1989) amongst others. This non-homogeneity arises by adopting the so-called Double Summation Method (DSM) for directional wave generation. Within this approach, the wave components of the same frequency are assigned different directions, creating standing wave patterns. To circumvent this unwanted effect, Latheef et al. (2017) have introduced the Random Directional Method (RDM), in which the problem of non-homogeneity is resolved by adopting a single directional component for each frequency. For more details, the reader is referred to Latheef et al. (2017). As such, the RDM was adopted in the experimental studies employed for validating HOSM in §4.4.

In contrast, in HOSM simulations, the input wave components populate a (k_x, k_y)

rectangular grid, with the angular resolution increasing with increasing k_x. Thus, the nature of the numerical model imposes a wavenumber equivalent DSM. To verify whether the adopted spectral resolution is sufficient to guaranty homogeneity, the spatial variation of the ensemble-averaged significant wave height, H_s, and ensemble-averaged kurtosis λ_{40} arising from 330 linear random sea-state simulations were considered. While each sea-state was simulated for a duration of $60T_p$, similarly to the simulations presented in Chapter 4 and 5. The spatial variation of H_s and λ_{40} is presented in Figure C.2; with sub-figure C.2(A) referring to H_s and sub-figure C.2(B) to λ_{40}. In considering the results in Figure C.2 as a whole, the maximum deviation from the theoretical/target Gaussian values at any spatial location does not exceed 1.5% and 3.5% for the H_s and λ_{40}, respectively. Hence, the wavefield is considered homogeneous.

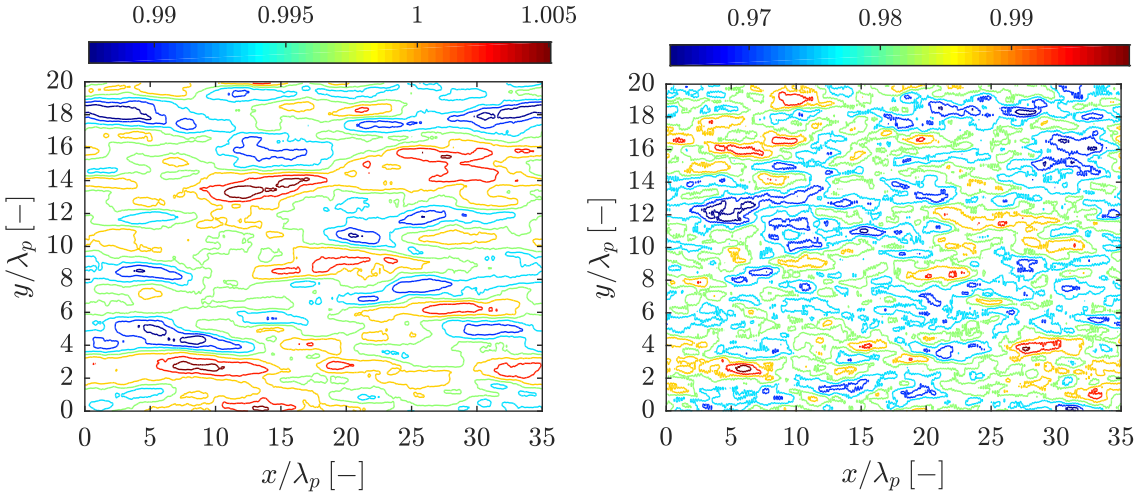


Figure C.2: Spatial variation of (A) the ensemble-averaged significant wave height, H_s and (B) the ensemble-averaged kurtosis, λ_{40}, for a linear wavefield of $k_p d = 5.03$, $\gamma = 2.5$ and $\sigma_\theta = 10°$. Both quantities are normalised by the expected or target value from linear wave theory. In each sub-figure, the axes are normalised by the wavelength corresponding to the spectral peak frequency.

C.4 Separation of nonlinear contributions in directionally spread seas

In simulating the directionally spread sea-states in Chapter 4, the nonlinear order within HOSM was set to $M = 3$. This includes the leading order near-resonant quartet interactions but omits higher order near-resonant interactions. Hence, the effect of

increasing M should be verified.

Moreover, in the context of the uni-directional simulations, presented Chapter 3, it was shown that (1) a ramp-function defined by $T_a = 4T_p$ is sufficient to suppress the spurious waves, generated due to the linear initialisation of the wavefields and (2) that a shorter ramp function would not be effective. This section aims to verify these findings for directional simulations. Finally, in performing the above analysis, the effective separation of the various nonlinear contributions should also tested.

Based on the above, this section includes the following analyses:

i) Verification of the effect of the nonlinearity parameter M within directional HOSM simulations to the nonlinear contributions.

ii) Verification of the methodology adopted for the separation of the nonlinear contributions within directional HOSM simulations.

iii) Identification of the minimum required ramp-function duration for the effective suppression of spurious-wave generation. As well as, the overall assessment of the effectiveness of the ramp function.

C.4.1 Preliminary results on the effect of M

To study the effect of the nonlinearity parameter M on the crest-height statistics, the shallowest ($k_p d = 0.87$) and deepest ($k_p d = 5.03$) effective water depths of the cases presented in Section 4.3 were adopted, characterised by the highest sea-state steepness of $\frac{1}{2} H_s kp = 0.105$. Moreover, for each effective water depth, sea-states of $\sigma_\theta = 10^\circ$ and 20° were simulated, with the peak enhancement factor of the adopted JONSWAP spectrum being set to $\gamma = 1, 2.5$ and 5. These correspond to the full set of γ values investigated in Chapter 4. Moreover, the adopted numerical setup was identical to the one adopted in Chapter 4 and presented in Table C.1. In this preliminary investigation, only the statistics of the total free surface were considered.

Figure C.3 presents the crest-height distributions for the four sea-states of $\gamma = 2.5$ and for all three values of M; each sub-figure referring to a different sea-state. All data correspond to an evolution time of $t = 25T_p$, referring to the steady state of nonlinear evolution. For reference, the (linear) Rayleigh and the second-order directional distribution of Forristall (2000) are also added. Considering these comparisons, it is revealed that an increase in M above 3 has a minimal effect on the crest-height

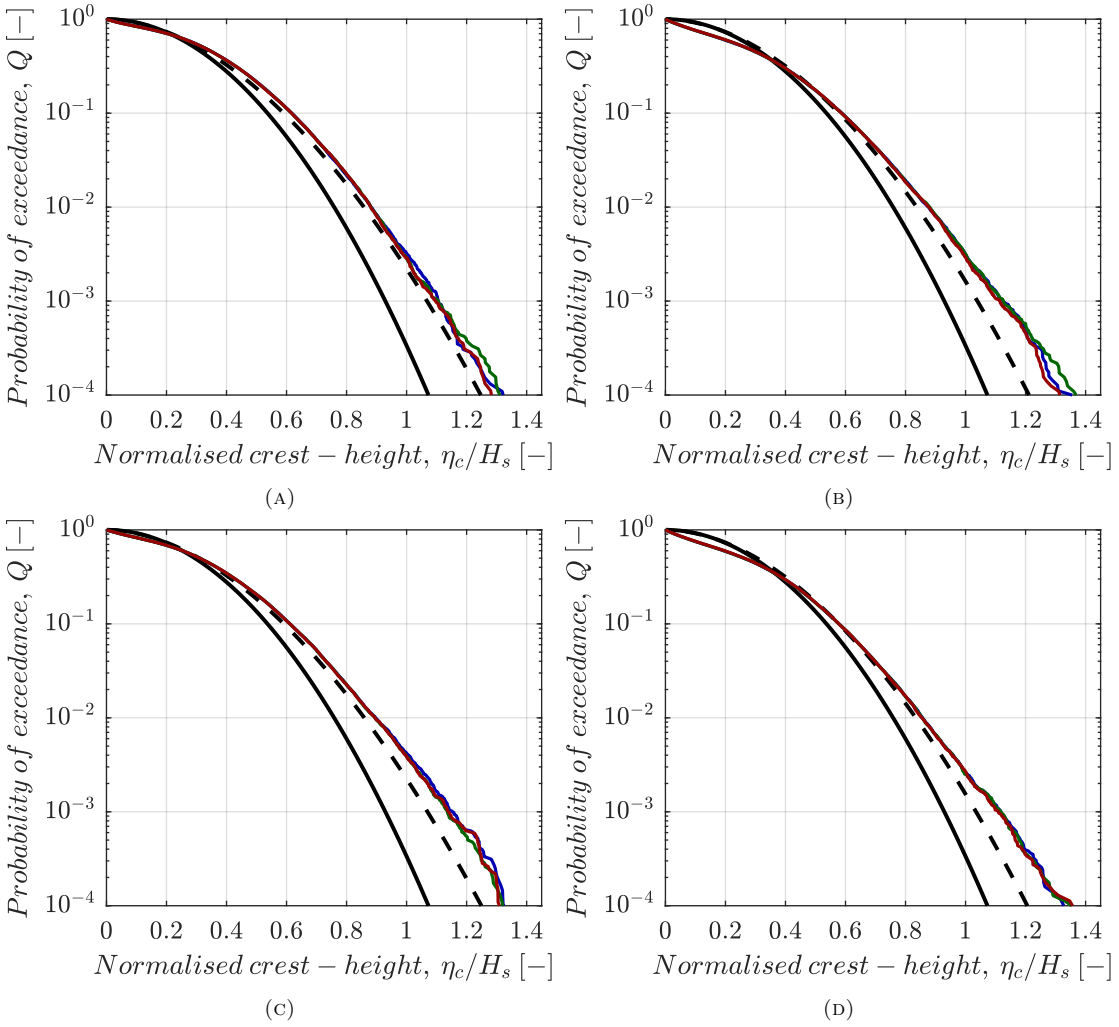


Figure C.3: Normalised crest-height,η_c/H_s, distribution of exceedance obtained arising from HOSM simulations of directional sea-states for varying nonlinear order M: (A) for $k_pd = 0.87$ and $\sigma_\theta = 10°$, (B) for $k_pd = 5.03$ and $\sigma_\theta = 10°$, (C) for $k_pd = 0.87$ and $\sigma_\theta = 20°$, (D) for $k_pd = 5.03$ and $\sigma_\theta = 20°$. In all cases the selected sea-state steepness is $\frac{1}{2}H_sk_p = 0.1052$, the JONSWAP peakedness parameter $\gamma = 2.5$ and the evolution time is $t = 25T_p$. The different lines refer to $M = 3$ ( ), $M = 4$ ( ), $M = 5$ ( ). The Rayleigh ( ) and Forristall (2000) 3D ( ) distributions are also added for reference.

distribution for all sea-states considered. Importantly, this outcome was also found to hold for the different spectral bandwidths ($\gamma = 1.0$ and 5.0) in both water depths; the results not been presented here for brevity.

To verify the effect of M in more detail, snapshots of selected wave events with crest heights corresponding to a probability of exceedance of $Q \approx 10^{-4}$ are presented in Figure C.4. In each case, a wave event was selected from the simulations of $M = 3$, and it was reproduced for $M = 4$ and 5, using the same sets of inputs but with the

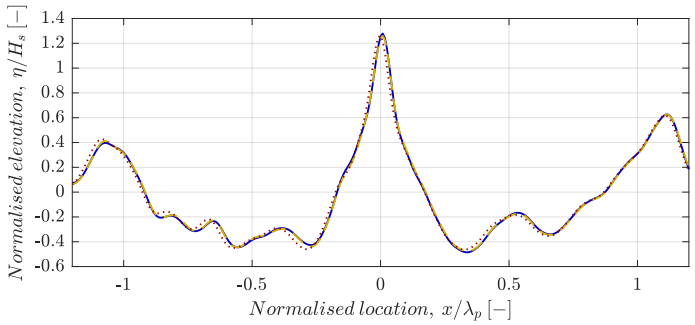
nonlinear order, M, altered. It is observed that in increasing M from 3 to 4 the wave shape is not altered. However, for $M = 5$, the x coordinate at which the maximum elevation is recorded is slightly lower compared to lower M. This reveals a slight phase-shift of the different wave components. This shift is believed to originate from the introduction of near-resonant interactions of higher than third-order that are not present in the $M = 3$ and $M = 4$ simulations. Nonetheless, this difference is considered very small and, hence, it does not pose any concerns with respect to the convergence of the results. In summary, the results in Figure C.3 and C.4 indicate that the total free surface is indeed converged with respect to M for $M = 3$. However, the present comparisons do not demonstrate convergence of the underlying nonlinear contributions. This point is verified in the following section.

Effect of M on the time-evolution of the nonlinear contributions

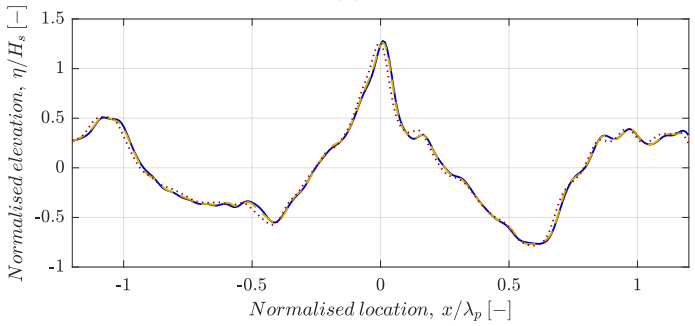
Having verified the convergence of the total crest-height distribution at steady state with respect to M, this section investigates the equivalent convergence of the time-evolution of the different nonlinear contributions. To achieve this, three sea-states were selected, characterised by $k_p d = 5.03$, 1.28 and 0.87 with $\frac{1}{2} H_s k_p = 0.105$, $\sigma_\theta = 10^\circ$ and $\gamma = 2.5$. These sea-states correspond to those presented in the initial investigation of the nonlinear effects arising in directional sea-states in different effective water depths, presented in §4.5.2.

This reduced number of sea-states compared to those adopted in the the previous section was selected due to the increase in computational demand with increasing nonlinearity order. Indicatively, in simulating a sea-state with the numerical setup described in Table C.1, for four phase-shifts and for a simulation duration of $66T_p$ using $M = 3$, requires $\sim 23h$ of computation time. While a sea-state with $M = 5$ requires $\sim 69h$; three times more. This increase in the computational demand is due to the fact that with an increase in M, both the number of Dirichlet problems described in §2.2.5 and the required additional modes for a full de-alising is increased accordingly (Ducrozet et al., 2007).

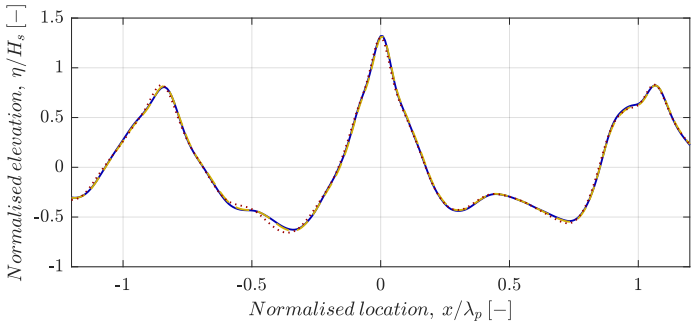
The resulted time-evolution of the statistical moments of the dynamic kurtosis, skewness and bound kurtosis for $M = 3$ and $M = 5$ is compared in Figure C.5. It should be noted that the results concerning the dynamic kurtosis (sub-figure C.5(a)) for $M = 3$ are those already presented in Figure 4.4. Taken the results in Figure



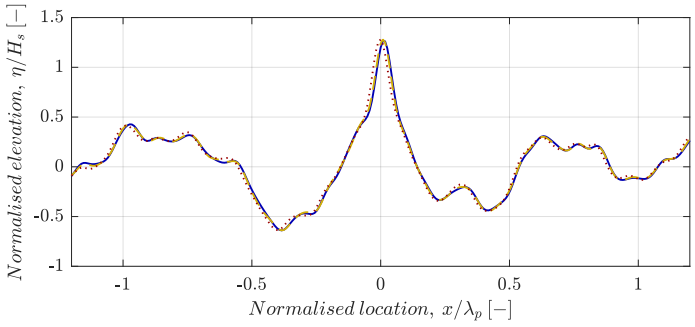
(A)



(B)



(C)



(D)

Figure C.4: Spatial profiles (along the x-axis) of wave events, normalised with respect to H_s, η/H_s, of wave events corresponding to a probability of exceedance of $Q = 10^{-4}$ for the sea-states presented in Figure C.3 for varying nonlinear order M: (A) for $k_p d = 0.87$ and $\sigma_\theta = 10°$, (B) for $k_p d = 5.03$ and $\sigma_\theta = 10°$, (C) for $k_p d = 0.87$ and $\sigma_\theta = 20°$ and (D) for $k_p d = 5.03$ and $\sigma_\theta = 20°$. The lines (——/– – –,····) refer to $M = 3$, 4 and 5, respectively.

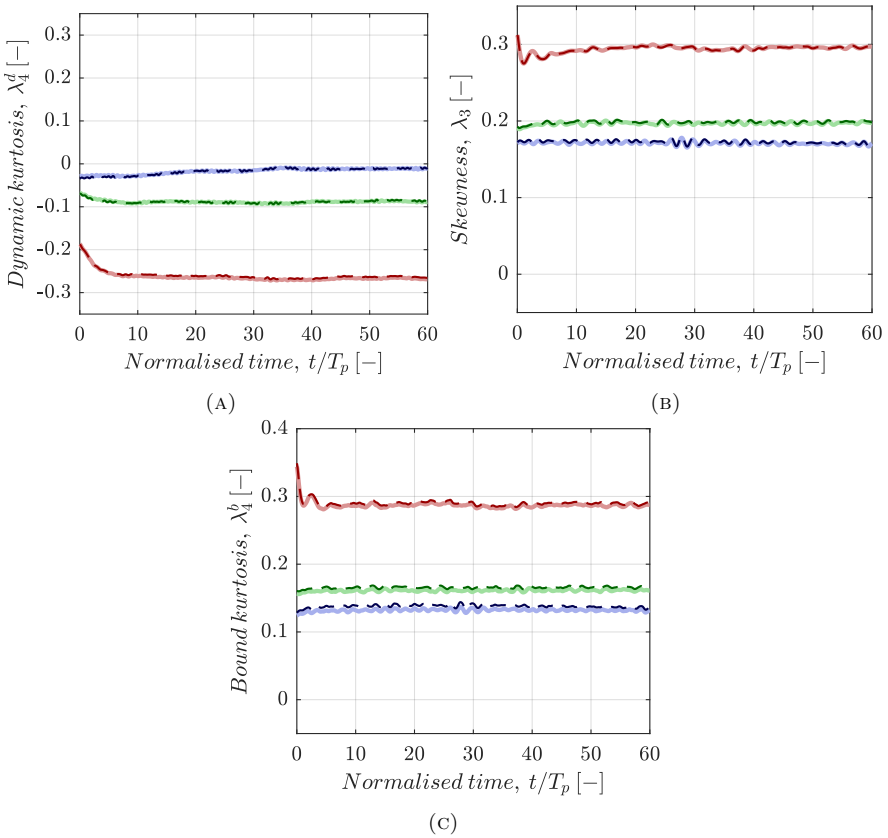


Figure C.5: Effect of the nonlinearity order M on the temporal evolution of the ensemble-averaged (A) dynamic kurtosis, (B) skewness and (C) bound kurtosis for directional sea-states of $\frac{1}{2}H_s k_p = 0.105$, $\gamma = 2.5$ and $\sigma = 10°$. The lines (/) refer to $k_p d = 5.03$, (/) to $k_p d = 1.28$ and (/) to $k_p d = 0.87$ for $M = 3$ and $M = 5$, respectively. The horizontal time-axis is normalised by the spectral peak period, T_p.

C.5 as a whole, it is shown that the nonlinearity order M has a minimal (negligible) effect on the statistical moments for the entire nonlinear evolution process. This demonstrates that higher-order near-resonant or bound contributions than those simulated using $M = 3$ are not significant. At least when the statistical moments are concerned.

To verify that the nonlinear crest-height contributions are also not affected by an increase in M, Figure C.6 compares their time-evolution for a probability of exceedance of $Q = 10^{-3}$ using $M = 3$ and $M = 5$. The results corresponding to $M = 3$ are supplied with confidence intervals, the latter obtained using the bootstrap method (Efron, 1979). The format of this figure is similar to the earlier Figure 4.7, presented in §4.5.2. In more detail, the left column of sub-figures presents the crest-heights of the total free surface and of the free-waves part, the latter being isolated

using the four-phase manipulation method. While the sub-figures on the right present the bound-wave contributions. Finally, all crest heights are normalised by the linear (Rayleigh) predictions.

Taken together, the comparisons in Figure C.6 demonstrate that an increase in M from 3 to 5 does not affect the magnitude of the nonlinear contributions at any stage of the nonlinear evolution. To quantify the differences between the two sets of simulations, the time-averaged values of the nonlinear contributions at steady state were obtained and the results are shown with horizontal grey lines in each sub-figure. The difference between these lines is $\leq 1\%$ of the linear crest-height prediction in all cases. Specifically, the maximum difference is $\sim 1\%$ for the bound contributions in deep water ($k_p d = 5.03$), with $M = 5$ resulting to slightly lower elevations. However, this difference is not considered important. Interestingly, this difference is also observed in the evolution of bound kurtosis in Figure C.5; once again demonstrating the link between the statistical moments and the crest heights.

C.4.2 Wavenumber-frequency spectra

The remainder of this appendix aims to verify that the trends observed in Figure 4.7 and C.6 are not affected by the presence of spurious waves generated due to an ineffective ramping of the nonlinear boundary conditions (see §3.5.1 in the context of uni-directional simulations) and to demonstrate the overall performance of the four-phase manipulation method presented in §2.2.6 in the context of directional simulations.

To achieve this, results for the deepest ($k_p d = 5.03$) and shallowest ($k_p d = 1.28$) sea-states of the previous section are presented; the sea-state with $k_p d = 1.28$ being omitted to reduce the number of presented figures. Following the same logic as §2.2.6, a wavenumber-frequency spectrum is sought to be extracted for each harmonic contribution in order to verify that the corresponding energy distribution is located appropriately in the wavenumber-frequency domain.

For this, a three-dimensional Discrete Fast Fourier Transform (2D-FFT) was performed in the entire spatio-temporal wave records of each harmonic contribution in the time-interval $t \in [0, 50T_p]$. This interval was selected as a compromise between a fine temporal resolution and focus on the initial part of the nonlinear evolution. Moreover, similarly to §2.2.6, a Tukey window function was applied in the

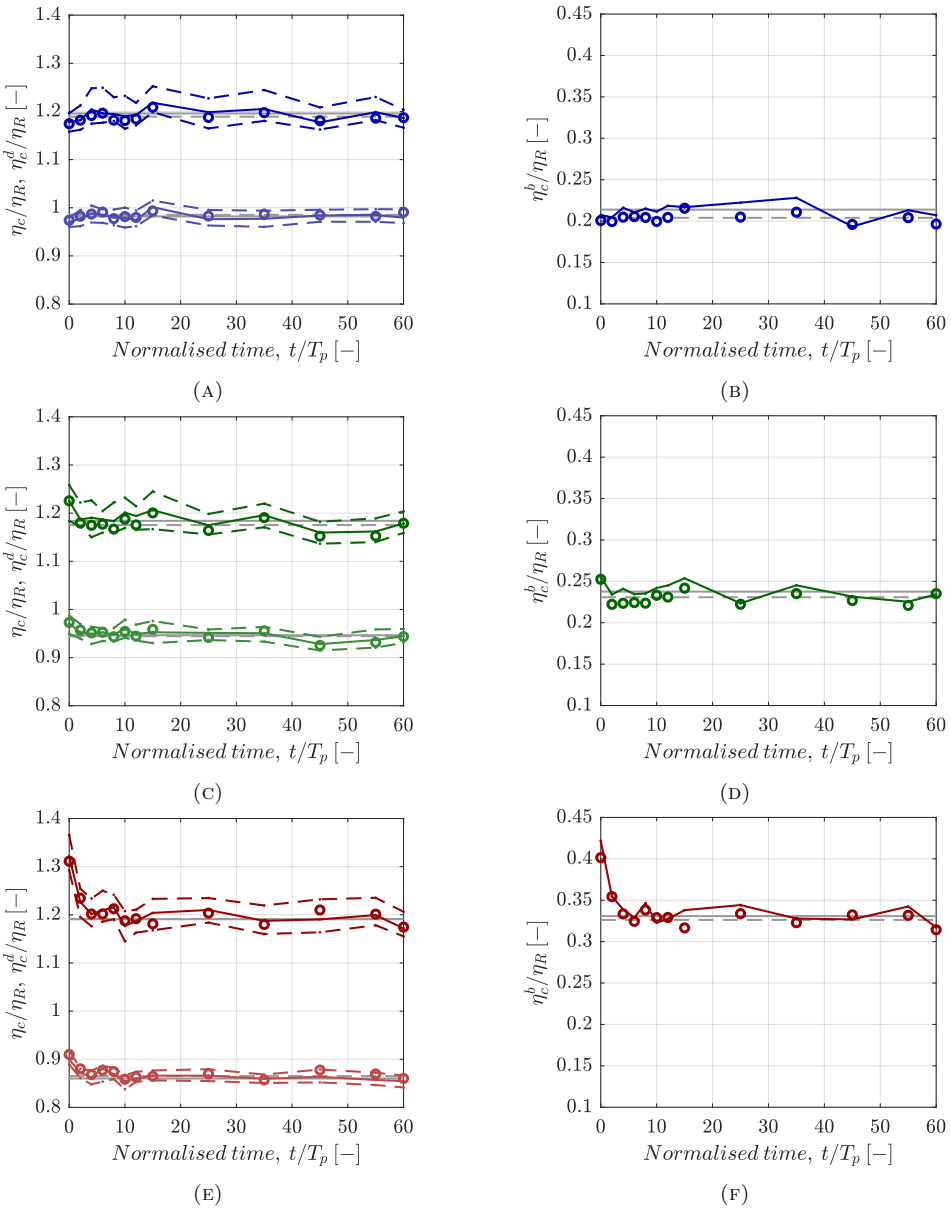
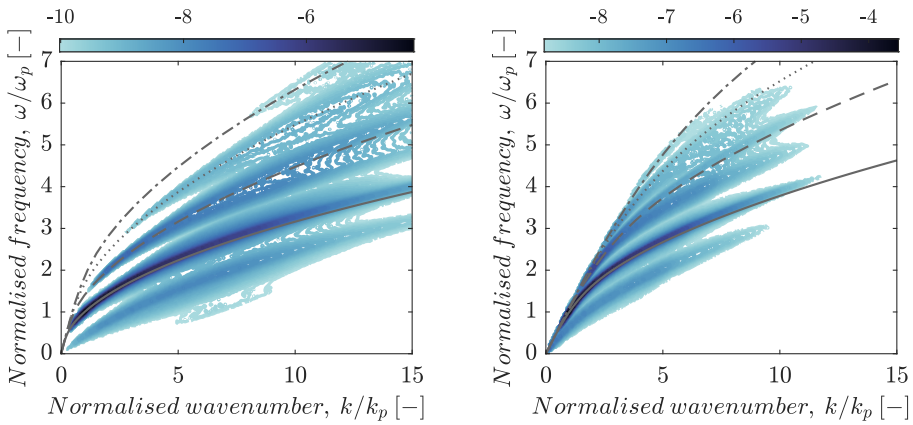


Figure C.6: Effect of the nonlinearity order M on the temporal evolution of the normalised crest height, η_c/η_R, and its underlying nonlinear contributions corresponding to a probability of exceedance of $Q = 10^{-3}$ for directional sea-states of $\sigma_\theta = 10°$, $\gamma = 2.5$ and $\frac{1}{2}H_s k_p = 0.105$. The left column refers to the total free-surface and the freely propagating part, and the right column to the total bound-wave contributions. The sub-figures (A) & (B) refer to $k_p d = 5.03$, (C) & (D) to $k_p d = 1.28$ and (E) & (F) to $k_p d = 0.87$. In (A), (C) and (E) (—— / —— / ——) refer to the total free surface obtained using $M = 3$. The same notation is also adopted in (B), (D) and (F) for the bound-waves part. While, the free-waves part is denoted with (—— / —— / ——). In all sub-figures the markers (○ / ○ / ○) and (○ / ○ / ○) refer to the results for the same sea-states obtained using $M = 5$. The dash-dotted lines in (A), (C) and (E) correspond to 95% confidence intervals. In all sub-figures the time-averaged values for $t > 10T_p$ are denoted with (——) for $M = 3$ and (— —) for $M = 5$.

time domain to avoid energy leakage due to the non-periodicity of the records. The three-dimensional results of the 2D-FFT referring to the (k_x, k_y, ω) domain were represented in two-dimensions by considering the absolute wavenumber $k = \sqrt{k_x^2 + k_y^2}$.

Considering first the total free-surface, the resulted two-dimensional wavenumber-frequency spectra ($\frac{1}{2}a_i^2$, a_i being the Fourier amplitudes) are shown in Figure C.7; sub-figure C.7(A) corresponding to $k_p d = 5.03$ and sub-figure C.7(B) to $k_p d = 0.87$. In observing these figures it becomes evident that the total free surface contains energy both below and above the linear dispersion line corresponding to frequency-difference and frequency-sum terms respectively. Interestingly, it is observed that bound contributions up to fourth order are present in the wavefield.



(A) (B)

Figure C.7: Contour plot of the spectral energy ($\frac{1}{2}a^2$) of the total free-surface elevation: (A) for $k_p d = 5.03$ and (B) for $k_p d = 0.87$ arising in directional JONSWAP ($\gamma = 2.5$) sea-states with $\frac{1}{2}H_s k_p = 0.105$ and $\sigma_\theta = 10°$. The line (——) corresponds to the linear dispersion equation, while the lines (— — /· · · · /— · —) correspond to integer multiples of the dispersion relation, with $n = 2, 3$ and 4 respectively. The contours are presented in log-scale such that the energy of the different harmonics is visible. For these simulations the T_a parameter of the ramp function was set to $4T_p$. Note that the results are truncated to 6 significant orders to avoid visualising insignificant energy contaminated by numerical noise or energy leakage.

Harmonic separation

The wavenumber-frequency spectra of the different harmonic contributions resulting from the four-phase manipulation method are shown in Figure C.8 for $k_p d = 5.03$ and Figure C.9 for $k_p d = 0.87$. In these figures, each sub-figure corresponds to a different harmonic contribution. However, it should be reminded that in applying the four-phase manipulation method, the zeroth and fourth-harmonic contributions

are not separated. In obtaining, therefore, sub-figure (c) in each of the above figures, only the energy below the second-order bound-waves dispersion line was plotted. While to obtain sub-figure (e) the energy above this line was plotted. These results have been obtained for $T_a = 4T_p$ and $M = 5$, the latter allowing the full extent of nonlinear interactions to take place. Thereby any higher-order resonant or near-resonant interactions are also modelled.

Considering first the results of the first harmonic (sub-figures (a) and (a)) it becomes evident that the significant energy allocated to the bound waves observed in Figure C.7 is eliminated. Specifically, the majority of the wave energy follows closely the linear dispersion relation, with only a minor part travelling faster. In this regard, it should be noted that the data in these sub-figures are presented in log scale hence the importance of these latter components are visually exaggerated. Interestingly, Gibson & Swan (2007) have also identified the spread of energy above the linear dispersion line at high frequencies during the evolution of quasi-deterministic wave groups in deep water. A phenomenon that is attributed to third-order near-resonant interactions. The same effect appears to be present in random sea-states in both deep and finite water depths.

Considering the bound-wave harmonics, it is demonstrated that, indeed, the majority of their energy occupies regions in the wavenumber-frequency domain in accordance with the expectation from Stoke's theory (see discussion in §2.2.6). However, in both effective water depths, the zeroth harmonic (Figures C.8(c) and C.9(c)) contains a small part of energy around the linear dispersion line. This energy is believed to be associated with fourth-order quintet resonant or near-resonant interactions. Interestingly, this effect was also noted by Gibson & Swan (2007) in their study of quasi-deterministic wave groups in deep water and in the uni-directional sea-state simulations presented in §2.2.6.

In this regard, it is relatively well-known that the fourth-order quintet interactions are more important for non-collinear disturbances than collinear in both deep and finite water depths (McLean 1982a, Fructus et al. 2005). Hence, it is not surprising that these components appear in the present directional simulations for $k_p d = 0.87$ and do not appear in the equivalent uni-directional results presented in §2.2.6. While, for the directional simulations in $k_p d = 5.03$ appear somewhat increased compared to the equivalent uni-directional results, in accordance with expectation. The present

results are important in that they demonstrate that their effect is insignificant compared to the dominant quartet interactions in directionally spread seas. A result that has already been revealed by Gibson & Swan (2007) and Katsardi & Swan (2011) in the context of uni-directional isolated wave groups and is confirmed here for random directional seas.

In addition, it should be noted that a small proportion of free-wave energy appears in the third-harmonic for $k_p d = 5.03$. A possible origin for this energy is the firth-order sextet resonant or near-resonant interactions that again are more important for non-collinear disturbances than collinear (McLean 1982a, Kharif & Ramamonjiarisoa 1988). In this respect, it was verified that, by increasing the nonlinearity order to $M = 7$, the results for $M = 5$ were entirely reproduced. Hence, any higher resonant interactions were not found to be relevant, and the sextet resonant or near-resonant interactions are represented appropriately when $M = 5$ is adopted. Finally, the energy laying below the linear dispersion line was also observed in the equivalent uni-directional results presented in Figure 2.6. This energy relates to third-order frequency-difference terms, as discussed in the context of this latter figure.

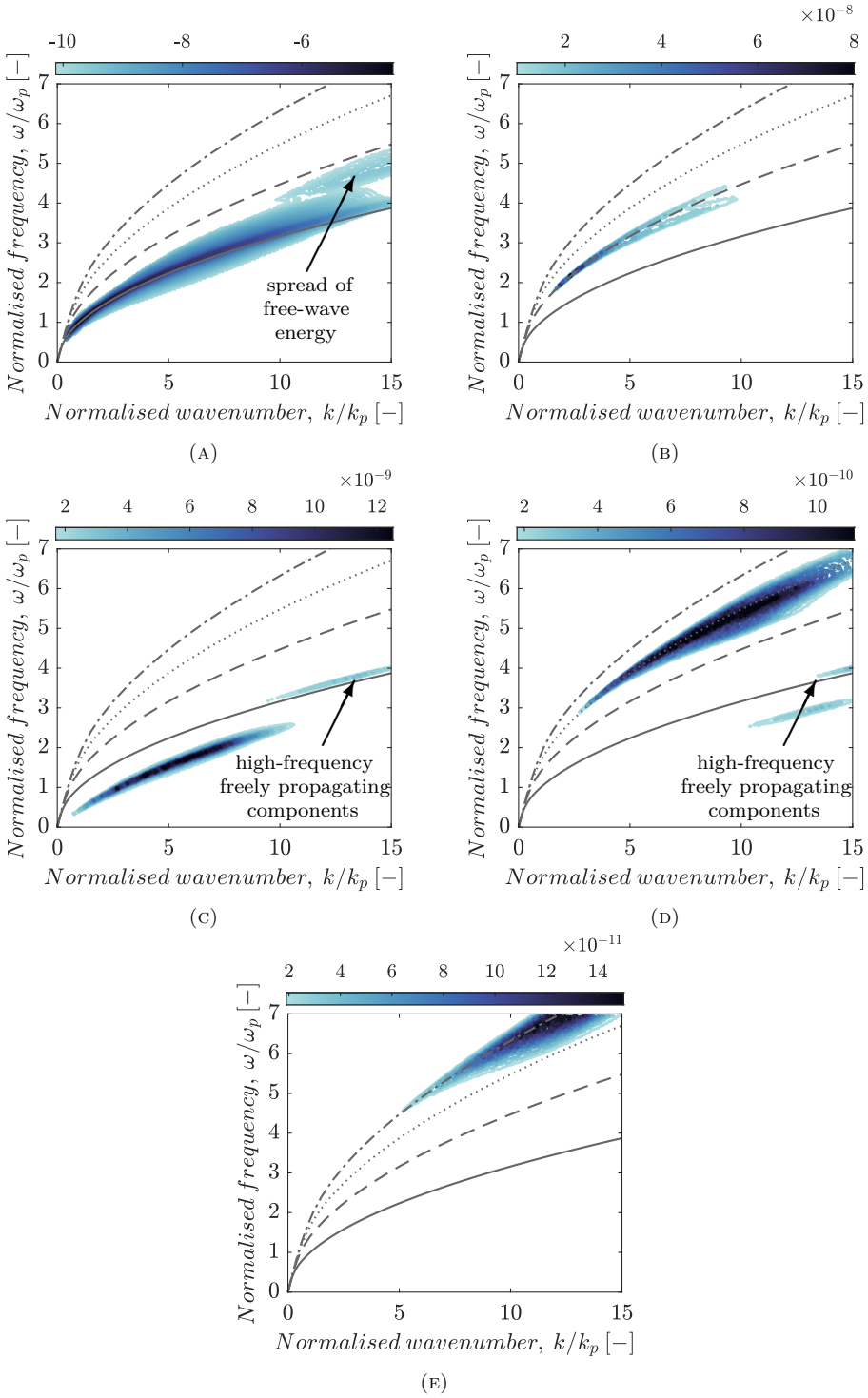


Figure C.8: Contour plot of the spectral energy ($\frac{1}{2}a^2$) of the extracted bound-harmonic contributions arising in a directional JONSWAP ($\gamma = 2.5$) sea-state with $\frac{1}{2}H_s k_p = 0.105$ and $\sigma_\theta = 10°$ in $k_p d = 5.03$: (A) first ($\eta^{1^{st}}$), (B) second ($\eta^{2^{nd}}$), (C) zeroth ($\eta^{0^{th}}$), (D) third ($\eta^{3^{rd}}$), and (E) fourth ($\eta^{4^{th}}$) harmonic contributions. The line (——) corresponds to the linear dispersion equation, while the lines (— — / · · · · / — · —) correspond to multiples of the dispersion relation, with $n = 2, 3$ and 4 respectively. In obtaining these results, the nonlinearity parameter was set to $M = 5$ and the ramp function is defined by $T_a = 4T_p$. The first harmonic appears in log-scale and the results are truncated to 6 significant orders.

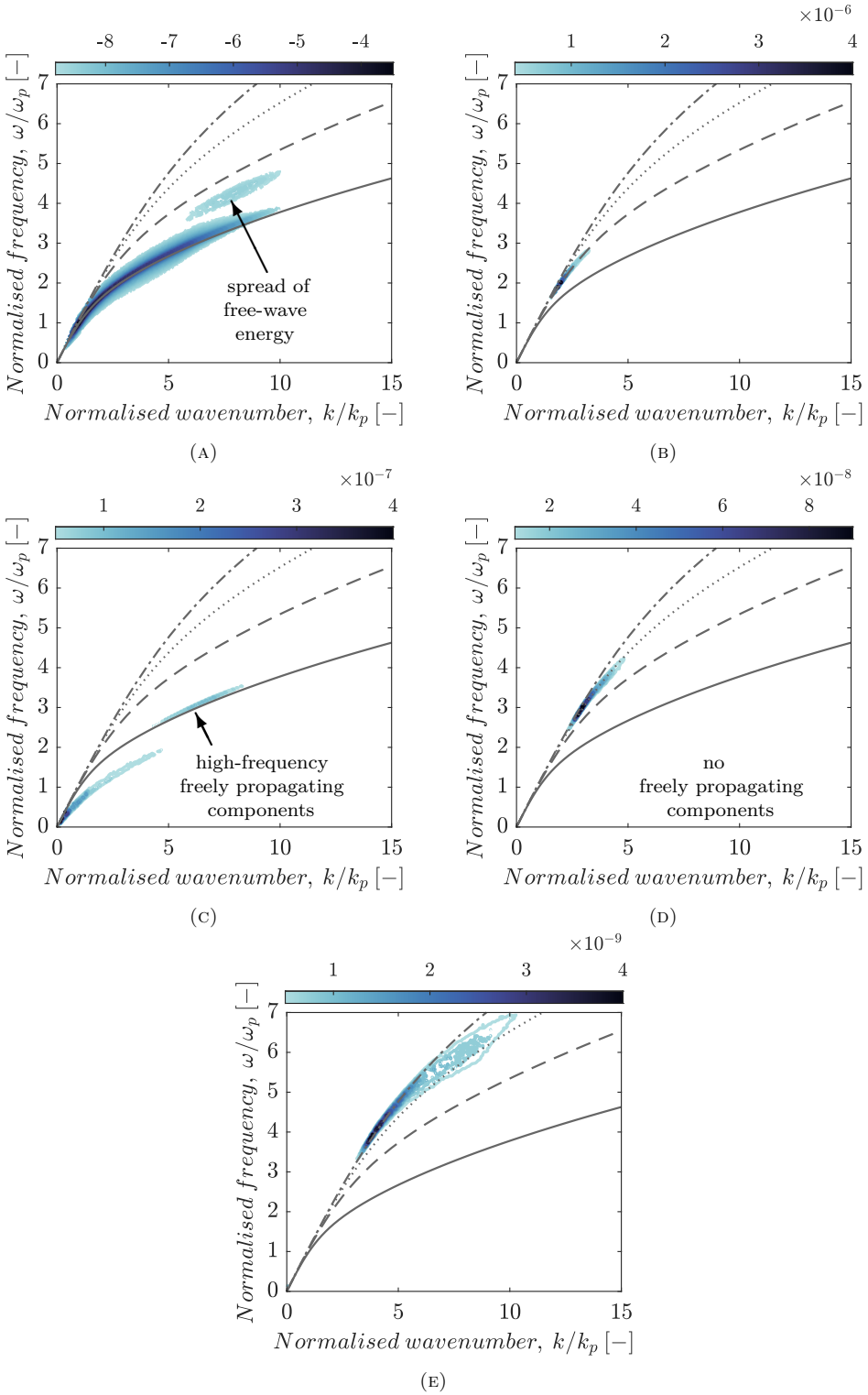


Figure C.9: Same as Figure C.8 but for an effective water depth of $k_p d = 0.87$.

Effect of the ramp function

Having identified the different interactions that take place in directionally spread seas, this section aims to verify that the results presented in Figures C.8 and C.9 are independent of the length of the ramp function and that the latter effectively suppresses any spurious waves.

For this, the parameter T_a defining the length of the ramp function was set to 0, $2T_p$, $4T_p$ and $8T_p$. The first value defines no ramping, the second a shorter ramping than what was used in the simulations of Figures C.8 and C.9 ($T_a = 4T_p$) and the last longer. In essence, this investigation aims to explore if a shorter ramp function than $T_a = 4T_p$ would be sufficient to suppress any spurious waves and if the adoption of a longer ramp would lead to identical results to Figures C.8 and C.9.

To verify the above, Figures C.10, C.11 and Figure C.12 present the wavenumber-frequency spectra of the second, zeroth and third harmonics respectively for the different ramp function lengths and for the same sea-states presented in Figures C.8 and C.9. In each figure, the left column concerns sea-states in $k_pd = 5.03$ and the left column in $k_pd = 0.87$. While from top to bottom T_a increases.

Taken together, Figures C.10, C.11 and Figure C.12 demonstrate that without the ramp function ($T_a = 0$) all harmonics in both effective water depths are contaminated by spurious free waves, similarly to Figure 3.14 presented in Chapter 3 concerning the second harmonic in uni-directional simulations. The presence of these waves is clearly undesirable. Interestingly, the majority of the spurious wave energy spans in the frequency range $\sim [1, 3]\omega_p$ for $k_pd = 5.03$ and $\sim [1, 2.5]\omega_p$ for $k_pd = 0.87$.

By introducing a relatively short ramp function of $T_a = 2T_p$, these spurious waves are reduced for both water depths In fact, in $k_pd = 5.03$ they are eliminated for the second and third harmonics. While the zeroth harmonic still includes a very small portion of free-wave energy in $\omega < 3\omega_p$. With an increase in T_a from $2T_p$ to $4T_p$, the free-wave energy in $\sim [1, 3]\omega_p$ for $k_pd = 5.03$ and $\sim [1, 2.5]\omega_p$ for $k_pd = 0.87$ is eliminated for all harmonics and any remaining free-wave energy is located outside these intervals. Importantly, for an even longer ramp of $8T_p$, the results are identical to $4T_p$. In this respect, given (1) the convergence of the results with T_a and (2) the elimination of the spurious free-wave energy in the original ranges, $\sim [1, 3]\omega_p$ for $k_pd = 5.03$ and $\sim [1, 2.5]\omega_p$ for $k_pd = 0.87$, the remaining small free-wave energy at the zeroth and third harmonics in $k_pd = 5.03$ and the

zeroth harmonic in $k_p d = 0.87$ is believed to not originate from spurious waves. In contrast, as mentioned above, it is believed to be due to higher than third-order near-resonant interactions. At present, providing an independent verification for this point is not possible. A possible approach in tackling this would be to simulate random sea-states with a fifth, or sixth-order Zakharov (1968) equation. However, to the author's knowledge, such equation is not presently available, and if it was, the computational burden associated with directional simulations would make its application practically unfeasible; this latter point being discussed by Hadjigeorgiou (2018).

Given that spurious waves do not contaminate the present directional simulations, the trends observed in Figure C.6 are not affected by the initial conditions. It should be mentioned that in obtaining these trends, the adopted ramp function was long enough ($T_a = 4T_p$) to suppress such spurious waves.

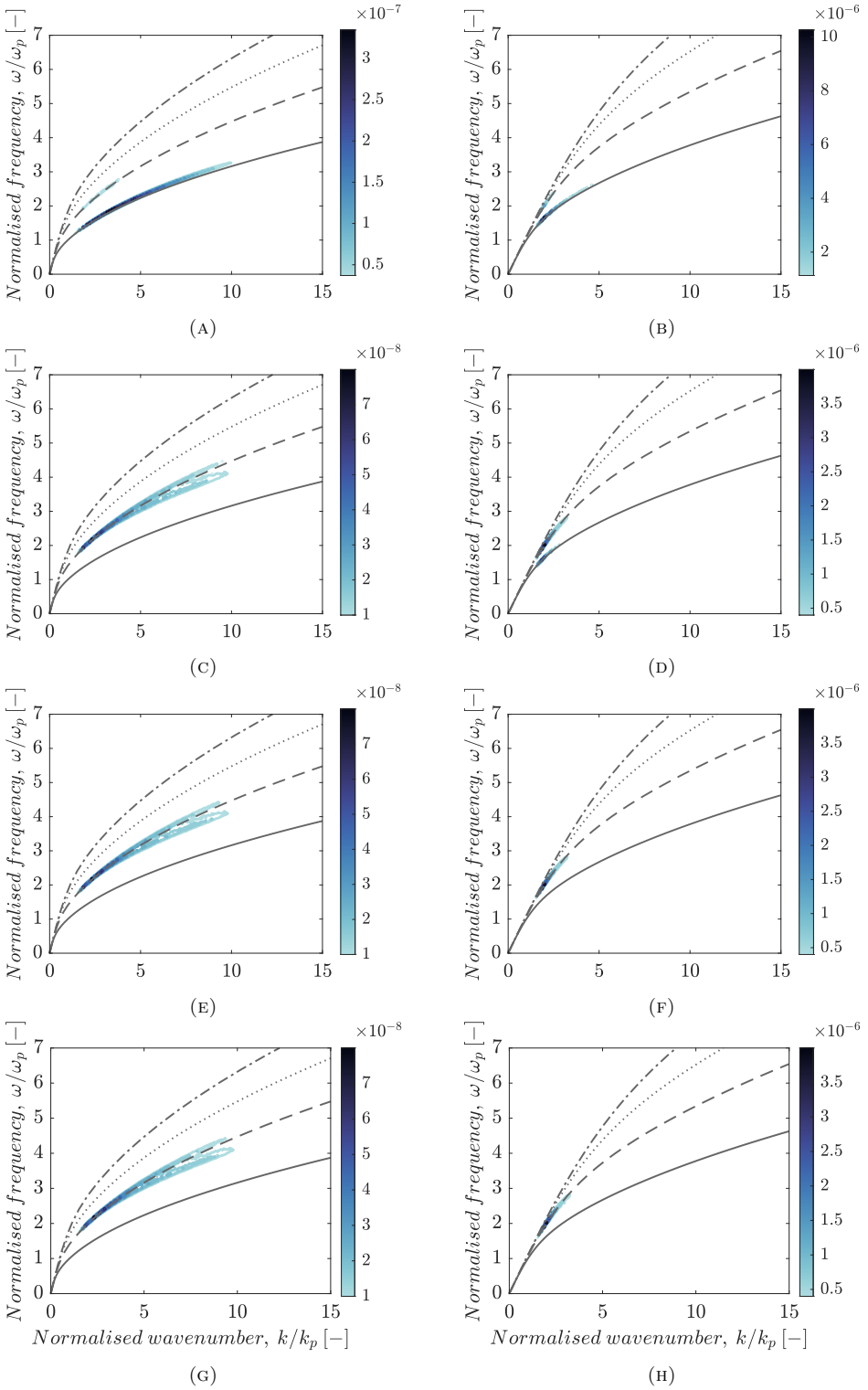


Figure C.10: Contour plot of the spectral energy ($\frac{1}{2}a^2$) of the second-harmonic for different ramp-function lengths, for sea-states with $\frac{1}{2}H_s k_p = 0.105$, $\sigma_\theta = 10°$ and $\gamma = 2.5$. Left column for $k_p d = 5.03$ and right column for $k_p d = 0.87$. (A)-(B) for $T_a = 0$, (C)-(D) for $T_a = 2T_p$ (E)-(F) for $T_a = 4T_p$ and (G)-(H) for $T_a = 8T_p$. The line (——) corresponds to the linear dispersion equation, while the lines (– – / · · · · / – · – ·) correspond to integer multiples of the linear dispersion relation of 2, 3 and 4 respectively.

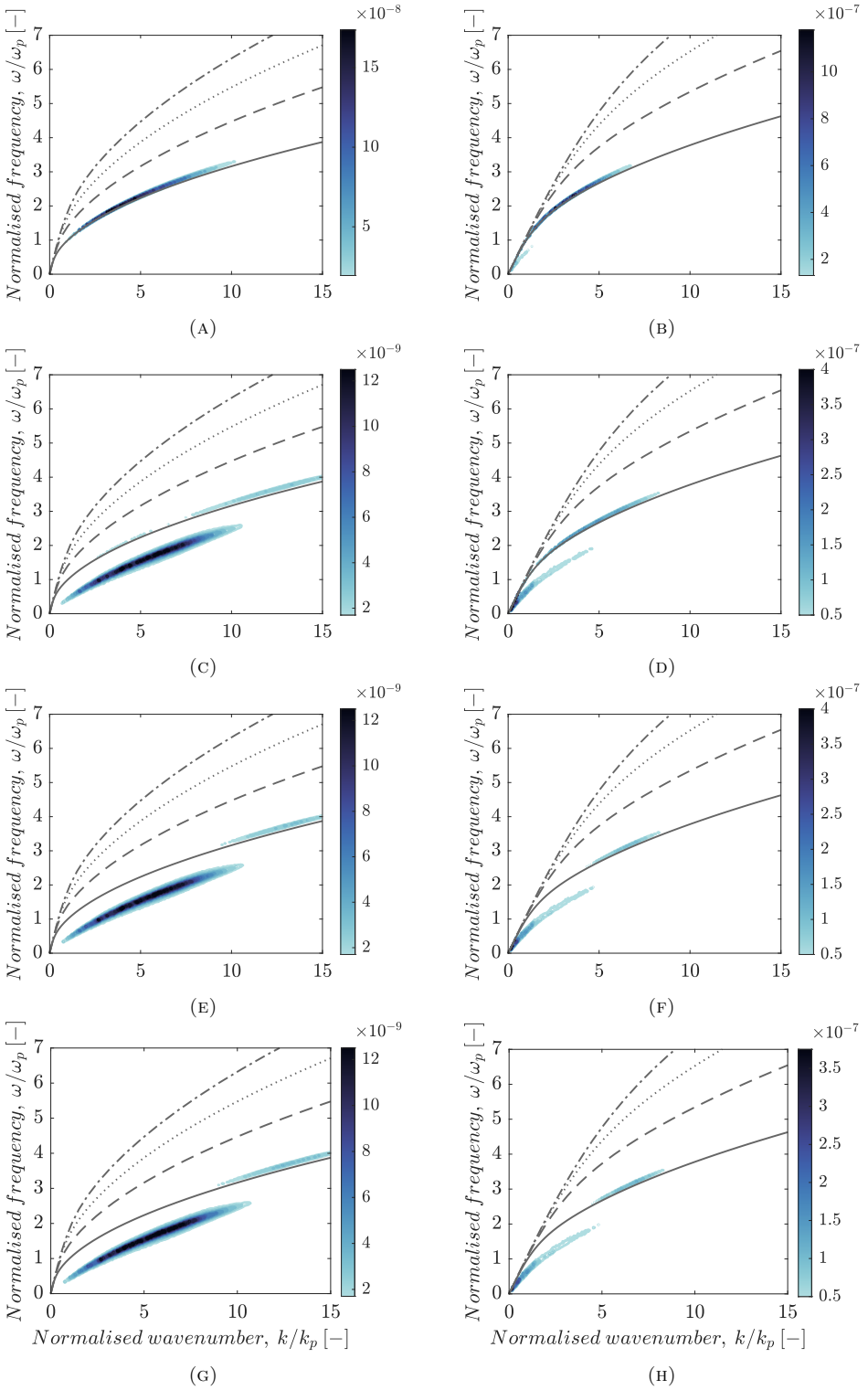


Figure C.11: Contour plot of the spectral energy ($\frac{1}{2}a^2$) of the zeroth-harmonic for different ramp-function lengths, for sea-states with $\frac{1}{2}H_s k_p = 0.105$, $\sigma_\theta = 10°$ and $\gamma = 2.5$. Left column for $k_p d = 5.03$ and right column for $k_p d = 0.87$. (A)-(B) for $T_a = 0$, (C)-(D) for $T_a = 2T_p$ (E)-(F) for $T_a = 4T_p$ and (G)-(H) for $T_a = 8T_p$. The line (——) corresponds to the linear dispersion equation, while the lines (– – / · · · · / – · – ·) correspond to integer multiples of the linear dispersion relation of 2, 3 and 4 respectively.

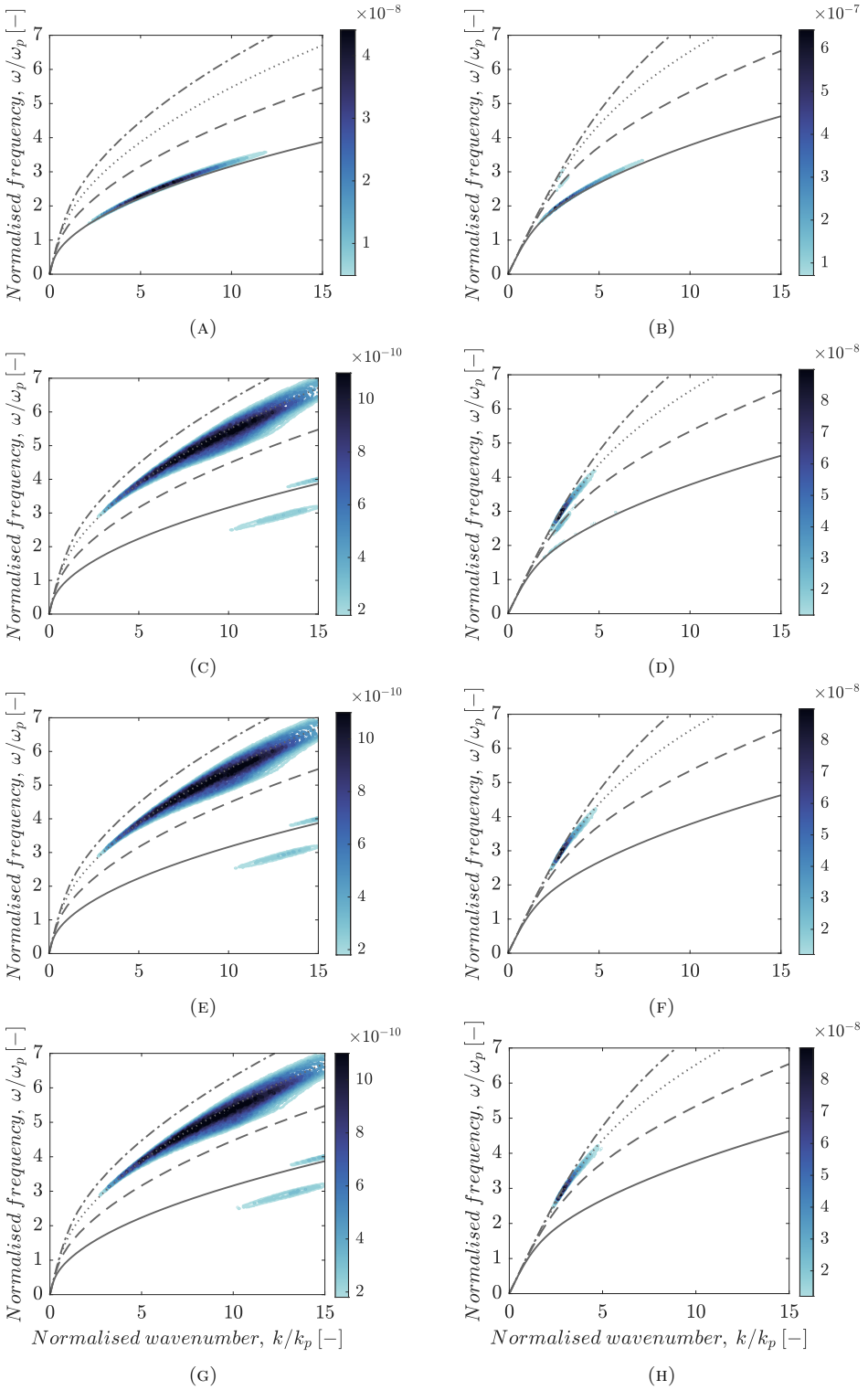


Figure C.12: Contour plot of the spectral energy ($\frac{1}{2}a^2$) of the third-harmonic for different ramp-function lengths, for sea-states with $\frac{1}{2}H_s k_p = 0.105$, $\sigma_\theta = 10°$ and $\gamma = 2.5$. Left column for $k_p d = 5.03$ and right column for $k_p d = 0.87$. (A)-(B) for $T_a = 0$, (C)-(D) for $T_a = 2T_p$ (E)-(F) for $T_a = 4T_p$ and (G)-(H) for $T_a = 8T_p$. The line (——) corresponds to the linear dispersion equation, while the lines (– – / · · · · / – · – ·) correspond to integer multiples of the linear dispersion relation of 2, 3 and 4 respectively.

D

Spectral evolution within directional HOSM simulations

The present appendix is devoted to the analysis of the nonlinear evolution of the directional wave spectra arising in directional sea-state simulations presented in Chapter 4. With the nonlinear interactions evolving in time, this investigation is deemed necessary for assessing the degree of the stationarity of the simulations. In doing so, transparency can be gained regarding the relevance of the initial directional characteristics of the adopted spectra. However, whilst the present results are essential for clarifying some crucial aspects of the directional simulations, they are not included in the main body of the thesis, as they do not directly relate to the primary purposes of the investigation.

D.1 Evolution of the free-wave spectra

To begin, in deep water, it is relatively well-established that directional spectra tend to broaden within phase-resolved random-wave simulations during time scales of evolution similar to the ones considered in this thesis. Evidence for this can be found in previous studies based either on the BMNLS equation (Dysthe et al. 2003, Socquet-Juglard et al. 2005, Simanesew et al. 2016) or the HOSM model (Xiao et al. 2013, Toffoli et al. 2010b)

This spectral broadening has also been predicted analytically by Longuet-Higgins

(1976). Specifically, Longuet-Higgins (1976) showed that for very narrow-banded spectra, there is a transfer of wave energy from the spectral peak towards wavenumbers forming an angle of $\arctan(1/\sqrt{2}) = 35.26°$ with respect to the mean wave direction. An angle that corresponds to the tangent at the origin of the *degenerate* resonance loop of Phillips (1960) (Figure 2.1). This evolution originates from the so-called *degenerate* interactions for which the resonance condition ($\mathbf{k_0} + \mathbf{k_1} = \mathbf{k_2} + \mathbf{k_3}$) involves self-interaction terms ($\mathbf{k_0} = \mathbf{k_1}$ or $\mathbf{k_0} = \mathbf{k_1} = \mathbf{k_2} = \mathbf{k_3}$), these being particularly relevant to narrow-banded conditions.

However, for sea-states in finite water depth, the features of directional spectral evolution are not well established. Notably, in the directional HOSM simulations performed by Toffoli et al. (2009), it was shown that the wavenumber-average directional spreading increases with evolution time for any sea-state in the effective water depth range $k_p d \in [0.8, 20]$. While this increase was reduced with a reduction in effective water depth.

In considering the above, the following questions arise:

- Is the increase of the average directional spreading observed in Toffoli et al. (2009) representative to the entire frequency range?
- Starting with a frequency-independent directional spreading is frequency dependence developed over the time-scales ($t \in [0, 60]T_p$) considered in the present simulations?

To answer the above questions, sea-states with an initial directional spread of $\sigma_\theta = 10°$ have been employed, with a steepness of $\frac{1}{2}H_s k_p = 0.105$. These were found to be representative of the full set of the available simulated sea-states produced in the course of the present study. To this end, it should be noted that the adopted numerical setup for the directional HOSM simulations, outlined in Table C.1, includes a combination of lateral domain length, L_y, and number of nodes in y, n_y, that lead to a maximum lateral wavenumber $k_{y,max}$ which permits any spectral broadening to take place without restriction. Specifically, considering the wavenumber $k_{y,s}$ for which the square-root of the spectral energy has decayed to 0.5% of the peak value at $k_x = k_p$, the ratio $k_{y,max}/k_{y,s}$ can be considered as an indicator of the available 'room' for lateral spectral evolution. This ratio in the present simulations corresponds to $k_{y,max}/k_{y,s} \approx 14.2, 6.7, 3.7, 4.3, 2.8$ and 2.1 for $\sigma_\theta = 5, 10, 15, 20, 25, 30°$, respectively,

which allows energy transfers to lateral wavenumbers extending more than 100% beyond the input range.

Figure D.1 presents the wavenumber spectra of the underlying *free waves* corresponding to evolution times of $t = 0$, $25T_p$ and $60T_p$, for the three effective depths of $k_p d = 0.87, 1.28$ and 5.03; its row of sub-figures corresponding to a different effective water depth. It is shown that the spectra indeed tend to broaden with evolution time irrespective of the water depth. Notably, this observation is in qualitative agreement with the results presented Toffoli et al. (2009) relating to the mean directional spreading of the total free surface.

D.2 Spectral energy transfers

Based on the above, it is instructive to explore the regions of spectral energy movements and identify how these are affected by the effective water depth. For this, the spectra at the end of the ramp function ($t = 0$) were subtracted from the evolved spectra for longer evolution times ($t > 0$). The resulted energy transfers for the longest evolution time of $t = 60T_p$ are shown in Figure D.2; each sub-figure corresponding to a different effective water depth. In each sub-figure, dashed lines that form an angle of 35.26° with respect to $k_y = 0$ are presented corresponding to the theoretical result of Longuet-Higgins (1976), together with the resonance loop of Phillips (1960) obtained using the finite-depth dispersion relation.

In considering Figure D.2, it is observed that there is a transfer of energy from wave components laying close to the mean wave direction ($k_y = 0$) towards wave components that travel close to the angle of 35.26° of Longuet-Higgins (1976), irrespective of the water depth. These results are in accordance with an equivalent deep-water investigation using HOSM by Toffoli et al. (2010b). However, Toffoli et al. (2010b) used an initial frequency-dependent directional distribution of Mitsuyasu et al. (1975). Moreover, the present results directly relate to the investigation presented by Simanesew et al. (2016) on the basis of the BMNLS equation. In this latter investigation the authors showed that an initially frequency-independent spectrum in deep water tends to develop frequency dependence under the effect of near-resonant interactions; evidence provided by both experimental data and numerical simulations based on the BMNLS equation. As such, the present numerical results extend

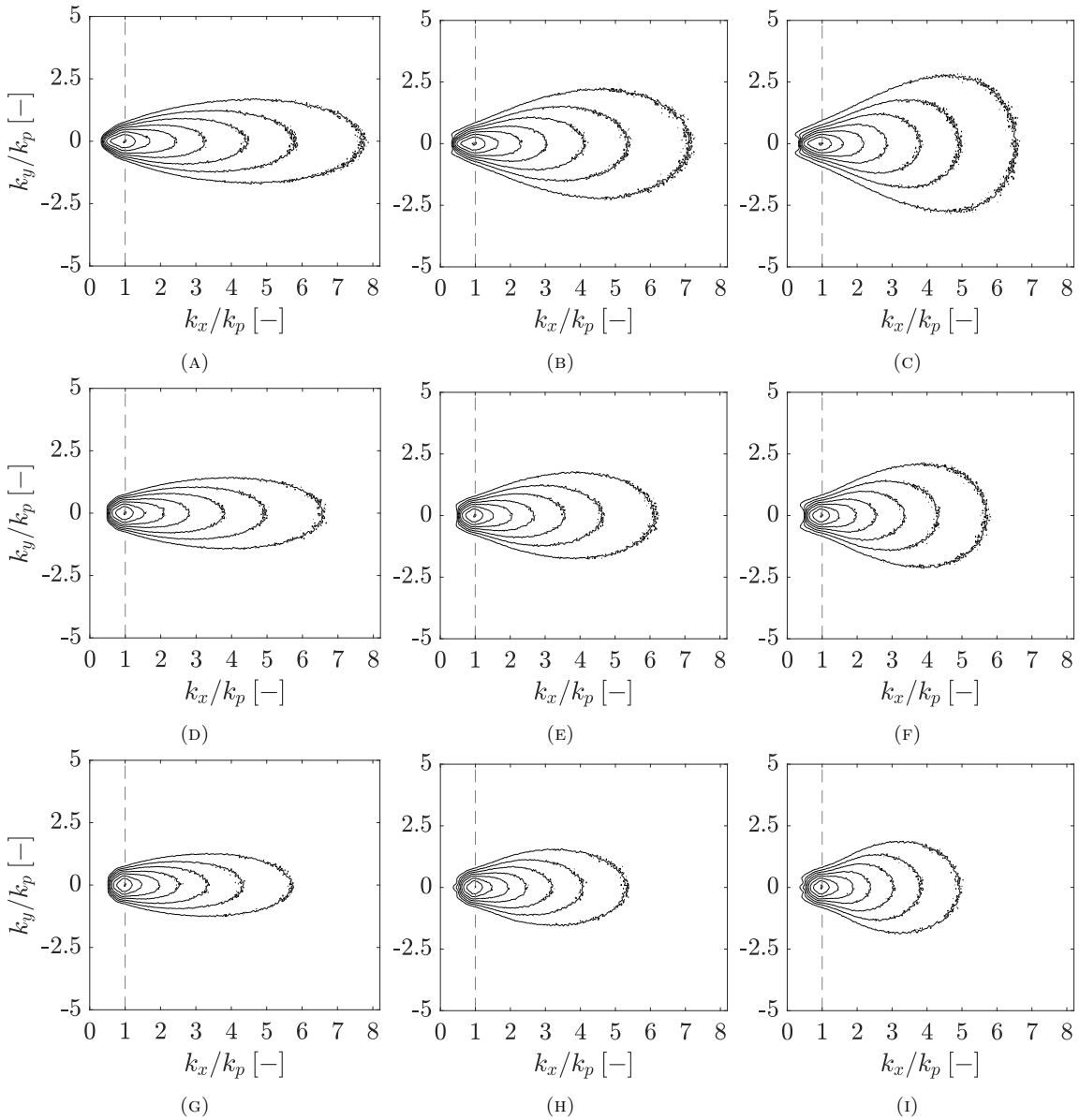


Figure D.1: Normalised ensemble-averaged wavenumber spectra, $S_{\eta\eta}(k_x, k_y)/S_{\eta\eta}(k_p, 0)$, of the free waves for different evolution times corresponding to sea-states of $\frac{1}{2}H_s k_p = 0.1052$, $\gamma = 2.5$ and $\sigma_\theta = 10°$; (A)-(C) for $k_p d = 5.03$, (D)-(F) for $k_p d = 1.28$ and (G)-(I) for $k_p d = 0.87$. From left-to-right, (A), (D), (G) correspond to $t = 0$, (B),(E),(H) to $t = 25T_p$ and (C),(F),(I) to $t = 60T_p$. The contours follow a logarithmic spacing with levels: 0.95, $3{\cdot}10^{-1}$, 10^{-1}, $3{\cdot}10^{-2}$, 10^{-2}, $3{\cdot}10^{-3}$, 10^{-3} and $3{\cdot}10^{-4}$ as moving away from the central wavenumber. The grey dashed line marks the wavenumber, $k_x = k_p$, corresponding to the initial spectral peak period.

the earlier findings of Toffoli et al. (2010b) and Simanesew et al. (2016) to finite water depth, whilst ensuring that the simulations are not bandwidth-restricted.

In exploring the origins of these energy transfers, it is worth noting that the angle of 35.26° of Longuet-Higgins (1976) corresponds to the angle for which the nonlinear and dispersive terms in the NLS equation change sign. As such, for greater angles modulational instability does not occur in a narrow-band setting. Hence, the spectral broadening discussed by Longuet-Higgins (1976) expresses the process in which an initially unstable random sea-state tends to transfer energy towards stable regions. A process that could potentially explain the present results, despite that instabilities are not prominent in a broad-band setting.

In addition, it is observed that there is an increase of the spectral energy in $k_x < k_p$, whereas there is a decrease in $k_x > k_p$ for small angles of wave propagation. In seeking to explain this type of energy transfers, it is instructive to consider the *degenerate* resonance loops of Phillips (1960) shown in Figure D.2. These resonance loops correspond to the case where $\mathbf{k_0} = \mathbf{k_1} = (k_p, 0)$ in the usual resonance condition of Equation 2.23 and can largely explain the energy transfers around the loops. In more detail, wave components at (or very close to) the spectral peak, interact resonantly (or near-resonantly) with wave-components, $\mathbf{k_2}$, laying on (or close to) the right hand side of the loop. This interaction transfers energy to wave-components, $\mathbf{k_3} = 2\mathbf{k_0} - \mathbf{k_2}$, that are anti-symmetric to $\mathbf{k_2}$ with respect to the two axes of symmetry of the loop (noted as $k_x = k_p$ and $k_y = 0$) and lay on the left hand side of the loop (see also Figure 2.1).

However, it is noted that the resonance loop presented in each of the cases of Figure D.2 is only one of many other possible loops corresponding to $\mathbf{k_0}$ different than the spectral peak. Nonetheless, the energy located around the spectral peak is higher than in other areas of the spectrum. Therefore, the presented resonance loop is shown to have a dominant effect on the energy transfers. Likewise, there exist resonance curves for *non-degenerate* interactions (when three *different* wave components interact to transfer energy to a fourth wave component) which lead to energy transfers in other areas of the wavenumber domain. These are responsible for energy transfers in angles different from the 35.26°.

Finally, the angle of maximum increase in the spectral energy was found to be influenced by the initial directional spreading. In more detail, this angle was $\sim$

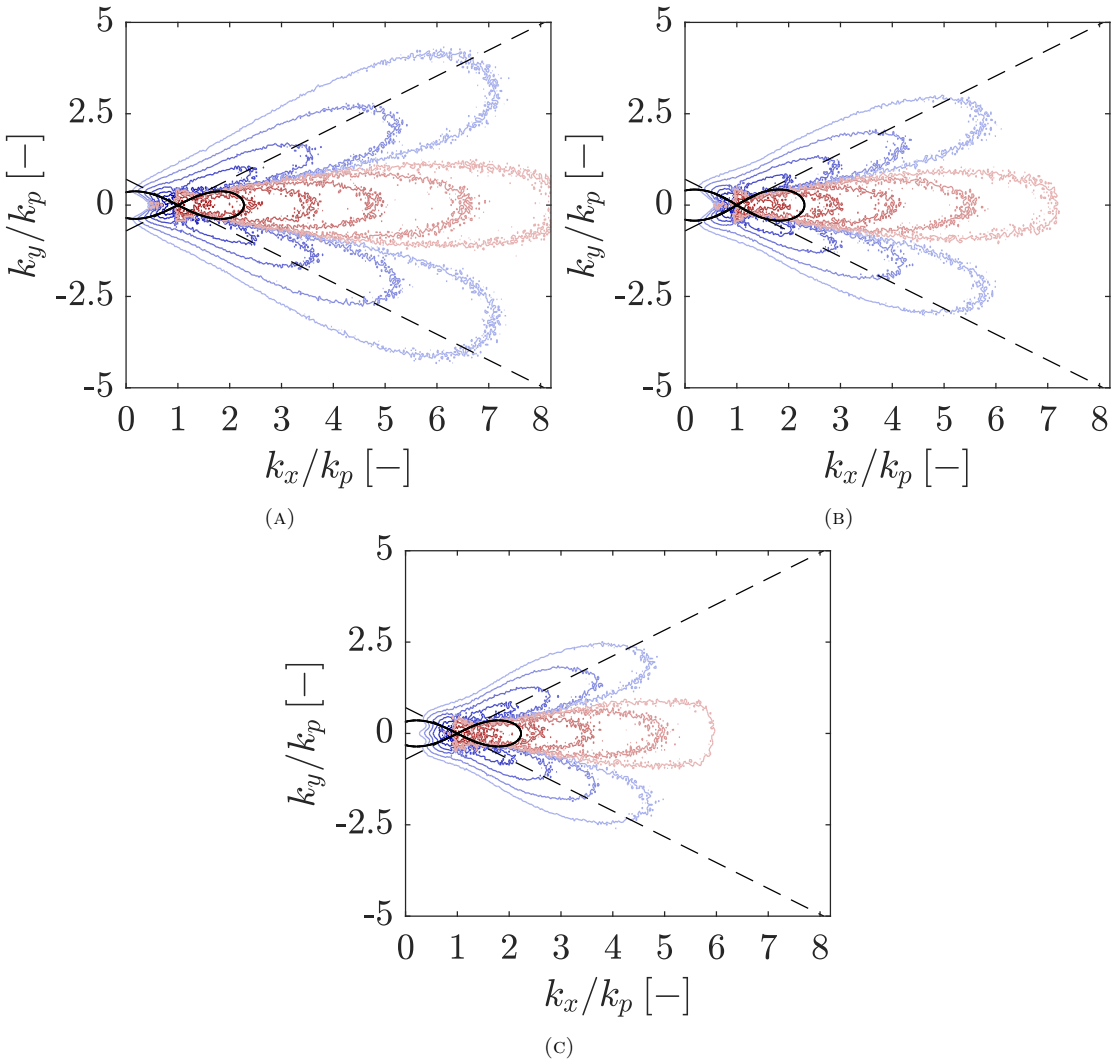


Figure D.2: Energy movement in the directional wave spectra of Figure D.1, expressed as $\Delta S_{\eta\eta}(k_x, k_y)/S_{\eta\eta}(k_p, 0)$, where $\Delta S_{\eta\eta}(k_x, k_y) = S_{\eta\eta}(k_x, k_y)|_{t=60T_p} - S_{\eta\eta}(k_x, k_y)|_{t=0}$. The different sub-figures correspond to different effective water depths, with (A) for $k_p d = 5.03$, (B) for $k_p d = 1.28$ and (C) for $k_p d = 0.87$. Red-coloured contours refer to $\Delta S_{\eta\eta} < 0$, while blue-coloured contours refer to $\Delta S_{\eta\eta} > 0$. The contour levels follow a logarithmic spacing corresponding to values of $\pm$ [10^{-1}, $3{\cdot}10^{-2}$, 10^{-2}, $3{\cdot}10^{-3}$, 10^{-3}, $3{\cdot}10^{-4}$, 10^{-4}], denoted with (/ / / / /) for positive values and with (/ / / / /) for negative values. The angle 35.26° of Longuet-Higgins (1976) is shown with ( ) and the resonance loop of Phillips (1960) is shown with ( ).

20, 31, 39, 44, 48 and 53° for $\sigma_\theta = 5, 10, 15, 20, 25$ and 30°, respectively, at the end of the simulations. Moreover, this angle was largely independent of the effective water depth and spectral bandwidth; the latter being already observed by Toffoli et al. (2010b). However, a more detailed account of such transfers is beyond the scope of the present investigation.

D.3 Time-evolution of mean directional spread and the effect of bound waves

In seeking to quantify the spectral changes observed in Figure D.1 the second-order moment of the directional distribution can be considered (Hwang et al. 2000, Toffoli et al. 2009 and Toffoli et al. 2010a). This is given by:

$$\sigma_2(k) = \frac{\int_0^{\pi/2} \theta^2 S_{\eta\eta}(k,\theta) d\theta}{\int_0^{\pi/2} S_{\eta\eta}(k,\theta) d\theta}. \tag{D.1}$$

The mean directional spread of the sea-state, σ_{2m}, can be calculated by averaging Equation D.1 across k. Notably, in adopting σ_{2m}, one recovers the standard deviation σ_θ of the Gaussian DSF employed here. As such, the time-evolution of $\sigma_{2m}/\sigma_\theta$ can give an quantitative indication on the importance of the spectral broadening observed in Figure D.1. For this, two wave-number ranges for the evaluation of σ_{2m} were considered. These correspond to $f/f_p \in [0.5, 3]$ and $f/f_p \in [0.9, 1.1]$. The first range includes the majority of the wave energy, excluding areas of the spectrum with very small or even non-existent wave energy, whereas the second range corresponds to the area around the spectral peak. The resulted evolution of the ratio $\sigma_{2m}/\sigma_\theta$ evaluated using the free-wave spectra for these two ranges is shown in Figure D.3 for the same sea-states adopted in producing the results in Figure D.1.

In observing Figure D.3, it can be concluded that the spectral broadening in the wide range of $f/f_p \in [0.5, 3]$ is significant leading to evolved σ_{2m} of as much as $\approx 18, 16, 15°$ in $k_p d = 5.03, 1.28$ and 0.87, respectively, for an initial spreading of $\sigma_\theta = 10°$. While this is not the case for the distribution of energy around the spectral peak, for which the mean directional spreading remains practically unchanged. The latter is important in that it supports the relevance of the initial directional spreading, when the statistics arising during the nonlinear evolution are considered.

Moreover, in considering the role of the bound-wave contributions on the directional properties, Figure D.3 includes also the evolution of $\sigma_{2m}/\sigma_\theta$ evaluated upon the spectrum of the *total* free surface. In observing these trends, the mean angles evaluated upon the range $f/f_p \in [0.9, 1.1]$ are not affected by the inclusion of bound terms; owing to the absence of bound terms in this region. While the mean angles evaluated upon the range $f/f_p \in [0.5, 3]$ are only weakly affected by bound terms;

the latter leading to the slight reduction in directionality of the order of $1-3\%$ for all evolution times and effective water depths.

Furthermore, it should be emphasised that the mean directional spreading has not reached a steady-state value at the end of the present simulations. In this respect, the analysis of Toffoli et al. (2010b) revealed that such a steady state is reached after a duration of $\sim 400T_p$ in deep water. To this end, the study of nonlinear evolution for such a long duration has not been attempted here due to (1) the excessive computational requirements and (2) the main focus of the investigation being the time-evolution of the crest-height statistics, rather than the spectral evolution itself. This is particularly supported by the fact that the crest heights statistics do not appear to be influenced by the spectral evolution in the wide frequency range ($f/f_p \in [0.5, 3]$).

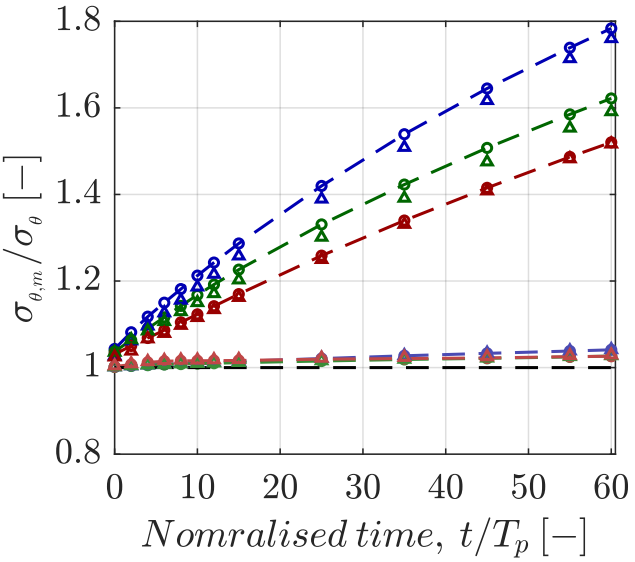


Figure D.3: Temporal evolution of the ratio $\sigma_{2m}/\sigma_\theta$ for sea-states with $\frac{1}{2}H_s k_p = 0.105$, $\gamma = 2.5$ and $\sigma = 10°$. The lines (−○− /−○− /−○−) refer to the freely propagating part of the free surface for $f/f_p \in [0.5, 3]$, the lines (−○− /−○− /−○−) refer to the freely propagating part of the free surface $f/f_p \in [0.9, 1.1]$; while the markers (△/△/△) refer to the total free surface for $f/f_p \in [0.5, 3]$, and finally the markers (△/△/△) refer to the total free surface for $f/f_p \in [0.9, 1.1]$. In all cases, the colour ordering refers to $k_p d = 5.03, 1.28$ and 0.87, respectively. The horizontal line (— —) is added for reference and reflects no change in σ_{2m}.

Finally, the same qualitative conclusions have also been drawn for the full range of sea-states presented in §4.3. It was observed that the relative increase in the mean directional spreading evaluated in the range $f/f_p \in [0.5, 3]$ becomes less intense with an increase in directionality (as also noted in Xiao et al. (2013)) and decrease in

spectral bandwidth. While the corresponding change in the range of $f/f_p \in [0.9, 1.1]$ is minimal ($\leq 8\%$) in all cases. The only exception refers to the sea-states of $\sigma_\theta = 5^\circ$, the spreading of which was increased by $\sim 10 - 20\%$ at the end of the simulations. Nonetheless, this leads to a maximum effective directional spread of $\sigma_\theta \approx 6^\circ$, which is very close to the initial value ($\sigma_\theta = 5^\circ$). Finally, the frequency-bandwidth parameters ν and q_p were found to vary from the initial values by less than $\sim 7\%$ for all the sea-states. Hence, the spectral broadening observed in $k_p d = 0.87$ in uni-directional seas (§3.6) was not reproduced in the directionally spread simulations.

E

Statistical moments arising in second-order sea-states

The present appendix aims to verify the applicability of Equation 4.4 in predicting the skewness arising within second-order random wave simulations of broad-banded directional sea-states. As well as the applibability of existing narrow-band second-order theoretical solutions on the relation between the skewness and bound kurtosis. These two aspects are discussed in §E.1 and §E.2, respectively.

E.1 On the performance of Equation 4.4 in predicting the skewness

Before assessing the predictive performance of Equation 4.4 for second-order sea-states, it should be noted that, within the second-order theory, the nominator of the expression that defines the skewness ($\lambda_3 = E[\eta^3]/\sigma_\eta^3$), the free-surface variance, does not remain unchanged with respect to the linear one. Following Tayfun (1994), the variance of the total second-order free surface is given by,

$$\begin{aligned}{\sigma'_\eta}^2 &= E[\eta^2] = E[(\eta^{(1)})^2] + E[(\eta^{(2)})^2] = \\ &= m_0 + \frac{1}{4}\int_0^\infty\int_0^\infty\int_0^{2\pi}\int_0^{2\pi} S_{\eta\eta}(\omega_i,\theta_i)S_{\eta\eta}(\omega_j,\theta_j)[(A_{ij}^+)^2 + (A_{ij}^-)^2]d\theta_i d\theta_j d\omega_i d\omega_j\end{aligned} \tag{E.1}$$

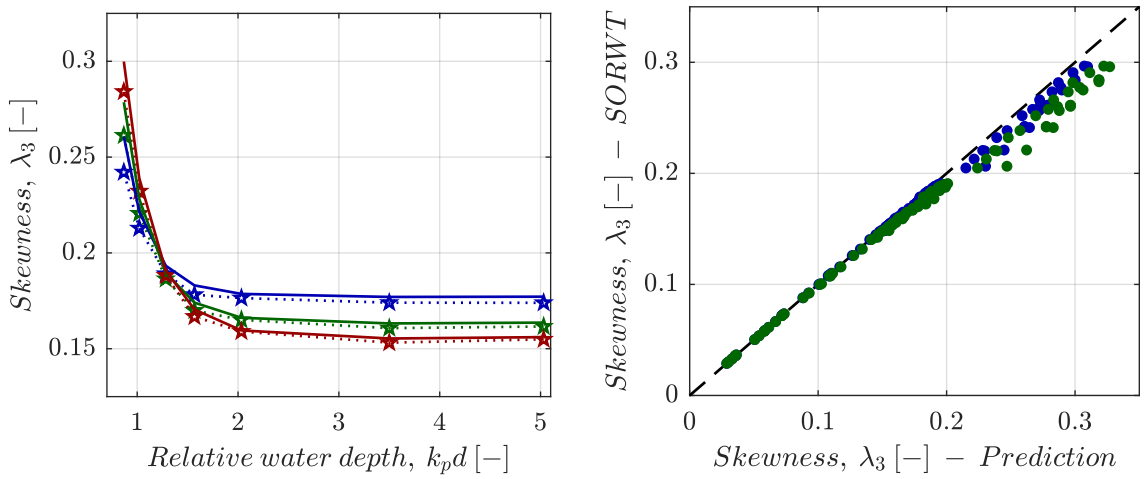
with the second term in the summation being always positive. In Equation E.1, $\eta^{(1)}$ is the linear part of the free surface (Equation 2.13) and $\eta^{(2)}$ is the second-order part (Equation 2.18). Moreover, m_0 is the zeroth spectral moment, $S_{\eta\eta}(\omega,\theta)$ is the directional wave spectrum and $A_{ij}^{\pm}$ refer to the second-order interaction kernels between pairs of interacting wave components i and j (see Equation 2.18). This change in the variance signifies a change in the available wave energy, which is not a physical phenomenon. To this end, as indicated by Janssen (2009) using the Zakharov equation, the free-surface variance remains unchanged and equal to m_0 in the presence of nonlinear effects beyond second-order. Consequently, caution should be paid in adopting the appropriate measure for the variance at each order of nonlinearity.

To assess the applicability of Equation 4.4 for second-order sea-states, an extensive set of 120 directional sea-states were simulated using SORWT; with the sea-state parameters laying in the ranges $k_p d \in [0.87, 5.03]$, $\sigma \in [5, 30]$ and $\gamma \in [1, 5]$. In more detail, for each sea-state the ensemble-averaged skewness from 50 $\sim$3-hour random records sampled at 12.8Hz (full scale) was calculated; each record corresponding to a different set of random phases, amplitudes and directions.

To obtain such an extensive set of simulations, an acceleration procedure was conceptualised and implemented to evaluate the second-order free surface. This procedure circumvents the need to evaluate computationally intensive double summations of the form of Equation 2.18, and it is described in Appendix F. Based on this approach, the computational time for evaluating the free surface for a single random seed of $\sim$3-hours duration is as low as $\sim 2.5s$; in an HP Z400 workstation using standard MATLAB routines. While the required computational time for the entire set of simulations was only $\sim 4h$.

In addition, to account for the effect of the (small) sample variability, the ensemble-averaged skewness of the underlying linear free surface (which, in theory, is zero) was subtracted from the ensemble-averaged skewness of the total second-order free surface. Based on this approach, the nonlinear ensemble-averaged skewness from 50 random seeds coincided with the values from 200 random seeds; for which the ensemble-averaged skewness is converged to $> 99.5\%$[1]. Finally, the numerical eval-

[1]the convergence being assessed in terms of the relative difference between the mean skewness from 150 and 200 seeds



(A) (B)

Figure E.1: Comparison of the time-and ensemble-averaged skewness arising from SORWT simulations to the analytical predictions of Equation 4.4 to predict the skewness parameter (λ_3). (A) refers to sea-states of $\frac{1}{2}H_sk_p = 0.105$ and $\sigma_\theta = 10°$ for varying effective water depth, k_pd; with the lines (·★· · / · ★· · / · ★· ·) referring to SORWT and (—— / —— / ——) to the predictions of Equation 4.4 for $\gamma = 1.0, 2.5$ and 5.0, respectively. (B) refers to comparisons for the full set of 120 simulated sea-states; with (•) denoting predictions incorporating the change in free-surface variance predicted by Equation E.1 and (•) that do not. While, the diagonal line (— —) defines perfect agreement.

uation of both Equations 4.4 and E.1 was found to not be sensitive to the spectral resolution, and the evaluation of the skewness based on SORWT time records was insensitive to an increase in the sampling rate.

Figure E.1 presents comparisons between the numerical (Equation 2.57) and analytical results (Equations 4.4 and E.1). Specifically, sub-figure (A) presents comparisons for sea-states of $\frac{1}{2}H_sk_p = 0.105$, $\sigma_\theta = 10°$, $\gamma = 1, 2.5, 5$ with varying effective water depth k_pd; these sea-states coinciding to those presented in Figure 4.17, albeit with the latter simulated using SORWT. These comparisons demonstrate that Equation 4.4 in conjunction with Equation E.1 performs very well in predicting the measured skewness. However, a small over-prediction is observed, which increases with a reduction in the effective water depth and increase in spectral bandwidth. Indicatively, this over-prediction is of the order of 1% in $k_pd = 5.03$ and 5% in $k_pd = 0.87$ for $\gamma = 1$. This increase in the error with increasing spectral bandwidth and effective water depth is in line with the corresponding increase of the slopes $\partial\eta^{(1)}/\partial t$ and $\nabla\eta^{(1)}$, respectively. Hence, it can be attributed to the leading order truncation of the theoretical solution. However, to be certain about the origins of the

observed errors, the accuracy of Equation E.1 in predicting the free-surface variance needs to be assessed as well. To this end, unlike Equation 4.4, the evaluation of the variance based on Equation E.1 is exact, with the maximum relative deviation between the measured values from time traces and Equation E.1 being only 0.075%. As such, the error associated with the free-surface variance is deemed negligible.

Taking into account the full set of sea-states, Figure E.1(b) presents the measured vs the calculated skewness. Specifically, the markers in green refer to predictions that do not include the change in the free-surface variance and the markers in blue refer to predictions that include it. It is shown that the difference between the two approaches becomes larger for increased values of the skewness. These are associated with the shallowest cases, $k_p d = 0.87$, for which the increase in variance is in the order of 3%. The comparisons given on Figure E.1(b) indicate that including the change in variance is essential for a more accurate prediction of the skewness arising from sorwt. As the blue markers lay reasonably close to the perfect fit, and the green lay further apart. Therefore, based on the above, Equation 4.4 performs very well in predicting the skewness arising from sorwt simulations, as long as the change in variance is accounted for.

E.2 On the relation between the skewness and kurtosis

As mentioned in §4.6.2 the identification of the relation between skewness and kurtosis can be of practical interest. In the context of second-order theory and for narrow-banded long-crested waves Marthinsen & Winterstein (1992) have shown that the second-order contribution to the bound kurtosis in deep water is given by $\lambda_{40}^b = 4/3\lambda_3^2$. As such, it is worth exploring if the quadratic relationship of Marthinsen & Winterstein (1992) holds for realistic bandwidth directional second-order sea-states; this represents an intermediate step before exploring the fully non-linear problem in §4.6.2.

Figure E.2 presents the measured bound kurtosis vs the measured skewness arising from the 120 simulated sea-states using sorwt; the latter described in the context of Figure E.1. More specifically, the three sub-figures comprising Figure E.2 refer to the same data, but with the markers coloured according to different sea-state param-

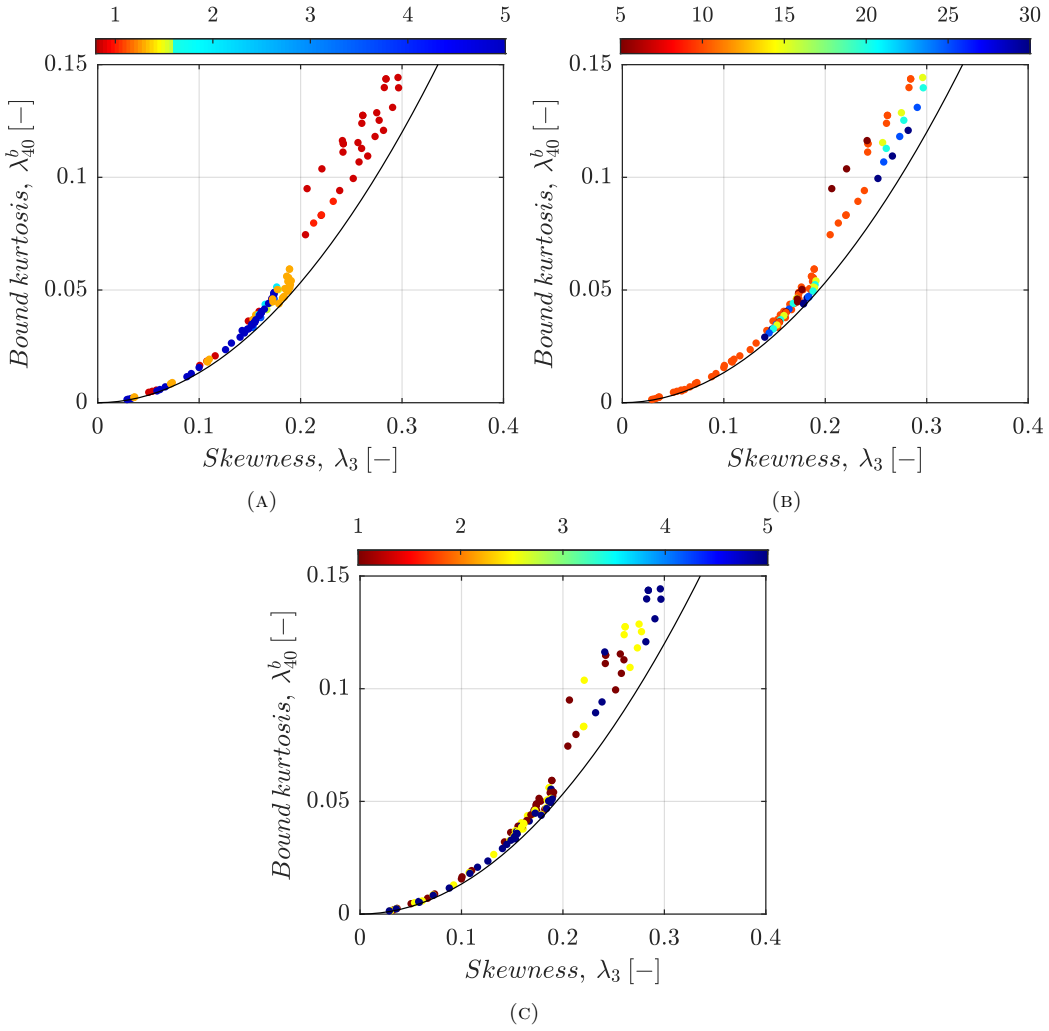


Figure E.2: Bound kurtosis against measured skewness arising from SORWT simulations for 120 sea-states shown with (•). All three sub-plots refer to the same data. In (a) the markers are coloured according to the $k_p d$ value, in (b) according to σ_θ and in (c) according to γ. The deep-water narrow-band theoretical relation of Marthinsen & Winterstein (1992) (——) has also been added for reference.

eters. Namely, in sub-figure (A) the markers are coloured according to the value of the effective water depth $k_p d$, in (B) according to the degree of directionality, σ_θ, and in (C) according to the peak enhancement factor, γ. In all sub-figures, the theoretical solution of Marthinsen & Winterstein (1992) is also added for comparison. Taking the different sub-figures together, the following points are observed:

- The relationship between the skewness and the bound kurtosis for broad-banded directionally spread seas is largely quadratic.
- The theoretical solution of Marthinsen & Winterstein (1992) performs well in predicting the bound kurtosis for $k_p d > 1$. However, for $k_p d < 1$, it under-predicts the numerical data.
- The scatter of the data for $k_p d < 1$ can be explained by the different directional spreads considered. In contrast, the effect of spectral bandwidth appears to be less important. This scatter originates from the rapid increase of the second-order difference terms with a reduction in directionality. As a result, this increase ultimately leads to a reduced skewness with reducing directionality. This, in turn, disrupts the one-to-one relationship between the skewness and bound kurtosis.

However, despite the noted discrepancies, the theoretical solution of Marthinsen & Winterstein (1992) is able to provide an estimate of the second-order contribution to the bound kurtosis.

F

Acceleration method for obtaining the second-order free surface

The evaluation of the free-surface elevation using the second-order random wave theory of Equation 2.18 can be a very computationally intensive task when random sea-state statistics are sought. More specifically, following a direct evaluation of the summations involved in Equation 2.18, the order of computation is $O(N^2)$, where N is the number of spectral wave components. In the following discussion, a simple methodology for reducing the computational cost to $O(2N)$ is presented. This is based on a simple algebraic manipulation prior to evaluating the time-series of the second-order free surface.

Following the discussion in §2.2.2, the evaluation of the total second-order free surface, in any given location, involves the computation of the following summations (following a complex notation):

$$\begin{aligned} \eta^{(2)+}(t) &= \Re[\frac{1}{4}\sum_{i=0}^{N}\sum_{j=0}^{N} a_i a_j A_{ij}^{+} \exp(-i\omega_{ij}^{+}t)] \\ \eta^{(2)-}(t) &= \Re[\frac{1}{4}\sum_{i=0}^{N}\sum_{j=0}^{N} a_i a_j^{*} A_{ij}^{-} \exp(-i\omega_{ij}^{-}t)], \end{aligned} \tag{F.1}$$

where $\eta^{(2)+}(t)$ is the sum-frequencies second-order elevation and $\eta^{(2)-}(t)$ is the difference-frequencies one. While, $\omega_{ij}^{+} = \omega_i + \omega_j$ and $\omega_{ij}^{-} = \omega_i - \omega_j$ refer to the sum and difference frequencies respectively.

The bottleneck in computing the above double summations is that the term involving the time vector, t, $(\exp(-i\omega_{ij}^{+,-}t))$ has to be evaluated N^2 times, as many times as the number of the involved interactions. However, in considering the full set of sum and difference frequencies involved in the summations of Equation F.1, for equally spaced frequency discretisation of frequency increment, $\Delta\omega$, the sum and difference frequencies are not unique.

This can be illustrated by considering the frequency matrices $\omega_{ij}^{+,-}$, shown in Equations F.2 and F.3 and appearing in Equation F.1. In more detail, by considering for example two interacting wave components of $\omega_i = 2\Delta\omega$ and $\omega_j = 3\Delta\omega$, the frequency of the sum term is $\omega_{ij}^{+} = 5\Delta\omega$. Now, taking into account two different interacting components of $\omega_i = 1\Delta\omega$ and $\omega_j = 4\Delta\omega$, the sum term is again $\omega_{ij}^{+} = 5\Delta\omega$. Thus, considering the entire set of interactions among the N^2 elements of the matrices F.2 and F.3, there are only $2N$ unique elements for each matrice that are repeated.

$$\begin{bmatrix} \omega_{00}^{+} & \omega_{01}^{+} & \omega_{02}^{+} & \dots & \omega_{0N}^{+} \\ \omega_{10}^{+} & \omega_{11}^{+} & \omega_{12}^{+} & \dots & \omega_{1N}^{+} \\ \omega_{20}^{+} & \omega_{21}^{+} & \omega_{22}^{+} & \dots & \omega_{2N}^{+} \\ \vdots & \vdots & \vdots & \ddots & \vdots \\ \omega_{N0}^{+} & \omega_{N1}^{+} & \omega_{N2}^{+} & \dots & \omega_{NN}^{+} \end{bmatrix} = \begin{bmatrix} \omega_0 & \omega_1 & \omega_2 & \dots & \omega_N \\ \omega_1 & \omega_2 & \omega_3 & \dots & \omega_{N+1} \\ \omega_2 & \omega_3 & \omega_4 & \dots & \omega_{N+2} \\ \vdots & \vdots & \vdots & \ddots & \vdots \\ \omega_N & \omega_{N+1} & \omega_{N+2} & \dots & \omega_{2N} \end{bmatrix} \tag{F.2}$$

and

$$\begin{bmatrix} \omega_{00}^{-} & \omega_{01}^{-} & \omega_{02}^{-} & \dots & \omega_{0N}^{-} \\ \omega_{10}^{-} & \omega_{11}^{-} & \omega_{12}^{-} & \dots & \omega_{1N}^{-} \\ \omega_{20}^{-} & \omega_{21}^{-} & \omega_{22}^{-} & \dots & \omega_{2N}^{-} \\ \vdots & \vdots & \vdots & \ddots & \vdots \\ \omega_{N0}^{-} & \omega_{N1}^{-} & \omega_{N2}^{-} & \dots & \omega_{NN}^{-} \end{bmatrix} = \begin{bmatrix} \omega_0 & \omega_{-1} & \omega_{-2} & \dots & \omega_{-N} \\ \omega_1 & \omega_0 & \omega_{-1} & \dots & \omega_{1-N} \\ \omega_2 & \omega_1 & \omega_0 & \dots & \omega_{2-N} \\ \vdots & \vdots & \vdots & \ddots & \vdots \\ \omega_N & \omega_{N-1} & \omega_{N-2} & \dots & \omega_0 \end{bmatrix}, \tag{F.3}$$

where $\omega_i = i\Delta\omega$.

By making the above observation, the amplitudes of the second-order components, $\frac{1}{4}a_i a_j A_{ij}^{+,-}$, corresponding to the unique frequencies $[\omega_0, \omega_1, \cdots \omega_{2N}]$ for the

sum terms, and $[\omega_{-N}, \omega_{-N+1}, \cdots \omega_N]$ for the difference terms can be summed before calculating the time-dependant part of Equation F.1, according to:

$$\begin{aligned} B_n^+ &= \frac{1}{4}\sum_{i=0}^{N}\sum_{j=0}^{N} a_i a_j A_{ij}^+ \Delta_{i+j-n} \quad n = 0, 1, 2, 3, 4, ..., 2N \\ B_n^- &= \frac{1}{4}\sum_{i=0}^{N}\sum_{j=0}^{N} a_i a_j A_{ij}^- \Delta_{i-j-n} \quad n = -N, -N+1, ..., 0, 1, ..., N, \end{aligned} \tag{F.4}$$

where Δ_e is the Kronecker delta and it is equal to 1 for $e = 0$ and equal to 0 otherwise.

As such, given this simple consideration the double summations in Equation F.1 can be replaced by following single summations:

$$\begin{aligned} \eta^+(t) &= \Re[\sum_{n=0}^{2N} B_n^+ \exp(-i\omega_n t)] \\ \eta^-(t) &= \Re[\sum_{n=-N}^{N} B_n^- \exp(-i\omega_n t)]. \end{aligned} \tag{F.5}$$

This simplification not only reduces the number of the required summations, but also enables the use of the inverse Fast Fourier Transform algorithm for evaluating the expressions in Equation F.5.

Moreover, the above procedure can be adopted for other types of second-order quantities: such as the second-order kinematics, second-order radiated/diffracted wave-fields arising from the interaction of waves with floating structures and their second-order forcing or motion response (see, for example, Kim & Yue (1990)).

G

On the applicability of the Gram-Charlier series

Whilst Chapter 5 presented a novel crest-height model that is fully predictive and accurate, the accuracy of the most common alternative higher-order crest-height model based on the Gram-Charlier series (see §2.3.3) is assessed in the present appendix.

This investigation was carried out prior to devising the new model. It was considered essential owing to both popularity of the Gram-Charlier series and their potential suitability in representing higher-order crest-height distributions. As such, the assessment of the Gram-Charlier series crest-height model served as initial guidance as to whether it would be worth devoting further efforts into casting its predictions entirely predictive. Or whether an alternative approach was required to model the third-order nonlinearity effectively. To this end, the applicability of the Gram-Charlier series was assessed for the full set of sea-states presented in Chapters 3 and 4. This presents the widest assessment of the model to date.

Furthermore, the crest-height predictions of the Gram-Charlier series model involve the assumption that third-order nonlinearity characterising the wave crests is identical to the third-order corrections to the envelope of the free surface. Whilst this argument is valid for narrow-band waves, its applicability to broad-band waves is questionable. Hence, here the Gram-Charlier series is first applied in its simplest form in §G.1, referring to the statistical description of the free surface itself, for which the effect of spectral bandwidth is not involved in any assumption underpinning the

theory. Following on, §G.2 assesses the Gram-Charlier series ability to capture the magnitude of the crest heights.

G.1 Probability density function of the free surface

Following Longuet-Higgins (1963), the starting point for devising the Gram-Charlier representation of the probability density function (PDF) of the nonlinear free surface is based on the expression of the free-surface elevation according to,

$$\eta = \sum_{i=1}^{\infty} \tilde{a}_i \zeta_i + \sum_{i=1}^{\infty}\sum_{j=1}^{\infty} \tilde{b}_i \tilde{b}_j \zeta_i \zeta_j + \sum_{i=1}^{\infty}\sum_{j=1}^{\infty}\sum_{l=1}^{\infty} \tilde{c}_i \tilde{c}_j \tilde{c}_l \zeta_i \zeta_j \zeta_l + ..., \tag{G.1}$$

where ζ_i are symmetric independent random variables and $[\tilde{a}_i,\ \tilde{b}_i,\ \tilde{b}_j,\ \tilde{c}_i,\ \tilde{c}_j,\ \tilde{c}_l]$ are constants. Whilst this representation of the free surface incorporates third-order effects, it does not include the coupling of the free-wave components.

Longuet-Higgins (1963) have shown that the PDF of η given in Equation G.1 can be expressed as,

$$p(\eta) = \frac{1}{2\pi\sqrt{m_0}} e^{-\frac{1}{2}\frac{\eta^2}{m_0}} [1 + \frac{1}{6}\lambda_3 H_3 + \Big(\frac{1}{24}\lambda_{40} H_4 + \frac{1}{72}\lambda_3^2 H_6\Big) + ...], \tag{G.2}$$

where m_0 is the free-surface variance, λ_3 is the skewness of η and λ_{40} is the kurtosis of η. Finally, H_i are the Hermite polynomials given by,

$$H_3 = f^3 - 3f, \quad H_4 = f^4 - 6f^2 + 3, \quad H_6 = f^6 - 15f^4 + 45f^2 - 15, \tag{G.3}$$

where $f = \eta/\sqrt{m_0}$. As should be the case, for $\lambda_3 = 0$ and $\lambda_{40} = 0$, one recovers the the Gaussian distribution.

To assess Equation G.2, Figure G.1 concerns the comparison between predictions based on Equation G.2 with PDFs obtained from HOSM simulations. In more detail, these comparisons refer to the steady-state part ($t = 55T_p$) of nonlinear evolution for uni-directional sea-states of $\frac{1}{2}H_s k_p = 0.105$ and $k_p d = 5.03, 1.28$ and 0.87. This enables to test Equation G.2 in situations where significant nonlinear focusing ($k_p d = 5.03$), defocusing ($k_p d = 0.87$) and neither (substantial) focusing nor defocusing is observed ($k_p d = 1.28$). While in applying Equation G.2, the values of the statistical moments were obtained directly from the free-surface measurements.

More specifically, the left column of sub-figures (sub-figures (A), (C) and (E)) refers to the free-waves part of the free surface and the right column (sub-figures (B), (D) and (F)) to the total free surface. Moreover, each row corresponds to a different effective water depth, with (A) and (B) referring to $k_p d = 5.03$, (C) and (D) to $k_p d = 1.28$, and (E) and (F) to $k_p d = 0.87$. In each sub-figure, the (linear) Gaussian distribution is also added for reference and all distributions are normalised by the H_s of each sea-state.

In observing Figure G.1, firstly, it is interesting to note that the PDF of the free waves is symmetric to the zero (mean) elevation, revealing that the near-resonant interactions affect both the positive and negative elevations in the same manner. This observation has perhaps important consequences for the trough-to-crest wave heights. The present results highlight that attenuation in the wave heights compared to commonly employed weakly nonlinear distributions in the defocusing regime can originate from the effect of near-resonant interactions, in addition to the effect of wave breaking; the latter noted by Karmpadakis (2018).

Considering the comparisons presented in sub-figures (A), (C) and (E), Equation G.2 is shown to predict the PDF reasonably well even if wave dynamics are not explicitly accounted for in its derivation. Interestingly, it is shown that a non-zero value for the kurtosis, in conjunction with a zero value for the skewness, leads to symmetric with respect to $\eta = 0$ changes in $p(\eta)$. However, in $k_p d = 5.03$, the magnitude of both the highest and lowest elevations is somewhat under-predicted. Whereas in $k_p d = 0.87$ the values of the PDF are negative at the highest absolute elevations. In fact, this is a known potential issue in applying Equation G.2, as discussed in Huang & Long (1980) amongst others.

Taking into account the PDF of the total free surface, sub-figures (B), (D) and (F) show comparisons of both Equation G.2 and the second-order solution of Socquet-Juglard et al. (2005). The latter shows symmetric increase of both positive and negative elevations, whereas the former does not; owing to the effect of third-order nonlinearity. It is shown that the negative elevations, which are affected by both second-order bound waves and third-order near-resonant interactions, are predicted very well by the Gram-Charlier series (Equation G.2). While Socquet-Juglard et al. (2005) fails to predict the magnitude of the negative elevations, especially when nonlinear focusing or defocusing is important.

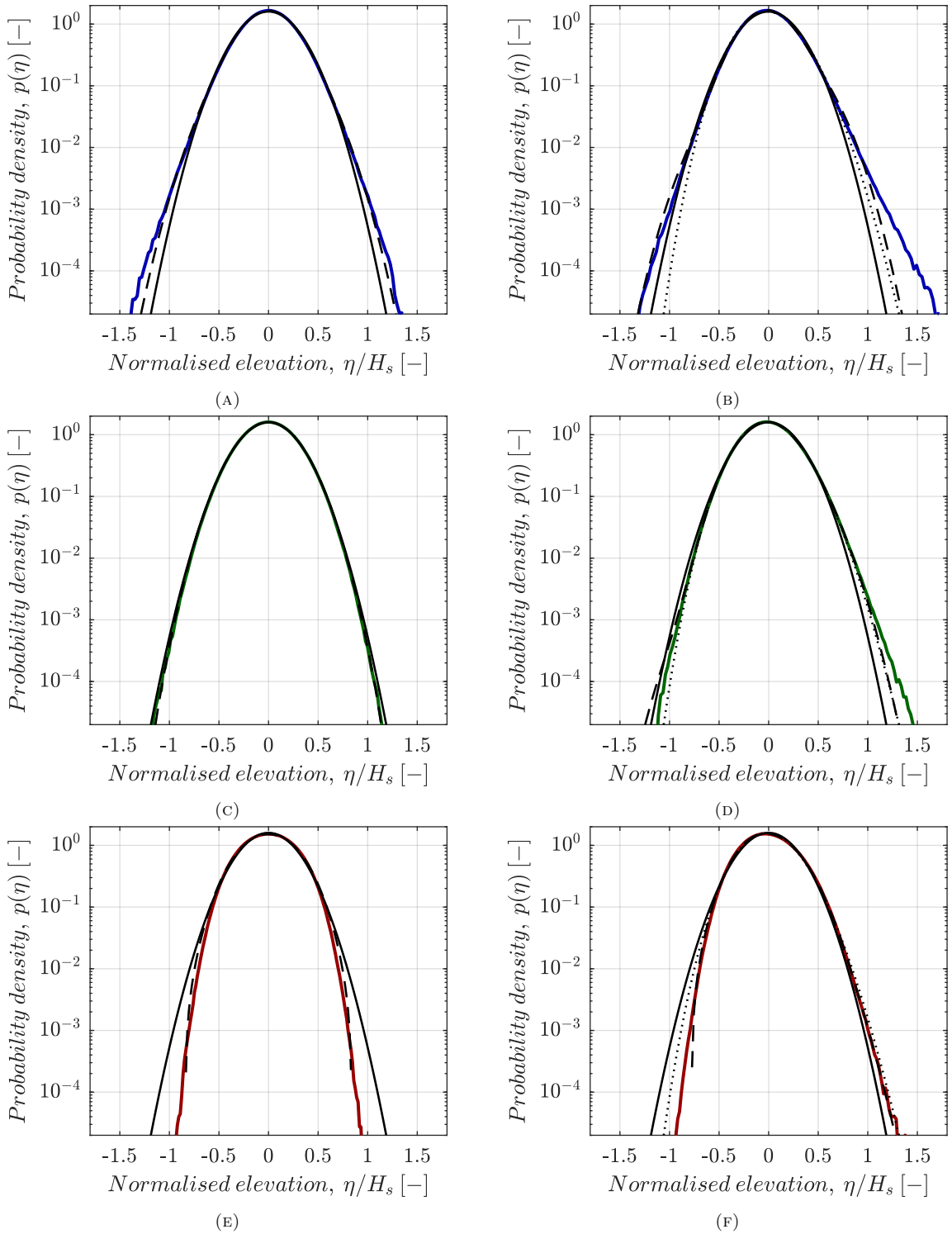


Figure G.1: Comparison of the probability density function of the free surface, $p(\eta)$, arising from HOSM simulations (—— / —— / ——) to the Gram-Charlier series (— —) predictions based on Equation G.2. The comparisons refer to uni-directional sea-states ($\sigma_\theta = 0$) of $\frac{1}{2}H_s k_p = 0.105$ and $\gamma = 2.5$ at steady state ($t = 55T_p$) in effective water depths of $k_p d = 5.03$ ((A) & (B)), $k_p d = 1.28$ ((C) & (D)) and $k_p d = 0.87$ ((E) & (F)). The left column refers to the dynamic part of the free surface, while the right column to the total free surface. The (linear) Gaussian distribution (——) is also added for reference in all sub-plots.

However, Equation G.2 under-predicts the positive elevations for $k_pd = 1.28$ and 5.03, especially in deep water ($k_pd = 5.03$) for which energy focusing is present. These results reveal that the contributions to the positive elevations from bound waves are not predicted well by Equation G.2. A potential explanation for this is:

1. the presence of fourth-order bound terms that, whilst are accounted for in the measured values of skewness, they are not represented appropriately by Equation G.2,

2. the coupling of the bound terms to the underlying free waves and

3. the bound kurtosis and dynamic kurtosis not affecting the free-surface elevation in the same way. Hence, they can not be represented by the same factor, i.e. the total kurtosis.

The last point (point (3)) directly relates to Figure 3.34, where the bound contribution to the kurtosis (affecting the positive elevations) has been shown to relate to more significant increases in the crest-heights than the dynamic kurtosis. More specifically, it was shown that the effect of dynamic kurtosis on the crest-height amplification is $\sim 1/3$ of the equivalent effect of the bound kurtosis. To this end, for $k_pd = 1.28$, for which wave dynamics are not important, the under-prediction of the positive elevations probably relates to points (1) & (3) above.

Finally, the Gram-Charlier series are found to capture very well the entire PDF for $k_pd = 0.87$. However, with the assumptions underpinning the derivation of Equation G.2 being clearly violated, this agreement is believed to be merely due to the negation of the terms involving λ_{40} and λ_3^2 in Equation G.2.

Having identified some key features of the performance and limitations of the Gram-Charlier-series PDF predictions, next, the Gram-Charlier-series crest-height predictions are assessed.

G.2 Crest-height exceedance distribution

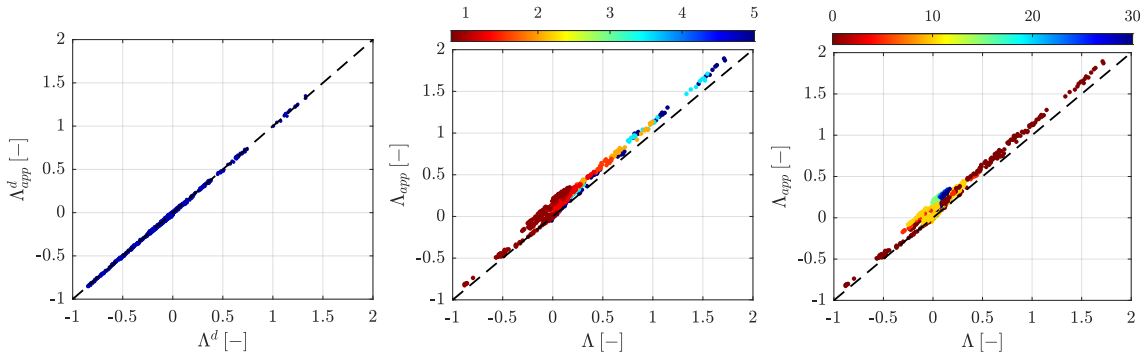
The exceedance probability of crest heights according to the Gram-Charlier series was presented in §2.3.3. To this end, it was highlighted that the model requires the values of the skewness, λ_3, and the fourth-order normalised joint cumulants between the free surface and its Hilbert transform: λ_{40}, λ_{22}, and λ_{04} (see Equation 2.57).

These fourth-order cummulants are used in the evaluation of the parameter Λ (see Equation 2.53) according to $\Lambda = \lambda_{40} + 2\lambda_{22} + \lambda_{04}$.

However, for simplification, in some studies (for example Tayfun & Fedele (2007) and Fedele et al. (2016)), the narrow-band approximation $\Lambda_{app} = 8\lambda_{40}/3$ has been used, which only depends on the total kurtosis, λ_{40}. To this end, Mori & Janssen (2006) have shown analytically that for the dynamic part of the free surface, the two parameters coincide: $\Lambda_{app} = \Lambda$. Hence, any difference between the two originates from bound-wave contributions. Building upon these considerations, it is worth clarifying the relationship between Λ and Λ_{app}. Particularly, for the dynamic part of the free surface, which will enable to explore whether the theoretical considerations of Mori & Janssen (2006) hold. This will serve as an additional means for verifying the effectiveness of separating the free waves from bound waves.

To this end, Figure G.2 contrasts the ensemble-averaged values of Λ and Λ_{app} at steady state [1] for all available evolution times arising from the entire set of HOSM simulations presented in Chapters 3 and 4, comprising a set of 84 sea-states. Specifically, sub-figure (A) presents the comparison between Λ and Λ_{app} for the free waves, referred to as Λ^d and Λ^d_{app}, respectively. It is shown that the two parameters are in excellent agreement, in line with Mori & Janssen (2006). Following on, sub-figures (B) and (C) present comparisons for the total free surface. These sub-figures present the same set of comparisons, the difference between the two being the colouring of the markers. In more detail, in sub-figure (B) the markers are coloured according to $k_p d$, while in sub-figure (C) they are coloured according to σ_θ. In considering the results presented in the two sub-figures, it is first shown that no clear relationship between Λ and Λ_{app} exists, as the points are scattered. This scattering becomes more significant in the shallowest effective water depths ($k_p d < 1$), and it is induced by the inclusion of a wide range of directional spreadings, as shown in sub-figure (C). Despite the observed scatter, Λ_{app} is systematically larger than Λ; the average difference between the two being ~ 0.08. This observation is in line with similar comparisons conducted by Cherneva et al. (2009) and Cherneva et al. (2013) for a limited number of sea-states in deep water. While it contradicts the notion that $\Lambda < \Lambda_{app}$ based on second-order theory (Tayfun & Lo, 1990). This arises due to the effect of third-order

[1] Specifically, for $t > 45Tp$ for the uni-directional sea-states and for $t > 10T_p$ for the directional sea-states



(A) (B) (C)

FIGURE G.2: Comparison between Λ and Λ_{app} for the full set of available HOSM simulations. (A) refers to the dynamic part of the free surface, while (B) and (C) refer to the total free surface. In (B) the markers are colored according to $k_p d$ and in (C) according to σ_θ. In all sub-figures, the diagonal line (— —) refers to one-to-one relationship, signifying perfect agreement.

bound contributions. Importantly, the differences between Λ and Λ_{app} indicate that the choice of Λ over Λ_{app} could potentially lead to different crest-height predictions.

Following the preliminary analysis regarding the parameter, Λ, Figure G.3 concerns the performance of the Gram-Charlier series crest-height predictions. These predictions have been obtained on the basis of both Λ and Λ_{app}. While their performance is assessed through comparisons to crest heights arising from both uni-directional ($\sigma_\theta = 0$) and directionally spread ($\sigma_\theta = 10°$) HOSM simulations of sea-states with $1/2H_s k_p = 0.105$ and $\gamma = 2.5$ at $k_p d = 0.87$, 1.28 and 5.03. The sub-figures at the left-hand side refer to $\sigma_\theta = 0$ and the sub-figures on the right-hand side to $\sigma_\theta = 10°$. All crest-height distributions refer to the steady-state part of the nonlinear evolution. The uni-directional results were obtained at $t = 55T_p$ and the directional results at $t = 25T_p$.

Considering first the uni-directional sea-states, the Gram-Charlier series are shown to under-predict the crest heights laying at the tail of the crest-height distribution for all effective water depths, similarly to the comparison of the PDF in Figure G.1. However, this under-prediction appears more intense in the shallowest case of $k_p d = 0.87$ for the crest heights than the PDF. This is explained by the negative values of the fourth-order cumulants, which, unlike Equation G.2, solely account for the effect of third-order nonlinearity on the crest heights. Hence, the observed discrepancies largely originate from the assumptions underpinning the derivation of the Gram-Charlier series in the first place and not the derivation of Equation 2.53 itself.

Considering the comparisons of the directional sea-states, the Gram-Charlier pre-

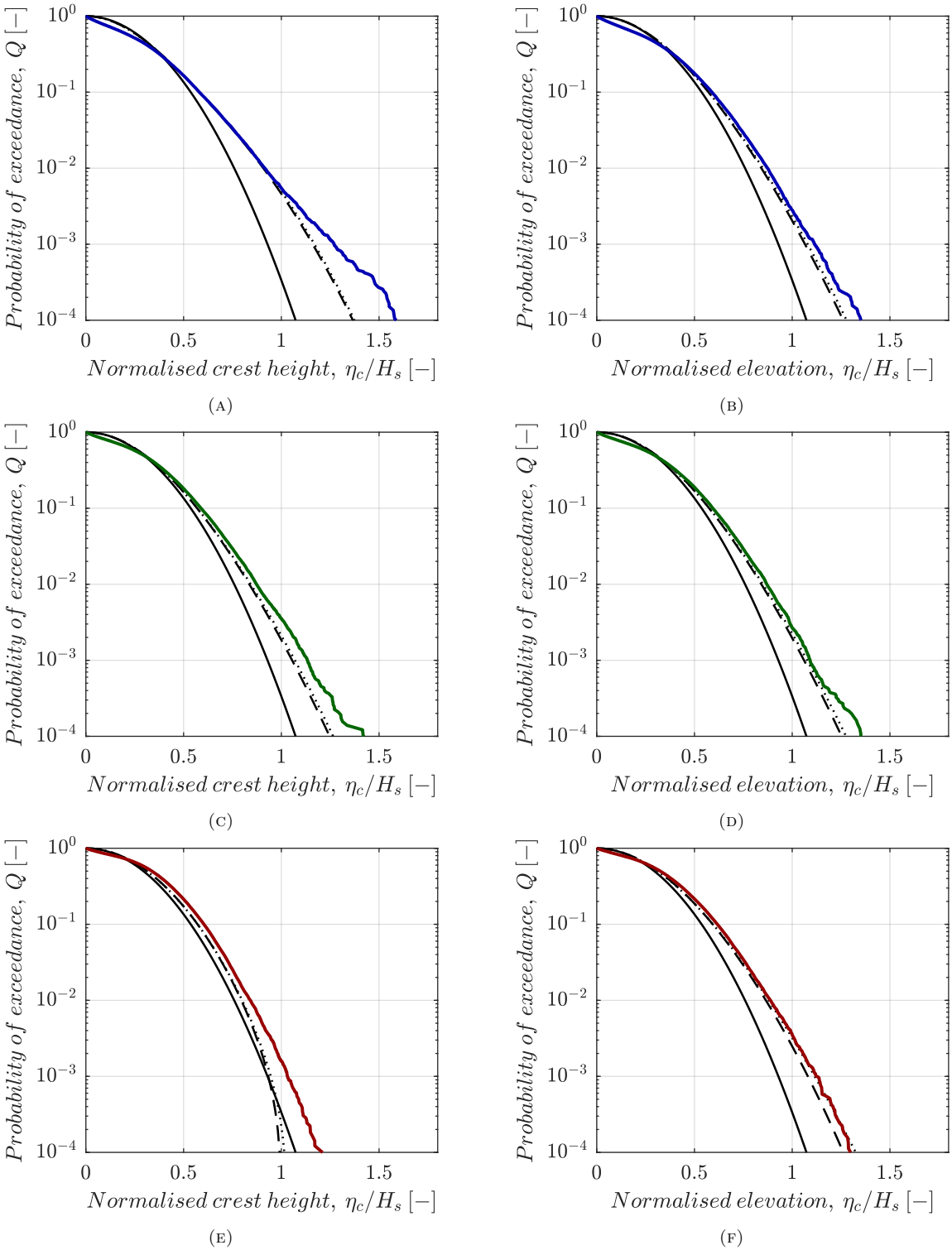


Figure G.3: Comparison of crest-height distributions arising from HOSM simulations (—— / —— / ——) to Gram-Charlier series predictions; the latter being denoted with (— —) and (▪ ▪ ▪ ▪) using Λ and Λ_{app}, respectively. The left column refers to uni-directional sea-states ($\sigma_\theta = 0$), while the right column to directionally spread sea-states of $\sigma_\theta = 10°$. From top to bottom, (A) & (B) refer to in effective water depths of $k_p d = 5.03$, (C) & (D) to $k_p d = 1.28$ and (E) & (F) to $k_p d = 0.87$. The (linear) Rayleigh distribution (——) is also added for reference in all sub-plots.

dictions are more accurate than in the uni-directional sea-states. This arises due to the reduced effect of the near-resonant interactions. However, the predictions using Λ are shown to lay consistently below the numerical data. To this end, it is interesting to note that the difference in the predictions obtained using Λ_{app} over Λ is not significant, with the predictions based on Λ_{app} laying slightly above the predictions based on Λ. This leads to an agreement between predictions and numerical data for $k_p d = 0.87$, for which the difference between Λ_{app} and Λ is the highest. Despite this, the predictions based on Λ_{app} still lead to the underestimation of the crest heights in deeper effective water depths.

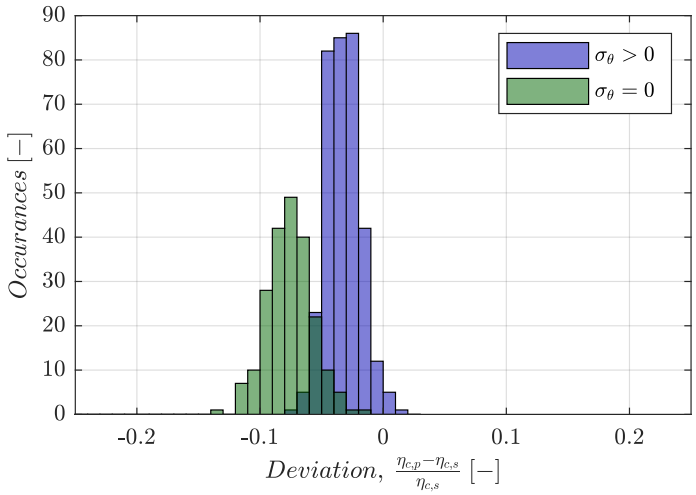


Figure G.4: Histogram of relative deviation, $(\eta_{c,p} - \eta_{c,s})/\eta_{c,s}$, between the crest heights corresponding to an exceedance probability level of $Q = 10^{-3}$ obtained from the Gram-Charlier series crest-height model and from HOSM simulations.

To present an overview of the performance of the Gram-Charlier-series crest-height predictions, Figure G.4 presents the histogram of the relative deviation [1] of the Gram-Charlier series predictions to the numerical data arising at an exceedance probability level of $Q = 10^{-3}$ for all available 84 sea-states and for all evolution times belonging to the steady-state part of nonlinear evolution. It is shown that apart from a small portion of the data which are slightly over-predicted (corresponding to the sea-states of the lowest steepnesses), the Gram-Charlier series consistently under-predict the numerical results, for both uni-directional and directionally spread sea-states. Indicatively, the mean deviation for the steepest sea-states of $\frac{1}{2}H_s k_p = 0.105$

[1] defined by $(\eta_{c,p} - \eta_{c,s})/\eta_{c,s}$, where $\eta_{c,p}$ refers to the Gram-Charlier-series prediction and $\eta_{c,s}$ to the numerical data.

is $\sim -8\%$ for $\sigma_\theta = 0$ and $\sim -3\%$ for $\sigma_\theta > 0$. While the maximum absolute deviation for the same set of sea-states is $\sim 13\%$ for $\sigma_\theta = 0$ and $\sim 7\%$ for $\sigma_\theta > 0$. Interestingly, the magnitude of the deviations presented in Figure G.4 is significantly larger than the deviations arising from the HOE-EANN predictions (Figure 5.23(A)), confirming the outperformance of HOE-EANN in relation to the Gram-Charlier predictions.

H

Short description of additional meta-models

The present appendix is devoted to the description of the Gaussian Process Emulator (GPE) and Support Vector Machines (SVM) for regression meta-models used in §5.2.2. This is a short desciption of the methods and it is provided for completeness. More information can be found in the references provided herein and in the main text. In §H.1 the GPE is introduced, followed by §H.2 where the SVM is presented. It is noted that the adopted mathematical notation applies to each section individually.

H.1 Gaussian Process Emulator

A Gaussian Process Emulator (GPE) is a meta-model that is formulated on the basis that a joint Gaussian distribution links the output data used for its training and the GPE predictions.

The functional form of a GPE with input variables $\mathbf{x} = [x_1, x_2, ..., x_N]$ (N being the number of input variables) and output y is given by:

$$y(\mathbf{x}) = \boldsymbol{\beta}^T \mathbf{f}(\mathbf{x}) + \sigma^2 Z(\mathbf{x}), \tag{H.1}$$

where, unlike other meta-models, the output is a probabilistic quantity.

The first term in Equation H.1 represents the mean trend ($E[y]$) and the second

term the variance ($Var[y]$) associated with the predictions. This variance reflects the uncertainty due to the limited number of data points used in training the GPE. Consequently, the variance at the training data points is zero, whereas it increases as one moves away from the training data points. However, if the meta-model predictions are to be used in a deterministic fashion, the mean trend should be adopted.

The mean trend consists of the multiplication of the regression coefficients $\boldsymbol{\beta} = [\beta_1, \beta_2, ..., \beta_P]$ and the basis functions $\mathbf{f} = [f_1, f_2, ..., f_P]$. The regression coefficients are determined during the training process. While the functional form of the basis functions is pre-selected by the user. To this end, a common choice for the basis functions is polynomials of a selected order, and it has been adopted in the present study.

The variance of y results from the multiplication of σ^2, which is the variance of the GPE and has a constant value, with the zero-mean unit-variance stationary Gaussian process $Z(\mathbf{x})$. The latter is defined by the covariance matrix $Cov[Z(\mathbf{x}), Z(\mathbf{x}')] = R(\mathbf{x}, \mathbf{x}'; \boldsymbol{\theta})$, which describes the correlation between two input data points $\mathbf{x}$ and $\mathbf{x}'$. Moreover, R represents a correlation function family defined by the hyper-parameters $\boldsymbol{\theta} = [\theta_1, \theta_2, ..., \theta_N]$. The functional form of the correlation function family is determined by the user and the hyper-parameters $\boldsymbol{\theta}$ are defined during the training.

Based on the above, the correlation matrix between the outputs of the training data set $\mathbf{y}_T = [y_1, y_2, ..., y_M]$ and the output of a new prediction, y, is defined by,

$$C(y, \mathbf{y_T}) = \begin{bmatrix} 1 & \mathbf{r}^T(\mathbf{x}) \\ \mathbf{r}(\mathbf{x}) & \mathbf{R} \end{bmatrix} \tag{H.2}$$

where

- $\mathbf{r} = [\mathbf{r}_1, \mathbf{r}_2, ..., \mathbf{r}_M]$ refers to the vector of cross-correlations between the input vector $\mathbf{x}$ of a new prediction with each one of the input vectors $\mathbf{x}_{T,i}$ $(i = 1, 2, ..., M)$ used in the training, and it is given by $\mathbf{r}_i = R(\mathbf{x}_{T,i}, \mathbf{x}; \boldsymbol{\theta})$

- $\mathbf{R}$ is the correlation matrix between all input vectors of the training dataset with elements, $R_{ij} = R(\mathbf{x}_{T,i}, \mathbf{x}_{T,j}; \boldsymbol{\theta}) \quad i, j = 1, 2, ..., M$.

Following the above formulation, the mean and variance of the GPE prediction

can then be calculated according to (Rasmussen & Williams, 2006):

$$\begin{aligned} E[y] &= \mathbf{f}(\mathbf{x})^T\boldsymbol{\beta} + \mathbf{r}(\mathbf{x})^T\mathbf{R}^{-1}(\mathbf{y}_T - \mathbf{F}\boldsymbol{\beta}) \\ Var[y] &= \sigma^2\Big(1 - \mathbf{r}^T(\mathbf{x})\mathbf{R}^{-1}\mathbf{r}(\mathbf{x}) + \mathbf{u}^T(\mathbf{x})\Big(\mathbf{F}^T\mathbf{R}^{-1}\mathbf{F}\Big)^{-1}\mathbf{u}(\mathbf{x})\Big) \end{aligned} \tag{H.3}$$

where

$$\mathbf{u}(\mathbf{x}) = \mathbf{F}^T\mathbf{R}^{-1}\mathbf{r}(\mathbf{x}) - \mathbf{f}(\mathbf{x}) \tag{H.4}$$

$$\boldsymbol{\beta} = \Big(\mathbf{F}^T\mathbf{R}^{-1}\mathbf{F}\Big)^{-1}\mathbf{F}^T\mathbf{R}^{-1}\mathbf{y}_T \tag{H.5}$$

and

$$\sigma^2 = \frac{1}{M}\Big(\mathbf{y}_T - \mathbf{F}\boldsymbol{\beta}\Big)^T\mathbf{R}^{-1}(\mathbf{y}_T - \mathbf{F}\boldsymbol{\beta}\Big). \tag{H.6}$$

While $\mathbf{F}$ is the matrix whose elements are $F_{ij} = f_j(\mathbf{x}_{T,i}) \quad i = 1, 2, ..., M,\ j = 1, 2, ..., P$.

Thus, both the mean trend and the variance depend upon the hyper-parameters $\boldsymbol{\theta}$, which are optimised to minimise the leave-one-out cross-validation error (see §5.2.2).

In the course of the present analysis, the numerical implementation of GPE developed by Marelli & Sudret (2014) was utilised. Different combinations of basis functions, correlation function families and optimisation algorithms were trialled for training the GPE. These formed a full matrix of possible combinations and the resulted optimum configuration is reported in Table H.1.

Table H.1: Characteristics of the GPE configuration. Where HCMAES refers to Covariance Matrix Adaptation - Evolution Strategy (CMA-ES, Hansen & Ostermeier 2001) followed by a gradient descent optimisation algorithm.

Basis function type	Linear
One-dimensional correlation function type	Matèrn 3/2
Multi-dimensional correlation type	Unisotropic separable
Error measure for the hyperparameters optimisation	Leave-one-out cross-validation
Hyper-parameters optimisation method	HCMAES

H.2 Support Vector Machines for regression

Unlike the GPE, the Support Vector Machines (SVM) for regression provides only a mean trend. The general form of the SVM predictions is given by,

$$y(\mathbf{x}) = \mathbf{w}^T H(\mathbf{x}) + b, \tag{H.7}$$

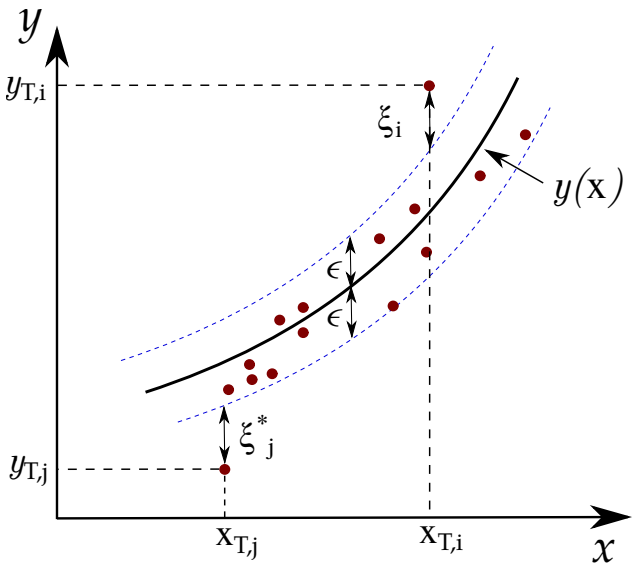
where $\mathbf{w}$ is a vector of weights, b is an offset, $\mathbf{x}$ is the vector of input variables $\mathbf{x} = [x_1, x_2, ..., x_N]$ and H is a mapping function; the latter introduced to account for nonlinearity between inputs and outputs. In the case that $H(\mathbf{x}) = \mathbf{x}$, Equation H.7 represents the solution to a standard linear multivariate regression problem.

However, the formulation of the SVM methodology presents some important differences to a classic regression analysis. This stems from the introduction of the so-called *ϵ-insensitive loss function*, l. During the calibration of the SVM model, based on a set of inputs $\mathbf{x}_T = [\mathbf{x}_{T,1}, \mathbf{x}_{T,2}, ..., \mathbf{x}_{T,M}]$ and outputs $\mathbf{y}_T = [y_{T,1}, y_{T,2}, ..., y_{T,M}]$, this function leads to the penalisation of a point i only if its distance from the prediction $y(\mathbf{x}_{T,i})$ is higher than ϵ. An illustration of this procedure is provided in Figure H.1.

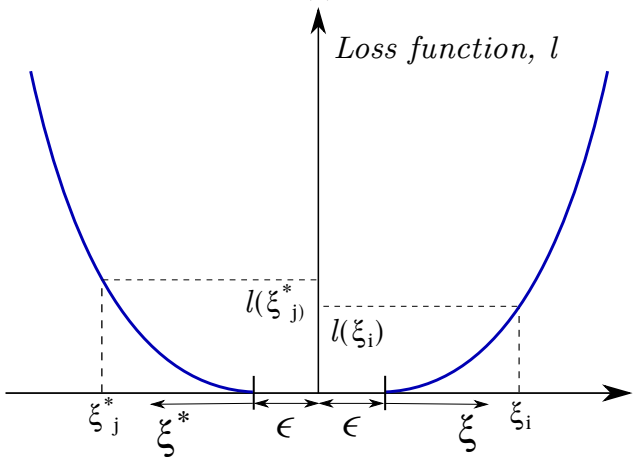
In considering Figure H.1(A), the points laying between the blue dashed lines are not penalised (or in other words considered in the loss function). In contrast, points laying outside these curves are penalised. Thus, the SVM regression gives more weight to 'outliers' when compared to a standard multivariate regression analysis. This ensurs a better generalisation performance (Cristianini et al., 2000). The the loss function is then applied to the so-called *slack* variables ξ, ξ^*, as shown in Figure H.1(B). These variables refer to the distances of the points to be penalised from the *ϵ-insensitive 'tube'*. The latter refers to the edges of the volume between the blue dashed lines in Figure (A).

Based on the above, the optimisation problem to be solved is formulated according to:

$$\min_{\mathbf{w}} \frac{1}{2}||\mathbf{w}||^2 + C\sum_{i=1}^{N} l(\xi_i) + l(\xi_i^*), \tag{H.8}$$



(A)



(B)

Figure H.1: Illustration of the principal elements of the SVM formulation. (A) shows the prediction trend (———), the limits of the ϵ-insensitive 'tube' (– –), the training points (•), the ϵ-insensitive width (ϵ) and the slack variables ξ and ξ^*. While (B) shows how the loss function (———) is applied upon the slack variables.

subject to the following constrains:

$$\begin{aligned} & y_{T,i} - \mathbf{w}^T H(\mathbf{x}_{T,i}) - b \leq \epsilon + \xi_i \\ & \mathbf{w}^T H(\mathbf{x}_{T,i}) + b - y_{T,i} \leq \epsilon + \xi_i^* \\ & \xi_i, \xi_i^* \geq 0. \end{aligned} \tag{H.9}$$

Where $C > 0$ is a factor that regularises the contribution from the penalised terms.

This constraint optimisation problem is more easily solved when it is expressed in its dual form, i.e. when a *Lagrange* function is constructed according to:

$$\begin{aligned} L(\mathbf{w}, b, \xi, \xi^*) = & \frac{1}{2}||\mathbf{w}||^2 + C \sum_{i=1}^{M} l(\xi_i) + l(\xi_i^*) \\ & - \sum_{i=1}^{M} (\kappa_i \xi_i + \kappa_i^* \xi_i^*) \\ & - \sum_{i=1}^{M} \alpha_i (\epsilon + \xi_i - y_{T,i} + \mathbf{w}^T H(\mathbf{x}_{T,i}) + b) \\ & - \sum_{i=1}^{M} \alpha_i^* (\epsilon + \xi_i^* + y_{T,i} - \mathbf{w}^T H(\mathbf{x}_{T,i}) - b), \end{aligned} \tag{H.10}$$

where α_i, α_i^*, κ_i and $\kappa_i^* \geq 0$ are Lagrange multipliers.

Solving for the saddle point of L (i.e. for $\nabla L = 0$) leads to the following optimisation problem to be solved:

$$\begin{aligned} \max_{\alpha} & - \frac{1}{2} \sum_{i,j=1}^{M} (\alpha_i - \alpha_i^*)(\alpha_j - \alpha_j^*) \Phi(\mathbf{x}_{T,i})^T \Phi(\mathbf{x}_{T,j}) \\ & - \epsilon \sum_{i=1}^{M} (\alpha_i + \alpha_i^*) \\ & + \sum_{i=1}^{M} y_{T,i} (\alpha_i + \alpha_i^*) \\ & + C \sum_{i=1}^{M} T(\xi_i) + T(\xi_i^*). \end{aligned} \tag{H.11}$$

Subject to:

$$\sum_{i=1}^{M} (\alpha_i - \alpha_i^*) = 0, \tag{H.12}$$

where the variables κ_i and κ_i^* have been eliminated (see Smola & Schölkopf 2004) and $T(\xi) = l(\xi) - \xi \partial_\xi l(\xi)$. The solution to the above optimisation problem is usually

solved based on an interior-point optimisation algorithm, resulting to the optimum coefficients α_i and α_i^* (and b).

Based on α_i and α_i^*, the SVM prediction of Equation H.7 can be reformulated into (Smola & Schölkopf, 2004),

$$y(\mathbf{x}) = \sum_{i=1}^{N}(\alpha_i - \alpha_i^*)\Phi(\mathbf{x}_{T,i})^T\Phi(\mathbf{x}) + b. \tag{H.13}$$

While, in practice, the inner product $\Phi(\mathbf{x}_{T,i})^T\Phi(\mathbf{x})$ is defined by a basis or kernel function $k(\mathbf{x}_{T,i}, \mathbf{x}; \boldsymbol{\theta}_i) \quad \boldsymbol{\theta}_i = [\boldsymbol{\theta}_1, \boldsymbol{\theta}_2, ..., \boldsymbol{\theta}_N]$. This should be positive and satisfy the so-called Mercer's conditions (see Smola & Schölkopf 2004).

It is interesting to note that the coefficients α_i and α_i^* are non-zero only if the point $\mathbf{x}_i$ is penalised: i.e. if it lays beyond the ϵ margins (Figure H.1). This implies that α_i and α_i^* cannot be non-zero simultaneously, as the output or response $y_{T,i}$ associated to $\mathbf{x}_i$ lays either above or below $y(\mathbf{x}_i)$. A such, the points for which either α_i or α_i^* are non-zero are referred to as *support vectors* and α_i or α_i^* as *support vector coefficients*.

In considering the above, the ϵ-insensitive width, the regularisation factor C and the parameters θ associated with the basis functions are free variables and consist of the hyper-parameters of the problem that ought to be optimised. In the present analysis, the SVM implementation provied by Marelli & Sudret (2014) was adopted. In applying this, different different loss function types (linear and quadratic), basis function types and optimisation algorithms were utilised. The optimum configuration resulted from this investigation is reported in Table H.2.

Table H.2: Characteristics of the SVM configuration. Where HCMAES refers to Covariance Matrix Adaptation - Evolution Strategy (CMA-ES, Hansen & Ostermeier 2001) followed by a gradient descent optimisation algorithm.

Property	Selection
Loss function for penalization of deviations	Linear
Basis function type	Matèrn 3/2
Solver for evaluating the support vector coefficients	Interior-point
Error measure for the hyper-parameters optimisation	Leave-one-out cross-validation
Hyper-parameters optimisation method	HCMAES

I

Range of validity of the Ensemble Artificial Neural Network predictions

The base for the HOE-EANN crest-height predictions, defined in Chapter 5, is the prediction of the statistical moments of skewness, bound kurtosis and dynamic kurtosis based on the Ensemble Artificial Neural Network (EANN) approach. As is the case for any model calibrated based on a finite set of data, it is crucial to define the range of validity of the predictions. To this end, the data used for the training of the EANN were generated using HOSM and cover the range $k_pd \in [0.87, 5.03]$ and $\frac{1}{2}H_sk_p \in [0, 0.105]$; with different directional spreadings (σ_θ) and spectral bandwidths (γ) being employed. As such, if the HOE-EANN model is to be used outside these limits, EANN has to extrapolate or generalise reasonably. In §5.3.2 it was shown that indeed EANN generalises very well when applied to lower ($k_pd = 0.8$) and higher ($k_pd = 8.0$) effective water-depths.

In assessing the generalisation of the EANN predictions for an even wider range of conditions and specifically for $k_pd < 0.8$ the trends of the moments in this region can be considered. Specifically, the skewness parameter should exhibit a linear variation with an increase in the steepness (Mori & Janssen 2006, Tayfun 2006), the bound kurtosis should exhibit a quasi-parabolic trend (Mori & Janssen 2006) and the dynamic kurtosis, a quasi-linear trend according to Figure 4.8(A).

To this end, Figure I.1 presents the variation of the statistical moments with increasing sea-state steepness for different effective water depths in the range $k_pd \in$

$[0.5, 3.0]$ (with an increment in k_pd of 0.1) for sea-states with $\sigma_\theta = 20°$. Each column of sub-figures corresponds to a different statistical moment. From left to right: sub-figures (A), (D) and (G) refer to the skewness, sub-figures (B), (E) and (H) to the bound kurtosis and sub-figures (C), (F) and (I) to the dynamic kurtosis. From top to bottom, each row of sub-figures corresponds to a different spectral bandwidth (γ); the latter being defined according to $\gamma = 1.0, 2.5$ and 5.0.

Considering first the skewness parameter, the trends are shown to start deviating from linearity after a certain steepness; this steepness being lower as the effective water depth (k_pd) reduces for all γ values. For example, this steepness appears to be as low as $\frac{1}{2}H_sk_p = 0.08$ at $k_pd = 0.5$. Likewise, the bound kurtosis also starts to deviate from a quasi-parabolic variation as the steepness increases; again this deviation becoming noticeable for a progressively lower steepness as k_pd reduces. Qualitatively similar results also underpin the trends of the dynamic kurtosis. The dynamic kurtosis is shown to deviate from a quasi-linear variation with an increase in steepness: the steepness marking the end of a quasi-linear variation of the dynamic kurtosis is similar to the steepness marking the end of the expected variation of the skewness and bound kurtosis.

This limiting or maximum allowable steepness, denoted with $\frac{1}{2}H_sk_p|_{max}$, at each effective water depth was found to be approximated well by the following functional form:

$$\frac{1}{2}H_sk_p|_{max} = 0.19\tanh(k_pd). \tag{I.1}$$

The values of the statistical moments corresponding to $\frac{1}{2}H_sk_p|_{max}$ are shown with black markers connected by a black dashed line in each sub-figure of Figure I.1. It should be noted that the criterion upon which this limiting steepness has been defined is somewhat relaxed when the bound kurtosis in deep water is considered. However, with the bound kurtosis contributing less than the other statistical moments to the crest-height elevations, this somewhat relaxed condition is not considered to be detrimental for the HOE-EANN predictions. As already noted in §5.3.2, a deviation of the bound kurtosis in the order of $\sim 20\%$ is not as significant as to affect the accuracy of the final predictions of the crest-height model.

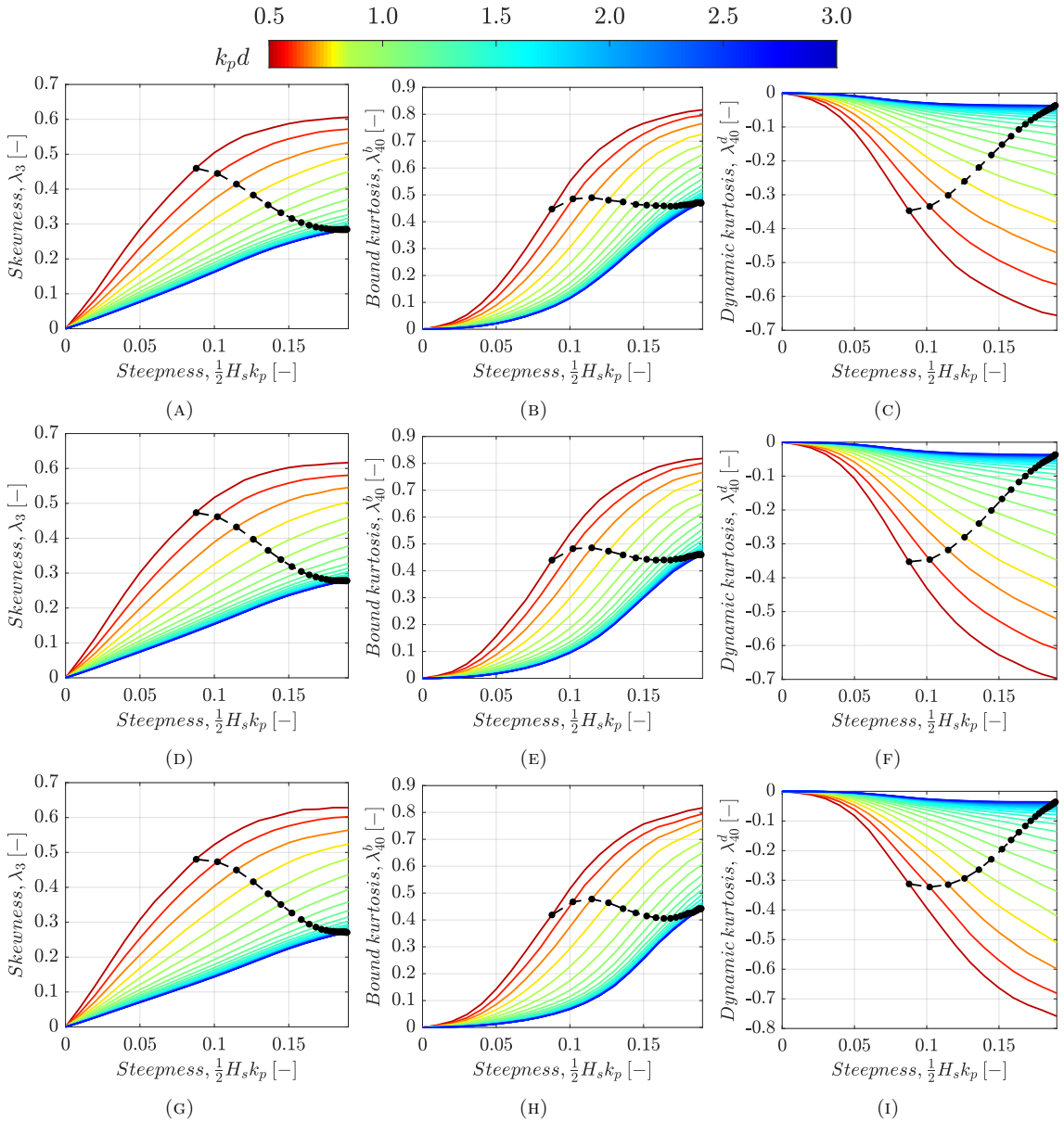


Figure I.1: Variation of the EANN predictions for the statistical parameters of (A), (D) & (G) skewness, λ_3, (B), (E) & (H) bound kurtosis, λ_{40}^b, and (C), (F) & (I) dynamic kurtosis, λ_{40}^d, with increasing steepness for sea-states with $\sigma_\theta = 20°$; each line corresponding to a different effective water depth in $k_pd \in [0.5, 0, 8]$ with an increment of 0.1. The k_pd value of each line is defined in the provided colour-scale. From top to bottom, (A), (B) & (C) refer to $\gamma = 1$, (D), (E) & (F) to $\gamma = 2.5$ and (G), (H) & (I) to $\gamma = 5$. The line (−•−) refers to the values of the statistical moments at the maximum steepness; the latter given by Equation I.1.

J

On the performance of the Karmpadakis & Swan (2022) model

In §2.3.3 the analytic model of Tayfun & Fedele (2007) and the semi-empirical model proposed by Karmpadakis & Swan (2022) were identified as the current state-of-the-art higher-order crest-height models, applicable in finite water depth conditions.

To this end, the model of Tayfun & Fedele (2007) has been shown in Appendix G to consistently under-predict the fully nonlinear numerical crest-height distributions obtained from HOSM simulations. This revealed the need for an alternative formulation. In this regard, the Karmpadakis & Swan (2022) model, whilst not been published, presents the only currenlty alternative model, applicable to the sea-state conditions considered in the present thesis. Thus, the present appendix aims to assess the performance of Karmpadakis & Swan (2022) in capturing the effects of nonlinear interactions and wave-breaking on the crest heights. This is deemed an important investigation in demonstrating the advancements that the crest-height model proposed in Chapter 5 offers.

J.1 Test cases

Based on the above, in §J.2, the Karmpadakis & Swan (2022) model is compared to available numerical data obtained using HOSM. These data refer to directional sea-states covering the effective water-depth range $k_p d \in [0.87, 5.03]$ and having steepness

$\frac{1}{2}H_s k_p = 0.105$. While they were used in calibrating the fully nonlinear model proposed in Chapter 5 referred to as HOE-EANN. Since these data do not include the effect of wave-breaking, the fully nonlinear formulation (without breaking) proposed by Karmpadakis & Swan (2022) was employed for these initial comparisons. Moreover, in assessing the performance of the Karmpadakis & Swan (2022) model in even lower effective water depths, field data in the range $k_p d \in [0.5, 0.8]$ were also employed. These field data are characterised by $H_s/d \leq 0.20$ for which wave breaking is not expected to affect the tail of the distribution, evidence of which is provided in Karmpadakis (2018).

Subsequently, in §J.3, the Karmpadakis & Swan (2022) model is compared against experimental data with $\frac{1}{2}H_s k_p > 0.105$ in $k_p d > 1.0$ and field data with $H_s/d > 0.24$ in $k_p d < 1.0$. In both cases, wave breaking is expected to dissipate the largest waves. As such, for these comparisons the breaking-corrected Karmpadakis & Swan (2022) predictions were employed. It is noted that these data correspond to those used to validate the breaking-corrected HOE-EANN predictions referred to as HOE-EANN-B in §5.4.

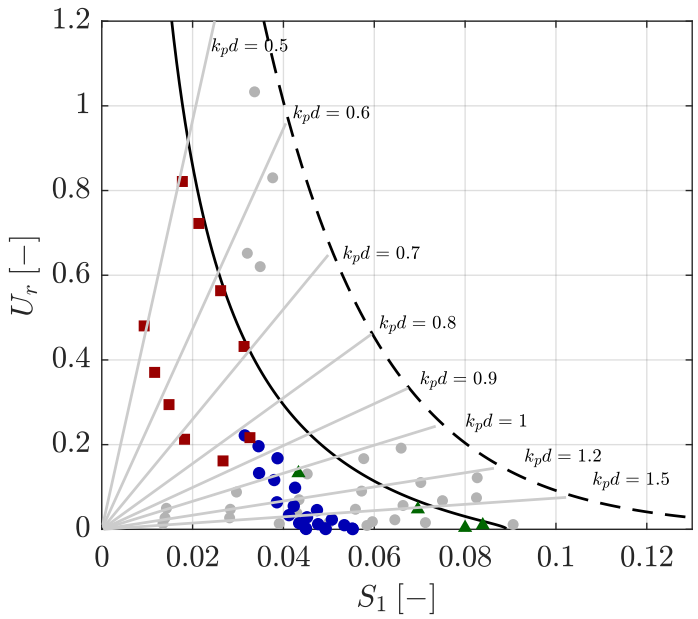


Figure J.1: Sea-state characteristics used for assessing the performance of the Karmpadakis & Swan (2022) model, represented in the (S_1, U_r) parameter space. The lines (——) and (– –) refer to the proposed limits of validity of HOE-EANN-B and Karmpadakis & Swan (2022), respectively. The markers (•) refer to numerical (HOSM), (▲) experimental and (■) field data. While (•) refer to the sea-states used in the calibration of Karmpadakis & Swan (2022). The grey lines refer to iso-$k_p d$ lines for increasing steepness $\frac{1}{2}H_s k_p$.

To illustrate the sea-state conditions used in the present appendix to assess the Karmpadakis & Swan (2022) model performance, Figure J.1 presents the sea-state characteristics of the numerical, experimental and field data in the (S_1, Ur) parameter space, the space where Karmpadakis & Swan (2022) is defined. Each source of data is denoted with a different marker style. Moreover, the sea-states used by Karmpadakis & Swan (2022) to calibrate their model have also been added and appear with grey circular markers. While the proposed range of validity of both the HOE-EANN-B and Karmpadakis & Swan (2022) models are also added. In addition, for reference, iso-k_pd lines for sea-states with increasing $\frac{1}{2}H_sk_p$ have been added. These were obtained on the basis of $\gamma = 2.5$. To this end, it should be noted that γ affects the estimation of T_1 and hence both S_1 and Ur but not significantly.

In considering Figure J.1, it is shown that the range of validity of the Karmpadakis & Swan (2022) model extends to steeper sea-states than HOE-EANN-B. Moreover, the sea-states employed in the present appendix lay within the proposed range of validity of the Karmpadakis & Swan (2022) model, whilst covering regions in the (S_1, Ur) parameter space that were not used for its calibration. Specifically, sea-states with $k_pd \in [0.65, 1.0]$ and any steepness, as well sea-states in $k_pd < 0.65$ laying within the range of mutual validity of HOE-EANN-B and Karmpadakis & Swan (2022) have not been considered by Karmpadakis & Swan (2022). Hence, it is interesting to see how the Karmpadakis & Swan (2022) model performs in these regions.

J.2 Assessment of the fully nonlinear predictions: Comparison to numerical and field data

J.2.1 Numerical data obtained using HOSM

The numerical data used for assessing Karmpadakis & Swan (2022) refer to the sea-states presented in Tables 4.2 and 4.3. These sea-states are characterised by the highest available steepness of $\frac{1}{2}H_sk_p = 0.105$ and include different spectral bandwidths ($\gamma \in [1, 5]$) and directional spreadings ($\sigma_\theta \in [5, 30]^\circ$). To provide fair comparisons, uni-directional sea-states ($\sigma_\theta = 0$) have been excluded from the present analysis. As the model of Karmpadakis & Swan (2022) has not considered such sea-states.

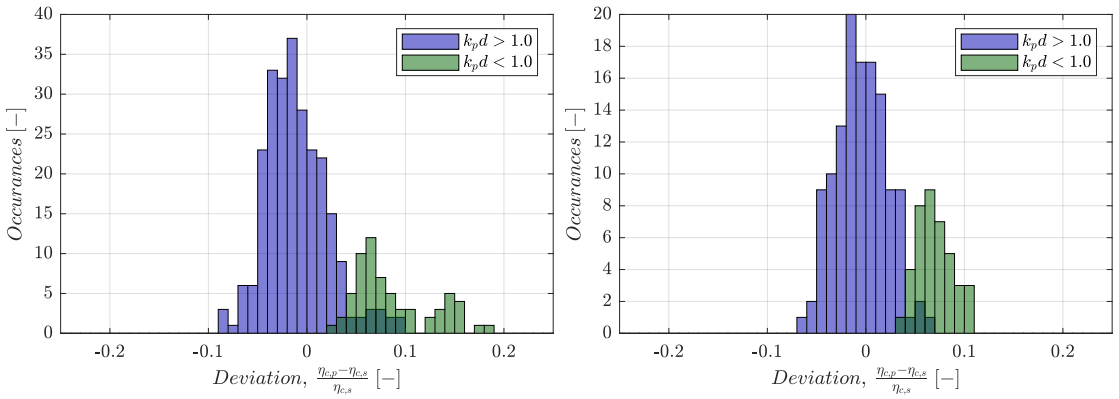
Moreover, to provide a compact assessment of the performance of Karmpadakis

& Swan (2022), the relative deviation, $(\eta_{c,p} - \eta_{c,s})/\eta_{c,s}$, between the the predicted crest height, $\eta_{c,p}$, and the measured crest height, $\eta_{c,s}$ at an exceedance probability of $Q = 10^{-3}$ was computed for all the selected sea-states and all available evolution times at the steady state of the nonlinear evolution. The histogram of the computed relative deviations is presented in Figure J.2(A). In this Figure, the data have been partitioned according to the effective water-depth. Particularly two histograms are presented corresponding to $k_p d < 1.0$ and $k_p d > 1.0$. This partition has been performed based on the fact that the majority of the data used for calibrating the Karmpadakis & Swan (2022) model laid in $k_p d \geq 1.02$. And only a small subset of field data in $k_p d \approx 0.5 - 0.65$ was utilised to extend the applicability of the model in $k_p d < 1.0$, as shown in Figure J.1.

The results in Figure J.2(A) demonstrate that whilst for $k_p d > 1.0$ the deviations are centred around zero, and hence the model is unbiased, this is not the case for $k_p d < 1.0$. In this latter case, Karmpadakis & Swan (2022) systematically over-predicts the crest-heights. This over-prediction stems from the fact that sea-states in $k_p d < 1.0$ were under-represented by Karmpadakis & Swan (2022). This has already been demonstrated in Figure J.1 where only 4 sea-states are shown to lay around $k_p d \approx 0.5 - 0.65$. These latter sea-states are such that wave breaking dominates the tail of the distribution. As such, the effect of nonlinear interactions in $k_p d < 1.0$ is based on extrapolation of the nonlinear correction factors calibrated for sea-states in $k_p d > 1.0$. In performing such extrapolation, the effect of energy defocusing which becomes increasingly important in $k_p d \lesssim 1.0$ (§4.5.5) is not accounted for.

In considering Figure J.2(A) in more detail, it is shown that the spread of deviations even for $k_p d > 1.0$ is higher to those produced by the HOE-EANN model, presented in Figure 5.23(A). This could be because the Karmpadakis & Swan (2022) model does not account for the different directional spreadings and spectral bandwidths. To verify this, Figure J.2(B) presents the histogram of the deviations for sea-states with $\sigma_\theta \geq 10^\circ$ and $\gamma = 2.5$; thereby matching the conditions upon which the model was calibrated.

In contrasting Figure J.2(B) to J.2(A), it is shown that the spread of error is reduced for both $k_p d > 1.0$ and $k_p d < 1.0$. Specifically, the root-mean-square relative deviation in Figure J.2(A) is $\sim 3.5\%$ and $\sim 9.5\%$, for $k_p d > 1.0$ and $k_p d < 1.0$, respectively. Whereas in Figure J.2(B) it is $\sim 2.5\%$ and $\sim 7\%$, respectively. This



(A) (B)

FIGURE J.2: Histogram of relative deviation, $(\eta_{c,p} - \eta_{c,s})/\eta_{c,s}$, between the predicted crest heights by Karmpadakis & Swan (2022) at an exceedance probability level of $Q = 10^{-3}$ and the corresponding crest heights from numerical (HOSM) data. (A) for sea-states of $\sigma_\theta > 0$ and any $\gamma \in [1, 5]$ and (B) for sea-states of $\sigma_\theta > 10°$ and $\gamma = 2.5$. All sea-states refer to $\frac{1}{2}H_s k_p = 0.105$. While the numerical data correspond to steady-state conditions.

suggests that the Karmpadakis & Swan (2022) model could be further improved if it could account for the degree of directionality and γ. However, the systematic over-prediction of the crest heights at $k_pd < 1.0$ is still present in Figure J.2(B) despite the selection of more favourable sea-state conditions.

To illustrate the advancements that the HOE-EANN model offers over Karmpadakis & Swan (2022), Figure J.3 presents the equivalent to Figure J.2 deviations obtained utilising the HOE-EANN model. Similarly to Figure J.2, sub-figure (A) refers to all the available directional sea-states with $\frac{1}{2}H_s k_p = 0.105$. While sub-figure (B) refers to sea-states with $\sigma_\theta \geq 10°$ and $\gamma = 2.5$. The deviations observed in Figures J.3(A) and J.3(B) are of the same magnitude. This suggests that the deviations produced by HOE-EANN are not dependant upon any of the sea-state parameters (k_pd, σ_θ and γ); the observed deviations being merely the result of the sample variability associated to the empirical distribution functions. Moreover, the spread of deviations is much smaller than what was observed in Figure J.2, with the root-mean-square relative deviation being $\sim 1.5\%$ in all cases. This suggests that the HOE-EANN model is more accurate than Karmpadakis & Swan (2022) even for sea-states in $k_pd > 1.0$. This is explained by the inclusion of the effects of spectral bandwidth and directionality within HOE-EANN, as opposed to Karmpadakis & Swan (2022). As well as due to the different formulation of the two models.

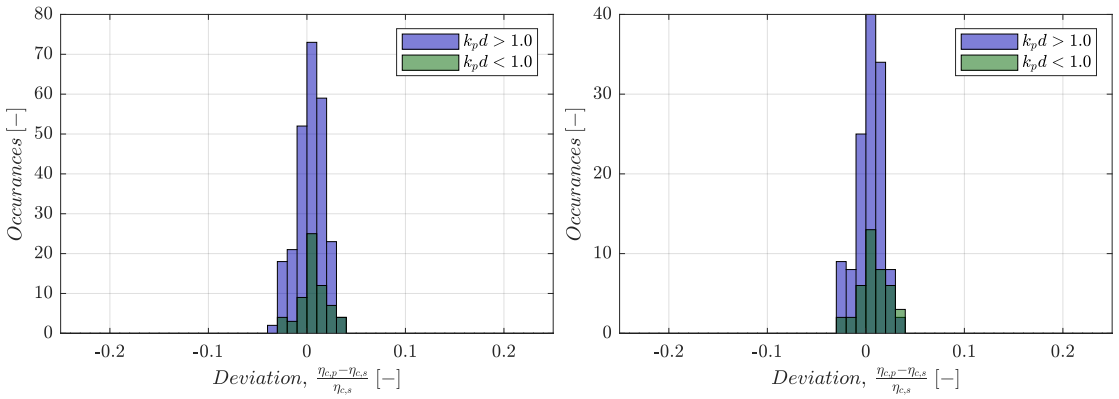


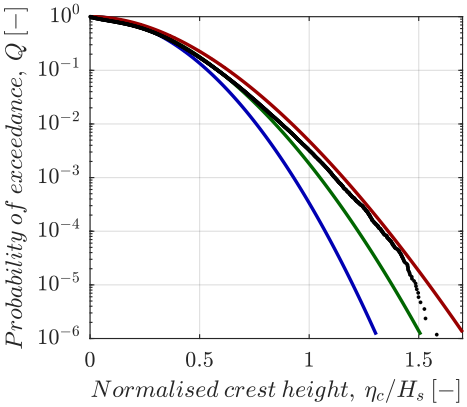
Figure J.3: Histogram of the relative deviations, $(\eta_{c,p} - \eta_{c,s})/\eta_{c,s}$, between the predicted crest-heights by HOE-EANN at an exceedance probability level of $Q = 10^{-3}$ and the corresponding crest heights from numerical (HOSM) data. (A) for sea-states of $\sigma_\theta > 0$ and any $\gamma \in [1, 5]$ and (B) for sea-states of $\sigma_\theta > 10^\circ$ and $\gamma = 2.5$. All sea-states refer to $\frac{1}{2}H_s k_p = 0.105$. While the numerical data correspond to steady-state conditions.

J.2.2 Field data

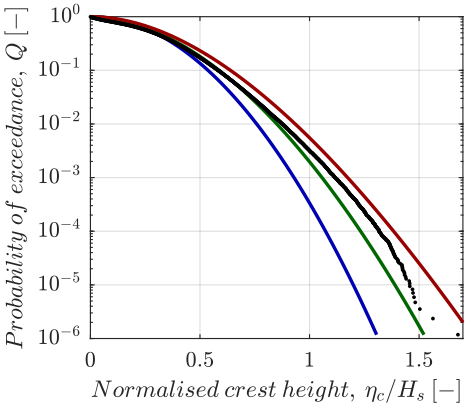
Having gained an insight on the Karmpadakis & Swan (2022) performance in the k_pd range $[0.87, 5.03]$, here additional comparisons to field data are presented. These refer to $k_pd \in [0.48, 0.8]$. As mentioned in §J.1, these sea-states are characterised by $H_s/d \leq 0.20$ for which wave breaking is not expected to be important according to Karmpadakis (2018).

The comparisons between the nonlinear Karmpadakis & Swan (2022) model without incorporating the wave-breaking correction and the field data are presented in Figure J.4. Each sub-figure corresponds to a different sea-state. While the characteristics of each sea-state are provided in the caption of each sub-figure. Moreover, in all plots, the linear (Rayleigh) and second-order (Forristall, 2000) distributions have been added for reference.

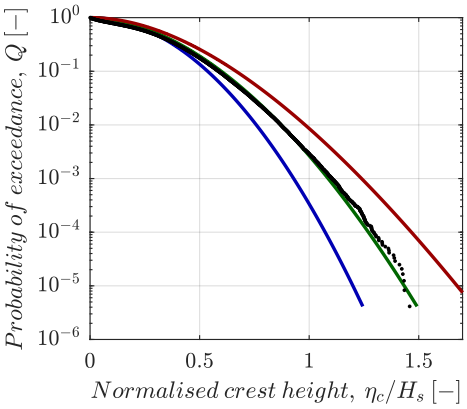
It is again noted that these sea-state conditions belong to a region in the (S_1, Ur) parameter space that has not been considered by Karmpadakis & Swan (2022). Specifically, the employed sea-states correspond to those with $S_1 \in [0, 0.02]$ & $Ur \in [0, 0.5]$ in Figure J.1. Importantly, it was found that for most of these cases (apart from the shallowest of $k_pd = 0.48$), the breaking factor incorrectly increases the crest-heights. This is a non-physical behaviour owing to inadequate performace of the factor for all combinations of S_1 and Ur. Hence, the wave-breaking correction factor within Karmpadakis & Swan (2022) should be revisited to cover sea-states of



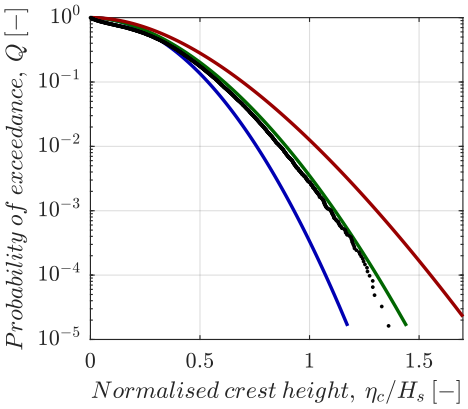
(A) $\frac{1}{2}H_s k_p = 0.08$ $k_p d = 0.8$ $\gamma = 1.5$ $H_s/d = 0.20$



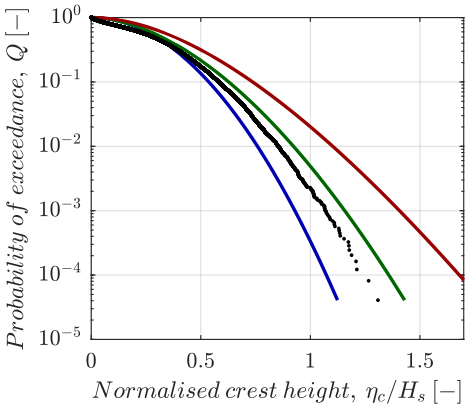
(B) $\frac{1}{2}H_s k_p = 0.06$ $k_p d = 0.7$ $\gamma = 1.6$ $H_s/d = 0.18$



(C) $\frac{1}{2}H_s k_p = 0.055$ $k_p d = 0.6$ $\gamma = 1.6$ $H_s/d = 0.18$



(D) $\frac{1}{2}H_s k_p = 0.05$ $k_p d = 0.53$ $\gamma = 1.3$ $H_s/d = 0.18$



(E) $\frac{1}{2}H_s k_p = 0.04$ $k_p d = 0.48$ $\gamma = 1.4$ $H_s/d = 0.18$

Figure J.4: Comparison of the Karmpadakis & Swan (2022) predictions to crest-height distributions from field data for non-breaking sea-states in $k_p d < 1.0$. The sea-state characteristics are provided in the caption of each sub-figure. The different lines refer to: (———) Rayleigh, (———) directional Forristall (2000), (———) model prediction without breaking factor and (•) field data.

mild severity in low effective water depths.

In considering the comparisons presented in Figure J.4, whilst the observations are shown to lay above the Forristall (2000) predictions in $k_pd = 0.08$, with reduction in k_pd the observed amplifications are diminished. While for $k_pd = 0.48$ the crest-heights lay below Forristall (2000). This behaviour is not captured by Karmpadakis & Swan (2022). In fact, Karmpadakis & Swan (2022) predicts an increase of the amplifications beyond Forristall (2000) with reduction in k_pd. This is in qualitative agreement with the increase of the *bound-wave* contributions with reducing k_pd, as shown in Figure 4.14(A). As such, similarly to §J.2.1, the Karmpadakis & Swan (2022) model is shown to significantly over-predict the observed crest heights in most of the cases. Specifically, whilst for $k_pd = 0.8$ the over-predictions are not very significant, they become increasingly more important with reduction in k_pd. This observation is again explained by the omission of the effect of energy defocusing due to near-resonant interactions that tends to reduce the crest heights. Notably, the HOE-EANN model that accounts for this effect has provided very good comparisons to these field data in Figures 5.32(B) and 5.42.

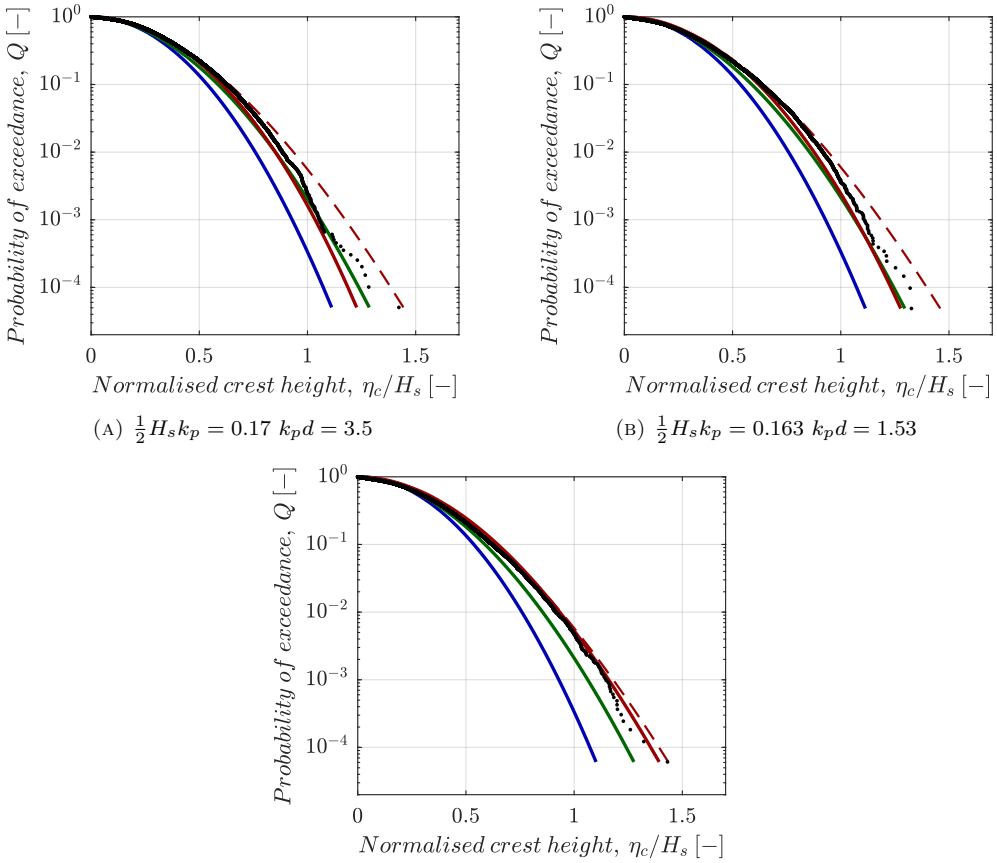
Having assessed the predictions of the nonlinear Karmpadakis & Swan (2022) model for sea-states of mild severity, the following section is devoted to the assessment of the breaking-corrected Karmpadakis & Swan (2022) predictions for more severe sea-state conditions.

J.3 Assessment of the breaking-corrected predictions: Comparison to experimental and field data

As discussed in §J.1 two complementary sources of data were employed to assess the breaking-corrected Karmpadakis & Swan (2022) prediction. These refer to experimental data in $k_pd > 1.0$ and field data in $k_pd < 1.0$. These are the data used for testing the HOE-EANN-B model in §5.4 and they correspond to breaking sea-states. Hence, it is interesting to see how the Karmpadakis & Swan (2022) model performs for the same cases. It is noted that these experimental data were used in calibrating Karmpadakis & Swan (2022), while the field data were not.

Experimental data in $\mathbf{k_p d > 1.0}$

Comparisons between the Karmpadakis & Swan (2022) predictions and the selected experimental data are presented in Figures J.5 and J.6 for $\sigma_\theta = 10°$ and $\sigma_\theta = 20°$, respectively. It is noted that the comparisons include both the breaking-corrected predictions as well as the nonlinear predictions without breaking. Moreover, the sea-state characteristics and the origin of the experimental data are presented in the provided captions. In all plots, the linear (Rayleigh) and second-order (Forristall, 2000) distributions have been added to facilitate the comparisons.



(A) $\frac{1}{2}H_s k_p = 0.17$ $k_p d = 3.5$ (B) $\frac{1}{2}H_s k_p = 0.163$ $k_p d = 1.53$

(C) $\frac{1}{2}H_s k_p = 0.12$ $k_p d = 1.02$

Figure J.5: Comparison of the Karmpadakis & Swan (2022) predictions to experimental crest-height distributions. The sea-state characteristics are defined in each sub-figure's caption. The different lines refer to: (———) Rayleigh, (———) Forristall (2000), (———) model prediction with breaking factor, (– – –) model prediction without breaking factor, (•) experimental data. The data in (A) originate from McCarthy (2018) and the data in (B) to (C) from Karmpadakis et al. (2019a). For all sea-states $\sigma_\theta = 10°$ and $\gamma = 2.5$.

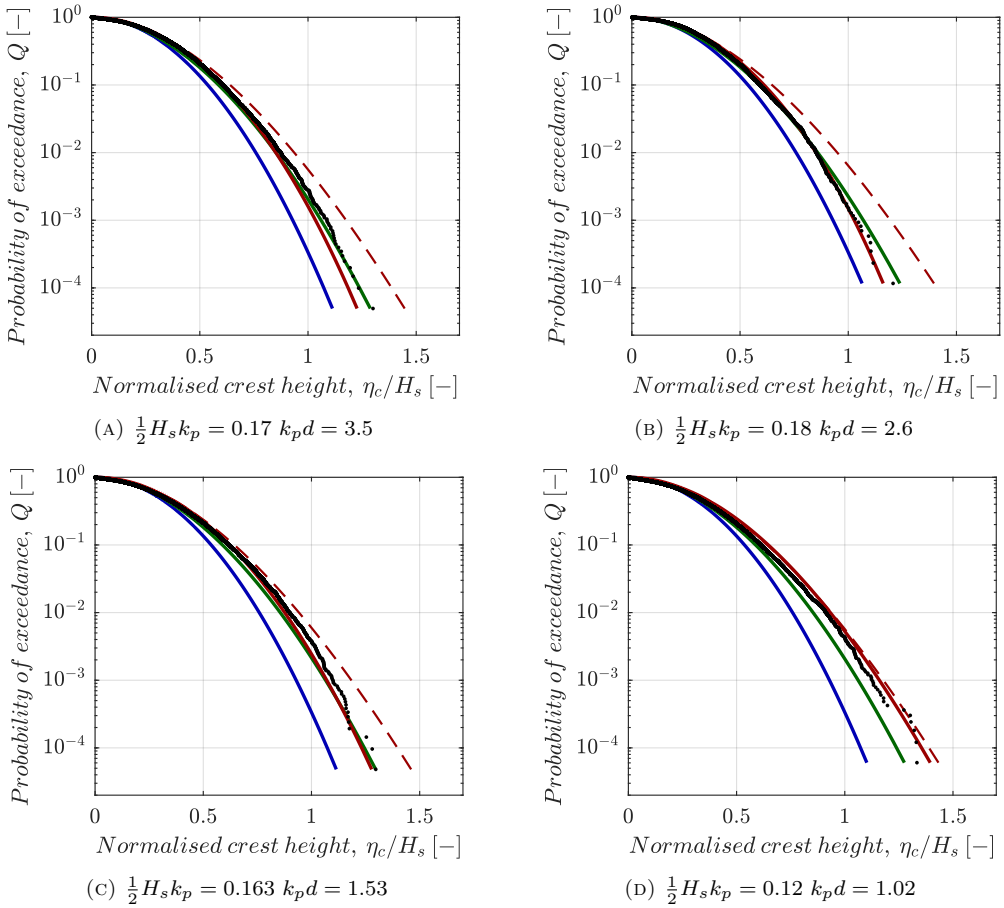


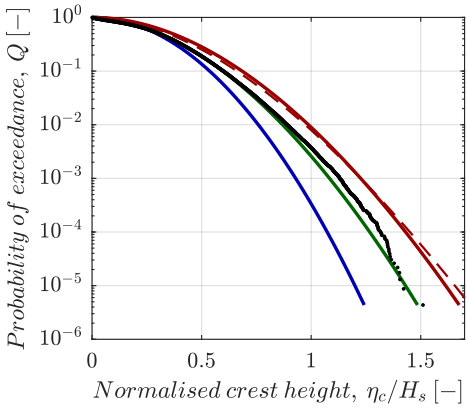
Figure J.6: Same as Figure J.5, but for sea-states with $\sigma_\theta = 20°$ and $\gamma = 2.5$. The data in (A) and (B) originate from McCarthy (2018) and the data in (C) and (D) from Karmpadakis et al. (2019a).

The comparisons in Figures J.5 and J.6 show that the breaking-corrected Karmpadakis & Swan (2022) predictions match very well the experimental data and they outperform those provided by the second-order model of Forristall (2000). However, as noted by Karmpadakis & Swan (2022), the crest-heights are slightly underpredicted in some cases. This is observed in the present comparisons as well, particularly for $k_p d > 1.5$. However, the observed differences are small, and the model is considered valid in general.

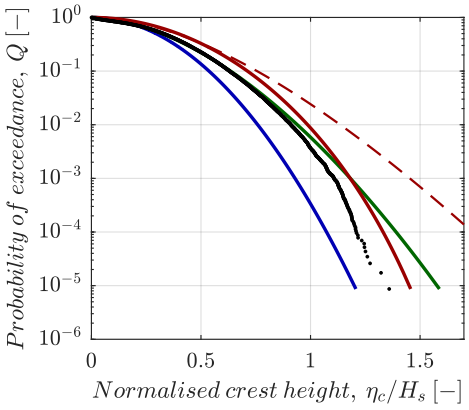
Field data in $\mathbf{k_p d < 1.0}$

Having assessed the performance of the Karmpadakis & Swan (2022) model against experimental data in steep (breaking) sea-states for $k_p d > 1.0$, here, the model is compared to field data corresponding to breaking sea-states for $k_p d < 1.0$. These sea-states refer to the same effective water depths employed in Figure J.4 but the

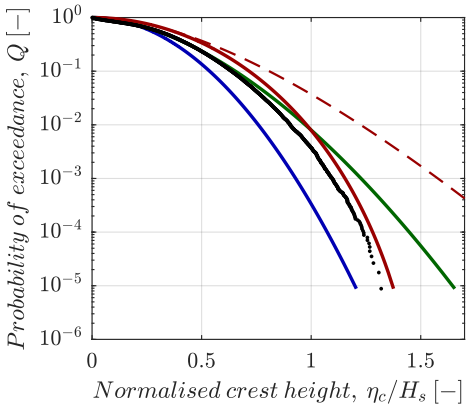
sea-state severity is now higher.



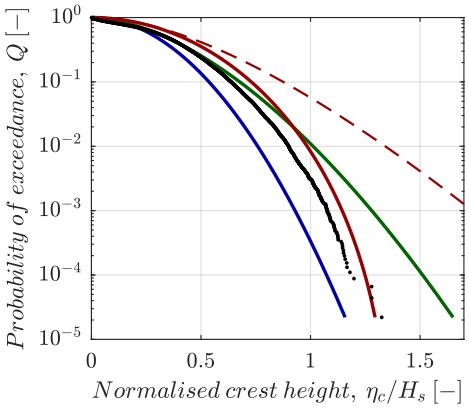
(A) $\frac{1}{2}H_s k_p = 0.10$ $k_p d = 0.8$ $\gamma = 1.7$ $H_s/d = 0.25$



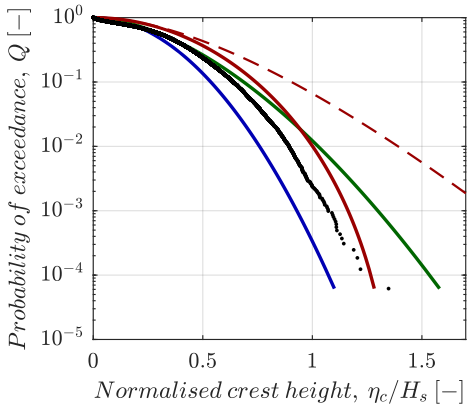
(B) $\frac{1}{2}H_s k_p = 0.11$ $k_p d = 0.7$ $\gamma = 2.0$ $H_s/d = 0.34$



(C) $\frac{1}{2}H_s k_p = 0.10$ $k_p d = 0.6$ $\gamma = 1.9$ $H_s/d = 0.34$



(D) $\frac{1}{2}H_s k_p = 0.09$ $k_p d = 0.53$ $\gamma = 1.7$ $H_s/d = 0.34$



(E) $\frac{1}{2}H_s k_p = 0.08$ $k_p d = 0.48$ $\gamma = 1.4$ $H_s/d = 0.34$

Figure J.7: Comparison of the Karmpadakis & Swan (2022) predictions to crest-height distributions from field data for breaking sea-states in $k_p d < 1.0$. The sea-state characteristics are provided in the caption of each sub-figure. The different lines refer to: (———) Rayleigh, (———) directional Forristall (2000), (———) model prediction with breaking factor, (– – –) model prediction without breaking factor and (•) field data.

Figure J.7 presents comparisons between the Karmpadakis & Swan (2022) model predictions and the additional set of field data; each sub-figure corresponding to a different sea-state. The sea-state parameters are given in the corresponding caption of each sub-figure, and the linear and second-order predictions are again included for reference. It is noted that equivalent comparisons between the HOE-EANN-B model and these data have been presented in Figures 5.38 and 5.42 with excellent agreement being observed between the two.

In considering Figure J.7, it is shown that the Karmpadakis & Swan (2022) model still over-estimates the crest-heights significantly, similarly to Figure J.4. However, this time the over-estimation is somewhat reduced and the predictions appear closer to the observations. This reduction stems from the fact that these sea-states lay closer to those used for calibrating the Karmpadakis & Swan (2022) model, as shown in Figure J.1.

Taken together, the breaking-corrected Karmpadakis & Swan (2022) model predictions are effective in $k_p d > 1.0$. However, they fail to provide satisfactory results in $k_p d < 1.0$ for a wide set of sea-state conditions, obtained by numerical simulations and field measurements.